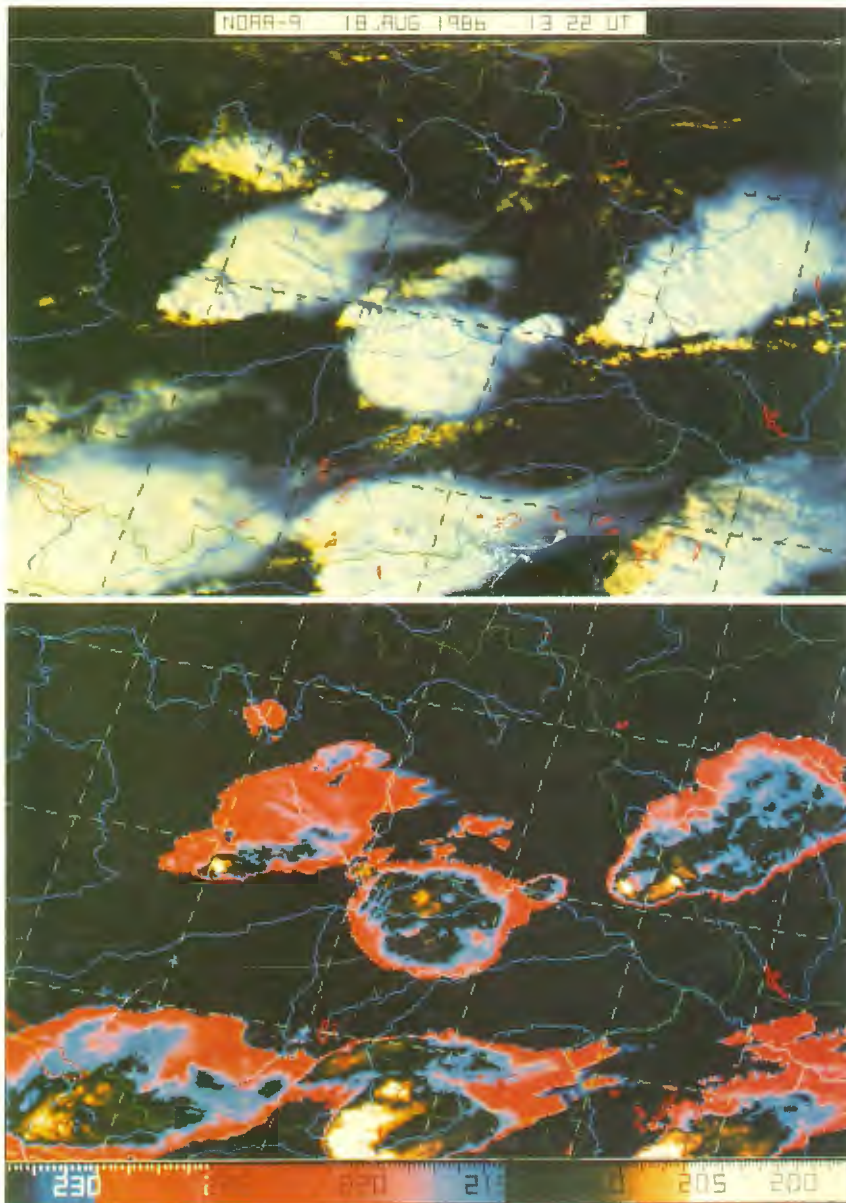


# 10th International Cloud Physics Conference

## Preprints

### Volume I

Bad Homburg v. d. H., F. R. G.  
August 15 – 20, 1988



# **10th International Cloud Physics Conference**

## **Preprints**

### **Volume I**

**Bad Homburg v. d. H., F. R. G.  
August 15 – 20, 1988**

The manuscripts provided as preprints for the 10th International Cloud Physics Conference 1988 are extended abstracts. The authors are responsible for the contents. The reproduction of these summaries does not prevent a subsequent presentation of the lectures and their publication by the authors somewhere else.

#### **Legend to the cover page**

Hailstorms on August 18, 1986, 13 : 22 UT in the lower Alpine region, observed with NOAA-9 satellite, visible and infrared channel. The northwesterly storm is located near Augsburg. Later in the afternoon hail was reported in this area on the ground. The cloud top temperature estimated from the IR channel is in accordance with the radar-observed top (see cover picture Volume 2) and the temperature profile of this day. The satellite data processing has been performed by the Applied Data Technology Division of DFVLR, Oberpfaffenhofen.

---

Editor and publishing house:  
Deutscher Wetterdienst  
Frankfurter Straße 135  
D-6050 Offenbach am Main  
Federal Republic of Germany

---

These proceedings are also published in the series „Annalen der Meteorologie” as No. 25. ISBN 3-88148-240-7.

---

Copy dead line: May 10, 1988

## **International Sponsors**

International Association of Meteorology and Atmospheric Physics (IAMAP)

International Commission on Cloud Physics (ICCP)

USAF European Office of Aerospace Research and Development, London

US Army Research Office, London

## **Sponsors in the Federal Republic of Germany**

Ministry for Research and Technology (BMFT)

German Weather Service (DWD)

German Meteorological Society (DMG)

German Aerospace Research Establishment (DFVLR)

The City of Bad Homburg

## **International Program Committee**

Prof. Dr. P. V. Hobbs (USA),  
(Chairman)

Dr. A. A. Chernikov (USSR)

Dr. A. J. Heymsfield (USA)

Dr. P. Jonas (UK)

Prof. Dr. Z. Levin (Israel)

Prof. Dr. R. List (Canada)

Prof. Dr. H. D. Orville (USA)

Prof. Dr. H. R. Pruppacher (FRG)

Prof. Dr. R. G. Soulage (France)

Dr. T. Takeda (Japan)

Prof. Dr. B. Zhao (PRC)

## **National Organizing Committee**

Prof. Dr. H. R. Pruppacher (Chairman)

Prof. Dr. H. W. Georgii

Prof. Dr. H. Grassl

Prof. Dr. F. Herbert

Prof. Dr. E. Raschke

Dr. H. Reiser

Prof. Dr. U. Schumann



TABLE OF CONTENTS	Page
Author Index .....	XXIV
Preface.....	1

### SESSION 1: CLOUD MICROPHYSICS I: LABORATORY STUDIES

THE EFFECT OF CHARGE ON THE COALESCENCE OF SMALL PRECIPITATION DROPS AT TERMINAL VELOCITY .....	4
<i>H. T. Ochs III, R. R. Czys and J. Q. Feng, Illinois State Water Survey, Champaign, IL, USA</i>	
WAKE-EXITED RAINDROP OSCILLATIONS .....	7
<i>K. V. Beard and H. T. Ochs, Illinois State Water Survey, Champaign, IL, USA</i>	
TEMPORAL VARIATIONS OF SNOW CRYSTAL GROWTH PARAMETERS. ....	9
<i>T. Takahashi*, N. Fukuta**, T. Endoh* and G. Wakabama*, *The Institute of Low Temperature Science, Hokkaido University, Sapporo, JAPAN, **University of Utah, Salt Lake City, UT, USA</i>	
EMPIRICAL EQUATIONS OF ICE CRYSTAL GROWTH MICROPHYSICS FOR MODELLING AND ANALYSIS.....	12
<i>C. R. Redder and N. Fukuta, University of Utah, Salt Lake City, UT, USA</i>	
THE CONTRAST STUDY OF NEW MODEL ON ICE CRYSTAL GROWTH. ....	15
<i>A.-S. Wang, Institute of Atmospheric Physics, Academia Sinica, Beijing, PRC</i>	
A WIND TUNNEL STUDY ON THE MELTING OF SNOW FLAKES. ....	18
<i>S. K. Mitra, O. Vohl, H. R. Pruppacher, Johannes Gutenberg-Universität, Mainz, FRG</i>	
EVAPORATION AND MELTING OF ICE CRYSTALS: A LABORATORY STUDY.....	22
<i>R. G. Oraltay and J. Hallett, Desert Research Institute, Reno, NV, USA</i>	
A NEW MECHANISM FOR ICE INITIATION IN WARM-BASED MIDWESTERN CUMULI.....	25
<i>R. R. Czys, Illinois State Water Survey, Champaign, IL, USA</i>	
SPREADING OF SUPERCOOLED WATER DROPLETS ON AN ICE SURFACE.....	28
<i>Y. Dong and J. Hallett, Desert Research Institute, Reno, NV, USA</i>	
A MODEL OF THE ELECTROSTATIC-AERODYNAMIC SHAPE OF RAINDROPS.....	31
<i>C. Chuang and K. V. Beard, University of Illinois, Urbana, IL, USA</i>	

### SESSION 2: CLOUD MICROPHYSICS II: FIELD MEASUREMENTS AND THEORY

MEASUREMENTS OF THE PARTITIONING OF AEROSOL MASS AND NUMBER BETWEEN CLOUD DROPLETS AND INTERSTITIAL AIR.....	34
<i>J. Ogren, J. Heintzenberg and K. Noone, University of Stockholm, Stockholm, SWEDEN</i>	
THE CALCULATION OF SUPERSATURATIONS AND GROWTH OF DROPLETS IN CONTINENTAL CUMULUS CLOUDS.....	37
<i>K. N. Bower and T. W. Chouartton, UMIST, Manchester, UK</i>	
ON THE OBSERVATIONS OF CLOUD TEMPERATURE AND LIQUID WATER CONTENT USING A LYMAN- $\alpha$ AND AN FSSP SENSOR. ....	40
<i>J. B. Jensen and D. Baumgartner, NCAR, Boulder, CO, USA and G. B. Raga, University of Washington, Seattle, WA, USA</i>	
EVALUATION OF DROPLET GROWTH RATES IN HAWAIIAN OROGRAPHIC CLOUDS. ....	43
<i>D. Baumgartner, NCAR, Boulder, CO, USA</i>	

STUDIES OF WARM-RAIN DEVELOPMENT.....	46
<i>W. A. Cooper, NCAR, Boulder, CO, USA</i>	
RADAR OBSERVATIONS AND MODELLING OF WARM RAIN INITIATION. ....	49
<i>A. J. Illingworth and I. J. Caylor, UMIST, Manchester, UK</i>	
A TEST OF ICE CRYSTAL PRODUCTION BY AIRCRAFT.....	52
<i>G. Vali, R. D. Kelly and F. Serrano, University of Wyoming, Laramie, WY, USA</i>	
AIRBORNE STUDIES OF THE ICE PHASE IN MARITIME CLOUDS AROUND THE BRITISH ISLES.....	55
<i>P. R. A. Brown, Meteorological Office, Bracknell, Berkshire, UK and T. W. Choullarton, UMIST, UK</i>	
PRECIPITATION INITIATION MECHANISMS IN CLOUDS OVER NORTH INDIA.....	58
<i>R. N. Chatterjee, P. Prakash, G. Singh and R. K. Kapoor, Indian Institute of Tropical Meteorology, Pune, INDIA</i>	
EVIDENCE OF PREFERENTIAL ZONES OF ICE MULTIPLICATION BY SPLINTERING IN CONVECTIVE CELLS. ....	62
<i>J.-F. Gayet, C. Duroure and R. G. Soulage, LAMP, Aubière, FRANCE</i>	
MICROPHYSICAL CHARACTERISTICS OF WARM-BASED CUMULI: OBSERVATIONS AT $-10^{\circ}$ C.....	64
<i>R. R. Cyzs, Illinois State Water Survey, Champaign, IL, USA</i>	

### SESSION 3: CLOUD MICROPHYSICS III. ENTRAINMENT AND MIXING

A COMPARATIVE STUDY OF LABORATORY THERMALS AND ATMOSPHERIC CLOUDS. ....	67
<i>H. Johari*, G. Taylor**, M. Baker** and R. Breidenthal*, *Dept. of Aeronautics and Astronautics, **Geophysics Program, University of Washington, Seattle, USA</i>	
ENTRAINMENT AND FINE-SCALE (MOLECULAR) MIXING.....	70
<i>I. R. Paluch and D. G. Baumgardner, NCAR, CO, USA</i>	
AIRBORNE STUDIES OF THE INFLUENCE OF ENTRAINMENT ON THE VERTICAL AND HORIZONTAL MICROPHYSICAL STRUCTURE OF SMALL CUMULUS CLOUDS. ....	73
<i>J. Latham, UMIST, Manchester, UK, and A. M. Blyth, New Mexico Institute of Mining &amp; Technology, Socorro, NM, USA</i>	
ENTRAINMENT SITES, MIXING PROCESSES IN WARM CONVECTIVE CLOUDS. EFFECT ON DROPLET GROWTH. ....	76
<i>E. Hicks, A. Rigaud, J. Gagneux, C. Pontikis, Météorologie Nationale EERM/CRPA, Magny les Hameaux, FRANCE</i>	
STRUCTURE OF UPPER CLOUDS BOUNDARY USING THE LIDAR DATA. ....	79
<i>V. E. Zuev, V. S. Shamanaev, I. E. Penner and I. V. Samokhvalov, Institute of Atmospheric Optics, Siberian Branch USSR Academy of Sciences, Tomsk, USSR</i>	
TURBULENT TRANSPORT PROCESSES WITHIN AND BELOW SMALL CUMULUS CLOUDS. ....	82
<i>A. M. Jochum, Institut für Physik der Atmosphäre, DFVLR, Oberpfaffenhofen, FRG</i>	
INSTABILITY THEORY IN CLOUDS AND THE PARAMETRIZATION OF EDDY VISCOSITY COEFFICIENTS. ....	85
<i>Y. Takaya, Meteorological Research Institute, Tsukuba, JAPAN</i>	
THREE DIMENSIONAL CUMULUS ENTRAINMENT STUDIES.....	88
<i>T. L. Clark, P. K. Smolarkiewicz and W. D. Hall, NCAR, Boulder, CO, USA</i>	
HETEROGENEOUS MIXING MEASUREMENTS IN SMALL NON PRECIPITATING CUMULI. ....	91
<i>J. L. Brenguier, Direction de la Météorologie Nationale EERM/CNRM, Toulouse Cedex, FRANCE</i>	

## SESSION 4: CLOUD MICROPHYSICS IV: NUMERICAL MODELING

THE CASE FOR SUBGRID-SCALE CONDENSATION IN NUMERICAL CLOUD MODELS.....	94
<i>F. B. Lipps and R. S. Hemler, Princeton University, Princeton, NJ, USA</i>	
THE EFFECT OF TURBULENCE ON THE COLLECTION OF CLOUD DROPS: A STOCHASTIC MODEL.....	97
<i>G. W. Reuter, McGill University, Montreal, CANADA</i>	
THE EFFECT OF ICE PHYSICAL PROCESSES ON THE NUMERICAL SIMULATION OF WEST AFRICAN SQUALL LINES.....	100
<i>W. D. Hall, NCAR, Boulder, CO, USA, and J. P. Lafore, CNRM, Toulouse, FRANCE</i>	
NUMERICAL SIMULATION OF MICROPHYSICAL PROCESSES IN CUMULONIMBUS.....	103
<i>Z. Hu and G. He, Academy of Meteorological Sciences, Beijing, PRC</i>	
A COMPARATIVE STUDY OF TWO MICROPHYSICAL SCHEMES IN A $\beta$ MESOSCALE MODEL.....	106
<i>E. Richard and N. Chaumerliac, LAMP, OPGC, Clermont-Ferrand, FRANCE</i>	
GENERALIZED MICROPHYSICS SCHEME FOR USE IN MESOSCALE/CLOUD MODELS. ....	109
<i>G. J. Tripoli, University of Wisconsin, Madison, WI, USA, and P. J. Flatau and W. R. Cotton, Colorado State University, Fort Collins, CO, USA</i>	
THE STUDY OF NUMERICAL SIMULATION ON THE FORMATION OF THE CLOUD DROPLET SPECTRA IN CUMULUS CLOUDS.....	112
<i>H. Xiao, H. XU, and M. Huang, Institute of Atmospheric Physics, Academia Sinica, Beijing, PRC</i>	

## SESSION 5: CLOUDS AND RADIATION

SOME OUTSTANDING PROBLEMS ON THE INFLUENCE OF CLOUDS ON RADIATION.....	115
<i>G. L. Stephens, Colorado State University, Fort Collins, CO, USA</i>	
THEORY ON THE UNCERTAINTY IN CLOUD MICROPHYSICAL PROCESSES AND CLIMATE. ....	118
<i>K. N. Liou and S. C. Ou, University of Utah, Salt Lake City, UT, USA</i>	
IN SITU MEASUREMENTS OF "SHIP TRACKS". ....	121
<i>L. F. Radke, J. H. Lyons and P. V. Hobbs, University of Washington, Seattle, USA, and J. E. Coakley, NCAR, Boulder, CO, USA</i>	
RADIATION INDUCES GROWTH AND EVAPORATION OF DROPLETS IN BOUNDARY LAYER CLOUDS. ....	124
<i>R. Davies, McGill University, Montreal, Quebec, CANADA</i>	
CLOUD AND AEROSOL OPTICAL DEPTHS: PRELIMINARY RESULTS FROM FIFE. ....	125
<i>R. F. Pueschel*, P. B. Russell*, T. P. Ackerman**, D. S. Colburn*, R. C. Wrigley*, M. A. Spanner***, and J. M. Livingston****;</i> <i>*NASA, Ames Research Center, Moffett Field, CA, USA,</i> <i>**Pennsylvania State University, PA, USA,</i> <i>***TGS Technology, Moffett Field, CA, USA,</i> <i>****SRI International, Menlo Park, CA, USA</i>	
AN OBSERVATIONAL STUDY OF RADIATIVELY DRIVEN CONVECTION.....	127
<i>S. Nicholls, Meteorological Office, Bracknell, Berkshire, UK</i>	
RADIATIVE INFLUENCES ON PRECIPITATING MESOSCALE SYSTEMS. ....	130
<i>W. R. Cotton and S. Chen, Colorado State University, Fort Collins, CO, USA, and G. Tripoli, University of Wisconsin, Madison, WI, USA</i>	

CIRRUS MICROPHYSICS AND INFRARED RADIATIVE TRANSFER: A CASE STUDY. ....	133
<i>T. P. Ackerman*</i> , <i>A. J. Heymsfield**</i> , <i>F. P. J. Valero***</i> and <i>St. Kinne***</i>	
<i>*Dept. of Meteorology, Pennsylvania State University, PA, USA</i>	
<i>**NCAR, Boulder, CO, USA,</i>	
<i>***NASA, Ames Research Center, Space Science Division Moffett, CA, USA</i>	

#### POSTER SESSION A: CLOUD MICROPHYSICS AND CHEMISTRY

THE COLLECTION EFFICIENCY OF A MASSIVE FOG COLLECTOR. ....	135
<i>R. S. Schemenauer and P. I. Joe, Atmospheric Environment Service, Downsview, Ontario, CANADA</i>	
THE USE OF AUTOMATIC PARTICLE RECOGNITION TO IMPROVE THE DETERMINATION OF BULK QUANTITIES FROM PMS 2-D PROBE DATA IN CIRRUS. ....	138
<i>A. G. Darlison and P. R. A. Brown, Meteorological Office, Bracknell, Berkshire, UK</i>	
THE COMPARISON OF HOLOGRAPHIC AND 2-D PROBE MEASUREMENTS OF ICE CRYSTALS. ....	141
<i>P. R. A. Brown and A. G. Darlison, Meteorological Office, Bracknell, Berkshire, UK</i>	
DEVELOPMENT OF HYDROMETEOR VIDEO SONDE. ....	144
<i>M. Murakami and T. Matsuo, Meteorological Research Institute, Tsukuba, JAPAN</i>	
THE STUDY OF THE INTERSTITIAL AEROSOL PARTICLES AND CLOUD DROPLETS WITH DIGITAL IMAGE ANALYSIS OF DIFFRACTION IMAGES. ....	148
<i>R. Jaenicke and R. Sørensen, University of Mainz, Mainz, FRG</i>	
ON THE DETERMINATION OF DROPLET SIZE DISTRIBUTIONS WITH THE CONTERFLOW VIRTUAL IMPACTOR. ....	151
<i>B. Johansson and J. Heintzenberg, University of Stockholm, Stockholm, SWEDEN</i>	
MULTIPARAMETER CHARACTERIZATION OF RAINDROP SIZE DISTRIBUTION BY THE POLARIMETRIC DFVLR RADAR: FIRST RESULTS. ....	154
<i>M. Chandra, A. Schroth and E. Lüneburg, DFVLR, Institut für HF-Technik, Weßling, FRG</i>	
AN INVESTIGATION OF THE EFFECT OF ELECTRICAL CHARGES ON THE COLLISION EFFICIENCY OF CLOUD DROPS. ....	158
<i>V. M. Kim, Institute of Experimental Meteorology, Obninsk, USSR</i>	
MICROPHYSICAL AND ELECTRICAL PHENOMENA DURING FREEZING OF WATER DROPS. ....	161
<i>A. Kh. Adzhiev and S. T. Tomazov, High Mountain Geophysical Institute, Nalchik, USSR</i>	
A DESCRIPTION OF CONDENSATION PROCESSES IN A TURBULENT THREE-PHASE CLOUD. ....	164
<i>L. N. Novosyolov and A. S. Stepanov, Institute of Experimental Meteorology, Obninsk, USSR</i>	
EFFECT OF THE ELECTRIC FIELD ON THE RAINDROP SHAPE. ....	166
<i>G. G. Magradze, Academy of Sciences of the Georgian SSR, Tbilisi, USSR</i>	
DAMPED OSCILLATION REPRESENTATION OF DROP-SPECTRUM EVOLUTION DUE TO COALESCENCE AND BREAKUP. ....	169
<i>P. S. Brown, Trinity College, Hartford, CT, USA</i>	
KINETIC EQUATION FOR POLLUTED CLOUD DROPLET SPECTRUM. ....	172
<i>I. M. Erukashvily, Israel Meteorological Service, Bet-Dagan, ISRAEL</i>	
LIQUID WATER CONTENT, MEDIAN VOLUME DIAMETER, AND TEMPERATURE IN DEPENDENCE ON THE HEIGHT ABOVE THE CLOUD BASE FOR DIFFERENT TYPES OF CLOUDS. ....	175
<i>H.-E. Hoffmann and R. Roth, DFVLR-Oberpfaffenhofen, Institut Physik der Atmosphäre, Weßling, FRG</i>	

A DETAILED EXAMINATION OF DISCONTINUITIES IN NATURAL RAIN SPECTRA .....	178
<i>H. C. Vaughan, Iowa State University, Ames, IA, USA</i>	
CRYSTALLIZATION OF SUPERCOOLED SOLUTIONS.....	180
<i>K. Harrison and J. Hallett, Desert Research Institute, Reno, NV, USA</i>	
KINETICS OF ICE CRYSTAL FORMATION ON AEROSOL PARTICLES IN SUPERCOOLED FOG.....	183
<i>B. Z. Gorbunov, A. E. Paschenko and H. Kakutkina, Institute of Chem. Kinetics and Combustion, Novosibirsk, USSR</i>	
ABOUT SECONDARY ICE CRYSTAL PRODUCTION.....	185
<i>T. G. Gzirisvili and V. G. Khorguany, Academy of Sciences of the Georgian SSR, Tbilisi, USSR</i>	
EXPERIMENTAL STUDIES ON SECONDARY ICE PARTICLE PRODUCTION. ..	188
<i>A. Yamashita, H. Konishi, W. Shimada, M. Miyatake and K. Tani, Osaka Kyoiku University, Osaka, JAPAN</i>	
PROPORTION OF RIMING GROWTH PROCESS IN SNOWFALL PHENOMENA.....	190
<i>T. Harimaya and M. Sato, Hokkaido University, Sapporo, JAPAN</i>	
THREE-DIMENSIONAL STRUCTURES OF SNOW CRYSTALS SHOWN BY STEREO-PHOTOMICROGRAPHS. ....	193
<i>K. Iwai, Shinshu University, Nagano, JAPAN</i>	
ON THE VARIATION OF FALLING VELOCITY OF EARLY SNOWFLAKES.....	196
<i>M. Kajikawa, Akita University, Akita, JAPAN</i>	
A PARAMETERIZATION SCHEME FOR THE COALESCENCE OF WATER DROPS USING THE STOCHASTIC COLLECTION EQUATION. ....	199
<i>C. Lüpkes, K. D. Beheng and G. Doms, Johann Wolfgang Goethe-Universität, Frankfurt am Main, FRG</i>	
ON THE DYNAMICS OF THE FALLING ICE CRYSTAL ZONE. ....	202
<i>J. Podzimek, University of Missouri, Rolla, MO, USA</i>	
A NEW DATABASE OF ICE PARTICLE SIZE SPECTRA FOR ALTITUDES UP TO 10 KM, (30,000 FT).....	205
<i>R. K. Jeck, Naval Research Laboratory, Washington, DC, USA</i>	
A VERTICAL WIND TUNNEL FOR THE STUDY OF SNOWFLAKES AND EFFECTS OF ACCUMULATED SNOW ON MATERIALS.....	208
<i>K. Isono, Nagoya University, Tokyo, JAPAN; J. Kobayashi, Japan Weather Association, Tokyo, JAPAN; T. Gonda, Science University of Tokyo, Chiba, JAPAN; Y. Sasyo, and T. Mori, Suga Test Instruments Co. Ltd., JAPAN</i>	
PROPERTIES OF THE PRECIPITATION EMBRYOS EVOLUTION IN CHARACTERISTIC HAWAIIAN BANDCLOUDS.....	211
<i>A. Rigaud, E. Hicks, J. Gagneux and C. Pontikis, Direction Météorologique Nationale EERM/CRPA, Magny les Hameaux, FRANCE</i>	
PATTERN OF AIR BUBBLE INCLUSIONS IN ATMOSPHERIC ICE FORMED DURING ACCRETION GROWTH.....	214
<i>P. Gribelin, P. Personne and H. Isaka, LAMP, Aubière, FRANCE</i>	
ANALYSIS OF HAILSTONES FROM A SEVERE STORM AND THEIR SIMULATED EVOLUTION.....	217
<i>L. Levi, Consejo Nacional de Investigaciones Científicas y Técnicas, ARGENTINA, and L. Lubart, Servicio Meteorológico Nacional, Buenos Aires, ARGENTINA</i>	
THE COLLECTION EFFICIENCIES OF SOFT-HAILSTONES FOR SUPER-COOLED WATER DROPLETS AND ICE CRYSTALS.....	220
<i>W. D. Keith and C. P. R. Saunders, UMIST, Manchester, UK</i>	

SIMULATION OF CONICAL GRAUPEL BY USING A BALLISTIC MODEL. ....	223
<i>P. Personne, Chr. Duroure and H. Isaka, LAMP, Aubière, FRANCE</i>	
COMPARISON OF MODEL RESULTS FOR MODELS OF DIFFERING MICROPHYSICAL DETAIL.....	226
<i>R. D. Farley and H. D. Orville, South Dakota School of Mines and Technology, Rapid City, SD, USA</i>	
AIRBORNE "CLOUD SIEVING".....	229
<i>E. E. Hindman, Physics and Atmospheric Science Department, Drexel University, PA, USA</i>	
CLOUD CAPTURE BY A MOUNTAIN TOP FOREST: ACIDITY AND DOSAGE DURATION. ....	232
<i>V. K. Saxena and N.-H. Lin, North Carolina State University, Raleigh, NC, USA</i>	
DETERMINATION OF CHEMICAL REACTION RATES IN FOG. ....	235
<i>R. Dlugi and W. Seidl, Meteorologisches Institut der Universität München, Munich, FRG</i>	
INSOLUBLE PARTICLES IN HYDROMETEORS. ....	238
<i>M. Krämer and L. Schütz, University of Mainz, FRG</i>	
BELOW CLOUD SCAVENGING BY RAIN AND DRIZZLE. ....	241
<i>B. T. McGann and S. G. Jennings, University College, Galway, IRELAND</i>	
STUDIES OF CLOUD MICRO-CHEMICAL PHYSICS. ....	243
<i>R. L. Pitter and W. G. Finnegan, Desert Research Institute, Reno, NV, USA</i>	
KINETICS AND MECHANISM OF THE Fe-CATALYZED AUTO-OXIDATION OF S(IV)-OXIDES IN AQUEOUS SOLUTION. ....	246
<i>J. Kraft, M. Dellert, P. Braun and R. Van Eldik, University of Witten/Herdecke, FRG</i>	
THE EFFECT OF AEROSOLS ON THE pH OF SNOWFALLS.....	249
<i>M. Kumai, U.S. Army Cold Regions Research and Engineering Laboratory, Hannover, NH, USA</i>	
IONIC CONCENTRATIONS OF RIME ICE AND SNOW AND BERGERON PROCESS. ....	251
<i>S. H. Huang, Nanjing University, Nanjing, PRC, R. A. Castillo, Western Connecticut State University, Danbury, CT, USA, and V. A. Monhen, ASCR, SUNY, NY, USA</i>	
CHEMICAL NATURE OF PRECIPITATION AT VISAKHAPATNAM. ....	254
<i>S. Nizamuddin, Andhra University, Waltair, INDIA</i>	
A ONE-DIMENSIONAL NUMERICAL MODEL TO SIMULATE LIQUID PHASE CHEMICAL REACTIONS WITHIN RADIATION FOG. ....	255
<i>R. Forkel and W. Seidl, Meteorologisches Institut der Universität München, Munich, FRG</i>	

**SESSION 6: CLOUD CHEMISTRY AND ACIDIC PRECIPITATION  
I: MEASUREMENTS**

THE EFFECT OF FREEZING ON THE COMPOSITION OF CLOUD DROPLETS. ....	258
<i>J. V. Iribarne and T. Pyshtov, University of Toronto, Toronto, Ontario, CANADA</i>	
SOME EFFECTS OF CLOUD MICROPHYSICS ON CLOUD CHEMISTRY.....	261
<i>D. A. Hegg and P. V. Hobbs, University of Washington, Seattle, WA, USA</i>	
PROCESSES DETERMINING CLOUDWATER COMPOSITION: FIELD EVIDENCE FOR INCLOUD REACTIVE SCAVENGING OF SO <sub>2</sub> .....	264
<i>P. H. Daum, Brookhaven National Laboratory, Upton, NY, USA</i>	
ACIDIFICATION OF STRATIFORM CLOUDS AND THEIR AEROSOL SCAVENGING PROPERTIES. ....	267
<i>R. A. Castillo, Western Connecticut State University, Danbury, CT, USA, and J. Deluisi, NOAA, Boulder, CO, USA</i>	

MICROPHYSICAL, DYNAMICAL AND CHEMICAL ASPECTS OF SCAVENGING PROCESSES DURING WINTER PRECIPITATION. ....	270
<i>A. Waldvogel, T. Schumann and B. Zinder, Atmospheric Physics ETH, Zürich, SWITZERLAND</i>	
VERTICAL PROFILES OF POLLUTANTS INSIDE AND OUTSIDE OF CLOUD. ..	273
<i>G. A. Isaac and W. R. Leitch, Atmospheric Environment Service, Downsview, Ontario, CANADA</i>	
RESULTS OF TIME AND HEIGHT RESOLVED SCAVENGING EXPERIMENTS. ....	276
<i>L. Kins, Universität München, Munich, FRG, and F. X. Meixner, Fraunhofer Institut für Atmosph., Garmisch-Partenkirchen, FRG, and K. P. Müller, Kernforschungsanlage Jülich, Institut für Atmosph. Chemie, Jülich, FRG</i>	
OXIDATION REGIMES IN OROGRAPHIC CAPPING CLOUD.....	279
<i>P. A. Clark, G. P. Gervat, T. A. Hill, and A. R. W. Marsh, Central Electricity Research Laboratories, Leatherhead, Surrey, UK, and A. S. Chandler, T. W. Choularton, and M. J. Gay, UMIST, Manchester, UK</i>	
AN EXAMINATION OF THE CHEMICAL AND PHYSICAL VARIABILITY OF CLOUDS AT A MOUNTAIN-TOP SITE IN CENTRAL SWEDEN. ....	282
<i>K. J. Noone, J. A. Ogren and J. Heintzenberg, Stockholm University, Stockholm, SWEDEN</i>	
INFLUENCES OF CLOUD MICROPHYSIC ON CONTINENTAL AND MARINE PRECIPITATION CHEMISTRY. ....	285
<i>F. Parungo and C. Nagamoto, NOAA/ERL, Boulder, CO, USA</i>	
CONCENTRATIONS IN RAIN EVENTS COLLECTED SEQUENTIALLY: MEASUREMENTS VERSUS RESULTS OF A SIMPLE SCAVENGING MODEL.....	288
<i>J.-L. Jaffrezo and J.-L. Colin, Université Paris, Paris Cedex, FRANCE</i>	
EXPERIMENTS ON MICROPHYSICS AND CHEMISTRY OF RADIATION FOGS.....	291
<i>K. H. Enderle, H. Oberland, and W. Jaeschke, Johann Wolfgang-Goethe Universität, Frankfurt am Main, FRG</i>	

## SESSION 7: CLOUD CHEMISTRY AND ACIDIC PRECIPITATION II: NUMERICAL MODELING

CHEMICAL EVOLUTION WITHIN A CLOUD MODEL FEATURING A POLYDISPERSE DROPLET SIZE SPECTRUM. ....	294
<i>T. A. Hill, UMIST, Manchester, UK</i>	
MODELING STUDIES ON THE FORMATION, GROWTH, DISSIPATION, AND ACIDIFICATION OF CUMULUS CLOUDS. ....	297
<i>S. K. Nair and L. K. Peters, University of Kentucky, Lexington, KY, USA</i>	
A NUMERICAL INVESTIGATION OF SULFATE PRODUCTION AND DEPOSITION IN MIDLATITUDE CONTINENTAL CUMULUS CLOUDS.....	300
<i>G. Taylor, University of Washington, Seattle, WA, USA</i>	
A NUMERICAL SIMULATION OF THE ACIDIFICATION PROCESS OF RAIN WATER BELOW THE CLOUD AND THE MECHANISM OF ACID RAIN FORMATION IN AREA OF CHONGQING.....	303
<i>M. Huang and S. Liu, Institute of Atmospheric Physics, Academia Sinica, Beijing, PRC</i>	
EFFECTS OF CLOUD MICROPHYSICAL PROCESSES ON TRACE CHEMICAL REMOVAL EFFICIENCIES. ....	306
<i>D. Lamb and J. P. Chen, The Pennsylvania State University, University Park, PA, USA</i>	
DYNAMIC, RADIATIVE AND CHEMICAL EFFECTS OF CLOUDS ON TROPOSPHERIC TRACE GASES.....	309
<i>C. J. Walcek, SUNY, Albany, NY, USA</i>	

PARAMETERIZATIONS OF MICROPHYSICAL PROCESSES IN CLOUDS FOR APPLICATION IN MODELS OF REGIONAL ATMOSPHERIC DEPOSITION.....	312
<i>I. Y. Lee, Argonne National Laboratory, Argonne, IL, USA</i>	
A MODEL OF WET DEPOSITION TO COMPLEX TERRAIN BY THE SEEDER-FEEDER PROCESS.....	316
<i>A. Jones and T. W. Choularton, UMIST, Manchester, UK</i>	
METEOROLOGICAL AND CHEMICAL INFLUENCING FACTORS ON ACIDITY PRODUCTION IN A MESOSCALE MODEL WITH QUASI-SPECTRAL MICROPHYSICS.....	319
<i>N. Chaumerliac and R. Rosset, LAMP, Aubière, FRANCE</i>	

## SESSION 8: INSTRUMENTATION

A COMPARISON OF RADIOMETRIC AND IMMERSION TEMPERATURE MEASUREMENTS IN WATER CLOUDS. ....	322
<i>S. Nicholls, E. L. Simmons, N. C. Atkinson and S. D. Rudman, Meteorological Office, Bracknell, Berkshire, UK</i>	
CALIBRATION OF PMS FSSP AND 1D-C PROBES FOR CLOUD DROPLET MEASUREMENTS. ....	325
<i>J.-F. Gayet, LAMP, Aubière, FRANCE</i>	
RADAR OBSERVATIONS OF PRECIPITATION MICROSTRUCTURE: THE MORPHOLOGY OF LINEAR DEPOLARIZATION MEASUREMENTS IN CLOUD. ....	328
<i>P. H. Herzegh, NCAR, Boulder, CO, USA, and A. R. Jameson, Applied Research Corporation, Landover, MD, USA</i>	
MULTIPARAMETER DOPPLER RADAR OBSERVATIONS OF A SQUALL LINE WITH THE POLARIMETRIC DFVLR RADAR. ....	330
<i>P. Meischner, V. N. Bringi and T. Jank; DFVLR-Oberpfaffenhofen, Weßling, FRG</i>	
A POOR MANS OPTICAL FOG DETECTOR. ....	333
<i>R. K. A. M. Mallant, Netherlands Energy Research Foundation, ECN, Petten, THE NETHERLANDS</i>	
APPLICATIONS OF THE NCAR ELECTRA DOPPLER RADAR FOR THE STUDY OF PHYSICAL PARAMETERS OF CLOUDS. ....	335
<i>C. Walther, C. Frush and P. Hildebrand, NCAR, Boulder, CO, USA</i>	
INTERCOMPARISONS OF AIRCRAFT MEASUREMENTS WITH LIDAR RETURNS FROM AEROSOL, ICE CRYSTALS, AND WATER DROPLETS. ....	338
<i>W. R. Leaitch and R. M. Hoff, Atmospheric Environment Service, Downsview Ontario, CANADA, and A. I. Carswell, S. Pal and G. A. Cunningham, York University, Downsview, Ontario, CANADA</i>	
A NEW AIRBORNE DEVICE FOR MEASUREMENT OF CLOUD PARTICLES USING VIDEO-MICROSCOPE. ....	341
<i>T. Tanaka, T. Matsuo, K. Okada, and I. Ichimura, Meteorological Research Institute, Ibaraki, JAPAN, and S. Ichikawa and A. Tokuda, Sankei Co. Ltd., JAPAN</i>	

## SESSION 9: OROGRAPHIC CLOUDS

ON THE SMALL SCALE TOPOGRAPHICAL INFLUENCES ON PRECIPITATION. ....	344
<i>W. W. Grabowski, Polish Academy of Science, Warsaw, POLAND</i>	
A NUMERICAL INVESTIGATION OF AN OROGRAPHIC PRECIPITATION EVENT. ....	347
<i>M. P. Meyers and W. R. Cotton, Colorado State University, Fort Collins, CO, USA</i>	
COMPLEX MICROPHYSICAL INTERACTIONS WITHIN A CENTRAL SIERRA NEVADA OROGRAPHIC CLOUD SYSTEM.....	350
<i>R. M. Rauber, University of Illinois, Urbana, IL, USA</i>	

COMPARISON OF OROGRAPHIC CLOUD AND PRECIPITATION DEVELOPMENT OF THREE DIFFERENT GEOGRAPHIC LOCATIONS USING A 3-D NESTED GRID CLOUD MODEL. ....	353
<i>R. M. Rasmussen, Bureau of Reclamation, Denver, CO, USA, and P. Smolarkiewicz, W. D. Hall and T. Clark, NCAR, Boulder, CO, USA</i>	
MICROPHYSICAL OBSERVATIONS OVER THE ATLAS MOUNTAINS IN MAROCCO. ....	356
<i>O. Baddour, Météorologie Nationale, Casablanca, Royaume du Maroc, and R. M. Rasmussen, Bureau of Reclamation, Denver, CO, USA</i>	
MICROPHYSICAL AND DYNAMICAL INTERACTIONS IN COLORADO FRONT RANGE UPSLOPE STORMS. ....	359
<i>D. A. Wesley, M. J. Weisbluth, R. A. Pielke and W. R. Cotton, Colorado State University, Fort Collins, CO, USA</i>	
CHARACTERISTICS OF RADAR ECHO OF A SNOWBAND FORMED IN THE LEE SIDE OF A MOUNTAIN. ....	362
<i>Y. Fujiyoshi, T. Endoh and G. Wakabana, Institute of Low Temperature Science, Hokkaido University, Sapporo, JAPAN</i>	

**POSTER SESSION B: CLOUD MACROPHYSICS**

STUDY ON CLOUD AND RAIN PROCESS BY MICROWAVE RADIOMETER OBSERVATION. ....	364
<i>B. Zhao, Peking University, Beijing, PRC</i>	
A NEW DROPSONDE FOR CLOUD PROBINGS. ....	366
<i>D. E. Gaytandjiev, Hydrometeorological Service, Sofia, BULGARIA</i>	
HUMIDITY MEASUREMENTS DURING CLOUD FORMATION USING INFRARED HYGROMETRY. ....	369
<i>P. J. DeMott and D. C. Rogers, Colorado State University, Fort Collins, CO, USA</i>	
IDENTIFICATION OF PRECIPITATION PARTICLES USING DUAL POLARIZATION RADAR. ....	372
<i>A. J. Illingworth and I. J. Caylor, UMIST, Manchester, UK</i>	
Z-R RELATIONS FORM AIRBORNE 2D-P MEASUREMENTS IN HAWAIIAN SHOWERS. ....	375
<i>R. J. Kubesh, K. V. Beard and D. B. Johnson, Illinois State Water Survey, Champaign, IL, USA</i>	
COMPARISON BETWEEN AIRCRAFT AND DOPPLER RADAR MEASUREMENTS DURING ENCC (VOVES 1983). ....	378
<i>H. Sauvageot, Laboratoire Aérologie Campistrous, FRANCE, and A. Rigaud, E. Hicks and C. Pontikis, Météorologie Nationale EERM/CRPA, Magny les Hameaux, FRANCE</i>	
EHF ATTENUATION THROUGH THE MELTING LAYER. ....	380
<i>A. J. Barnes, Jr., Air Force Geophysics Laboratory, Hanscom AFB, MA, USA</i>	
SIZE DISTRIBUTION OF PRECIPITATION PARTICLES IN MIDLATITUDE MESOSCALE CONVECTIVE COMPLEXES. ....	383
<i>J. D. Yeh, B. F. Fan and W. R. Cotton, Colorado State University, Fort Collins, CO, USA</i>	
A PRELIMINARY RESEARCH ON THE RADIATION FOG IN XISHUANG BANNA. ....	386
<i>Y. Huang, W. Xu, Meteorological Bureau of Yunnan Province, Yunnan, PRC, Z. Li, W. Huang, L. Fan, Nanjing Institute of Meteorology, Nanjing, PRC</i>	
THE BASIC CHARACTERISTICS OF THE WINTER NORTHERN XINJIANG STRATIFORM CLOUD SYSTEM. ....	389
<i>Z. Gao and J. Zhang, Weather Modification Office, Xinjiang, PRC</i>	
THE RAINFALL ENHANCEMENT BY TWO LAYER CLOUD STRUCTURE OBSERVED AT OROFURE MOUNTAIN RANGE, HOKKAIDO, JAPAN. ....	393
<i>K. Kikuchi, K. Iwanami and T. Taniguchi, Hokkaido University, Sapporo, Japan</i>	

NUMERICAL SIMULATION OF COASTAL CLOUDS WHEN SOLAR RADIATION IS BLOCKED BY SMOKE.....	396
<i>C. R. Molenkamp, Lawrence Livermore National Laboratory, Livermore, CA, USA</i>	
LONG-LIVED HAWAIIAN RAIN BANDS.....	398
<i>P. Smolarkiewicz, and T. L. Clark, NCAR, Boulder, CO, USA, and R. Rasmussen, Bureau of Reclamation, Denver, CO, USA</i>	
A LONG-LASTING RAINSTORM TRAVELLING ALONG A STATIONARY FRONT.....	401
<i>H. Sakakibara and A. Tabata, Meteorological Research Institute, Ibaraki, JAPAN</i>	
THREE-DIMENSIONAL AIRFLOW AND VORTICITY BUDGET OF RAINBANDS IN A WARM OCCLUSION.....	404
<i>O. Hertzman and P. V. Hobbs, University of Washington, Seattle, WA, USA</i>	
DOPPLER RADAR OBSERVATION OF CONVERGENCE BAND CLOUD FORMED ON THE WEST COAST OF HOKKAIDO ISLAND, JAPAN.....	407
<i>Y. Fujiyoshi, K. Tsuboki and G. Wakabama, Institute of Low Temperature Science, Hokkaido University, Sapporo, JAPAN</i>	
THE USE OF OXYGEN ISOTOPES IN STUDIES OF ICE PHASE PRECIPITATION FROM WINTER STORMS .....	410
<i>B. Demoz, J. A. Warburton and R. L. Stone, Desert Research Institute, Reno, NV, USA</i>	
NUMERICAL SENSITIVITY STUDY OF THE MORPHOLOGY OF LAKE-EFFECT SNOW STORMS OVER LAKE MICHIGAN .....	413
<i>M. Hjelmfelt, NCAR, Boulder, CO, USA</i>	
DOPPLER RADAR OBSERVATIONS OF SNOW PARTICLES IN WINTER CONVECTIVE CLOUDS .....	416
<i>H. Konishi, Osaka Kyoiku University, Osaka, Japan, and T. Endoh and G. Wakabama, Institute of Low Temperature Science, Hokkaido University, Sapporo, JAPAN</i>	
THE RELATIONSHIP BETWEEN ENTRAINMENT RATE AND SOME PRODUCTS OF 1-D C <sub>b</sub> MODEL.....	419
<i>M. Curic and D. Janc, University of Belgrad, Beograd, YUGOSLAVIA</i>	
ON THE ENTRAINMENT IN CUMULI – A CONTRIBUTION TO A CASE STUDY .....	422
<i>I. Nemesova, Institute of the Physics of the Atmosphere, Prague, CZECHOSLOVAKIA</i>	
A FINE RESOLUTION TWO-DIMENSIONAL NUMERICAL STUDY OF A CLOUD-CAPPED BOUNDARY LAYER.....	425
<i>M. K. MacVean and S. Nicholls, Meteorological Office, Bracknell, Berkshire, UK</i>	
A NUMERICAL METHOD FOR INTEGRATING THE THERMAL CONVECTION EQUATIONS IN THE ATMOSPHERE .....	428
<i>I. M. Enukashvily, Israel Meteorological Service, Bet-Dagan, ISRAEL</i>	
A DIAGNOSTIC STUDY OF VERTICAL FLUXES IN CUMULUS CLOUDS USING MODEL OUTPUT DATA.....	431
<i>M. J. Weissbluth and W. R. Cotton, Colorado State University, Fort Collins, CO, USA</i>	
EFFICIENCY OF DEEP CONVECTIVE CLOUDS RELATED WITH SOME PARAMETERS OF OCCURRENCE OVER THE ARGENTIN TERRITORY.....	434
<i>M. E. Saluzzi, Universidad de Buenos Aires, Conicet, Buenos Aires, ARGENTINA</i>	
CHARACTERISTICS OF MESOSCALE CLOUD SYSTEMS DEVELOPED IN THE MARITIME SUBTROPICS .....	437
<i>M. Ishihara, A. Tabata, K. Akaeda, T. Yokoyama and H. Sakakibara, Meteorological Research Institute, Ibaraki, JAPAN</i>	
ON THE MERGER OF TWO SMALL CONVECTIVE RADAR ECHOES .....	440
<i>B. Ackerman and P. C. Kennedy, Illinois State Water Survey, Champaign, IL, USA</i>	

MULTIPLE DOPPLER RADAR OBSERVATIONS OF AIRFLOW FIELDS DURING CONVECTIVE ECHO MERGERS.....	443
<i>P. C. Kennedy, Illinois State Water Survey, Champaign, IL, USA</i>	
RESULTS FROM WARM RAIN STUDIES IN PENANG, MALAYSIA.....	446
<i>R. List, D. Hudak and R. Nissen, University of Toronto, Toronto, Ontario, CANADA, and N. P. Tung, S. K. Soo and T. S. Kang, Malaysian Meteorological Service, Petaling Jaya, MALAYSIA</i>	
THE KINEMATICS OF MESO-GAMMA SCALE PRECIPITATION SYSTEMS .....	449
<i>P. I. Joe, C. L. Crozier and T. R. Nichols, Atmospheric Environment Service, Downsview, Ontario, CANADA</i>	
THE ORIGIN OF AIR MASSES LEADING TO SEVERE HAILSTORMS IN SOUTHWESTERN FRANCE.....	452
<i>J. Dessens, Centre de Recherches Atmosphériques, Lannemezan, FRANCE, and Fournier d'Albe, Dormont, Saint-Pierre de Bailleul, FRANCE</i>	
RADAR REMOTE SENSING OF MELTING HAIL.....	455
<i>V. N. Bringi and P. Meischner, DFVLR, Institut für Physik der Atmosphäre, Weßling, FRG</i>	
TEST OF PARAMETERIZATION SCHEMES FOR CLOUD MICROPHYSICAL PROCESSES IN A 3-D MESOSCALE MODEL .....	458
<i>L. Levkov, D. Jacob, D. Eppel and H. Graßl, Forschungszentrum Geesthacht, Geesthacht, FRG</i>	
DEVELOPMENT OF ANALYTICAL METHODS FOR THE INVESTIGATION OF CLOUDS, FOG AND RAIN, TOGETHER WITH THE GASEOUS PHASE, AND RESULTS OF FIELD MEASUREMENTS .....	461
<i>K. Bächmann, U. Sprenger, G. R. Fuchs-Pohl, W. Schmied, and P. Zeißler, Technische Hochschule Darmstadt, FRG</i>	
RAIN AEROSOL COUPLING IN MARITIME, URBAN AND RURAL AREA. SCAVENGING RATIOS MEASUREMENTS IN RELATION WITH TRANSPORT.....	463
<i>J. L. Colin and J. L. Jaffrezo, Université Paris, Paris Cedex, FRANCE</i>	
THE RAINOUT REMOVAL OF SULFUR DIOXIDE AND ACIDIFICATION OF PRECIPITATION FROM STRATIFORM CLOUDS .....	466
<i>Q. Yu, Peking University, Beijing, PRC</i>	

## SESSION 10: CIRRUS CLOUDS

STRUCTURAL AND TEXTURAL CHARACTERISTICS OF CIRRUS CLOUDS.....	468
<i>K. S. Kuo, R. M. Welch and S. K. Sengupta, South Dakota School of Mines and Technology, Rapid City, SD, USA</i>	
CIRRUS CLOUDS AND MESOSCALE ATMOSPHERIC PROCESSES .....	471
<i>E. P. Borisenkov and T. A. Bazlova, Main Geophysical Observatory, Leningrad, USSR</i>	
MESOSCALE AND MICROSCALE STRUCTURE OF CIRRUS CLOUDS: THREE CASE STUDIES .....	473
<i>K. Sassen and M. Griffin, University of Utah, Salt Lake City, UT, USA</i>	
VERTICAL VELOCITIES WITHIN A CIRRUS CLOUD FROM DOPPLER LIDAR AND AIRCRAFT MEASUREMENTS DURING "FIRE": IMPLICATIONS FOR PARTICLE GROWTH.....	476
<i>I. Gultepe and A. Heymsfield, NCAR, Boulder, CO, USA</i>	
HYDROMETEOR DEVELOPMENT IN COLD CLOUDS IN "FIRE".....	479
<i>A. J. Heymsfield and N. C. Knight, NCAR, Boulder, CO, USA</i>	

THE EMPIRICAL MODEL OF THE STRUCTURE OF CIRRUS CLOUDS IN MIDDLE LATITUDES .....	482
<i>A. L. Kosarev, I. P. Mazin and A. N. Neuzorov, Central Aerological Observatory, Moscow Region, USSR</i>	
MODELLING THE INITIAL ICE CRYSTAL SPECTRUM IN CIRRUS CLOUD.....	485
<i>A. G. Darlison, Meteorological Office, Bracknell, Berkshire, UK</i>	
EFFECTS OF CIRRUS COMPOSITION ON ATMOSPHERIC RADIATION BUDGETS .....	488
<i>St. Kinne, NASA Ames Research Center, Moffett Field, CA, USA, and K. N. Liou, University of Utah, Salt Lake City, UT, USA</i>	

#### SESSION 11: BOUNDARY-LAYER PROCESSES, FOGS AND LAYER CLOUDS

A RADIATION-FOG MODEL WITH DETAILED MICROPHYSICS .....	490
<i>A. Bott, U. Sievers and W. Zdankowski, Johannes Gutenberg-Universität, Mainz, FRG</i>	
SMALL SCALE STRUCTURE OF A RADIATIVE FOG: A NUMERICAL STUDY .....	493
<i>P. K. Smolarkiewicz, NCAR, Boulder, CO, USA, and D. Fitzjarrald, State University of New York, Albany, NY, USA</i>	
NUMERICAL STUDIES ON THE EVOLUTION OF RADIATION FOG.....	496
<i>W. Wobrock, Johann Wolfgang-Goethe Universität, Frankfurt am Main, FRG</i>	
A NUMERICAL STUDY OF MESOSCALE PERTURBATIONS IN STRATIFORM BOUNDARY LAYER CLOUD FIELDS.....	499
<i>M. Tjernström, Uppsala University, Uppsala, SWEDEN</i>	
A NUMERICAL STUDY OF RADIATION FOG OVER THE YANGTZE RIVER.....	503
<i>M.-W. Qian and X. Lei, Institute of Atmospheric Physics, Academia Sinica, Beijing, PRC</i>	
PRECIPITATION MECHANISM OF PRECIPITUS STRATIFORMIS OVER JILIN PROVINCE IN SPRING.....	507
<i>X.-L. Wang, D.-Z. Jin, Y.-Z. Li and C. R. Zheng, Meteorological Institute of Jilin Province, Changchun, PRC</i>	
AIRCRAFT OBSERVATIONS AND SIMULATIONS OF ARCTIC STRATUS CLOUDS.....	509
<i>J. E. Finger and P. Wendling, Institut für Physik der Atmosphäre, DFVLR, Weßling, FRG</i>	
DIURNAL VARIATION OF A STRATOCUMULUS-TOPPED ATMOSPHERIC BOUNDARY LAYER OVER SEA.....	511
<i>P. G. Duynkerke, KNMI, AE De Bilt, THE NETHERLANDS</i>	
INTEGRATED FOG WATER SAMPLING SYSTEM.....	514
<i>L. Schütz, M. Krämer, B. Friederich and F. Franken, Johannes Gutenberg-Universität, Mainz, FRG</i>	
USE OF LIDAR DATA IN SHORT-TERM FORECAST OF STRATIFORM CLOUDINESS BASE HEIGHT .....	515
<i>S. I. Kolev*, O. P. Parvanov**, L. A. Kostadinov***, and I. N. Kolev**, *Institute of Hydrology and Meteorology, Sofia, BULGARIA, **Institute of Electronics, Sofia, BULGARIA, ***Hydrometeorological Service, Sofia, BULGARIA</i>	

#### SESSION 12: CYCLONES, FRONTS AND RAINBANDS

WATER CONTENT OF WINTER CLOUDS OVER ETS .....	518
<i>A. S. Azarov, N. A. Bezrukova, N. F. Buranbaev, A. V. Coldaev and A. A. Chernikov, Central Aerological Observatory, Dolgoprudny, Moscow Region, USSR</i>	

MICROPHYSICAL STRUCTURE OF JAPANESE WARM-FRONTAL CLOUDS OBSERVED WITH A NEW TYPE SONDE (HYVIS) .....	521
<i>M. Murakami, T. Matsuo, H. Mizuno and Y. Yamada, Meteorological Research Institute, Ibaraki, JAPAN</i>	
COLD FRONTAL PASSAGE OVER THE SIERRA BARRIER .....	525
<i>J. D. Marwitz, University of Wyoming, Laramie, WY, USA</i>	
A NUMERICAL MODELING STUDY OF COLD-FRONTAL RAINBANDS .....	527
<i>D. J. Knight and P. V. Hobbs, University of Washington, Seattle, WA, USA</i>	
NUMERICAL SIMULATION OF RAINBANDS CAUSED BY MESO- $\beta$ SCALE POTENTIAL VORTICITY ANOMALIES .....	529
<i>H. R. Cho and D. S. T. Chan, University of Toronto, Toronto, Ontario, CANADA</i>	
SIMULATION OF FRONTAL CLOUDS AND PRECIPITATION USING A MESOSCALE WEATHER PREDICTION MODEL .....	532
<i>E. Müller and U. Wacker, Deutscher Wetterdienst, Offenbach/M., FRG</i>	
LONG LASTING TRADE WIND RAINBANDS .....	535
<i>T. Takahashi, Kyushu University, Fukuoka, JAPAN</i>	
CHARACTERISTICS OF CUMULUS BANDCLOUDS OFF THE COAST OF HAWAII .....	538
<i>G. B. Raga*, J. B. Jensen**, J. Wettlaufer*, and M. B. Baker*, *University of Washington, Seattle, WA, USA, **NCAR Boulder, CO, USA</i>	
STRUCTURE OF LAYER CLOUDS AS OBSERVED SIMULTANEOUSLY BY A MICROWAVE RADIOMETER AND AN 8.6 MM RADAR .....	541
<i>G. Liu and T. Takeda, Water Research Institute, Nagoya University, Nagoya, JAPAN</i>	
ANALYSIS OF SINGLE DOPPLER RADAR DATA: WIND FIELD AND PRECIPITATION OBSERVATIONS DURING A FRONTAL PASSAGE .....	544
<i>M. Hagen, Institut für Physik der Atmosphäre – DFVLR, Oberpfaffenhofen, FRG</i>	
THE OCCURRENCE OF ICE IN CLOUDS ASSOCIATED WITH EXTRATROPICAL CYCLONES .....	547
<i>R. T. Bruintjes, South African Weather Bureau, Pretoria, REPUBLIC OF SOUTH AFRICA</i>	

### SESSION 13: GRAUPEL AND HAIL

THE SUPERCOOLING OF SURFACE WATER SKINS OF SPHERICAL AND SPHEROIDAL HAILSTONES .....	551
<i>R. List, F. Garcia-Garcia, R. Kuhn and B. Greenan, University of Toronto, Toronto, Ontario, CANADA</i>	
MICROPHYSICAL CONCEPT OF HAIL FORMATION .....	554
<i>M. I. Tisov and V. G. Khorguani, High-Mountain Geophysical Institute, Nalchik, USSR</i>	
STUDIES OF ARTIFICIAL HAILSTONES UNDER DIFFERENT EXPERIMENTAL CONDITIONS .....	557
<i>F. Prodi, Istituto FISBAT-CNR, Bologna, ITALY, and A.-S. Wang, Institute of Atmospheric Physics, Academia Sinica, Beijing, PRC</i>	
WIND TUNNEL HAILSTONE GROWTH USING DOPPLER RADAR DERIVED TRAJECTORIES .....	560
<i>G. B. Lesins, University of Oklahoma, Norman, OK, USA</i>	
THE EFFECT OF SUPERCOOLED DROPLET ELECTRICAL CHARGES ON THE HAIL GROWTH COAGULATIVE PROCESS .....	563
<i>T. G. Bliadze, A. I. Kartsvadze, A. M. Okudjava and T. N. Saliasbvili, Institute of Geophysics, Georgian Academy of Sciences, Tbilisi, USSR</i>	

GROWTH OF HAILSTONES IN CONVECTIVE CLOUDS. RESULTS OF MEASUREMENTS AND NUMERICAL EXPERIMENTS .....	566
<i>S. Stoyanov, Hydrometeorological Service, Sofia, BULGARIA, M. Tisov, High Mountain Geophysical Institute, Nalchik, USSR, and I. Geresdi, Cs. Zoltán, Cs. Székely, K. Molnár, Meteorological Service, Szalánta, HUNGARY</i>	
HAIL IMPACTS, HAIL NETS AND DAMAGE.....	569
<i>D. Roos, Council for Scientific and Industrial Research, Pretoria, SOUTH AFRICA, and S. F. Durrant, University of Surrey, Guildford, UK</i>	
COMPARISON OF THE SHAPE AND SIZE DISTRIBUTIONS OF RAINDROPS AND HAILSTONES.....	572
<i>P. K. Wang, University of Wisconsin, Madison, Wisconsin, USA</i>	
TWO STAGE HAILSTONE GROWTH IN THE AUGUST 1, 1981 CCOPE STORM .....	574
<i>J. C. Pflaum, University of Oklahoma, Norman, OK, USA, and R. M. Rasmussen, Bureau of Reclamation, Denver, CO, USA</i>	
ON SOME CHARACTERISTICS DETERMINING THE DEVELOPMENT OF HAIL PROCESSES IN BULGARIA .....	576
<i>P. Simeonov, Hydrometeorological Service, Sofia, BULGARIA, and D. Sirakov, Sofia University, Sofia, BULGARIA</i>	

#### SESSION 14: CONVECTIVE CLOUDS I: MEASUREMENTS

MEASUREMENTS OF CLOUD DROPS; THEIR AEROSOL CONTENT AND CLOUD INTERSTITIAL NUCLEI NEAR THE BASES OF CONVECTIVE CLOUDS IN ISRAEL.....	579
<i>Z. Levin, E. Ganor, C. Price and D. Pardess, Tel Aviv University, Ramat Aviv, ISRAEL</i>	
MICROPHYSICAL CHARACTERISTICS OF CONVECTIVE CLOUDS OVER THE SOUTH-CENTRAL UNITED STATES .....	582
<i>M. R. Poellot, University of North Dakota, Grand Forks, ND, USA, and J. C. Pflaum, University of Oklahoma, Norman, OK, USA</i>	
INVESTIGATION BY TRACER METHOD OF THE CONVECTIVE CELLS OF CUMULONIMBUS CLOUDS .....	585
<i>L. A. Dinevich, State Hydrometeorological Committee, USSR, and S. S. Salavejus, Institute of Physics of the Academy of Sciences, Lithuanian SSR</i>	
INVESTIGATING MIXING AND THE ACTIVATION OF ICE WITH GASEOUS TRACER TECHNIQUES.....	588
<i>J. L. Stith, University of North Dakota, Grand Forks, ND, USA, M. K. Politovich and R. F. Reinking, NOAA/ERL, Boulder, CO, USA, and A. Detwiler and P. L. Smith, South Dakota School of Mines and Technology, Rapid City, SD, USA</i>	
FIRST FORMATION OF PRECIPITATION IN AN ISOLATED CONVECTIVE CLOUD .....	591
<i>C. A. Knight, NCAR, Boulder, CO, USA</i>	
RETRIEVAL OF DYNAMIC VARIABLES IN DOPPLER-OBSERVED CONVECTIVE CLOUD SYSTEMS .....	594
<i>C. E. Hane, National Severe Storms Laboratory NOAA, Norman, OK, USA</i>	
THE EFFECTS OF THE EXISTENCE OF STRATIFORM CLOUD ON THE DEVELOPMENT OF CUMULUS CLOUD AND ITS PRECIPITATION.....	597
<i>M. Huang, Y. Hong, H. Xu and H. Zhou, Institute of Atmospheric Physics, Academia Sinica, Beijing, PRC</i>	
A CASE STUDY OF A SLOW-MOVING CONVECTIVE BAND OBSERVED BY A DOPPLER RADAR .....	600
<i>K. Akaeda, M. Ishihara, A. Tabata, T. Yokoyama and H. Sakakibara, Meteorological Research Institute, Ibaraki, JAPAN</i>	

## SESSION 15: CONVECTIVE CLOUDS II: THEORY AND NUMERICAL MODELING

ANALYSIS OF DIFFERENT APPROACHES TO MATHEMATICAL DESCRIPTION OF CONVECTION.....	603
<i>M. V. Buikov, Ukrainian Regional Research Institute, Kiev, USSR</i>	
ORGANIZATION OF CLOUD CONVECTION BY GRAVITY WAVES IN THE LOWER TROPOSPHERE.....	606
<i>J. M. Radziwill, University of Warsaw, POLAND</i>	
DRAG EFFECT IN CONVECTIVE DRAFTS .....	609
<i>K. E. Haman and S. P. Malinowski, University of Warsaw, Warsaw, POLAND</i>	
MOISTURE CONVERGENCE AS A SOURCE OF EXPLOSIVE GROWTH IN MODELED CUMULUS CLOUDS .....	612
<i>J. H. Helsdon, Jr., H. D. Orville, R. D. Farley and F. J. Kopp, South Dakota School of Mines and Technology, Rapid City, SD, USA</i>	
THE EFFECTS OF COLD WATER SURFACE ON WARM CUMULUS CLOUDS-NUMERICAL EXPERIMENT .....	615
<i>F. Kong, M. Huang and H. Xu, Institute of Atmospheric Physics, Academia Sinica, Beijing, PRC</i>	
COMPREHENSIVE RESEARCH OF CONVECTIVE CLOUD DYNAMICS FROM THE DATA OF AIRCRAFT AND NUMERICAL EXPERIMENTS.....	618
<i>J. A. Dovgaljuk, V. P. Drachova, A. D. Egorov, A. A. Sinkevich, E. N. Stankova, V. D. Stepanenko, Main Geophysical Observatory, Leningrad, USSR</i>	
A STUDY ON NUMERICAL SIMULATION OF CLOUD MERGERS AND INTERACTIONS.....	621
<i>M. Huang, H. Xu and W. Ji, Institute of Atmospheric Physics, Academia Sinica, Beijing, PRC</i>	
SMOOTH PARTICLE HYDRODYNAMICS AS APPLIED TO 2-D CUMMULUS TYPE CONVECTION.....	624
<i>A. Gadian, UMIST, Manchester, UK</i>	
CONVECTION WAVES AND THEIR STRUCTURAL IMPACT ON CLOUD FIELDS .....	626
<i>T. Hauf and T. L. Clark, NCAR, Boulder, CO, USA</i>	
COMPARISON BETWEEN NUMERICAL CLOUD RESULTS AND OBSERVATIONS .....	629
<i>B. Mitzeva and V. Andreev, University of Sofia, Sofia, BULGARIA</i>	

## SESSION 16: THUNDERSTORMS

LOCAL ENVIRONMENTAL CONDITIONS INFLUENCING THE GROWTH AND INTERNAL STRUCTURE OF NON SEVERE THUNDERSTORMS.....	632
<i>N. E. Westcott, Illinois State Water Survey, Champaign, IL, USA</i>	
DOPPLER RADAR STUDY OF A WEAKLY SHEARED THUNDERSTORM .....	635
<i>D. J. Raymond and A. M. Blyth, New Mexico Institute of Mining &amp; Technology, Socorro, NM, USA</i>	
INTERIOR CHARACTERISTICS AT MID LEVELS OF THUNDERSTORMS IN THE SOUTHEASTERN UNITED STATES.....	638
<i>D. F. Musil and P. L. Smith, South Dakota School of Mines and Technology, Rapid City, SD, USA</i>	
ELECTRIFICATION OF THE 31 JULY 1984 NEW MEXICO MOUNTAIN THUNDERSTORM .....	641
<i>C. L. Ziegler, National Severe Storms Laboratory, Norman, OK, USA, and P. S. Ray and S. L. Lang, Florida State University, Tallahassee, FL, USA</i>	

RETRIEVAL OF MICROPHYSICAL VARIABLES IN NEW MEXICAN MOUNTAIN THUNDERSTORMS FROM DOPPLER RADAR DATA.....	644
<i>P. S. Ray*, C. L. Ziegler**, and S. L. Lang*, *Florida State University, Tallahassee, FL, USA, **National Severe Storms Laboratory, Norman, OK, USA</i>	
ON THE ROLE OF PRECIPITATION IN MAINTENANCE OF DOWNDRAFTS IN CUMULONIMBUS CLOUDS .....	647
<i>H. Pawelowska-Mankiewicz, University of Warsaw, POLAND</i>	
INFLUENCE OF THUNDERSTORM-GENERATED ACOUSTIC WAVE ON COAGULATION.....	650
<i>M. Curic, University of Belgrad, Beograd, YUGOSLAVIA, and Z. Vukovic, Hydrometeorological Institute of Serbia, Beograd, YUGOSLAVIA</i>	

#### SESSION 17: SATELLITE STUDIES

SATELLITE-SURFACE LINKAGE TO ESTIMATE MID-LATITUDINAL PRECIPITATION FEATURES.....	653
<i>M. Scholl, Freie Universität Berlin, Berlin, FRG</i>	
RESULTS FROM THE RAINFALL ESTIMATION STUDIES BASED ON METEOSAT DATA.....	656
<i>O. M. Turpeinen, European Space Operations Centre, Darmstadt, FRG</i>	
COMPARISON OF SATELLITE DATA WITH SURFACE-BASED REMOTE SENSING MEASUREMENTS IN UTAH WINTER OROGRAPHIC STORMS.....	659
<i>D. C. Rogers, Colorado State University, Fort Collins, CO, USA, and K. Sassen and G. C. Dodd, University of Utah, Salt Lake City, UT, USA</i>	
PASSIVE MICROWAVE OBSERVATIONS OF THUNDERSTORMS FROM HIGH-ALTITUDE AIRCRAFT .....	662
<i>G. M. Heymsfield, NASA Goddard Space Flight Center, Greenbelt, MD, USA, and R. Fulton, General Sciences Corporation, Laurel, MD, USA</i>	
NUMERICAL FRONTAL ANALYSIS SCHEME FOR OPERATIONAL INTERPRETATIONS OF SATELLITE PICTURES AND PRECIPITATION ESTIMATIONS.....	665
<i>L. Lesch, Institut für Meteorologie, Freie Universität Berlin, Berlin, FRG</i>	

#### SESSION 18: SEVERE STORMS AND HURRICANES

A MIDDLE LATITUDE SQUALL LINE IN FRANCE.....	666
<i>G. Jaubert, M. Chong and J. M. Giudicelli, Direction de la Météorologie Nationale (EERM/CNRM), Toulouse Cedex, FRANCE</i>	
A STUDY OF THE DYNAMICS OF SQUALL LINES USING A NON-HYDROSTATIC CLOUD MODEL .....	669
<i>D. B. Parsons, R. Rotunno, J. B. Klemp and M. L. Weisman, NCAR, Boulder, CO, USA</i>	
PHYSICAL PROCESSES AND OBSERVED FEATURES IN MICROBURST-PRODUCING STORMS .....	672
<i>M. Hjelmfelt and C. Kessinger, NCAR, Boulder, CO, USA</i>	
ON THE MICROPHYSICS OF MICROBURSTS.....	675
<i>H. D. Orville, F. J. Kopp, R. D. Farley and Y. C. Chi, South Dakota School of Mines and Technology, Rapid City, SD, USA</i>	
OBSERVATION OF MICROBURSTS FROM SNOW CLOUDS IN WINTER MONSOON SEASON .....	678
<i>H. Uyeda, R. Shirooka and K. Kikuchi, Hokkaido University, Sapporo, JAPAN</i>	
EVOLUTION OF CONVECTIVE STORM ALONG BOUNDARY LAYER CONVERGENCE LINES.....	681
<i>J. Wilson and C. Müller, NCAR, Boulder, CO, USA</i>	

THE STRUCTURE OF THE CONVECTIVE CELLS AND THE DYNAMICS OF HAILSTORM DEVELOPMENT IN ALAZANI VALLEY.....	684
<i>A. I. Kartsivadze, T. G. Salukvadze, R. I. Doreuli, E. I. Khelaya, and A. Sh. Balavadze, Institute of Geophysics, Georgian Academy of Sciences, Tbilisi, USSR</i>	
EVOLUTION OF MESOCYCLONIC CIRCULATION IN SEVERE STORMS .....	687
<i>P. I. Joe and C. L. Crozier, Atmospheric Environment Service, Toronto, Ontario, CANADA</i>	
A NUMERICAL STUDY OF MULTICELLULAR SEVERE CONVECTIVE STORMS FOLLOWED BY LONG-LASTING HEAVY RAINFALL .....	690
<i>J. Shiino, Meteorological Research Institute, Ibaraki, JAPAN</i>	
3-D NUMERICAL MODELING AND RADAR OBSERVATIONS OF DEEP CONVECTIVE CLOUDS.....	693
<i>H. Höller, Institut für Physik der Atmosphäre, DFVLR-Oberpfaffenhofen, Weßling, FRG</i>	
OBSERVED STRUCTURE AND EVOLUTION OF A MESOVORTEX IN THE TRAILING STRATIFORM REGION OF A MCC.....	696
<i>J. Verlinde and W. R. Cotton, Colorado State University, Fort Collins, CO, USA</i>	
MELTING LAYER STRUCTURE IN MCC STRATIFORM PRECIPITATION .....	699
<i>P. T. Willis, Atlantic Oceanographic and Meteorological Laboratories, Miami, FL, USA, and A. J. Heymsfield, NCAR, Boulder, CO, USA</i>	
DUAL-DOPPLER AND AIRBORNE MICROPHYSICAL OBSERVATIONS IN THE STRATIFORM REGION OF THE 10-11 JUNE MCS OVER KANSAS DURING PRESTORM.....	702
<i>S. A. Rutledge*, R. A. Houze Jr.**, A. J. Heymsfield***, and M. I. Biggerstaff** *Oregon State University, Corvallis, OR, USA, **University of Washington, Seattle, WA, USA, ***NCAR, Boulder, CO, USA</i>	
VERTICAL DRAFTS IN THE CONVECTIVE REGIONS OF MESOSCALE CONVECTIVE SYSTEMS IN KANSAS.....	705
<i>M. I. Biggerstaff and R. A. Houze, Jr., University of Washington, Seattle, WA, USA, and S. A. Rutledge, Oregon State University, Corvallis, OR, USA</i>	
MESOSCALE PATTERNS OF ICE PARTICLE CHARACTERISTICS IN HURRICANE NORBERT .....	708
<i>R. A. Houze, Jr., University of Washington, Seattle, WA, USA, and F. D. Marks, Jr., and R. A. Black, Hurricane Research Division NOAA/AOML, Miami, FL, USA</i>	
THE BULK WATER BUDGET OF HURRICANE NORBERT (1984) AS DETERMINED FROM THERMODYNAMIC AND MICROPHYSICAL ANALYSES RETRIEVED FROM AIRBORNE DOPPLER RADAR.....	711
<i>J. F. Gamache, F. D. Marks, Jr. and R. A. Black, Hurricane Research Division, NOAA/AOML, Miami, FL, USA, and R. A. Houze, Jr., University of Washington, Seattle, WA, USA</i>	
MICROPHYSICS IN A CONVECTIVE CLOUD SYSTEM ASSOCIATED WITH A MESOSCALE CONVECTIVE COMPLEX - AND NUMERICAL SIMULATION.....	714
<i>B. F. Fan, J. D. Yeh and W. R. Cotton, Colorado State University, Fort Collins, CO, USA, and G. J. Tripoli, University of Wisconsin, Madison, WI, USA</i>	
OBSERVATIONAL ANALYSIS OF MESOSCALE CONVECTIVE SYSTEM GROWTH AND STRUCTURE .....	717
<i>K. R. Knupp, University of Alabama, Huntsville, AL, USA</i>	
INVESTIGATION OF THUNDER AND HAIL CLOUDS USING REMOTE METHODS.....	719
<i>M. R. Vatyán, M. G. Bakhsoliani, N. E. Lomidze, G. B. Brylev, B. E. Peskov, USSR</i>	
STUDIES OF CONVECTIVE CLOUDS DEVELOPMENT IN CENTRAL ASIA.....	723
<i>A. D. Dzshuraev, H. A. Imamdzhánov, B. Sh. Kadyrov and V. P. Kurbatkin, The Bugaev Central Asian Regional Research Institute, Tashkent, USSR</i>	

Author Index

- Ackerman, B. 440  
 Ackerman, T.P. 125, 133,  
 Adzhiev, A.Kh. 161  
 Akaeda, K. 437, 600  
 Andreev, V. 629  
 Atkinson, N.C. 322  
 Azarov, A.S. 518
- Baddour, O. 356  
 Baechmann, K. 461  
 Baker, M. B. 67, 538  
 Bakhsoliani, M.G. 719  
 Balavadze, A.Sh. 684  
 Barnes jr., A.J. 380  
 Baumgardner, D.G. 40, 43, 70  
 Bazlova, T.A. 471  
 Beard, K.V. 7, 31, 375  
 Beheng, K.D. 199  
 Bezrukova, N.A. 518  
 Biggerstaff, M.I. 702, 705  
 Black, R.A. 708, 711  
 Bliadze, T.G. 563  
 Blyth, A.M. 73, 635  
 Borisenkov, E.P. 471  
 Bott, A. 490  
 Bower, K. 37  
 Braun, P. 246  
 Breidenthal, R. 67  
 Brenguier, J.L. 91  
 Bringi, V.N. 330, 455  
 Brown jr., Ph. S. 169  
 Brown, P.R.A. 55, 138, 141  
 Bruintjes, R.T. 547  
 Brylev, G.B. 719  
 Biukov, M.V. 603  
 Buranbaev, N.F. 518
- Carswell, A.I. 338  
 Castillo, R.A. 251, 267  
 Caylor, I.J. 49, 372  
 Chan, D.S.T. 529  
 Chandler, A.S. 279  
 Chandra, M. 154  
 Chatterjee, R.N. 58  
 Chaumerliac, N. 106, 319  
 Chen, J.P. 306  
 Chen, S. 130  
 Chernikov, A.A. 518  
 Chi, Y.C. 675  
 Cho, H.R. 529  
 Chong, M. 666  
 Choularton, T.W. 37, 55, 279,  
 316  
 Chuang, C. 31  
 Clark, P.A. 279  
 Clark, T.L. 88, 353, 398, 626
- Coakley, J.E. 121  
 Colburn, D.C. 125  
 Coldaev, A.V. 518  
 Colin, J.-L. 288, 463  
 Cooper, W.A. 46  
 Cotton, W.R. 109, 130, 347, 359,  
 383, 431, 699, 714  
 Crozier, C.L. 449, 687, 696  
 Cunningham, G.A. 338  
 Curic, M. 419, 650  
 Czys, R.R. 4, 25, 64
- Darlison, A.G. 138, 141, 485  
 Daum, P.H. 264  
 Davies, R. 124  
 Dellert, M. 246  
 Deluisi, J. 267  
 DeMott, P.J. 369  
 Demoz, B. 410  
 Dessens, J. 452  
 Detwiler, A. 588  
 Dinevich, L.A. 585  
 Dlugi, R. 235  
 Dodd, G.C. 659  
 Doms, G. 199  
 Dong, Y. 28  
 Doreuli, R.I. 684  
 Dovgaljuk, J.A. 618  
 Drachova, V.P. 618  
 Duroure, Chr. 62, 223  
 Durrant, S.F. 569  
 Duynkerke, P.G. 511  
 Dzhuraev, A.D. 723
- Egorov, A.D. 618  
 Eldik, R. v. 246  
 Enderle, K.H. 291  
 Endoh, T. 9, 362, 416  
 Erukashvily, I.M. 172, 428  
 Eppel, D. 458
- Fan, B.F. 383, 714  
 Fan, L. 386  
 Farley, R.D. 226, 612, 675  
 Feng, J.Q. 4  
 Finger, J.E. 509  
 Finnegan, W.G. 243  
 Fitzjarrald, D. 493  
 Flatau, P.J. 109  
 Forkel, R. 255  
 Fournier d'Albe, E.M. 452  
 Franken, F. 514  
 Friederich, B. 514  
 Frush, C. 335  
 Fuchs-Pohl, G.R. 461

Fujiyoshi, Y. 362, 407  
 Fukuta, N. 9, 12  
 Fulton, R. 662

Gadian, A. 624  
 Gagneux, J. 76, 211  
 Gamache, J.F. 711  
 Ganor, E. 579  
 Gao, Z. 389  
 Garcia-Garcia, F. 551  
 Gay, M.J. 279  
 Gayet, J.-F. 62, 325  
 Gaytandjiev, D.E. 366  
 Geresdi, I. 566  
 Gervat, G.P. 279  
 Giudicelli., J.M. 666  
 Gonda, T. 208  
 Gorbunov, B. 183  
 Grabowski, W.W. 344  
 Grassl, H. 458  
 Greenan, B. 551  
 Gribelin, P. 214  
 Griffin, M. 473  
 Gutelpe, I. 476  
 Gzirishvili, T. 185

Hagen, M. 544  
 Hall, W.D. 88, 100, 353  
 Hallett, J. 22, 28, 180  
 Haman, K.E. 609  
 Hane, C.E. 594  
 Harimaya, T. 190  
 Harrison, K. 180  
 Hauf, T. 626  
 He, G. 103  
 Hegg, D.A. 261  
 Heintzenberg, J. 34, 151, 282  
 Helsdon jr., J.H. 612  
 Hemler, R.S. 94  
 Hertzman, O. 404  
 Herzegh, P.H. 328  
 Heymsfield, A.J. 133, 476, 479,  
   699, 702  
 Heymsfield, G.M. 662  
 Hicks, E. 76, 211, 378  
 Hildebrand, P. 335  
 Hill, T.A. 279, 294  
 Hindman, E.E. 229  
 Hjelmfelt, M. 413, 672  
 Hobbs, P.V. 1, 121, 261, 404,  
   527  
 Hoeller, H. 693  
 Hoff, R.M. 338  
 Hoffmann, H.-E. 175  
 Hong, Y. 597  
 Houze jr., R.A. 702, 705, 708,  
   711  
 Hu, Z. 103  
 Huang, M. 112, 303, 597,  
   615, 621

Huang, S.H. 251  
 Huang, W. 386  
 Huang, Y. 386  
 Hudak, D. 446

Ichikawa, S. 341  
 Ichimura, I. 341  
 Illingworth, A.J. 49, 372  
 Imamdzhanov, H.A. 723  
 Iribarne, J.V. 258  
 Isaac, G.A. 273  
 Isaka, H. 214, 223  
 Ishihara, M. 437, 600  
 Isono, K. 208  
 Iwai, K. 193  
 Iwanami, K. 393

Jacob, D. 458  
 Jaenicke, R. 148  
 Jaeschke, W. 291  
 Jaffrezo, J.-L. 288, 463  
 Jameson, A.R. 328  
 Janc, D. 419  
 Jank, T. 330  
 Jaubert, G. 666  
 Jeck, R. 205  
 Jennings, S.G. 241  
 Jensen, J.B. 40, 538  
 Ji, W. 621  
 Jin, D.-Z. 507  
 Jochum, A.M. 82  
 Joe, P.I. 135, 449, 687  
 Johansson, B. 151  
 Johari, H. 67  
 Johnson, D.B. 375  
 Jones, A. 316

Kadyrov, B.Sh. 723  
 Kajikawa, M. 196  
 Kakutkina, H. 183  
 Kang, T.S. 446  
 Kapoor, R.K. 58  
 Kartsivadze, A.I. 563, 684  
 Keith, W.D. 220  
 Kelly, R.D. 52  
 Kennedy, P.C. 440, 443  
 Kessinger, C. 672  
 Khelaya, E.I. 684  
 Khorguani, V. 185  
 Kikuchi, K. 393, 678  
 Kim, V.M. 158  
 Kinne, St. 133, 488  
 Kins, L. 276  
 Klemp, J.B. 669  
 Knight, C.A. 591  
 Knight, D.J. 527  
 Knight, N.C. 479  
 Knupp, K.R. 717  
 Kobayashi, J. 208

Kolev, I.N. 515  
 Kolev, S.I. 515  
 Kong, F. 615  
 Konishi, H. 188, 416  
 Kopp, F.J. 612, 675  
 Kosarev, A.L. 482  
 Kostadinov, L.A. 515  
 Kraemer, M. 238, 514  
 Kraft, J. 246  
 Kubesh, R.J. 375  
 Kuhn, R. 551  
 Kumai, M. 249  
 Kuo, K.S. 468  
 Kurbatkin, V.P. 723

Lafore, J.P. 100  
 Lamb, D. 306  
 Lang, S.L. 641, 644  
 Latham, J. 73  
 Leaitch, W.R. 273, 338  
 Lee, I.Y. 312  
 Lei, X. 503  
 Lesch, L. 665  
 Lesins, G.B. 560  
 Levi, L. 217  
 Levin, Z. 579  
 Levkov, L. 458  
 Li, Y.-Z. 507  
 Li, Z. 386  
 Lin, N.-H. 232  
 Liou, K.-N. 118, 488  
 Lipps, F.B. 94  
 List, R. 446, 551  
 Liu, G. 541  
 Liu, S. 303  
 Livingston, J.M. 125  
 Lomidze, N.E. 719  
 Lubart, L. 217  
 Lueneburg, E. 154  
 Luepkes, C. 199  
 Lyons, J.H. 121

MacVean, M.K. 425  
 Magradze, G. 166  
 Malinowski, S.P. 609  
 Mallant, R.K.A.M. 333  
 Marks jr., F.D. 708, 711  
 Marsh, A.R.W. 279  
 Marwitz, J.D. 525  
 Matsuo, T. 144, 341, 521  
 Mazin, I.P. 482  
 McGann, B.T. 241  
 Meischner, P. 330, 455  
 Meixner, F.X. 276  
 Meyers, M.P. 347  
 Mitra, S.K. 18  
 Mitzeva, B. 629  
 Mitzuno, H. 521  
 Miyatake, M. 188  
 Molenkamp, C.R. 396

Molnar, K. 566  
 Monhen, V.A. 251  
 Mori, T. 208  
 Mueller, C. 681  
 Mueller, E. 532  
 Mueller, K.P. 276  
 Murakami, M. 144, 521  
 Musil, D.F. 638

Nagamoto, C. 285  
 Nair, S.K. 297  
 Nemesova, I. 422  
 Nevzorov, A.N. 482  
 Nicholls, S. 127, 322, 425  
 Nichols, T.R. 449  
 Nissen, R. 446  
 Nizamuddin, S. 254  
 Noone, K. 34, 282  
 Novosyolov, L.N. 164

Obenland, H. 291  
 Ochs, H.T. 4, 7  
 Ogren, J. 34, 282  
 Okada, K. 341  
 Okudjava, A.M. 563  
 Oraltay, R.G. 22  
 Orville, H.D. 226, 612, 675  
 Ou, S.C. 118

Pal, S. 338  
 Paluch, I.R. 70  
 Pardess, D. 579  
 Parsons, D.B. 669  
 Parungo, F. 285  
 Parvanov, O.P. 515  
 Paschenko, A. 183  
 Pawloska-Mankiewicz, H. 647  
 Penner, I.E. 79  
 Personne, P. 214, 223  
 Peskov, B.E. 719  
 Peters, L.K. 297  
 Pflaum, J.C. 574, 582  
 Pielke, R.A. 359  
 Pitter, R.L. 243  
 Podzimek, J. 202  
 Poellot, M.R. 582  
 Politovich, M.K. 588  
 Pontikis, C. 76, 211, 378  
 Prakash, P. 58  
 Price, C. 579  
 Prodi, F. 557  
 Pruppacher, H.R. 18  
 Puschel, R.F. 125  
 Pyshnov, T. 258

Qian, M.-W. 503

Radke, L.F. 121  
Radziwill, J.M. 606  
Raga, G. 40, 538  
Rasmussen, R.M. 353, 356, 398,  
574  
Rauber, R.M. 350  
Ray, P.S. 641, 644  
Raymond, D.J. 635  
Redder, C.R. 12  
Reinking, R.F. 588  
Reuter, G. 97  
Richard, E. 106  
Rigaud, A. 76, 211, 378  
Rogers, D.C. 369, 659  
Roos, D. 569  
Rosset, R. 319  
Roth, R. 175  
Rotunno, R. 669  
Rudman, S.D. 322  
Russel, P.B. 125  
Rutledge, S.A. 702, 705  
  
Sakakibara, H. 401, 437, 600  
Salavejus, S.S. 585  
Saliashvili, T.N. 563  
Salukvadze, T.G. 684  
Saluzzi, M.E. 434  
Samokhvalov, I.V. 79  
Sassen, K. 473, 659  
Sasyo, Y. 208  
Sato, M. 190  
Saunders, C.P.R. 220  
Sauvageot, H. 378  
Saxena, V.K. 232  
Schemenauer R.S. 135  
Schmied, W. 461  
Scholl, M. 653  
Schroth, A. 154  
Schuetz, L. 238, 514  
Schumann, T. 270  
Seidl, W. 235, 255  
Sengupta, S.K. 468  
Serrano, F. 52  
Shamanaev, V.S. 79  
Shiino, J. 690  
Shimada, W. 188  
Shirooka, R. 678  
Sievers, U. 490  
Simeonov, P. 576  
Simmons, E.L. 322  
Singh, G. 58  
Sinkevich, A.A. 618  
Sirakov, D. 576  
Smith, P.L. 588, 638  
Smolarkiewicz, P.K. 88, 353,  
398, 493  
  
Soerensen, R. 148  
Soo, S.K. 446  
Soulage, R.G. 62  
Spanner, M.A. 125  
Sprenger, U. 461

Stankova, E.N. 618  
Stepanenko, V.D. 618  
Stepanov, A.S. 164  
Stephens, G.L. 115  
Stith, J.L. 588  
Stone, R.L. 410  
Stoyanov, S. 566  
Szekely, Cs. 566  
  
Tabata, A. 401, 437, 600  
Takahashi, T. 9, 535  
Takaya, Y. 85  
Takeda, T. 341, 541  
Tanaka, T. 341  
Tani, K. 188  
Taniguchi, T. 393  
Taylor, G. 67, 300  
Tjernstroem, M. 499  
Tlisov, M.I. 554, 566  
Tokuda, A. 341  
Tomazov, S.T. 161  
Tripoli, G.J. 109, 130, 714  
Tsuboki, K. 407  
Tung, N.P. 446  
Turpeinen, O.M. 656  
  
Uyeda, H. 678  
  
Valero, F.P.J. 133  
Vali, G. 52  
Vatyan, M.R. 719  
Vaughan, H.C. 178  
Verlinde, J. 696  
Vohl, O. 18  
Vukovic, Z. 650  
  
Wacker, U. 532  
Wakahama, G. 9, 362, 407,  
416  
Walcek, C.J. 309  
Waldvogel, A. 270  
Walther, C. 335  
Wang, A.-S. 15, 557  
Wang, P.K. 572  
Wang, X.-L. 507  
Warburton, J.A. 410  
Weisman, M.L. 669  
Weissbluth, M.J. 359, 431  
Welch, R.M. 468  
Wendling, P. 509  
Wesley, D.A. 359  
Westcott, N.E. 632  
Wettlaufer, J. 538  
Willis, P.T. 699  
Wilson, J. 681  
Wobrock, W. 496  
Wrigley, R.C. 125

Xiao, H. 112  
Xu, H. 112. 597, 615, 621  
Xu, W. 386

Yamada, Y. 521  
Yamashita, A. 188  
Yeh, J.D. 383, 714  
Yokoyama, T. 437, 603  
Yu, Q. 466

Zdunkowski, W. 490  
Zeissler, P. 461  
Zhang, J. 389  
Zhao, B. 364  
Zheng, C.R. 507  
Zhou, H. 597  
Ziegler, C.L. 641, 644  
Zinder, B. 270  
Zoltan, Cs. 566  
Zuev, V.E. 79

# P R E F A C E

## RESEARCH ON CLOUDS AND PRECIPITATION: PAST, PRESENT AND FUTURE

Peter V. Hobbs

President, International Commission on Cloud Physics, and Chairman  
International Program Committee for the 10th International Conference on Cloud Physics

It is now thirty-four years since the 1st International Conference on Cloud Physics was held in Switzerland. The 1988 Conference marks the tenth in this series of conferences. On this occasion it is, perhaps, appropriate to glance back to our origins, to reflect on the current situation, and to look to the future.

### 1. EARLY HISTORY\*

Questions concerning the nature of clouds, why it rains, will it rain tomorrow, what is thunder etc., must have been asked by prehistoric humans. Certainly, the ancient Greeks theorized on these matters; Aristotle appears to have known that clouds consist of water, and he speculated on the origins of hail. However, another two thousand years was to pass before it was realized that liquid water evaporates as water vapor and not air.

Chinese writings of the 2nd century B.C. associated the number six with water, and the first recorded observation that snow crystals exhibit hexagonal symmetry was made in China in 135 B.C.. Not until 1611 was the same observation made (by Kepler) in Europe. Correlations between the shapes of snow crystals and meteorological conditions were noted by Martens in 1675. By the 1760's, Wilcke was nucleating snow crystals with idoform and camphor, thereby anticipating artificial cloud seeding by 200 years!

Newton knew that moist air is less dense than dry air, but this concept was not generally understood until the latter half of the 18th century. In 1715 Barlow elaborated on an idea, the origins of which can be traced back to the 10th century, that raindrops form due to larger cloud drops overtaking and colliding with smaller drops.

Hamberger (1743) and Franklin (1749) noted that

---

\* Much of this material is abstracted from "A History of the Theories of Rain" by W. E. K. Middleton (Franklin Watts Inc., New York, 1965). Both Middleton's account, and my own, are biased toward contributions from the western hemisphere.

heating can cause air to rise, although it was not until 1834 that the term convection was introduced by Prout. Le Roy (1752) made great strides in clarifying ideas on dry and moist air and condensation. Du Carla (1780) had the general idea that expansion cools rising air and produces condensation, and, remarkably, he even stated that the precipitation rate is proportional to the rate of ascent. However, it was Erasmus Darwin who first stated clearly the connection between expansion, cooling and condensation (1788). Darwin also extended to the atmosphere Black's ideas on latent heat release, although it was not until the 1830's that its importance in clouds was generally recognized.

The 19th century opened with the first useful classification of clouds by Howard (1803). Cooling and warming of air by expansion and compression were described mathematically by Poisson (1823). Dove (1828) discussed cooling due to orographic ascent and to the upward flow of warm air over colder air.

The middle of the 19th century saw great activity in the studies of tornados, hurricanes and (what were later to be called) cyclones. Redfield (1836) showed that tropical storms are vortices. Espy (1841) put forward the idea that air in large weather systems may converge along a line; an idea that was developed by Loomis (1841). Over half a century was to pass before these ideas were taken up in the Norwegian frontal model of a cyclone.

Espy (1835) noted that latent heat release due to condensation reduces the rate of cooling by expansion of rising air parcels. Maille (1836) estimated the magnitude of this effect; he also calculated the precipitable water in a column and showed it could explain heavy rain. Thomson (later Lord Kelvin) derived analytical expressions for the dry and saturated lapse rates (1862). By 1868 Peslin had produced a clear description of stability and instability in the vertical displacement of air parcels.

The question of cloud droplet growth was tackled in earnest in the latter half of the 19th century. Following Thomson's (1870) theoretical determination of equilibrium vapor pressure as a function of drop size, Reynolds (1877) showed that growth by condensation is too slow to explain the formation of raindrops. By the turn of the century, Lenard (1904) and Defant (1905) had deduced that collisions between droplets play an important role in the growth of raindrops.

As early as 1672, Guericke had hinted at the role of particles in the formation of drops by condensation, but this idea was not confirmed until the elegant experiments of Coulier (1875) and Aitken (1881).

Fahrenheit (1724) noted that ice appeared in a flask of cold water when it was shaken, but it was de Saussure (1783) who first pointed out that water in clouds resists freezing even at low temperatures. The suggestion that hailstones may grow by collecting supercooled drops followed shortly after (Nöllner, 1853; Maille, 1853). Maille also noted that the different layers in hailstones might be due to their recycling in a cloud.

In 1789 Franklin suggested "... much of what is rain, when it occurs at the surface of the earth, might have been snow, when it began its descent ...". But it was not until the 20th century that this conjecture was put on a firm foundation by Wegener (1911), Bergeron (1933) and Findeisen (1938). Bergeron also realized that ice particles from high clouds might grow by collection as they fall through lower clouds (the "seeder-feeder" mechanism), although this idea can be traced back to Renou (1866).

This brief review of the early history of cloud physics research serves to remind us, to paraphrase Newton, that we "... stand on the shoulders of giants".

## 2. THE MODERN ERA

Bergeron marked the beginning of the "modern era" of cloud physics research. During this period the pace of research accelerated enormously, but we are probably too close to it to assess its overall importance. We can, however, obtain an idea of changes in the level and types of research activity by briefly reviewing the contents of the international conferences on cloud physics.

A measure of the growth in the subject is provided by the number of papers at these conferences (Fig. 1). The 1954 Conference consisted of just 20 invited papers. Since then the numbers of papers has increased sharply. At this conference (1988), 376 papers were submitted and 284 accepted. This growth is even more remarkable when it is realized that during this same period cloud physics spawned international conferences in Atmospheric Aerosols and Nucleation, Atmospheric Electricity, Weather Modification and Cloud Modeling.

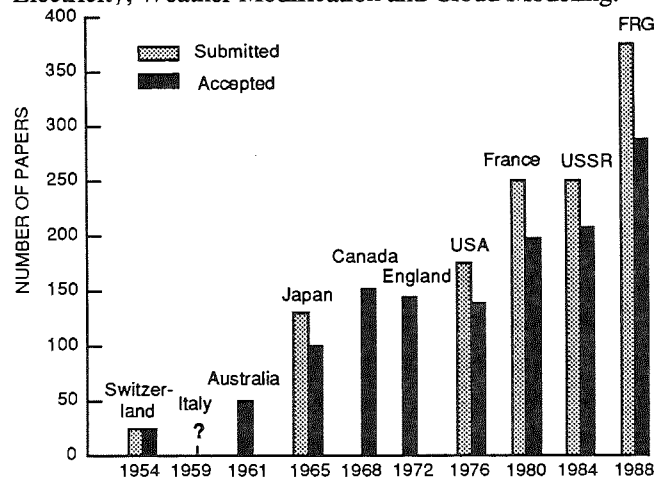


Figure 1. Trends in numbers of papers for the International Cloud Physics Conferences.

Shifts in research emphasis are reflected in the papers presented at the conferences. In the 1968 Conference about 75% of the papers were concerned with cloud microphysics, and the rest with larger-scale processes. In the 1988 Conference about 56% of the papers are concerned with microphysics and 44% with macrophysics. If the papers presented in 1968 are divided into field, laboratory, theoretical and numerical modeling studies, the respective percentages are 36, 33, 23 and 8. The corresponding percentages for the 1988 Conference are 51, 7, 15 and 27. Clearly, in the past 20 years a more reasonable balance has evolved between microphysical and macrophysical studies, and numerical modeling has come on very strongly. Laboratory studies, on the other hand, have fallen off sharply, to what might be less than an optimum level.

Another important development in recent years has been a broadening of the subject. The 1988 Conference contains sessions on clouds and radiation, cloud chemistry and acidic precipitation, boundary-layer processes and satellite studies. At this conference we have assembled a group of scientists with a broader range of interests in clouds than has probably ever before collected in one place.

Yet, despite these signs of significant progress, one might characterize the present period by Dickens' phrase: "... the best of times, ... the worst of times". The best of times, because we have at hand the tools to unravel complex cloud and precipitation processes. The worst of times, perhaps, because we must strive harder than ever before to obtain the resources to pursue these tasks in the face of mounting competition from many other areas of science and from societal needs in general.

### 3. THE FUTURE

The 13th International Conference on Cloud Physics should be held in year 2000. How will the subject have evolved by that time?

My first prediction is that the conference will not be entitled "Cloud Physics". This is a misnomer even now, as we can see from the 1988 Conference which contains many papers that are not well described by this title. For this reason alone, the conference might be called something like "International Conference on Cloud and Precipitation Processes". However, I believe the title will be even broader than this, for the reasons given below.

Wiscombe and Ramanathan (1985) have pointed out that since the 1940's meteorology has been dominated by dynamic and synoptic meteorology, but that it is now moving into an era that requires a multidisciplinary approach involving meteorology, geophysics, chemistry and biology. This realization has culminated in the International Geosphere-Biosphere Program: A Study of Global Change (IGBP), which focuses on cross-disciplinary studies related to changes in the global environment. I anticipate that the concept of the IGBP will dominate atmospheric research for the remainder of this century.

Clouds play a significant role in global change. For example, a few percent increase in low-level global cloud cover, or their optical properties, could offset the warming of the earth due to a doubling in CO<sub>2</sub>. A recent theory proposes that a relatively small change in DMS emissions from phytoplankton in the oceans could affect the optical properties of marine clouds. Studies of the Antarctic ozone hole point to the crucial role played by polar stratospheric clouds. Cloud chemistry and precipitation scavenging contribute significantly to acid

deposition. Clouds affect the vertical distribution of trace species. The effects of clouds are being incorporated into numerical forecasting models. Tropical clouds play a key role in the general circulation of the atmosphere. The list could go on, but the message is clear: cloud studies should form an integral component of the IGBP.

What can we do to meet the challenge of the future?

First, we must look outward from our discipline. To be sure, we must continue to work on unsolved core problems; we must better integrate observational, theoretical and modeling studies and, in particular, we must work on the scale-interaction problem. However, we must give increasing attention to tilling the fertile fields that border our discipline. This latter task will require a broad educational base. Cloud physics evolved as much from classical physics as it did from meteorology, but in the past twenty years it has rightly shifted firmly into meteorology. In the next twenty years it will need to widen even further, to include overlapping areas with chemistry, biology and geophysics. A goal for future researchers might be to have, in addition to a core discipline, at least one interdisciplinary interface.

Predictions are fraught with danger. Perhaps, in the year 2000, the president of the ICCP will amuse the 13th Conference by recalling my crystal-ball gazing.

### 4. ACKNOWLEDGEMENTS

Planning for this conference began four years ago, while the 9th Conference was still in progress. Since then, the planning has increased in pace each year and involved increasing numbers of individuals. Unfortunately, it is not possible for me to list all those that have helped bring the conference to fruition. I must, however, express my sincere thanks to Professor Hans R. Pruppacher, not only for the most efficient way in which he has organized the local and national arrangements, but also for raising funds without which the conference would be much the poorer. It has been a great pleasure to work with him. I also thank the members of the International Program Committee and the National Organizing Committee for their help and support.

The work of these committees is now nearing an end. It remains for the conferees, through their presentations and discussions, to make the 10th Conference a success.

# The Effect of Charge on the Coalescence of Small Precipitation Drops at Terminal Velocity

Harry T. Ochs III, Robert R. Czys and James Q. Feng

Climate and Meteorology Section  
Illinois State Water Survey  
Champaign, Illinois USA

It has long been recognized that charge can affect the results of collisions in streams of drops (Rayleigh, 1879; Goyer, *et al.*, 1960), between drops and a flat water surface (Jayaratne and Mason, 1964), between two drop streams (Park, 1970; Sartor and Abbott, 1972; Brazier-Smith, *et al.*, 1972), and for drops fired at suspended drops (List and Whelpdale, 1969; Whelpdale and List, 1971). We present the first observations of the effect of charge on the coalescence of colliding water drops that were initially falling freely at terminal velocity. Other experiments using uncharged drops show large discrepancies between drop stream or suspended drop results and free fall, terminal velocity results (Beard and Ochs, 1983; Ochs and Beard, 1984; Ochs, *et al.*, 1986). Therefore, it is probable that previous work on charge effects should not be directly applied to cloud situations. The present findings support this contention, because the charge required to induce complete coalescence differs from previous results at similar drop sizes and size ratios by an order of magnitude. The following new features of charged drop interactions were observed: a unique impact angle dividing the coalescence from the non-coalescence region that is independent of charge; a two-order of magnitude range of relative charge between drop bounce and complete charge-induced coalescence; a wide range of charge where a satellite drop occurs with temporary coalescence; and, at higher charge levels, the beginning of charge-induced permanent coalescence at the most grazing collisions.

The range of charges used in this experiment coincide closely with charges observed in nature: about  $1.0 \times 10^{-16}$  C for drops in developing cumulus clouds to about  $1.0 \times 10^{-12}$  C for drops in thunderstorms (Takahashi, 1972). Observations were taken with eight positive charges and three negative charges on the large drop with a constant small drop positive charge for more than 5000 interactions between a  $340 \mu\text{m}$  and a  $190 \mu\text{m}$  radius drop. These drop sizes are typical of drizzle drops or small precipitation drops. Charges of like sign were emphasized since drizzle drops in clouds are likely to have the same polarity (Pruppacher and Klett, 1978).

A unique computer controlled apparatus was developed to permit the study of repetitive isolated pairs of freely falling drops with independently controllable drop charge. The computer operated two drop generators, positioned the drop collisions in the camera field of view, and synchronized camera and strobe

operations. The drop generators used hollow cylindrical piezoelectric transducers that vibrated radially to induce capillary waves on a jet caused by forcing water through a pin hole. The jet broke up into a stream of uniformly sized drops. Most of the drops were highly charged using a cylindrical electrode around the point of jet breakup. These drops were deflected into a gutter as they fell through a strong horizontal electric field. A switching circuit controlled by the computer periodically imposed a pulse on the drop charging voltage. This produced individual drops with lower charge which fell through the horizontal electric field and into the experiment chamber. The charge on the large and small drops was measured frequently and adjustments were made to maintain desired drop charges. Two cameras were used to record the collisions from orthogonal directions in a horizontal plane. Incandescent lamps located behind and  $30^\circ$  above each camera's optical axis illuminated the falling drops and produced streaks on the film. The impact angle for each collision was obtained from the distance separating the streaks.

The examples of streak signatures shown in Fig. 1 are from one orthogonal camera view. When the two drops don't collide the image in Fig. 1a resulted. Coalescence (Fig. 1b) occurred when two falling drops collided, made contact and united to form a single drop. Oscillation of the newly coalesced drop caused the waviness of the streak below the collision-coalescence point. Bounce is shown in Fig. 1c. Temporary coalescence is shown in Fig. 1d and the short streak extending to the right was caused by a satellite drop. An average satellite radius of about  $80 \mu\text{m}$  (about

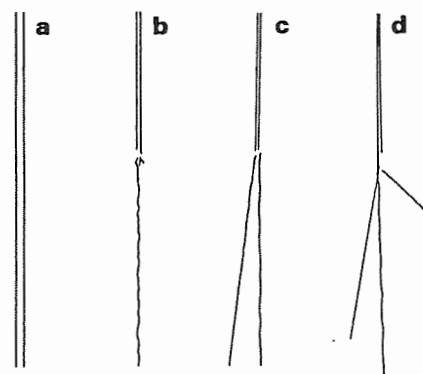


Figure 1. Tracings of streak photography images: (a) miss, (b) coalescence, (c) bounce and (d) temporary coalescence. Each image corresponds to a single frame of film. Examples without the strobe flash were chosen to better illustrate the streak images.

Table 1. Summary of Experiment Parameters.

Experiment	N	R	r	$Q_R$	$Q_r$	$Q_R - Q_r$	$\Phi_c$
		$\mu\text{m}$	$\mu\text{m}$	$\times 10^{-14}$ C	$\times 10^{-14}$ C	$\times 10^{-14}$ C	deg.
1	66	329	193	1.0	-0.1	1.1	44
2	37	340	191	3.9	3.0	0.9	42
3	45	341	193	0.2	2.1	-2.0	44
4	81	342	192	11.0	2.3	8.7	42
5	42	331	186	35.2	1.8	33.4	44
6	77	336	192	41.0	1.7	39.4	44
7	93	340	191	84.4	2.8	81.5	43
8	50	341	197	129.7	3.8	125.4	--
9	160	339	192	208.0	2.9	205.0	--
10	47	339	198	-3.5	2.3	-5.7	40
11	45	338	197	-19.6	2.3	-21.9	42
12	42	351	195	-99.2	3.0	-102.1	44
13	130	341	194	40.1	23.4	16.7	42

7% of the small drop mass) was measured on low intensity strobe exposures superimposed on the streak images.

The parameters used are shown in Table 1. Collision results for the positively charged drops (Runs 2-9) are displayed in Fig. 2 as a function of impact angle and magnitude of difference in mean drop charge. The small drop charge,  $Q_r$ , averaged  $2.5 \times 10^{-14}$  C (with a standard deviation of  $0.5 \times 10^{-14}$  C) while the large drop charge,  $Q_R$ , ranged from  $2.0 \times 10^{-15}$  to  $2.1 \times 10^{-12}$ . We observed an abrupt transition at a critical impact angle of  $43^\circ \pm 1^\circ$  from a coalescence to a non-coalescence region. Collisions occurring for impact angles  $< 43^\circ$  always resulted in coalescence regardless of drop charge. For impact angles  $> 43^\circ$ , the magnitude of the mean relative charge in Fig. 3 must exceed  $1.9 \times 10^{-14}$  C ( $Q_r =$

$2.1 \times 10^{-14}$  and  $Q_R = 2.0 \times 10^{-15}$  for the experiment in which this minimum was observed) before charge influenced the result of collisions. Once a relative charge of about  $3.0 \times 10^{-13}$  C was exceeded bounce was completely suppressed and temporary coalescence resulted. Interestingly, the probability of satellite production decreased with further increases in relative charge. At higher charge, coalescence was induced when the relative charge exceeded about  $8.0 \times 10^{-13}$  C. Fig. 3 shows that coalescence begins at large impact angles (about  $90^\circ$ ) and "creeps in" as charge increases. Permanent coalescence at all impact angles resulted when the relative charge exceeds  $2.0 \times 10^{-12}$  C. The results in Fig. 2 show that coalescence is promoted by charge even though both drops carry positive charge.

Three runs were conducted using about the same mean charge on the small drop as in Runs 2-9, but with negative charge on the large drop. The collision results using oppositely charged drops were found to be generally consistent with the results using positively charged drops. Runs 10 thru 12 have the same critical impact angle, fit the overall trend for bounce to be replaced initially by temporary coalescence and do not contradict the tendency for charge induced coalescence to begin for the most glancing collisions. The only inconsistency found in the data was in Run 12 which showed satellite production when the data for positively charged drops suggested none.

Run 1 was conducted with minimum charge on each drop. The results of this run clearly indicated that the collision results for "uncharged" drops are no different from the results for weakly charged drops.

Finally, Run 13 was conducted with an increased charge on the small drop and intermediate charge on the large drop to provide further information on using  $|Q_R - Q_r|$  to generalize the results. From Table 1  $|Q_R - Q_r|$  for Run 13 falls in a region where the data suggest a transition from mostly bounce to mostly temporary

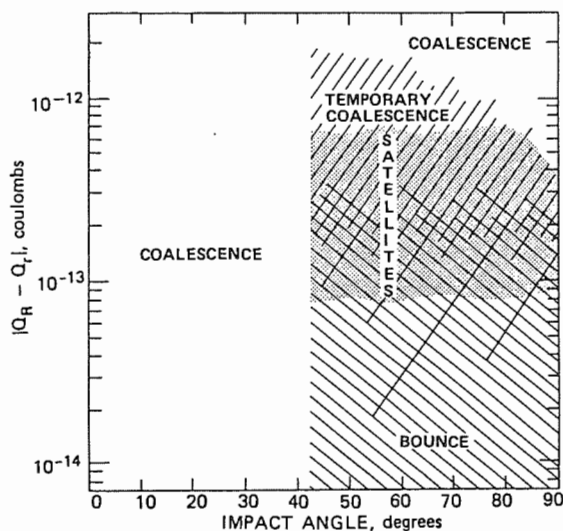


Figure 2. Collision outcome as a function of impact angle and mean relative charge. The charge on the small drop was fixed at  $2.5 \times 10^{-14}$  C and the large drop charge varied from  $1.5 \times 10^{-15}$  to  $2.1 \times 10^{-12}$  C in eight irregular steps. Coalescence occurs in the clear area. The hatched area sloping down from left to right indicates the area where bouncing occurs. The hatched area sloping up from left to right delineates the region of temporary coalescence. The stippled area covers the drop charges and impact angles for which satellite production is likely if temporary coalescence occurs. The concentration of hatched area overlap suggests the probability of bounce and temporary coalescence in the transition region.

coalescence with a satellite. Data from Run 13 had a critical impact angle of  $43^\circ$  and had a mixture of temporary coalescence and bounce that could be expected from the trends in the data from Runs 4, 5 and 11.

Previous laboratory investigations using suspended drops or drop streams have determined threshold relative charges for complete coalescence that have ranged over three orders of magnitude. A charge of  $3.0 \times 10^{-14}$  C caused a stream of drops to coalesce with a flat water surface (Jayaratne and Mason, 1964). Drops in continuous streams have been induced to coalesce by charges of about  $2.0 \times 10^{-13}$  C (Park, 1970; Sartor and Abbott, 1972) and  $4.0 \times 10^{-11}$  C (Brazier-Smith, *et al.*, 1972). A charge of  $3.0 \times 10^{-12}$  C (List and Whelpdale, 1969) and  $3.0 \times 10^{-11}$  C (Whelpdale and List, 1971) caused coalescence in suspended drop experiments. The first value is close to ours, however, their drop sizes and size ratios (0.07) are significantly different and thus comparisons are probably invalid. Charge-induced temporary coalescence has been reported (Jayaratne and Mason, 1964; Park, 1970; Whelpdale and List, 1971) but satellites have not. The wide range of charge required to induce coalescence in previous experiments ( $3\text{-}4000 \times 10^{-14}$  C) suggests that data on charge effects cannot be reliably extrapolated to drop interactions in clouds unless the conditions of the natural interactions are well simulated. This conclusion is supported by measurements using uncharged drops at terminal velocity (Beard and Ochs, 1983; Ochs and Beard, 1984; Ochs, *et al.*, 1986) in which results were found to differ significantly from drop stream and suspended drop experiments. The wide range of previous results from supported drops and drop streams and our unique ability to study drop interactions under free fall at terminal velocity give impetus to further research.

Our new data demonstrate that effects of charge on drop coalescence are significantly more complicated than had been previously thought. Several new phenomena were uncovered that remain unexplained. Of particular interest is the constant critical impact angle dividing permanent coalescence from bounce or temporary coalescence. Since drops colliding at angles  $< 43^\circ$  coalesce, one might expect that drops colliding at angles just  $> 43^\circ$  almost coalesce. Using this reasoning, as charge increases, coalescence should be induced for these collisions first, and the critical angle should steadily increase with increasing charge until permanent coalescence finally occurs for the largest impact angle. Figure 2 shows this logic to be incorrect. In addition, Fig. 2 shows that the lowest charge-induced permanent coalescence occurs at the largest impact angles where the drops follow grazing trajectories. These collisions have the least interaction time and, after coalescence, the largest angular momentum which should be most conducive to temporary coalescence (Brazier-Smith, *et al.*,

1972). Another interesting aspect of our results is that satellites form at the intermediate relative charges required for temporary coalescence and are suppressed at higher relative charges. Although more refined experiments may help to explain these observations, an adequate understanding will probably require complex modeling of coalescing drops.

Our data indicates that the outcome of drop collisions varies considerably over the natural range of electrical environment found in clouds. Such variability suggests important consequences for precipitation evolution. Traditionally, for lack of better information, calculations of precipitation drop spectra have assumed that every collision results in coalescence (Berry and Reinhardt, 1974). Recent experimental results suggest that this assumption is invalid for weakly charged drops since many collisions result in bounce rather than coalescence (Ochs, *et al.*, 1986). Comparisons between the computed evolution of precipitation utilizing the traditional assumption of coalescence and a more realistic assumption including drop bounce, have shown significant differences in the concentration at which large precipitation drops are produced (Ochs and Beard, 1985). Thus we expect that a transition between bounce and coalescence induced by charge will significantly impact subsequent precipitation development. The observations presented here indicate that, in addition, moderate amounts of charge will induce satellites which, in turn, can serve as embryos for new precipitation drops. Thus the electrical state of the cloud can influence the subsequent evolution of precipitation.

*Acknowledgement.* This research was supported by the National Science Foundation under grant NSFATM 8314072 and NSFATM 8601549.

## References

- Beard, K. V.; Ochs, H. T.: *J. Atmos. Sci.* **40** (1983) 146-153.  
Berry, E. X.; Reinhardt, R. L.: *J. Atmos. Sci.* **31** (1974) 1814-1831, 2118-2135.  
Brazier-Smith, P. R.; Jennings, S. G.; Latham, J.: *Proc. Roy. Soc. London* **A326** (1972) 393-408.  
Goyer, G. G.; McDonald, J. E.; Baer, F.; Braham, R. R.: *J. Meteor.* **17** (1960) 442-445.  
Jayaratne, O. W.; Mason, B. J.: *Proc. Roy. Soc. London* **A280** (1964) 545-565.  
List, R.; Whelpdale, D. M.: *J. Atmos. Sci.* **26** (1969) 305-308.  
Ochs, H. T.; Beard, K. V.: *J. Atmos. Sci.* **40** (1984) 863-867.  
Ochs, H. T.; Beard, K. V.: *J. Atmos. Sci.* **42** (1985) 1451-1454.  
Ochs, H. T.; Czys, R. R.; Beard, K. V.: *J. Atmos. Sci.* **43** (1986) 225-232.  
Park, R. W.: Ph.D. Thesis, University of Wisconsin (1970) 108-111.  
Pruppacher, H. R.; Klett, J. D.: Reidel (1978) 714 pp..  
Rayleigh, Lord: *Proc. Roy. Soc. London* **28** (1879) 406-409.  
Sartor, J. D.; Abbott, C. E.: *J. Rech. Atmos.* **6** (1972) 479-493.  
Takahashi, T.: *J. Geophys. Res.* **77** (1972) 3869-3878.  
Whelpdale, D. M.; List, R.: *J. Geophys. Res.* **76** (1971) 2836-2856.

# WAKE-EXCITED RAINDROP OSCILLATIONS

Kenneth V. Beard and Harry T. Ochs

Climate and Meteorology Section, Illinois State Water Survey  
2204 Griffith Drive, Champaign, Illinois 61820

## 1. INTRODUCTION

The notion that raindrop oscillations can be excited by eddies detaching from the drop originated with Gunn (1949) who postulated that the lateral drift behavior of 1 mm diameter drops might be caused by a mechanical distortion at resonance between the eddy shedding frequency and the oscillation frequency. In spite of the wide acceptance of this hypothesis as fact, the resonance phenomenon had not been observed. The major difficulty in studying wake-excited oscillations for water drops falling in air is the coincidental drift behavior; such drops cannot be contained within a wind tunnel or an acceleration column. We designed a special experiment to determine the effect of wake forcing on drop shape under free-fall conditions. The experimental approach minimized the lateral drift problem by generating drops at terminal velocity in still air whereby wake-excited oscillations were investigated over relatively short distances.

## 2. METHOD

Details of the design of our one-story experiment for measuring the axis ratio of small raindrops are given in Fig. 1. The upper third of equipment is the system for producing isolated, uniform drops (consisting of pressurized water supply, drop generator assembly, charging electrode, electrostatic deflection chamber and PC controls). The lower 2 chambers are for measuring drop velocity using a cathetometer and strobe (dark-field), and for bright-field photography drop silhouettes. The fall columns that extend the generator to camera distance from 1.5 to 2.5 m are not shown. The chambers and water reservoir are on separate platforms to isolate the experiment from vibrations. The camera, cathetometer and strobes are supported by a metal frame around the experiment that rests on the floor.

## 3. RESULTS

The major phase of our experimentation on wake forcing has been completed with results that are summarized by Fig. 2 where the axis ratio for small raindrops is given as a function of drop diameter. For the smaller drops ( $d \leq 1$  mm) our observations of axis ratios agree well with the perturbation theory (Pruppacher and Pitter, 1971) based on the numerical pressure

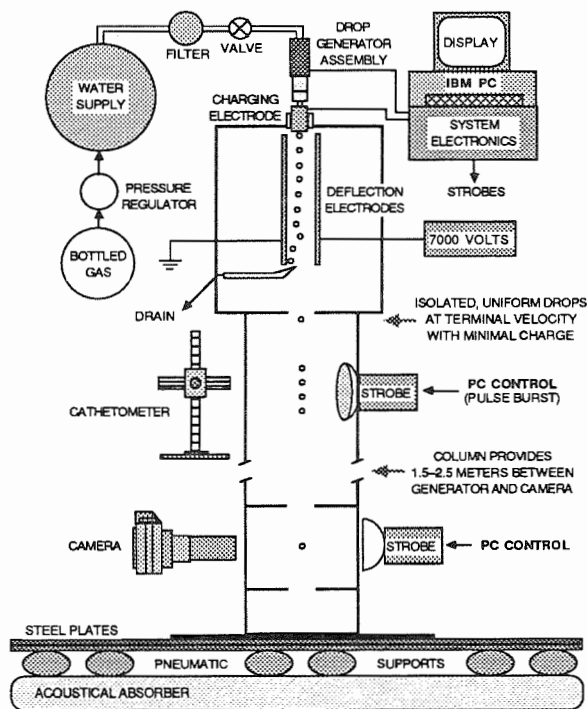


Fig. 1. Diagram of experimental apparatus.

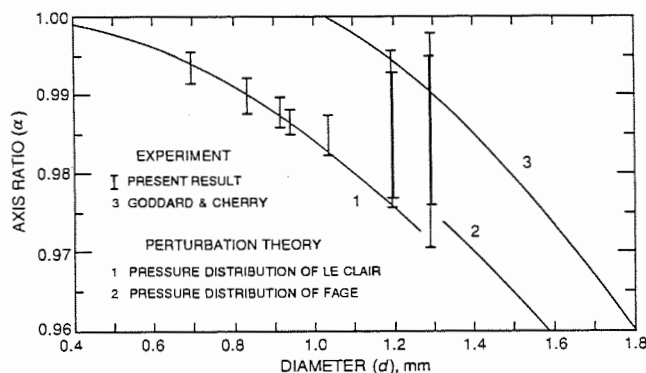


Fig. 2. Axis ratio as a function of raindrop diameter. Data are shown from present experiment as 95% confidence intervals for the mean axis ratio for smaller drops without oscillations ( $d = 0.7-1.03$  mm), and two standard deviations for axis ratios for larger drops with oscillations ( $d = 1.2-1.3$  mm).

distributions for steady state flow around a sphere. Above  $d = 1$  mm the axis ratios scatter *above* the theoretical curve. [Note: the data near  $d = 1.2$  and  $1.3$  mm are based on 58 observations of axis ratios.] We discovered that this one-sided scatter above the equilibrium axis ratios is consistent with oscillations only for the transverse mode of the two lower harmonics (frequencies). We also found that the transverse mode was the only oscillation response matching the forcing pattern expected from pressure changes as eddies detach from alternate sides of the upper pole.

The result of Goddard and Cherry (1984), shown as curve 3, is based on  $Z_{DR}$  measurements in rain, using the Chilbolton (UK) high resolution ( $1/4^\circ$  beam,  $0.5 \mu\text{s}$  pulse) dual-polarization radar and measurements of raindrops sizes using distrometers. The axis ratios given by curve 3 were used to rectify calculated values of  $Z_{DR}$  from the raindrop size distributions with the measured values of  $Z_{DR}$ . It seems plausible that raindrop oscillations of the type observed in our experiment might have been responsible for the shift in axis ratio, especially if oscillations also occurred at larger sizes.

It is clear from our experimental results that we have verified the long-standing hypothesis—*small raindrops oscillate because of resonant interaction with eddy shedding*—but for larger sizes, and possibly higher harmonics, than originally proposed by Gunn (1949). We plan to make additional measurements to extend the axis ratio measurements to about  $d = 1.5$  mm using the present apparatus [Experiments for larger drops will require a multi-story experiment.] Measurements will also be made near  $d = 1.1$  mm to help establish the transition size for resonant oscillations. We also plan to make frequency measurements to distinguish between the two possible harmonics using streak photographs of refracted and reflected light similar to the method shown in Ochs *et al.* (1986).

#### 4. ACKNOWLEDGMENTS

This material is based upon work supported by the National Science Foundation under Grants ATM84-19490 and ATM86-01549. Any opinions, findings, and conclusions or recommendations expressed in this material are those of the authors and do not necessarily reflect the views of the National Science Foundation.

#### 5. REFERENCES

- Goddard, J. W. F., and S. M. Cherry, 1984, The ability of dual-polarization radar (copolar linear) to predict rainfall rate and microwave attenuation. *Radio Sci.*, *19*, 201-208.
- Gunn, R., 1949: Mechanical resonance in freely falling drops. *J. Geophys. Res.*, *54*, 383-385.
- Ochs, H. T., R. R. Czys, and K. V. Beard, 1986: Laboratory measurements of coalescence efficiencies for small precipitation drops. *J. Atmos. Sci.*, *43*, 225-232.
- Pruppacher, H. R., and R. L. Pitter, 1971: A semi-empirical determination of the shape of cloud and raindrops. *J. Atmos. Sci.*, *28*, 86-94.

TEMPORAL VARIATIONS OF SNOW CRYSTAL GROWTH PARAMETERS

Tsuneya Takahashi\*, Norihiko Fukuta\*\*, Tatsuo Endoh\* and Gorow Wakahama\*

\* The Institute of Low Temp. Sci., Hokkaido Univ., Sapporo, 060 Japan

\*\* Dept. of Meteor., Univ. of Utah, Salt Lake City, Utah 84112, U.S.A.

1. INTRODUCTION

Accurate growth behavior of free-falling snow crystals reproduced under clearly controlled laboratory conditions is indispensable not only for studying snowfall mechanisms but also for planning cloud seeding and assessing the result.

Although there exists some information in the literature on relations between snow crystal growth parameters such as crystal masses, dimensions and velocities, temporal variations of these parameters are not sufficient (Fukuta, 1969; Ryan et al., 1976). Fukuta et al. (1982) succeeded in suspending and growing a snow crystal for 10 min using a newly devised super-cooled cloud tunnel which applied an aerodynamical mechanism for horizontal stability and de-

termined crystal growth parameters. Fukuta et al. (1984) experimentally showed that the isometric crystals grown around  $-10^{\circ}\text{C}$  have fast falling velocities and a tendency to develop appendages and become graupel.

In this paper, we shall report the results of measurements on temporal variations of snow crystal growth parameters by (1) vapor diffusion under water saturation and (2) riming around  $-10^{\circ}\text{C}$ . The present study was carried out using the improved version of the tunnel; the growth time in our measurements was up to 30 min.

2. RESULTS AND DISCUSSION

2-1 TEMPORAL VARIATIONS OF GROWTH PARAMETERS BY VAPOR DIFFUSION UNDER WATER SATURATION

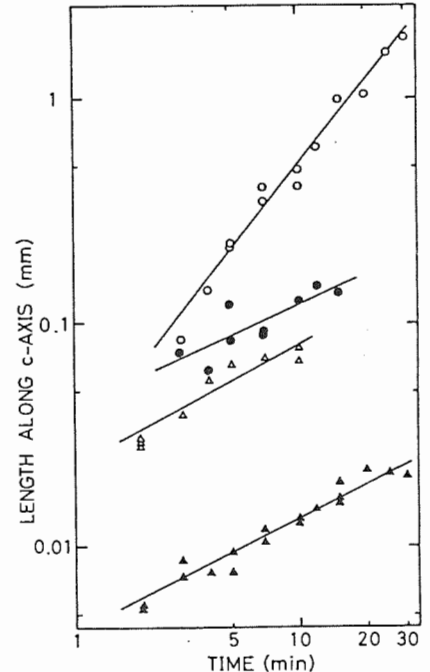
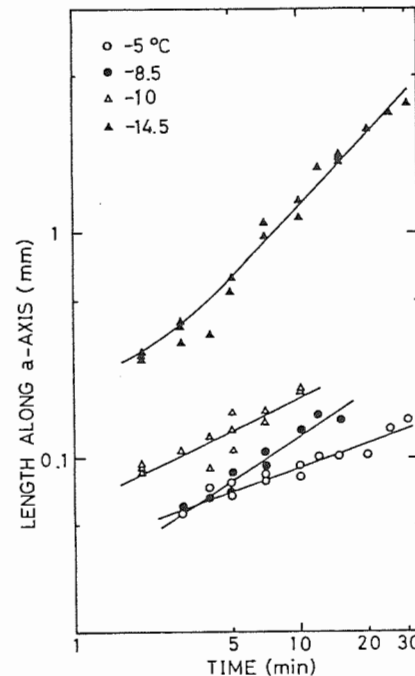
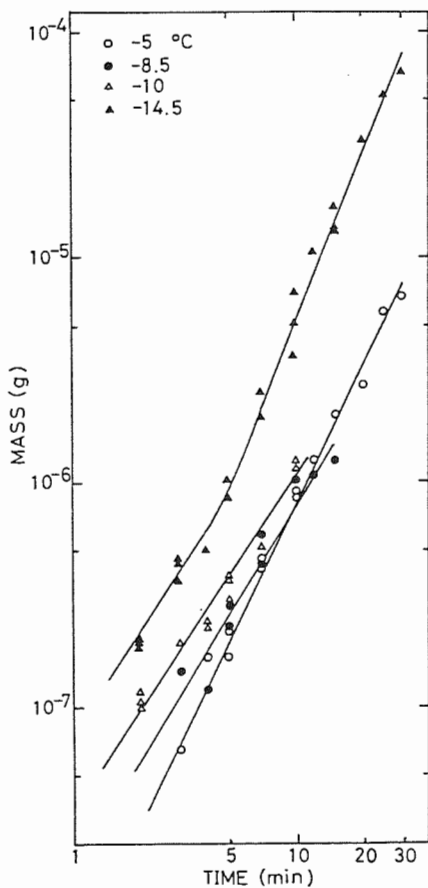


Fig. 2 Temporal variations of crystal dimensions.

Fig. 1 Temporal variations of crystal masses.

The observed crystal habits were needles at  $-5^{\circ}\text{C}$ , columns at  $-8.5^{\circ}\text{C}$  and double plates at  $-10^{\circ}\text{C}$ . At  $-14.5^{\circ}\text{C}$ , the crystal shape changed from sector to dendrite after 5 min of growth. At  $-8.5$  and  $-10^{\circ}\text{C}$ , the crystal shapes were isometric.

Figure 1 shows temporal variations of crystal masses. The slopes of isometric crystals were approximately Maxwellian value of 1.5. Those at  $-5$  and  $-14.5^{\circ}\text{C}$  were 2.0 and 1.6 (growth time  $< 5$  min) to 2.4 (growth time  $> 5$  min), respectively. Water vapor was deposited effectively on the dendrites and needles compared with plates and columns. Thus, the masses at  $-5^{\circ}\text{C}$  became greater than those at  $-8.5^{\circ}\text{C}$  after 10 min of growth.

Figure 2 shows temporal variations of crystal dimensions. At  $-8.5$  and  $-10^{\circ}\text{C}$ ,  $2a$  and  $c$  were approximately proportional to  $t^{0.5}$  respectively. Those relations can be explained by solving the vapor diffusion equation around a crystal face spreading out concentrically. When side stretching occurred, i.e. needles and dendrites grew,  $a \propto t^{0.36}$ ,  $c \propto t^{1.26}$  and  $a \propto t^{0.93}$ ,  $c \propto t^{0.51}$ , respectively.

Next, we discuss the ventilation factors ( $f_v$ ) of needles and dendrites (see Fig. 3).  $f_v$  was obtained using the following mass growth equation:

$$f_v = (dm/dt)(A+B)/4\pi C(S_i - 1)$$

where  $m$  is the crystal mass,  $C$  the crystal shape factor,  $S_i$  the ambient saturation ratio with respect to ice,  $A$  the heat conduction term and  $B$  the vapor diffusion term.  $dm/dt = (d \log m/d \log t)(m/t)$ :  $d \log m/d \log t$  was obtained using Fig. 1 and  $m/t$  the experimental values.  $f_v$  was underestimated to be less than 1 in the early growth stage because the shape factors calculated for prolate or oblate spheroids having the same maximum dimensions were a little large than those of the real crystals (McDonald, 1963). The ventilation effect became noticeable after the growth time of 5 min in case of dendrites. On the other hand, it was not evident in case of needles. These results were probably related with the experimental fact that dendrites grow only over sev-

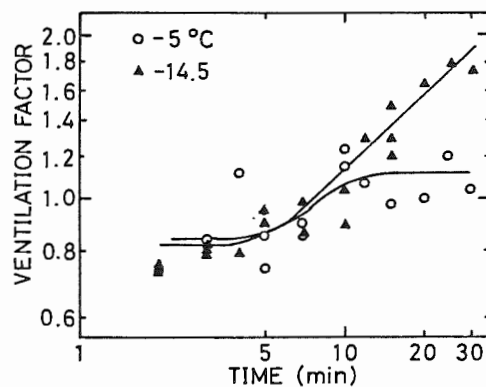


Fig. 3 Temporal variations of ventilation factors at  $-5$  and  $-14.5^{\circ}\text{C}$ .

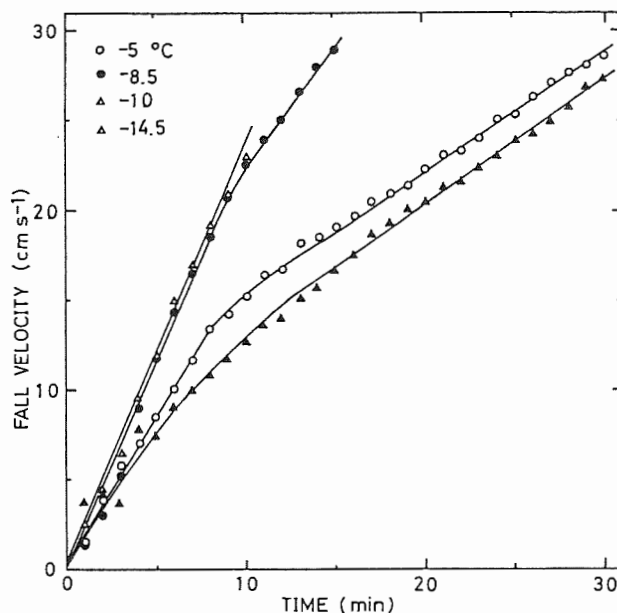


Fig. 4 Temporal variations of crystal fall velocities.

eral percents of the supersaturation with respect to water, although needles develop even under water saturation in the static chamber (Kobayashi, 1961). That is, dendrites grew due to the increased apparent vapor density at the crystal edges by the ventilation effect; this result was similar to Keller and Hallett's (1982) result under the forced ventilation.

Figure 4 shows temporal variations of crystal fall velocities. The relations can be represented by a straight line at  $-10^{\circ}\text{C}$ , two straight lines at  $-5$  and  $-8.5^{\circ}\text{C}$  and a convex curve and a straight line at  $-14.5^{\circ}\text{C}$ . The relation that fall velocity became constant when a dendrite grew beyond 1 mm in diameter (Nakaya and Terada, 1935), was not observed.

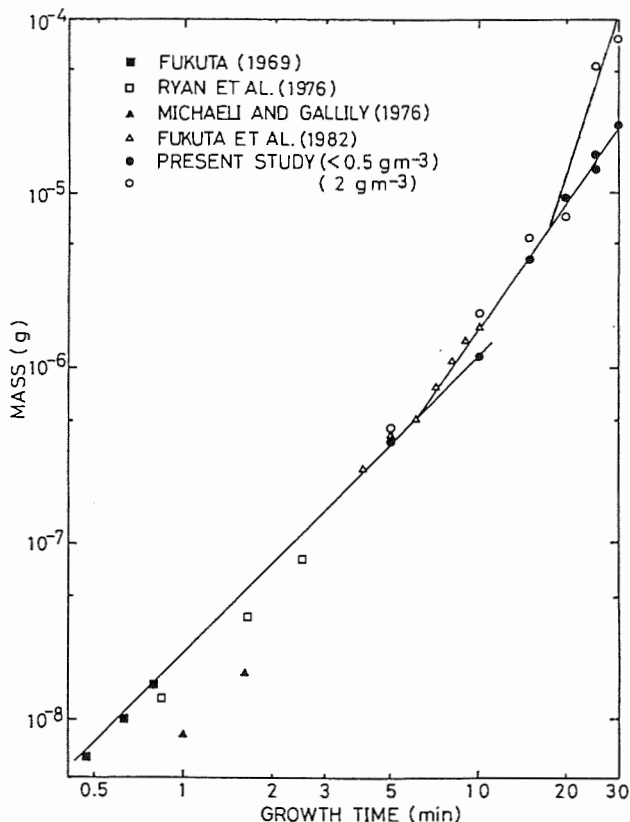


Fig. 5 Temporal variation of crystal masses at  $-10^{\circ}\text{C}$ .

#### PARAMETERS BY RIMING AROUND $-10^{\circ}\text{C}$

Temporal variation of crystal masses for  $-10^{\circ}\text{C}$  on the liquid water content below  $0.5 \text{ g m}^{-3}$  and of  $2 \text{ g m}^{-3}$  was plotted in Fig. 5. The figure also gives the results obtained by Fukuta (1969), Ryan et al. (1976), Michaeli and Gallily (1976) and Fukuta et al. (1982). The variation was represented by three stages:

Stage I: Vapor diffusional growth stage  
( $d \log m / d \log t = 1.6$ )

Stage II: Transitional growth stage  
( $d \log m / d \log t = 2.3$ )

Stage III: Graupel growth stage  
( $d \log m / d \log t = 6.2$ )

In stage III, the slope was nearly equal to the theoretical value of graupel growth, 6, obtained by Fukuta (1980). The particle shape was nearly spherical: this was probably indication of particle rotation. In stage II, droplets were captured only on the edges of crystal surfaces perpendicular to flow. In stage I and III, the particles followed Stokes' law and Newton's law of resistance, respectively.

**ACKNOWLEDGMENTS** This work was partially supported by the Division of Atmospheric Sciences, National Science Foundation under Grant ATM-82-18966 and Scientific Research Funds, Japan Ministry of Education under Grant 61020001.

#### REFERENCES

- Fukuta, N.: Experimental studies on the growth of small ice crystals. *J. Atmos. Sci.* 26 (1969), 522-531.
- \_\_\_: Development of fast falling ice crystals in clouds at  $-10^{\circ}\text{C}$  and its consequence in ice phase processes. *Proc. 8th. Internat. Conf. on Cloud Phys.* (1980), 97-100.
- \_\_\_, M. W. Kowa and N. H. Gong: Determination of ice crystal growth parameters in a new supercooled cloud tunnel. *Preprints Conf. on Cloud Phys.* (1982), 325-328.
- \_\_\_, N. H. Gong and A. S. Wang: A microphysical origin of graupel and hail. *Proc. 9th Internat. Conf. on Cloud Phys.* (1984), 257-260.
- Keller, V. W. and J. Hallett: Influence of air velocity on the habit of ice crystal growth from the vapor. *J. Crystal Growth* 60 (1982), 91-106.
- Kobayashi, T.: The growth of snow crystals at low supersaturations. *Phil. Mag.* 6 (1961), 1363-1370.
- McDonald, J. E.: Use of the electrostatic analogy in studies of ice crystal growth. *Z. Angew. Math. Phys.* 14 (1963), 610-619.
- Michaeli, G. and I. Gallily: Growth rates of freely falling ice crystals. *Nature* 259 (1976), 110.
- Nakaya, U. and T. Terada: Simultaneous observations of the mass, falling velocity and form of individual snow crystals. *J. Fac. Sci., Hokkaido, Univ. Ser. II*, 1 (1935), 191-201.
- Ryan, B. F., E. R. Wishart and D. E. Shaw: The growth rates and densities of ice crystals between  $-3^{\circ}\text{C}$  and  $-21^{\circ}\text{C}$ . *J. Atmos. Sci.* 33 (1976), 842-850.

C.R. Redder and N. Fukuta

Department of Meteorology, University of Utah  
Salt Lake City, Utah 84112, U.S.A.

1. INTRODUCTION

Microphysical behaviors of ice crystals growing in supercooled clouds are an indispensable knowledge to understand subsequent ice phase processes. Existing theories are limited in their applicable ranges and need to be verified with experimental data. Using a unique, vertical, supercooled cloud tunnel, we have been measuring microphysical parameters of ice crystal growth. By comparing the cloud tunnel data (Fukuta et al., 1979; Kowa, 1981; Gong and Fukuta, 1985; Takahashi and Fukuta, to be published) and others (Fukuta, 1969; Ryan et al., 1976) with existing theories of ice crystal growth, we have recently deduced empirical expressions as a function of time up to 30 min at different temperatures in the range from -4 to -20°C, suitable for use in modeling and analysis. The expressions preserve the functional styles while being made to best match the experimental data. This paper reports the results.

2. EMPIRICAL EQUATIONS

When a small particle grows in a supersaturated environment, it is known that accommodation coefficients for mass and heat exchanges play an important role (diffusion-kinetic equation, Fukuta and Walter, 1970). For a spherical ice crystal, the mass may be expressed as

$$m = m_0 [(1 + C_{m1}t)^{1/2} - 1]^3, \quad (1)$$

where

$$m_0 = \frac{\pi \rho_i}{3} \left(\frac{C_1}{C_2}\right)^3,$$

$$C_{m1} = \frac{4C_2}{C_1^2},$$

$$C_1 = \frac{\rho_i}{(S-1)} \left( \frac{L^2 \alpha}{KR_V T_\infty^2} + \frac{l_\gamma}{D \rho_{\infty, \text{sat}}} \right),$$

$$C_2 = \frac{\rho_i}{2(S-1)} \left( \frac{L^2}{KR_V T_\infty^2} + \frac{1}{D \rho_{\infty, \text{sat}}} \right),$$

$$l_\alpha = \frac{(2 - \alpha)K(2\pi R_a T)^{1/2}}{2\alpha p(c_v + R_a/2)},$$

$$l_\gamma = \frac{(2 - \gamma)D}{2\gamma} \left(\frac{2\pi}{R_V T_\infty}\right)^{1/2},$$

and  $t$  the time,  $\rho_i$  the density of ice,  $S$  the saturation ratio of the environment with respect to ice,  $L$  the latent heat of deposition per unit mass,  $K$  the thermal conductivity of air,  $R_V$  and  $R_a$  the specific gas constant for water vapor and air, respectively,  $T_\infty$  and  $\rho_{\infty, \text{sat}}$  the absolute temperature and the saturation vapor density in the environment,  $p$  the pressure,  $c_v$  the specific heat at constant volume,  $D$  the diffusivity of water vapor in air,  $\alpha$  the thermal accommodation coefficient of air and  $\gamma$  the deposition coefficient of water vapor.

Equation (1) gives  $m \propto t^3$  when  $t \rightarrow 0$  which is the mass increase under free-molecular flows, and  $m \propto t^{1.5}$  when  $t \rightarrow \infty$ , which is the growth condition of the Maxwellian theory. When the crystal grows under the influences of coexisting supercooled cloud droplets and the fall, additional effects of fog vapor field, ventilation and riming have to be considered. Experimental data for long growth period (Gong and Fukuta, 1985; Takahashi and Fukuta, to be published) show that the exponent of  $t$  increases towards 6 (Fukuta, 1980), which is the ideal case of graupel and hail growth. Then raising the value of the exponent to the half way to accommodate the above effects except for the graupel and hail process, equation (1) may be modified to

$$m = m'_0 [(1 + C_{m1}t)^{1/2} - 1] + C_{m2}t^3, \quad (2)$$

where  $m'_0$  is equivalent to  $m_0$  but includes additional effects such as fog and ventilation, and  $C_{m2}$  a constant to be determined empirically.

For ice crystals whose shapes are nearly independent of time, the diameter,  $2a$ , and the  $c$ -axial length,  $c$ , may be expressed in a manner similar to equation (2). However, for very short growth time zone, data are scarce and it does not affect the behavior of ice crystal growth in the long time zone. Therefore, we ignore the former or the diffusion-kinetic effect dominated zone caused by thermal accommodation and deposition coefficients in the corresponding free molecular transportation. Then, we can write

$$2a = C_{a1}t^{1/2} + C_{a2}t, \quad (3)$$

Table 1. Constants for empirical equations of m, 2a, c and w determined from experimental data.

T	m' <sub>0</sub>	C <sub>m1</sub>	C <sub>m2</sub>	C <sub>a1</sub>	C <sub>a2</sub>	C <sub>c1</sub>	C <sub>c2</sub>	w <sub>0</sub>	C <sub>w1</sub>
°C	μg	s <sup>-1</sup>	μg/s <sup>3</sup>	mm/s <sup>1/2</sup>	mm/s	mm/s <sup>1/2</sup>	mm/s	cm/s	s <sup>-1</sup>
-4	6.22e-4	1.78e-1	5.35e-10	2.94e-3	2.42e-5	1.77e-3	3.30e-4	8.88e0	7.76e-3
-5	3.99e-3	9.10e-2	6.85e-10	2.88e-3	3.52e-5	1.49e-3	9.39e-4	5.23e0	1.46e-2
-6	2.22e-4	4.85e-1	1.71e-9	2.84e-3	4.65e-5	2.24e-3	9.03e-4	6.40e0	1.21e-2
-7	8.58e-5	8.62e-1	1.62e-9	2.69e-3	6.91e-5	5.27e-3	4.24e-4	1.98e1	3.75e-3
-8	1.70e-4	5.60e-1	1.89e-9	2.16e-3	1.45e-4	6.48e-3	1.34e-4	5.68e1	1.35e-3
-9	2.86e-4	4.30e-1	2.52e-9	1.96e-3	2.35e-4	5.21e-3	9.29e-5	5.98e1	1.44e-3
-10	2.25e-4	5.32e-1	3.06e-9	2.33e-3	3.00e-4	4.05e-3	6.72e-5	2.38e1	4.39e-3
-11	7.25e-5	1.19e0	2.82e-9	4.00e-3	3.24e-4	2.70e-3	5.77e-5	1.37e1	8.37e-3
-12	4.59e-5	1.76e0	2.96e-9	5.40e-3	4.20e-4	2.17e-3	3.33e-5	7.22e0	1.68e-2
-13	8.06e-5	1.42e0	5.05e-9	5.44e-3	8.41e-4	1.70e-3	1.01e-5	2.26e0	6.17e-2
-14	5.03e-6	8.98e0	1.25e-8	1.58e-3	1.84e-3	1.54e-3	1.93e-6	7.98e-1	2.19e-1
-15	3.46e-4	7.28e-1	1.62e-8	4.32e-4	2.32e-3	1.40e-3	3.74e-6	3.97e-1	5.44e-1
-16	9.16e-5	1.57e0	5.80e-9	6.89e-3	1.33e-3	1.40e-3	5.20e-6	3.95e-1	5.75e-1
-17	1.31e-6	2.18e1	1.71e-9	1.08e-2	4.74e-4	1.64e-3	1.74e-5	9.30e-1	1.99e-1
-18	2.89e-8	2.54e2	1.36e-9	9.21e-3	3.37e-4	3.26e-3	6.92e-5	1.56e0	1.06e-1
-19	3.72e-9	9.97e2	1.30e-9	7.07e-3	3.20e-4	5.98e-3	3.54e-4	2.77e0	4.98e-2
-20	1.84e-4	8.73e-1	1.81e-9	5.46e-3	3.68e-4	4.79e-3	5.63e-4	4.25e0	2.81e-2

$$c = C_{c1}t^{1/2} + C_{c2}t, \quad (4)$$

where C<sub>a1</sub>, C<sub>a2</sub>, C<sub>c1</sub>, and C<sub>c2</sub> are constants to be determined by fitting these functions to experimental data.

Equations (2) through (4) give apparent density of the crystals. The density values thus obtained create no serious inconsistencies.

For relatively small crystals, combination of the Maxwellian theory of growth and the Stokes law of fall velocity for a spherical ice gives the fall velocity  $w \propto t$ . Whereas, for graupel growth combined with Newton's parabolic law of terminal velocity under turbulent resistance also leads to  $w \propto t$  (Fukuta, 1980). However, between these two extremes, there exists ice crystal shape enhancing zone mainly due to the ventilation effect where the fall velocity development is expected to be slower. Towards the end of this zone, riming will become more and more noticeable. For this zone before strong riming to take place, we may describe

$$w = w_0[(1 + C_{w1}t)^{2/3} - 1], \quad (5)$$

where w<sub>0</sub> and C<sub>w1</sub> are empirical constants to be determined from the experimental data. The shape enhancing effect is small for isometric crystals at around -10°C (Fukuta, 1980).

Table 1 shows constants determined for empirical equations (2) through (5) from experimental data for m, 2a, c and w as a function of t under constant temperatures.

### 3. COMPARISON BETWEEN THE EMPIRICAL EQUATIONS AND EXPERIMENTAL DATA

Figure 1 compares the computed (solid lines) values with experimental data of the four growth parameters as a function of time at -11°C. Since this is the temperature close to the zone of isometric crystal growth, the

shape enhancement is minimal and velocity development does not appreciably slow down.

Figure 2 gives the comparison in temperature plot. The inverted triangles indicate the computed values. a and c values are for 10 min growth and m and w values for 20 min, without correction of pressure effect which is small compared with other errors. The computed values show deviation mostly less than 30% from the respective averages of experimental data in the time range up to 30 min. For further information, see Redder (1988).

Acknowledgments. This work was jointly supported by the Division of Atmospheric Sciences, N.S.F. under Grant ATM-8616568 and Utah/NOAA Weather Modification Program under Contract No. 87-1999.

### REFERENCES

- Fukuta, N., 1969: Experimental studies on the small ice crystals. *J. Atmos. Sci.*, 26, 522 - 531.
- Fukuta, N., L.R. Neubauer and D.D. Erickson, 1979: Laboratory studies of organic ice nuclei smoke under simulated seeding conditions: Ice crystal growth. Final Rept. to NSF under Grant No. ENV77-15346, January 1979.
- Fukuta, N., 1980: Development of fast falling ice crystals in clouds at -10°C and its consequence in ice phase processes. Preprints 8th International Conference Cloud Physics, Clermont-Ferrand, France, 97 - 100.
- Fukuta, N. and L.A. Walter, 1970: Kinetics of hydrometeor growth from a vapor-spherical model. *J. Atmos. Sci.*, 27, 1160 - 1172.
- Gong, N.-H. and N. Fukuta, 1985: Supercooled cloud tunnel studies of ice crystal growth for extended periods of time. Plateau

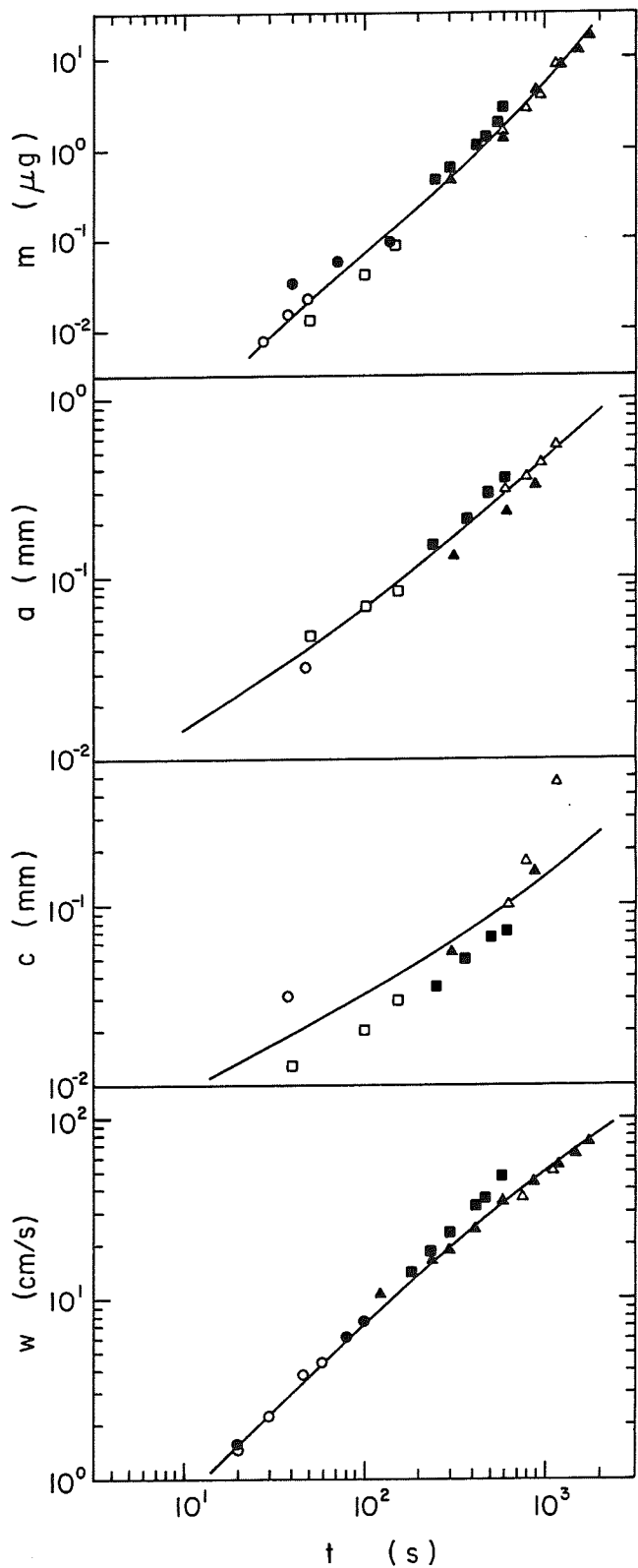


Fig. 1. Ice crystal growth parameters plotted as a function of time at  $-11^{\circ}\text{C}$ . The solid curves represent the empirical equations. The geometric symbols correspond to data from the following investigations:  $\circ$ -Fukuta (1969),  $\bullet$ -Fukuta et al. (1979),  $\square$ -Ryan et al. (1976),  $\blacksquare$ -Kowa (1981),  $\triangle$ -Gong and Fukuta (1985),  $\blacktriangle$ -Takahashi and Fukuta (to be published).

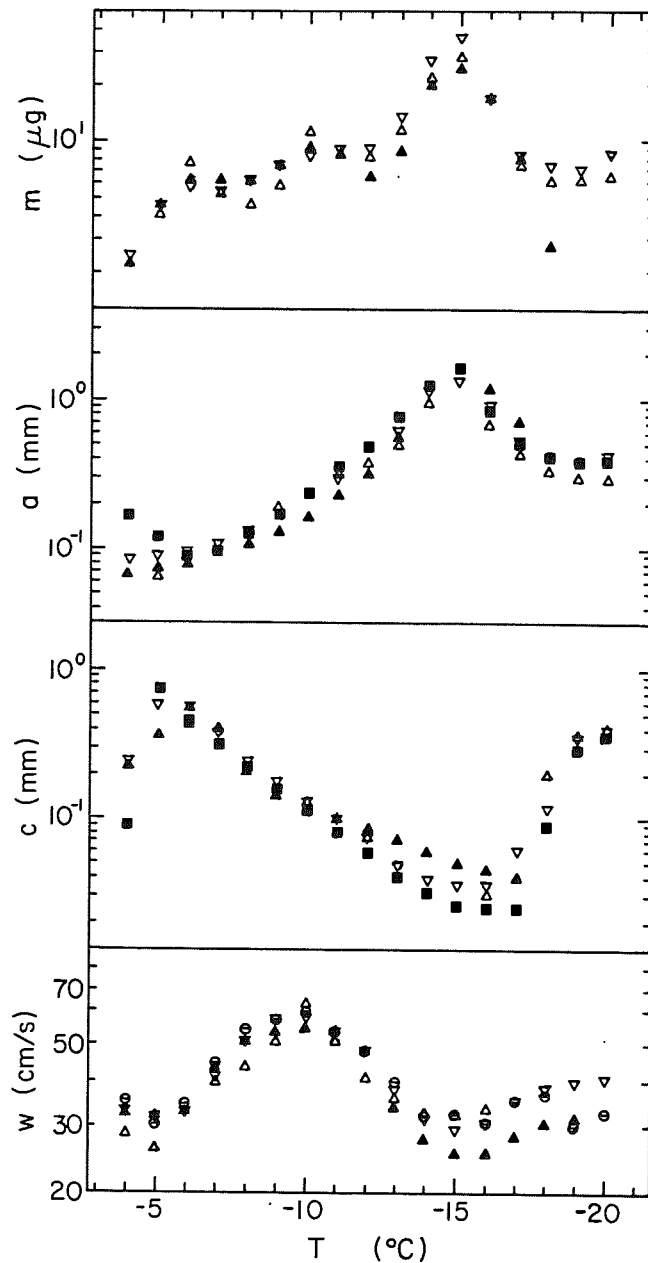


Fig. 2. Ice crystal growth parameters plotted as a function of temperature. Growth time for  $a$  and  $c$  is 10 min and that for  $m$  and  $w$  20 min. For symbols, see Fig. 1 except that  $\nabla$ - calculated from empirical equation,  $\ominus$ - calculated by another method to be published.

*Meteorology*, 4, 293 - 302.

Kowa, M.W., 1981: Determination of ice crystal growth parameters in a supercooled cloud tunnel. M.S. Thesis, Univ. of Utah, 1981.

Redder, C.R., Development of ice crystal growth microphysics for modeling and analysis. M.S. Thesis, Univ. of Utah, 1988, (in preparation).

Ryan, B.F., E.R. Wishart and E.W. Holroyd, III, 1976: The growth rates and densities of ice crystals between  $-3^{\circ}\text{C}$  and  $-21^{\circ}\text{C}$ . *J. Atmos. Sci.*, 33, 842 - 850.

Takahashi, T. and N. Fukuta: Supercooled cloud tunnel studies on the growth of snow crystals between  $-4$  and  $-20^{\circ}\text{C}$  (in preparation).

# THE CONTRAST STUDY OF NEW MODEL ON ICE CRYSTAL GROWTH

Wang Ang-Sheng

Institute of Atmospheric Physics, Academia Sinica  
Beijing, The People's Republic of China

## 1. INTRODUCTION

The growth and shape variation of ice crystals under different environmental conditions are the most important and basic problems in atmospheric physics. In this field, the works of U. Nakaya (1954), J. Hallett and B. J. Mason (1958), and T. Kobayashi (1961) were important. But there were several flaws which need to improve and modify; and many scientists engaged this work (Wang Ang-Sheng, 1984).

Since new law of ice crystal growth was found in a wedge shaped chamber and new model was presented by Wang Ang-Sheng and N. Fukuta (1984), and Wang Ang-Sheng (1984), the quantitative growth law and Wang-Fukuta's model were payed wide attention. As a deeply study, authors will study the comparisons between new results with qualitative study, with Kobayashi's model, with dynamic experiment and with field data of natural ice crystal etc. They will presented in this paper.

## 2. THE CONTRAST WITH QUALITATIVE STUDY

It is well known that since 1949, the law of ice crystal growth was studied. There were some famous models in this field, for example, M. Hamajima (1949), U. Nakaya (1954), J. Hallett and B. J. Mason (1958), and T. Kobayashi (1961) et al. They are qualitative results. Due to these model were wide used in atmospheric physics, so it is very important to contrast new model with them.

Firstly we must point out that in the qualitative studied, there is no quantitative concept, so the boundary lines between different kinds of ice crystals (for example, plate and prism or prism and needle and so on) were decided by the shapes of ice crystal, of course, it is not clear. In new quantitative result, the forms of ice crystal were decided by  $2a/c$  (Wang Ang-Sheng, 1984). In there,  $2a$  is the longest dimension of basal plane, and  $c$  is the height of ice crystal. Their boundary lines between different kinds

of ice crystal are very clear and decided by quantitative value  $2a/c$ . This is best result. Now, the contrast of Wang-Fukuta's result with above qualitative model is shown in Table 1. From this Table, we can find that there have a best similarity between new result and above famous model in the shapes of ice crystal. When we use Wang-Fukuta's model (Wang Ang-Sheng, 1984; and 1987) to contrast with old models (M. Hanajima, 1949; U. Nakaya, 1954; J. Hallett and B. J. Mason, 1958; and T. Kobayashi, 1961), it is very clear that all results are close in the region where is higher than water saturation. This means new result has good unanimity with above models in above region. But there are different from above old models below water saturation region (Wang Ang-Sheng, 1984, and 1987). This is new important development of new work which will be given in the next section.

## 3. THE CONTRAST WITH KOBAYASHI-PRUPPACHER'S MODEL

Among the above models, Kobayashi's model has been frequently quoted, and Pruppacher improved it in some parts by using several results (H. R. Pruppacher and J.D. Klett, 1978). But, we pointed out that there have some flaws in the Kobayashi-Pruppacher's model (Wang Ang-Sheng and Fukuta, 1985; and Wang Ang-Sheng, 1987).

As a important advance, we contrast new result with Kobayashi-Pruppacher's model. In Fig. 1 and Fig. 2, we give Wang-Fukuta's result (Fig. 1, 1984) and Kobayashi's model (Fig. 2, 1961). Because they have same size in the figures, the comparison is easily. As mentioned above, it is clear that most situations are close in the region where is over water saturation. But they are different each other in another part which is below water saturation. Due to the limit of experimental data, the shapes of ice crystal are decided by temperature and vapor density excess in the Kobayashi-Pruppacher's model. But there were only few data in the region below water

saturation for Kobayashi's experiment; and their error was larger (Kobayashi, 1961); so we must to do more experiments to find the best result.

More than 4000 quantitative data were obtained in a wedge-shaped ice thermal diffusion chamber by Wang Ang-Sheng and N. Fukuta (1984), and there were about half of above 4000 data in the region where is below water saturation. These data had exact and quantitative measurements. So they are the best results until today (Wang Ang-Sheng and Fukuta, 1984). According to these new data, one result (at 50 min) of above work is shown in Fig. 1. In the Fig. 1, we can find there are four regions, i.e. Wulff's region, rapid changing region, large  $2a/c$  value region (very thin plate) and low  $2a/c$  value region (needle region) etc. (Wang Ang-Sheng, 1984 and 1987). These are different from Kobayashi-Pruppacher's model. So, Wang Ang-Sheng and Fukuta model was built in 1984 (Wang Ang-Sheng, 1984). This was an important development for this field.

#### 4. THE CONTRAST WITH DYNAMIC EXPERIMENTS

In general, the static experiments have wide range of  $T$  and  $(Si-1)$  field and can be used to get an overall law of ice crystal growth. Although dynamic experiments have narrow region on above field (only close water saturation), then the situation is closer to natural conditions. Due to there are some differents between static and dynamic experiments of ice crystal growth, the contrast is not easy. In Fig. 3 and Fig. 4, the quantitative comparison of Wang and Fukuta's static data (1982,  $t = 50$  min) with Yamashita's (1974) and Gong and Fukuta's (1982) dynamic data are given respectively (Wang Ang-Sheng, 1987).

In Fig. 3, we can find that although the growth time of ice crystals in above experimens was not same, the  $2a/c$  value which decides the ice crystal form is close under the close temperature. For example, at  $-9^{\circ}\text{C}$ ,  $c/2a$  equals 0.67 - 1.0 in Yamashita's data, then our data equal 0.9 (10 min) and 0.62 (50 min). That means the results of the above two works are close to each other. In Fig. 3, it is clear that although in above experiments the growth methods and time were different each other, their forms of ice crystls were similar. That means the temperature is very important in ice crystal growth under water

saturation.

The comparison of Wang and Fukuta's quantitative results with Gong and Fukuta's dynamic results was shown in Fig. 4. From Fig. 4, we can find that two curves of  $\log(2a/c) - T$  ( $^{\circ}\text{C}$ ) tend unanimously. For example, at  $-3^{\circ}\text{C}$ ,  $\log(2a/c)$  of two data equals 0.45. The minimum of two curves is found near  $-5$  or  $-6^{\circ}\text{C}$ ; and the maximum of above curves is found near  $-15$  or  $-16^{\circ}\text{C}$ . Of course, the curves are not unanimous at all points, because their growth methods were different each other.

As mentioned above, the quantitative comparison between static and dynamic experiments shows our work was supported by dynamic experiments under water saturation. This condition is close natural condition.

Owing to the limitation of our extended abstract, the sections 5 and 6 were omitted.

#### REFERENCES

- Hallett, J. and B. J. Mason, 1958: The influence of temperature and supersaturation on the habit of ice crystals grown from the vapour. *Roc. R. Soc.*, A247, 440-453.
- Hanaijma, M., 1949: On the growth condition of man-made snow. *Low. Tem. Sci. A2*, 23-29.
- Kobayashi, T., 1961: The growth of snow crystals at low supersaturations. *Phil. Mag.*, 6, 1363-1370.
- Nakaya, U., 1954: *Snow Crystla*. Harvard University Press. 1-551.
- Pruppacher, H. R. and J. D. Klett, 1978: *Microphysics of clouds and precipitation*. D. Reidel. 1-714.
- Wang Ang-Sheng, 1984: New models of ice crystal growth law in temperature - ice supersaturation or vapor density excess field. 9th International Cloud Physics Conference. 21 -28 August 1984, Tallinn, USSR. 179-182.
- \_\_\_\_\_, 1987: Quantitative growth law of ice crystals. *Advances in Atmospheric Sciences*. Vol. 4, No. 4, 414-431.
- \_\_\_\_\_ and N. Fukuta, 1984: Studies of ice crystal habit development in a new wedge-shaped ice thermal diffusion chamber. *Scientia Sinica*. 1984, No. 12. 1155-1162.
- \_\_\_\_\_ and \_\_\_\_\_, 1985: The quantitative studies on the growth law of ice crystal. *Advances in Atmospheric Scien ces*. Vol. 2, No. 1, 46-53.
- Yamashita, Akira 1974: Studies of crystal using a large cold box. *Kisho Kenkyn Note*. No. 123, 47-94.

Table 1

A. S. Wang & N. Fukuta's data (1982)		M. Hamajima (1949) and V. Nakaya's (1954) data	B. J. Mason (1957) and T. Kobayashi's (1981) data
$2a/c$ value	form name		
$2a/c > 20^*$	Dendritic or spatial plate	Dendritic	Dendritic
$2a/c > 20$	Very thin plate	Spatial plate	Plate and sector
$20 > 2a/c > 5$	Thin plate	Plate and sector	
$5 > 2a/c > 2$	Thick plate	Thick plate	Thick plate
$2 > 2a/c > 1$	Prism	Column	Solid column, very thick plate
$1 > 2a/c > 0.1$	Long prism	Scroll or cup	
$0.1 > 2a/c$	Needle	Needle	Needle

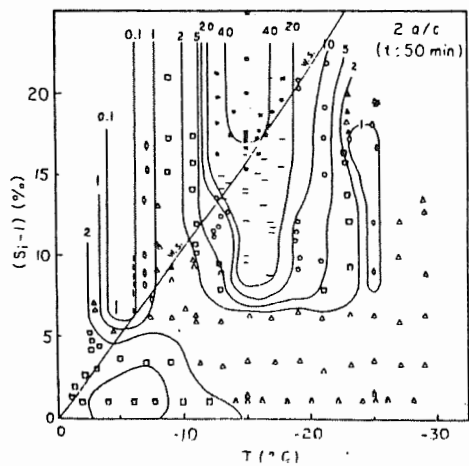


Fig. 1

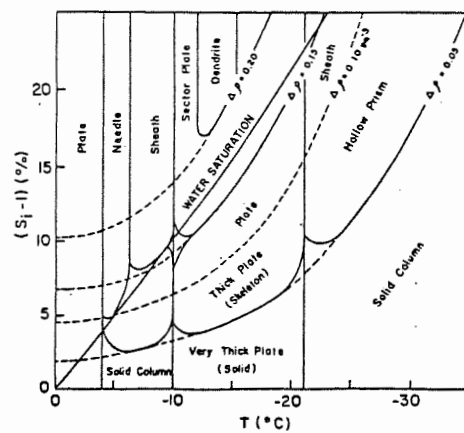


Fig. 2

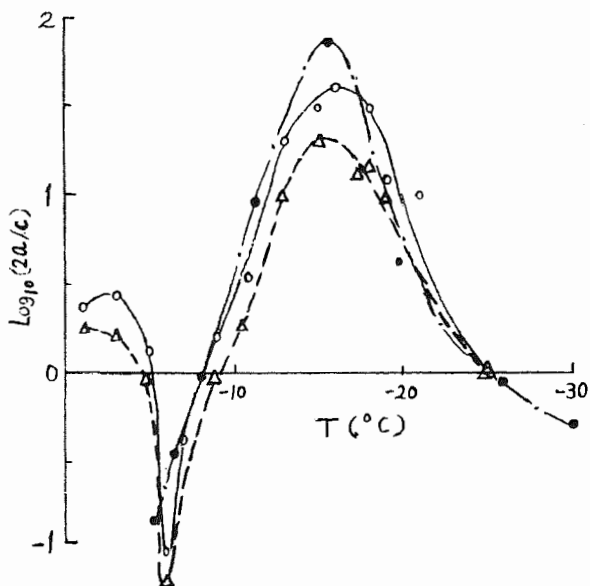


Fig. 3

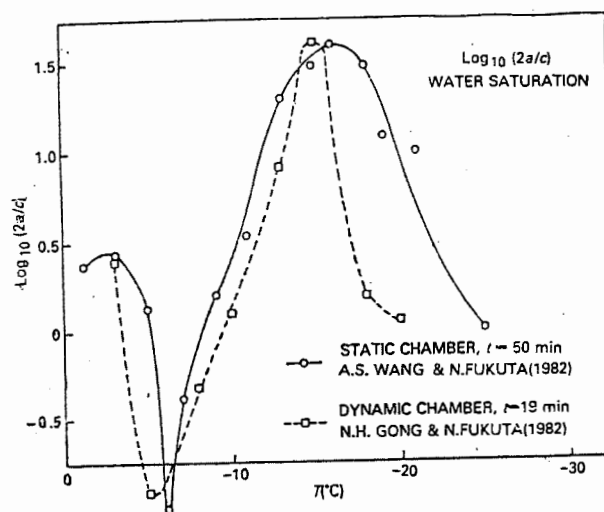


Fig. 4

# A WIND TUNNEL STUDY ON THE MELTING OF SNOW FLAKES

S.K. Mitra, O. Vohl and H.R. Pruppacher  
Johannes Gutenberg-Universität, Mainz, FRG

## 1. INTRODUCTION

The process of snow flake melting plays an important role in precipitation physics considering that in many midlatitude spring-, fall-, and winter storms precipitation develops as a result of individual snow crystals aggregating to larger snow crystal-aggregates or snow flakes which, on their way from the cloud to the ground, melt into raindrops. The process of melting is also of considerable significance to the dynamic behaviour of clouds as the latent heat released during melting becomes added to the buoyancy of the cloud air.

Melting in atmospheric precipitating clouds is indicated very prominently on Radar RHI displays as a zone of increased intensity of the backscattered radiation. This so called "bright band" is of typical vertical extent between 100 and 500 m with an average extent of about 300 m. This bright band, investigated by many Radar studies (for a summary see Stewart *et al.*, 1984) is essentially a result of four mechanisms acting: Between about  $-5^{\circ}\text{C}$  and  $0^{\circ}\text{C}$  snow crystals of different sizes and fall velocities exhibit strong aggregation to form flakes of very similar fall velocity, thus increasing the size of the precipitation particles and decreasing their number concentration. As these flakes pass through the  $0^{\circ}\text{C}$  level they become wet, causing the dielectric constant of the particle to become almost that of water which strongly enhances the Radar reflectivity. Following a change of shape the flakes, upon completion of melting, collapse to raindrops of sizes much smaller than those of the snow flakes but with widely different fall speeds which

are much larger than those of the original flakes. This acts to decrease the concentration of the precipitation particles and thus the Radar reflectivity. Above the melting level snow crystal aggregates were found to have diameters reaching 5 to 11 mm with fall velocities between 1 and 1.5 m/sec. They were found to melt between 0 and  $+5^{\circ}\text{C}$  to raindrops of equivalent diameters reaching 1.1 to 2.6 mm with terminal velocities at sea level reaching 4.3 to 7.6 m/sec, depending on the density of the individual snow flakes (see Locatelli and Hobbs, 1974; Matsuo and Sasyo, 1981a). Of specific interest for calculating the precipitation intensity *below* the melting layer from snow flake size distributions *above* the melting layer is the question as to whether the equivalent drop size distribution derived from the masses of the snow flakes above the melting layer changes as the flakes pass through the melting layer. Such changes could be the result of breakup of the flakes as they melt, or due to the coalescence of melting flakes. Past Radar studies present diverging points of view. Some support the idea that melting flakes break up or believe that melting snow flakes grow by coalescence within the melting layer, while others appear to have evidence that neither coalescence growth, nor breakup occurs in the melting layer.

In order to approach these problems, Matsuo and Sasyo (1981b) undertook a laboratory study in which they melted individual snow flakes, collected during natural snow falls. During melting the flakes were held on a net of thin nylon threads exposed to an air stream of fixed velocity of 1 m/sec and

+5.5°C. From photographic records they deduced the rate of melting of the flakes.

Unfortunately nylon threads considerably influence the melting behaviour in attracting the water to the string binding the flake to the net. In an attempt to improve on the drawbacks of the experimental set-up of Matsuo and Sasyo (1981a) we undertook our own laboratory study.

## 2. THE EXPERIMENTAL SET-UP

Our study was carried out with the help of a recently completed vertical wind tunnel at the University of Mainz. This wind tunnel represents a second generation of the type, built at the University of California in 1968, and described in detail by Beard and Pruppacher (1969). The present wind tunnel built at Mainz incorporates several important improvements over the earlier tunnel built at UCLA. One of these improvements consists of a positive control of the rate of cooling and warming of the air in the tunnel, such that these rates are independent of the vertical velocity of the air in the observation section of the tunnel. This feature allows to study in detail the melting behaviour of atmospheric ice particles which can be kept at their terminal velocity freely "floating" in the tunnel air while the tunnel air is warmed or cooled at a desired rate.

For our melting studies three experimental set-ups were used. In the *first set-up*, natural or "artificial" snow flakes from laboratory grown snow crystals were placed on a net of nylon threads of 0.1 mm diameter mounted inside the vertical observation section of the tunnel. The tunnel air was adjusted to the terminal velocity of the flake such that it almost hovered on the net. This set-up was chosen to study the flake surface during the initial stages of the snow flake melting. In the *second set-up* natural or "artificial" snow flakes were held into the tunnel air while being suspended on a thin nylon fiber. In this set-up, the tunnel air was continuously adjusted such that the nylon

fiber was completely loose and without tension, thus insuring that the flake was at its terminal velocity. Sideways motions of the flake were, however, restricted. In the *third set-up* the snow flakes were freely suspended in the air stream of the wind tunnel. During melting of the flake the speed of the air stream was continually adjusted to keep the melting flake at its terminal velocity such that the flake remained at a fixed vertical position in the observation section. Unfortunately, in free fall, it was not possible to observe the melting of the flake to the very end of the melting since the fall speed increased rather abruptly during the final transition to a drop, and the erratic sailing motions of the flake became very intense.

The air speed of the tunnel was calibrated by means of a calibrated TSI hot wire anemometer system. The dew point, i.e. the relative humidity of the tunnel air was monitored by a Cambridge systems dew point hygrometer. The relative humidity was about 90% during all experiments. The temperature of the tunnel air was monitored by calibrated thermocouples and Platinum resistance thermometers. The rate of warming of the tunnel air was about 1.5°C/min corresponding to temperature gradients between 1.25°C/100 m and 0.35°C/100 m for the falling snow flake, considering its changing fall speed as it melted. The natural snow flakes were obtained from freshly fallen snow captured on mink fur just outside the laboratory. The "artificial" snow flakes were formed by a specially developed technique from individual dendritic and needle crystals grown from the vapor in our large walk-in cold chamber. Most of the experiments were carried out with flakes of about 10 mm diameter, corresponding to masses of about 2 mg to 11 mg, depending on the density of the individual flakes. These flakes melted into drops of 1.5 mm to 2.0 mm diameter with fall velocities of 5.4 m/sec to 7.6 m/sec. The sizes, masses and fall velocities of the present flakes correspond well to those given by Locatelli and

Hobbs (1974) and by Matsuo and Sasyo (1981a). All observations on the melting snow flakes were documented by still- and motion picture photography.

### 3. RESULTS

The results of our observations on melting snow flakes can be summarized as follows:

(1) All snow flakes studied melted within a fall distance of 500 m from the 0°C level for typical atmospheric temperature gradients encountered by the flakes. Most flakes melted, however, within a 300 m fall. Thus the flakes were melted into raindrops before they reached a temperature level of 2 to maximally 5°C.

(2) "Dry" snow flakes exercise a spinning, helical and shaking motion whose frequency of rotation and oscillation depends much on the overall size and on the porosity of the flake. As soon as melting starts, the frequency of rotation and oscillation changes and sideways-sailing sets in. During continued melting the way of turning of the flake may change abruptly, and one or the other motion may interrupt for a brief period, all resulting from a rearrangement of the flake's internal structure. Upon the collapse of the ice framework of the flake's uncontrollable erratic downward and sideways motion sets in. Tumbling over, however, was never observed. The intense erratic sideways motions of melting flakes suggest that the growth of melting flakes by coalescence continues in the upper portion of the melting layer, the liquid portion of the flake guaranteeing a 100% coalescence efficiency upon collision.

(3) In agreement with the observation of Matsuo and Sasyo (1981a) and Knight (1979) we found that the melting of a snow flake may be divided into four stages:

(a) *Stage 1*: Small drops of tens of microns in diameter appear at the tips of the crystal branches which make up a flake, melting being most intense at the periphery and lower side of the flake.

(b) *Stage 2*: By capillary action and by surface tension effects which attempt to minimize the total surface energy, the melted water flows from the periphery effectively to the intersections of the snow crystal branches. There the water accumulates, leaving the "surface" of the flake essentially uncovered of water. Since the main ice frame remains intact a "ragged" surface of the flake is maintained. Thus, the water acts as a powerful "cement" for the flake during the melting, helping to keep the aggregate together, but at the same time attempting to collapse the particle into a more compact shape.

(c) *Stage 3*: The smallest branches of the flake's inside melt and the water also flows to the intersection of the main branches. This allows structural rearrangement to take place since the main framework is now less confined. Thus the main branches may bulge out or be flipped inward. The crystal mesh of the flake changes from one with many small openings to one with few large ones.

(d) *Stage 4*: The main ice frame collapses suddenly. The water covers it and pulls its shape together into that of a drop.

(4) Although the breakup of melting snow flakes was found not to occur as a rule, particularly not for flakes smaller than about 5 mm in diameter, three types of breakup were observed:

(a) Small pieces of ice or micron sized drops left the melting flake.

(b) Larger flakes with an off-center mass distribution, whose connecting small crystal branches melted during stage 3 broke mechanically apart into pieces.

(c) Larger flakes whose off-center mass distribution melted locally lost this water through drop shedding. In these cases the drop terminal velocities were larger than those of the flakes (e.g., a drop of about 300  $\mu\text{m}$  diameter may have a terminal velocity larger than that of a flake).

(5) Rough estimates from our film and still pictures give for air of 90% relative humidity, typical atmospheric temperature gradients, and snow flakes of about 10 mm diameter the following relations:

(a) 0, 30, 70, 90% water in flake after 30, 50, 70 and 90% "melt distance", resp.

(b) 0, 15, 40, 80% of total size change taken place after 30, 50, 70, and 90% "melt distance", resp.

(c) 0, 15, 30, 50, 75% of the terminal velocity of the drop into which the flake melted after 30, 50, 70, 90, 95% "melt distance", resp.

As "melt distance" we considered the distance between the 0°C level and the level at which the flake had melted completely into a drop. The above numbers appear to verify qualitatively the results derived by Matsuo and Sasyo (1981 a,b) from their semi-empirical heat transfer theory for snow flakes.

#### REFERENCES:

- BEARD, K.V., and H.R. PRUPPACHER, 1969: A wind tunnel determination of the terminal velocity and drag of small water drops. *J. Atmos. Sci.*, 26, 1066-1072
- KNIGHT, C.A., 1979: Observations of the morphology of melting snow. *J. Atmos. Sci.*, 36, 1123-1130
- LOCATELLI, J.D., and P.V. HOBBS, 1974: Fall speeds and masses of solid precipitation particles. *J. Geophys. Res.*, 79, 2185-2197
- MATSUO, T., and Y. SASYO, 1981a: Melting of snow flakes below freezing levels in the atmosphere. *J. Meteor. Soc. Japan*, 59, 10-25
- MATSUO, T., and Y. SASYO, 1981b: Empirical formulas for the melting rate of snow flakes. *J. Meteor. Soc. Japan*, 59, 1-8.
- STEWART, R.E., J.D. MARWITZ and I.C. PACE, 1984: Characteristics through the melting layer of stratiform clouds. *J. Atmos. Sci.*, 41, 3227-3236

EVAPORATION AND MELTING OF ICE CRYSTALS:  
A LABORATORY STUDY

Riza G. Oraitay and John Hallett  
Desert Research Institute  
Reno, Nevada 89506

1. INTRODUCTION

Melting and evaporation of ice crystals during free fall are important in interpretation of the radar bright band, understanding the thermodynamics of the melting layer and the ice crystal economy of cloud systems. Information on the morphology of melting relies on a limited number of observational and experimental studies (KNIGHT 1971, p.1123; MATSUO and SASYO 1981, p.1; RASMUSSEN ET AL. 1983, p.381; FUJIYOSHI 1986, p.307) while little laboratory work is available on the morphology of evaporation. We used a thermal diffusion chamber (KELLER and HALLETT 1982, p.91) to grow ice crystals (dendrites, columns and plates) as a function of supersaturation, temperature and air flow velocity and studied melting or evaporation under controlled relative humidity, temperature and fall velocity.

2. EXPERIMENTAL STUDY

After the crystals were grown the air flow was reversed through separate temperature and moisture conditioners. The temperature of the air was raised to a fixed value at controlled relative humidity. Air flow velocity was adjusted approximately equal to the fall velocity of the ice crystals. The morphology of evaporation and melting was observed through a video camera.

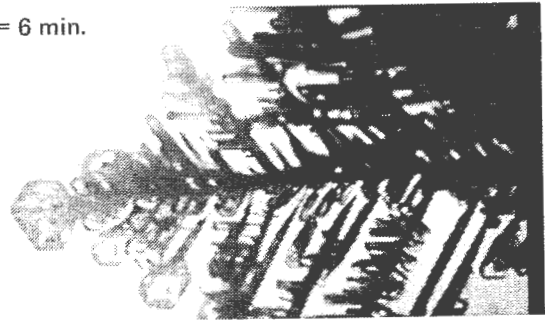
3. RESULTS AND DISCUSSION

3.1 MORPHOLOGY OF DENDRITIC CRYSTALS:

At low relative humidity and ice bulb temperature only evaporation was observed. As the ice bulb temperature approached  $\sim -0.5^{\circ}\text{C}$ , evaporation caused breakup of ice particles

(Fig. 1). A crystal of 5 mm in size produced 7 to 10 ice particles in a range  $50\mu\text{m}$  to 1mm.

t = 6 min.



t = 15 min.



t = 19 min.

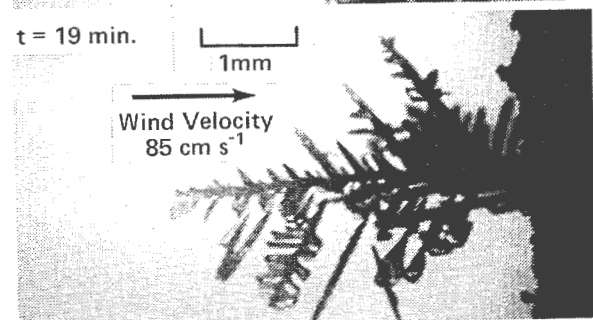


Fig. 1: Evaporation of a dendrite at  $T_a = +1^{\circ}\text{C}$ ,  $T_i = \sim 0^{\circ}\text{C}$ , Relative Humidity 80%.

With increasing ambient air temperature, the wet bulb temperature exceeded  $0^{\circ}\text{C}$  and melting occurred. At low relative humidity ( $\text{RH} < 80\%$ ), melted water accumulated in the interstices. The ice pieces between them eroded very quickly, leading to shedding of water droplets containing ice pieces (about five drops  $25\mu\text{m}$  to  $400\mu\text{m}$  in diameter). At higher relative humidities, melted water

covered most of the crystal and water shedding took place at the later stages of melting (Fig. 2). At high relative humidity and temperature ( $RH > 90\%$ ,  $T_a > 4^\circ\text{C}$ ), crystals were moulded aerodynamically in the air flow and no shedding was observed.

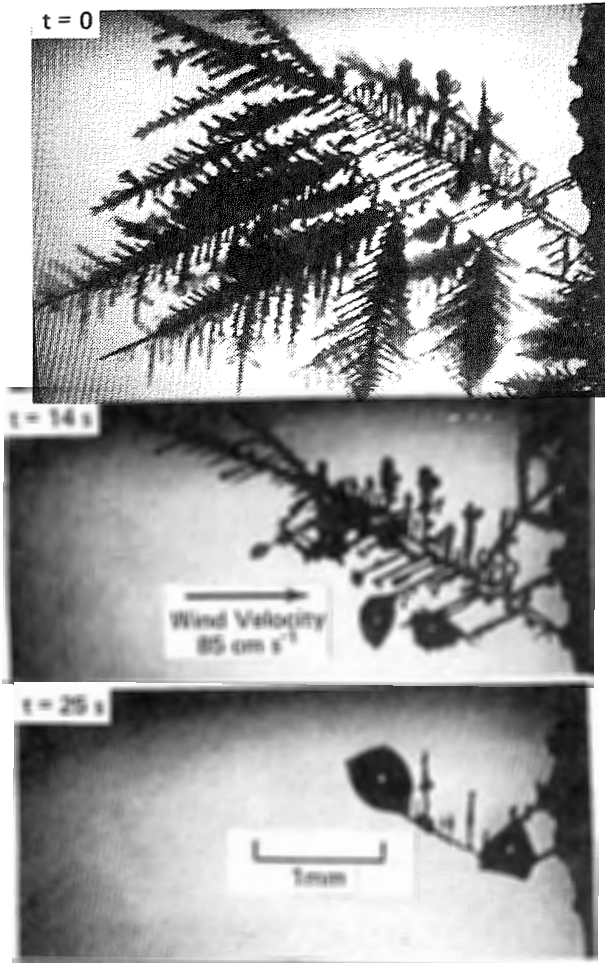


Fig. 2: Melting of dendritic crystals at  $T_a = +3^\circ\text{C}$ ,  $T_w = +2.1^\circ\text{C}$  and 85% Relative Humidity.

### 3.2 MORPHOLOGY OF COLUMNS:

Melting of a cluster of columns is shown in Fig. 3. Melted water first filled the hollow inside of the columns, then accumulated at the forks. Usually one droplet formed in the middle of each crystal, and was shed when it reached a diameter of about  $400\mu\text{m}$ . In most of the cases a second droplet of a smaller size (about  $25\mu\text{m}$ ) was formed and shed. Water droplets which were produced during the melting of columns did not contain ice pieces.

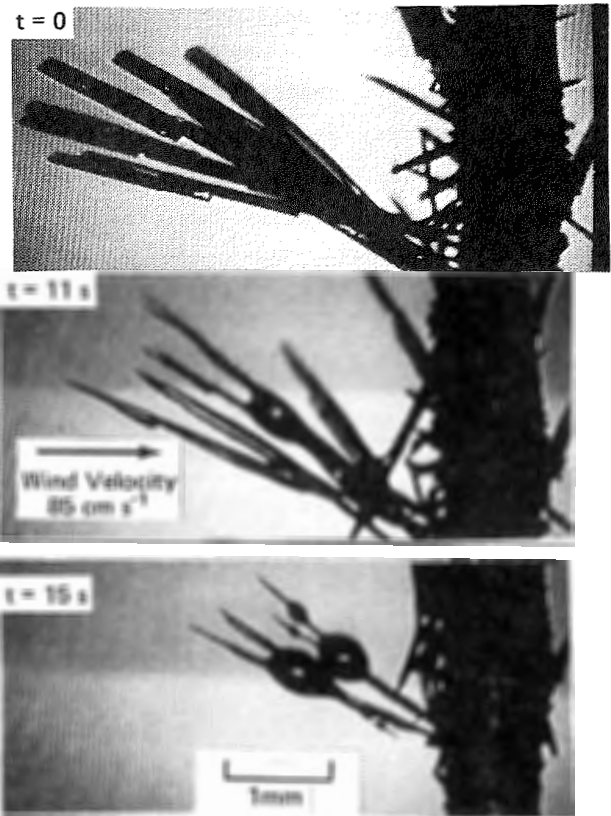


Fig. 3: Melting of columns at  $T_a = +1.5^\circ\text{C}$ ,  $T_w = +0.4^\circ\text{C}$  and 80% Relative Humidity.

### 3.3 MORPHOLOGY OF PLATES:

Melting of plates was different from dendrites and columns, melted water spread over the surface and covered the crystals. Neither breakup nor shedding was observed (Fig. 4).

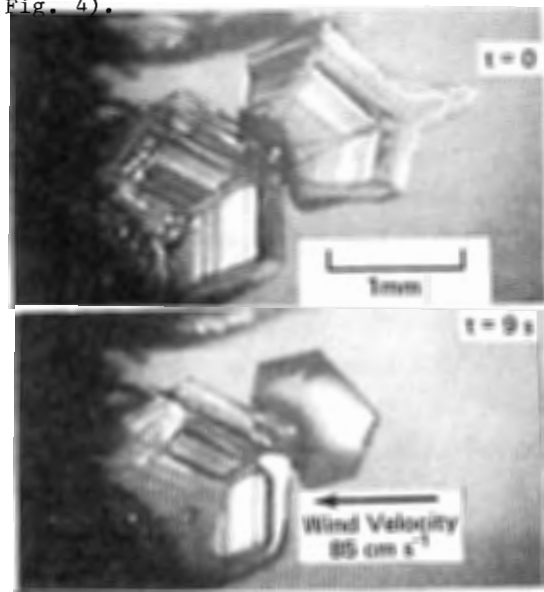


Fig. 4: Melting of a plate at  $T_a = +1.5^\circ\text{C}$ ,  $T_w = +0.4^\circ\text{C}$  and 80% Relative Humidity.

### 3.4 MELTING RATES

The rate of change of linear dimensions along a or c axis of dendritic crystals at 90% Relative Humidity as a function of temperature is shown in Fig. 5. Measurement of the rates at lower relative humidity was difficult due to shedding and breakup.

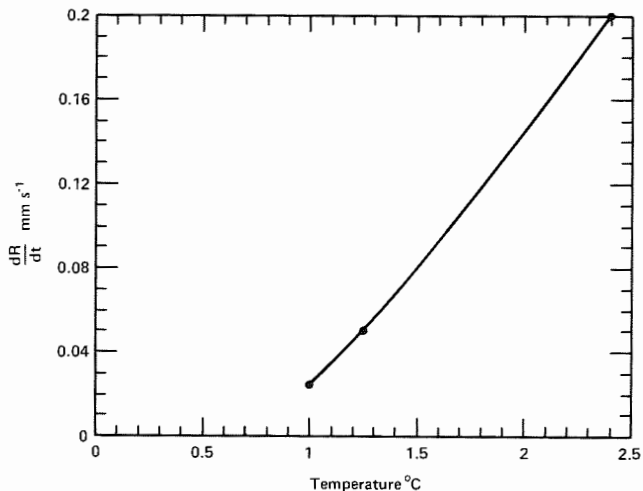


Fig. 5: Rate of change of linear dimensions along a or c axis at 90% Relative Humidity.

### 4. CONCLUSIONS

- i. During the evaporation of columns and plates, no ice breakup was observed.
- ii. Evaporation of dendritic ice crystals at low relative humidity and ice bulb temperature proceeded without any ice breakup. As the ice bulb temperature approached 0°C, significant ice breakup (7 to 10 pieces per crystal) was observed. For positive values of wet bulb temperature around 0°C, shedding of mixed droplets and ice pieces occurred. As wet bulb temperature increased, beyond about 2°C, only shedding of water was observed.
- iii. With the further increase of relative humidity and ambient air temperature, shedding of water decreased.
- iv. During the melting of columns, an average number of two droplets (about 400  $\mu$ m and 25  $\mu$ m) were shed. Melting of plates did not produce any secondary droplets.

It is inferred from our laboratory results that, the occurrence of breakup and shedding will be determined by the temperature and relative humidity of the ambient air and will result in quite different structures of the radar bright band. Secondary particle production will occur only for specific crystal habits (dendrites). The importance of recirculation of both large drops and ice particles on the overall microphysical development (TELFORD 1986, p.555) will depend on the probability of reincorporation of such particles into an appropriate updraft.

This work was carried out under Contract #ATM 8715636, Division of Atmospheric Science, National Science Foundation, Washington, D.C.

### 5. REFERENCES

- FUJIYOSHI, Y.: Melting Snowflakes, *J. Atmos. Sci.* 43 (1986), 307 - 311.
- KELLER, V.W. and HALLETT, J.: Influence of Air Velocity on the Habit of Ice crystal Growth from the Vapor. *J. Cryst. Growth* 60 (1982), 91 - 106.
- KNIGHT, C.A.: Observations of the Morphology of Melting. *J. Atmos. Sci.* 29 (1971), 1123 - 1130.
- MATSUO, T. and SASYO, Y.: Empirical Formula for the Melting Rate of the Snowflakes. *J. Met. Soc. Japan* 59 (1981), 1 - 8.
- RASMUSSEN, R.M.; LEVIZZANI, and PRUPPACHER, H.: A Wind Tunnel and Theoretical Study on the Melting Behaviour of Atmospheric Ice Particles: III. *J. Atmos. Sci.* 41 (1983), 381 - 387.
- TELFORD, J.W.: Comment on the paper "Microphysical Properties of Supercooled Cumulus Clouds in which an Ice Particle Multiplication Process Operated" by MOSSOP, S.C. *Quart. J.R. Met. Soc.* 112 (1986), 555-560.

A NEW MECHANISM FOR ICE INITIATION IN  
WARM-BASED MIDWESTERN CUMULI

Robert R. Czys

Illinois State Water Survey  
Climate and Meteorology Section  
Champaign, Illinois USA

1. INTRODUCTION

Collisions between supercooled precipitation drops are examined as a possible source for ice in the warm-based summer convective clouds of the central United States. Microphysical observations taken during the summer of 1986 as part of the Precipitation Augmentation for Crops Experiment (PACE) have shown, as was originally reported from Project Whitetop (Braham, 1964), that ice can originate at temperatures warmer and in concentrations higher than might be expected solely from ice-forming nuclei (IFN).

On two days during July 1986, PACE collected microphysical data at the  $-10^{\circ}\text{C}$  level. Initial ice concentrations determined from 2-D images were as much as 35 times larger than typical summer IFN concentrations measured over the central United States using membrane filters (Czys, 1977). It was not unusual for PACE86 clouds to develop graupel concentrations between 10 to 20  $\text{L}^{-1}$  with mean diameters from 125 to 325  $\mu\text{m}$  before cloud top temperature reached  $-11^{\circ}\text{C}$ . All clouds developed ice in the presence of supercooled rain and this is one clue that has led to the consideration of freezing as a product of an active supercooled coalescence (cold-rain) process.

2. LABORATORY EVIDENCE

An exploratory investigation was conducted to determine if supercooled distilled deionized water could be made to freeze when subjected to mechanic shocks. In each of four experiments about two dozen millimeter-size drops ( $\approx 100 \mu\text{l}$  per drop) were placed

on a chrome stage smoothly coated with petroleum jelly. The stage was then placed in an open-top cold box and the drops were slowly cooled to a temperature below  $0^{\circ}\text{C}$ .

Data was obtained at constant temperature for drops cooled to  $-10^{\circ}\text{C}$  and for drops cooled to  $-15^{\circ}\text{C}$ . The air temperature in the vicinity of the drops was  $-13^{\circ}\text{C}$  and  $-16^{\circ}\text{C}$ , respectively. Here only data for the experiment at  $-10^{\circ}\text{C}$  is reported. After the drops had been cooled to these temperatures a length of time elapsed and then mechanical shocks were transmitted to the cooling stage by repeated tapping with a plastic mallet.

Figure 1 shows drop freezing probability with time for drops cooled to  $-10^{\circ}\text{C}$  for two different trials distinguished by the dashed and solid line. The time at which the drops began to receive mechanical shocks is indicated by the arrows. As can be seen in Fig. 1 undisturbed, most of the drops re-

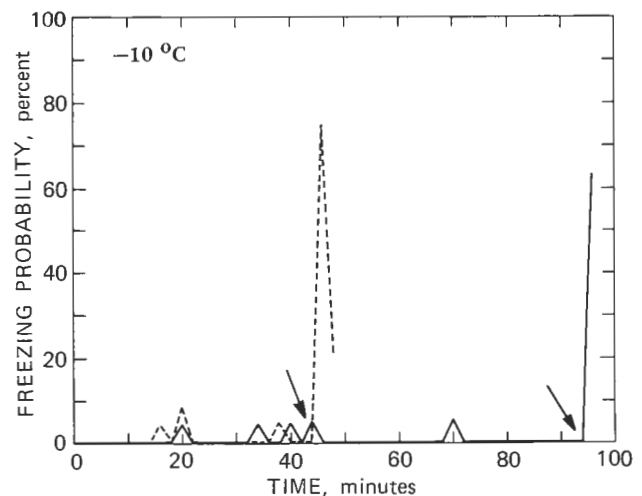


Figure 1. Freezing probability verses time for drops cooled to  $-10^{\circ}\text{C}$ .

mained supercooled for lengths of time far in excess of the 3 minutes or so it takes for a cloudy air parcel to pass from 0 °C to -10°C at  $\approx 8 \text{ m s}^{-1}$ . At -10°C only 5 drops in 24 froze during the 90 minutes preceding mechanical disturbance and for the other run only 4 drops in 24 froze during 45 minutes. Nearly identical results were obtained in the experiment at -15°C.

Fig. 1 also shows that freezing probability jumps sharply precisely at the onset of mechanical disturbances. This result suggests that more than chance was involved in the freezing of the drops. However, further investigation is warranted since these results are prone to uncertainties introduced from the use of a supporting substrate.

### 3. PHYSICAL MECHANISM

Adiabatic cooling in the vicinity of mechanically induced bubble nucleation is proposed as the physical mechanism for ice nucleation. If a liquid is subjected to a sufficient pressure decrease (or a temperature increase or both), bubble growth occurs and the associated local temperature effects depend on growth rate relative to the rate at which dissolved air can come out of solution. Net adiabatic cooling is possible if the bubble expands faster than the dissolved air is drawn out of solution. Once a bubble forms its collapse is always limited by the slow rate at which the air dissolves back into the water.

A simple calculation suggests that adiabatic temperature decreases on the order of 100°C are possible assuming that a spherical cluster of gas molecules expands to 0.5  $\mu\text{m}$  radius. Thus, ice nucleation may occur spontaneously. However, expansion may not be perfectly adiabatic since some addition of gas molecules to the bubble occurs. Thus in some cases, only enough cooling may be produced to activate a submerged IFN.

Estimates of the amount of pressure difference needed to cause a bubble vary from -500 mb for homogeneous nucleation to a lower limit of -5 mb for aerated tap water (Hueter and Bolt, 1955). Actual thresholds may be lower given the difficulty of bubble detection and the fact that cloud and rain drops may contain large amounts of impurities.

Admittedly, the physical mechanism presented here is based on conjecture, but since bubble formation should precede ice nucleation (Goyer *et al.*, 1965), the occurrence of a bubble may at least have predictive value.

### 4. DROP-FREEZING POSSIBILITY

In a numerical simulation of drop rebound, Foote (1975) has shown that an intricate pressure field evolves within a drop during the period of compression to eventually produce a negative pressure difference of 2.4 mb. Foote's calculation is for an initially spherical drop, 1.19 mm diameter impacting a wall at  $30 \text{ cm s}^{-1}$  and is characterized by a Weber Number of 1.42. The Weber Number gives a non-dimensional measure of drop deformation from the ratio of impact pressure to curvature pressure.

At impact, the pressure field takes the form of a sharp spike with maximum and minimum of 35 and 2.5 mb. Simultaneously, a circular surface wave propagates away from the impact point and associated with it an internal circulation evolves. When the wave reaches the top of the drop where the internal circulation reverses, the pressure field shows a maximum and minimum of 3.8 and -2.4 mb.

The pressure difference in Foote's calculation does not exceed the -5 mb criteria for heterogeneous bubble formation, but is close enough to suspect that pressure differences sufficient for bubble growth may occur for re-

bounds characterized by larger Weber Numbers.

Figure 2 shows lines of constant Weber Number (WE) and was calculated using the equation:

$$WE = (\rho_w r \Delta V^2) / \sigma \quad (1)$$

where  $\rho_w$  is the density of water,  $\Delta V^2$  is the differential terminal velocity and  $\sigma$  is surface tension of water. This equation is slightly different from the one used by Foote (1975) since small drop radius is used to better represent deformation curvature in collisions between dissimilarly sized drops (Ochs *et al.*, 1986).

For Fig. 2 the linear relationship  $WE = 0.60 \times \Delta P$  was used to extrapolate from Foote's work. Thus negative pressure differences greater than 5 mb correspond to collisions with  $WE > 3$  and  $\Delta P < -500$  mb for  $WE > 300$ . The stippled area in Fig. 2 delineates the region of  $WE > 3$  and hence the drop sizes for which heterogeneous bubble formation may be suspected. The lack of stippling for drops with  $R > 1000$   $\mu\text{m}$  and drops with  $r > 300$   $\mu\text{m}$ , indicates collisions with sufficient energy for drop breakup (Whelpdale and List, 1971). Use of Eq. 1 produced a maximum Weber Number of  $\approx 280$ , just smaller than defined for the homogeneous bubble nucleation.

Figure 2 suggests that bubble formation might be possible for drop rebound in clouds once precipitation-size collector drops are produced. Whether the large drop, small one, both or neither freezes in rebound is a matter for future investigation as are the freezing possibilities of temporary and permanent coalescence.

## 5. SUMMARY

Previous considerations of cloud microphysical processes leading to ice initiation have generally ignored the active, supercooled coalescence mecha-

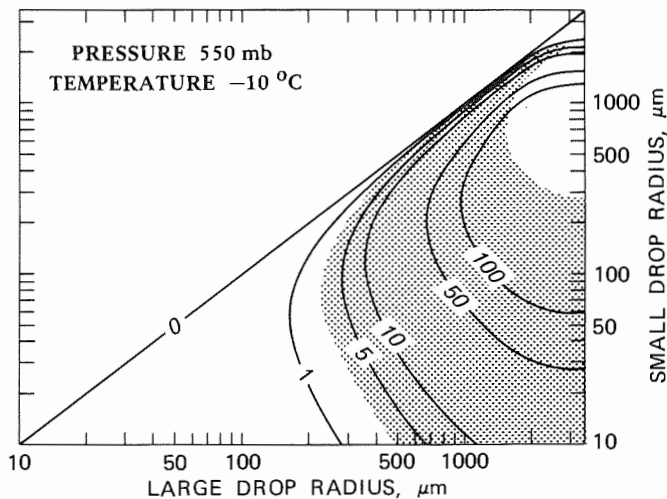


Figure 2. Lines of constant Weber Number. The stippled area delineates  $WE > 3$ .

nism that occurs in the warm-based cumulus of the central United States. In this paper it has been suggested that some collisions between supercooled drops may result in freezing and thus be a strong source of ice having powerful influence over the spectral evolution of liquid and solid particles.

*Acknowledgement.* This research has been conducted under cooperative agreement with the National Oceanic and Atmospheric Administration under contracts COMM NA86RAH06051 and COMM NA87RAH07077. The author wishes to thank Professor Roscoe R. Braham, Jr. for use of his drop freezing apparatus.

## REFERENCES

- Braham, R. R., 1964: *J. Atmos. Sci.*, 21, 640-645.
- Czys, R. R., 1977: *Proc. Sixth Conf. on Inadvertent and Planned Weather Modification*, Champaign, Illinois, 29-32.
- Goyer, G. G., T. C. Nhadra and S. Gitlin, 1965: *J. Appl. Met.*, 4, 156-160.
- Foote, G. B., 1975: *J. Atmos. Sci.*, 32, 390-402.
- Hueter, T. F. and R. H. Bolt, 1955: *Sonics*. John Wiley and Sons, p 230.
- Ochs, H. T., R. R. Czys and K. V. Beard, 1986: *J. Atmos. Sci.*, 43, 225-232.
- Whelpdale, D. M., and R. List, 1971: *J. Geophys. Res.*, 76, 2836-2856.

SPREADING OF SUPERCOOLED WATER DROPLETS  
ON AN ICE SURFACE

Ya Yi Dong and John Hallett  
Desert Research Institute  
Reno, Nevada 89506

### 1. INTRODUCTION

In spite of its importance in graupel formation, the spreading processes of water droplets are poorly understood. One of the difficulties is that the surface energy between ice and water, which is extremely important in the spreading process, cannot be measured directly because of the non-equilibrium state during freezing. On other hand, the effects of the so-called quasi-liquid layer on an ice surface on spreading have not been carefully considered. The present experiment was designed to investigate behaviour of supercooled water droplets spreading on different ice surfaces under various temperatures. It was found that the spreading ratio of water droplets slowly increases with temperature on a "dry" ice surface, but increases rapidly with temperature when a quasi-liquid layer exists on the ice surface above  $-4^{\circ}\text{C}$ . It was also found that the curvature of the ice surface has a strong influence on the water spreading. The traditional concept of contact angle is not applicable in this case.

### 2. EXPERIMENT

A brass tower temperature conditioner is set up in a freezer to minimize the effects from the environment. The tower is about 80 cm in height, 18 cm in diameter and is cooled by circulating antifreeze. A thermo-electric plate is located on the bottom of the tower to obtain better temperature control. A microscope is set up in the same freezer, so that the samples can be examined as soon as possible after they are removed

from the thermo-electric plate. Ice crystals are selected from a freezing water surface and the crystal axis orientation checked by crossed polaroids. Water droplets are fed from the tower top at least 10 minutes after the ice sample is put on the thermo-electric plate and temperature equilibrium is reached. The water droplets fall through the tower and accrete on the ice surface at terminal velocity. Only limited number of droplets are fed to minimize effects of latent heat and obtain clear pictures of individual events. The ice samples are then removed and examined under the microscope. The whole procedure is carried out in the freezer, and finished in 5-10 minutes so that effect of evaporation is negligible.

### 3. RESULTS

The experiment was carried out for basal and high index surface at temperatures from  $-18^{\circ}\text{C}$  to  $-1^{\circ}\text{C}$ . Fig. 1 shows the spreading ratio, which is defined as a ratio of radius of a spread droplet base to its height, is different on basal and high index surfaces at  $-3^{\circ}\text{C}$ . It is interesting to note that the spreading ratio increases relatively slowly with temperature under  $-2^{\circ}\text{C}$  on basal surface, and increases dramatically above  $-2^{\circ}\text{C}$ . The same behaviour was observed on high index surfaces but the transition point is about  $-4^{\circ}\text{C}$ . This observation implies that the spreading ratio is influenced by the thickness of quasi-liquid layer (FURUKAWA, 1987, p.665). The spreading ratio as a function of temperature



a) Droplet spread on a basal surface



b) Droplet spread on a high index surface

100  $\mu\text{m}$

Fig. 1: Different spreading ratios of supercooled droplets on different ice crystal surfaces near melting point. Temperature  $-3^{\circ}\text{C}$ .

is plotted in Fig. 2. Over the whole temperature region examined, the droplets spread and freeze as cones with a tip on top. The angle between the side of the cone and the ice substrate is strongly dependent on temperature (Fig. 3). This result agrees well with Hansman's experiment (1988). The observation also reveals an interesting phenomenon: at low temperature ( $<-10^{\circ}\text{C}$ ),

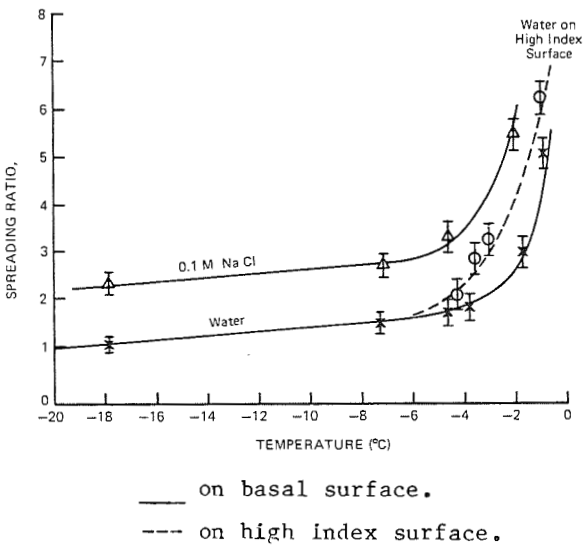


Fig. 2: Spreading ratio as a function of temperature.

the ice substrate is strongly dependent on temperature, which is plotted in Fig. 3.

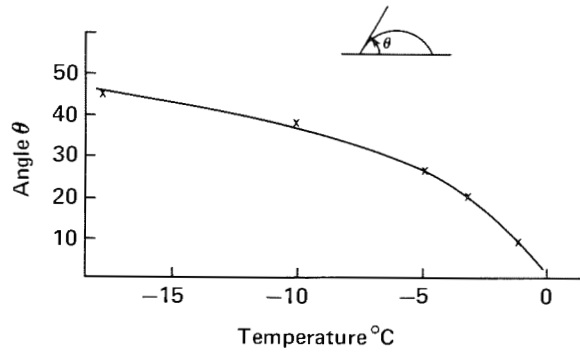


Fig. 3: Angle between cone side and flat ice surface as a function of temperature.

supercooled water droplets freeze as individual spheres when they land on a curved ice surface through they would spread as cones on flat surface under the same conditions. Fig. 4 shows an example.

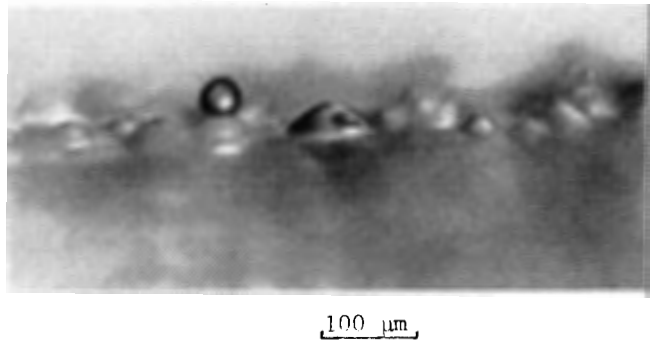


Fig. 4: An example of spherical frozen droplet on a curved surface.

#### 4. DISCUSSION

The above observation demonstrates an important spreading behaviour related to the riming process. A number of previous studies showed some disagreements in shape of freezing droplets because the effects of quasi-liquid layer and curvature of the collector was not considered. When a water droplet reaches a flat ice surface, it is nucleated immediately at the contact point, the released latent heat warms up the substrate (near the landing point) to near  $0^{\circ}\text{C}$ . A quasi-liquid layer will form in this

area. The water droplet will continue to spread until it is completely frozen. The final shape depends on freezing time and spreading time. The mean velocity of dendrite growth was estimated by HALLETT (1964, p.667)  $v = 0.08 T^2 \text{ cm s}^{-1}$ . Deformation speed can be taken as the initial droplet velocity for a first estimate. In the region of interest, these speeds can be of the same order. On a curved surface, the ratio of freezing speed to spreading speed (the speed of the droplet to cover ice surface) is higher than that on a flat surface. Therefore, droplets are more likely to freeze as spheres instead of cones on a curved surface. The two processes are shown in the Fig. 5. The result implies that

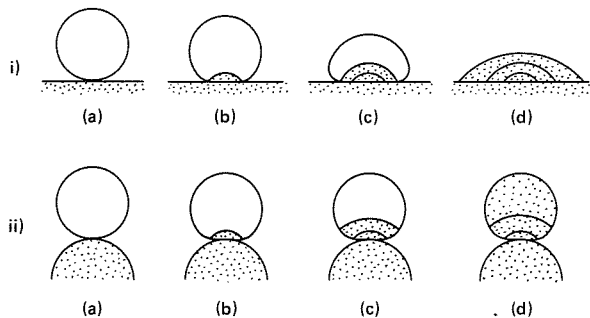


Fig. 5: A model of spreading on flat and curved surface.

riming behaviour is strongly dependent not only on temperature and kinetic energy, but also the size and curvature of ice particles and droplets. Small droplets retain their original shape when they are collected by small ice particles, but spread on relatively flat surfaces. Finally, it should be pointed out that the concept of contact angle is not applicable in this case. The final angle between the surface of frozen droplet and substrate can be as large as about  $100^\circ$  for collector surfaces with different curvature. From the view point of free energy, the wettability  $S$  of water on ice is:  $S = \gamma_{sv}^\circ - (\gamma_{sl} + \gamma_{lv}^\circ)$  (ZISMAN 1964, p.1) where  $\gamma_{sv}^\circ$  is free energy of interface, and  $\gamma_{lv}^\circ$  the term for the

liquid-vapor interface. In the temperature region  $0^\circ\text{C}$  to  $-40^\circ\text{C}$ , the value of the term  $(\gamma_{sl} + \gamma_{lv}^\circ)$  remains constant or increases slightly with temperature decrease (PRUPPACHER 1978, p. 104 and 129);  $\gamma_{sv}^\circ$  increases with temperature decrease. Since  $S > 0$  at  $0^\circ\text{C}$ , we can conclude that supercooled water droplets would spread over ice surface with contact angle of zero at any temperature, if freezing were not taking place; this can give an apparent constant angle (KNIGHT 1967, p.250). The dominant factor of spreading on ice is the ratio of spreading speed and freezing speed, but not surface free energy.

This work was carried out under NSF Contract #ATM-8715636, Division of Atmospheric Science, National Science Foundation, Washington, D.C.

## 5. REFERENCES

- FURUKAWA, Y.; KURODA, I; and YAMAMOTO, M.: Study of the transition layer on the surface of an ice crystal. *J. Crystal Growth*. 29 (1986), 82, p.665-677.
- HALLETT, J.: Experimental studies of the crystallization of supercooled water. *J. Atmos. Sci.* 21 (1964), p.677-682.
- HANSMAN, R.J.; Jr. and TURNOCK, S.R.: Investigation of surface water behaviour during glacial ice accretion. AIAA 26th Aerospace Sciences Meeting. AIAA (1988), paper 0015.
- KNIGHT, C.A.: The contact angle of water on ice. *J. Coll. and Int. Sci.* 25 (1967) p.280.
- KURODA, T. and LACHMANN R.: Growth kinetics of ice from the vapour phase and its growth forms. *J. Crystal Growth* 56 (1982), p.189-205.
- PRUPPACHER, H.R.: Microphysics of cloud and precipitation. 1978, p.104-129. D. Reidel Publishing Company, Dordrecht, Holland.
- ZISMAN, W.A.: Relation of equilibrium contact angle to liquid and solid constitution. Contact Angle wettability and adhesion. *Advances in Chemistry series 43* (1964), p.1-51.

# A MODEL OF THE ELECTROSTATIC-AERODYNAMIC SHAPE OF RAINDROPS

Catherine Chuang and Kenneth V. Beard

Department of Atmospheric Sciences, University of Illinois  
105 S. Gregory Avenue, Urbana, Illinois 61801

## 1. INTRODUCTION

Early theoretical and semiempirical models to predict the shape of raindrops have been subject to varying restrictions either in physical realism or in applications. A new model based on the equilibrium equation across a curved surface was developed by incorporating an aerodynamic pressure and electrostatic effects. The method of applying an empirical pressure distribution around a sphere, originally proposed by Savic, has been refined to include variations in the pressure distribution with Reynolds number and drop distortion. A finite volume technique was used to calculate the shape dependent electric effect with a numerically generated boundary-fitted coordinate system.

## 2. EQUILIBRIUM EQUATION

The equilibrium shape of an interface was determined by Laplace's pressure balance at each point on the surface

$$\sigma(1/R_1 + 1/R_2) = \Delta P \quad (1)$$

where  $\sigma$  is the surface tension,  $R_1$  and  $R_2$  are the principal curvature radii, and  $\Delta P$  is the net pressure. The curvatures were evaluated using a tangent angle coordinate system in a vertical plane (Hartland and Hartley, 1976), where  $1/R_1 = d\phi/ds$  and  $1/R_2 = \sin\phi/x$  (see Fig. 1).

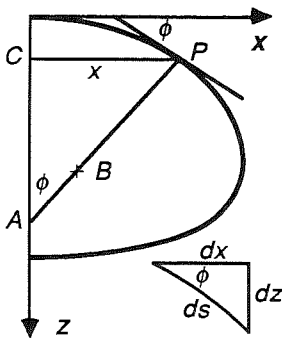


Fig. 1. Diagram for the drop surface with  $R_1$  given by  $BP$  and  $R_2$  by  $AP$ .

There are five physical factors which are expected to control the shape of raindrops: surface tension, hydrostatic pressure, aerodynamic pressure, internal circulation and electric stress. The initial step in developing the model was a force balance among the first three factors

$$\sigma(d\phi/ds + \sin\phi/x) = 2\sigma/R_t + \Delta\rho gz + (P_{\text{top}} - P)_a \quad (2)$$

where  $R_t$  is the radius of curvature at the top,  $\Delta\rho$  is the density difference between water and air, and  $(P_{\text{top}} - P)_a$  is the aerodynamic pressure change from the upper pole.

The accumulated upward force due to airflow past the raindrop can be computed by integration of the aerodynamic pressure acting on the total drop surface  $A$ :

$$-\int_A P_a \cos\phi dA = mg \quad (3)$$

Eq (3) implies that the supporting force from aerodynamic pressure must equal the total weight to satisfy the requirement of mechanical equilibrium. The shape was calculated by forward integration of  $d\phi/ds$  for assumed values of the initial curvature at the top with a boundary condition  $d\phi/ds = \sin\phi/x = 1/R_t$ , where  $x = z = \phi = 0$ . An iterative scheme is applied to determine the initial curvature at the top ( $1/R_t$ ) necessary to achieve the proper volume for a particular drop size.

## 3. MODIFYING THE PRESSURE DISTRIBUTION

Before each computation of drop shape, the aerodynamic pressure distribution was adjusted for the effects of drag beginning with an appropriate distribution for a sphere. Measurements of the surface pressure around rigid spheres at very large Reynolds number ( $Re = 10^4 - 10^5$ ) and numerical results ( $Re = 400$ ) are practically identical in the unseparated region. The distributions for high Reynolds number are rather flat behind the separation point and show only a few degrees variation in the location and breadth of the pressure dip. The distribution of Fage (1937) was used, but instead of applying the data directly to the calculation as in the

perturbation model of Savic (1953) and Pruppacher and Pitter (1971), an adjustment was made before each calculation to obtain the appropriate pressure drag for a particular Reynolds number.

In the range of Reynolds number applicable to larger raindrops ( $d = 2 - 9$  mm) the pressure drag ( $C_{dp}$ ) was approximated by an empirical formula as

$$C_{dp} = C_d [1 - 13.4 Re^{-0.58}] \quad (4)$$

where  $C_d$  is the total drag. This interpolation formula was obtained by using end points from LeClair *et al.* (1970) at  $Re = 400$  and Achenbach (1972) at  $Re = 75\,000$ .

The adjustment of pressure drag was made by altering the pressure distribution of Fage in the wake region ( $88^\circ$  to  $180^\circ$ ) and the intermediate region ( $72^\circ - 88^\circ$ ) using

$$\begin{aligned} \kappa'(\psi) &= 1 - \Gamma [1 - \kappa_{fage}(\psi)] & 88^\circ \leq \psi \leq 180^\circ \\ \kappa'(\psi) &= 1 - \Gamma' [1 - \kappa_{fage}(\psi)] & 72^\circ < \psi < 88^\circ \end{aligned} \quad (5)$$

where  $\Gamma$  is a constant and  $\Gamma' = 1 - (1 - \Gamma)(\psi - 72^\circ)/16$  provides a linear transition between the unseparated region at  $72^\circ$  and the wake at  $88^\circ$ . The value of  $\Gamma$  was adjusted before the shape calculation so that the pressure drag, obtained by integration  $\kappa'(\psi)$  over the surface of a sphere, was the appropriate fraction of the weight as given by (4).

#### 4. AERODYNAMIC SHAPE OF RAINDROPS

As discussed in Beard and Chuang (1987) an excessive pressure amplitude is required to offset the entire weight, since the pressure drag can offset only the fraction  $C_{dp}/C_d$ . A mean weight was used by replacing the density difference in (2) by  $0.5(1 + C_{dp}/C_d)\Delta\rho$ . The amplitude of the pressure distribution  $\kappa'$  was readjusted before every calculation, by using  $\kappa = \Lambda \kappa'$ , where the constant  $\Lambda$  is determined by integration such that the pressure drag equals the mean weight. This step was needed to adjust for the effect of distortion.

Successive calculations were made using an updated pressure distribution based on the previous drop shape, with  $\kappa'$  obtained from a new value of  $\Gamma$  to satisfied (4), and with  $\kappa$  obtained from a new value of  $\Lambda$ . Iteration was stopped after the raindrop shapes were sufficiently converged (typically 4-8 cycles). The final pressure distributions are similar to those shown in Beard and Chuang where the pressure amplitudes increase with distortion, *i.e.*, the pressure dip lowers.

The computed aerodynamic shape of raindrops are

shown in Fig. 2 for  $d = 1$  to 6 mm. The drop shapes are placed with the center of mass at the origin with corresponding dashed circles having the radius of the equivalent volume sphere. The flatter base for larger raindrop results from the increasing influence of hydrostatic and aerodynamic effects. Because of the absence of a dimple in the base, the raindrop cross sections in Fig. 2 are also profiles.

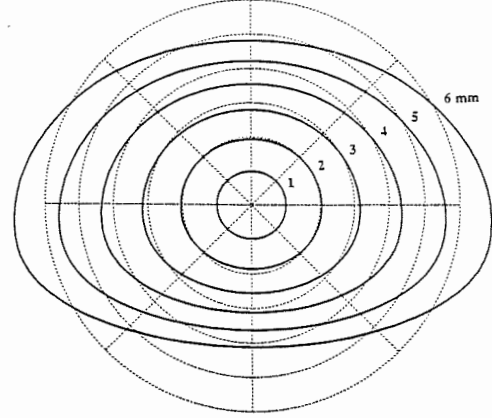


Fig. 2. Model results for aerodynamic drops.

#### 5. ELECTROSTATIC EFFECT ON DROP SHAPE

In the absence of space charge, the static potential distribution for any conductor configuration can be determined from Laplace's equation. The electric stress from either an applied electric field or surface charges will decrease the pressure difference  $\Delta P$  by an amount  $E_s^2/8\pi$  which modifies the equilibrium equation to

$$\sigma(d\phi/ds + \sin\phi/x) - E_s^2/8\pi = 2\sigma/R_t + \Delta\rho g z + (P_{top} - P)_a \quad (6)$$

where  $E_s$  is the magnitude of electric field in electrostatic units (e.s.u.) at the outside surface of drop. The main difficulty in solving for the electrostatic effect is that the drop shape must be known. A numerical iterative method was used to solve the unknown boundary shape. In order to avoid loss of accuracy, Laplace's equation for the electric potential was solved in a domain with boundaries that are coincident with the drop surface. The boundary-fitted coordinate systems was numerically generated by taking the transformed curvilinear coordinates to be solutions of a suitable elliptic partial differential equation in the physical plane (Thompson *et al.*, 1974). Laplace's equation was solved by a finite volume method to simplify the Neumann boundary condition on the polar axis.

The effect of a uniform vertical electric field on the drop shape is illustrated in Fig. 3 for  $d = 1 - 6$  mm and  $E = 9$  kV/cm. Stronger electric stress in the regions of the poles makes the shape more rounded than the aerodynamic shape. The axis ratio ( $\alpha_e$ ) under different magnitudes of vertical electric field are given in Table 1.

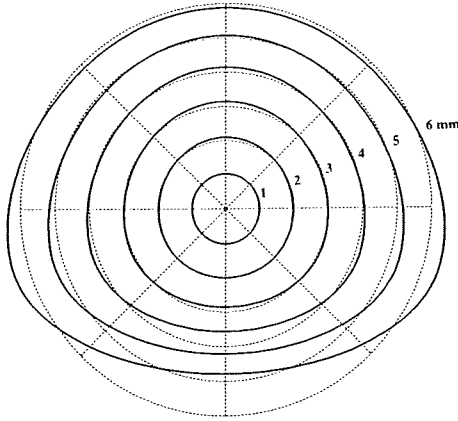


Fig. 3. Model results for aerodynamic-electrostatic drops.

TABLE 1. Axis ratios for drops in a vertical electric field.

$E$ (kV/cm)	Axis Ratio			
	$d = 2$	3	4	5
1.0	0.847	0.768	0.703	0.649
2.0	0.851	0.773	0.708	0.654
3.0	0.858	0.781	0.716	0.661
4.0	0.869	0.792	0.727	0.672
5.0	0.884	0.809	0.743	0.688
6.0	0.903	0.830	0.765	0.708
7.0	0.928	0.859	0.794	0.737
8.0	0.961	0.897	0.835	0.776
9.0	1.005	0.950	0.895	0.836

## 6. DISCUSSION

Model results for aerodynamic shapes when compared with observations in wind tunnels follow the trend in measurements of the equilibrium axis ratios even for extremely large drops. The computed shapes for the pure electrostatic distortion are very close to the theoretical study by Taylor (1964). The results for aerodynamic-electrostatic drops are similar to the mean shapes and axis ratios obtained by Richards and Dawson (1973) from photographs of drops in a wind tunnel with a vertical electric field.

## 7. ACKNOWLEDGMENTS

This material is based upon work supported by the National Science Foundation under Grants ATM84-19490 and ATM86-01549. Any opinions, findings, and conclusions or recommendations expressed in this material are those of the authors and do not necessarily reflect the views of the National Science Foundation.

## 8. REFERENCES

- Achenbach, E., 1972: Experiments on the flow past spheres at very high Reynolds numbers. *J. Fluid Mech.*, 54, 565-575.
- Beard, K. V., and C. Chuang, 1987: A new model for the equilibrium shape of raindrops. *J. Atmos. Sci.*, 44, 1509-1524.
- Page, A., 1937: Experiments on a sphere at critical Reynolds Numbers. Aero. Res. Comm., England, Rep. and Memo. No. 1766, 20 pp.
- Hartland, S., and R. W. Hartley, 1976: *Axisymmetric Fluid-Liquid Interfaces*. Elsevier, 782pp.
- LeClair, B. P., A. E. Hamielec and H. R. Pruppacher, 1970: A numerical study of the drag on a sphere at low and intermediate Reynolds number. *J. Atmos. Sci.*, 27, 308-315.
- Pruppacher, H. R., and J. D. Klett, 1978: *Microphysics of Clouds and Precipitation*. Reidel, Boston, 714 pp.
- Pruppacher, H. R., and R. L. Pitter, 1971: A semi-empirical determination of the shape of cloud and rain drops. *J. Atmos. Sci.*, 28, 86-94.
- Richards, C. N., and G. A. Dawson, 1973: Stress on a raindrop falling at terminal velocity in a vertical electric field - A numerical method. *Phys. Fluids*, 16, 796-800.
- Savic, P., 1953: Circulation and distortion of liquid drops falling through a viscous medium. Natl. Res. Council, Canada, Rep. NRC-MT-22, 50 pp.
- Taylor, G., 1964: Disintegration of water drops in an electric field. *Proc. Roy. Soc. London*, A280, 383-397.
- Thompson, J. F., F. C. Thames, and C. W. Mastin, 1974: Automatic numerical generation of body-fitted curvilinear coordinate system for field containing any number of arbitrary two-dimensional bodies. *J. Comp. Phys.*, 15, 299-319.

MEASUREMENTS OF THE PARTITIONING OF AEROSOL MASS AND NUMBER  
BETWEEN CLOUD DROPLETS AND INTERSTITIAL AIR

John Ogren, Jost Heintzenberg and Kevin Noone

Department of Meteorology, University of Stockholm,  
S-106 91 Stockholm, Sweden

## 1 INTRODUCTION

The incorporation of aerosol particles into clouds is of central importance to both cloud chemistry and cloud physics. The number of cloud droplets is determined by the number of aerosol particles that act as cloud condensation nuclei, while the mass of aerosol particles scavenged by the droplets determines to a large extent the chemical composition of the droplets. In a recent study, TEN BRINK ET AL. (1987) reviewed the available measurements of the efficiency of nucleation scavenging of aerosol particles by clouds and reported that "there have been few measurements that have unambiguously and precisely determined the efficiency of this process in natural clouds.

Model calculations (JENSEN AND CHARLSON, 1984) suggest that the mass scavenging efficiency is a function of the mass of submicrometer particles and the updraft velocity, but little experimental evidence is available to confirm this functionality. Measurements by LEITCH ET AL. (1986) are consistent with the model predictions, showing that lower number and mass scavenging efficiencies are associated with higher aerosol loadings, but the measurements of TEN BRINK ET AL. (1987) showed uniformly high mass scavenging efficiencies regardless of the aerosol mass loading.

Interpretation of the available measurements is hindered by one or both of the following limitations in the experimental methods: the total number

and mass of aerosol particles (scavenged plus unscavenged) are unavailable, or the time resolution of the measurements is too low to resolve inhomogeneities in the cloud. Most of the works to date have relied on a comparison of in-cloud and out-of-cloud measurements to derive the scavenging efficiency, but have not measured the total mass and number of aerosol particles within the cloud. As a result, interpretation of the data requires assumptions about the relationship between total aerosol mass and number within and outside of the cloud. Interpretation of measurements obtained with low time resolution (e.g., those based on collected samples of interstitial air) may also require the assumption that the cloud was present during the entire sampling interval.

Both of the above limitations apply to the present work. However, these limitations are the result of the current implementation of the sampling technique, not of the technique itself. Accordingly, the focus of this paper is to describe our approach to measuring scavenging efficiencies and to present data demonstrating the feasibility of the method.

## 2 EXPERIMENTAL APPROACH

Measurements were performed in stratocumulus clouds on Mt. Åreskutan in central Sweden (63°26'N, 13°6'E, 1250 m asl) during the summer of 1986. Cloud droplets greater than 4  $\mu\text{m}$  radius were sampled with a counterflow virtual

impactor operated in a vertical wind tunnel (OGREN et al., 1985; NOONE et al., 1988). The sampled droplets were evaporated and then counted with a condensation nucleus counter (TSI model 3020). The light scattering coefficient ( $\sigma_{sp}$ ) of the residual aerosol particles, determined with an integrating nephelometer, was used as a surrogate for the mass of aerosol particles. The liquid water content (LWC) of the cloud was determined by measuring the water vapor concentration resulting from evaporation of the cloud droplets, using a Lyman-alpha hygrometer (ZUBER and WITT, 1987). An identical nephelometer and condensation nucleus counter sampled particles smaller than 1  $\mu\text{m}$  radius following removal of larger particles and droplets with a cyclone. The nephelometers were of a design similar to that reported by HEINTZENBERG and BÄCKLIN (1983), with a detection limit of  $10^{-7} \text{ m}^{-1}$ . This sensitivity allowed even the very low aerosol light scattering coefficients in cloud interstitial air to be quantified.

The submicrometer aerosol measurements were obtained during field testing of a system for baseline measurements in Arctic air, and were recorded as five-minute medians of 1 Hz measurements. This time resolution was optimized for variations occurring over synoptic time scales, rather than cloud time scales. As a result, inhomogeneities in the clouds on time scales shorter than 5 minutes (of order 2 km) could not be resolved in the submicrometer aerosol measurements. The measurements obtained with the CVI system were recorded with time resolutions of 1-10 seconds, and frequently showed rapid variations in drop number concentration and LWC that were not apparent in the submicrometer aerosol data.

### 3 RESULTS

Submicrometer aerosol  $\sigma_{sp}$  typically dropped by at least a factor of ten when clouds were present, while the number concentration (N) of submicrometer particles rarely decreased by more than 50 percent. An example of the effect of cloud passage on  $\sigma_{sp}$  is illustrated in Fig. 1. During periods when a cloud was present, as indicated by LWC (inoperative prior to 11:50) and  $\sigma_{sp}$  of the cloud droplet residues, the sum of the light scattering coefficients of the submicrometer aerosol particles and residual cloud droplets was lower than the out-of-cloud submicrometer aerosol  $\sigma_{sp}$ . This is attributed to the presence of unsampled droplets between 1 and 4  $\mu\text{m}$  radius. Assuming that the total aerosol light scattering coefficient was constant within the cloud, examination of Fig. 1 suggests that the mass of particles associated with droplets in the 1-4  $\mu\text{m}$  range in the dense portion of the cloud

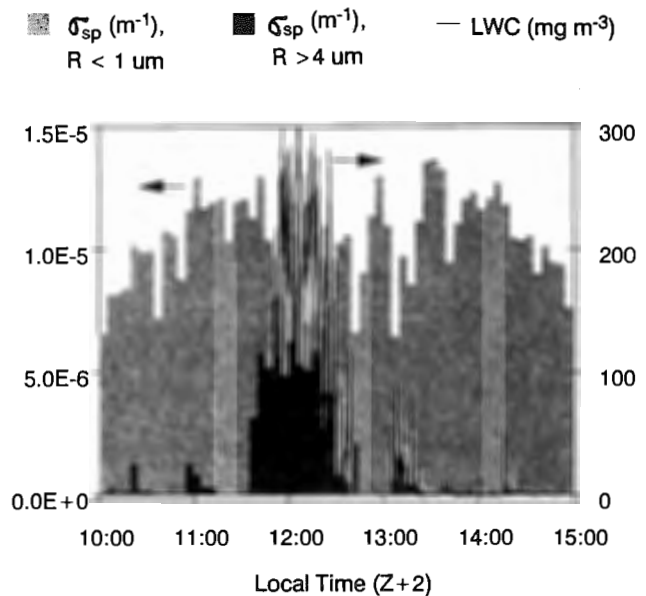


Fig. 1: Variation of LWC and  $\sigma_{sp}$  associated with submicrometer particles (light-shaded area) and cloud droplets (dark-shaded area) during passage of a cloud. Note that the height of the stacked bars corresponds to the sum.

(around 12:00, when the sampling site was about 300 m above cloud base) was comparable to the mass of particles associated with droplets greater than 4  $\mu\text{m}$ .

The corresponding picture for the effect of clouds on N (Fig. 2) is quite different. Here, the number of cloud droplets larger than 4  $\mu\text{m}$  radius was less than 2% of the number of particles outside of the cloud, while the total dropped by about 20% in the cloud (again, the "missing" particles are thought to be associated with 1-4  $\mu\text{m}$  droplets). The low scavenging efficiency for particle number, combined with the high scavenging efficiency for particle mass, suggests that the unscavenged particles were quite small. This finding is consistent with simultaneous measurements of the size distribution of the interstitial particles, which typically showed a mode under 0.1  $\mu\text{m}$  radius.

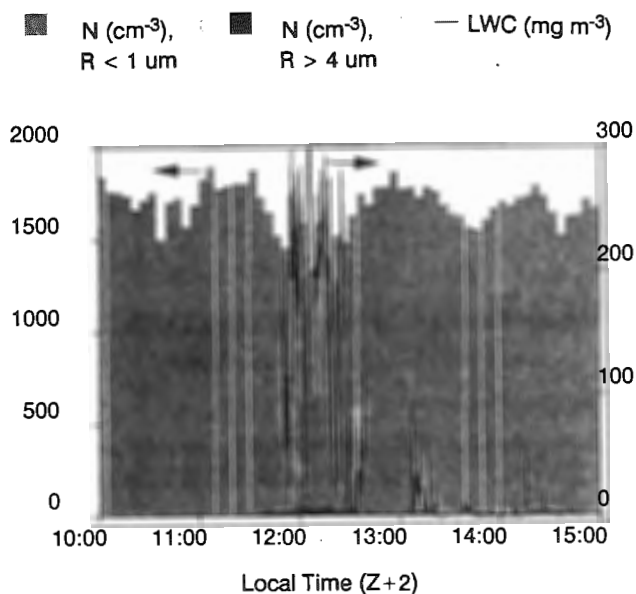


Fig. 2: Variation of LWC and N, as in Fig. 1.

#### 4 CONCLUSION

In the relatively unpolluted, strato-cumulus clouds frequently encountered at the site, well over half of the mass of submicrometer particles was typically found in the droplets. In contrast, fewer than half of the number of submicrometer particles was contained in the cloud droplets. In order to obtain more precise determinations of the scavenging efficiencies, the CVI is being redesigned to allow sampling of droplets down to 1  $\mu\text{m}$  radius, and the time resolution of the submicrometer aerosol data is being improved.

#### 5 REFERENCES

- HEINTZENBERG, J.; BÄCKLIN, L.: A high sensitivity integrating nephelometer for airborne air pollution studies. *Atmos. Environ.* 17 (1983), p. 433-436.
- JENSEN, J.; CHARLSON, R.: On the efficiency of nucleation scavenging. *Tellus 36B* (1985), p. 367-375.
- LEAITCH, W.; STRAPP, J.; ISAAC, G.; HUDSON, J.: Cloud droplet nucleation and cloud scavenging of aerosol sulphate in polluted atmospheres. *Tellus 38B* (1986), p. 328-344.
- NOONE, K.; CHARLSON, R.; COVERT, D.; OGREN, J.; HEINTZENBERG, J.: Cloud droplets: Solute concentration is size dependent. *J. Geophys. Res.* (1988), in press.
- OGREN, J.; HEINTZENBERG, J.; CHARLSON, R.: In-situ sampling of clouds with a droplet to aerosol converter. *Geophys. Res. Lett.* 12 (1985), p. 121-124.
- TEN BRINK, H.; SCHWARTZ, S.; DAUM, P.: Efficient scavenging of aerosol sulfate by liquid-water clouds. *Atmos. Environ.* 21 (1987), p. 2035-2052.
- ZUBER, A.; WITT, G.: Optical hygrometer using differential absorption of hydrogen Lyman- $\alpha$  radiation. *Appl. Optics* 26 (1987), p. 3083-3089.

THE CALCULATION OF SUPERSATURATIONS AND GROWTH OF DROPLETS  
IN CONTINENTAL CUMULUS CLOUDS

Keith Bower and Tom Choularton

Dept. of Pure and Applied Physics

University of Manchester Institute of Science and Technology

P O Box 88

Manchester M60 1QD, UK

There has been much recent debate concerning the mechanism by which drops in continental cumulus clouds are able to grow to radii in excess of  $25 \mu\text{m}$ , to enable the initiation of further growth by coalescence to produce warm rain. In-cloud measurements have shown that enhanced growth of up to  $5 \mu\text{m}$  beyond the largest radii predicted by adiabatic growth is often observed (HILL and CHOULARTON, 1985, BLYTH and LATHAM, 1985) and this is consistent with the work of other authors (eg. BAKER et al, 1980, TELFORD and CHAI, 1980) who envisage dry air entrainment as playing a major role in droplet growth in such clouds.

A model has been developed by HILL and CHOULARTON, 1986, to include the effects of dry tropospheric air entrainment on the growth of a droplet spectrum in cumulus clouds. Such entrainment is considered to occur on localised scales, and in the model discrete blobs of dry tropospheric air gradually mix with the surrounding cloud, evaporating totally those drops nearest to the blob but causing little or no evaporation of more remote drops. This leads to the evaporative cooling of the blob as it becomes saturated, but the region mixes with surrounding cloud and continues to rise if sufficient momentum can be entrained. This will cause a high supersaturation to develop which will then decline rapidly as cloud condensation nuclei (CCN) become activated. Hence the model predicts that such mixing will have the effect of reducing the number concentration of droplets of all sizes but with the spectra retaining the same overall shape. The effects of several such events will cause cloud supersaturations to be higher than corresponding adiabatic

values, and they will not be closely tied to updraught speed. Increased supersaturations are expected to be responsible for the observed enhanced growth, and further results of mixing are expected to include an increase in the bimodality of spectra, and a reduction in mean droplet lifetime when compared to the ascent times of air parcels travelling from cloud base to cloud top.

Observations from several aircraft passes through continental cumulus clouds obtained during the CCOPE experiment on 12 July, 1981, have been analysed in an attempt to test these predicted results of dry air entrainment. The general properties of one such pass are shown in Figure 1. In general there exist broad regions (500-1500 m across) of similar droplet number concentrations  $N$ , liquid water contents  $L$ , and mixing history (eg. regions A, B, C). In addition, there are smaller regions  $l$ , (<200 m wide) showing negative deviations of  $N$ ,  $L$ , updraught  $W$ , and temperature  $T$ , which cannot be attributable to sampling error, and are considered to be regions of recent entrainment. A comparison of average droplet spectra from such regions with those obtained from neighbouring broader regions is shown in Figure 2 for four passes. It can be seen that a reduction in  $N$  across the whole spectrum has occurred. The general spectral shape is retained for droplet sizes above  $5 \mu\text{m}$ , but below this there is evidence of the CCN reactivation expected to occur in the high supersaturations following a mixing event.

A method to calculate supersaturations present in the CCOPE passes was devised using the observed values of  $T$ , pressure  $p$ ,  $W$ , and

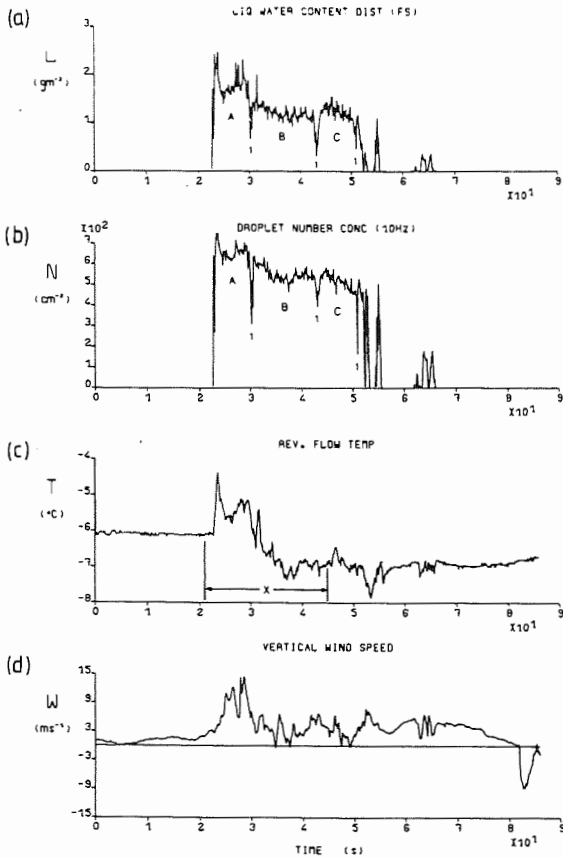


Figure 1. Distribution of (a) FSSP total liquid water content  $L$ , (b) number concentration  $N$ , (c) dry bulb temperature  $T$ , and (d) vertical wind velocity  $W$ , all measured at 10Hz for pass 13.

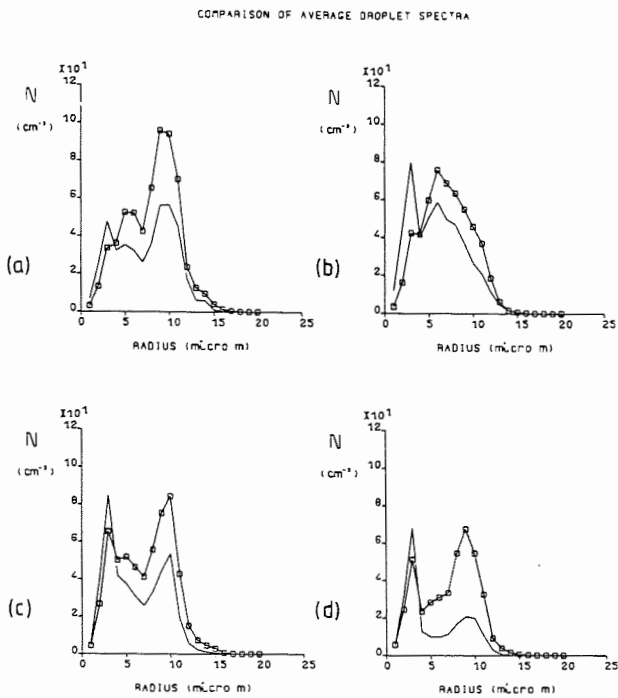


Figure 2. Comparison of average droplet spectra from regions (1) of recent entrainment (curve with no symbols), with average spectra from neighbouring cloud regions (curve with symbols) for (a) Pass 6, (b) Pass 13, (c) Pass 7 and (d) Pass 14.

droplet spectra. These were included in an adiabatic growth model, with a prescribed initial supersaturation of 0.1%. Integrating the model forward with a timestep of 0.01 s, the equilibrium supersaturations were calculated (usually within an altitude change of 7 m, and development time of 1.29 s). Figure 3 shows the supersaturations  $S$ , and updraughts,  $W$ , used in their calculation for one cloud pass. Figure 4 shows the corresponding  $S$  versus  $W$  plot, and as predicted illustrates that the two parameters are not related closely except in regions of similar mixing history.

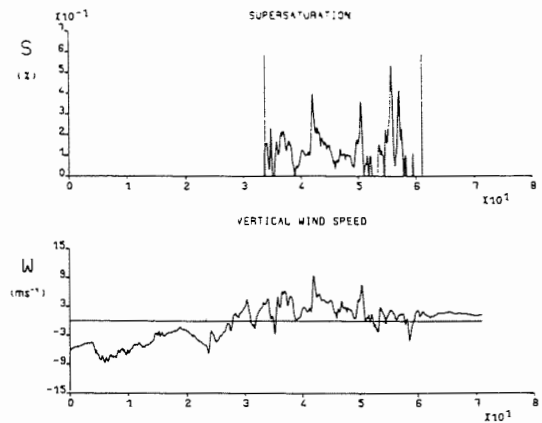


Figure 3. Distributions of calculated supersaturation and vertical velocity for Pass 5.

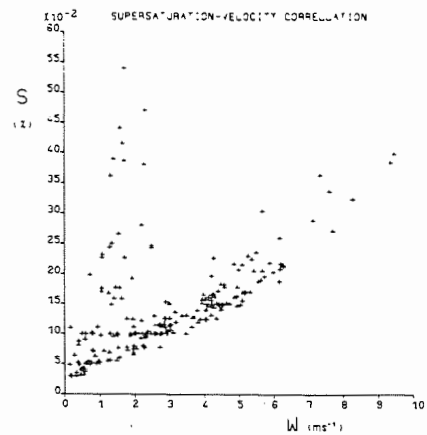


Figure 4. Calculated supersaturation versus vertical velocity for Pass 5.

For comparison purposes, a representative droplet spectrum developed from a measured CCN distribution was allowed to develop adiabatically, from the observed cloud base conditions in a constant updraught profile to the

observation level. Number concentrations of activated droplets were adjusted to reproduce the observed values of  $N$ . In total, eight sets of data were allowed to develop to the observation level and cloud top in this way, and the resultant adiabatic spectra were found to be much narrower than the observed with a very much higher liquid water content. A comparison of maximum droplet radii revealed that the adiabatic values were on average 19% smaller than the observed, corresponding to a difference of 3-4  $\mu\text{m}$ , and that the corresponding adiabatic supersaturations were 26% lower.

The effect of the enhanced supersaturation on droplet growth was then modelled by reducing the number concentration of activated droplets in the adiabatic model so as to reproduce the observed supersaturations at the observation level. This resulted in the average maximum droplet size being increased by 16% but it was still 6% smaller than the average observed maximum. However, this process takes no account of the statistically favoured droplets which are envisaged to avoid evaporation following entrainment in the model, but which do experience the high  $S$  pulses. Hence number concentrations were reduced still further in the adiabatic model so as to reproduce the 'observed' potential supersaturations at the observation level. This increased maximum droplet sizes to within 1% on average of the observed values (although there was a large spread of  $\pm 6\%$  in results). It therefore seems reasonable to suggest that the enhanced growth can be accounted for taking into consideration the enhanced observed supersaturations which occur following several dry air entrainment events.

Finally, average droplet lifetimes were calculated by considering the time taken for embryo droplets to develop to an average size equal to the observed value in an adiabatic model. Starting at cloud base or from some higher level under observed conditions, esti-

mates of mean lifetime of between 1.5 and 4.5 minutes were obtained depending on the updraught profiles prescribed. With a profile which increased linearly from the cloud base updraught to the observation level value, an average mean lifetime of 3 mins was obtained. As predicted this is considerably shorter (by a factor of about 0.2) than the parcel ascent time from cloud base to the observation level, and is similarly shorter than the average reported age of these clouds. In addition, a mean droplet lifetime of less than 5 mins, which is also a measure of the average interval between mixing events, has important consequences for the chemistry occurring within the droplets, especially so for the aqueous phase oxidation of sulphur dioxide by hydrogen peroxide and ozone. Only the former process will be important, the latter requiring a timescale of several tens of minutes. The entrainment process will also help to replenish the oxidant, thus enhancing sulphate production in the drops.

#### REFERENCES

- BAKER, M.B.; CORBIN, R.G; LATHAM, J.: The Influence of Entrainment on the Evolution of Cloud Droplet Spectra: I. A Model of Inhomogeneous Mixing. *Quart. J. Roy. Met. Soc.* 106 (1980) 581-598.
- BLYTH, A.M.; LATHAM, J.: An Airborne Study of Vertical Structure and Microphysical Variability Within a Small Cumulus. *Quart. J. R. Met. Soc.* 111 (1985) 773-792
- HILL, T.A.; CHOULARTON, T.W.: An Airborne Study of the Microphysical Structure of Cumulus Clouds. *Quart. J. R. Met. Soc.* 111 (1985) 517-544.
- HILL, T.A.; CHOULARTON, T.W.: A Model of the Development of the Droplet Spectrum in a Growing Cumulus Turret. *Quart. J.R. Met. Soc.* 112 (1986) 531-554.
- TELFORD, J.W.; CHAI, S.K.: A New Aspect of Condensation Theory. *Pageoph* 118 (1980) 720-741.

# ON THE OBSERVATIONS OF CLOUD TEMPERATURE AND LIQUID WATER CONTENT USING A LYMAN- $\alpha$ AND AN FSSP SENSOR

Jørgen B. Jensen, Darrel Baumgardner

National Center for Atmospheric Research<sup>1</sup> Boulder, CO 80307

Graciela Raga

Department of Atmospheric Sciences, University of Washington, Seattle, WA 98195

## 1. INTRODUCTION

The 1985 Joint Hawaiian Warm Rain Project was an aircraft experiment designed to explore the processes leading to warm rain in cumulus clouds off the coast of Hawaii. During the five weeks of the experiment a very large number of cumuli were sampled by the University of Wyoming King Air in a systematic manner.

For a detailed discussion of the aircraft instrumentation we refer to COOPER *et al.* (1984); here we will only discuss the reverse flow temperature sensor, the EG&G dew-point thermometer, a Lyman- $\alpha$  humidity sensor mounted with a reverse flow shielding inside the fuselage, and a PMS FSSP.

We have analyzed 134 penetrations from 22 clouds sampled on six days during July of 1985. A total of 3126 1-second samples were classified as in-cloud.

## 2. RAW TEMPERATURE MEASUREMENTS

Wetting of temperature sensor elements during certain circumstances have previously been described by e.g. LENSCHOW and PENNELL (1974). Wetting of heating of air passing by the sensor evaporates some of the water and cools the sensor element. The adiabatic heating depends on the aircraft true air speed and this effect is corrected for; there is no correction for the effect of evaporative cooling.

The evidence for sensor wetting is twofold: (i) A comparison between parcel buoyancy and vertical wind speed showed that most parcels were both negatively buoyant *and* ascending. (ii) A transient "cooling spike" was commonly found upon exit from cloud,

when the wet sensor element suddenly is immersed in highly sub-saturated air. Therefore we have chosen to use the Lyman- $\alpha$  sensor on the aircraft to estimate the temperature of saturated, cloudy air.

## 3. CALIBRATION OF THE LYMAN- $\alpha$ SENSOR

Descriptions of Lyman- $\alpha$  sensors for measurements of atmospheric water vapor have been given by eg. TILLMAN (1965). Since the present calibration technique differs from previous methods, we will describe it in some detail. After calibration we can calculate a Lyman- $\alpha$  derived dew-point temperature,  $T_{L\alpha}$ . This is useful as a fast response dew-point temperature measurement outside cloud as well as an estimate of the temperature of saturated cloudy air.

In the following calculation we will assume that collimated light with wavelengths between  $\lambda_{min} = 115$  nm and  $\lambda_{max} = 132$  nm is emitted with intensity  $I_0(\lambda)$  and that it is detected with intensity  $I$ . Given that water vapor and oxygen are the only significant absorbers for this wavelength range in the lower atmosphere, we can write the Beer law as:

$$I = \int_{\lambda_{min}}^{\lambda_{max}} I_0(\lambda) \exp \left\{ -\frac{k_v(\lambda)\rho_v\Delta s}{\rho_{vref}} - \frac{k_z(\lambda)\rho_z\Delta s}{\rho_{zref}} \right\} d\lambda \quad (1)$$

Here  $k_v(\lambda)$  and  $k_z(\lambda)$  are the absorption coefficients for water vapor and oxygen respectively,  $\rho_v$  and  $\rho_z$  are the vapor and oxygen densities,  $\rho_{vref}$  and  $\rho_{zref}$  are the reference densities of vapor and oxygen at STP, and  $\Delta s$  is the pathlength. Since both  $I_0(\lambda)$ ,  $k_v(\lambda)$  and  $k_z(\lambda)$  depend strongly on  $\lambda$  and since  $I_0(\lambda)$  may change with time, it is next to impossible to evaluate

eq. (1) exactly. We will therefore simplify eq. (1) by using average values of  $I_0(\lambda)$ ,  $k_v(\lambda)$  and  $k_z(\lambda)$ , i.e.:

$$I = I_0 \exp \left\{ -\frac{k_v \rho_v \Delta s}{\rho_{vref}} - \frac{k_z \rho_z \Delta s}{\rho_{zref}} \right\} \quad (2)$$

For the subsequent processing we have:

$$V_{out} = c_4 \ln \{c_1 c_2 I + c_3\} + c_5 \quad (3)$$

where  $V_{out}$  is the voltage which is stored on tape,  $c_1$  and  $c_3$  are unknown constants, and  $c_2$ ,  $c_4$  and  $c_5$  are laboratory measured constants.

Combining eqs. (2) and (3) and reorganizing yields:

$$\begin{aligned} \frac{\rho_v}{\rho_{vref}} k_v \Delta s + \frac{\rho_z}{\rho_{zref}} k_z \Delta s - \ln \{c_1 c_3 I_0\} = \\ - \ln \left[ \exp \left\{ \frac{1}{c_4} (V_{out} - c_5) \right\} - c_3 \right] \quad (4) \end{aligned}$$

From day to day the maximum value of  $V_{out}$  increased until an upper limit of about 3.2 Volts was reached. At this point we found that the current-to-voltage converter offset,  $c_3 = 0.0028$  Volt.

By taking three segments with constant dew-point temperature from an environmental sounding we can use the EG&G dew-point sensor in combination with the pressure and reverse flow sensors to "calibrate" the Lyman- $\alpha$ . For the three sounding segments we can calculate  $(\rho_{v1}, \rho_{v2}, \rho_{v3})$ ,  $(\rho_{z1}, \rho_{z2}, \rho_{z3})$ , and (eq. (4):  $RHS_1, RHS_2, RHS_3$ ). Using eq. (4) to form three equations with three unknowns, we can solve for  $k_v \Delta s$ ,  $k_z \Delta s$  and  $\ln(c_1 c_3 I_0)$ ; i.e. the Lyman- $\alpha$  sensor is "calibrated". For 15 calibrations we find that the average  $k_v/k_z \approx 10$ .

After a calibration has been made, a double iteration is used to find the Lyman- $\alpha$  temperature. First step is to guess the water vapor density,  $\rho_v$ . Secondly we iterate  $T_{L\alpha}$  until the equation of state for water vapor is satisfied to a sufficient degree, calculate oxygen density and test if the LHS and RHS of eq. (4) matches sufficiently.

One final adjustment to  $T_{L\alpha}$  was made in the following way. At cloud base there will normally be a small difference between the Lyman- $\alpha$  and reverse flow temperature due to a slight offset between the

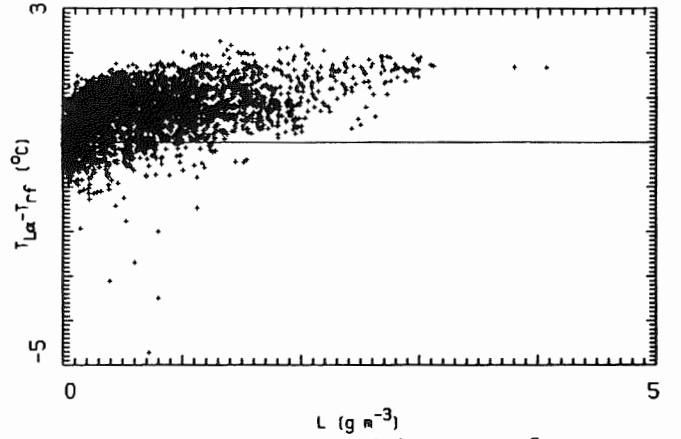


Fig. 1. Cooling,  $T_{L\alpha} - T_{rf}$ , of the reverse flow sensor with respect to the Lyman- $\alpha$  sensor due to wetting shown as function of the liquid water content,  $L$ .

sensors. This offset was added to the EG&G dewpoint temperature and the solution of the three equations with three unknowns repeated until the reverse flow temperature and the Lyman- $\alpha$  temperature were equal at cloud base.

#### 4. CORRECTED TEMPERATURE MEASUREMENTS

Fig. 1 shows the difference,  $T_{L\alpha} - T_{rf}$ , for all cloudy 1-second samples. Most of the samples show less than 1.5 °C cooling from wetting; maximum values are close to 2 °C. This compares favorably with the theoretical predictions by LENSCHOW and PENNELL (1974).

Using the Lyman- $\alpha$  derived temperature we find that most ascending parcels indeed are positively buoyant.

The deviation of the cloudy air temperature from the adiabatic temperature,  $T_{L\alpha} - T_a$ , as function of height,  $z$ , is shown in Fig. 2. If we estimate an uncertainty in the cloud base temperature of  $\pm 0.5$  °C, which translates into an uncertainty of  $T_a$  of  $\pm 0.5$  °C, it seems reasonable to assign an uncertainty in  $T_{L\alpha}$  of  $\pm 0.5$  °C. Fig. 2 shows that a large number of the cloudy samples have temperatures which can not be discerned from the adiabatic values. 49 % of the samples have  $-1$  °C  $< (T_{L\alpha} - T_a) < 1$  °C; these occur all the way from cloud base to cloud top.

#### 5. CORRECTIONS TO LWC MEASUREMENTS

The liquid water content, LWC, was derived from droplet size distribution measured with a PMS FSSP

probe. The observed liquid water mixing ratios were compared to the values predicted from adiabatic ascent from cloud base. Fig. 3 shows that the observed values never exceed 0.4 of the adiabatic values. Entrainment and mixing is expected to dilute many of the samples; however, it is disturbing that none of the data approach adiabatic values.

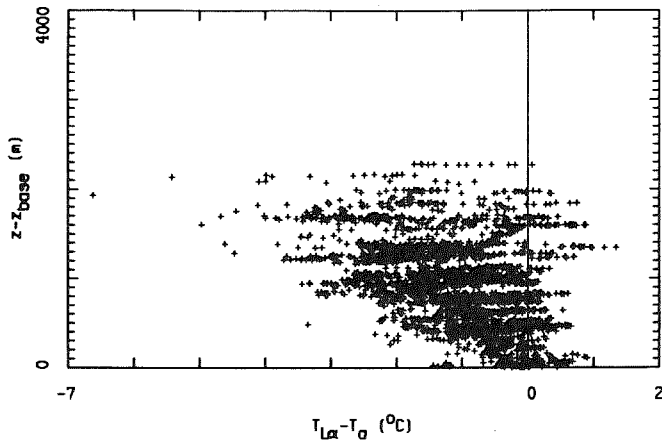


Fig. 2. Cooling of cloudy parcels due to entrainment,  $T_{L\alpha} - T_a$ , shown as function of flight level above cloud base,  $p_{base} - p$ .

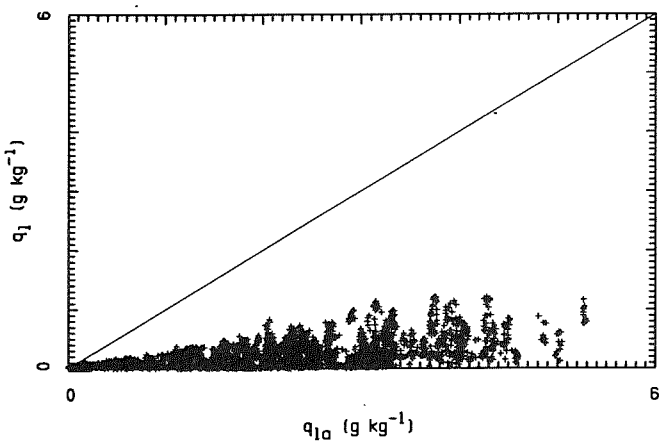


Fig. 3. Raw FSSP liquid water mixing ratio as function of adiabatic liquid water mixing ratio.

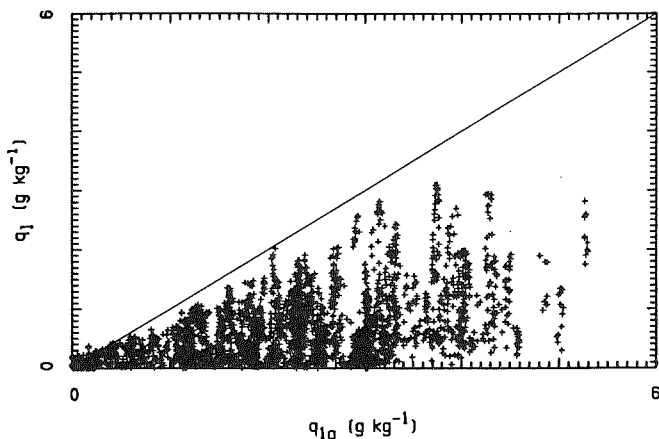


Fig. 4. Corrected FSSP liquid water mixing ratio as function of adiabatic liquid water mixing ratio.

An in-depth analysis of the FSSP (BAUMGARDNER, 1988) showed that significant corrections to the measurements were necessary to correct for sample volume variations, for undersizing that result from electronic response time limitations and for laser beam inhomogeneities. These effects are especially significant when droplet spectra are as broad as they were in the Hawaii trade clouds.

Correction algorithms were derived based on the operating characteristics of the FSSP and were applied to the measurements from this study. The results are shown in Fig. 4 where the comparison between observed and predicted values appear more sensible.

**ACKNOWLEDGMENTS** Thanks are due to Dr. W.A. Cooper of NCAR and Dr. A. Rodi from University of Wyoming for much help and many stimulating discussions. The present study was in part supported by National Science Foundation under grant ATM 8420816.

#### REFERENCE LIST

- BAUMGARDNER, D. (1988): Cloud droplet growth in Hawaii orographic clouds. *Ph. D. Dissertation*, University of Wyoming, 311 pp.
- COOPER, W.A. (1978): Cloud physics investigations by the University of Wyoming in HIPLEX 1977. Rept. #AS119, Dept. of Atmos. Sci., Univ. of Wyoming, Laramie, Wyoming, 321 pp.
- LENSCHOW, D.H. and W.T. PENNELL (1974): On the measurement of in-cloud and wet-bulb temperature from an aircraft. *Mon. Wea. Rev.*, **102**, 447-454.
- RAGA, G., J.B. JENSEN, J. WEWTLAUFER and M.B. BAKER (1988): Characteristics of cumulus band clouds off the coast of Hawaii. This volume.
- TILLMAN, J.E. (1965): Water vapor measurements utilizing the absorption of vacuum ultraviolet and infrared radiation. *Humidity and moisture, measurements and control in science and industry, 1, Principles and methods of measuring humidity in gasses*. R.E. Ruskin, Ed., New York, Reinhold, 428-433.

EVALUATION OF DROPLET GROWTH RATES  
IN HAWAIIAN OROGRAPHIC CLOUDS

Darrel Baumgardner

National Center for Atmospheric Research\*

Boulder, Colorado

1. INTRODUCTION

The present study was designed to provide more accurate and higher rate measurements of evolving cloud droplet populations than previously possible. The orographic clouds formed by the island of Hawaii were selected for evaluation because of their temporal stability, relatively low levels of turbulence, and warmer than freezing cloud tops. The results of these measurements are compared with predictions from a droplet growth model.

2. DROPLET GROWTH MODEL

In the one dimensional model that was developed the identity of each droplet is maintained after it is activated and until it coalesces with another droplet or leaves the cloud. This technique was utilized so that stochastic fluctuations could be evaluated during the growth process. The cloud condensation nuclei concentration,  $N$ , was parameterized as a function of the percent supersaturation,  $S$ , by using a power law relation,  $N = CS^k$ , where the values of  $C$  and  $k$  were measured (Hudson, private communication) as 34 and 0.55, respectively. The droplets initially grow by condensation during the parcel's adiabatic ascent and while coalescence is possible at any point during the growth process, it is insignificant until the median volume droplet diameter is greater than about 25  $\mu\text{m}$  (about 500 seconds of growth). Coalescence was modeled using the method of Gillespie (1975) where a Monte Carlo technique is used to generate the next time of coalescence and to select which two droplets

coalesce based upon a joint probability distribution established by the collection kernels of each droplet pair. This method was selected to examine the assumptions that are used when coalescence is modeled with the kinetic coagulation equation. The model was initialized with the measured cloud base temperature and pressure for each cloud study. The vertical motion of the air parcel was characterized by the measured profile of vertical velocity with altitude. The time period of the model was determined by the vertical velocity structure and depth of each of the three clouds that were evaluated.

3. MEASUREMENT METHODOLOGY

The primary variables measured were the cloud droplet size and number distributions. A forward scattering spectrometer probe (FSSP) and 260X one dimensional optical array probe, both manufactured by Particle Measuring Systems (PMS, INC., Boulder, Co.) provided measurements in the size range of 2  $\mu\text{m}$  to 150  $\mu\text{m}$ . An assessment of their operational and measurement limitations (Baumgardner, 1988) showed that differences could be resolved between droplet distributions that had grown for a minimum of 100 seconds. Figure 1 shows model results where droplet distributions were grown for 400 seconds (solid line) and 500 seconds (dashed line). The droplet spectra are displayed as if measured by the FSSP and 260X and have been adjusted to account for the inherent uncertainties and limitations imposed by the instruments. The measurement errors are estimated by using a Monte Carlo simulation of the instruments that accounts for the complex interactions among the factors that limit the instruments' operation. These errors are shown

\*Sponsored by the National Science Foundation

as vertical bars in each size channel. This figure shows how the measurement uncertainties can mask the differences in the spectra grown for different times.

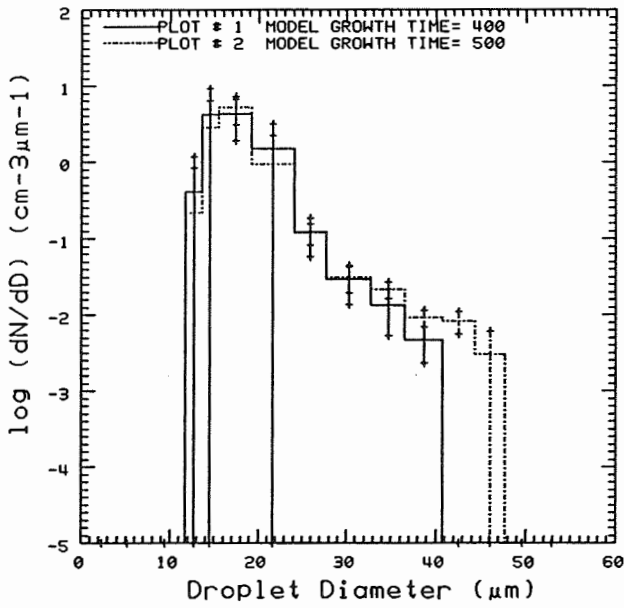


FIGURE 1

#### 4. RESULTS

Seventeen research flights were conducted during the field project to evaluate droplet growth rates. Three separate clouds are evaluated in the present study to illustrate particular similarities and differences between predicted and observed distributions. Each of the clouds had well-defined edges and eddy dissipation rates less than  $10 \text{ cm}^3 \text{ s}^{-3}$ . The clouds appeared laminar in structure and convective elements were neither observed visually or indicated by the measurements. The three clouds differed somewhat in general structure as summarized in the following table.

CASE	CLOUD BASE			CLOUD DEPTH (m)	CLOUD LENGTH (km)	MAX GROWTH (s)
	ALT. (m)	TEMP. ( $^{\circ}\text{C}$ )	PRESS. (mb)			
A	2900	7	705	$\approx 300$	$\approx 7$	300
B	2000	11	795	$\approx 400$	$\approx 10$	500
C	900	16	920	$\approx 600$	$\approx 25$	$> 2000$

The aircraft penetrated the clouds in successive upwind and downwind tracks that closely followed the ascending airflow.

Examples of predicted and observed measurements from each of the cloud studies are shown in Figures 2-4. The model results, adjusted for the measurement uncertainties, are shown as solid lines. The observed results, shown as dashed lines, are from measurements taken at altitudes where the estimated growth time from cloud base is within  $\pm 50$  seconds of the growth time used by the model. The shape parameters listed on the figures help identify similarities and differences between the predicted and measured spectra. The droplet diameter within which 95% of the water is

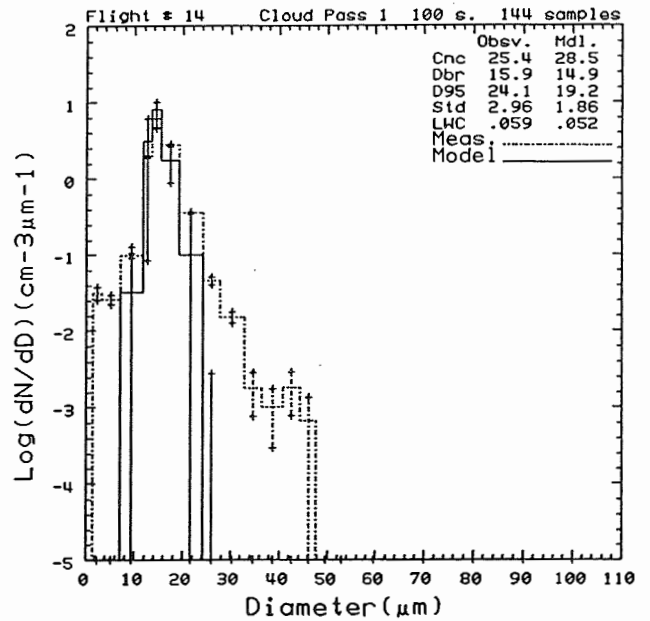


FIGURE 2

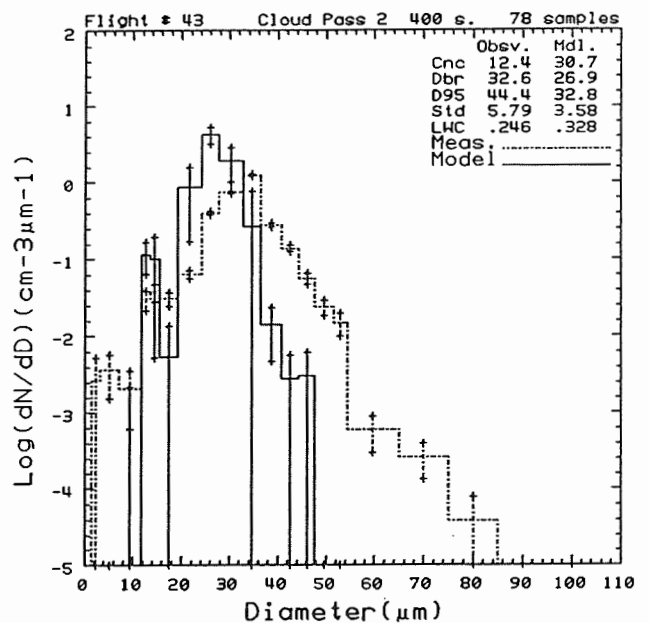


FIGURE 3

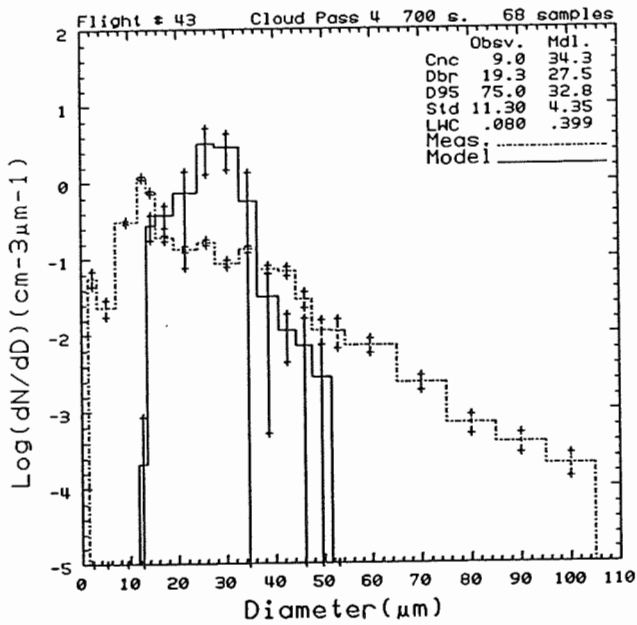


FIGURE 4

contained ( $D_{95}$ ) helps identify differences in the large droplet tail of the spectra. In all three cases there were larger droplets observed than were predicted, regardless of the growth time. In the first cloud study, the measured and predicted concentrations, mean diameters, and LWCs were in excellent agreement after 100 seconds growth and yet droplets were observed twice as large as predicted by the model. In the somewhat deeper and wider cloud of the second case, the differences are even more pronounced at the large droplet end of the spectrum. In this case the LWCs were in reasonable agreement but the measured concentrations are a factor of two lower than predicted. The measurements of the third cloud study show little agreement in concentration, mean diameter or LWC with the predicted results. In all three of these cases there was no evidence that measurements were contaminated by droplets from higher levels and yet much larger than predicted droplets are observed regardless of growth time or cloud depth. It is unlikely that the larger droplets are the product of coalescence in the first two cases because of the short growth periods and small collection kernels.

Initializing the model with additional giant salt nuclei in concentrations equivalent to those measured outside the cloud had a negligible effect on the resulting droplet

distribution. In the third case study the model had begun producing larger droplets by the selected growth time; however, these larger droplets did not account for those that were observed. Enhanced growth could be produced if elevated collection kernels were used in the coalescence calculation; however, these effects were offset if realistic concentrations were used in the model such as seen in the measurements. The comparisons of predicted and measured droplet distributions in the relatively simple case of low turbulent, orographic, warm clouds indicate that larger droplets appear in quantities greater than predicted from conventional theories. After a thorough scrutiny of the droplet growth model there does not appear to be a of the fundamental physical processes that govern droplet growth. The problem that the model did not address is the characterization of a fluctuating environment within which droplets grow and interact. Recent studies by Cooper et al (1986) show that fluctuations in the velocity and moisture fields surrounding cloud droplets will have major effects on their rates of growth. The focus of future research should be on the development of models that correctly characterize the structure of the environment.

## 5. REFERENCES

- Baumgardner, D., 1988: Cloud droplet growth in Hawaiian orographic clouds. Phd. Thesis, University of Wyoming. 311 pp.
- Cooper, W.A., D. Baumgardner, J.E. Dye, 1986: Evolution of the droplet spectra in Hawaiian orographic clouds. Preprints 23rd Conf. Cloud Physics. 52-55
- Gillespie, D.T., 1975: An exact method for numerically simulating the stochastic coalescence process in a cloud. J. Atmos. Sci., 32, 1977-1989.

# STUDIES OF WARM-RAIN DEVELOPMENT

William A. Cooper

National Center for Atmospheric Research\*  
Boulder, CO 80307, USA

## 1. INTRODUCTION

The development of rain in warm ( $>0^{\circ}\text{C}$ ) clouds must be due to the combined effects of condensation and coalescence following collisions, and the theoretical basis for each of these processes is well known. However, the detailed shape of the size distribution produced by condensation has a controlling influence on the rate of coalescence, and this shape is affected by entrainment of dry air, mixing of various cloud parcels, and radiative effects. In this paper, some aspects of these processes are examined in several cloud types where rain formed through warm-rain processes.

## 2. THEORETICAL DISCUSSION

The diffusional growth equation (and kinetic coefficients) of FUKUTA and WALTER (1970) were used in the following, and the integrations of the stochastic coalescence equation (SCE) were based on the techniques of BERRY and RINEHARDT (1974) and the collision efficiencies of KLETT and DAVIS (1973) or, at large size, those of BEARD and GROVER (1974).

The effects of fluctuations in the diffusional growth rates can be studied through use of the quasi-steady supersaturation,  $S_{qs} = a_1 W / (a_2 I)$  where  $W$  is the updraft,  $I$  the integral radius (equal to  $N\langle r \rangle$  where  $N$  is the droplet concentration and  $\langle r \rangle$  the mean radius), and  $a_1$  and  $a_2$  are coefficients first determined by SQUIRES (1952). The growth of a droplet is determined by  $\int S(t') dt'$  where  $S(t')$  is the time-dependent supersaturation in its environment, so its growth is determined by the integral

$$A_{qs}(t) = \int_0^t S_{qs}(t') dt' = \int_0^t \frac{a_1 W(t')}{a_2 I(t')} dt' \quad (1)$$

Let  $W$  and  $I$  be represented in terms of mean and fluctuating quantities:  $W(t') = W_0 + W'(t')$  and  $I(t') = I_0 + I'(t')$  where  $W_0$  and  $I_0$  are means for the period  $0 < t' < t$ . Then, expansion of (1) and neglect of higher-order terms in  $I'$  leads to

$$A_{qs}(t) \approx A_0 \left[ 1 - \frac{W_0 t}{Z} \left( \frac{\overline{I'}}{I_0} + \frac{\overline{I'W'}}{I_0 W_0} \right) \right] \quad (2)$$

where  $A_0 = (a_1 Z) / (a_2 I_0)$  and  $Z = \int W(t') dt'$ . In (2), an overbar indicates a time average so  $\overline{I'} = (1/t) \int I'(t') dt'$ . The effect discussed by BARTLETT and JONAS (1972) (whereby higher updrafts produce higher supersaturations accelerating droplet growth so as to cancel effects of fluctuations among droplets reaching a given altitude) is incorporated through the replacement  $Z = \int W(t') dt'$  which constrains the droplet to a given ascent. This constraint must also be applied to the remaining terms when the meaning of the overbars is interpreted.

The two fluctuating terms in (2) provide mechanisms for enhancement of droplet growth, if for a particular droplet either  $\overline{I'}$  or  $\overline{I'W'}$  is less than the corresponding ensemble mean. In the first term, the competition with neighboring droplets is reduced, and in the latter term the growth is enhanced by cycling along favored trajectories so that some droplets experience ascent in regions with low  $I$  (favoring growth) and descent in regions with high  $I$  (minimizing evaporation). For significant enhancement of growth, the first term is probably negligible because the effects must occur for one average ascent and cannot accumulate as

\*NCAR is sponsored by the National Science Foundation.

they can for the second term which can cause continued broadening and growth with time for appropriate trajectories.

The first term can represent the enhancement process suggested by BAKER and LATHAM (1979), while the process suggested by TELFORD and CHAI (1980) involves vertical cycling and so involves the second term as well. The approach taken in this paper will be to use the observed variability in  $I'$  or  $I'W'$  as a measure of the enhancement that might be possible through such processes.

GUZZI and RIZZI (1980) showed that the power radiated from a cloud droplet ( $Q$ ) changes the growth rate as if the supersaturation changed by  $C_I = L_v Q / (4\pi r \lambda R_w T)$  where  $L_v$  is the latent heat of vaporization,  $r$  the droplet radius,  $\lambda$  the conductivity (compensated for kinetic effects at the drop surface),  $R_w$  the gas constant for water vapor, and  $T$  the temperature. DAVIES and RIDGWAY (1984) found that  $Q$  varies approximately as  $r^{2.5}$ , and in that case  $C_I$  varies as  $r^{1.5}$ . Large droplets thus experience a larger effective supersaturation than small droplets, so this is a mechanism for broadening of a droplet spectrum near cloud tops or wherever there is a net power loss by the droplets. If values from ROACH (1976) are used for typical radiation losses by droplets, it can be shown (via a derivation too lengthy for this abstract) that the above process of broadening leads to doubling of the dispersion of the droplet size spectrum in about 15 min, and so can be an important factor broadening the droplet spectrum near the tops of clouds.

### 3. CLOUD TYPES CONSIDERED

#### 3.1 Hawaiian Wave Clouds

Cloud passes flown along airflow trajectories in shallow wave clouds over the southern end of the island of Hawaii were used to document the evolution of the droplet size distribution. These passes, discussed by COOPER et al. (1986), showed that the initial formation of the droplet spectrum was as expected from

calculations based on the observed updrafts and CCN spectra at cloud base. However, calculated coalescence rates in these clouds were negligible because liquid water contents were low ( $0.25 \text{ g/m}^3$ ) and mean droplet diameters were small (20-25  $\mu\text{m}$ ).

In contrast, the observations (Cooper et al., 1986; Baumgardner, 1988) showed that large droplets developed surprisingly fast. For diameters  $>80 \mu\text{m}$ , the concentration exceeded  $10/L$  after about 400 s of travel through the cloud, and some droplets were  $>150 \mu\text{m}$  in diameter. Drops of 500  $\mu\text{m}$  diameter also appeared below the downwind portions of some of these clouds. The development of these large droplets occurred after entrainment of dry air through the cloud top (at the trade inversion) partially evaporated portions of the cloud and produced a variable cloud structure.

COOPER et al. (1986) suggested that this mixing led to enhanced growth of some droplets. Two additional results can be added to support that contention. First, values of  $I'W'$  were highly variable, as shown in Table 1. Values of  $I'W'/(I_0W_0)$  as low as -3 were found, and there was poor correlation between  $I'$  and  $W'$  so a range of possible correlations could apply to various droplet trajectories. Second, a Monte Carlo calculation was used to simulate motion through the turbulent region of the clouds. In this calculation, the updraft fluctuated over the observed range (constrained so that the droplet remained in the cloud) but the integral radius was chosen randomly from among the observed values while both fluctuations changed randomly at 6 s intervals. The result was pronounced spreading of the droplet size distribution and production of 80-100  $\mu\text{m}$  droplets in concentrations comparable to those observed, even without any coalescence.

#### 3.2 Marine Stratocumulus Clouds

A shallow Sc layer located about 100 km west of San Francisco was observed to produce drizzle-size precipitation although it was only 350 m

thick and the temperature was everywhere above 9°C. Maximum droplet concentrations were about 250 cm<sup>-3</sup>, and mean diameters were <20 μm throughout the cloud. Again, calculations (with sizes and liquid water contents exceeding those observed) indicated that there would be little precipitation except after coalescence for >1.5 h with maximum liquid water content, and such times are unlikely for persistence of individual parcels or droplets in the Sc layer. There was less variability in available growth conditions than in the Hawaiian wave clouds, and the conditions seemed to be marginal or perhaps too weak to produce a significant enhancement of growth by condensation, as indicated in Table 1. Because of the long persistence times of these clouds, radiative cooling may contribute to the development of large droplets in a case such as this where conditions otherwise appear marginal for any development of drizzle or rain.

### 3.3 Cumulus Clouds

Similar enhancements of diffusional growth were sought in cumulus clouds, especially in the turbulent regions near cloud tops. Regions were often found having enough variability in I'W' to support some enhancement of droplet growth rates in the maritime (but, as yet, not the continental) cases. However, in these cases the sensitive dependence of the calculated coalescence rates on liquid water content makes the coalescence calculations unreliable guides to the expected rates of warm-rain formation. In Hawaiian cumulus clouds, the liquid water contents produced by adiabatic ascent would be 3-4 g/m<sup>3</sup> in the upper regions of the clouds, and if any parcels rose unmixed then the rates of coalescence would be so fast that the much slower potential enhancement of condensation rates by turbulent fluctuations (as in Table 1) would be insignificant. Enhancement of diffusional growth rates may be significant in cases where entrainment prevents adiabatic ascent of some parcels, but it appears more likely that the adiabatic ascent of a few parcels could initiate

coalescence growth and then drizzle-size droplets could spread through the cloud.

## 4. CONCLUSIONS

These results suggest that diffusional growth may be enhanced in some highly mixed regions of maritime Cu in a manner similar to that in the wave clouds, but that this effect is minor in updraft cores or in the Sc layers examined.

TABLE 1: EXAMPLES OF TERMS IN EQ. (2)

(W<sub>0</sub> estimated = Z/t for wave and Sc cases)

Cloud type	$\sigma_I/I_0$	$\sigma_{IW}/(I_0 W_0)$
Hawaiian wave	0.5	0.6
Hawaiian Cu:		
updrafts	0.2	0.15
cloud top	0.5	0.6
Marine Sc	0.25	0.3

ACKNOWLEDGMENTS: The aircraft support was provided by the Research Aviation Facility, National Center for Atmospheric Research, which is sponsored by the National Science Foundation, and by NASA contract NAS5-27783 to the University of Wyoming.

## REFERENCES

- BAKER, M. B. and J. LATHAM, 1979: The evolution of droplet spectra and the rate of production of embryonic raindrops in small cumulus clouds. *J. Atmos. Sci.*, 36, 1612-1615.
- BARTLETT, J. T. and P. R. JONAS, 1972: On the dispersion of the sizes of droplets growing by condensation in turbulent clouds. *Quart. J. Roy. Meteor. Soc.*, 98, 150-164.
- BAUMGARDNER, D. B., 1988: Evaluation of droplet growth rates in Hawaiian orographic clouds. 10th International Cloud Physics Conference.
- BEARD, K. V. and S. N. GROVER, 1974: Numerical collision efficiencies for small raindrops colliding with micron size particles. *J. Atmos. Sci.*, 31, 543-550.
- BERRY, E. X. and R. L. RINEHARDT, 1974: An analysis of cloud drop droptth by collection. Part I: Double distributions. *J. Atmos. Sci.*, 31, 1814-1824.
- COOPER, W. A., D. BAUMGARDNER and J. E. DYE, 1986: Evolution of the droplet spectra in Hawaiian orographic clouds. Preprints, Conf. on Cloud Physics, Snowmass, Amer. Meteor. Soc., C52-55.
- DAVIES, R. and W. RIDGWAY, 1984: Some effects of solar radiation on cloud microphysics. IRS 1984: Current Problems in Atmospheric Radiation, 171-173.
- FUKUTA, N. and L. A. WALTER, 1970: Kinematics of hydrometeor growth in a vapor-spherical model. *J. Atmos. Sci.*, 27, 1160-1172.
- GUZZI, R. and R. RIZZI, 1980: The effect of radiative exchange on the growth by condensation of a population of droplets. *Contributions to Atmos. Physics*, 53, 351-365.
- KLETT, J. D. and M. H. DAVIS, 1973: Theoretical collision efficiencies of cloud droplets at small Reynolds numbers. *J. Atmos. Sci.*, 30, 107-119.
- ROACH, W. T., 1976: On the effect of radiative exchange on the growth by condensation of a cloud or fog droplet. *Quart. J. Roy. Meteor. Soc.*, 102, 361-372.
- SQUIRES, P., 1952: The growth of cloud drops by condensation. *Aust. J. Sci. Res.*, 5, 66-86.
- TELFORD, J. W. and S. K. CHAI, 1980: A new aspect of condensation theory. *Pure Appl. Geophys.*, 19, 934-965.

RADAR OBSERVATIONS AND MODELLING OF WARM RAIN INITIATION

Anthony J Illingworth  
 Visiting Scientist  
 NCAR\*, Boulder  
 Colorado 80307, USA

and I Jeff Caylor  
 Dept. of Physics  
 UMIST  
 Manchester M60 1QD, UK

1. INTRODUCTION

Differential radar reflectivity observations of early echoes of rain in warm convective clouds in the UK and Alabama, USA, indicate that precipitation initially forms as raindrops greater than 4mm in size but present in concentrations of less than one per cubic meter. The differential reflectivity, ZDR, ( $10 \log (Z_H/Z_V)$ ), where  $Z_H$  and  $Z_V$  are the radar reflectivities measured with horizontal and vertical polarizations, respectively. ZDR provides a measure of the shape of the hydrometeors, and because raindrops are oblate to a degree which depends upon their size, the magnitude of ZDR is a unique function of raindrop size (Table 1). ZDR is a ratio and so is independent of concentrations, but once the mean size is known then the conventional reflectivity,  $Z_H$ , can be used to derive an estimate of raindrop concentration (SELIGA and BRINGI, 1976).

2. RAINDROP SIZE AND CONCENTRATIONS

If we assume an exponential raindrop size distribution:

$$N(D) = N_0 \exp(-3.67 D/D_0)$$

where  $N$  is the concentration of drops of diameter  $D$  and  $D_0$  is the equivolumetric diameter, then by summing the contributions of the various sizes of raindrops present we may calculate the values of ZDR as a function of  $D_0$  (Table 1, final columns, spectrum truncated at 8mm). The value of  $N_0$  is then linearly dependent upon the magnitude of  $Z_H$ . In Figure 1 the solid lines are the values of  $Z$  and ZDR as  $D_0$  varies but  $N_0$  is kept constant. The total drop concentration is given by  $N_0 D_0 / 3.67$ . Many observations have shown the average raindrop size distribution to be that proposed by Marshall and Palmer with  $N_0 = 8000 \text{ m}^{-3}$ . A long series of radar observations of  $Z$  and ZDR (CAYLOR and ILLINGWORTH, 1987) has confirmed that the average value of ZDR of rain for a given  $Z$  does indeed lie upon the  $N_0 = 8000$  curve in Figure 1.

We shall be discussing early echoes which have values of ZDR of 3 or 4dB, and would be expected to have  $Z$  values of 56 to 67dBZ for Marshall-Palmer rain. Instead the values are 30dBZ lower, implying values of  $N_0$  reduced by a factor of 1000. For example from Figure 1 we see that a value of  $Z$  of 15dBZ accompanied by a  $ZDR_{-1}$  of 3dB implies a value of  $N_0$  of only  $0.8 \text{ m}^{-3}$ , or a drop concentration ( $D_0 = 2.5 \text{ mm}$ ) of  $0.7 \text{ m}^{-3}$ .

3. CHILBOLTON RADAR (UK) OBSERVATIONS

A vertical section through a young convective cloud with anomalously high ZDR is displayed in Figure 2 (for other examples and details of the radar, see ILLINGWORTH et al, 1987). Values of  $Z$  of 30dBZ are accompanied by a ZDR above 4.5dB, which imply (Figure 1) large drops (6mm) in concentrations of only one per cubic meter. This cloud persisted for twenty minutes with no great change in character; the 2700 data points obtained during this period are displayed in Figure 3, where each star represents the average value of ZDR for every 2dBZ step in  $Z$ . The solid line in Figure 3 is the  $N_0 = 8000$  curve from Figure 1; showing that the low concentration of large raindrops persisted throughout the twenty minute period.

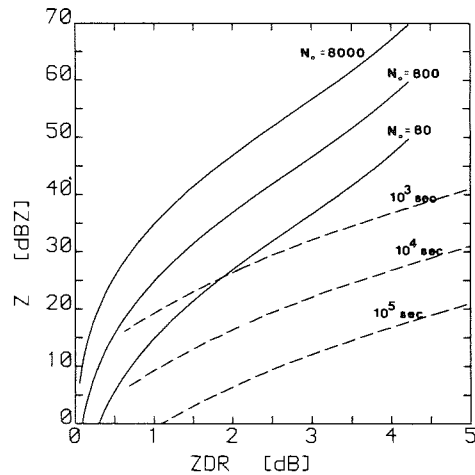


Figure 1. The variation of  $Z$  and ZDR as a function of 3 values of  $N_0$  (solid lines). The dashed lines show the expected lifetime for a 5mm diameter drop.

TABLE 1

Size (mm)	Axial Radial	ZDR(dB)	$D_0$ (mm)	ZDR(dB)
4	0.778	2.49	1	0.62
5	0.708	3.48	2	2.31
6	0.642	4.42	2.5	3.03
7	0.581	5.33	3	3.56
8	0.521	6.70	4	4.22

Values of axial ratio (from BEARD and CHUANG, 1987) and ZDR for various sizes of raindrop. The Mie-Gans calculations are supplied by Dr Holt, Department of Mathematics, University of Essex, and apply to raindrops at  $0^\circ\text{C}$  and 3.0765 GHz.

\*The National Centre for Atmospheric Research is sponsored by the National Science Foundation.

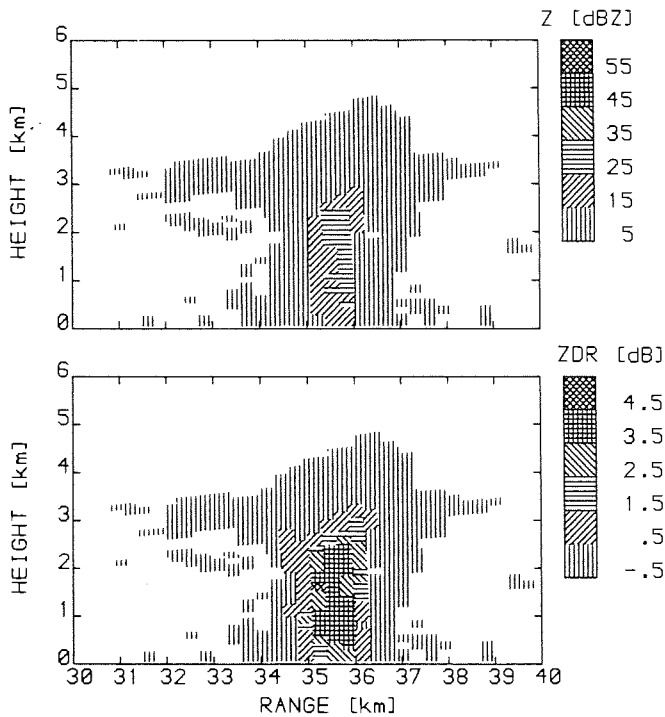


Figure 2. A vertical scan on 20 June 1980 displaying anomalously high ZDR.

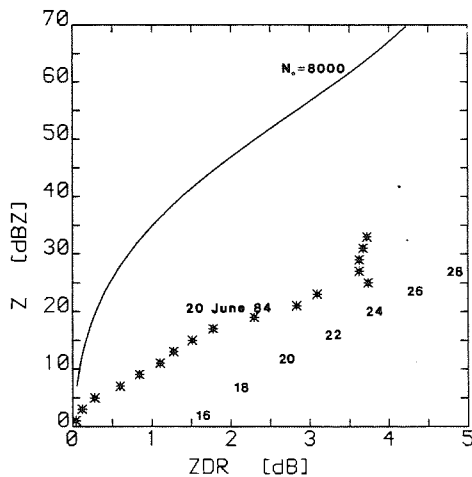


Figure 3. Averaged Z and ZDR over a 20 minute period for the cell in Figure 2. For comparison the model output as a function of time (minutes) and the Z and ZDR for a drop size distribution with  $N_0 = 8000$  are shown.

#### 4. GIANT NUCLEI MODEL

To explain such low concentrations of large raindrops, CAYLOR and ILLINGWORTH (1987) extended a suggestion (JOHNSON, 1982) that each large raindrop formed on an ultra giant nuclei ( $>30\mu\text{m}$ ), present in the background concentration at this low level (JUNGE, 1972). Figure 3 shows the prediction of the simple model in which Z and ZDR increase as the giant nuclei sweep out cloud water of  $\text{LWC } 2 \text{ g m}^{-3}$ , the numbers indicate time in minutes elapsed since initiation of the model with nuclei concentrations (in units of  $\text{m}^{-3}$  per unit log interval of radius) of  $10^3$  for  $10\mu\text{m}$  radius to  $3 \times 10^{-2}$  for  $100\mu\text{m}$ .

Only a few large raindrops grow, and the depletion of the cloud water is negligible. The model is linear in that increasing the LWC merely changes the time scale but not the Z/ZDR dependence; in addition, increasing the nuclei concentration merely scales up the values of Z leaving ZDR unchanged. The Chilbolton cloud persisted 20 minutes and it is not possible to give a specific age to various parts of the cloud. In view of the uncertainty of the absolute concentration of giant nuclei, the observed general dependence of Z with ZDR is consistent with the model.

#### 5. ALABAMA DATA, NCAR CP2 RADAR

First echoes formed at temperatures above zero on many days during the 1986 MIST (Microburst Severe Thunderstorm) project. These early echoes were also normally accompanied by anomalously high values of ZDR. A particularly clear example was on 10 July, when the evolution of a very weak echo less than 2km in diameter was observed in its entirety. In 20 minutes the echo grew from zero to 20dBZ and then collapsed; the top of the radar echo reached only 5km (slightly above the freezing level), but during this time values of ZDR in the cloud increased to 4dB, the ZDR core then descended as the rain fell to ground.

Figures 4 and 5 show the specific values of each Z/ZDR data point for two successive vertical sections through the maximum echo. The numbers plotted for each point represent the height of the data to the nearest kilometer. The evolution is consistent with the model in Figure 3, in that the concentration of drops is constant and less than one per cubic meter, 5 minutes after the appearance of the echo, the value of ZDR was 3dB, growing to 4dB in the subsequent three minutes. This is consistent with the maximum drop size increasing from 4.5 to 6mm (Table 1) by sweeping out cloud water of  $\text{LWC } 2 \text{ g m}^{-3}$ .

#### 6. CONCLUSIONS.

We have presented evidence that early echoes of warm clouds consist of a very few drops which grow to a large size by sweeping out cloud water. Because concentrations are so low this can happen without exhausting the supply of liquid water, and also with a negligible number of collisions causing the drops to break up. LOW and LIST (1982) found that for a collision to cause shattering, both raindrops must be larger than 1mm. For a given  $D_0$  the lifetime of a large raindrop will be inversely proportional to  $N_0$ ; in Figure 1 the dotted lines join the values of Z and ZDR for lifetimes of 1000, 10000, and 100000 seconds for a 5mm drop. The large raindrops in Figure 4 and 5 will survive for over an hour before collision-induced rupture. This situation should be contrasted to Figure 6 showing the Z/ZDR scatter plot for a normal mature cloud on 6 July 1986, the values are closer to the average  $N_0=8000$  curve, and the lifetime of the larger drops is less than a minute.

Warm rain measurements in Texas (CARBONE and NELSON, 1978) and in Hawaii (BEARD et al, 1986) also indicate low values of  $N_0$  and high  $D_0$ . Conventional airborne instruments do not generally have a large enough sample volume to obtain meaningful statistics of the very low concentrations inferred from the radar. In Hawaii one 8mm raindrop was sampled, supporting the idea that such raindrops are indeed stable in the atmosphere if they do not undergo collisions. Drops up to 9mm are stable in low turbulence wind tunnels (PRUPPACHER and BEARD, 1970).

We suggest that convective raindrops first form on embryos which are present in concentrations of about one per cubic meter. Such embryos could be giant nuclei, or alternatively could be ice crystals. The number of ice crystals seeding such a cloud might be expected to be more variable, and to be much greater if the cloud top was higher, yet the raindrop concentrations always seem to be very low. A raindrop distribution of a few large drops would appear to be very stable, but once break-up occurs, either due to the occasional collision or spontaneously if the drops become too large, then many small fragments are produced, and the distribution rapidly and irreversibly changes to the more normal Marshall-Palmer distribution.

#### ACKNOWLEDGEMENTS

This research was supported by the Meteorological Office, by NERC Grant GR3/5896 and by AFOSR-87-0046. Our co-workers S M Cherry and J W F Goddard pioneered the implementation and interpretation of the ZDR data at Chilbolton. We thank Profs Bringi, Forbes, Fujita and Wakimoto for allowing us access to the MIST data. IJC acknowledges the assistance of an ORS scholarship and AJI thanks members of the FOF at NCAR for many useful discussions.

#### REFERENCES

- BEARD, K.V.; JOHNSON, D.B.; BAUMGARDNER, D.: Geophys. Res. Letters. 13 (1986) 991-994.  
 BEARD, K.V.; CHUANG, D.: J. Atmos. Sci. 44 (1987) 1509-1524.  
 CARBONE, R.E.; NELSON, L.D.: J. Atmos. Sci. 35 (1978) 2302-2314.  
 CAYLOR, I.J.; ILLINGWORTH, A.J.: Q. J. Roy. Meteorol. Soc. 113 (1987) 1171-1191.  
 ILLINGWORTH, A.J.; GODDARD, J.W.F.; CHERRY, S.M.: Q. J. Roy. Meteorol. Soc. 113 (1987) 469-489.  
 JOHNSON, D.B.: J. Atmos. Sci. 39 (1982) 448-460.  
 JUNGE, C.E.; J. Geophys. Res. 77 (1972) 5183-5200.  
 LOWE, T.B.; LIST, R.: J. Atmos. Sci. 39 (1982) 1591-1618.  
 PRUPPACHER, H.R.; BEARD, K.V.: Q. J. Roy. Meteorol. Soc. 96 (1970) 247-256.  
 SELIGA, T.A.; BRINGI, V.N.: J. App. Meteorol. 15 (1976) 69-76.

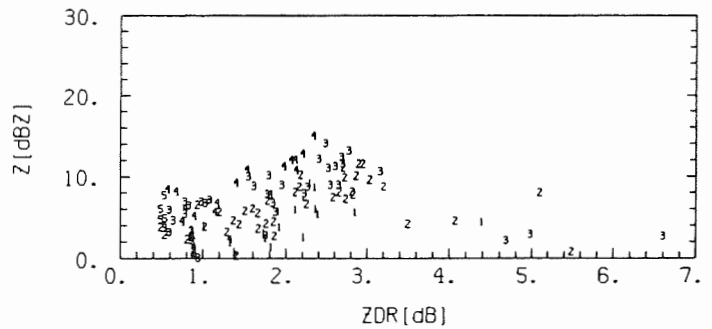


Figure 4. Scatter plot of Z and ZDR for each data point from a young echo on 10 July 1986 at 1301 CDT indicating low concentrations of large drops.

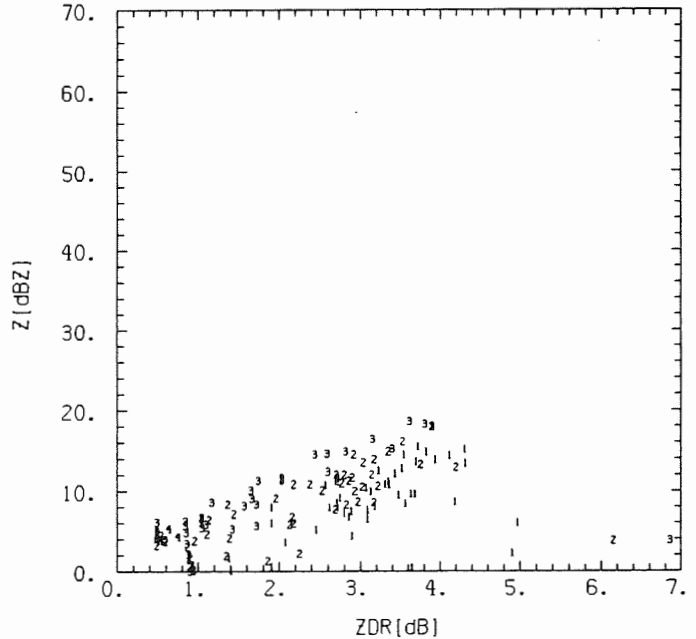


Figure 5. Values of Z and ZDR from the same cloud as Figure 4 observed 3 minutes later.

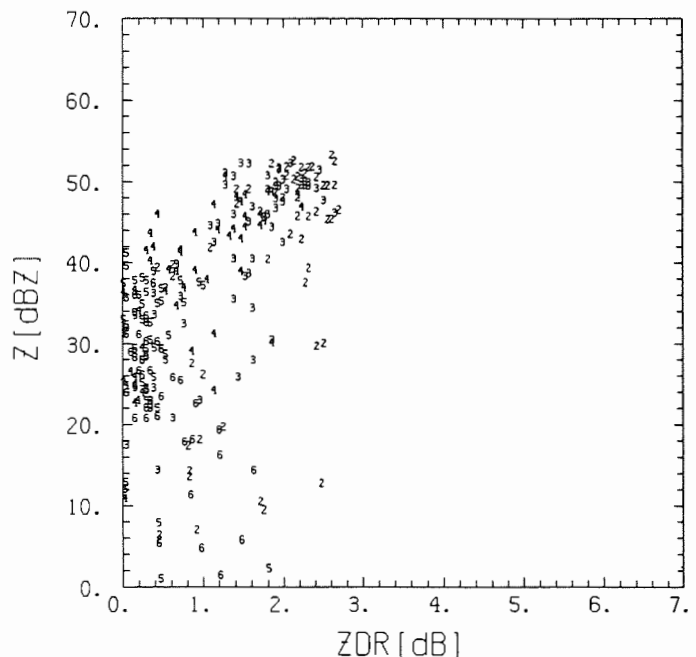


Figure 6. Z and ZDR data points from a mature convective cloud on 6 July 1986 at 1426 CDT indicating a Marshall-Palmer drop size distribution.

# A TEST OF ICE CRYSTAL PRODUCTION BY AIRCRAFT

Gabor Vali, R. D. Kelly and F. Serrano

Department of Atmospheric Science, University of Wyoming  
Laramie, WY 82071, U.S.A.

## 1. INTRODUCTION

In light of the importance of aircraft observations in the studies of cloud and precipitation processes, the possibility that the aircraft themselves may modify the clouds deserves serious consideration. Of the various microphysical and dynamical effects of aircraft on clouds, the generation of ice crystals (Aircraft Produced Ice Particles, APIP) has received most attention recently. The initial report of direct observations of this phenomenon (Rangno and Hobbs, 1983) was followed by further evidence (Rangno and Hobbs, 1984 - positive; Gordon and Marwitz, 1986 - negative), a discussion of possible implications (Mossop, 1984), and by a suggestion for the mechanism of APIP production (Vonnegut, 1986).

The experiments described here were undertaken in order to provide a broader data base on the conditions of APIP generation and on the controlling factors of the process. A tracer was used to ascertain proper sampling of the affected cloud volume so that both false positive and false negative conclusions could be avoided. This report is based on the first two attempts to carry out the experiment; the results must be considered preliminary.

## 2. TRACER TECHNIQUE

To clearly distinguish ice crystals produced by the passage of an aircraft through a cloud from ice crystals of other origins, it is necessary to intercept or re-trace the path of the aircraft as closely as possible. This requires navigation of the aircraft in an appropriate flight pattern with respect to the cloud (moving frame of reference). In order to

provide independent confirmation of interception, a tracer was employed, consisting of a pair of pulses of high concentrations of ice crystals. The use of ice crystals as tracers provided the important advantage that detection of these crystals could affirm not only that the aircraft path was intercepted, but also that the cloud conditions were such that ice crystals could grow and would thus permit APIP to be detected, if generated. The tracer pulses were generated over a small fraction of the flight path; the remainder of the path served as the region to examine for the presence of APIPs.

## 3. EXPERIMENTAL METHOD

The experiments were carried out using the University of Wyoming King Air 200T twin-engine turboprop aircraft. Instrumentation included particle imaging probes, a cloud droplet counter, two devices for liquid water content measurement, inertial navigation system, and temperature and humidity sensors. Tracer crystals were generated by the release of a liquid spray of freon, i.e. by homogeneous nucleation. Navigation with reference to the cloud was directed by a computer-generated vector giving the sum of the airspeed vectors over the lapse of time from the point of reference.

Flights along straight lines, through regions of supercooled liquid water content, constituted the test regions. Two pulses of tracers were generated approximately 1 km apart, followed by turns leading to a reverse path through the tracer pulses about 3-5 minutes later. Detection of high ice crystal concentrations from the freon releases was taken as

an indication that the plume originating along the earlier flight path was intercepted. The magnitude of the plume spread was calculated from the observed rate of turbulent energy dissipation; flight segments falling within the plume of an earlier flight track were designated as "plume" regions. So far, only cases in which the plume interception is confirmed by one tracer pulse have been obtained, but even one anchor point and identical aircraft heading on the initial and repeat passes provides a fairly long region over which sampling of the plume is assured. Detection of both tracer pulses, to define the line of the plume, would provide even greater confidence in sampling the plume.

Ice crystal concentrations, sizes and shapes were monitored using an optical array probe of 12  $\mu\text{m}/\text{element}$  resolution (1D-C probe), and two imaging probes of 25  $\mu\text{m}/\text{element}$  (2D-C) and 200  $\mu\text{m}/\text{element}$  resolution (2D-P). Concentrations to be presented here refer to those derived from the 1D-C probe, as it was the most sensitive to the small crystal sizes encountered in this work.

#### 4. RESULTS

Results from experiments in two different clouds are available so far, with two separate experiments in one of the clouds. *Of the three tests, two have shown no evidence for the generation of APIPs; in one case there is evidence for APIPs.*

The May 21, 1987 experiment near Laramie, Wyoming, was carried out in tenuous altostratus at  $-9.5^\circ\text{C}$ . The LWC was sporadic, with values  $<0.2 \text{ g m}^{-3}$ . Ice crystal concentrations were around 0.1 per liter. Of the two releases of freon, each along a 400 m flight segment, separated by 1.3 km, only one fell in a region of liquid water content. This pulse, when sampled 4 minutes later, was seen to have resulted in an ice crystal plume of  $>10 \text{ lit}^{-1}$  over 600 m. The rest of the 6.2 km long "plume" region was found to have remained

essentially unchanged both with respect to LWC and ice concentrations.

Two experiments were carried out on Nov. 20, 1986 near Sacramento, California, in a layer cloud of moderate LWC, through which ice crystals were falling from higher clouds. The temperature at the test level was  $-12^\circ\text{C}$ . LWC regions extended to 10-15 km regions with 0.2 to  $0.5 \text{ g m}^{-3}$ . The ice crystal precipitation falling through the cloud layer consisted of few tens of crystals per liter of up to 3 mm sizes.

One of the experiments on Nov. 20, 1986 produced essentially the same result as the May 21, 1987 test. The evidence is that no APIP were generated. The other experiment on Nov. 20, 1986 produced a different result. The procedure was similar to that already described, but only one tracer pulse was generated about midway along a 10-km flight leg. The relevant results are shown in Fig. 1. Portions C and D of the original flight track were re-traced about 3 min later, with a reverse heading.  $\text{FR}_D$  indicates the period of freon release,  $\text{P}_{D1}$  is the "plume" region corresponding to D,  $\text{FI}_{D1}$  shows where the tracer crystals are evident (highest concentrations), and  $\text{P}_C$  is the "plume" corresponding to segment C. The tracer plume was subsequently traversed at  $90^\circ$  with respect to the original heading; the detected plume is labelled  $\text{FI}_{D2}$ . The important observation in this test is that through  $\text{P}_{D1}$  there is a significant increase in ice concentration above the background values. The increase appears to be confined to a line along the flight track, as evidenced by the absence of similar increases on either side of  $\text{FI}_{D2}$ . In  $\text{P}_C$ , no increase above the background can be distinguished.

#### 5. ANALYSIS

The evidence shown in the foregoing section points to the conclusion that aircraft *may produce ice crystals when passing through supercooled water clouds, but only when certain combinations of conditions exist.* With the limited number of cases so far available it is

risky to try to delineate what those conditions are. The last of the cases described was different from the other two in the higher engine torque utilized (1540 ft-lb, versus ~1300 ft-lb for the other cases); this is indicative of greater airframe icing and is accompanied by greater fuel consumption. If the critical factor is related to engine torque, the difference between  $P_C$  and  $P_D$  would have to be ascribed to having missed the plume in  $P_C$ , where there was no tracer pulse to confirm proper positioning. Flight segments C and D were very similar, but a possibly significant difference was present in the size-distributions of cloud droplets. The possibility also has to be admitted that the ice crystals detected in  $P_D$  were of natural origin and had fallen from the sample altitude in the time interval between sampling  $P_D$  and  $FI_{D2}$ .

**Acknowledgement:** We thank our colleagues for building and operating the aircraft system. The National Science Foundation supported this work through Grant ATM 8611185.

REFERENCES:

GORDON, G. L.; MARWITZ, J. D.: APIP testing using a tracer. Preprints Tenth Conf. Wea. Modif., A.M.S., Arlington, Virginia, (1986), pp. 61-63

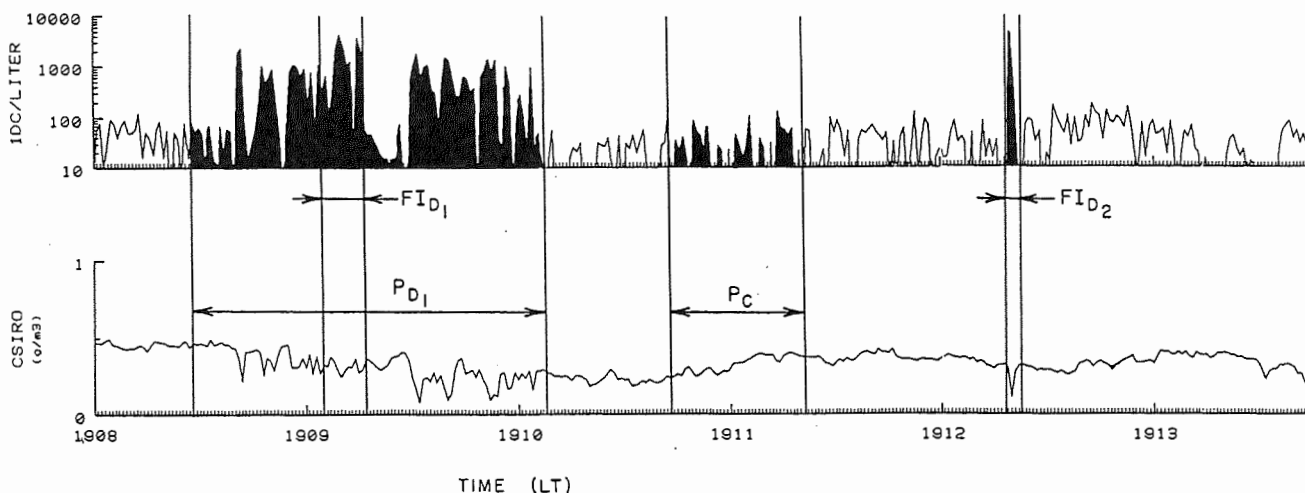
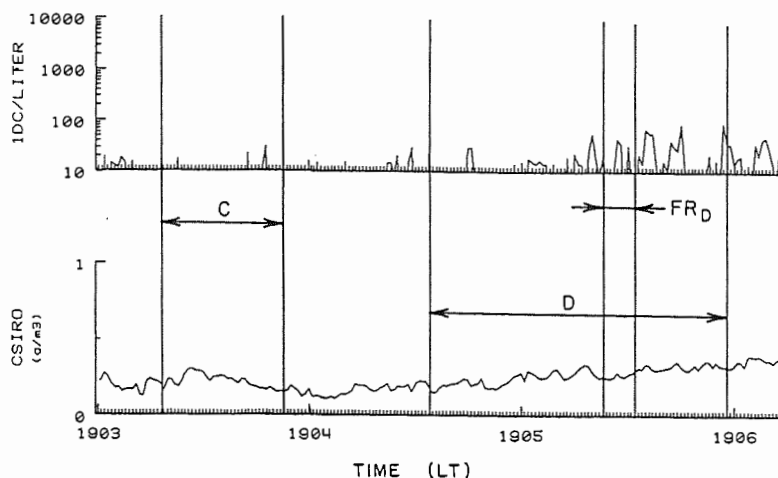
MOSSOP, S.C.: Comments on "Production of ice particles in clouds due to aircraft penetration". J. Clim. Appl. Meteor. 23 (1984), 345.

RANGNO, A. L.; HOBBS, P. V.: Production of ice particles in clouds due to aircraft penetrations. J. Clim. Appl. Meteor. 22 (1983), 214-232.

RANGNO, A. L.; HOBBS, P. V.: Further observations of the production of ice particles in clouds by aircraft. J. Clim. Appl. Meteor. 23 (1984), 985-987.

VONNEGUT, B: Nucleation of ice crystals in supercooled clouds caused by passage of an airplane. J. Clim. Appl. Meteor. 25 (1986), 98.

Figure 1. Flight data for LWC (CSIRO) and ice crystal concentration (IDC, per liter), for one of the test cases.



by

P.R.A. Brown<sup>1</sup> and T.W. Choulaton<sup>2</sup>

<sup>1</sup> Meteorological Office, Bracknell, UK., <sup>2</sup> UMIST, Manchester, UK.

1. INTRODUCTION

Evidence that the the Hallett-Mossop process of secondary ice production is active in natural clouds has been obtained on a number of occasions (e.g. MOSSOP, 1985). Theoretical (MASON, 1975) and experimental (KELLER AND SAX, 1981) studies have suggested the importance of the cloud dynamics in distributing the products of secondary ice production through the cloud and its effects on such factors as precipitation formation. We have examined data obtained in maritime clouds around the British Isles to study the formation and distribution of the ice phase in clouds with top temperatures in the range of -8 to -15 °C.

2. INSTRUMENTATION AND DATA

Ice crystal concentrations were measured using both standard PMS 2-D optical array probes and an airborne holographic system, which was also used to obtain the concentrations of cloud droplets larger than about 10 µm in diameter. Holographic measurements of ice columns exceed those from the 2-D cloud probe by a factor of about 5, due to detection and sizing errors in the 2-D probe itself and errors in the 2-D processing software which cause an overestimate of the effective sample volume (BROWN AND DARLISON, 1988).

Individual cloud cells were penetrated at different levels and no evidence was found of ice crystals generated by previous penetrations (RANGNO AND HOBBS, 1983). 2-D Cloud probe images from case H750 are shown in Fig. 1, the separate sections

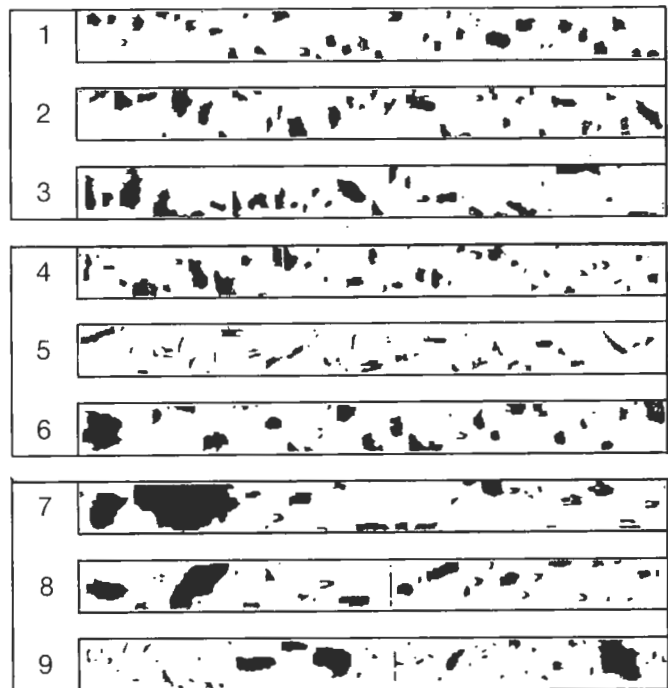


Fig. 1 2D Cloud probe images from Flight H750. The numbered sections correspond to those in Table 1.

corresponding to those of Table 1 which contains values of various parameters averaged over short periods during three penetrations of the cloud. This case illustrates several of the features which have been observed in clouds of a similar depth and which are described below.

3. SECONDARY ICE PRODUCTION AND THE EFFECTS OF CLOUD DYNAMICS.

A prominent feature is the increase in the concentration of ice columns in the main updraught between -4.6 and -8.3 °C. At the colder level, the column size spectrum has mode and maximum lengths of about 150 and 650 µm respectively. The latter corresponds to a fall velocity of about 0.8 ms<sup>-1</sup>, hence the columns are being transported upwards from

Table 1. Flight H750 18/09/85  
 Cloud-top temperature =  $-11.0^{\circ}\text{C}$   
 Cloud-base temperature =  $+5.1^{\circ}\text{C}$

Temperature of flight level ( $^{\circ}\text{C}$ )	Section	Vertical velocity ( $\text{m s}^{-1}$ )	Liquid water ( $\text{g m}^{-3}$ )	2DCloud probe		Holographic data		
				(a)	(b)	(c)	(d)	(e)
-10.2	1	0.17	0.00	4.7	26.8			
	2	0.87	0.04	18.3	27.8			
	3	0.27	0.03	12.9	26.2			
-8.3	4	-0.60	0.02	14.6	24.9	24.3	60.7	
	5	1.79	0.24	46.6	19.4	118.6	296.6	7.0
	6	-0.13	0.00	5.4	21.3			
-4.6	7	-0.05	0.20	25.7	19.4	34.1	26.7	
	8	3.37	0.52	9.8	11.0	19.3	11.9	18.4
	9	0.44	0.18	31.6	13.9	63.8	54.9	

(a), (d) Columns,  $L > 140 \mu\text{m}$  ( $\text{l}^{-1}$ )  
 (b) Irregular ice,  $L > 140 \mu\text{m}$  ( $\text{l}^{-1}$ )  
 (c) Columns,  $L < 140 \mu\text{m}$  ( $\text{l}^{-1}$ )  
 (e) Droplets ( $\text{cm}^{-3}$ )

warmer regions below. The presence of large rimed particles in concentrations of  $1\text{--}2 \text{ l}^{-1}$  together with substantial liquid water contents in the updraught at  $-4.6^{\circ}\text{C}$  suggests that the columns were produced by the Hallett-Mossop process of ice splinter production during riming (HALLETT AND MOSSOP, 1974). The mode and maximum lengths are in agreement with values calculated assuming that the base of the secondary production zone is at  $-2.5^{\circ}\text{C}$  with peak production at  $-4.5^{\circ}\text{C}$ .

Large concentrations of columns are also detected in regions of weak updraught less than  $1 \text{ ms}^{-1}$ . Holographic data show that a substantial fraction of these are smaller than  $140 \mu\text{m}$  in length. As water-saturated conditions still exist, the crystals will have a linear growth rate of about  $1 \mu\text{m s}^{-1}$  (RYAN et al., 1972). The small updraught and fall velocities suggest that the small columns will be detected close to their original formation level. In support of this, peak column concentrations in weak updraught regions tend to be found close to the  $-4.5^{\circ}\text{C}$  level of peak splinter production.

Clouds with stronger updraughts than the H750 case tend to have low column concentrations at all levels within the updraught core, probably due to the reduced time available

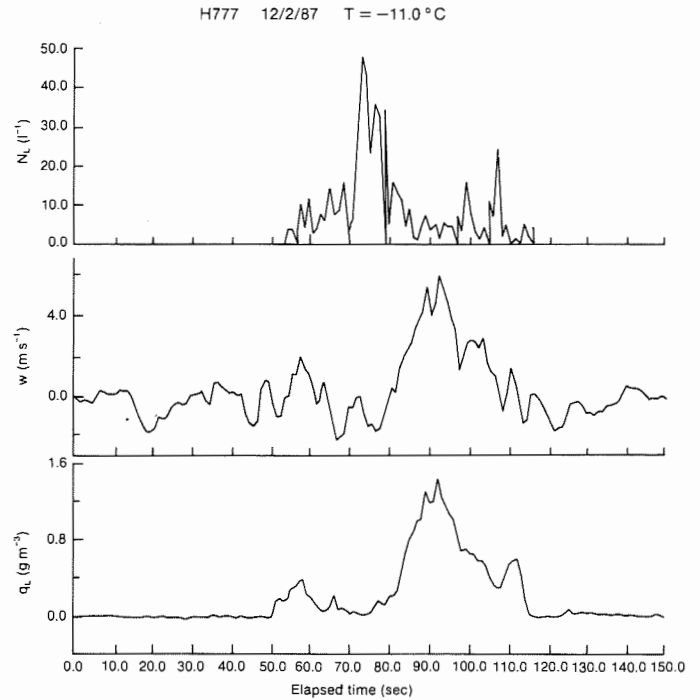


Fig. 2 Data from a single cloud penetration on Flight H777, when the cloud-top temperature was  $-15.0^{\circ}\text{C}$ .  $N_L$  is the concentration of crystals larger than  $300 \mu\text{m}$ ,  $w$  the vertical velocity, and  $q_L$  the liquid water content.

for splinter production in a parcel ascending through the splinter production zone. With top temperatures of nearer  $-15.0^{\circ}\text{C}$  found in these clouds, the ice distribution is dominated by rimed dendritic crystals presumed to have been generated at cloud-top and carried to lower levels in downdraughts (Fig. 2).

Since the cloud top is largely depleted of liquid water, the secondary columns will be unable to grow by riming unless they can be recirculated back into regions of ascent lower in the cloud. Data from another case shows evidence of this occurring at the  $-2.5^{\circ}\text{C}$  level of the base of the secondary ice generation zone.

#### 4. THE ICE PHASE IN CLOUD-TOP REGIONS

Near the top of the H750 cloud, irregular ice particles of  $150\text{--}300 \mu\text{m}$  in size are found in concentrations of  $15\text{--}25 \text{ l}^{-1}$  with a complete absence of liquid water (see Section 1, Fig. 1 and Table 1). They cannot therefore have acquired this shape by riming growth in-situ.

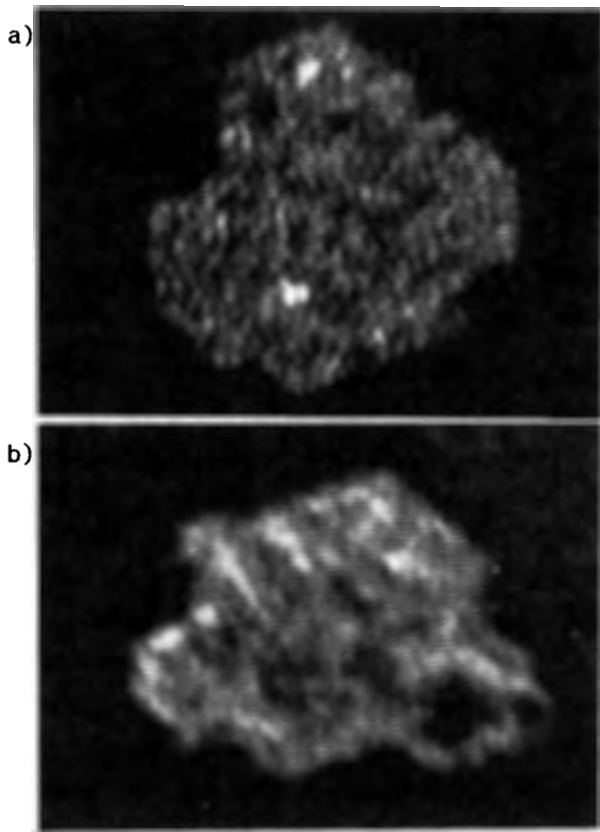


Fig. 3 Holographic images from near cloud top, Flight H708. Crystal dimensions are a) 220  $\mu\text{m}$ , b) 213  $\mu\text{m}$ .

It is also unlikely that they are the result of riming growth of secondary columns generated lower in the cloud, as holographic images of columns of about these dimensions show only very light riming. Crystals which have rimed sufficiently to have acquired a quasi-spherical appearance in 2-D images will thus be larger than the observed irregular particles.

Holographic images taken in these cloud-top regions show a number of examples of plate-like unrimed crystals of a size which could explain the appearance of the 2-D images (see Fig. 3). The plate-like habit suggests strongly that these crystals have formed and grown at temperatures close to cloud top. Other holographic images show frozen drops of 60–150  $\mu\text{m}$  in diameter. 2-D images from unglaciated clouds of a similar depth sampled on the same day as the H750 case show the presence of liquid drops of up

to 130  $\mu\text{m}$  in diameter at levels just below cloud top. It is thus conceivable that the irregular particles have been generated by a mechanism involving drop freezing, as suggested by HOBBS AND RANGNO (1985). It is not yet known whether this cloud top glaciation evolves independently of the processes occurring lower in the cloud. Data from more vigorous clouds does however suggest that cloud-top ice formation and its downwards transport may become the more dominant process as cloud top temperatures approach  $-15\text{ }^{\circ}\text{C}$ .

#### 5. SUMMARY.

The Hallett-Mossop process has been shown to be active within maritime convective clouds around the British Isles. The distribution of the secondary ice columns depends in detail on the cloud dynamics. Ice crystals are also generated separately at cloud top by a mechanism which we speculate may involve the freezing of large drops as suggested by HOBBS AND RANGNO (1985). The relationship between this process and the secondary ice production lower in the cloud has not yet been determined.

#### REFERENCES

- BROWN P.R.A and DARLISON A.G.: Preprints, 10th. Internatl. Cloud Physics Conf. 15–20 Aug. 1988.
- HALLETT J. and MOSSOP S.C.: Nature 249 (1974) pp26–28.
- HOBBS P.V. and RANGNO A.L.: J.Atmos.Sci. 42 (1985) pp2523–2549.
- KELLER V.W. and SAX R.I.: Quart.J.R.Met.Soc. 107 (1981) pp679–697.
- MASON B.J.: Quart.J.R.Met.Soc. 101 (1975) pp675–679.
- MOSSOP S.C.: Quart.J.R.Met.Soc. 111 (1985) pp183–198.
- RANGNO A.L. and HOBBS P.V.: J.Clim. and Appl.Meteor. 22 (1983) pp214–232
- RYAN B.F., WISHART E.R, and SHAW D.E.: J.Atmos.Sci. 33 (1972) pp842–850

# PRECIPITATION INITIATION MECHANISMS IN

## CLOUDS OVER NORTH INDIA

R.N. CHATTERJEE, P. PRAKASH, G. SINGH

AND

R.K. KAPOOR

INDIAN INSTITUTE OF TROPICAL METEOROLOGY

PUNE-411005, INDIA.

### 1 INTRODUCTION

Proper understanding of precipitation initiation mechanisms in clouds of any region is of fundamental importance. Occurrence of initial radar echo below or above freezing level, has been used by many investigators to study whether the collision-coalescence process or the Bergeron-Findeisen process is responsible in the release of precipitation. Battan (1953) based on the study of formation and spread of precipitation in 123 convective clouds under the Thunderstorm Project in U.S.A. during 1947 found that the initial echo formation was at temperatures warmer than  $0^{\circ}\text{C}$  in 60 per cent cases and therefore concluded that the mechanism of precipitation initiation in these clouds were purely due to collision-coalescence process. BRAHAM (1964) in project Whitetop observed his findings similar to those of BATTAN. BRAHAM found that about 50 % of the first echoes were entirely warmer than  $0^{\circ}\text{C}$ , 10% colder than  $0^{\circ}\text{C}$ , and 40% straddled the freezing level. Similarly, BRAHAM and DUNGEY (1976) in the St. Louis area under the Project METROMEX found 40% of the first echoes warmer than  $0^{\circ}\text{C}$ , 7% completely colder than  $0^{\circ}\text{C}$ , and 53% straddled the freezing level.

In India, a limited study over two years period, 1958 to 1959, was carried out in and around Delhi and the heights considered were the maximum reached by echo tops during the periods of survey. In particular, height determinations were repeated in case of cells which were below  $0^{\circ}\text{C}$  level, to see if any of these later developed into cold type. The

study showed that except during the winter when rain cells of warm type were of rare occurrence, about 30 to 40% of precipitating clouds during the monsoon season were of warm type (RAMANAMURTHY et al., 1960). Hereafter, we shall refer rain initiation mechanisms by Bergeron-Findeisen, coalescence-cum-ice and collision-coalescence processes respectively from a-, b-, and c-type rain cells. In a-type rain cells, widespread precipitation field giving echo with melting band appears. Rain on such occasions is usually of long duration and fairly steady in character. In b-type rain cells, observations reveal rain showers from tall convective clouds which do not exhibit any melting band feature, although the rain cell extends well above  $0^{\circ}\text{C}$  level. Rain on such occasions is of relatively short duration and high intensity, and is characterised by marked fluctuations in rates of precipitation. This is often called mixed process. In c-type rain cells, precipitation is mostly in the form of drizzle from warm convective clouds whose tops are limited to be below  $0^{\circ}\text{C}$  level. DE and RAKSHIT (1961) found that precipitation echoes from convective clouds in the Calcutta region were more than in 90% cases due to c-type process.

In this paper, an attempt has been made to study the role of different precipitation initiation mechanisms in clouds over Delhi region in north India during different seasons using radar observations of precipitation echoes collected during an extensive 16-years period from 1960-1975. A year consisted of four seasons, namely, winter (December to February), pre-monsoon (March to June),

monsoon (July to September) and post-monsoon (October to November). Heights of the freezing levels during winter, pre-monsoon, monsoon and post-monsoon seasons have been taken as 3.5, 5.0, 4.5 Kms respectively. Details of investigations are presented.

## 2 EQUIPMENT USED

NMD-451A, a Japanese make radar operating on 3.2 cm wave length and having peak output 250 KW has been used for the study. Its radiating system consists of a feed-horn and a parabolic reflector two meters in diameter, which shapes the beam to 1° in both azimuth and elevation. The duration of transmitted pulse is one microsecond and its repetition frequency is 300 per second. Minimum detectable signal is -90 dBm.

The radar is equipped, in addition to the conventional Plan Position (PPI), Range Height (RHI) and Amplitude Modulated (A-Scope) indicators, with a special arrangement called Range Elevation Indicator (REI) on which depth and elevation of echoes are displayed in true proportions when scanned at elevational angles between -1° and 90°. The maximum range of the radar is 300 km on PPI, REI and A-Scope, and 100 km on RHI. Range markers 2.5, 5, 10, 20 and 60 km apart are provided in the 10, 20, 50, 100 and 360 km ranges respectively. The RHI is supplied with height markers at intervals of 2.5 and 5 km respectively in its 10 km and 20 km height ranges. The overall sensitivity of the radar set is such that it can just detect raindrops of diameter about 0.33 mm at a distance of 100 km, if they are presented in concentration of 100 per litre.

## 3 METHOD OF OBSERVATIONS

The 3.2 cm weather radar was used to survey precipitation occurrences within 100 km around Delhi (28° 35'N, 77° 12'E, 210 m MSL), and data collected on rain cells were grouped

according to heights reached by their echo tops. For this purpose, an examination was firstly made, on the PPI scanning at near zero elevation, of the broad features of rain cells and their distribution. The cells are then randomly picked up and projected on RHI or REI to determine the heights of their tops. Generally, height measurements of individual echoes were repeated at intervals up to 5 minutes to determine their maximum vertical growth. To ensure correct height of the top-most part of the rain cell, the azimuth was fixed for scanning at each elevation that it passed through the brightest portion of echo at that level. This was necessary, as quite frequently it was seen that the azimuth corresponding to the highest point of echo from a rain cell was very different from that at which echo was strongest near ground. In this study hourly observations made from 1000 to 1700 hrs. IST have been used.

## 4 RESULTS AND DISCUSSIONS

### 4.1 FREQUENCY DISTRIBUTION OF PRECIPITATING CLOUDS

During winter, pre-monsoon, monsoon and post-monsoon seasons, a total of 7346 convective clouds were studied within 100 km around Delhi in 16-years period from 1960 to 1975. These were classified in the indicated class intervals and are shown in Table 1. The clouds which extended beyond 16 km were put under one category. It may be seen from Table 1 that during winter clouds had maximum echo top heights limited to 12 km. However, during pre-monsoon, monsoon and post-monsoon seasons, echo top heights extended beyond 16 km in 9,50 and 1 cloud cases respectively. During monsoon season in as much as 1.03% cases echo tops were above 16 km. The maximum echo top height encountered was 19 km.

### 4.2 DISTRIBUTION OF a-, b- AND c-TYPE RAIN CELLS.

Distribution of a-, b- and c-type rain cells of the above 7346 convective clouds studied is shown season-wise in Table 2. It may be noted from Table 2 that c-type rain cells were maximum during monsoon 2672 (54,9%) followed by winter, pre-monsoon and post-monsoon seasons; b-type rain cells were maximum in pre-monsoon or summer season 868 (57,0%) followed by winter, post-monsoon and winter seasons; a-type rain cells were found maximum during post-monsoon season 39 (30,5%). On annual basis a-, b- and c-type rain cells were 10.5, 41.2 and 48.3% respectively. The disparity noted compared to 1958 and 1959 observations especially in the case of c-type cells in winter is perhaps due to lesser data in that season.

REFERENCES:

BATTAN, L.J. (1953) J. Meteor., 10,311-323.  
 BRAHAM, R.R.JR (1964) J. Atmos. Sci., 20,563-568.  
 BBRAHAM R.R.JR and DUNGEY; M. (1976) Proc. Int. Conf. on Cloud Physics, July 26-30, 1976, Boulder Colo, U.S.A., 275-278.  
 DE, A.C. and RAKSHIT, D.K. (1961) Indian J. Met. Geophys., 12,2,289-298.  
 RAMANAMURTHY; BH. V., BISWAS; K.R. and B.K. GHOSH DASTIDAR (1960) Indian J. Met. Geophys., 11,4, 331-346.

**Table 1:** Frequency of occurrence of a-, b- and c-type rain cells among indicated height intervals in different seasons.

Season	Height (Km)					Total
	4.0	4.1-8.0	8.1-12.0	12.1-16.0	16.0	
Winter	249	543	36	-	-	828
Pre-monsoon	155	882	406	70	9	1522
Monsoon	939	2799	813	267	50	4868
Post-monsoon	17	90	14	6	1	128
Total	1360	4314	1269	343	60	7346

**Table 2:** Distribution of a-, b- and c-type rain cells in different seasons.

Season	a-type	b-type	c-type	Total
Winter	112	394	322	828
Pre-monsoon	133	868	521	1522
Monsoon	488	1708	2672	4868
Post-monsoon	39	57	32	128
Annual	772	3027	3547	7346

EVIDENCE OF PREFERENTIAL ZONES OF ICE MULTIPLICATION BY SPLINTERING IN  
CONVECTIVE CELLS

Jean-François Gayet, Christophe Duroure and R.G. Soulage  
LAMP, University of Clermont II, B.P. 45, 63170 Aubière (France)

1. INTRODUCTION

A lot of field situations have conformed so closely to the requirements of the HALLETT-MOSSOP (1974) splintering, as established by laboratory experiments, that there can be little doubt that it was an active process producing ice multiplication (MOSSOP, 1985). The purpose of this paper is to show, from a small scale analysis of in situ microphysical and dynamical measurements, that the "splintering" process occurs on preferential zones in convective cells. These measurements were collected during the "Landes-Fronts 84" experiment (held in the South-West of France in summer 1984) from an instrumented Transall aircraft together with a ground meteorological radar system. The aircraft was equipped with a complete set of microphysical probes (FSSP, 1D and 2D) (LAROCHE et al., 1985).

2. DESCRIPTION OF THE CLOUD SYSTEM

This study concerns the measurements collected on June 6th 1984. The radar analysis performed from the Rabelais system (8 mm wavelength; SAUVAGEOT, 1982) shows that the cloud system was characterized by several convective cells (Fig. 1) having a mean reflectivity of about 35 dBZ (maximum value 45 dBZ) and a cloud base and top of 1000 m (+3°C) and 5000 m (-20°C) respectively. The radiosounding (performed 1 h before the experiment) indicates a negligible vertical wind shear in intensity and direction on the cloud extent and a wet layer (80% humidity) up to 4000 m. The radar analysis also reveals a low reflectivity zone (-5 dBZ, Fig. 1) located between the 5000 and 7000 m levels which corresponds to the cirrus cloud observed from the aircraft and the ground. The flight track segment is reported on the

corresponding vertical reflectivity profile according to the tracking radar information (500 m accuracy on aircraft position). We shall discuss now the aircraft measurements obtained on this flight segment performed at 2700 m (-6°C) level.

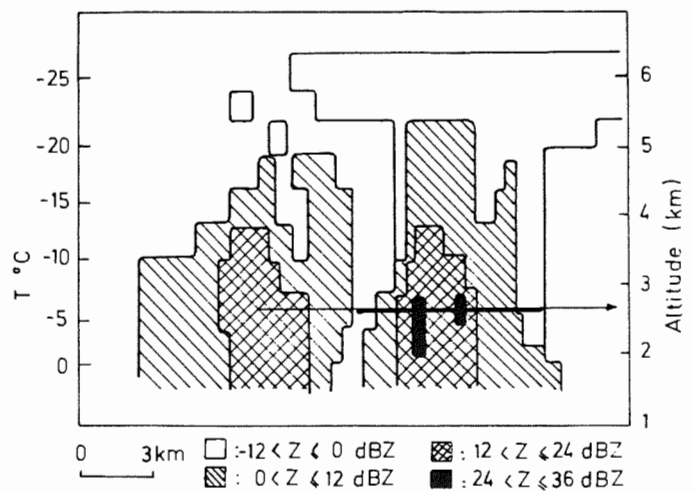


Fig.1 : Vertical profile of the reflectivity obtained from the Rabelais 8 mm radar.

3. EVIDENCE OF PREFERENTIAL ZONES OF SPLINTERING

3.1 EXAMPLE OF DATA OBTAINED AT -6°C

The example presented below is typical of the measurements obtained at this level in the cloud system of June 6th 1984. On Fig. 2 are reported time series (100 m space resolution) of microphysical parameters (LWC : liquid water content ; CI and DI : concentration and mean size of the ice particles greater than 60 μm ; CH and DH : concentration and mean size of precipitation particles greater than 250 μm) and the vertical airspeed (WA). In the main updraft region (5 m s<sup>-1</sup>) labelled A, the cell does not exhibit any ice particle on about 1000 m of horizontal extent and it is not mixed with the environmental air because of the liquid water

content which has a similar value as the adiabatic one ( $2 \text{ g m}^{-3}$ ). These characteristics contrast with those of regions labelled B in which high ice concentrations ( $100$  to  $600 \text{ l}^{-1}$ ) of small crystals ( $\sim 40 \text{ }\mu\text{m}$ ) are measured. These small particles have been identified as columns from the 2D-C probe (Fig. 3). Large graupels (Fig. 3) having a mean size ranged from  $1$  to  $2.5 \text{ mm}$  are also found in the B regions. As for the cloud droplets, they are characterized by a broad spectrum centered on  $21 \text{ }\mu\text{m}$  and having concentrations of droplets larger than  $24 \text{ }\mu\text{m}$  and smaller than  $13 \text{ }\mu\text{m}$ , of  $25 \text{ cm}^{-3}$  and  $15 \text{ cm}^{-3}$  respectively. All these characteristics are consistent with the HALLETT-MOSSOP (1974) ice multiplication criteria to explain the large ice crystal concentrations in the B regions.

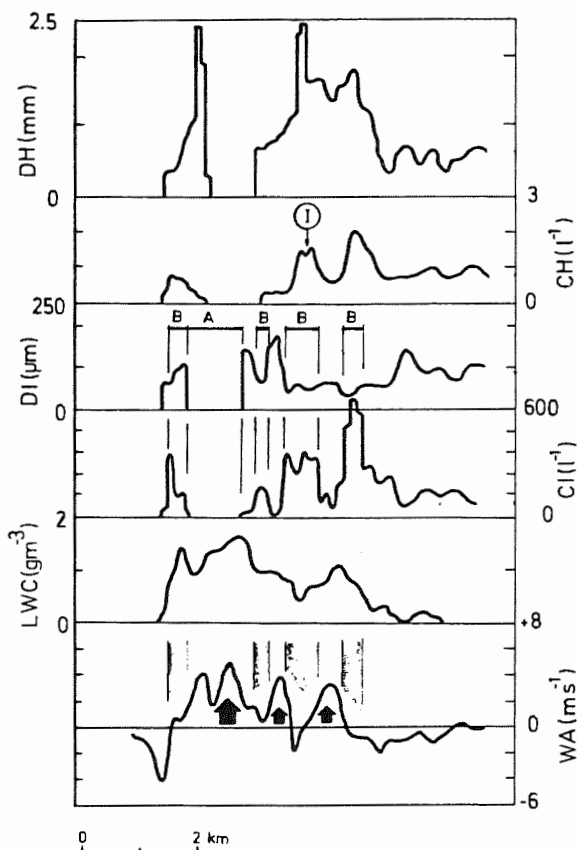


Fig. 2 : Time-series of microphysical parameters and vertical air velocity ( $2700\text{m}/-6^\circ\text{C}$  level). The corresponding aircraft segment is reported on Fig. 1 (thick line).

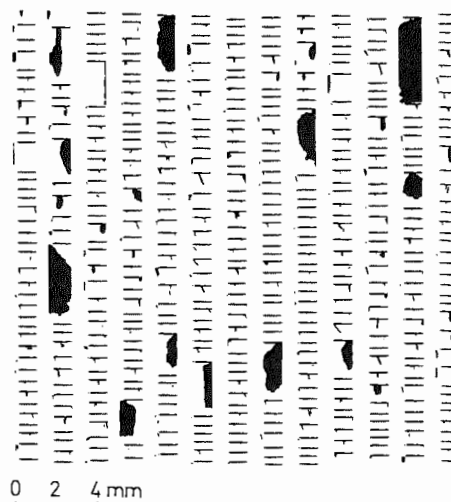


Fig.3 : Example of 2D-C images sampled at point I on Fig. 2.

### 3.2 DISCUSSION

A small scale analysis of the time series of Fig. 2 shows that the large ice concentrations of the B regions are firstly, extended on only a few hundred meters ( $200$  to  $400 \text{ m}$ ) and secondly, linked to the dynamical activity. As a matter of fact, these B regions are associated to the zones located on the edges both of the main and the secondary updrafts. On the contrary, the updraft regions (identified with dark arrows on Fig. 2) are characterized by zero or low values of ice crystal concentrations. It should be noted that the above characteristics were often evidenced in the Landes-Fronts 84 experiment, during the sampling of convective cells in which the splintering process was efficient. In order to exemplify more precisely this observation, we have reported (on Fig. 4) the mean values of the ice crystal concentration as a function of the mean vertical air velocity calculated in the cloud regions above-defined. The standard deviations of the vertical air velocity measurements are also reported on Fig. 4. Despite the fact that the limits of the cloud zones are arbitrarily defined, Fig. 4 clearly shows that the largest ice crystal concentrations are preferentially found outside (on the edges) of the updrafts. Furthermore, the correspondence between the ice crystal concentration (CI) and the mean size (DI) of these particles (Fig. 5) indicates that the largest concentrations ( $\sim 400 \text{ l}^{-1}$ ) are

associated with the smallest crystal size ( $\sim 40 \mu\text{m}$ ). This suggests that the origin of the small crystals issued from the splintering process takes place near the points of measurement that is to say not in the updraft cores but preferentially on the edges of the updraft (B regions). On the contrary, the updraft regions (Fig. 4) are characterized by much lower concentrations ( $< 50 \text{ l}^{-1}$ ) of large ice particles (rimed columns ranged from 80 to 200  $\mu\text{m}$ ). These observations indicate that these particles have a longer residence time in the cloud and may arise from the B regions by mixing or recycling. The low concentration of these recycled particles suggests that the mixing of the updrafts is not very efficient at this stage of cloud development. Our observations are consistent with the conceptual model of LAMB et al. (1978) which suggests, despite a rapid natural glaciation, that the heating that results tends to be ineffective in controlling the dynamic structure of the cell. This is due to the fact that this glaciation occurs in regions located outside the updraft cores where the buoyancy is considerably reduced or becomes negative and where the supply of supercooled water may be rapidly depleted or cut off.

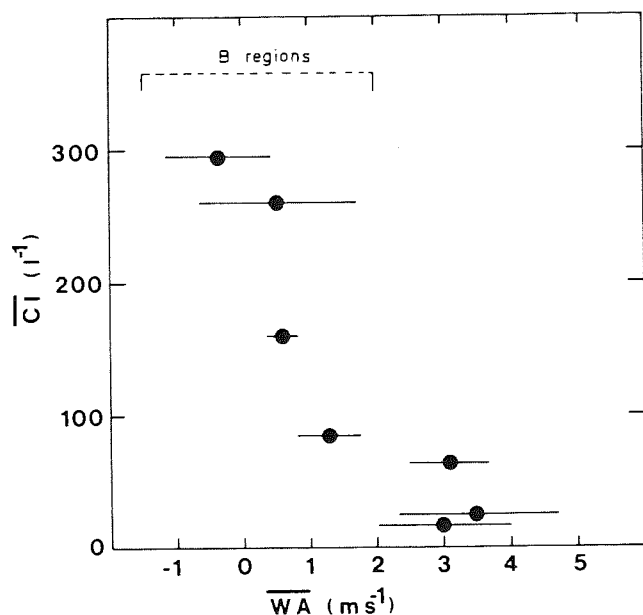


Fig. 4 : Mean ice crystal concentration versus the mean vertical air velocity.

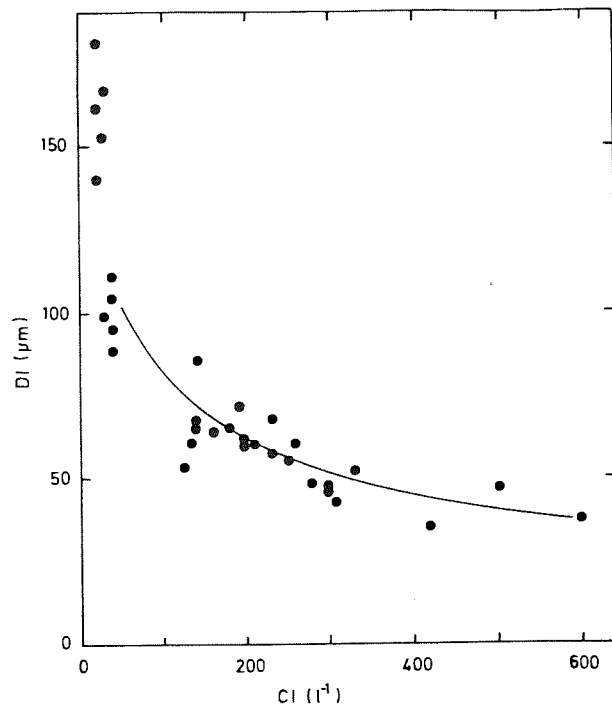


Fig. 5 : Correspondence between the concentration and the size of the ice crystals.

#### 4. ACKNOWLEDGEMENTS

This research was supported by the grants DRET/INSU n° 8334308 and 8534016. We would like to thank B. Campistron for his help in the 8 mm radar interpretation. The manuscript correction and typing is due to O. Guillot.

#### 5. REFERENCES

- HALLET J. and S.C. MOSSOP, 1974 : Production of secondary particles during the riming process. *Nature*, 249, 26-28.
- LAMB D., J. HALLET and R.I. SAX, 1978 : Microphysics of invigorated cumulus development. *Proc. AMS Conf. on Cloud Physics and Atmos. Electricity*, Issaquah, Wash.
- LAROCHE P. et al., 1985 : In-flight thunderstorm environmental measurements during the Landes 84 campaign. 10th Int. Aerospace and Ground Conf. on Lightning and Static Electricity, Paris.
- MOSSOP, S.C., 1985 : The origin and concentration of ice crystals in clouds. *Bull. American Meteor. Soc.*, 66, 264-272.
- SAUVAGEOT H., 1982 : *Radarmétéorologie. Télédétection active de l'atmosphère*. Eyrolles. Paris.

MICROPHYSICAL CHARACTERISTICS OF WARM-BASED CUMULI:  
OBSERVATIONS AT -10°C

Robert R. Czys

Illinois State Water Survey  
Climate and Meteorology Section  
Champaign, Illinois USA

## 1. INTRODUCTION

As part of the Precipitation Augmentation for Crops Experiment (PACE), the microphysical properties of untreated and treated (with either AgI or placebo) cumulus clouds are being investigated. PACE is a research program to determine precipitation alterations attainable by dynamic seeding during the growing season of the central United States and to determine the benefits and liabilities of such alterations. The overall goals and objectives of PACE have been discussed by Changnon (1986).

The exploratory phase of PACE began in the summer of 1986 with field operations using airplanes and radar. This paper reports on data collected in 20 natural clouds from 3 days in July 1986.

## 2. DATA

Table 1 gives a summary of microphysical properties of natural clouds measured at -10°C on three different days. On July 8, clouds feeding into an air mass thunderstorm positioned over the southeastern corner of Indianapolis, IN, were sampled. On July 24, data was obtained in 5 clouds feeding an air mass thunderstorm located northwest of St. Louis, MO. And, on July 30, data near -10°C was gathered for a cloud feeding a warm front thunderstorm. Each cloud is identified by the month, day, cloud number and penetration number. Missing data for clouds 708c2p1 and 708c6p1 was caused by momentary failure of the data acquisition system.

The clouds represented in Table 1 were mostly youthful, individual cumulus associated with a larger storm cloud. These were clouds which met the PACE visual criteria for seeding. They showed a hard "blocky" appearance, and had tops which were easily passing through the -10°C level which is approximately 20 kft over the central USA during the summer. The representative sounding for each day showed no evidence of either a shallow temperature inversion or a dry layer in mid-levels to restrict vertical cloud development. They were mostly warm-based and had base temperatures and heights of: +16C and 6000', +15C and 6500', and +8C and 11000', for July 8, 24, and 30, respectively. The airplane weather avoidance radar often displayed an echo during cloud approach.

Cloud maturities in Table 1 were approximated during cloud approach by the flight meteorologist and pilot from a visual estimation of the amount of cloud above flight level. Cloud top temperatures can be inferred from these maturities by assuming a moist adiabatic lapse rate of approximately -2°C/1000 ft at -10°C. Thus, estimated cloud top temperatures are approximately, -10 to -11°C for \*, -11 to -12°C for \*\*, -12 to -15°C for \*\*\*, -15 to -20°C for \*\*\*\* and colder than -20°C for \*\*\*\*\*.

### 2.1 SUPERCOOLED PRECIPITATION DROPS

Microphysical observations from 1986 confirm the existence of copious amounts of supercooled drizzle and rain drops at -10°C in moderately vig-

Table 1. Summary of Cloud Properties

Cloud ID	Penetration Time (CDT)	Duration (sec)	Maturity*	Cloud Dia. (km)	Cloud Temp. (°C)	Thermal Buoy. (°C)	Peak Updraft (m/sec)	Mean/Max FWC (g/m <sup>3</sup> )	Mean/Max JWC (g/m <sup>3</sup> )	Mean Drop Dia. (µm)	Mean Conc. (cm <sup>-3</sup> )	S.P.D.**
708c1p1	151643	42	**	2.5	-8.6	0.4	12	0.4 0.5	0.4 0.7	13	190	Yes
708c2p1	157751	--	**	---	---	---	--	---	---	--	---	Yes
708c3p1	153237	94	****	5.5	-9.3	1.2	15	0.2 0.3	0.0 0.2	17	80	No
708c3p2	153933	43	*****	1.6	-6.0	---	10	0.3 0.5	0.4 0.8	13	140	Yes
708c4p1	153418	58	****	2.8	-9.5	---	7	0.2 0.3	0.2 0.4	14	80	No
708c4p2	153827	62	*****	3.9	-7.9	---	3	0.1 0.3	0.1 0.2	19	20	No
708c5p1	154417	89	**	4.5	-8.9	0.4	17	0.4 0.8	0.7 2.9	15	140	Yes
708c6p1	154552	--	****	---	---	---	--	---	---	--	---	No
708c7p1	155828	68	**	4.4	-10.6	0.3	14	0.2 0.4	0.1 0.3	15	70	Yes
708c8p1	155958	73	****	4.7	-10.1	0.6	15	0.0 0.1	0.0 0.0	22	10	No
708c9p1	161419	56	**	4.3	-9.7	-0.3	17	0.1 0.6	0.0 2.4	13	140	Yes
708c10p1	162823	41	**	3.2	-8.4	0.7	5	0.1 0.2	0.0 0.1	22	20	Yes
708c11p1	162718	26	**	2.1	-8.7	1.1	15	0.7 1.0	3.5 3.8	16	250	Yes
708c12p1	162920	62	**	3.2	-8.8	0.4	15	0.3 0.5	0.3 0.5	15	120	Yes
724c1p1	142420	110	****	8.6	-9.3	1.2	15	0.3 0.8	0.3 0.9	14	130	Yes
724c2p1	143018	133	**	10.9	-10.5	0.4	5	0.2 0.6	0.1 0.7	16	50	No
724c3p1	144550	54	**	4.0	-8.1	-1.0	3	0.4 0.8	0.5 1.5	13	170	Yes
724c4p1	144941	75	****	5.4	-7.7	2.8	8	0.4 0.7	0.8 2.3	14	200	Yes
724c5p1	145612	43	**	3.0	-8.1	-0.6	3	0.2 0.6	0.2 0.7	13	110	Yes
730c6p1	172639	87	****	2.2	-10.9	-0.6	12	0.4 0.5	0.5 1.2	13	220	No

\* Maturity:                    \*        \*\*        \*\*\*        \*\*\*\*        \*\*\*\*\*  
 Estimated height of cloud top above flight level        100-500'        500-1000'        1000-2500'        2500-5000'        >5000'

\*\* S.P.D. = Supercooled Precipitation Drops

orous midwestern clouds with warm bases. The yes in the column labeled S.P.D. of Table 1 indicates that at least centimeter size splashes were observed on the airplane windshield during periods of positive vertical acceleration. These observations were later verified using the recording of a forward looking video camera.

These observations suggest that loading of the updraft by the bulk of the condensate mass is more severe in young clouds than older ones. Of the 11 clouds estimated to have tops no higher than 1000 ft above flight level, 10 contained supercooled rain. Comparatively, only 3 of the 9 clouds with tops higher than 2500 ft above flight level had supercooled rain drops as part of their composition.

Supercooled precipitation drops represent a substantial fraction of the total amount of supercooled water in

young clouds. Estimates of the liquid water content from the 2DC and 2DP records suggest that on average 60% of the total water content comes from drops larger than 50 µm diameter.

## 2.2 CLOUD BUOYANCY

Two physical effects must be taken into account when considering the net buoyancy of a cloudy parcel of air. The first effect is thermal and will produce a positive or negative component to the net buoyancy depending on the temperature difference between cloud and environment and the temperature must include an adjustment for water vapor content. The second component represents the negative effect of loading by the mass of the condensate contained in the parcel.

The buoyancies listed in Table 1 were calculated with respect to the temperature difference between the main cloud updraft and environment. They

do not include the effects of water vapor since we have little useful dew point data, nor do they reflect the mass of the cloud condensate. From representative thermodynamic soundings the relative humidity of the environment air was estimated to be 50% and if the cloudy parcel is assumed to be just saturated then buoyancy would be enhanced by 0.25°C due to the presence of water vapor. However, this enhancement is generally balanced by the mass of the cloud droplets ( $D < 45 \mu\text{m}$ ) since about  $0.5 \text{ g m}^{-3}$  corresponds to about  $-0.25^\circ\text{C}$ . Thus, to the extent larger hydrometeors are absent the buoyancies in Table 1 are a good first estimate.

If the negative effect of loading by large particles is taken into account using the 2DC and 2DP data, then most of the clouds in Table 1 are negatively buoyant. This suggests that the updrafts, typically peaking between 3 and  $17 \text{ m s}^{-1}$ , were in a state of deceleration. Hence, any buoyancy enhancements resulting from imposed glaciation may be expected to only reduce the rate of updraft deceleration.

The data also suggests that young clouds are less buoyant than older ones. This difference may be greater than indicated by the buoyancies in Table 1, since younger clouds tend to contain larger masses of liquid water than older and because older clouds may have received benefit from the release of latent heat as a product of natural glaciation.

### 2.3 ICE

Initial ice concentrations determined from the 2-D images of optical array probes (OAP) were as high as 35 times the ice nuclei concentration measured over the central United States using

membrane filters (Czys, 1977). The ice appeared mostly as graupel in sizes between 25 and  $1000 \mu\text{m}$  diameter. It was not unusual for clouds with tops no colder than  $-11^\circ\text{C}$  to develop graupel concentrations of 10 to  $20 \text{ l}^{-1}$  with mean diameters from 125 to  $325 \mu\text{m}$ . Low concentrations of rectangular-solid and rectangular-hollow OAP images, perhaps the shadows of columns, are the only evidence we have for the existence of vapor grown ice crystals.

### 3. SUMMARY

The microphysical features of the clouds observed suggest that supercooled liquid water is present in quantities sufficient for buoyancy enhancement by imposed glaciation. However, the clouds in this sample exhibited negative buoyancy by the time cloud top reached the  $-10^\circ\text{C}$  level. This suggests that the most attainable dynamic effect may be to only decrease the rate updraft deceleration.

### REFERENCES

- Changnon, 1986: Illinois weather modification program: PACE. Preprints Conf. on Weather Modification. Arlington, VA, 315-319.
- Czys, R. R., 1977: University of Chicago measurements of ice-forming nuclei from METROMEX. Proc. Sixth Conf. on Inadvertent and Planned Weather Modification, Champaign, IL, 29-32.

### ACKNOWLEDGEMENT

This research has been supported by the Precipitation Augmentation for Crops Experiment (PACE), conducted under cooperative agreement with the National Oceanic and Atmospheric Administration under contracts COMM NA86RAH06051 and COMM NA87RAH07077.

H. Johari\*, G. Taylor\*\*, M. Baker\*\* and R. Breidenthal\*

\*Department of Aeronautics and Astronautics, \*\* Geophysics Program  
University of Washington  
Seattle, WA 98195

## 1. INTRODUCTION

Recent field observations of convective clouds have revealed features of cloud structure which had not been predicted on the basis of early models. These observations have given rise to new conceptual models of cloud evolution. It is the purpose of this paper to examine these models in the light of laboratory simulations of convective cloud development.

The cloud features to be explained by a new conceptual model can be summarised as follows.

(1) Thermodynamic analysis of in-cloud air at a fixed level often reveals a single mixing line structure, which has been interpreted to mean that the source of entrained air within the sampled part of the cloud was restricted to a narrow layer within the environment. BOATMAN and AUER (1983), LA MONTAGNE and TELFORD (1983), JENSEN (1985), and others have shown that the source region is usually within a kilometer of the observation level, and often is slightly above it.

(2) Fine scale structure in microphysical fields (JENSEN ET AL., 1985) is often quite uniform over several hundreds of meters, even in cloudy air which has been substantially diluted by entrainment.

(3) Regions of undiluted cloudbase air, often several hundred meters in lateral extent, have been found in many convective clouds at altitudes far above cloud base.

(4) Cloud edges are 'hard' during cloud growth, suggesting that lateral diffusion is not an important entrainment mechanism, although regions of maximum liquid water content are usually near the center of the rising stream.

(5) As pointed out by WARNER (1970) and confirmed extensively since, the average ratio of observed to adiabatic liquid water content is always less than about 0.5, and declines slightly with height above the first few hundred meters. Laterally entraining similarity plume models which reproduce this average profile cannot reproduce observed cloudtop heights.

(6) Droplet spectral shapes suggest that entrainment takes place in localised events (BAKER ET AL., 1984) and that each cloud parcel undergoes only one or very few of these events (JENSEN ET AL., 1985).

## 2. LABORATORY SIMULATION

Our experiments consist of the release of a mixture of alcohol and glycol into a water tank which is neutrally stratified. When the release is instantaneous, we refer

to the buoyant fluid as a thermal and when the release is continuous over some time interval comparable with the time of rise of the buoyant fluid, the buoyant mass is said to form a plume. The parameters of the buoyant fluid at any point are described in terms of the density  $\rho(p)$ , where  $p$  is the fraction of the alcohol glycol mixture in the buoyant fluid. For certain compositions, the density of the mixed fluid is greater than that of the environment. The nonlinear relation only approximates the shape of the analogous atmospheric relation.

One measure of the effect of the buoyancy reversal on the 'cloud' dynamics is given by

$$D_* = \frac{1}{p_*} \frac{\rho(p_*) - \rho(0)}{\rho(1) - \rho(0)} \quad (1)$$

This parameter varies between 0 (for 'neutral' thermals and plumes) and 7.0 in our experiments. We stratify all the experimental results by this parameter in the following discussion.

### 2.1 THERMALS

Thermals were generated by overturning an inverted hemispherical cup at the bottom of the tank. A small volume of buoyant fluid initially confined by the cup then rises. In the first two diameters of its ascent, there is negligible mixing of the buoyant fluid with its environment. Mixing (defined as the molecular scale chemical process through which the buoyancy can change) begins after approximately one vortex revolution.

In the absence of buoyancy reversal,  $\rho(p)$  is a linear function of  $p$ . JOHARI (1988a) has measured the distance  $L$  which a thermal ascends before every parcel of released fluid mixes with at least  $\phi$  parcels of environmental fluid.  $\phi$  is termed the equivalence ratio, and is equal to  $(1 - p)/p$ .  $L$  is known as the flame length from the combustion literature.

Figure 1 shows  $L/d_0$  for thermals which are still rising, for a range of values of  $D_*$ . To within experimental accuracy,  $L/d_0$  is independent of  $D_*$ . Buoyancy reversal does not affect mixing rates in rising thermals.

The evolution of the thermals, however, is highly dependent on  $D_*$ . Whereas the neutral thermal leaves no wake, a wake is left behind in the buoyancy reversing case, and the amount of fluid left behind increases with  $D_*$ . For  $0.7 < D_* < 1.0$  the thermal often splits in two, part ascending and part descending. The altitude of the bifurcation is always  $4d_0$ . There are two remarkable features of the bifurcation: the two components

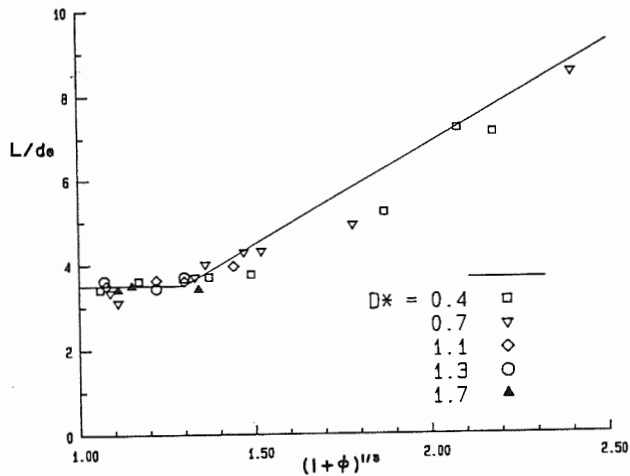


Fig. 1. Nondimensional flame length  $L/d_0$  plotted against a function of the equivalence ratio  $\phi$  (where  $1+\phi = 1/p$ ) for five different values of  $D_*$ . The line represents the behavior of inert thermals.

have approximately the same density, and that density is greater than that of the environment. The upper portion rises in spite of its negative buoyancy, apparently assisted by an impulse from the bifurcation itself.

## 2.2 PLUMES

Buoyant fluid is emitted at a constant speed,  $u$ , from a nozzle of diameter  $d_0$ . JOHARI (1988b) has measured the molecular mixing rate inside the plumes as a function of the initial Richardson's number,

$$Ri_0 = \frac{\rho(1) - \rho(0)}{\rho} \frac{g d_0}{u^2} \quad (2)$$

the ratio of buoyant to momentum forces at the nozzle. He shows that a dilution argument, following BROADWELL (1982), yields the following far field expression:

$$\frac{L}{d_0} = \text{const.} p^{-3/5} Ri_0^{-1/5} \quad (3)$$

For  $p \rightarrow 1$ , the maximum height of adiabatic transport in plumes is  $L/d_0 = 8$ , which is more than twice the value found for thermals.

## 3. DISCUSSION

Since the generation of buoyancy by latent heat is not simulated in the laboratory, we choose for our comparisons cloud cases in which the virtual moist adiabat more or less parallels the sounding within much of the cloud layer. We have examined data from the CCOPE (1981) and JHWRP (1985) experiments which meet this criterion. The height dependent values of  $D_*$  vary within a range roughly equal to that in the laboratory. Buoyancy sorting seems to be absent for mean cloud layer values of  $D_*$  less than about 1.0, and downward mixing is strongest for  $D_*$  greater than about 4.0-5.0, in nonprecipitating clouds.

The definition of cloud aspect ratio  $Z/d_0$ , where  $Z$  is cloudtop height, poses a problem. Using reasonable estimates for  $d_0$  yields aspect ratios of order 1-5. Thus we see that the finding of undiluted cloud base air near cloudtop is consistent with the laboratory results; in fact, in the absence of the topping inversion we might expect to see undiluted parcels at much higher levels.

The relevant Richardson number in the atmosphere is much larger than those in the laboratory. The dependence of the cloud properties on initial buoyancy and momentum is qualitatively similar to results of numerical model studies (TAYLOR, 1987; FERRIER, 1988) which show that excessive instability at low levels produces large entrainment rates there, and thus damps cloud growth.

## 4. CONCLUSIONS

According to recent models of convective clouds, developed to explain points (1)-(6) of our introduction, air rises adiabatically from cloud base in a thermal (RAYMOND and BLYTH, 1986) or plume (JENSEN, 1985). It mixes in a series of discrete gulps with the environment. After each gulp, the mixed fluid tends toward its position of hydrostatic equilibrium, as suggested earlier by TELFORD and WAGNER (1980). Most of the cloud mass is then this 'wake' of mixed fluid.

The crisp edges, small scale uniformity and extended adiabatic ascent of some parcels which characterize convective clouds are all found in the laboratory. The laboratory simulations suggest that evaporative cooling in buoyant flows can cause ejection of wake material, and that undiluted parcels can last through ascents of several diameters. It can be shown (RICHARDS, 1961) that passage of a thermal through a sharp inversion also causes ejection of fluid from the thermal; thus the effect of stratification in the environment may add to the wake produced by evaporative cooling. It appears from the laboratory simulations and atmospheric observations that the new models are physically realistic in this respect. However, the segregation of undiluted air in the early stages of ascent to cloudtop, as suggested by RAYMOND and BLYTH (1986), is not seen in the laboratory; we recall that even for high enough  $D_*$ , the laboratory thermals bifurcate, ascending and descending parcels have the same (dilute) mixture ratio.

While it appears necessary to invoke adiabatic ascent of some parcels to explain the observed heights of cloudtop, as well as the presence of undiluted cloudbase air aloft, it appears, for the reasons cited above, that the basic flow pattern inside convective clouds in some cases may be nearer that of starting plumes than that of thermals. Plumes have the same crisp edges and locally uniform interiors as thermals, but in plume parcels of different mixing ratio can coexist at the same level. The core of a starting plume can be almost undiluted while other regions at the same level within the plume are quite dilute. Recent numerical one-dimensional cloud models (FERRIER, 1988; TAYLOR, 1987), which are more plume-like than thermal-like, give satisfactory

agreement between cloud properties and observations in convective situations. We note that recent investigation of the in-cloud composition (TAYLOR and BAKER, unpublished) using such a model, shows that roughly half the air inside a convective cloud at any level has usually been entrained from the local environment. The starting plume model, moreover, is more consistent than the thermal model with observed time dependence of cloud properties.

It is, of course, clear that atmospheric clouds are more complex than the laboratory flows, that they probably consist of collections of convective elements, and that intermixing of fluid from different parts of the cloud produces effects quite unlike those which can be reproduced in these experiments. The examination of laboratory flows, however, is an enlightening method with which to investigate individually certain interesting aspects of the atmospheric phenomenon.

Acknowledgement: This research was partially supported by NSF grants ATM-8420816, 8609376 and 8611225.

#### REFERENCES:

- AUSTIN, P.; JENSEN, J.; BLYTH, A.; BAKER, M.: Turbulent Mixing and Microphysical Variability in Two Warm Cumulus Studies. *J. Atmos. Sci.* 42 (1985), 1123-1138.
- BAKER, M.; BREIDENTHAL, R.; CHOULARTON, T.; LATHAM, J.: The Effects of Turbulent Mixing in Clouds. *J. Atmos. Sci.*, 41 (1984), 299-304.
- BOATMAN, J.; AUER, A.: The Role of Cloud Top Entrainment in Cumulus Clouds. *J. Atmos. Sci.* 40 (1983), 1517-1534.
- BROADWELL, J.: A Model of Turbulent Diffusion Flames and Nitric Oxide Production. *TRW Doc. 38515-6001-UT-00*, 1982.
- FERRIER, B.: One Dimensional Time Dependent Modelling of Squal Line Convection. PhD Dissertation, U. Washington, 1988.
- JENSEN, J.: Turbulent Mixing, Droplet Spectral Evolution and Dynamics of Warm Cumulus Clouds. PhD Dissertation, U. Washington, 1985.
- JENSEN, J.; AUSTIN, P.; BAKER, M.; BLYTH, A.: Turbulent Mixing Droplet Spectral Evolution and Dynamics of Warm Cumulus Clouds. *J. Atmos. Sci.* 42 (1985), 173-192.
- JOHARI, H.: A Laboratory Study of Thermals with Evaporative Cooling. Eighth Symposium on Turbulence and Diffusion, AMS, San Diego, (1988a).
- JOHARI, H.: An Experimental Investigation of Mixing in Buoyant Flows. PhD dissertation, U. Washington, (1988b).
- LA MONTAGNE, R.; TELFORD, J.: Cloud Top Mixing in Small Cumulus. *J. Atmos. Sci.* 40, (1983), 2148-2156.
- PALUCH, I.: The Entrainment Mechanism in Colorado Cumuli. *J. Atmos. Sci.* 36 (1979), 2467-2478.
- RAYMOND, D.; BLYTH, A.: A Stochastic Mixing Model for Nonprecipitating Cumulus Clouds. *J. Atmos. Sci.* 43 (1986), 2708-2718.
- RICHARDS, J.: Experiments on the Penetration of an Interface by Buoyant Thermals. *J. Fl. Mechanics* 11 (1961), 369-385.
- TAYLOR, G.: A Numerical Investigation of Sulfate Production and Deposition in Midlatitude Continental Cumulus Clouds. PhD dissertation, U. Washington, (1987).
- TELFORD, J.; WAGNER, P.: The Dynamical and Liquid Water Structures of the Small Cumulus as Determined from Its Environment. *Pure and Appl. Geophys.* 118 (1980), 935-952.
- TURNER, J.: Jets and Plumes with Negative or Reversing Buoyancy. *J. Fluid Mech.* 26 (1966), 779-792.
- WARNER, J.: On Steady State One-Dimensional Models of Cumulus Convection. *J. Atmos. Sci.* 27 (1970), 1035-1040.

Ilga R. Paluch and Darrel G. BaumgardnerNational Center for Atmospheric Research\*  
Boulder, Colorado 80307, USA

## 1. INTRODUCTION

Recent fine-scale measurements of cloud-droplet concentrations indicate that entrainment in cumulus clouds can produce very nonuniform mixtures on the scale of meters. These data have been interpreted to imply that the larger turbulent eddies cause most of the bulk entrainment and coarse mixing, while fine-scale (molecular) mixing takes place within intermittent small eddies or vortex cores (Baker *et al.*, 1984). In the past it has been difficult to determine to what extent fine-scale mixing has taken place within a mixed cloud volume, because the sampling distances were too large to resolve its fine-scale structure.

## 2. LOCAL DROPLET CONCENTRATIONS

A new kind of measurement of the distribution of distances (or times) between droplet arrivals at the FSSP (Baumgardner, 1986) enables a "local droplet concentration" to be estimated regardless of the scale of the patchiness of the cloud. Droplets which have been well mixed in some particular volume will be randomly spaced within that volume. The distance,  $d$ , between one particle and the next is described by the exponential probability density function

$$P(d) = \alpha e^{-\alpha d}, \quad d > 0 \quad (1)$$

where  $1/\alpha$  is the average distance between particles. The spacing between particles is measured from an aircraft as an elapsed time,  $t$ ,  $d = Vt$ , where  $V$  is the airspeed, and  $1/\alpha$  is the average elapsed time between

particles which is determined by

$$\alpha = NAV \quad (2)$$

where  $N$  and  $A$  are the average droplet concentration and the FSSP sample area.

With the new method of measuring elapsed time between particles, the measured time is categorized in one of thirteen channels, where the width of each channel is 20  $\mu$ s, corresponding to a spacing interval of approximately 2 mm at a typical research speed of 100 m s<sup>-1</sup>. Elapsed times are accumulated in these size channels every 0.1 seconds, or approximately every 10 m. If the droplets are positioned randomly in space, the measured frequency distribution will take the form of the function given in (1), and a value for  $\alpha$  can be determined from the slope of the distribution. Then, using the known values for  $A$  and  $V$ , (2) is used to determine the local droplet concentration,  $N$ .

Figure 1 shows distance interval distributions of droplets measured upon entering cloud. When the calculated slope for randomly distributed droplets with the measured average concentration (light line) matches the slope of the histogram, then the droplets are randomly distributed throughout the sample volume. When the calculated slope is flatter than the observed, then the sample volume contains some empty or droplet-poor regions. The latter is typically observed within 20 or 30 m of clear-air samples. The data in the last four plots of Fig. 1 come from a high liquid water region where the droplet concentration is nearly constant. In this region the slopes of the interarrival distance distributions are constant and co-

\*The National Center for Atmospheric Research is sponsored by the National Science Foundation.

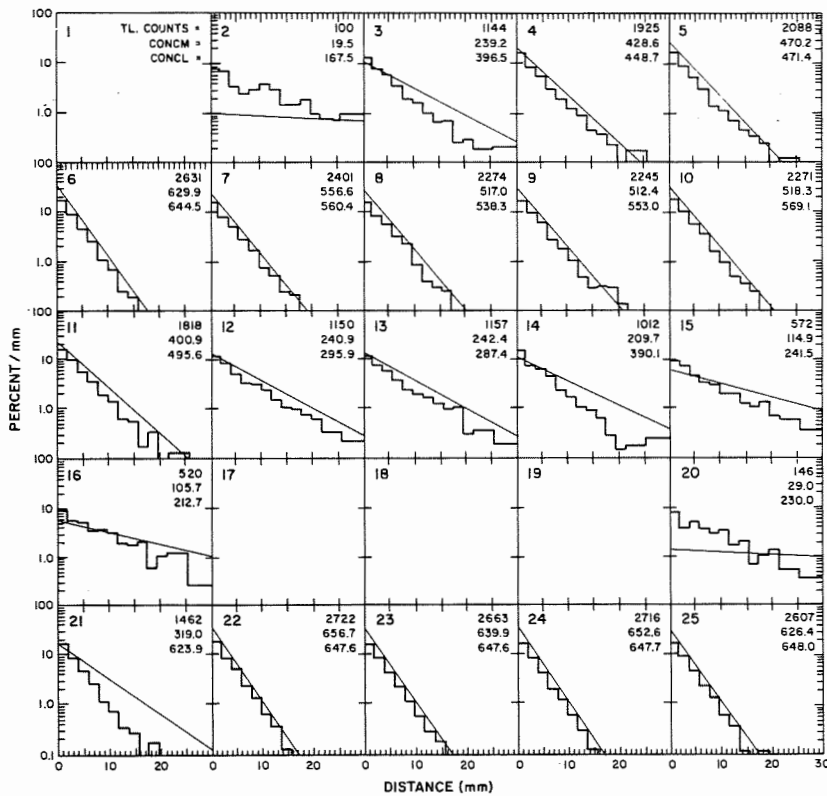


Fig. 1. Histograms of the distribution of distance between droplets arriving at the FSSP. The data are 10 m averages (10 Hz). CONCM is the average concentration, CONCL is the concentration derived from the droplet arrival time distribution slope. The latter ignores empty regions and represents the dominant local droplet concentration. The light line shows the expected slope for randomly distributed droplets corresponding to the measured average concentration.

incide with those computed from the measured average concentrations, indicating that the droplets are indeed randomly distributed throughout the sample volumes. Such uniformly random distributions were typically observed in adiabatic or nearly adiabatic cloud regions.

### 3. MIXING AT INTERFACES BETWEEN CLOUD AND CLEAR AIR

Comparisons between the average and local concentration can provide information about the structure of the interface. If an interface is diffuse, with a gradual increase in droplet concentration from cloud edge inward, then the average and local concentrations are approximately equal, and both increase gradually, as sketched in Fig. 2a. If the interface is irregular or patchy but there is no fine-scale mixing and thus the interface remains locally sharp, then the local concentration remains constant and it is always higher than the average concentration, as shown in Fig. 2b.

Examples of variation in the average and local concentration encountered near cloud and clear-air

boundaries are shown in Fig. 3. As can be seen the local concentration is usually significantly higher than the average concentration, indicating the presence of clear or droplet-poor air within the sample volumes. Simple diffuse interfaces, as in Fig. 2a, extending over distances of several tens of meters were not observed. Adiabatic local concentrations and low average concentrations, as in the case of the irregular interface in Fig. 2b, were also not observed. In most cases the local concentration decreases toward the cloud edge, but to a lesser extent than the average concentration, indicating that the interface is both

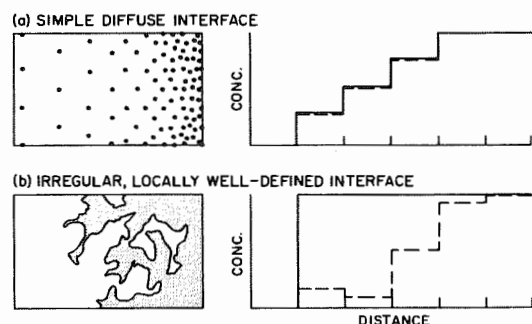


Fig. 2. Two kinds of interfaces and the expected changes in the dominant local concentration and the average concentrations with penetration distance (solid and dashed lines, respectively). a: simple diffuse interface; b: irregular but well-defined interface.

somewhat diffuse and irregular. This implies that coarse and fine-scale mixing take place concurrently within the same cloud volumes.

#### 4. IMPLICATIONS FOR CLOUD DROPLET GROWTH AND AIRPARCEL RECYCLING

The present observations indicate that most of the mixing takes place in narrow regions within tens of meters of clear-air boundaries. Substantially diluted, more-or-less uniformly mixed cloud volumes extending several hundreds of meters across are not observed, though such volumes are often postulated in microphysical parcel models. If the mixed airparcel concept is applicable to the type of continental cumulus investigated here, then the mixed airparcels must be much smaller in size, perhaps only several meters or a few tens of meters across.

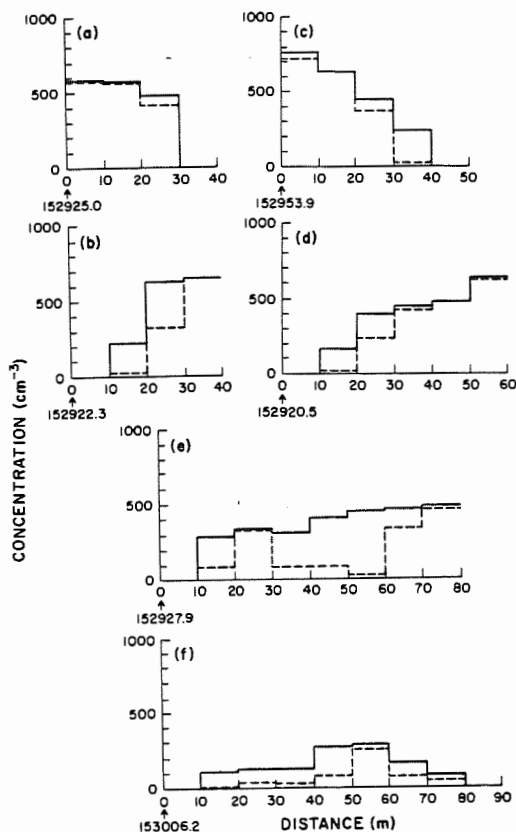


Fig. 3. Examples of interfaces encountered at cloud and clear-air boundaries. Solid line — dominant local concentration, dashed line — average concentration derived from the droplet arrival time distribution slope, both measured over 10 m penetration distances.

The fine-scale features of the mixing process together with the activation of new cloud droplets in ascending, diluted cloud volumes provide a plausible explanation of why mixing does not appear to promote cloud-droplet growth in continental cumulus clouds (Paluch and Baumgardner, 1988), contrary to what has been predicted in some microphysical parcel models (Baker and Latham, 1979; Telford and Chai, 1980). For continental clouds, estimates show that if activation of new droplets is taken into account, then to produce an increase in droplet size detectable with our present 1.5  $\mu\text{m}$  radius resolution the distances a diluted cloud volume must ascend are of the order of hundreds of meters or more. These distances are one or two orders of magnitude larger than the typical dimensions of the diluted cloud volumes. In the presence of turbulence, these mixed cloud volumes might be expected to rise without being destroyed through further mixing over distances several times their characteristic dimensions, but not over distances that are one or two orders of magnitude larger.

#### 5. REFERENCES

- BAKER, M. B., and J. Latham, 1979: The evolution of droplet spectra and the rate of production of embryonic raindrops in small cumulus clouds. *J. Atmos. Sci.*, **36**, 1612-1615.
- BAKER, M. B., R. E. Breidenthal, T. W. Choullarton, and J. Latham, 1984: The effects of turbulent mixing in clouds. *J. Atmos. Sci.*, **41**, 299-304.
- BAUMGARDNER, D., 1986: A new technique for the study of cloud microstructure. *J. Ocean and Atmos. Tech.*, **3**, 340-343.
- PALUCH, I. R., and D. G. Baumgardner, 1988: Entrainment and fine-scale mixing in a continental cloud. To be published in *J. Atmos. Sci.*
- TELFORD, J. W., and S. K. Chai, 1980: A new aspect of condensation theory. *Pure Appl. Geophys.*, **113**, 1067-1084.

AIRBORNE STUDIES OF THE INFLUENCE OF ENTRAINMENT ON THE VERTICAL AND HORIZONTAL  
MICROPHYSICAL STRUCTURE OF SMALL CUMULUS CLOUDS

John Latham\* and Alan M Blyth<sup>†</sup>

\*Physics Dept., University of Manchester Institute of Science and Technology

PO Box 88, Manchester M60 1QD, UK

<sup>†</sup>Physics Dept. and Geophysical Research Centre, N.M.I.M.T.

Socorro, New Mexico 87801, USA

Although recent major field experiments have yielded significant quantities of information on the fine-scale microphysical structure at essentially constant altitude within clouds, little data is available on the associated vertical structure. In an attempt to redress this deficiency we present and discuss measurements made using the University of Wyoming King Air research aeroplane, during the CCOPE experiment conducted in Montana, USA, in the summer of 1981. We restrict our attention to non-precipitating, essentially ice-free cumulus clouds which were studied either by making a series of horizontal penetrations at different altitudes encompassing almost all of the depth of the cloud (typically 2 to 3 km) over as short a period as possible. The principal microphysical measurements (obtained using a PMS Forward Scattering Spectrometer Probe, FSSP) were of liquid-water content (L, also measured with a Johnson-Williams device); cloud droplet size distribution ( $n(d)$ ), where  $d$  is the droplet diameter within the range 2 to 32  $\mu\text{m}$ ; and the droplet number concentration (N). These parameters were recorded at 10 Hz, corresponding to a spatial discrimination of about 10 m; information on N was also available at 50 Hz ( $\sim 2$  m). Standard meteorological parameters and size distributions of larger hydrometeors were also measured, but it was necessary to sacrifice the quantity of the dynamical data in order to minimise the time over which the vertical structure was determined.

We concentrate attention herein on describing the microphysical structure (especially in the vertical), examining the role of entrainment of environmental air in producing it, and discussing the embryonic raindrops which the PMS 1-D probe revealed were often present in particular regions of the clouds studied.

Information was gathered in flights through 7 clouds. On some occasions we present diagrams which superimpose data from all 7 clouds. On other occasions - where we are particularly concerned to examine fine structure - we present comprehensive data from one particular case study (Cloud A, 23 June), in which the observed relationships were characteristic of those found in all cases. Over the 7 case studies the cloud base temperature (TB), the cloud top temperature (TT) and the cloud depth (CD) ranged roughly from 13°C to -3°C, -6°C to -15°C and 1.5 km to 3.5 km respectively; the corresponding values of these parameters for Cloud A were 5.5°C, -15°C and 2.5 km.

Microphysical structure, generally speaking, was found almost everywhere within the clouds studied, independent of the distances from their horizontal and vertical boundaries at all scales down to the lowest limit of measurement ( $\sim 2$  m). Characteristic examples of significant fluctuations in L, N and mean droplet diameter  $\bar{d}$  measured at 10 Hz during horizontal penetrations through the upper and lower regions of Cloud A are shown in Figures 1 and 2 respectively. Consecutive droplet spectra, illustrating structure in  $n(d)$  on spatial scales down to 10 m in this cloud, are presented in Figure 3. Values of the coefficient of variability, K, are seen (Figure 4) to be usually in excess of unity at all 6 levels of penetration of Cloud A, indicating considerable structure in N, which is not simply due to random distributions of the droplets. On the other hand, on many occasions,  $K \sim 1$  in adiabatic regions.

Figures 5, 6 and 7 present 10 Hz scatterplots of L/LA (LA is the adiabatic liquid-water content), N and  $\bar{d}$  respectively for all altitudes, Z, above cloud base at which penetrations were made through Cloud A. The cloud is seen to be substantially sub-adiabatic at every level, with wide ranges in individual values of L/LA, and average values ranging from about 0.2 to 0.4. Individual values of N are seen to vary enormously at each level; the average values increasing slowly with Z. Less scatter is observed in the 10 Hz values of  $\bar{d}$ , the average values being substantially less than the calculated adiabatic ones, which always exceed the peak values of  $\bar{d}$ . Examination of Figures 5, 6 and 7 reveal that reductions in N and  $\bar{d}$  below the maximum (adiabatic) values at each level contribute about equally to the sub-adiabaticity in L.

There can be little doubt that the microphysical structure found in the clouds is a consequence of entrainment. Paluch analyses, which were performed where possible indicate that entrainment occurs at all levels, the source of the entrained air at any level lying between that level and no more than about 1 km above it. The substantial levels of sub-adiabaticity resulting from entrainment will shorten droplet lifetimes significantly, which may have important chemical implications - as might also, the role of entrainment in replenishing depleted supplies of oxidants.

Figures 8 and 9 show the distribution with Z of L/LA and N respectively for all clouds

studied. The scatter in L/LA is appreciable, but the tendency reported by Warner (1970) - curve displayed - for it to diminish rapidly with Z is not confirmed in our studies. In each, L/LA is roughly independent of Z. Substantial variability is found in N, with a tendency for the average droplet concentration to increase with altitude above cloud base, possibly as a consequence of activation of condensation nuclei at higher levels where the updraught is stronger and/or L has been diminished by entrainment.

Analysis of 1-D probe data for three particular detailed multipenetration studies of ice-free clouds on 27 July, revealed the presence of substantial concentrations ( $\sim 10$  /l of water drops in the approximate size range 60 to 120  $\mu\text{m}$  in the central and upper regions, but not near cloud base. Adiabatic spectra - determined from calculations based on measurements made in the lowest regions penetrated - indicate that the largest droplets grown by condensation are too small to produce the observed embryonic raindrops. The fact that they were not found in the lowest penetration through each cloud, and the observation (Figure 10) that their number concentrations at any level do not systematically increase with increasing L, militate against the idea that they were formed on giant nuclei. Whether or not their presence is attributable to the ingestion of the residue of a decaying thermal by a newer one, enhanced growth associated with entrainment or some other mechanism remains to be established.

REFERENCE

Warner, J.: 1970 On steady-state one-dimensional models of cumulus convection. J Atmos Sci, 27 (1970) 1035-1040.

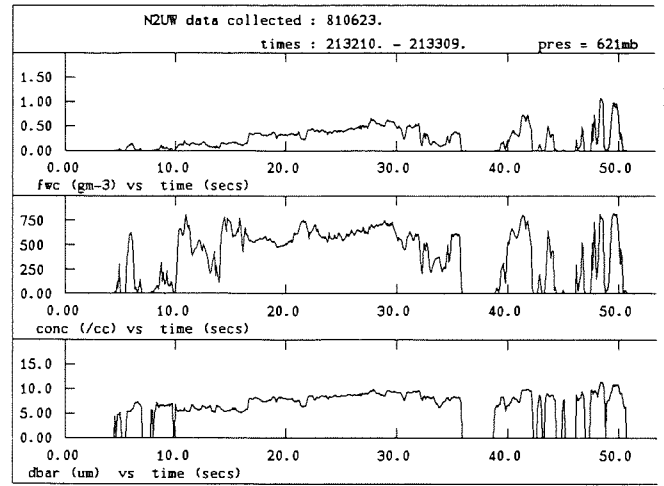


Figure 2. Cloud A. As Figure 1.

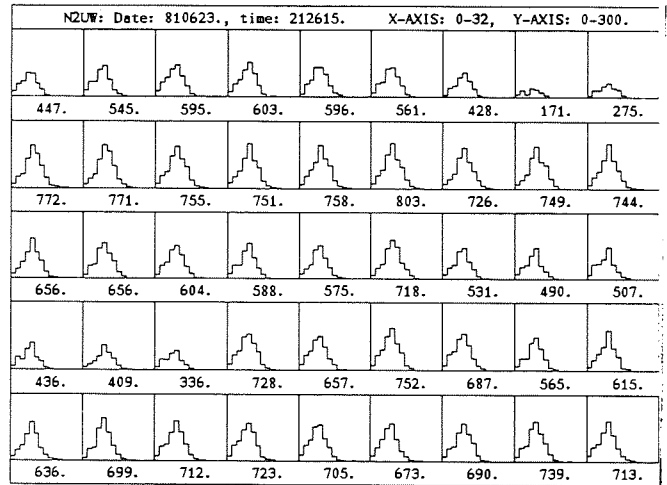


Figure 3. Cloud A. Consecutive 10 Hz droplet spectra. The number under each spectrum is  $N \text{ (cm}^{-3}\text{)}$ .

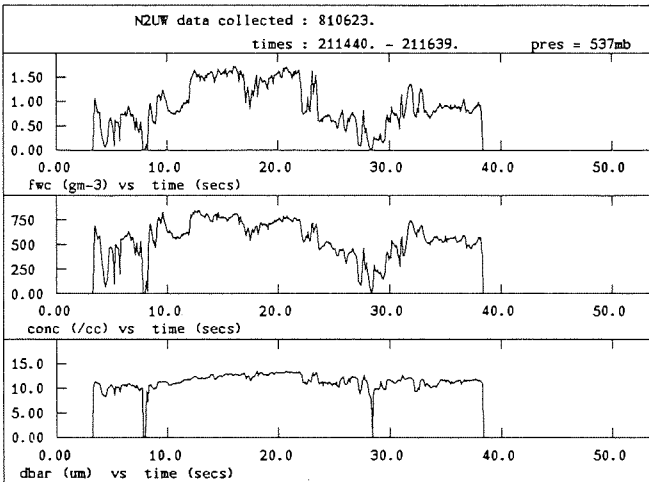


Figure 1. Cloud A. Variation of L, N and  $\bar{d}$  with time t for one penetration.

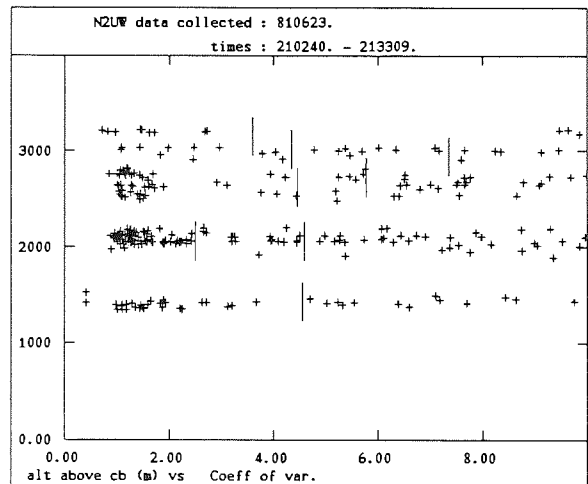


Figure 4. Cloud A. Values of K for each penetration.

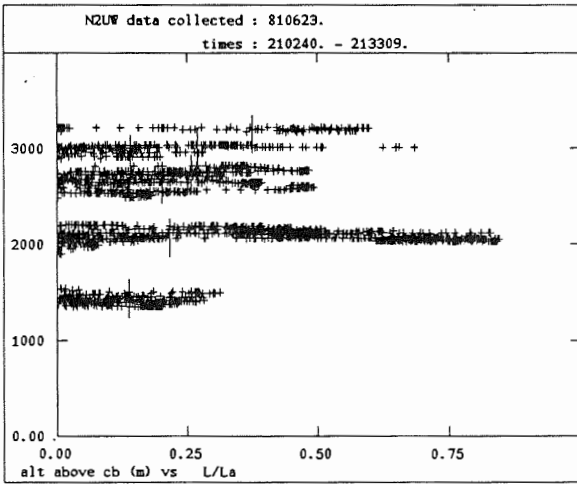


Figure 5. Cloud A. L/LA values for each penetration (10 Hz).

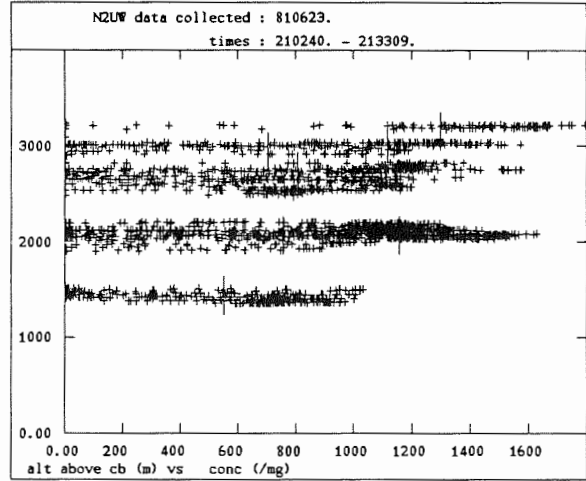


Figure 6. Cloud A. N values (/mg) for each penetration (10 Hz).

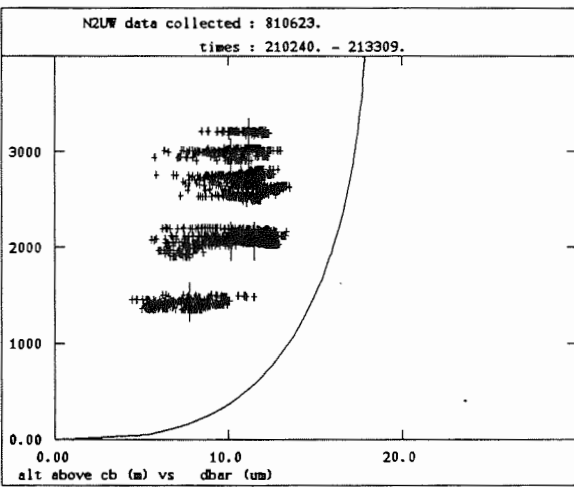


Figure 7. Cloud A.  $\bar{d}$  values ( $\mu\text{m}$ ) for each penetration (10 Hz). The solid line is for adiabatic growth.

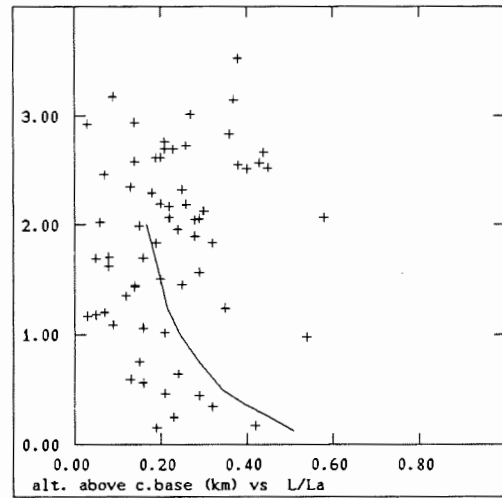


Figure 8. All 7 clouds. Variation of L/LA with height above cloud base. The solid line is from Warner (1970). Points are averages for each penetration.

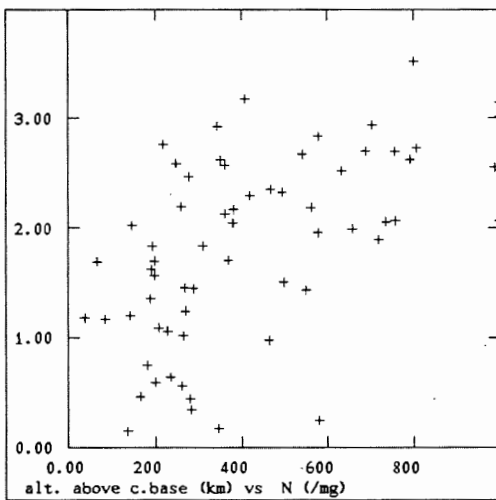


Figure 9. All 7 clouds. Variation of N (/mg) with height above cloud base. Points are averages for each penetration.

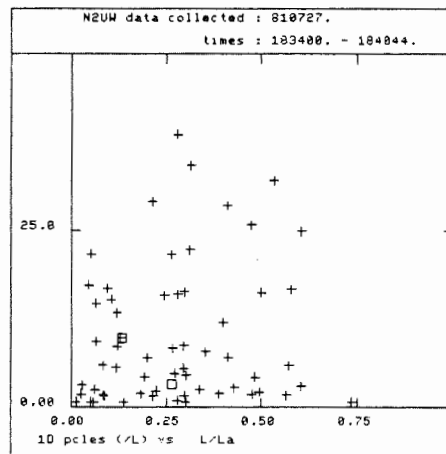


Figure 10. Variation of concentration of embryonic raindrops (/l) with L/LA. Cloud E (27 July)

# ENTRAINMENT SITES, MIXING PROCESSES IN WARM CONVECTIVE CLOUDS. EFFECT ON DROPLET GROWTH

Elizabeth Hicks, Arlette Rigaud, Jacqueline Gagneux and Constantin Pontikis

Météorologie Nationale, EERM-CRPA  
Magny-les -Hameaux (France)

## 1. INTRODUCTION

Entrainment and mixing of non cloudy air into cumulus clouds is currently proposed as a mechanism which broadens the droplet spectrum and creates larger droplets which are the first to start growing by coalescence and may initiate precipitation. In this paper we present the results of an analysis of data collected in September 1983 during a field experiment at Voves (France) which is focussed on the following questions: a) Do measurements made at different levels in a cloud indicate the same source of entrained air? b) Does the mixing process during an entrainment event support the droplet conserving or non conserving hypothesis? c) Does entrainment and mixing enhance cloud droplet growth in the condensation spectrum?

## 2. DATA

Three non precipitating shallow warm clouds, with depth ranging between 600 and 2300 meters, sampled on 9, 12 and 15 September have been selected for this analysis.

The environmental sounding and 1 Hz in-cloud measurements of pressure, temperature (Rosemount and Reverse-Flow sensors), dew-point temperature (G-E sensor), liquid water content (JW and FSSP) and droplet spectra (FSSP) were made by the instrumented EERM Piper Aztec aircraft. The FSSP value of the liquid water content  $Q_l$  and the Rosemount temperature were used in all thermodynamic analysis. The criteria used to ensure that samples were wholly in-cloud was  $Q_l > 0.1 \text{ gm}^{-3}$ .

The presence of precipitation-sized drops was detected by an 8mm Doppler radar and the study was limited to cloud regions with weak echo. An overview of this field experiment, instrumental accuracies is given in Pontikis et al.(1987).

## 3. ENTRAINMENT SOURCES

The source of entrained air is obtained by using Paluch's thermodynamic method where the total water mixing ratio  $Q$  is plotted against the wet equivalent potential temperature  $\theta_q$  for in-cloud measurements, cloud base and the environmental

sounding.

Table 1 summarizes the correlation coefficient of the linear regression through the in-cloud  $\theta_q, Q$  values for every penetration in the 3 clouds as well as information about cloud base, cloud top and entrainment levels. In most cases the in-cloud  $\theta_q, Q$  values form a fairly linear distribution (with more scatter towards cloud top) indicating a single source of entrainment. Every cloud undergoes cloud top entrainment.

date	N° cl.	Pmb base/top	Pmb obs. lev.	Pmb entr. lev.	Cor. Coef.
9/9	1	895/672	840 805 750	670 670 670	0.92 0.91 0.76
12/9	2	848/785	811 793	795 795	0.9 0.57
15/9	3	844/660	810 750 695	810 660 680	0.85 0.95 0.78

Table 1 : Cloud characteristics, entrainment levels associated to each traverse and the correlation coefficient of the regression line in the  $\theta_q - Q$  analysis.

Fig.1 (a,b,c) presents the Paluch diagrams for the 810mb, 750mb and 695mb levels of cloud 3. There are points with  $\theta_q, Q$  values larger than the mean base point values due to natural variability. Lateral entrainment at the lower level of the cloud (810mb) and cloud top entrainment at the higher levels (750 and 695mb) is observed.

The strong linearity of the in-cloud  $\theta_q, Q$  values at 750mb tend to indicate a single entrainment source at cloud top (660mb), although the cloud parcels have most probably already been diluted below. One would expect the in-cloud  $\theta_q, Q$  values to be therefore distributed in the area delimited by: a) the best fit line passing through the in-cloud  $\theta_q, Q$  values at 810 mb, b) the lines passing through the extreme  $\theta_q, Q$  values of the 810mb level and the  $\theta_q, Q$  value of the local environmental sounding which corresponds to the second source of entrained air (660mb). Such a pattern is observed and to a lesser extent for

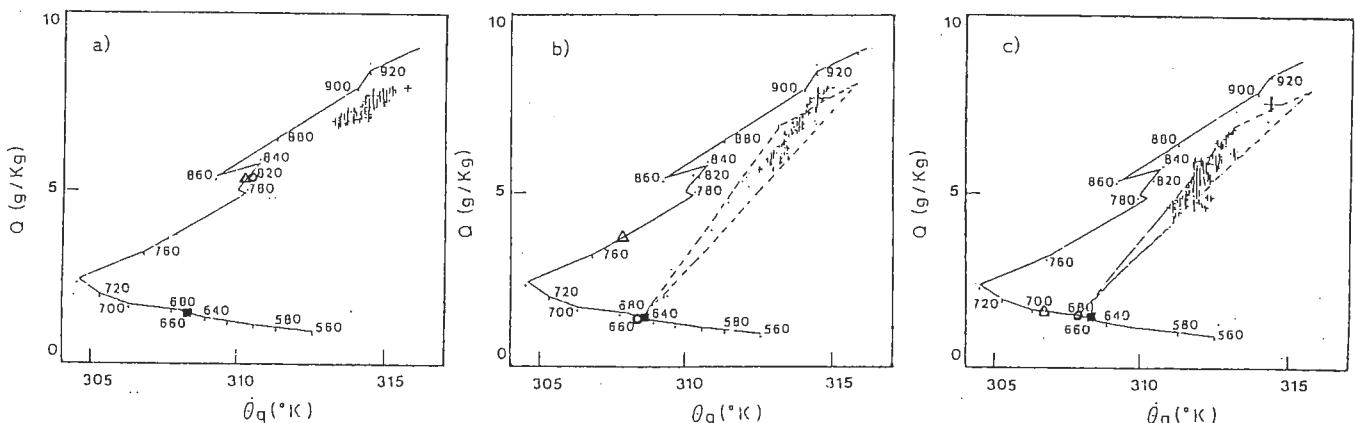


Fig. 1(a,b,c). Paluch diagrams for the 810(a), 750(b) and 695mb(c) levels of cloud 3. The symbols  $\Delta, \square$  on the environmental sounding denote respectively the levels of observation, entrainment and cloud top.

the 695 mb level where the entrainment source is situated at 680mb.

This is a confirmation of the validity of the Q-vs- $\theta_q$  diagrams but emphasizes the importance of multi-level penetrations in a cloud before concluding to cloud top entrainment as the only source of cloud dilution.

In the presence of cloud top entrainment, the dilution of the cloud is due to penetrative downdraughts and mixing between cloud parcels of varying degrees of dilution. In our study, penetrative downdraughts may reach 170mb under the entrainment level (cloud 1) and have similar depth to those which are responsible for the dilution of the clouds studied by Blyth and Latham (1985) and Paluch (1979).

#### 4. MIXING PROCESS

A similar analysis to Jensen's (1985) N-vs-F diagrams has been applied in order to determine the mixing process involved during entrainment events. When one source of entrained air is responsible for the dilution of the whole cloud, each cloudy parcel, independently of its life history and mixing state can be labelled by two quantities: F, the mass fraction of cloud base air it contains which is determined by the Paluch diagrams and R, the ratio between the measured and undiluted droplet number per unit mass. A parcel which is just saturated but droplet free is characterized by  $F=F_s$  and  $R=0$ . At a given level, the F, R values of each cloudy parcel may be plotted in a diagram and different hypothesis can be tested if the points lie within or beyond certain areas:

- homogeneous mixing (in the terminology of Baker and Latham (1979)): no droplets totally evaporate and the F,R points lie within the droplet conserving (D.C.) area delimited by  $F \cdot R_{min} < R < F \cdot R_{max}$ , up to  $F=F_s$ .

- inhomogeneous mixing: some droplets totally evaporate and F,R points are under the D.C. wedge. If a constant proportion K of droplets of all sizes totally evaporate during mixing to maintain saturation while the droplet size distribution does not change, the F,R points lie along the straight line  $R=F(1-K(F))$  passing through points (1,1) and ( $F_s$  min,0) where  $F_s$  min is the value of  $F_s$  at the entrainment level. When the observation level is lower than the entrainment level, the local value of  $F_s$  is higher than  $F_s$  min and only parcels with  $F > F_s$  will contain droplets.

If F,R points are scattered above the D.C. wedge, there has been secondary activation of droplets in the corresponding cloudy samples.

Fig.2 (a, b) presents R-F diagrams for two traverses respectively in cloud 1 and 3. At the 810 mb level of cloud 3 (Fig. 2a), lateral entrainment dilutes the cloud parcels. The absence of F, R points in the droplet conserving wedge for  $F < 0.93$  as well as the scatter of points along the  $R = F(1-K(F))$  line suggests an inhomogeneous mixing process between undiluted cloud parcels and environmental air. This is confirmed by the presence of similar spectral distributions in undiluted and diluted parcels with droplet number per unit mass differences larger than those due to natural variability.

Similar conclusions may be made for the 750 mb level of cloud 1 (Fig. 2b), but in this case, the entrainment event involves already mixed parcels, as most F, R points lie under the  $R = F(1-K(F))$  line.

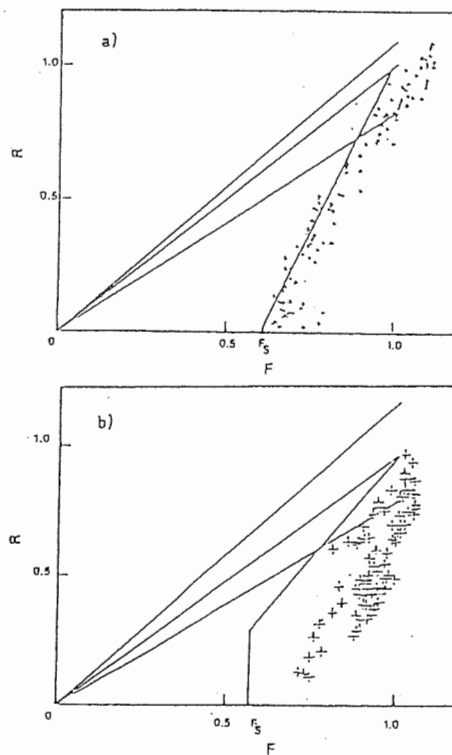


Fig. 2(a,b) R-F diagrams for a) 810mb (cloud 3) and b) 750mb (cloud 1) levels which support the droplet non conserving hypothesis.

Table 2 summarizes the results of the observation made in the R-F diagrams corresponding to all cloud penetrations.

In the case of cloud 1, the larger number of points within the droplet conserving limits is not a consequence of the mixing process itself but reflects the fact that many parcels were not greatly diluted at the time of observation.

The absence of samples with F, R values above the droplet conserving wedge tends to attenuate any assumption of secondary droplet activation.

N° cl.	Pmb	% R, F points			
		in D.C. F > 0.95	in D.C.	under D.C.	above D.C.
1	840	62	62	38	0
	805	24	43	57	0
	750	16	17	83	0
2	811	0	25	75	0
	793	33	72	28	0
3	810	35	37	63	0

Table 2: Pourcentage of droplet conserving and non conserving mixing events in each cloud (D.C. stands for droplet conserving wedge).

One may conclude that these data generally fail to support a droplet conserving hypothesis like in Jensen et al.'s studies (1985, 1986) but do agree with a mixing process where drop sizes do not change and a proportion of drops of all sizes are totally removed to reduce the liquid water content.

Similar observations were reported by Telford and Wagner (1981) from their measurements in the tops of marine stratus and were considered as a direct consequence of the ETEM process where "the thorough mixing inside the dry entity evaporates completely all the drops first entering it" (Telford et al. (1984)).

#### 5. INFLUENCE OF DILUTION ON DROPLET GROWTH

Droplets in ascending diluted cloud samples could grow by condensation to larger sizes than in undiluted parcels as the condensed water is released on fewer droplets.

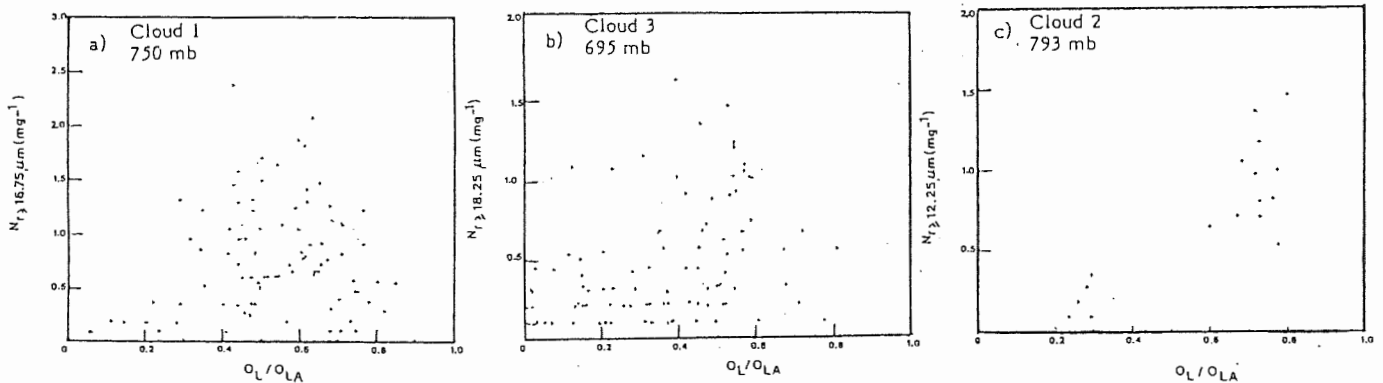


Fig.3(a,b,c) Largest droplet concentration plotted against  $Q_L/Q_{LA}$  for the highest traverses in the 3 clouds.

The examination of droplet spectra collected during the CCOPE experiment on different days have led to contradictory results concerning enhanced droplet growth due to mixing with environmental air (Blyth and Latham (1985), Hill and Choulaton (1985), Paluch and Knight (1986)).

We have plotted the concentration of the largest droplets against the ratio between the measured and adiabatic liquid water content which represents the degree of dilution of cloudy parcels (as  $F$  may not be used in all cases). The diagrams corresponding to the highest traverses in the 3 clouds, where there is the most opportunity in finding large droplets, are shown in Fig.3(a,b,c). For the deepest clouds, the data show great scatter and there is not a good correlation between the largest droplet concentration and  $Q_L/Q_{LA}$ . The highest concentrations of large droplets are found in parcels with an intermediate dilution degree ( $Q_L/Q_{LA}=0.4$ ). The deep downdraughts in the clouds and recycling of cloudy parcels (Telford and Chai (1980)) are the predominant factor of enhanced droplet growth in the case of cloud top entrainment whereas the nature of the mixing process (droplet conserving or non conserving) is secondary. However for the lower levels of cloud 3, the droplet non conserving mixing process associated to lateral entrainment events may also play a significant role in the creation of bigger droplets Baker et al.(1980)). In the most shallow cloud, at all levels, the largest droplet concentrations in undiluted parcels are higher than in the diluted ones. Recycling of parcels are limited to a very small depth and most probably when cloud top was sampled cloudy parcels had undergone insufficient cycling to create significant droplet growth.

Fig.4(a,b,c) presents histograms of the frequency of occurrence of droplets in the highest occupied channel (shaded histogram) compared to the frequency of occurrence of droplet concentrations at the highest traverse of each sampled cloud. The presence of large droplets is equally probable in parcels

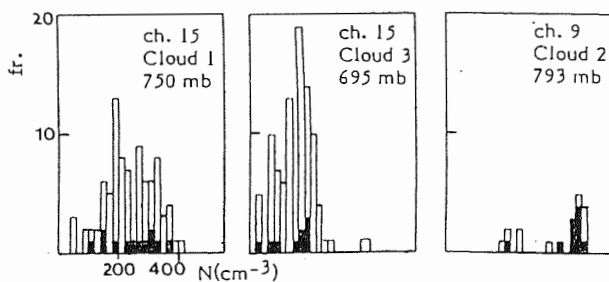


Fig. 4(a,b,c) Frequency of occurrence of droplets in a given FSSP channel (denoted by ch. in each box)(shaded histograms) compared to the frequency of occurrence of droplet concentrations.

with low or intermediate droplet concentrations, whereas they are absent in parcels with the highest concentrations, for cloud 1 and 3. However at the top of cloud 2, there is a higher probability of finding droplets with  $r \geq 13.75 \mu m$  in the least diluted parcels.

## 6. CONCLUSIONS

The conclusions from the results may be summarized as follows:  
 a) The source of entrained air observed at a given level is generally the cloud top, but lateral entrainment may affect the lower levels in a cloud.

b) Mixing is a droplet non-conserving process.

c) Dilution and buoyancy-driven recycling of cloudy parcels enhances droplet growth in shallow warm cumuli.

## REFERENCES

- Baker, M. B. and J. Latham, 1979 : The evolution of droplet spectra and the rate of production of embryonic raindrops in small cumulus clouds. *J. Atmos. Sci.*, 36, 1612-1615.
- Baker, M. B., R. G. Corbin and J. Latham, 1980 : The influence of entrainment on the evolution of cloud droplet spectra. I : A model of inhomogeneous mixing. *Quart. J. Roy. Meteor. Soc.*, 106, 581-598.
- Blyth, A. M. and J. Latham, 1985 : An airborne study of vertical structure and microphysical variability within a small cumulus. *Quart. J. Roy. Meteor. Soc.*, 111, 773-792.
- Hill, T. A. and T. W. Choulaton, 1985 : An airborne study of the microphysical structure of cumulus clouds. *Quart. J. Roy. Meteor. Soc.*, 111, 517-544.
- Jensen, J. B., P. H. Austin, M. B. Baker, and A. M. Blyth, 1985 : Turbulent mixing, spectral evolution and dynamics in a warm cumulus cloud. *J. Atmos. Sci.*, 42, 173-192.
- Jensen, J. B. and M. B. Baker, 1986 : Preprints, AMS Conf. Cloud Physics, Snowmass, 145-148.
- Paluch, I. R., 1979 : The entrainment mechanism in Colorado cumuli. *J. Atmos. Sci.*, 36, 2467-2478.
- Paluch, I. R. and C. R. Knight, 1986 : Does mixing promote cloud droplet growth? *J. Atmos. Sci.*, 43, 1994-1998.
- Pontikis, C., A. Rigaud and E. Hicks, 1987 : Entrainment and mixing as related to the microphysical properties of shallow warm cumulus clouds. *J. Atmos. Sci.*, 44, 2150-2165.
- Telford, J. W. and S. K. Chai, 1980 : A new aspect of condensation theory. *Pure and Appl. Geophys.*, 118, 720-742.
- Telford, J. W. and P. B. Wagner, 1981 : Observations of condensation growth determined by entity type mixing. *Pure Appl. Geophys.*, 119, 934-965.
- Telford, J. W., T. S. Keck and S. K. Chai, 1984 : Entrainment at cloud tops and the droplet spectra. *J. Atmos. Sci.*, 41, 3170-3179.

STRUCTURE OF UPPER CLOUDS BOUNDARY USING  
THE LIDAR DATA

V.E.Zuev, V.S.Shamanaev, I.E.Penner  
I.V.Samokhvalov

Institute of Atmospheric Optics, SB USSR Acad.Sci., Tomsk, 634055, USSR

## 1. INTRODUCTION

In solving many of the climatological and aerometeorological problems one should have a good knowledge of sizes and fluctuation characteristics of inhomogeneities forming the upper clouds boundary (UCB). An airborne lidar is a useful tool for these measurements.

## 2. METHOD OF OBSERVATION

### 2.1 INSTRUMENTATION

The measurements were carried out using a polarization lidar "Svetozar-3" (SHAMANAEV 1985) mounted on an IL-18 aircraft for sounding the clouds through the aircraft optical-glass window in the direction to the Earth. The laser wavelength was 532 nm, the transmitted beam divergence was 1.0 mrad, the angle of the receiver field of view was 1 to 13 mrad. The received signals were digitized with 3.75 m spatial resolution of the computer. The return signals were recorded on magnetic disks at intervals of 20 to 23 m over the entire flight range. Also, the radiation temperature of clouds was measured.

### 2.2 CRITERIA

The distance to UCB was measured using five criteria at a time. Two of them were employed in the paper: the distance from the aircraft to the signal start  $r_0$  and the signal maximum  $r_m$ . Based on these quantities the mean

gradient of scattering coefficient for UCB (that is, water content) was calculated as

$$\mu_G = \frac{1}{2(\Delta\tau)^2} \cdot \frac{\tau_0 - \Delta\tau}{\tau_0 + \Delta\tau} \quad (1)$$

where  $r = r_m - r_0$ .

To monitor the UCB phase state one calculated the lidar return depolarization ratio profile using formula  $D(H) = F_{\perp}(H)/F_{\parallel}(H)$ , where  $F_{\perp}$  and  $F_{\parallel}$  are the return-signal depolarization and polarization components, respectively. In order for the UCB behavior along the horizontal path to be analyzed, the UCB structural functions were calculated by the formula

$$b(\tau) = S^2 \frac{1}{n} \sum_{k=1}^n [H(\tau + l_k) - H(l_k)]^2, \quad (2)$$

where  $S^2$  is the UCB variance,  $l_k$  is the point on the flight path. In many of the situations UCB does not conform to the laws of stationary random processes. The correlation functions therefore are not always applicable.

### 2.3 THE FLIGHT SCHEME

The cloud field Sc was chosen for conducting the experiments. The flights were carried out during several days both along the perimeter and the diagonals of the square with the center in the Barents Sea and coordinates 74°45' N.L., 31° E.L. The observations with the cloud lidar instrument were also obtained during the flights in

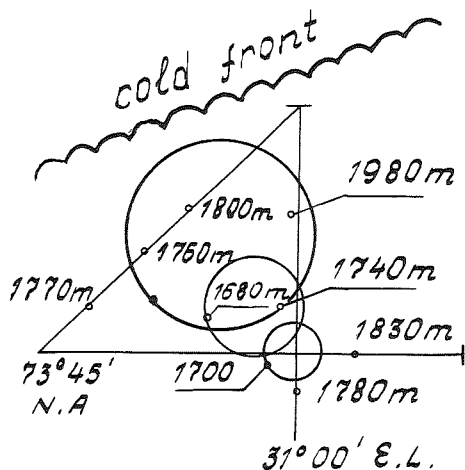


Fig. 1. Scheme of flight

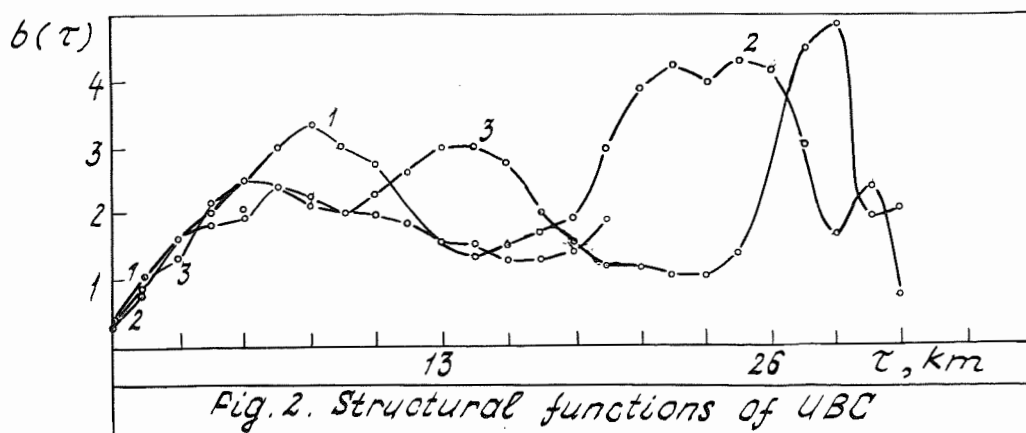
this area along the circumferences 10 km, 20 km and 40 km in diameter. As a rule, the wind distorted the shape of circles and drifted their centers from the point chosen, see Fig.1. The numbers here denote the average UCB above sea level during the flight on 27 February 1987.

### 3. RESULTS

The cloud field presented in Fig.1 was studied during 2 hours. In this area the average UCB of the Sc field was 1660 to 1830 m. Only in one segment of the flight path a local cloudiness "dome" to the 1980 m UCB was observed. The UCB structural functions are presented in Fig.2. Curve 1 is for the small circle (Fig.1); curve 2 is for the Western part of the middle circle; and curve 3 is for the Eastern part of the large circle. For the areas 2 and 3 there is a zone of mutual overlapping. Function  $b(\tau)$  was constructed with the interval  $\tau = 1300$  m with averaging over 20 laser flashes. For the small circle, the mean UCB height  $H = 1720$  m with the r.m.s. de-

viation  $H = 114$  m. For the areas of the middle and large circles analyzed in Fig.2,  $H = (1680 \pm 60)$  m and  $H = (178 \pm 55)$  m, respectively. All the three circles have a common horizontal characteristic length of UCB inhomogeneities 5 to 8 km. In addition the middle circle has UCB fluctuations with 21 to 26 km characteristic length, and in the large circle, it is 13 and 28 km. It is interesting to note that the structural functions  $b(\tau)$  constructed with a minimal interval along the flight line (20-50 m) never have a saturation area smaller than 1 km. That is the small-scale UCB fluctuations (tens of meters) cannot be considered as a stationary random process on the flight paths shorter than 1 km. The radiation temperature of clouds varied along the flight path by not more than  $3^\circ\text{C}$  and did not correlate with the UCB fluctuations.

For example, in the Northern part of the large circle, the scattering coefficient gradient  $\mu_G = (1.3 \pm 1) 10^3 \text{ km}^{-2}$ . The value of the scattering coefficient  $\sigma$  varies from  $20 \text{ km}^{-1}$  to  $31 \text{ km}^{-1}$  with 50% fluctuations for the upper 50-m cloud layer. The depolarization gradient  $\mu_D$  was also measured in the upper 50-m cloud layer. For example, in the central part of the large circle  $\mu_D$  has the values  $(4.6 \pm 1.0) \text{ km}^{-2}$  to  $(2.9 \pm 0.9) \text{ km}^{-2}$ . As shown in the papers (SAMOKHVALOV 1982, p.1050; ZUEV 1984, p.38), this is consistent with the UCB water droplet state.



SAMOKHVALOV, I.V.; SHAMANAEV, V.S.:  
 Izv.Akad.Nauk SSSR Fiz.Atmos.Okeanà  
 18 (1982) N. 10, p.1050-1055.

SHAMANAEV, V.S.; ABRAMOCHKIN, A.I.:  
 Airborne polarization lidar "Sveto-  
 zar-3". 1985.Rukopis' dep. VINITI  
 N. 6225-85 Dep.

ZUEV, V.E.; KREKOV, G.M.; SAMOKHVA-  
 LOV, I.V. et al. : Meteorologiya i  
 gidrologiya, 1984, N.4, p.38-45.

# TURBULENT TRANSPORT PROCESSES WITHIN AND BELOW SMALL CUMULUS CLOUDS

Anne M. Jochum

DFVLR, Institut für Physik der Atmosphäre  
D-8031 Oberpfaffenhofen, Fed. Rep. of Germany

## 1. INTRODUCTION

In 1986 multiple aircraft measurements were conducted in the cloud-topped convective boundary layer (cbl) over complex terrain in South Germany to investigate the structure of turbulence and transport processes within and below clouds and to study the interaction between cloud- and sub-cloud-layer.

Three powered gliders and a jet aircraft all equipped for turbulence measurements were simultaneously flying along the same horizontal flight leg with fixed vertical spacing. The use of several research aircraft provides a very good spatial and temporal resolution. The gliders were scanning the subcloud boundary layer whereas the jet was collecting data (including microphysics) within and above the clouds. The data from the different aircraft are combined to yield vertical profiles of mean fluxes and spectral characteristics as well as information on the mean horizontal structure of thermal or cloud up- and downdrafts in various heights. Vertical profiles of mean meteorological parameters were obtained from rawinsondes and an additional aircraft. Airborne downward looking lidar gives information on the structure of the inversion zone and of the cloud layer.

Quadrant analysis and conditional sampling techniques are used to identify and investigate the main physical processes and scales contributing to vertical transport. First results from a case study with weak ambient winds are presented. There the observed clouds appear to be closely related to thermals in the mixed layer. Therefore the emphasis is laid on turbulence structure and transport rather than microphysical or radiative processes.

## 2. OBSERVATIONAL DATA

The measurements were conducted in the convective boundary layer over hilly terrain (maximum height variation 100m) in South Germany. Three instrumented powered gliders (Jochum et al., 1987) and the jet research aircraft Falcon-E (Fimpel, 1987) were simultaneously flying along the same horizontal flight leg with fixed vertical spacing to measure turbulence data. Wind profiles are derived from occasional ascents or descents of the Falcon. During selected runs above the inversion a downward scanning lidar onboard the Falcon

(Mörl et al., 1981) delivered two-dimensional cross sections of the cbl structure as shown in Figure 1.

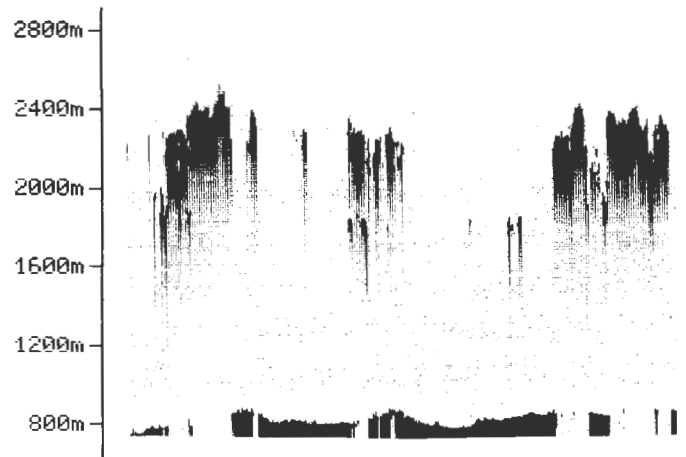


Figure 1. Lidar scan of cbl structure 14.07.1986.

The observational period covered four days in July 1986 characterized by high pressure, light to moderate winds, fair weather with varying light cloud cover. Results from a day (14.07.1986 noon) with weak ambient wind and 2-3/8 small cumulus cloud cover are presented. The data (11-13 local time) cover 26 individual measurement runs. The turbulence data are low-pass filtered to eliminate high frequency noise beyond sensor resolution, and high-pass filtered to remove scales larger than the convective scale. The resulting scale range is from 17m to 3.5km.

In order to understand the physical processes involved in turbulent heat transfer and its relation to the turbulence structure, two different methods of analysis have been pursued. For conditional sampling vertical velocity was chosen as the indicator series to distinguish a convective element (updraft) from its environment. The threshold defined to separate 'updraft' (larger than mean plus threshold) from 'environment' values is set to half the standard deviation of the indicator function, sensitive to the exact magnitude of the threshold. A minimum event length of 100m (except where otherwise mentioned) is specified in order to prevent very small bursts within larger events from splitting these coherent structures.

Another method of analysis consists of partitioning time series of temperature and vertical wind into the four quadrants of the  $\theta' - w'$ -plane and of computing fluxes and other quantities for each of

these quadrants which represent different physical processes (for details of the method see e.g. Grossman, 1984): Warm updrafts ( $\theta' > 0$  and  $w' > 0$ ) are thermal motions, cold updrafts penetrating thermals, warm downdrafts represent entrainment of warm air from aloft, cold downdrafts are compensating sinking motions. Contributions from each of these processes to total transport and area fractions covered by the corresponding motions are computed this way.

### 3. RESULTS

The data from the different aircraft are combined. All heights are normalized with the inversion height  $z_i$ . The composite vertical profiles in Figures 2-3 are derived by interpolating data from individual runs to normalized heights of multiples of 0.1 $z_i$  and averaging consecutive profiles over quasistationary periods of time. Figures 4-6 show the individual data points to illustrate the degree of scatter.

Three classes of length scales are introduced by appropriately filtering the data. Figure 2 shows the contributions of these scale ranges to sensible heat flux. The class covering eddies smaller than 170m represents turbulence of stochastic character. Its contribution of less than 10% is limited to the lowest third of the cbl. The class of intermediate size scales contains motions forming organized motions up length scales comparable to the cbl depth. They are most important in the lower half of the cloud-topped cbl, whereas in a cloudfree cbl they contribute significantly to the negative total flux in the upper third of the cbl (Jochum, 1988). The scales larger than cbl depth carry most of the flux in the upper half of the cbl.

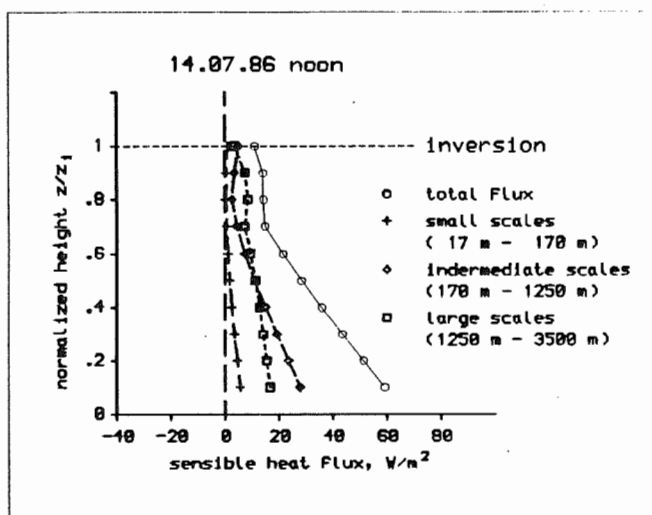


Figure 2. Scale ranges contributing to sensible heat flux. See text for details. Height is normalized by inversion height  $z_i$ .

The contributions of different physical processes to total sensible heat flux are identified using quadrant analysis. Figure 3 shows that everywhere in the cloud-topped cbl the vertical heat flux is dominated by warm updrafts (thermals). Cold downdrafts (compensating sinking motions) are also important, contribution to total flux about half as much as warm updrafts. In the upper half, two more types of motion (penetrative thermals and entrainment of warm air from aloft) contribute to total flux but they are much less significant than in cloudfree cases (Jochum, 1988).

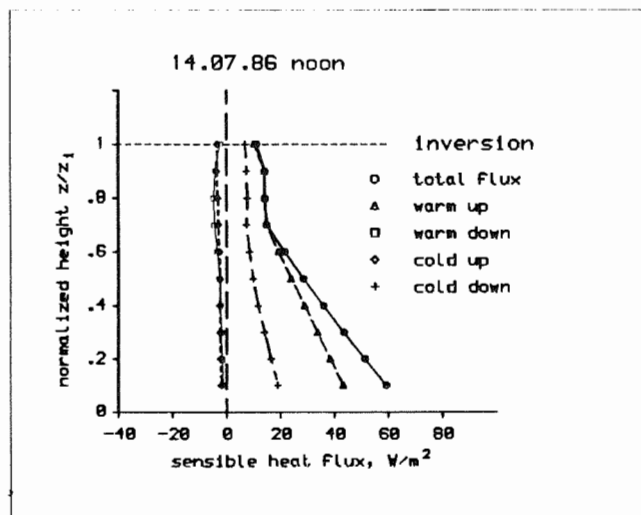


Figure 3. Physical processes contributing to sensible heat flux. See text for details.

Some statistics of updrafts are shown in Figure 4: the average thermal intersection length for events larger than 100m on the left, and the average number of updrafts per 10km on the right. In order to get information on smaller scale structure the minimum event length of 35m was evaluated additionally and is plotted in Figure 4 as crosses. Smaller events are most important in the lowest part of the boundary layer. Data from a cloudfree day which had otherwise comparable conditions are shown in the same figure as solid and dashed curves.

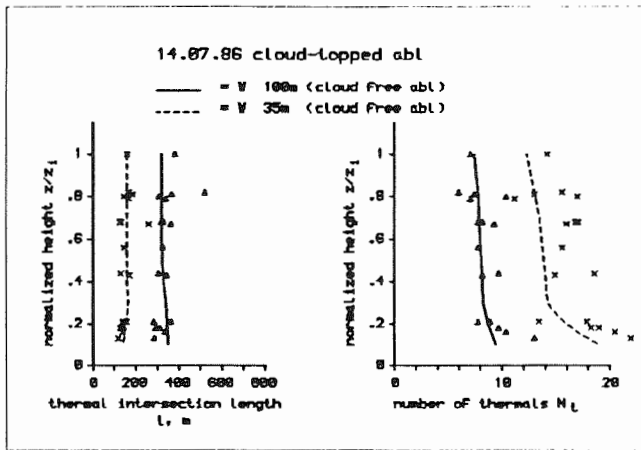


Figure 4. Mean updraft intersection length and average number of updraft intersections per 10km.

Physical properties of convective elements were also derived from the conditional sampling data. The average temperature excess of updrafts compared to their environment is shown in Figure 5. For the cloud-topped boundary layer investigated here there is no region of negative buoyancy below the inversion, whereas in cloudfree cases the level of neutral buoyancy is in the upper third of the cbl. The average vertical wind velocity excess as shown in Figure 6 increases upwards in contrast to the cloudfree case shown as solid line.

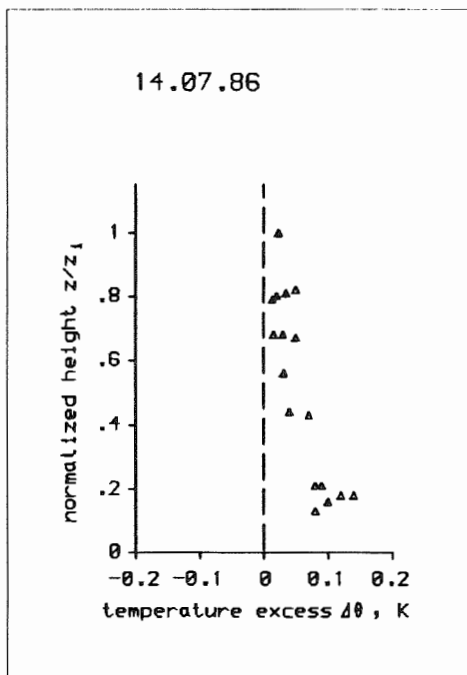


Figure 5. Mean temperature excess of updrafts over environment.

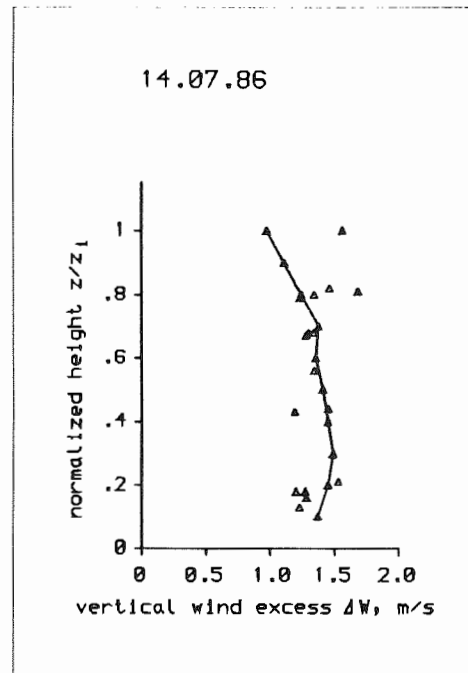


Figure 6. Mean vertical wind velocity excess of updrafts over environment. Solid line shows cloudfree case.

#### REFERENCES

Fimpel, H.P., 1987: The DFVLR meteorological research aircraft Falcon-E: Instrumentation and examples of measured data. *Proc. Sixth Sympos. on Meteorological Observations and Instrumentation, New Orleans, 10-16 Jan 1987, Amer. Meteor. Soc.*, 212-216.

Grossman, R.L., 1984: Bivariate conditional sampling of moisture flux over a tropical ocean. *J. Atmos. Sci.*, **41**, 3238-3253.

Jochum, A.M., 1988: Turbulent transport in the convective boundary layer over complex terrain. *Proc. Eighth Sympos. on Turbulence and Diffusion, San Diego, 25-29 April 1988, Amer. Meteor. Soc.*

Jochum, A.M., M.E. Reinhardt and H. Willeke, 1987: Three DFVLR powered gliders - a meteorological measurement system for the investigation of the atmospheric boundary layer. *Proc. Sixth Sympos. on Meteorological Observations and Instrumentation, New Orleans, 10-16 Jan 1987, Amer. Meteor. Soc.*, 217-220.

Mörl, P., M.E. Reinhardt, W. Renger and R. Schellhase, 1981: The use of the airborne LIDAR System 'ALEX F 1' for aerosol tracing in the lower troposphere. *Beitr. Phys. Atmosph.*, **54**, 403-410.

INSTABILITY THEORY IN CLOUDS AND THE  
PARAMETERIZATION OF EDDY VISCOSITY COEFFICIENTS

Yoshimasa Takaya

Meteorological Research Institute  
Tsukuba, 305 JAPAN

1 INTRODUCTION

We propose a theory which describes the mechanism of the entrainment or mixing between cloudy air and the surrounding clear air which is a generalization of the conditional instability of the first kind. There, the tilted stratification of the thermodynamical and cloud-physical variables in the cloud plays an important role. This theory explains the fractal-like structure of the convective cloud and predicts the horizontal angle of the node or the hollow of the cloud. Further we take the effect of this instability into our numerical simulation of the convective cloud as the eddy terms and obtain the result that the history of the collective motion of the convective clouds sensitively depends on these eddy terms.

2. INSTABILITY THEORY IN CONVECTIVE CLOUDS

In order to exploit the instability theory in convective clouds, we think a system whose physical variables are velocity fields, potential temperature, water-vapour mixing-ratio and cloud-water mixing-ratio whose stratification is tilted nearly along the boundary of the cloud. We divide each variable into three parts; hydrostatic part, spatially meaned dynamical part and turbulent part. We obtain a set of equations for these turbulent variables with linear approximation. If we assume the normal mode solution to these variables

$$\exp(\sigma t - ip \cdot r), \quad (2.1)$$

where  $\sigma$  is interpreted to be a growth-rate of the turbulence if it is real and positive.  $p$  is a wave number vector and  $r$  is a coordinate vector. Eigenvalue equation becomes simply a following quadratic equation in  $\sigma$  if we assume the shape of the meaned cloud is

either cylindrically symmetric or slab-symmetric;

$$\sigma^2 + \tau_{22}\sigma - g(i_2 \cdot k)(i_2 \cdot B) = 0, \quad (2.2)$$

where  $k$  is a unit vector which points to the vertical,  $i_2$  is a unit vector which is defined by

$$i_2 = p \times (k \times p) / (|p| |k \times p|)$$

and which parallels to the turbulent velocity  $v'$ .  $\bar{V}$  is meaned velocity and  $\tau_{22}$  is a component of meaned shear tensor defined along the unit vector  $i_2$

$$\tau_{22} = (i_2 \cdot \nabla)(i_2 \cdot \bar{V}).$$

The vector  $B$  is defined by hydrostatic part and meaned part of thermodynamical and cloud-physical variables and their gradients. The physical meaning of  $B$  is as follows. If a parcel in a cloud experiences a virtual displacement along  $B$ , it acquires the maximum increase of buoyancy. The discrepancy between the direction of  $B$  and vertical comes from the tilted stratification in a cloud. Note that Eq.(2.2) does not depend on the length of the  $p$  but only on the direction of it. By changing the direction of  $i_2$ , the eigenvalue will be changed. Then the direction of  $i_2$  which corresponds to the maximum growth-rate will be realized in nature. By calculating this direction at the peripheral part of the cloud, we can predict the direction of the node or the hollow of the convective cloud. The physical interpretation of this solution is as follows. The direction of buoyancy is vertical and simple parcel method can only say that the parcel must go up or down vertically. If we neglect the effect of the second part of Eq.(2.2), the most unstable mode selects the direction of  $i_2$  just the middle of the

vertical and direction of B. It shows that the real motion of the cloudy air and the result of the parcel method are lead to different movements. The second term of Eq.(2.2) represents the effect of the advection of the meaned velocity by turbulent velocity. Therefore the most unstable mode is determined by a balance of the three effects; the vertically directed buoyancy itself, the maximum increase of buoyancy and the effect of advection of meaned velocity by turbulent velocity. The relative phases between the turbulent variables show that this mode transports heat, water-vapour and cloud water from inside of the cloud to the surrounding clear air and dilutes the cloud. Instead of the observational data, we borrow thermodynamical and cloud-physical data from our numerical simulation. In Fig.1 we predict the distribution of the growth-rate and the direction of the most unstable mode at each grid point of the right half part of the simulated slab-symmetric cloud. These

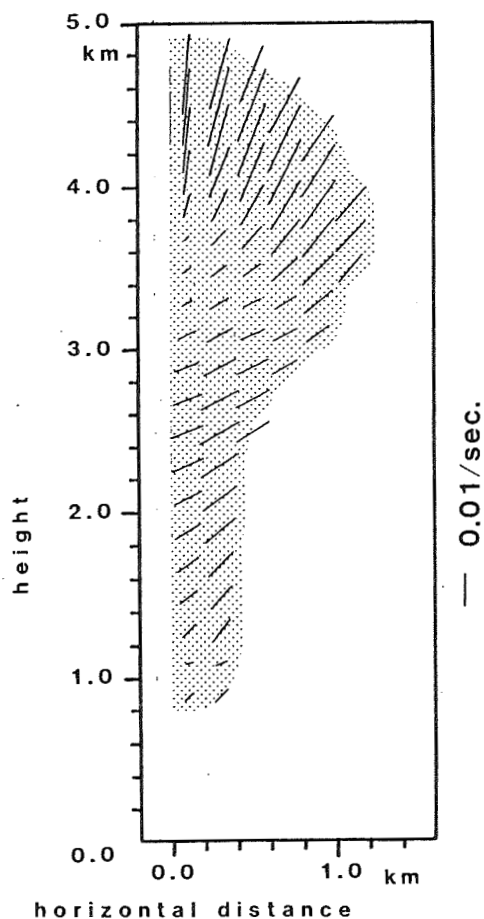


Fig.1 A right half part of the distribution of the most unstable direction of turbulent velocity. The length of the bar shows the magnitude of the growth-rate. Cloud region is indicated by the shaded region.

directions at the outer part of the cloud point to almost the middle of the vertical and the direction perpendicular to the surface of the cloud. The second point of our prediction is that the growth-rate is larger at the outer part of the cloud, especially at the cloud top, and smaller at the inner part. The third point is that our theory explains the fractal-like structure of the convective cloud. It tells that there exists the most unstable direction at each part of the cloud. Therefore a node at a moment, for example, is changed into the shape with nodes and hollows of smaller scale according to the instability at each point of that node and so on.

### 3. OBSERVATIONAL RESULTS

By using the time-lapse video recorder, we analyzed the progressive change of the shape of the convective cloud. In Fig.2, we show a frame of the videograph in which the direction of jetting out of the node is denoted by black arrow. The size of the arrow corresponds to the size of the node. Seeing this we recognize the fractal-like structure of the convective cloud. The direction of each arrow is generally steeper than that of the normal to the surface of the cloud, which agrees to our prediction. The second prediction in the former section is clearly seen in the observation by J. Warner(Ref.1).

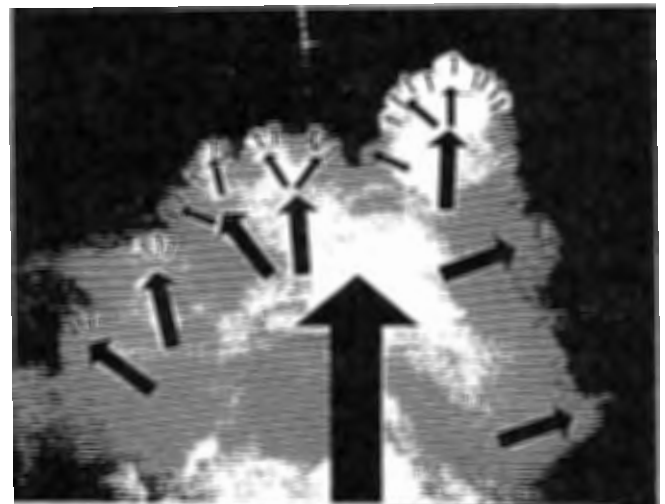


Fig.2 A frame of videograph which was taken on August 14, 1987 at Tsukuba. It shows the fractal-like structure of the convective cloud. Each black arrow shows the direction of the growing node and their size corresponds to the scale of the node.

#### 4. PARAMETERIZATION OF EDDY TERMS IN CLOUDS

In order to parameterize the eddy viscosity terms in convective clouds, we assume that they are represented by the mode of the maximum growth-rate about which we studied in the former section. But our instability theory is linear, so that the absolute value of the amplitudes cannot be determined. In order to complete the parameterization, we must fix the mean-square of the turbulent velocity  $\overline{v'}^2$ . It should be determined by observational study. But at this stage our data is not enough to do it. Therefore we propose a following tentative parameterization to be

$$\overline{v'}^2 = v_0^2(100 \times \sigma)^2.$$

It means that the root-mean-square of the turbulent velocity may be proportional to the growth-rate itself. The value of  $v_0$  is selected appropriately through the results of our numerical simulations which include this parameterization. In making our numerical model, we have no principles to fix the eddy terms at the outside of the cloud. Therefore we assume to add eddy viscosity terms with constant viscosity coefficients  $\mu$  at each grid point. The results of the numerical simulation sensitively depend on the parameter  $\mu$  and  $v_0$ . When we compare two cases in which  $\mu$  is taken to be 25 m<sup>2</sup>/sec. or 200 m<sup>2</sup>/sec with other conditions being the same, the cloud easily rise in the former case. The reason is that in the former case the updraft and downdraft occur without difficulty because of the low viscosity at the outside of the clouds. Further we compare the two cases in which the parameter  $v_0$  is 1 m/sec or 0 with other conditions to be the same. In the former case, the dilution of cloud occurs strongly at the outer part of the cloud in its growing stage. Therefore the conversion of the cloud-water to rain water is interrupted and the decrease of the total water-vapour in the domain is slower. In a simulation in which supply of the sensible heat is continued, the increase of the kinetic energy connected with the more of the water-vapour remained in the domain finally causes a formation of strong convective clouds.

#### 5. CONCLUSIONS

The instability theory in convective cloud is proposed which is obtained by the combination of the observational study, theoretical study and numerical study. This theory predicts the fractal-like structure and the horizontal angle of the node or the hollow of the convective cloud. It also predicts that the entrainment or the mixing occurs most strongly at the cloud top and that the turbulence is rather weak at the inner part and stronger at the outer part of the convective cloud. These results agree qualitatively with the observations. Further this theory is applied to parameterize the eddy viscosity terms in numerical simulations of the convective clouds. There strong dilution of cloud occurs at the outer part of the cloud, especially at the cloud top. Then water-vapour is radiated around the cloud and the conversion of the cloud-water to rain-water is suppressed. Therefore the decrease of the water-vapour remained in the domain is delayed compared with the simulation in which the eddy terms are not included ( $v_0=0$ ). If the supply of the water-vapour and sensible heat are continued, it is possible to rise finally a strong convective cloud. It shows that when we study the collective motion of the convective clouds, the eddy terms play a very important role.

#### REFERENCES

1. Warner, J.,1970: The microstructure of cumulus cloud. Part . The nature of the Updraft. J.Atmos. Sci.,27,682-688. (Fig.2)

Fig. 2 shows the total reset  $n_d$  as a function of the measured activity  $A_m$  compared to the predicted values given by Eq. 3 and 4, for different values of  $\tau$ . The observed values are in agreement with the theory for transit times  $\tau$  fluctuating from  $2\mu\text{s}$  to  $3.5\mu\text{s}$ .

The values of the actual droplet rate  $n$  and of the corresponding transit time  $\tau$  are iteratively estimated by adjusting the measured parameters  $n_d$  and  $A_m$  to the predicted ones. To select the homogeneous samples, where the mean density is constant, an homogeneity factor,  $H_m$ , has been deduced from the 5 sub-countings of the droplet spectra,  $n_{mi}$ . The associated droplet rate (after D.O.F. and velocity rejection) is roughly proportional to  $n_d$  except for fluctuations of the rejection criteria which are studied in Brenguier (1988). The homogeneity is expressed as:

$$H_m = \frac{n_m}{5 \max(n_{mi})} \quad \text{where} \quad n_m = \sum_{i=1}^5 n_{mi}. \quad (5)$$

The estimated values of  $\tau$  are inversely proportional to the aircraft velocity,  $v_a$ , in the range  $58 \text{ m s}^{-1}$  to  $80 \text{ m s}^{-1}$ , with a slope  $\pi d/4$  equal to  $150 \mu\text{m}$ , i.e.  $d = 190 \mu\text{m}$ . This is in agreement with the values measured on our FSSP, which are slowly increasing from  $160 \mu\text{m}$  in the middle of the DOF to  $220 \mu\text{m}$  at the limits of the sensible area. The difference between  $\pi d/4 v_a$  and the estimated value of  $\tau$  is due to a lengthening of the transit-time in the amplifiers and depends on the droplet diameter. Laboratory tests of the probe give an estimate of this lengthening and the transit-time can, then, be calculated by:

$$\tau = \pi d/4 v_a + (0.03 \bar{\phi} + 0.035) 10^{-6} \quad (6)$$

where  $\bar{\phi}$  is the mean diameter of the droplet spectrum.

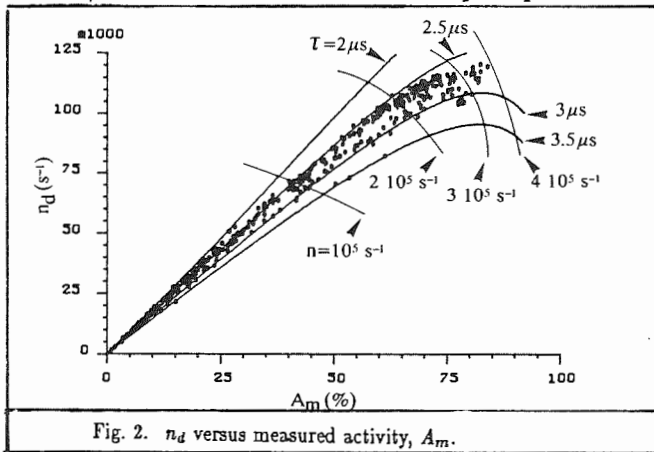


Fig. 2.  $n_d$  versus measured activity,  $A_m$ .

#### 4. CORRECTION PROCEDURE

In 1981, Baumgardner proposed an empirical formula to estimate the actual droplet rate:

$$n = \frac{n_d}{1 - m A} \quad (7)$$

where  $m$  ranges between 0.5 and 0.8.

Eq. 3 and 4 give the limit of  $m$  at low droplet rates:

$$\lim_{n \rightarrow 0} m = \frac{(1 - D)\tau + D\tau_{d2}}{\tau + \tau_d}, \quad \text{where} \quad \tau_d = (1 - D)\tau_{d1} + D\tau_{d2} \quad (8)$$

The correction factor  $m$  is estimated from the data points corresponding to the homogeneous samples:

$$m = 1/A_m(1 - n_d/n) \quad (9)$$

It is compared to the predicted values on Fig. 3. The lower  $m$  value in our FSSP is between 0.62 and 0.63, but it increases rapidly from 0.7 at  $A_m \approx 0.50$  to 0.8 at  $A_m \approx 0.80$ .

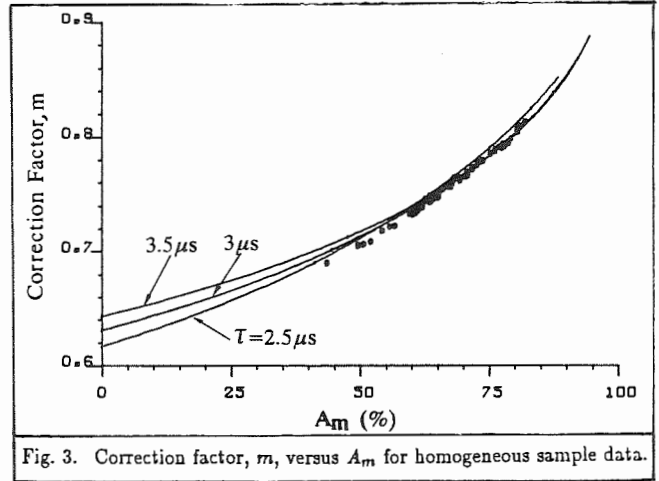


Fig. 3. Correction factor,  $m$ , versus  $A_m$  for homogeneous sample data.

The proposed correction scheme is based on the comparison of the measured and predicted values of the mean transit duration of the coincident droplet series:

$$\bar{T} = A_m/n_d - \tau_d \quad (10)$$

In an heterogeneous sample, this mean duration is the weighted average of the local values while  $n_d$  and  $A$  are the sum of the sub-values. This parameter is displayed on Fig. 4 as a function of the measured activity. Homogeneous sample values lie along the predicted curve while heterogeneous samples have values higher than the predicted one. This result is reasonable because the Poisson distribution is the random distribution which minimizes the probability of coincidence. The actual droplet rate is then estimated by calculating the individual droplet transit-time  $\tau$  from the aircraft velocity and the measured mean droplet diameter (Eq. 6) and by iteratively comparing the measured values of  $\bar{T}$  to the values deduced from Eq. 3 and 4, where  $D$  is the measured value of the DOF ratio.

At low activity, inaccurate estimations of  $\bar{T}$  are lower than the minimum predicted value and  $n$  is estimated by comparing the measured to the predicted activity.

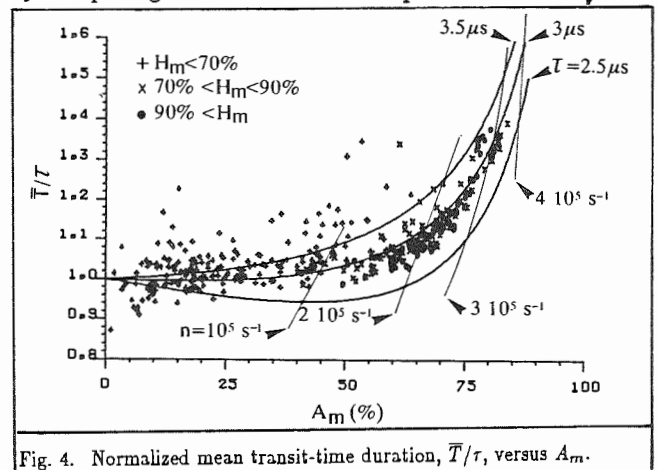


Fig. 4. Normalized mean transit-time duration,  $\bar{T}/\tau$ , versus  $A_m$ .

Fig. 5 shows the measured droplet rate (a) as a function of the static pressure compared to the droplet rate corrected with Eq. 9 (b) and with the results of the proposed correction scheme (c). The measured droplet rate is limited to  $120\,000\text{ s}^{-1}$ ; values up to  $250\,000\text{ s}^{-1}$  are obtained from Eq. 9, while values as high as  $4 \cdot 10^5\text{ s}^{-1}$  are estimated with the proposed scheme. The total sensible length of the laser beam measured in the laboratory is approximately  $14\text{ mm}$ . With a beam diameter  $\approx 190\ \mu\text{m}$ , the sampled volume at an aircraft velocity of  $75\text{ m s}^{-1}$ , is then  $200\text{ cm}^{-3}$ . With estimated droplet rates between  $3 \cdot 10^5\text{ s}^{-1}$  and  $4 \cdot 10^5\text{ s}^{-1}$  the droplet concentration ranges between  $1500\text{ cm}^{-3}$  and  $2000\text{ cm}^{-3}$ . These concentrations, covering a range of droplet diameters between  $2\ \mu\text{m}$  and  $20\ \mu\text{m}$ , are very high compared to the currently measured values. Relations (1) and (2) have been tested in our laboratory with a random pulse generator (Brenquier, 1988) and confirm the measured values of the characteristic times of our FSSP:  $\tau$ ,  $\tau_{d1}$  and  $\tau_{d2}$ . This agreement is reflected on Fig. 4, where data points follow the predicted behavior. For these reasons, we are confident on the high concentration estimations. However, by this procedure, we estimate the probability of coincidence and the related concentration for droplets randomly dispersed according to a Poisson distribution. The high values can be interpreted as cloud regions where the droplets are not randomly distributed but organized in clusters, where the local probability of coincidence is much higher.

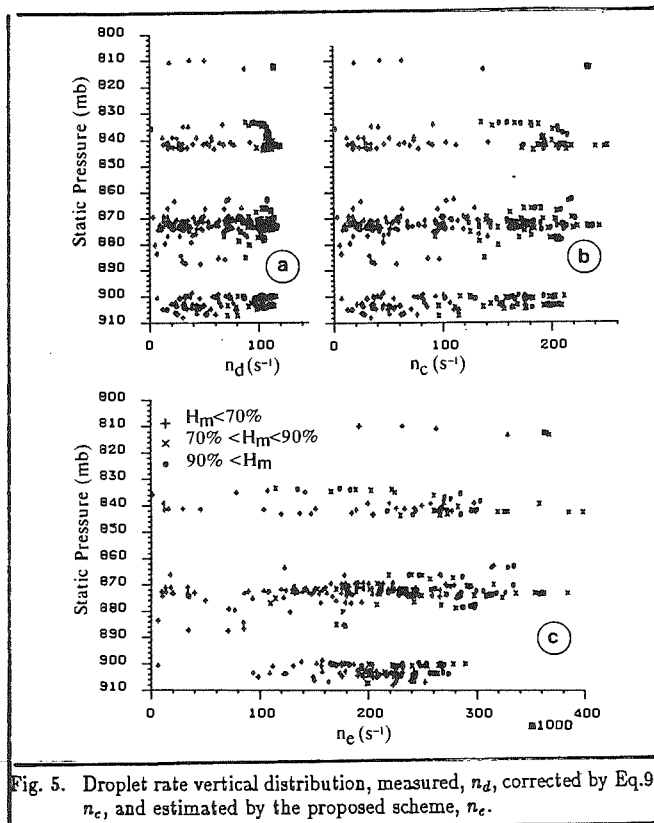


Fig. 5. Droplet rate vertical distribution, measured,  $n_d$ , corrected by Eq.9,  $n_c$ , and estimated by the proposed scheme,  $n_e$ .

## 5. HETEROGENEOUS SAMPLES

By using the mean transit duration to estimate the actual droplet rate, we have supposed that the heterogeneous samples are partly made of cloudy homogeneous regions, the rest being clear of droplet. The ratio of the

measured activity to the predicted one is then equivalent to the evaluation of the homogeneity obtained with the 5 Hz sub-countings (Eq. 5), except that it applies at any scale. These parameters are compared on Fig. 6 which shows a good correlation between them. Estimated values equal to 1 correspond to values of  $\bar{T}$  lower than the minimum predicted one ( activity  $< 0.25$  ). Both these parameters being completely independent, this result corroborates the proposed correction scheme.

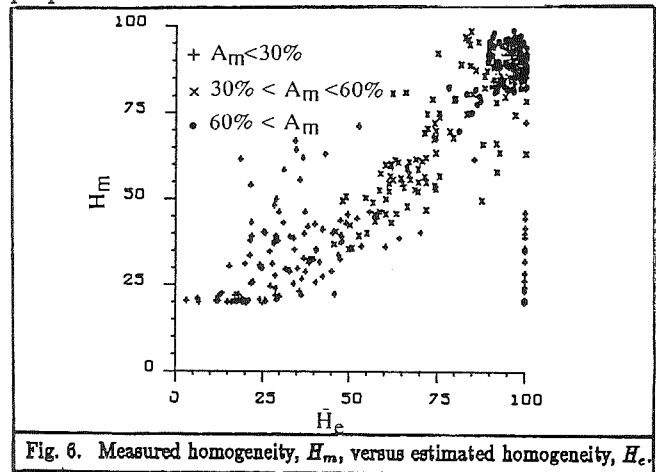


Fig. 6. Measured homogeneity,  $H_m$ , versus estimated homogeneity,  $H_e$ .

## 6. CONCLUSION

A new method has been proposed to correct the coincidence and dead-time losses in the FSSP. By adjusting the measured data to the predicted values of two independent parameters ( $n_d$  and  $A$ ), it is possible to estimate high droplet rates for which the correction factor is important ( $n_d/n \approx 3$ ).

The estimated values of the concentration are very high ( $\approx 2000\text{ cm}^{-3}$ ) compared to the values measured in the past. The method is also powerful to estimate the homogeneity of the samples. Thus it appears that 1 second samples, with a low concentration (low values of  $n_d$  and  $A$ ) are in fact very heterogeneous ( high value of the mean transit duration ). These regions are better described as a succession of cloudy patches inserted in clear air. This observation is confirmed by the fluctuations of the droplet counts measured at an higher rate ( 5 Hz ).

The method is based on the evaluation of the probability of coincidence referred to as a Poisson distribution. The very high values of the concentration shows that droplets are probably distributed in space less uniformly than provided by this ideal distribution.

## REFERENCES

- Baumgardner, D.,W. Strapp and J. Dye, 1985: Evaluation of the Forward Scattering Spectrometer Probe. Part II: Corrections for coincidence and dead-time losses. *J. Atmos. Oceanic. Technol.*, **2**, 626-632.
- Brenquier, J.L. and L. Amodei, 1988: Coincidence and dead-time corrections for the particle counters. Submitted to *J. Atmos. Oceanic. Technol.*.
- Brenquier, J.L.,1988: High concentration measurements with an FSSP. Submitted to *J. Atmos. Oceanic. Technol.*.
- Chalon, J.P., 1987: Landes-Fronts 84, une expérience d'étude des bandes convectives associées aux systèmes frontaux. *La Météorologie VII*, 7-23.
- Cerni, T.A., 1983: Determination of the size and concentration of cloud drops with an FSSP. *J. Climate Appl. Meteor.*, **22**, 1346-1355.
- Dye, J.E. and D. Baumgardner, 1984: Evaluation of the Forward Scattering Spectrometer Probe. Part I: Electronic and optical studies. *J. Atmos. Oceanic. Technol.*, **1**, 329-344.

Frank B. Lipps and Richard S. Hemler

Geophysical Fluid Dynamics Laboratory/NOAA  
Princeton, New Jersey, USA

### 1. INTRODUCTION

Recent calculations have been carried out simulating both mid-latitude and tropical convection using a three-dimensional numerical cloud model with a Kessler-type warm rain bulk cloud physics. Inside of clouds, where condensation is taking place, conservation of equivalent potential temperature  $\theta_e$  is assumed for the subgrid-scale turbulence parameterization. In clear air, conservation of virtual potential temperature  $\theta_v$  is assumed. Due to these different forms of turbulent mixing in clear and cloudy air, subgrid-scale condensation SGC occurs just below cloud base with resultant latent heat release. For both shallow and deep convection, this low level heating produces a more uniform vertical velocity maximum with time and maintains the cloud over a longer lifetime. For shallow convection, the rain reaching the ground is increased significantly.

### 2. THE SUBGRID-SCALE CONDENSATION

The formulation of the numerical model is similar to that given in Lipps and Hemler (1982, 1986a). In this section we describe the subgrid-scale turbulence parameterization which includes the subgrid-scale condensation SGC. The SGC was not present in earlier models due to an inconsistent treatment of the turbulent mixing of cloud water  $q_c$ . In the current model, prognostic equations are solved for the water vapor mixing ratio  $q_v$  and for the total  $q$  which is the sum of water vapor  $q_v$  and cloud water  $q_c$ . As in the earlier models, prognostic equations are solved for the rain water  $q_r$  and the potential temperature  $\theta$ .

The role of the SGC can be seen by examining the vertical subgrid-scale fluxes  $\rho_0 \overline{w'q'}$  for the total  $q$  and  $\rho_0 \overline{w'q'_v}$  for the water vapor  $q_v$ . Following Lipps (1977), these fluxes are obtained from the subgrid-scale turbulence equations:

$$0 = -\frac{2}{3} E \frac{\partial q}{\partial z} - \frac{c_s}{\Delta} E^{1/2} \overline{w'q'} \quad (1)$$

$$0 = -\frac{2}{3} E \frac{\partial q_v}{\partial z} - \overline{w'C'_d} - \frac{c_s}{\Delta} E^{1/2} \overline{w'q'_v} \quad (2)$$

where  $c_s$  is a constant,  $\Delta = (\Delta x \cdot \Delta y \cdot \Delta z)^{1/3}$ ,  $E$  is the subgrid-scale kinetic energy and  $\overline{w'C'_d}$  is a subgrid-scale correlation associated with the condensation  $C_d$ . Compared with the treatment in Lipps (1977), gravitational buoyancy terms have been neglected in (1) and (2). The eddy diffusivity  $K_h$  is defined by

$$K_h = \frac{2}{3} \frac{\Delta}{c_s} E^{1/2} \quad (3)$$

so that we may write

$$-\rho_0 \overline{w'q'} = \rho_0 K_h \frac{\partial q}{\partial z} \quad (4)$$

$$-\rho_0 \overline{w'q'_v} = \rho_0 K_h \left( \frac{\partial q_v}{\partial z} + \left(\frac{2}{3} E\right)^{-1} \overline{w'C'_d} \right) \quad (5)$$

where  $\rho_0$  is the base state density.

The equation for  $\overline{w'C'_d}$  is obtained as in Lipps (1977):

$$\overline{w'C'_d} = \frac{2}{3} E \frac{f}{(1+\beta\gamma)} \left( \beta \frac{\partial \theta}{\partial z} - \frac{\partial q_{vs}}{\partial z} \right) \quad (6)$$

where  $q_{vs}$  is the saturation water vapor mixing ratio and  $f$  is a parameter to indicate whether the particular grid point is in cloudy or clear air. Inside of clouds  $f=1$ , in clear air  $f=0$ , and near a cloud edge  $f$  is a fraction as described below. The parameters  $\beta$  and  $\gamma$  are specified as in Appendix A of Lipps and Hemler (1982):

$$\beta = \frac{L q_{vs} (1 + 1.608 q_{vs})}{R_v T_0 \theta_0}, \quad \gamma = \frac{L}{c_p \pi_0} \quad (7)$$

Here  $L$  is the latent heat of vaporization,  $c_p$  is the specific heat of dry air,  $R_v$  is the gas constant for water vapor, and  $T_0$ ,  $\theta_0$  and  $\pi_0$  are the base state temperature, potential temperature and Exner pressure function.

The numerical grid is staggered in the vertical as shown in Fig. 1. Here we assume the cloud base is between the two grid points where  $\theta$ ,  $q_v$ ,  $q$  and  $q_c$  are evaluated. The vertical velocity  $w$  and the correlation  $w'C_d^1$  are evaluated at intermediate grid points. Note that in the cloud  $q_v=q_{vs}$  and outside the cloud  $q_{vs}-q_v > 0$  and  $q_c=0$ . The value of  $f$  near cloud base is given by

$$f = \frac{q_c}{(q_{vs} - q_v) + q_c} \quad (8)$$

where  $q_c$  is evaluated at the upper grid point inside the cloud and  $(q_{vs}-q_v)$  is given for the lower grid point below cloud base.

For the point below cloud base shown in Fig. 1,  $q=q_v$  since  $q_c=0$  there. The prognostic equations for  $q$  and  $q_v$  are different at this point, however, primarily because the forms of  $-\rho_0 w'q'$  and  $-\rho_0 w'q_v'$  are different as indicated by equations (4) and (5). In order to allow  $q=q_v$  at this point, we must add the subgrid-scale condensation SGC term in the  $q_v$ -prognostic equation. The requirement  $q=q_v$  gives for SGC:

$$\rho_0 SGC = \frac{\rho_0 w q_c}{\Delta z} - \frac{\rho_0 K_h q_c}{(\Delta z)^2} + \frac{\rho_0 K_h}{(\Delta z)} \cdot \left(\frac{2}{3} E\right)^{-1} \overline{w'C_d^1} \quad (9)$$

where  $\Delta z$  is the vertical grid interval. The first two terms on the right are small numerical truncation effects. The primary

### STAGGERED GRID

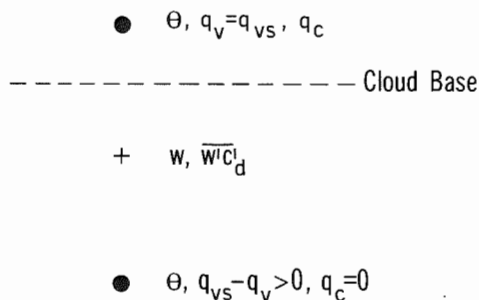


Fig. 1 The staggered grid in the vertical. Variables  $\theta$ ,  $q$ ,  $q_v$  and  $q_c$  are evaluated at the dark points and  $w$  and  $w'C_d^1$  are evaluated at the cross point. Dashed line is cloud base. See text.

contribution to  $\overline{SGC}$  is through the third term which involves  $w'C_d^1$ . Using (6) for  $w'C_d^1$  we find approximately:

$$\rho_0 SGC \approx \frac{\rho_0 K_h}{(\Delta z)} \frac{f}{(1+\beta\gamma)} \left( \beta \frac{\partial \theta}{\partial z} - \frac{\partial q_{vs}}{\partial z} \right) \quad (10)$$

where  $f$  is evaluated from (8).

Thus  $\overline{w'C_d^1}$  plays a key role in the turbulence parameterization of moist convection. Inside of cloud, where equivalent potential temperature  $\theta_e$  is conserved, the vertical fluxes  $\rho_0 w'\theta'$  and  $\rho_0 w'q_v'$  are specified by (A14) and (A15) of Lipps and Hemler (1982). Both of these vertical fluxes involve  $w'C_d^1$  as given by equation (6) above. In clear air, where  $w'C_d^1 = 0$ , both fluxes are downgradient in  $\theta$  and  $q_v$  respectively.

### 3. MODEL CALCULATIONS

Three-dimensional numerical calculations have been carried out to simulate the deep moist convection observed in the central United States on 22 May 1976 (Ogura and Liou, 1980).

Four-hour simulations were performed for a model domain of 96 km in the east-west direction, 32 km in the north-south direction, and a vertical depth of 17 km. The horizontal and vertical grid lengths were 1 km and 0.5 km respectively. Open lateral boundary conditions were applied on the east and west boundaries and periodicity was assumed for the north and south boundaries. The convection was initiated with a warm bubble which resulted in a strong initial cell and secondary gust front outflows. These gust fronts initiated more realistic convection which had a squall line configuration in the north-south direction after 2.5 hours into the simulation.

In Fig. 2 is shown the maximum vertical velocity  $W$  with time for the calculation with the subgrid-scale condensation SGC (solid curve) and for the calculation without SGC (dashed curve). With SGC, it is seen that the vertical velocity of the first cell is maintained with time, and furthermore, a second major cell develops at 90 min which is stronger than any comparable cell in the calculation without SGC. After two hours, the two calculations are much more similar in appearance; however, the maximum vertical velocity remains somewhat larger for the simulation with SGC included.

In Fig. 3 is plotted the volume-mean, density-weighted condensation rates for the two calculations for the first hour of the simulation. The solid curve, for the calculation with SGC, indicates that the condensation did not decrease nearly as rapidly with time after the first cell developed. This result is consistent with

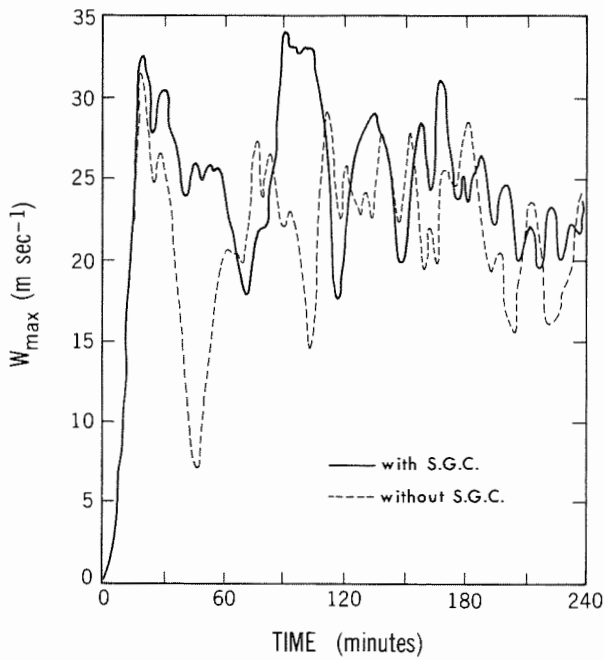


Fig. 2 Variation of maximum vertical velocity  $W$  with time for deep continental convection. Solid curve has SGC included. Dashed curve does not have SGC.

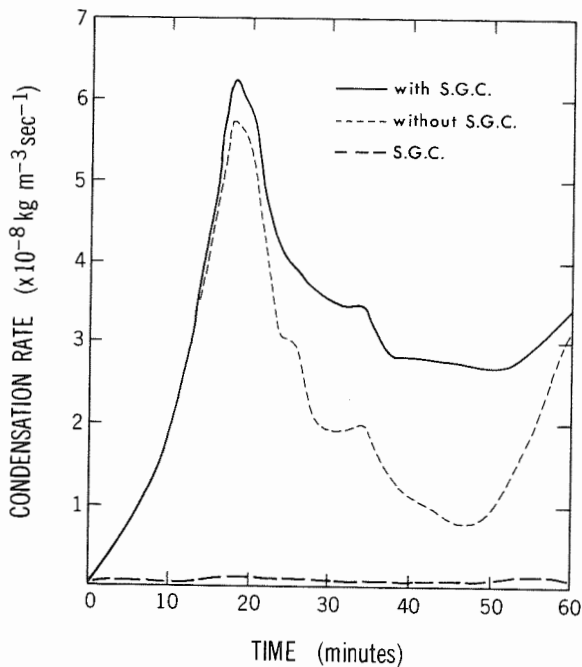


Fig. 3 Volume-mean, density-weighted condensation rate with time for deep continental convection. Solid curve has SGC included. Dashed curve does not have SGC. Long-dashed curve is that volume-mean  $\rho_0$  SGC.

the maintenance of strong vertical velocity for the first cell as seen in Fig. 2. The long-dashed curve in Fig. 3 is for the volume-mean  $\rho_0$  SGC. Although the SGC is at least an order of magnitude smaller than the total condensation, it is seen that its inclusion in the model has an important effect on the dynamics of the convection.

The SGC has been included in the shallow GATE simulations described by Lipps and Hemler (1986b). The increased values of maximum vertical velocity and of volume-mean condensation noted above were also found for the shallow GATE convection. In general, it appears that shallow convection is more sensitive to the inclusion of SGC. The rainfall reaching the ocean surface was slightly more than a factor of three larger for the simulation with SGC included. These values of precipitation are much closer to the observed rainfall rates.

#### REFERENCES

- Lipps, F.B., 1977: A study of turbulence parameterization in a cloud model. *J. Atmos. Sci.*, **34**, 1751-1772.
- Lipps, F.B., and R.S. Hemler, 1982: A scale analysis of deep moist convection and some related numerical calculations. *J. Atmos. Sci.*, **39**, 2192-2210.
- \_\_\_\_\_, and \_\_\_\_\_, 1986a: Numerical simulation of deep tropical convection associated with large-scale convergence. *J. Atmos. Sci.*, **43**, 1796-1816.
- \_\_\_\_\_, and \_\_\_\_\_, 1986b: Numerical modelling of a line of towering cumulus on Day 226 of GATE. WMO Weather Modification Research Programme. Report of the International Cloud modelling Workshop/Conference, WMO/TD-No. 139, pp. 187-191.
- Ogura, Y., and M.-T. Liou, 1980: The structure of a midlatitude squall line: A case study. *J. Atmos. Sci.*, **37**, 553-567.

THE EFFECT OF TURBULENCE ON THE COLLECTION OF CLOUD DROPS:  
A STOCHASTIC MODEL

Gerhard Reuter

McGill University, Montreal

1. INTRODUCTION

Turbulent motions in convective clouds affect the collision-coalescence of water droplets via two different mechanisms. The first mechanism results from the fact that drops of different sizes respond with different inertia to a fluctuating turbulent velocity field. DE ALMEIDA (1979) modelled the effect of turbulent drag on the collection process. He found that the contribution of turbulent drag collection is dramatic for drops of sizes 10-30  $\mu\text{m}$ .

A second mechanism affecting the coalescence of drops in turbulent air is active for drops having the same or different sizes. This mechanism is related to the eddy structure of a turbulent velocity field. At a given time, cloud drops can be contained in two spatially separated eddies. At a later stage, it might happen that these two eddies overlap and this might result in collision and merging of some of the drops in these eddies. This mechanism has been modelled by REUTER et al. (1988). The turbulent collection kernel can be computed with this stochastic model which is based on stochastic differential equations.

In this paper we will show the results of the growth of a cloud droplet population affected by gravitational collection and coalescence caused by overlapping eddies in turbulent air. The collection equation is solved by a very economical numerical scheme (EYRE et al., 1988) and the collection kernel is approximated with the stochastic model of REUTER et al. (1988).

2. MODEL DESCRIPTION

The classical kinetic (coagulation) equation is used to model the collision-coalescence among a population of cloud droplets. The dynamics of the collection process is contained in the collection kernel the form of which will be discussed later. The kinetic equation is solved using the numerical scheme of EYRE et al. (1988). This scheme is very economical as it makes use of adaptive mesh grading. The mass spectrum of droplets (ranging several orders of magnitude) is mapped to the interval  $(-1,1)$ . The solution function is then approximated using a linear combination of cubic splines. The positions of the nodal points are allowed to move and are chosen optimally at regular time intervals. The optimization is performed by distributing the nodal points equally with respect to the arc lengths of the approximate solution function. Collocation reduces the problem to one of solving a system of ODE's for the expansion coefficients.

The collection kernel is computed using the stochastic model of REUTER et al. (1988). In addition to gravitational collection, the kernel is also affected by the probability of coalescence due to overlapping of turbulent eddies. The model is based on stochastic differential equations that govern the relative motion of two drops. The turbulence causes a random fluctuation to the relative droplet velocities. The magnitude of these random perturbations is related to the turbulent eddy diffusion coefficient. A detailed description of the model assumptions, the finite difference scheme and sample results are presented

in REUTER et al. (1988).

To solve the collection problem efficiently, we prefer to have an analytic formula for the collection kernel  $K(r, R, \epsilon)$  for a given pair of drops with radii  $r$  and  $R$  in a turbulent air characterized by an energy dissipation rate  $\epsilon$ . The following formula approximates the values of  $K$  computed with the stochastic model.

$$K(r, R, \epsilon) = \pi(r+R)^2 E(r, R) \cdot \left\{ \left| u(r) - u(R) \right| + 3,25 \epsilon^{1/3} (r+R)^{1/3} \right\}$$

Here  $u(r)$  is the terminal fall speed of a drop with radius  $r$  and  $E(r, R)$  is the collection efficiency. The coalescence efficiencies are assumed to be unity. The collision efficiencies are specified with the formula of SCOTT and CHEN (1976) which provides a close fit for the Shafrir-Neiburger and Davis-Sartor collision efficiencies.

### 3. RESULTS

Numerical experiments are made with an exponential initial volume distribution. The liquid water content is  $1 \text{ gm}^{-3}$  and the mean initial radius is  $25 \text{ }\mu\text{m}$ . Figure 1 shows the evolution of the droplet population in turbulent air with  $\epsilon = 1000 \text{ cm}^2 \text{ s}^{-3}$ . The results are given in terms of the droplet mass distribution  $\tilde{N}(r)$  which is defined such that  $\tilde{N}(r)dr$  equals the mass of droplets per unit volume of air with radii in the interval  $dr$ . (The mass distribution emphasizes the larger droplets more so than the usual size spectrum.) The curves show that the development of the coalescence is rather slow even for strong turbulence. If the turbulence is weaker, the growth is slower (Figure 2). Yet the results certainly show that overlapping of turbulent eddies contributes to the collection process.

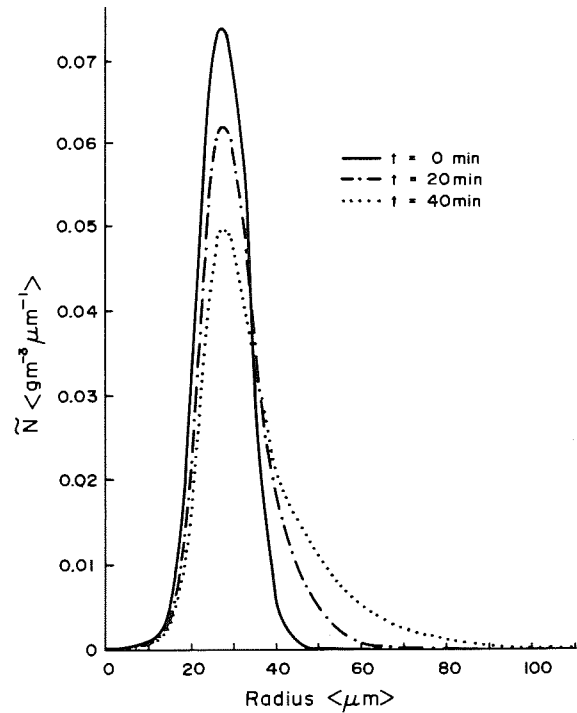


FIG. 1. Evolution of droplet mass distribution in turbulent air ( $\epsilon = 1000 \text{ cm}^2 \text{ s}^{-3}$ ).

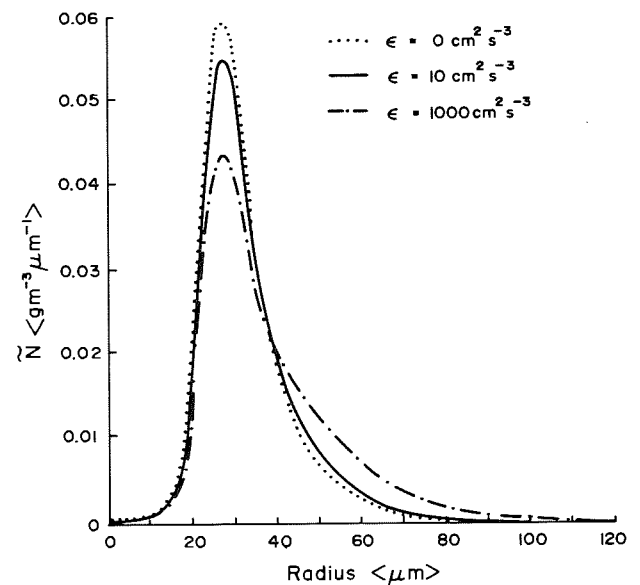


FIG. 2. Comparison of droplet mass distribution at 40 min for different values of turbulent energy dissipation rate  $\epsilon$ .

#### 4. REFERENCES

DE ALMEIDA, F.C.: The effects of small-scale turbulent motions on the growth of a cloud droplet spectrum. *J. Atmos. Sci.* 36 (1979), p. 1557-1563.

EYRE, D.; WRIGHT, C.J.; REUTER, G.W.: Spline-collocation with adaptive mesh grading for solving the stochastic collection equation. *J. Comput. Physics* (1988), in press.

REUTER, G.W.; DE VILLIERS, R.; YAVIN, Y.: The collection kernel for two falling cloud drops subjected to random perturbations in a turbulent air flow: A stochastic model. *J. Atmos. Sci.* (1988), in press.

SCOTT, W.T.; CHEN, C.-Y.: Approximate formulas fitted to the Davis-Sartor-Schafirir-Neiburger droplet collision efficiency calculations. *J. Atmos. Sci.* 27 (1970), p. 698-700.

# THE EFFECT OF ICE PHYSICAL PROCESSES ON THE NUMERICAL SIMULATION OF WEST AFRICAN SQUALL LINES.

William D. Hall

National Center for Atmospheric Research<sup>1</sup>  
Boulder, Colorado, U.S.A.

Jean Philippe Lafore

Etablissement d'Etudes et de Recherches Meteorologiques  
CNRM/Toulouse, France

Tropical squall lines are a subject of great research interest since they provide a significant amount of precipitation to many areas in the tropics. An important question that is often asked is "What is the role of ice microphysical processes on tropical squall line mesoscale structures and precipitation characteristics?" The present study is inspired by the works of Dudhia, Moncrieff and So (1987), DMS, and Lafore and Moncrieff (1988), LM. These authors successfully quantified the observed dynamical structure of a fast moving (15 m/sec) tropical squall line using a two-dimensional model applied to a West African environment.

The present paper describes two-dimensional nested grid numerical experiments of Clark's 3-D cloud model. Calculations were performed to study the thermodynamic and dynamic response of tropical squall lines by ice phase microphysical processes. These simulations incorporate temperature and velocity profiles observed in the COPT 1981 field experiment. The numerical framework consists of three nested models with increasing resolution moving at a constant speed to insure that the squall line remains in the center of the highest resolution domain. Results of two numerical experiments with and without ice are presented. In the ice case the Koenig and Murray (1976) ice parameterization with a high seeding nucleation rate is applied; in the no ice or warm rain case the parameterization of Kessler described by Clark (1979). In both experiments the model is initialized as in DMS and LM with a cooling rate of  $-0.01^{\circ}\text{C}/\text{sec}$  maintained for ten minutes over a 12 km region above the ground with a depth of 3 km. The observed June 22, 1981 presquall sounding is used.

Figures 1 through 4 show the cloud water, rain water, buoyancy, and horizontal velocity perturbation fields for the warm rain case after 200 minutes of

integration. Figures 5 through 10 show the cloud water, rain water, cloud ice, graupel, buoyancy, and horizontal velocity perturbation for the ice case at the same time. In both cases the propagation speed of the squall lines are similar (15 m/sec) and the convective region of the squall lines are characterized by a quasi-periodic sequence of convective cells moving at about one half the speed of the gust front. These convective cells first form on or near the gust front, move into the trailing region, and eventually dissipate. There are, however, marked differences between these two experiments. In the warm rain case, the density current is much stronger and concentrated near the ground. This resulted in larger vertical velocities near the gust front at this time. These differences were caused by the greater amount of rain in the warm rain case reaching ground and consequently more evaporative cooling resulted. The larger rain amount is a direct result of the Kessler parameterization. In both cases the autoconversion of cloud water to rain water occurred when the cloud water exceeded 1 gram per cubic meter. When competing ice processes were present, less cloud water was available for autoconversion to occur. The second striking difference is the character of the rear inflow jet 75 to 120 km. behind the squall line. LM presented an hydrostatic argument which explained that the rear inflow jet is caused by horizontal gradients of buoyancy behind the squall line. In the ice case the combined differences of latent heat release into the upper levels, melting below 4.5 km., and precipitation loading resulted in a different the buoyancy field. This caused in the rear inflow jet position for the ice case to be at a higher level than in the warm rain case.

In these preliminary results it has been shown that the inclusion of simple ice phase microphysics can significantly alter the simulated results of a fast moving tropical squall line. Many other features such

<sup>1</sup>The National Center for Atmospheric Research is sponsored by the National Science Foundation

as the mesoscale accent within the stratiform anvil region, maintenance of the density current, and the resulting precipitation distribution of the simulated squall lines are currently being studied. Simulation results will be compared with the COPT field studies of Chong et. al. (1987).

**REFERENCES:**

CHONG, M., AMAYENC, P., SCIALOM, G., TESTUD, J.: A tropical squall line observed during the COPT 81 experiment in West Africa. Part 1: Kinematic structure inferred from dual-doppler radar data. *Mon. Wea. Rev.* **115** (1987) 670-694.

CLARK, T. L.: Numerical simulations with a three-dimensional cloud model: lateral boundary condition experiments and multicellular severe storm simulations. *J. Atmos. Sci.* **36** (1977) 2191-2215.

DUDHIA, J., Moncrieff, M. W., and So, D. W. K.: The two-dimensional dynamics of West African squall lines. *Quart. J. Roy. Meteor. Soc.*, **113** (1987) 121-146.

KOENIG, L. R. and MURRAY, F. W.: Ice-Bering cumulus cloud evolution: numerical simulation and general comparison against observations, *J. Appl. Meteor.*, **15** (1976) 747-762.

LAFORE, J. P. and MONCRIEFF, M. W.: A numerical investigation of the scale-interaction between a tropical squall line and its environment., submitted to *J. Atmos. Sci.* (1988)

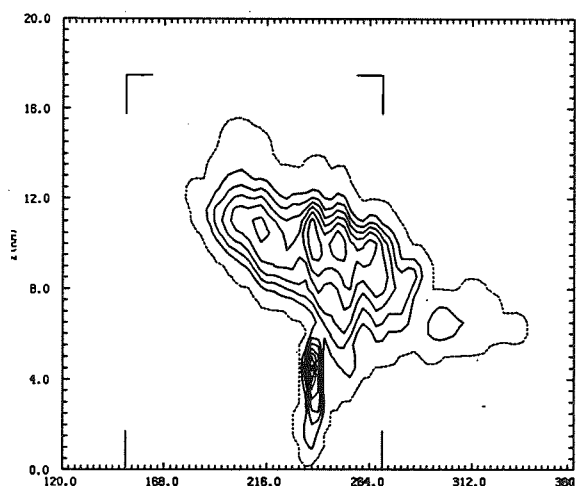


Figure 1. Cloud water field  
Contour interval .5 g/kg

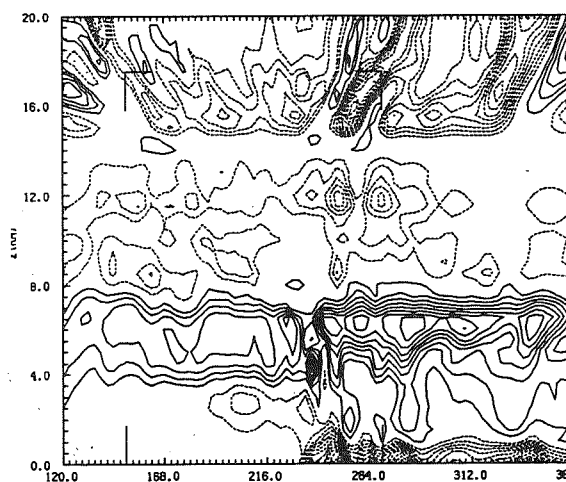


Figure 3. Bouyancy field  
Contour interval .5°C

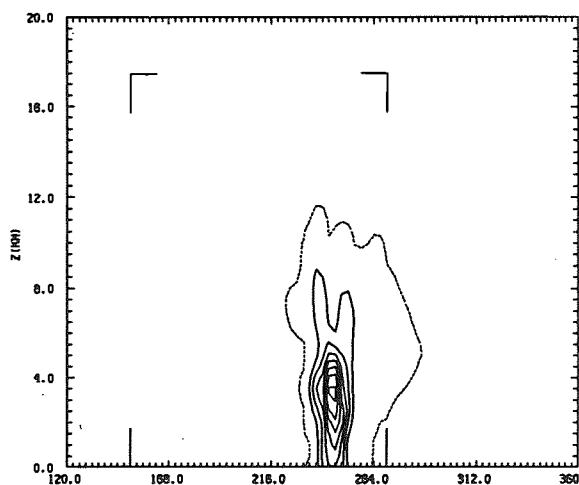


Figure 2. Rain water field  
Contour interval .5 g/kg

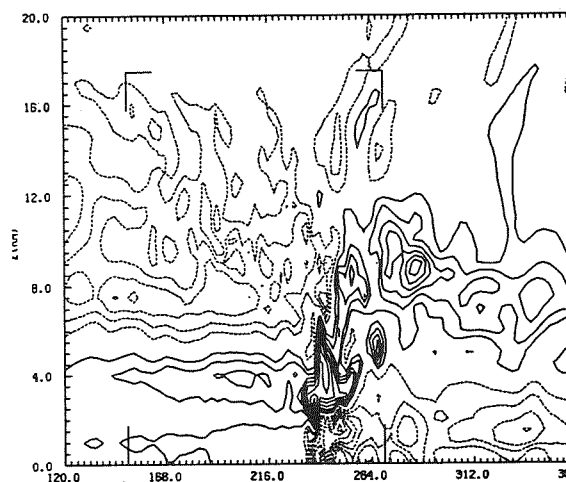


Figure 4. Horizontal velocity perturbation field  
Contour interval 2 m/sec.

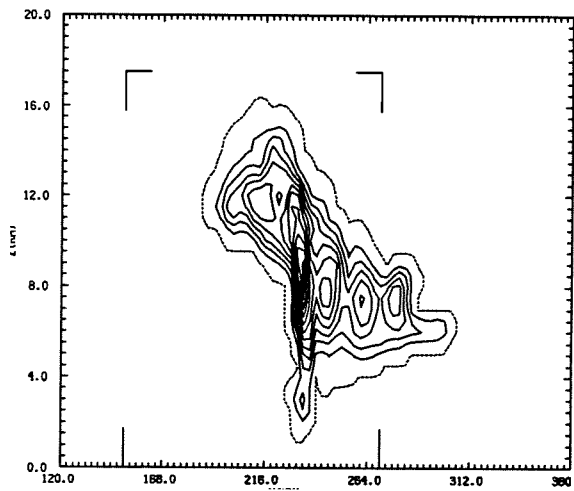


Figure 5. Cloud water field  
Contour interval .5 g/kg

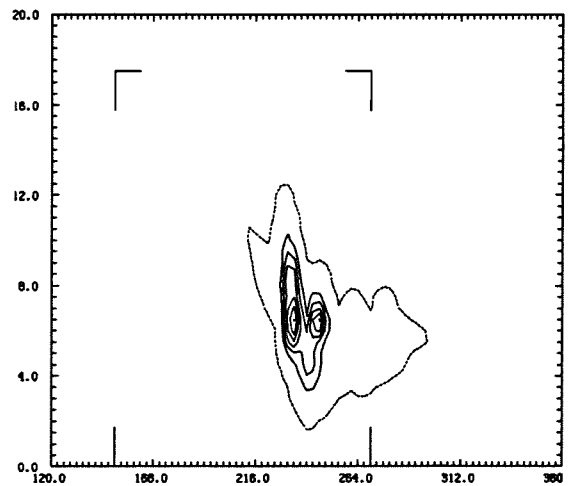


Figure 8. Graupel field  
Contour interval .5 g/kg

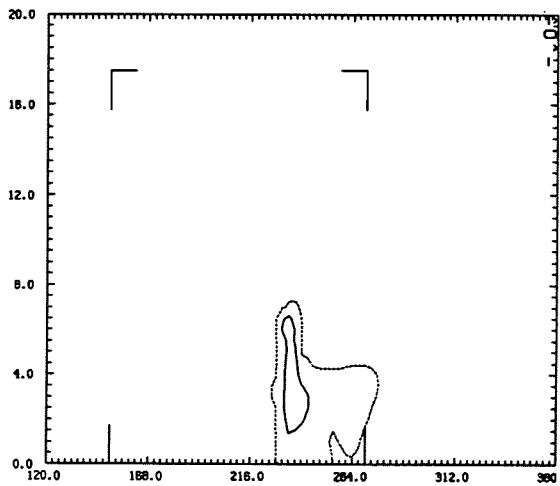


Figure 6. Rain water field  
Contour interval .5 g/kg

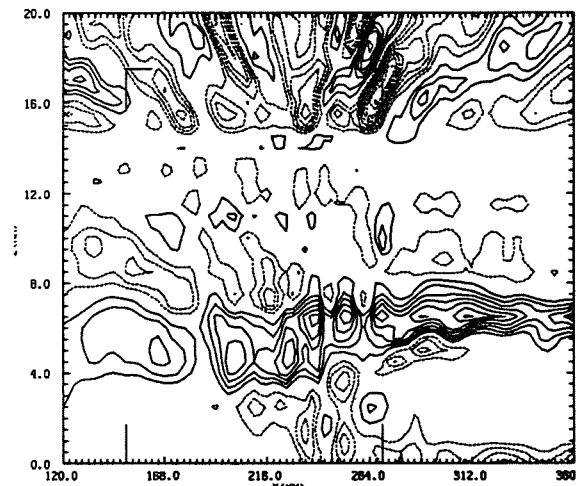


Figure 9. Bouyancy field  
Contour interval .5°C

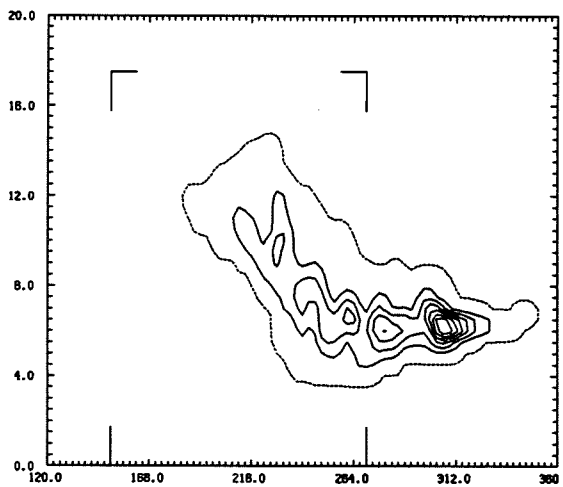


Figure 7. Cloud ice field  
Contour interval .5 g/kg

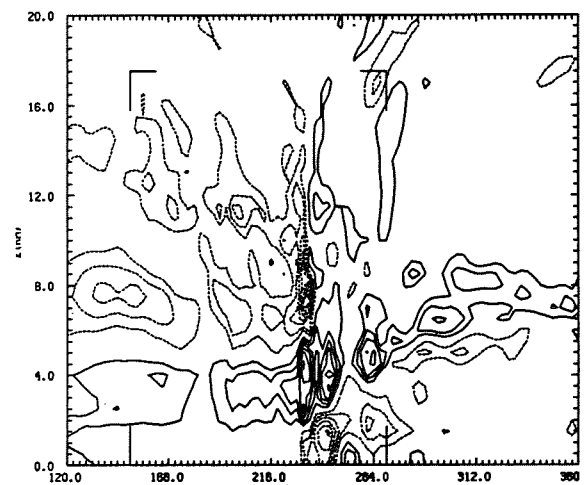


Figure 10. Horizontal velocity perturbation field  
Contour interval 2 m/sec

# NUMERICAL SIMULATION OF MICROPHYSICAL PROCESSES IN CUMULONIMBUS

Hu Zhijin      He Gaunfang

Academy of Meteorological Science ,

State Meteorological Administration, Beijing, China

## 1. INTRODUCTION

Parameterized model is widely used for simulation of the microphysical processes in clouds. In its usual form the parameter  $N_0$  for particle size distribution is assumed to be constant, then the number concentrations of particles ( $N$ ) are diagnosed from their mass content ( $Q$ ). This assumption does not agree with the observations and causes serious errors in simulation of some important microphysical processes. For example the ice nucleation and multiplication have small effect on  $Q_i$ , but increase  $N_i$  significantly. According to Bergeron theory  $N_i$  have large effect on precipitation efficiency. It makes the basis of weather modification. A parameterized model prognosing both  $Q$  and  $N$  of various water particles (two-parameter model) had been established by Hu (1984) for stratiform clouds. Here a two-parameter model is presented for simulating the microphysical processes in cumulonimbus clouds. All the water substance is divided into 6 categories: vapor ( $V$ ), cloud drops ( $C$ ), rain drops ( $r$ ), ice crystals ( $i$ ), graupels ( $g$ ), and Hailstones ( $h$ ). Hails have diameter larger

than  $D^*=0.5$  cm. The particle size distributions are assumed to be the Gamma functions. A truncated Gamma function is assumed for hails:  $N(D)=0$  for  $D < D_*$ ;  $N(D)=N_0 \exp(-\lambda D)$ , for  $D \geq D_*$ . Both parameters  $N_0$  and  $\lambda$  are variables and can be deduced from  $N$  and  $Q$ . For example,  $N_i = N_{0i} \exp(-\lambda_i D_{*i}) \lambda_i^{-1}$ ,  $Q_i = 6 N_i \lambda_i^{-3} A_{mi} \left[ 1 + \lambda_i D_{*i} + \frac{1}{2} (\lambda_i D_{*i})^2 + \frac{1}{6} (\lambda_i D_{*i})^3 \right]$  where  $A_{mi} = 0.471 \text{ g cm}^{-3}$ .

## 2. MICROPHYSICAL EQUATIONS

Every microphysical variable, such as  $Q_v, Q_c, Q_r, Q_i, Q_g, Q_h, N_r, N_i, N_g, N_h$ , can be prognosed with consideration of advection, turbulent, fall-out and sources:

$$\frac{\partial M}{\partial t} = -(W - V_m) \frac{\partial M}{\partial z} + k \frac{\partial^2 M}{\partial z^2} - E(M - M_0) + \frac{M}{\rho} \frac{\partial \rho V_m}{\partial z} + \frac{\delta M}{\delta t}$$

26 kinds of microprocesses are considered including condensation (deposition, evaporation) of cloud, ice, rain, graupel and hail ( $S_{vc}, S_{vi}, S_{vr}, S_{vg}, S_{vh}$ ); collection of cloud droplets by ice, rain, graupel and hail ( $C_{ci}, C_{cr}, C_{cg}, C_{ch}$ ); collection of rain by ice, graupel and hail ( $C_{ri}, C_{rg}, C_{rh}$ ); collection of ice by rain, graupel and hail ( $C_{ir}, C_{ig}, C_{ih}$ ); ice nucleation and multiplication ( $P_{vi}, P_{ci}$ ); autoconversions

of cloud-rain, ice-graupel and graupel-hail (Acr, Aig, Agh); freezing of rain (Mrg); melting of ice, graupel and hail (Mir, Mgr, Mhr); ice-ice and rain-rain collection (Cii, Crr).

The source term for each variable are as following :

$$\frac{\delta Q_r}{\delta t} = -S_{v,r} - S_{r,r} - S_{v,i} - S_{v,s} - S_{v,h} - NP_{v,i} Q_{v,o}$$

$$\frac{\delta Q_s}{\delta t} = S_{v,s} - C_{c,r} - C_{c,r} - C_{c,s} - C_{c,h} - A_{c,r} - NP_{v,i} Q_{v,o}$$

$$\left\{ \begin{array}{l} \frac{\delta Q_r}{\delta t} = S_{v,r} + C_{c,r} + A_{c,r} + M_{g,r} + M_{i,r} + M_{h,r} - M_{r,g} \\ \text{If } T \geq 273 \text{ K, } +C_{i,h} + C_{i,r} \\ \text{if } T < 273 \text{ K, } -C_{r,h} - C_{r,r} - C_{r,i} \quad (kk=0) \\ \quad -C_{w,h} + C_{w,h} - C_{r,g} - C_{r,i} \quad (kk=1) \end{array} \right.$$

$$\left\{ \begin{array}{l} \frac{\delta N_r}{\delta t} = NS_{v,r} + A_{c,r}/Q_{v,o} + NM_{g,r} + NM_{i,r} \\ \quad - NM_{r,g} + NC_{c,r} \\ \text{If } T \geq 273 \text{ K, } (M_{h,r} + C_{i,h})/Q_{h,o} \\ \text{if } T < 273 \text{ K, } -NC_{r,h} - NC_{r,g} - NC_{r,i} \quad (kk=0) \\ \quad -NC_{r,h} - NC_{r,g} - NC_{r,i} - (C_{w,h} + C_{r,h} \\ \quad - C_{w,h})/Q_{h,o} \quad (kk=1) \end{array} \right.$$

$$\frac{\delta Q_i}{\delta t} = S_{v,i} + C_{c,i} - C_{i,r} - M_{i,r} - C_{i,g} - C_{i,h} - A_{i,g} \\ + NP_{v,i} Q_{v,o} + NP_{v,i} Q_{v,o}$$

$$\frac{\delta N_i}{\delta t} = NS_{v,i} - NC_{i,r} - NM_{i,r} - NC_{i,g} - NC_{i,h} - NA_{i,g} \\ + NP_{v,i} + NP_{v,i} + NC_{i,i}$$

$$\left\{ \begin{array}{l} \frac{\delta Q_g}{\delta t} = S_{r,g} + C_{c,g} + C_{i,g} - C_{g,h} + A_{i,g} + M_{r,g} \\ \quad - M_{g,r} - A_{g,h} \\ \text{If } T < 273 \text{ K, } +C_{r,g} + C_{r,r} + C_{r,i} \end{array} \right.$$

$$\left\{ \begin{array}{l} \frac{\delta N_g}{\delta t} = NS_{v,g} + NA_{i,g} - NA_{g,h} + NM_{r,g} - NM_{g,r} \\ \quad - NC_{g,h} \end{array} \right.$$

$$\left\{ \begin{array}{l} \text{If } T < 273 \text{ K} \quad +N_{o,i} \end{array} \right.$$

$$\left\{ \begin{array}{l} \frac{\delta \theta_h}{\delta t} = S_{v,h} + C_{c,h} + C_{i,h} - M_{h,r} + A_{g,h} \\ \text{If } T < 273 \text{ K} \quad +C_{o,h} + C_{r,h} \quad (kk=0) \\ \quad +C_{w,h} \quad (kk=1) \end{array} \right.$$

$$\frac{\delta N_h}{\delta t} = NA_{g,h} - NM_{h,r}$$

where Pvi, NPvi, Mgr, NMgr etc. is the mass transformation rate and the number change rate due to ice nucleation, graupel melting, etc. respectively. Qvo, Qro, Qho is the initial mass of a nucleated ice, secondary ice, autoconverted raindrop and shedded water drop from hail respectively. Cwh is the threshold value of hail wet growth rate, which determines whether the hail is in dry growth regime (kk=0) or in wet growth regime (kk=1). Fc is a parameter describing the "width of cloud droplet spectrum" and prognosed:

$$\frac{\partial F_c}{\partial t} = -W \frac{\partial F_c}{\partial z} + k \frac{\partial^2 F_c}{\partial z^2} + \frac{\delta F_c}{\delta t}$$

$$\frac{\delta F_c}{\delta t} = \rho^2 Q_v^2 [120 \rho Q_v + 1.6 N_i / D_i]^{-1}$$

Equations for Svr, Svg, Cci, Ccr, Ccg, Cii, Crr, Pvi, Pci, Acr have little change from that of our stratiform cloud model (Hu 1984). The others cannot be presented here due to limitation of space.

### 3. CASE STUDIES

Some case studies had been done by this model combined with an one-dimensional time-dependent cumulus model after Hu (1985). Here are 3 typical examples.

#### 3.1 SMALL CUMULONIMBUS CASE

The simulated convective cloud looked like a Cu cong. cloud, but transformed into Ci not. cloud after precipitation. The cloud top reached 7.7 km (-12°C). Calculated characteristics agreed with observations. It was shown that preci-

precipitation formed through the warm-rain process (Acr, Ccr). Some of the raindrops froze into graupel by collection of ice (Cri). Ice multiplied by Hallett-Mossop process (Pci). Its rate increased with the accumulation of rain and graupel in the upper part of the cloud and reached  $500 \text{ (kg.s)}^{-1}$ , being 100 times as much as ice nucleation rate in this cloud.

### 3.2 HAILSTORM CASE

Simulated hailstorm was associated with a severe squall line. The height of radar echo was 9--12 km. Rainfall was weak, Max. accumulated hailstones on the ground was  $436/\text{m}^2$  with mean diameter of 9 mm. Model output agreed with observation in many aspects. It showed that the updraft was strong (22 m/s). Raindrops formed through the warm-rain process in the upper part of cloud, where temperature was  $-24-- -32^\circ\text{C}$ . They froze into graupel (Mrg) rapidly. The Bergeron process (Svi, Aig) was not effective. Graupel grew by riming (Ccg) and were suspended in the upper part of cloud. Only a few of them grew into hailstones and fell on the ground. Most of them evaporated with the dissipation of cloud, so the precipitation efficiency was very low.

### 3.3 TERRESTRIAL RAIN CASE

Simulated "75.8" terrestrial rain brought very great losses. The max. rainfall of 7 Aug. 1975 was 1005 mm. Calcula-

tion showed that the updraft was not strong (about 4--5 m/s), and precipitation could fall out through the updraft. Rain was prolonged during the simulated time (144 min) and its total amount reached 186 mm. Precipitation formed mainly by the warm-rain process. Graupels formed by Cri and grew by Ccg, Crg. Ice formed mainly due to Pci. The Bergeron process (Svi, Aig) was not important. Water drops shed from hailstones had some influence on precipitation development. The interactions of updraft, cloud and precipitation caused a periodic variation in their development with a period of 0.5--1 hour.

### 4. REFERENCES

- Hu Zhijin. Yan Caifan: A Numerical Model of Stratiform Clouds, Papers Presented at 9th International Cloud Physics Conference, Tallinn, USSR, 1984.
- Hu Zhijin, Yan Caifan: The Effect of Salt-seeding in Warm Cumulus With Various Lifetimes. Papers Presented at 4th WMO Conference On Weather Modification, Honolulu, USA., WMO Report 2, p 353, 1985.

A COMPARATIVE STUDY OF TWO MICROPHYSICAL SCHEMES  
IN A  $\beta$  MESOSCALE MODEL

Evelyne Richard and Nadine Chaumerliac

LAMP/OPGC, Clermont-Ferrand

1. INTRODUCTION

Two sets of microphysical parameterizations are compared under various orographic situations in a  $\beta$  mesoscale model (NICKERSON et al. 1986). One is the currently used Kessler parameterization (KESSLER, 1969) and the other is based upon Berry and Reinhardt's work (1973). These two parameterizations will be quoted as "K" and "BR" in the following. In both cases, cloud water mixing ratio is diagnosed from the predicted value of  $q$  (equal to the sum of the vapor mixing ratio,  $q_v$  and the cloud water mixing ratio,  $q_{cw}$ ). In case of supersaturation,  $q_v$  is set equal to the saturated vapor mixing ratio and excess vapor is converted into cloud water.

There are two main differences in the K and BR parameterizations : the number of predictive variables and the assumed raindrop spectrum. For the K parameterization, the rainwater mixing ratio ( $q_{rw}$ ) is predicted assuming a Marshall Palmer distribution function of the raindrops. For BR parameterization, both rainwater mixing ratio and total number concentration of raindrops ( $N_{rw}$ ) are predictive variables, the raindrops being assumed lognormally distributed. In both cases, the processes taken into account are autoconversion, accretion, evaporation and sedimentation. Self collection of the raindrops is only considered in case of BR parameterization.

The autoconversion rates are expressed as

$$\left. \frac{d\rho_a q_{rw}}{dt} \right]_{\text{aut. K}} = \begin{cases} 10^{-3} (\rho_a q_{cw} - 0.5 \cdot 10^{-3}) \\ 0 \end{cases}$$

if  $\rho_a q_{cw} > 0.5 \text{ g/m}^3$

if not

$$\left. \frac{d\rho_a q_{rw}}{dt} \right]_{\text{aut. BR}} = \alpha (\rho_a q_{cw})^2$$

where  $\rho_a$  is the air density and  $\alpha$  a function of the cloud spectrum parameters. Setting the dispersion parameter to 0.2775 (typical maritime value),  $\alpha$  is equal to 0.66 for a mean cloud diameter of 35  $\mu\text{m}$  (BR1) and to 0.15 for a diameter of 27.5  $\mu\text{m}$  (BR2).

Note that in contrast to Kessler's rate, BR's rates allow for production of rainwater even for low cloud water contents. For cloud water content greater than 0.5  $\text{g/m}^3$ , Kessler's rate is in between the two Berry's rates.

2. MOUNTAIN WAVE SIMULATIONS

In order to compare the two parameterisations, the model is first run over an idealized two-dimensional bell-shaped mountain. A two layer atmosphere is considered with a lower layer of constant lapse rate up to 8 km and a isothermal layer aloft. The initial horizontal wind speed is uniformly 20 m/s and the relative humidity is 80 % below 3 km.

In Fig. 1 are plotted the vertical cross sections of the cloud water mixing ratios, rainwater mixing ratios and precipitations rates, computed after 6 hours of simulation for the Kessler parameterization and the BR1 and BR2 parameterizations. Cloud water fields are similar for K and BR2 while BR1 cloud is weaker due to more efficient conversion of cloud into rain. Precipitation intensities are also comparable between K and BR2 but the precipitation extends further downwind in case of BR2. It should be noticed that the corresponding rain water mixing ratios are quite different, BR2 rainwater mixing ratio being twice as

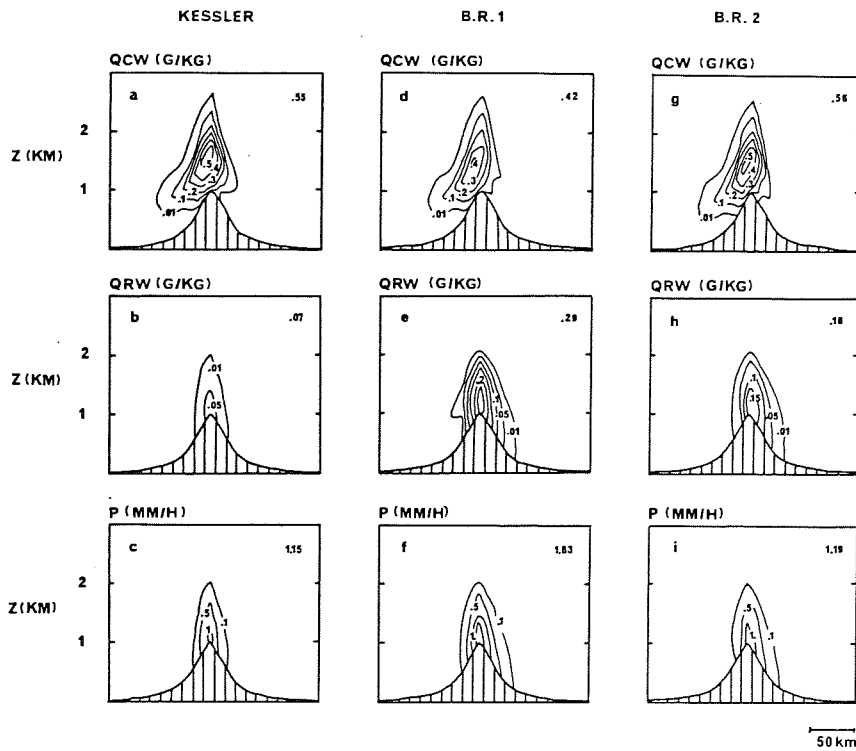


Fig. 1  
Vertical cross sections of cloud water mixing ratio ( $q_{cw}$ ), rain water mixing ratio ( $q_{rw}$ ) and precipitation rate ( $P$ )

large as in the K case. This indicates that rainwater is carried by much larger drops in K than in BR2. As a consequence, the BR2 raindrops are more sensitive to the wind drift. This should be related to the differences already noticed in the spatial distribution of the precipitation.

### 3. FEEDER SEEDER CLOUD SIMULATIONS

The model is now applied to the problem of orographic enhancement of rain via the feeder-seeder mechanism. This precipitation enhancement results from the washout of small cloud droplets orographically generated by raindrops originating in higher level large scale clouds. A detailed study of 14 seeding events observed in Southern Wales was presented by HILL et al, 1981. These observational data have been used to initialize the model (sounding, seeding precipitation rate) and to control the quality of the results (precipitation enhancement). Further details can be found in RICHARD et al, 1987. All the 14 cases have been run with the K, BR1, BR2 parameterizations. Fig. 2 shows for each parameterization a case by case comparison between observations and computations. BR1 and BR2 give much better agreement than K and BR1 is slightly better than BR2. Looking

more closely at the results, cases 1 to 4, characterized by strong low level wind speed are systematically underestimated by the K parameterization. Fig. 3 gives the precipitation enhancements as a function of the low level wind speeds for the observations and the results from the three parameterizations. The four data sets have been fitted by a curve,  $\Delta P = av^k$ . All the parameterizations slightly underestimate the orographic enhancement in the range 10 to 20 m/s. For stronger wind values, there are larger discrepancies between the observations and the K results. Only the BR parameterizations are able to reproduce the observed dependency of the orographic enhancement on the low level wind speed.

This is mainly due to the fact that Kessler's parameterization produces fewer but larger raindrops than BR's parameterization. The K raindrops falling faster are then less advected and the residence time of the seeding raindrops within the cloud is shorter especially in case of strong low level winds.

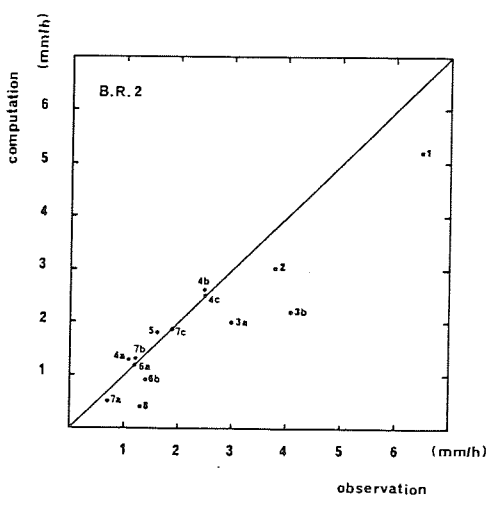
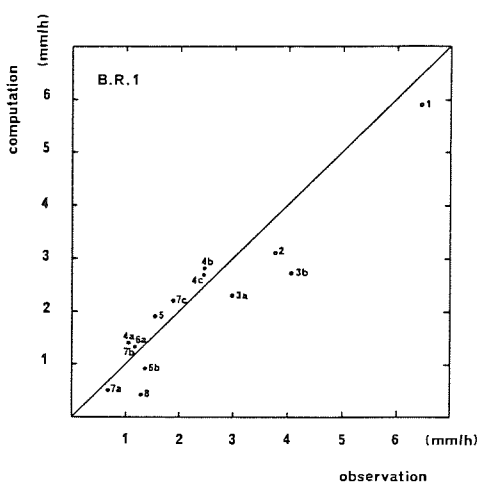
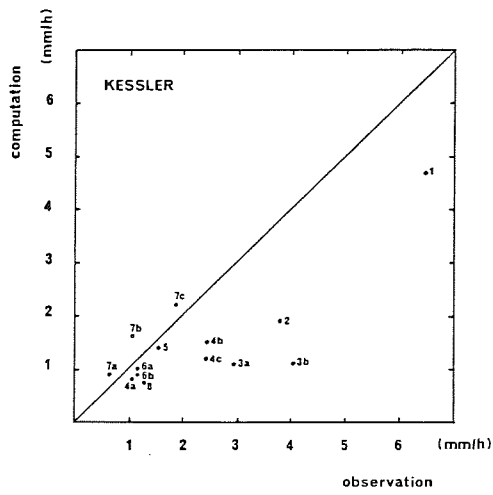


Fig. 2 : Computed orographic precipitation enhancement versus the observed one for 14 cases.

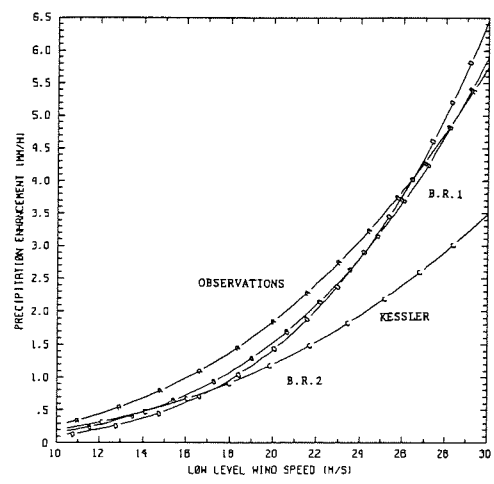


Fig. 3 : Variation of the orographic precipitation enhancement as a function of the mean low level wind speed

4. REFERENCES

BERRY E.X.; REINHARDT R.L. : Modeling of condensation and collection within clouds D.R.I. Phys. Sci. Pub.,Nr 16 (1973) Univ. of Nevada

HILL F.F.; BROWNING K.A.; BADER M.J. : Radar and raingage observations of orographic rain over South Wales. Quart. J. Roy. Meteor. Soc., Nr 107 (1981), P. 643-670

KESSLER E. : On the distribution and continuity of water substance in atmospheric circulations. Meteorological Monographs, 10-32 (1969) A.M.S., Boston

NICKERSON E.C.; RICHARD E.; ROSSET R.; SMITH D.R. : The numerical simulation of clouds, rain and airflow over the Vosges and Black Forest Mountains, a meso- $\beta$  model with parameterized microphysics. Mon. Wea. Rev., Nr.114 (1986), P 398-414.

RICHARD E.; CHAUMERLIAC N.; MAHFOUF J.F.; NICKERSON E.C. : Numerical simulation of orographic enhancement of rain with a mesoscale model. J. Clim. Appl. Meteor., Nr 26 (1987), P. 661-669.

Gregory J. Tripoli

University of Wisconsin, Dept. of Meteorology, Madison, WI 53715

Piotr J. Flatau and William R. Cotton

Dept. of Atmospheric Science, Colorado State University, Fort Collins, CO 80523

## 1 Introduction

Because of the diverse applications we envision for the Colorado State University RAMS (Regional Atmospheric Modeling System), we demand greater skill and flexibility in the formulation of our microphysics parameterization scheme than in previous models. Historically the number of categories of hydrometeors and the size-distribution of hydrometeors assumed in a model vary from investigator to investigator. It seems that there is an almost infinite set of combinations of particle size distributions, particles size-distribution parameters, and hydrometeor types that can be formulated in a cloud model. However, we have found that it is possible to express almost any microphysical parameterization in a common or universal format. We have therefore developed a *generalized* bulk microphysics parameterization capable of meeting our current and projected needs with a high degree of flexibility.

In spite of the apparent diversity of distributions used to define the sizes of particles in atmospheric polydisperse media (Feingold and Levin, 1986) (clouds, fogs, aerosols), only a few basic types arise. These are: the generalized gamma distribution and its special cases, the normal distribution and its transformation (e.g., log-normal), the constant distribution, and the power law. The generalized or *modified gamma* function defines special cases: gamma, truncated gamma, Marshall-Palmer (or exponential), Khrgian-Mazin, doubly truncated Marshall-Palmer, and half-normal. Even the normal and log-normal size spectra can be linked to some of the mathematics arising in generalized gamma calculations.

In a bulk microphysical scheme, several water and (or) aerosol classes are usually considered, such as cloud droplets, rain, aggregates, graupel, pristine ice, aerosol, and hail. The cloud water may be taken as constant size, but rain drops are usually considered to be distributed according to Marshall-Palmer or log-normal functions. Assuming a constant size precludes coagulation (same terminal velocity), and it may be advantageous to consider cloud particles as distributed according to some other probability function, such as gamma.

The optimum distribution chosen for a given water class will depend on the application. For instance, a distribution which describes averaged terminal velocity well, may not be suitable to describe the radiative properties of the medium. In most cases, there is no universal physical principle behind the choice of the *hard-wired* distribution around which a given parameterization is usually built. Thus we would like to have the flexibility to switch fairly easily from one type of distribution to another.

The discretization of a continuous spectrum of liquid and frozen hydrometeors into arbitrary categories is another feature traditionally "hard wired" into bulk microphysics parameterizations. These categorizations are an attempt to include the gross characteristics of several identifiable ice and droplet habits into a cost-effective scheme. As with the choices of a distribution, the choice of discretization is not always universally applicable. We also would like to have the flexibility to easily redefine the properties and the number of hydrometeor categories.

The following paper summarizes methodology described more fully in Tripoli *et al.* (1988).

## 2 Size Spectra and Their Moments

### 2.1 Basic concepts

Several empirical formulas have been proposed for the spectra of various water categories. The spectral density  $n(D)$  is defined such that  $n(D)dD$  is the total number of particles, whose diameter is between  $D$  and  $D + dD$ , per unit volume of air. Hence

$$N_t = \int_0^D n(D)dD, \quad (1)$$

is the total concentration of particles of diameters smaller than  $D$ , per unit volume of air. To describe the particle size spectrum we choose the suitable probability density function (p.d.f)  $f(D)$  defined on interval  $(D_{min}, D_{max})$ , with, most commonly,  $D_{min} = 0$  and  $D_{max} = \infty$ . This p.d.f. is normalized to one, i.e.,

$$\int_0^{\infty} f(D)dD = 1. \quad (2)$$

In the development of a bulk parameterization scheme one is ultimately interested in the total mass or number density of the hydrometeors involved in a process, or in a numerical or mass weighted average of a quantity. For example, the total downward mass flux of water due to precipitation settling is obtained by integrating the mass flux of a single hydrometeor at each size over the whole distribution. Such an integration appears in the form:

$$\bar{g} = \int_{D_{min}}^{D_{max}} g(D)n(D)dD. \quad (3)$$

Normally, the function  $g$  exhibits the power law dependence,

$$g(D) = cD^p \quad (4)$$

where  $c$  and  $p$  are constants. In such case the problem reduces to finding generalized moment of the p.d.f.  $f(D)$ :

$$I(p) = \int_{D_{min}}^{D_{max}} D^p f(D)dD = D_n^p F(p). \quad (5)$$

Function  $F$  depends only on the distribution and the limits over which it is integrated.  $D_n$  is the *characteristic* diameter. In other words most of equations of the bulk parameterization schemes in use now (Cotton *et al.*, 1982; Lin *et al.*, 1983; Nickerson *et al.*, 1986), can be written in one single and simple form:

$$\bar{g} = g(D_n)N_t F(p). \quad (6)$$

An implication of this result is that one can develop a universal scheme which can be applied to any one of several particle size-distribution functions.

One example of the moment is the water content, defined as

$$\rho_l = \int_{D_{min}}^{D_{max}} m(D)n(D)dD, \quad (7)$$

where  $\rho_l$  is the bulk water density and  $m(D)$  the mass of a particle of diameter  $D$ . For spherical particles we have

$$m(D) = \frac{\pi}{6} D^3 \rho_w, \quad (8)$$

where  $\rho_w$  is density of the particle. From (8), (7) and (5):

$$\rho_l = \frac{\pi}{6} N_t I(3) = m(D_n) N_t F(3). \quad (9)$$

Now we have to specify functions  $F(p)$  and characteristic diameter  $D_n$ .

## 2.2 Distributions

### 2.2.1 Generalized gamma distribution

A popular choice for a spectral density function to describe sizes of atmospheric particles is a generalized gamma function. Its definition is

$$f_{mg}(D) = \frac{c}{\Gamma(\nu)} \left(\frac{D}{D_n}\right)^{c\nu-1} \frac{1}{D_n} \exp\left[-\left(\frac{D}{D_n}\right)^c\right], \quad (10)$$

where  $D$  is diameter of particle. Constants  $\nu$  and  $c$  define the *shape* of the distribution and with the *normalization* constant  $N_t$  the spectral density function is completely specified.

The p-moment of the generalized gamma distribution (10) is

$$I_{mg}(p) = \int_{D_{min}}^{D_{max}} D^p f_{mg}(D) dD = D_n^p F_{mg}(p), \quad (11)$$

where subscript *mg* stands for *modified gamma* and

$$F_{mg}(p) = \frac{\Gamma(\nu + p/c)}{\Gamma(\nu)}. \quad (12)$$

Thus the liquid water content for the modified gamma distribution is:

$$\rho_l = \frac{\pi}{6} N_t D_n^3 \rho_w \frac{\Gamma(\nu + 3/c)}{\Gamma(\nu)}. \quad (13)$$

The *gamma* distribution is obtained by setting  $c = 1$  in all formulas in this section.

Table 1 summarizes the characteristics of seven specific distributions commonly used. The first five are special cases of the generalized gamma distribution. One of the the most commonly used distribution in atmospheric cloud physics is the Marshall-Palmer type wherein  $c = 1$  and  $\nu = 1$ .

Distribution	Symbol	$D_{min}$	$D_{max}$	$c$	$\nu$
Modified gamma	<i>mg</i>	0	$\infty$	$c$	$\nu$
Gamma	<i>gam</i>	0	$\infty$	1	$\nu$
Exponential (Marshall-Palmer)	<i>MP</i>	0	$\infty$	1	1
Truncated Marshall-Palmer	<i>tMP</i>	$D_{min}$	$D_{max}$	1	1
Half-normal	<i>hn</i>	0	$\infty$	2	1/2
Normal	<i>nor</i>	$-\infty$	$\infty$	-	-
Log-normal	<i>log</i>	0	$\infty$	-	-

Table 1: Summary of the size distributions and the shape parameters  $c$  and  $\nu$ .

Name	Modified gamma	Log-normal
$F(p)$	$\Gamma(\nu + p/c)/\Gamma(\nu)$	$\exp(\sigma^2 p^2/2)$
$D_{mean}$	$\Gamma(\nu + 1/c)/\Gamma(\nu) D_n$	$\exp(\sigma^2/2) D_n$
$D_{mode}$	$(\nu - 1/c)^{1/c} D_n$	$\exp(-\sigma^2) D_n$
Water content $q$	$m(D_n) N_t \frac{\Gamma(\nu+3/c)}{\Gamma(\nu)}$	$m(D_n) N_t \exp(\frac{9\sigma^2}{2})$

Table 2: Special moments of size distributions

### 2.2.2 Normal distributions

The normal and log-normal distributions do not fit the family of gamma distributions. The general methodology for integration over the spectral density outlined above is entirely applicable however. The form of a normal distribution and log-normal distribution are respectively:

$$f_{nor}(D) = \frac{1}{\sqrt{2\pi}\sigma D} \exp\left[-\left(\frac{D - D_n}{\sqrt{2}\sigma}\right)^2\right], \quad D \in (-\infty, \infty), \quad (14)$$

and

$$f_{log}(D) = \frac{1}{\sqrt{2\pi}\sigma D} \exp\left[-\left(\frac{\ln(D/D_n)}{\sqrt{2}\sigma}\right)^2\right], \quad D \in (0, \infty). \quad (15)$$

The log-normal distribution is becoming widely used in bulk parameterizations. In the case of the log-normal distribution,  $F(p)$  is simply defined:

$$F_{log}(p) = \exp\left(\frac{\sigma^2 p^2}{2}\right). \quad (16)$$

Characteristics of the family of normal distributions are also described in Table 1. Table 2 defines the function  $F(p)$  for the modified gamma and log-normal distributions as functions of several common moments.

## 2.3 Example of bulk parameterization formula: Mass-weighted terminal velocity

We can not provide here details of the microphysics parameterization. A detailed technical report is being prepared Tripoli *et al.* (1988). As an example let us consider mass-weighted terminal velocity, given by

$$\bar{v}_i = \frac{1}{\bar{r}_i \rho_0} \int_{D_{min}}^{D_{max}} v_i(D_i) m_i(D_i) n(D_i) dD_i, \quad (17)$$

where  $i$  indicates one of several classes of hydrometeors in the model. After integration we obtain

$$\bar{v}_i = \frac{1}{\bar{r}_i \rho_0} v_i(D_{ni}) m_i(D_{ni}) N_{ti} F(p_{mi} + p_{vi}), \quad (18)$$

where  $p_{vi}$  and  $p_{mi}$  are powers of velocity- and mass-diameter dependence. Hence, we can change distributions by simply redefining  $F$ . The parameterization is written by forming a table of  $F(p)$  for each distribution function. Then the appropriate table is called, based on the desired form of the distribution.

All other processes such as: mass-diameter, density-diameter, vapor deposition, terminal velocities, coagulation growth (aggregation and collection) and nucleation are coded according to the same principle: determine power  $p$ , diagnose from the model characteristic diameter  $D_n$  and total concentration  $N_t$ , and find distribution-averaged quantities.

## 3 Hydrometeor classes and their interaction

Several different bulk microphysical parameterization schemes have been proposed in the literature, each dividing ice, water and aerosol into several assumed categories. In general, time dependent continuity equations are formed for the mass and in some cases there is a continuity equation for number concentration. In some log-normal-based predictive schemes, a third parameter is sometimes predicted. The water continuity equations are normally written in the form:

$$\frac{dr_i}{dt} = \sum_{j=1}^N CN_{j,i,i} - \sum_{j=1}^N CN_{i,j,i} + P_i \quad (19)$$

and

$$\rho_o \frac{dN_i/\rho_o}{dt} = \sum_{j=1}^N NCN_{j,i,i} - \sum_{j=1}^N NCN_{i,j,i} + NP_i, \quad (20)$$

where  $r_i$  and  $N_i$  are the mixing ratio and number concentration for category  $i$ ,  $\rho_o$  is the air density,  $CN_{l,m,n}$  designates the positive definite mixing ratio conversion tendency to category  $n$  resulting from the conversion of mass from hydrometeor category  $l$  to the category  $m$ ,  $N$  is the number of categories, and  $P_i$  is the mixing ratio tendency of category  $i$  due to precipitation settling.  $NCN$  and  $NP$  are analogous tendencies for number concentrations. For mass continuity, it is required that  $CN_{i,j,i} = CN_{i,j,j}$ , although  $NCN_{i,j,i} \neq NCN_{i,j,j}$ .

The art of microphysical parameterization is found in the formulation of  $NCN$  and  $CN$ . Generally, a conversion tendency can be expressed in the form:

$$CN_{l,m,n} = H_{l,m,n}(CL_{l,m}, VD_{n,v}, ML_{n,k}, NU_{k,v}), \quad (21)$$

where  $H$  is the arbitrary parameterization which is a function of several standard interaction terms.  $CL_{l,m}$  is the collection of category  $l$  by category  $m$ ,  $VD_{n,v}$  is the vapor deposition (evaporation, or sublimation) of category  $n$  to the vapor category and  $ML_{n,k}$  is the melting of category  $n$  into category  $k$  and  $NU_{n,v}$  is nucleation of category  $n$  from vapor  $v$ .

Nucleation would be non-zero only when  $l$  is a vapor category and  $m = k$  is a particular crystal category. The term may contain splintering, sorption/deposition, and phoretic effects. In some cases, nucleation tendency itself may depend on interaction terms. For instance, splintering will depend upon riming rate contained in  $CL_{cloud,ice}$ .

$VD_{n,v}$  and  $ML_{n,k}$  are nonzero only if  $m = v$  and  $m = k$  respectively. The computed interaction term may or may not be used for the actual conversion tendency. For instance, the amount of rain collected by cloud water is not used as a tendency for the growth of cloud water, whereas the amount of cloud water collected by rain is used as loss to cloud water. On the other hand, both the amount of ice crystals collected by rain and the amount of rain collected by ice crystals may become a tendency for graupel. Hence the conversion term from category  $l$  to category  $m$  could be based on the interaction between  $l$  and a third category.

The conversion may also include such things as the arbitrary reclassification of a portion of the mass of one category to another. Auto-conversion of category  $l$  to another is typically expressed as a function of  $CL_{l,l}$ .

A similar form of the conversion tendency is give for  $NCN$ . The standard interaction terms can be formulated arbitrarily independent of the distribution using the methodology described in Section 2. Hence, given a complete set of  $CL_{i,j}$ ,  $VD_{i,v}$ ,  $ML_{i,k}$  and  $NU_{n,v}$ , virtually any arbitrary parameterization is expressed by (21). Some additional *parameterization specific* features are found in the basic interaction equations themselves, most of which can be separated out. Such features include collision and coalescence efficiencies among others. Many *parameterization specific* features arise from simplifying approximations, which we attempt to eliminate.

## 4 Implementation

It is beyond the scope of this paper to specifically describe the implementation. Basically, we first diagnose all distribution parameters for each category based on either one or two predicted distribution parameters. We then compute all values of  $CL$ ,  $VD$ ,  $ML$  and  $NU$  among all categories. A set of conversions among

categories is then computed based on these values. The conversion computation is modularized and can be changed easily. The collision and coalescence efficiencies are also modularized and easily varied.

The diagnosis of distributions and distribution parameters is defined either on input or in a modular form so it can be easily changed. The parameterization determines mixing ratio tendencies and, as an option, particle concentration tendencies for any hydrometeor category. Tendencies are based on an initially prescribed mixing ratio and second distribution parameter for each category. The second parameter may be a predicted concentration or a specified slope, intercept, or concentration. Depending on which second parameter is specified, the parameterization diagnostic routine will diagnose the others. In addition, the diagnostic routine (one for each category) prescribes which distribution is to be used and other pertinent things such as the terminal velocity-diameter and density-diameter relationships, habits and so on.

### Acknowledgements

Research described here have been supported by the National Science Foundation Grant ATM-8512480.

## References

- Cotton, W. R., M. A. Stephens, T. Nehr Korn, and G. J. Tripoli, 1982: The Colorado State University three-dimensional cloud/mesoscale model - 1982. *J. Rech. Atmos.*, **16**, 295-320.
- Feingold, G. and Z. Levin, 1986: The lognormal fit to raindrop spectra from frontal convective clouds in Israel. *J. Atmos. Sci.*, **25**, 1346-1363.
- Lin, Y., R. D. Farley, and H. D. Orville, 1983: Bulk parameterization of the snow field in a cloud model. *J. Atmos. Sci.*, **22**, 1065-1089.
- Nickerson, E. C., E. Richard, R. Rosset, and D. R. Smith, 1986: The numerical simulation of clouds, rain, and airflow over the Vosges and Black Forest Mountains: A meso- $\beta$  model with parameterized microphysics. *Mon. Wea. Rev.*, **114**, 398-414.
- Tripoli, G. J., P. J. Flatau, and W. R. Cotton, 1988: *Generalized microphysics scheme for use in mesoscale/cloud models*. Technical Report, Colo. State University, Fort Collins.

# THE STUDY OF NUMERICAL SIMULATION ON THE FORMATION OF THE CLOUD DROPLET SPECTRA IN CUMULUS CLOUDS

Xiao Hui Xu Huaying Huang Meiyuan

Institute of Atmospheric Physics, Academia Sinica, Beijing, People's Republic of China

## 1. INTRODUCTION

As for the question about the relative roles of various collection processes in the formation of cloud-droplet spectra, there have been many studies, such as Gu Zhenchao (1980) and de Almeida (1979a), but most of them confined to analysing the microphysical processes. However, in a cloud the formation of cloud-droplet spectra is affected heavily by various macro variables of cloud as well. Precisely because of this, we will put the question into a dynamic model of cumulus cloud to discuss in this paper. In addition, we will still analyse the physical process of the formation of bimodal cloud-droplet spectrum in the cloud.

## 2. MODEL

The one-dimensional and time-dependent cylindrical cumulus cloud model adopted in this paper is similar to Xu Huaying et al. (1983) in basic structures (or confer Takahashi, 1976). But according to our researching questions, the model is improved in some aspects.

The values of gravitational collision efficiency used here are those given by de Almeida (1979b) in the case of turbulent energy dissipation rate  $\epsilon = 0 \text{ cm}^2 \text{ s}^{-3}$  (pure gravitation). In addition, we will use the two collision efficiencies under  $\epsilon = 1$  and  $10 \text{ cm}^2 \text{ s}^{-3}$  and the electric collision efficiency, to discuss the effects of various collection processes on the formation of cloud-droplet spectra.

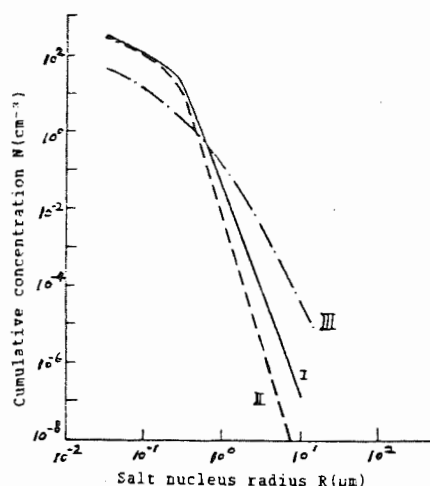


Fig.1. Initial dry salt nucleus spectra. Curves I and II represent the spectra of continental dry salt nuclei in the layers of from the ground to 200m height and from 200 to 4000m, respectively. Curve III represents the spectrum of maritime dry salt nuclei in the layer of the ground to 4000m height.

The environmental values are taken as the initial values of all variables in the cumulus air column. A cloud saturated initially from 400 to 1200m is stimulated by introducing a small disturbance updraft in the layer below 2000m. A typical, conditional, unstable stratification is used as environmental vertical distribution of temperature and humidity.

Here suppose that the cloud condensation nuclei are all taken as NaCl salt nuclei. Their radii are all greater than  $0.03125 \mu\text{m}$  and spectra are shown as Fig.1. The spectrum of maritime salt nuclei is that given by Woodcock (1972). The spectra of the continental salt nuclei with  $R \geq 1 \mu\text{m}$  are those given by Huang Meiyuan et al. (1982), and the spectra of  $R < 1 \mu\text{m}$  are given by extrapolating. The total concentrations of the nuclei are about  $300 \text{ cm}^{-3}$  for spectra I and II and about  $55 \text{ cm}^{-3}$  for spectrum III.

## 3. COMPUTATION RESULTS AND DISCUSSIONS

### 3.1 The Basic Characteristics of The Cloud-Droplet Spectra

It can be seen in Fig.2 that for both the droplet spectra of the continental cloud and those of the maritime cloud, they are all widening with height, their peak radii increasing and peak concentrations decreasing, only near the cloud top their widths decreasing again. These characteristics agree with the vertical distribution characteristics of macro variables of the modeling clouds (the figure is omitted). So it can be used that the characteristics of the widest cloud-droplet spectrum in cumulus cloud represent some basic characteristics of micro-structures of the cloud.

According to our computation results, it was found that in the cloud the total concentration of cloud-droplets changes smaller with height, however, the concentration of big droplet of  $R > 25 \mu\text{m}$  first increases with height and attains to its maximum in the middle-upper part of the cloud, and then decreases rapidly again.

### 3.2 The Bimodal Structure of The Cloud-Droplet Spectrum

Spectrum E in Fig.2a and that in Fig.2b show markedly bimodal structure. It is thus evident that the cloud-droplet spectra near the top of whether the continental or the maritime cumulus cloud appear this structure. The two peak radii in the continental case are about  $4 \mu\text{m}$  and  $10 \mu\text{m}$  at 15 min, while in the maritime case they are about  $4 \mu\text{m}$  and  $15 \mu\text{m}$ .

According to the macro-features of the modeling cumulus cloud, it can be known that at the height appearing bimodal spectra, there is a stronger divergent air-flow. In the divergent region, for the salt nuclei and

relatively dry air of environment, only a few of them can be entered into the inside of the cloud by turbulence process. Such air-flow structure is advantageous to the condensation growth of small cloud drop-lets and salt-nuclei in the cloud. So larger concentration of the cloud-droplets appears at the radius of about  $4 \mu\text{m}$ . Simultaneously, although a few of droplets with  $R > 10 \mu\text{m}$  are decreased because of being entrained into the outside cloud, the original shape and peak radius of the spectrum of large cloud-droplets are still remained. Therefore, a bimodal droplet spectrum appears there. So it can be thought that the appearing of bimodal droplet spectrum has to do with the entrainment process of cloud.

### 3.3 The Relative Roles of Various Collection Processes in The Formation of Cloud-Droplet Spectra

It was found from our computations that the effects of following various collection processes on the spectrum distributions of droplets in the continental cloud are much the same as those in the maritime cloud. So we will only give the computation results of the former case, shown as Fig.3 and Table 1, and discuss them in detail. Following the symbol NC denotes no collection (pure condensation),  $C_1$  the turbulent and gravitational collection in the case of  $\varepsilon = 1 \text{ cm}^2\text{s}^{-3}$ ,  $C_e$  the electric collection. And  $C_1C_e$  denotes the turbulent and gravitational collection in the case of  $\varepsilon = 1 \text{ cm}^2\text{s}^{-3}$  and the electric collection simultaneously. The rest is by analogy.

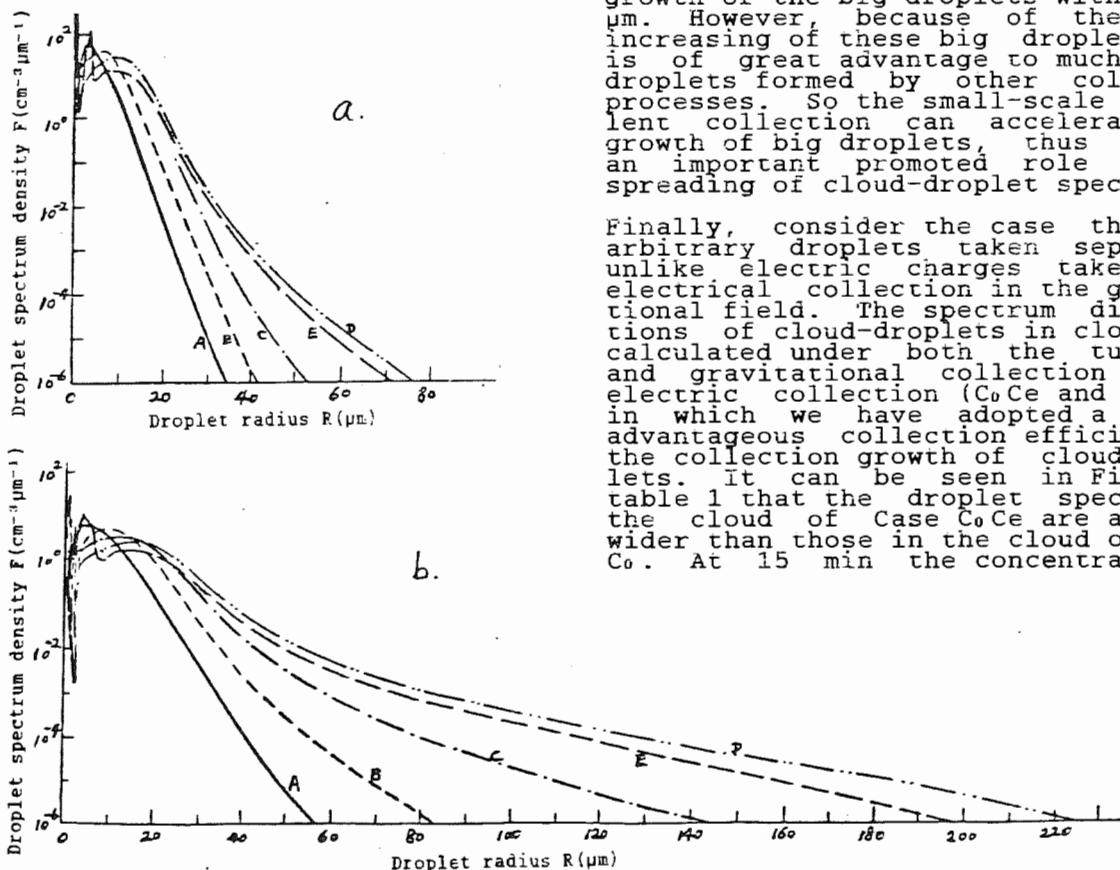


Fig.2. The distributions of cloud-droplet spectra in cumulus clouds at various heights (a. continental cloud; b. maritime cloud, both at 15 min). The symbols A, B, C, D and E represent the cloud-droplet spectra at 1000, 1400, 2000, 2600 and 2800 m height (the cloud base at 800m), respectively.

Firstly, Consider the case of the role of gravitational collection ( $C_0$ ). As a comparison, the case of no collection (NC) is also calculated. It can be seen in Fig.3 and Table 1 that under the consideration of the gravitational collection, the cloud-droplet spectra are much wider than those under only considering the condensation, and to the concentration of large cloud drop-lets, such as  $R \geq 40 \mu\text{m}$ , its growth rate is also increasing.

It can also be seen in Fig.3 and Table 1 that to the concentration of large cloud-droplets, its growth rate is increasing after considering small-scale turbulence. At 15 min the concentration of the droplets of  $R \geq 40 \mu\text{m}$  in Case  $C_1$  attains to  $2.91 \times 10^{-3} \text{ cm}^{-3}$  and that of  $R \geq 100 \mu\text{m}$  comes up to  $1.84 \text{ m}^{-3}$ , which are 3.6 times and 8.7 times larger than corresponding one in Case  $C_0$ . As to Case  $C_{10}$ , there are the same results as well. The above results show that in the spreading of the cloud-droplet spectra in the earlier developing stage of cumulus cloud, the collection caused by small-scale turbulence plays a greatly promoted role, which can make the growth rate of the concentration of large cloud droplets to be over three times larger than that one corresponding to the case of the gravitational collection process without considering turbulence.

Analysing the collection efficiencies under the three  $\varepsilon$  values given by de Almeida(1979b), we can know that there is a direct influence of small-scale turbulence mainly on the collection growth of the big droplets with  $R < 40 \mu\text{m}$ . However, because of the quick increasing of these big droplets, it is of great advantage to much bigger droplets formed by other collection processes. So the small-scale turbulent collection can accelerate the growth of big droplets, thus playing an important promoted role in the spreading of cloud-droplet spectra.

Finally, consider the case that two arbitrary droplets taken separately unlike electric charges take place electrical collection in the gravitational field. The spectrum distributions of cloud-droplets in clouds are calculated under both the turbulent and gravitational collection and the electric collection ( $C_0C_e$  and  $C_1C_e$ ), in which we have adopted a extreme advantageous collection efficiency to the collection growth of cloud droplets. It can be seen in Fig.3 and table 1 that the droplet spectra in the cloud of Case  $C_0C_e$  are a little wider than those in the cloud of Case  $C_0$ . At 15 min the concentration of

Table 1. The variables of the cloud-droplets at the heights of appearing the largest water contents (LWC) in continental cumulus clouds under the conditions of various collection processes. In this table, No.1, 2, 3, 4, 5 and 6 represent the collection processes of NC, C<sub>0</sub>, C<sub>1</sub>, C<sub>0</sub>Ce, C<sub>1</sub>Ce and C<sub>10</sub>, respectively. R denotes the cloud-droplet radius in  $\mu\text{m}$ .

Time	5 min						10 min						15 min					
	Droplet concent. ( $\text{cm}^{-3}$ )			LWC (g/kg)	Height (m)	Droplet concent. ( $\text{cm}^{-3}$ )			LWC (g/kg)	Height (m)	Droplet concent. ( $\text{cm}^{-3}$ )			LWC (g/kg)	Height (m)			
	20SR<40	40SR<100	100SR			20SR<40	40SR<100	100SR			20SR<40	40SR<100	100SR					
1	0.577	1.493E-7	7.578E-20	0.774	1400	2.460	1.113E-4	4.441E-17	1.245	2000	3.958	4.841E-4	7.616E-15	1.509	2600			
2	0.582	4.420E-7	1.475E-15	0.774	1400	2.474	9.326E-4	4.203E-12	1.245	2000	3.984	6.388E-3	1.932E-7	1.509	2600			
3	0.834	1.412E-6	2.137E-15	0.775	1400	3.213	4.413E-3	2.721E-11	1.246	2000	5.291	2.911E-2	1.839E-6	1.515	2600			
4	0.760	7.526E-7	1.664E-15	0.772	1400	2.932	1.554E-3	1.060E-11	1.240	2000	4.878	9.972E-3	4.790E-7	1.504	2600			
5	1.013	2.377E-6	2.263E-15	0.773	1400	3.663	6.625E-3	6.921E-11	1.241	2000	6.069	3.995E-2	4.053E-6	1.506	2600			
6	0.697	1.714E-6	1.404E-17	0.767	1400	2.917	6.528E-3	3.676E-11	1.233	2000	4.715	4.289E-2	2.499E-6	1.496	2600			

(\* here  $1.493\text{E}-7 = 1.493 \times 10^{-7}$ )

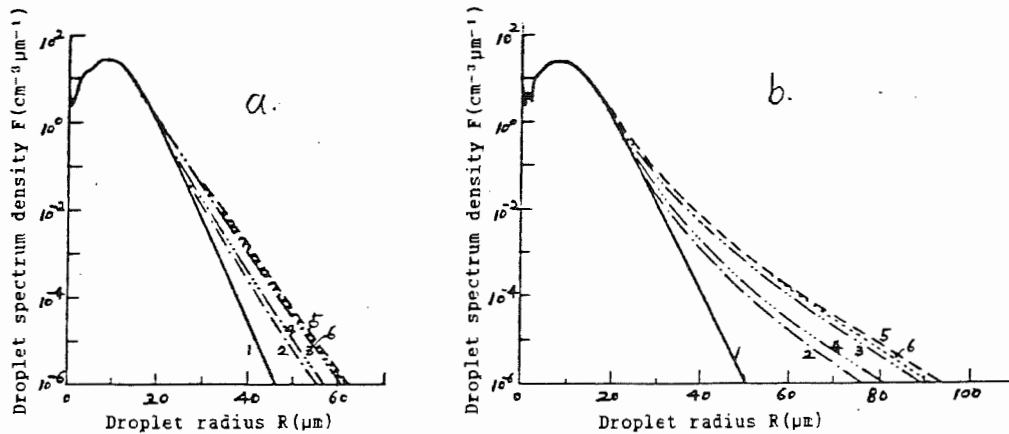


Fig.3. The cloud-droplet spectra in the continental cumulus clouds under the conditions of various collection processes (a. at 10 min and 2000m height; b. at 15 min and 2600m). Curves 1, 2, 3, 4, 5 and 6 in the Figure represent the collection processes of NC, C<sub>0</sub>, C<sub>1</sub>, C<sub>0</sub>Ce, C<sub>1</sub>Ce and C<sub>10</sub>, respectively.

the droplets of  $R \geq 40 \mu\text{m}$  and that of  $R \geq 100 \mu\text{m}$  in Case C<sub>0</sub>Ce are 0.56 times and 1.5 times larger than corresponding ones in Case C<sub>0</sub>. Similarly, at the same time, the concentration of the droplets of  $R \geq 40 \mu\text{m}$  and that of  $R \geq 100 \mu\text{m}$  in the cloud of Case C<sub>1</sub>Ce are 0.37 times and 1.2 times larger than corresponding ones in Case C<sub>1</sub>. These computation results show that the role of electric collection is not large, even if such great advantageous condition of the cloud-droplet growth as above was used. Therefore, it can be thought that there is no large role of the electric collection mechanism in the growth process of small cloud-droplet in the earlier developing stage of cumulus cloud.

#### 4. CONCLUSIONS

Based on the above analyses and discussions, we can obtain the several conclusions as follows.

1) The total concentration of cloud droplets in cumulus cloud has few changes with height, while the concentration of large cloud-droplets increases firstly with height in the middle-lower layer of cloud, and comes up to its maximum in the middle-upper part, and then decreases rapidly again.

2) The spectra of cloud-droplets near the cloud top have obvious bimodal structure, which has something to do with the entrainment characteristics between inside and outside of cloud at that height.

3) In the spreading of the cloud droplet spectra in the earlier developing stage of cumulus clouds, the gravitational collection process plays the most obvious role, the collection process caused by small-scale turbulence plays a greatly promoted role, which can accelerate the growth of big cloud-droplets, while the role of electric collection process is not significant.

#### REFERENCES

- de Almeida, F.C., 1979a: The effects of small-scale turbulent motions on the growth of a cloud droplet spectrum, *J. Atmos. Sci.*, 36: 1557-1563.
- de Almeida, F.C., 1979b: The collisional problem of cloud droplets moving in a turbulent environment--Part II. Turbulent collision efficiencies. *J. Atmos. Sci.*, 36: 1564-1576.
- Gu Zhenchao, 1980: *The Physics Fundamentals of Clouds, Fogs and Precipitation*. Science Press, Beijing, 1-29, 137-145 and 154-161.
- Huang Meiyuan et al., 1982: Distributions of giant salt nuclei inside and outside cloud over the basin of Xin An Jiang, *Scientia Atmospherica Sinica*, 6: 301-307. (in Chinese with English abstract)
- Takahashi, T., 1976: Warm rain, giant nuclei and chemical balance--A numerical model. *J. Atmos. Sci.*, 33: 269-286.
- Woodcock, A.H., 1972: Smaller salt particles in oceanic air and bubble behavior in the sea. *J. Geophys. Res.*, 77: 5316-5321.
- Xu Huaying et al., 1983: A study on the growth of cloud droplets by condensation in cumulus clouds. *Scientia Atmospherica Sinica*, 7: 249-259. (in Chinese with English abstract)

# Some Outstanding Problems on the Influence of Clouds on Radiation

Graeme I. Stephens

*Department of Atmospheric Science, Colorado State University, Fort Collins, CO 80523*

## 1. Introduction

The interaction of radiation with clouds is a topic of considerable interest to both the atmospheric radiation and cloud physics communities. It is also a topic germane to problems encountered in remote sensing and satellite meteorology and is of great importance in studies of climate and climate change. For many problems it is not only the manner in which clouds influence the radiative transfer processes that is important but also the way in which radiation might in turn change cloud is also crucial. The link between these two types of problems lies in the way that radiative transfer processes are related to the micro- and macro-properties of the cloud. This paper reviews some of the outstanding issues that impact on our ability to provide a meaningful description of the radiative processes in cloud both from the point of view of characterizing the radiative energy budgets of clouds and from the perspective of the remote sensing of cloud properties.

## 2. Relationship between radiative processes and microphysics

The two important parameters that influence the radiative transfer through clouds are cloud optical thickness  $\tau$ , a product of the geometric depth ( $\Delta z$ ) and extinction coefficient ( $\alpha$ ), and the single scatter albedo  $\tilde{\omega}_0$ . The bulk radiative properties of cloud, such as the albedo  $\mathcal{R}$  and absorptance  $\mathcal{A}$  depend on the combination of these parameters in the form (Ackerman and Stephens, 1987)

$$\mathcal{R}, \mathcal{A} \rightarrow (1 - \tilde{\omega}_0)\tau. \quad (1)$$

Thus parameterization of the cloud albedo, radiative heating and cooling and emission in terms of cloud properties requires some sort of relationship between  $\alpha$  and  $\tilde{\omega}_0$  and these cloud properties. The relation between  $\alpha$  and  $\tilde{\omega}_0$  and the cloud microphysics is now discussed.

### 2.1 Volume extinction

Volume extinction is related to the cloud microphysics through the formula

$$\alpha = \int_0^\infty n(\ell)a(\ell)Q_{ext}d\ell \quad (2)$$

where  $n(\ell)$  is the cloud particle size distribution,  $\ell$  is some characteristic size of the cloud particle,  $Q_{ext}$  is the extinction efficiency and  $a(\ell)$  is the cross sectional area of the particle of size  $\ell$ . Consider spherical cloud droplets for the present discussion. Under many circumstances  $Q_{ext} \approx 2$  and (2) becomes

$$\alpha \approx 2A, \quad (3)$$

where  $A$  is the cross sectional area of the distribution  $n(r)$  where  $r$  is now the droplet radius. Current radiation parameterizations relate the properly  $\alpha$  to the cloud liquid water content  $w$  through the relationship

$$\alpha \sim \frac{3w}{2r_e}, \quad (4)$$

where  $r_e$  corresponds to the volume  $V$  to area  $A$  ratio of the size distribution. The extent to which  $\alpha$  can be parameterized solely in terms of  $w$  alone depends on the degree that  $V$  and  $A$  are correlated, and thus the extent to which  $r_e$  is determined by  $w$ . To illustrate the relationships between  $V$  and  $A$ , consider  $n(r)$  as given by

$$n(r) = \text{const.}r^{\beta-1}e^{-r/a}. \quad (5)$$

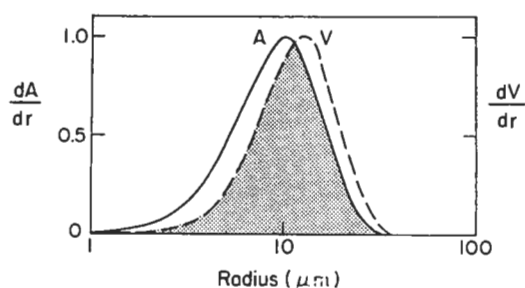


Fig. 1 Surface ( $S$ ) and volume ( $V$ ) distributions based on the size distribution expressed by (5) with  $\beta = 3$  and  $a = 10\mu\text{m}$ . Note that the contributions to most of the total area and volume come from contributions by particles of the same size (shaded region).

Fig. 1 shows the cross sectional area and volume distributions calculated using (5) as a function droplet radius and demonstrate a high degree of correlation for the example given. However, the relationship between  $V$  and  $A$  varies considerably according to  $n(r)$ . Consider a distribution of the type

$$n(r) \approx C_1 r^{\beta-1} e^{-r/a_1} + C_2 e^{-r/a_2} \quad (6)$$

which has an elongated large particle tail. The extent to which  $A$  and  $V$  overlap for this case depends on the relative concentrations of small to large particles (Fig. 2).

The simple analysis given above emphasizes current problems encountered in radiation modeling and parameterization of cirrus cloud in particular. Among these are:

- the need to know the abundance of small ice particles and the ratio of small to large ice particle concentrations (Fig. 3). This information then provides some indication of whether the radiative properties of ice clouds can be expected to be functions of ice water path alone. The example given in Fig. 2a is one for which this relationship would not be expected to be unique.

- The extent to which scattering properties like  $Q_{ext}$  depend on crystal habit and if so what is the "characteristic" dimension of the crystal?

Another example that provides for ambiguous radiation - cloud water relationships is now illustrated. Twomey (1977) noted that the effects of pollution on radiation might be most notable through the influence of pollution on cloud microphysics rather than directly

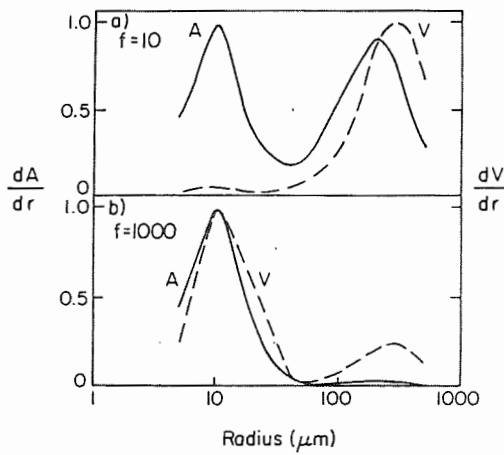


Fig. 2 Surface (*S*) and volume (*V*) distributions based on the size distribution expressed by (6) with  $\beta = 3$ ,  $a_1 = 10\mu\text{m}$  and  $a_2 = 100\mu\text{m}$  and for different ratios of  $C_1$  to  $C_2$ . These ratios are expressed by the factor  $f$  which is the ratio of small to large particles. For large values of  $f$ ,  $A$  and  $V$  are highly correlated (b).

on radiation itself. Twomey argued that an increase in pollution generally implied an increase in cloud nucleus concentrations and thus to an increase of cloud droplets. A more colloiddally stable cloud, according to (4), has associated with it a smaller  $r_e$  for the same liquid water content; this leads to an increase of optical thickness and hence an increase of cloud albedo - the latter depending to some extent on the absorption characteristics of the aerosol. This argument seems to be supported in AVHRR satellite images of  $3.7\mu\text{m}$  radiation which clearly show the localized effects of ship tracks on cloud albedo (Coakley, et al., 1987).

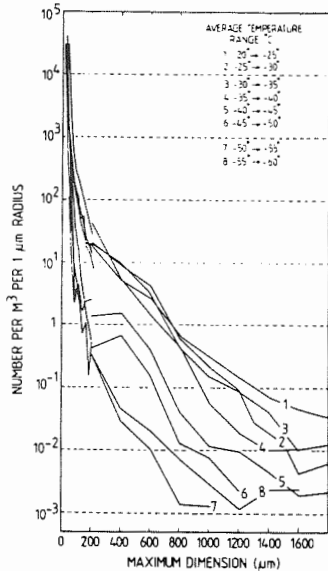


Fig. 3 The size distribution of ice crystals with a the maximum dimension range of 20 - 1800 $\mu\text{m}$  and for the eight temperature ranges indicated.

## 2.2 The single scattering albedo

The single scattering albedo  $\tilde{\omega}_o$  is also an important parameter as it characterizes the absorption of a single cloud particle or a small volume of cloud containing a distribution of particles. Unfortunately the dependence of the single scatter albedo on the size distribution  $n(r)$  is extremely complex. Ackerman and Stephens (1987) using a simplified scattering theory were able to demonstrate

that

$$1 - \tilde{\omega}_o \sim 1 + c\kappa^{-1}r_e^p \quad (7)$$

where  $\kappa$  is the absorption coefficient for water and  $c$  and  $p$  are constants. Those authors demonstrated that  $p$  in fact depends on the strength of absorption, i.e., on  $\kappa$  (Fig. 4) and therefore provided an illustration and understanding of how the bulk absorption and reflection properties of clouds depend on  $r_e$  and the vertically integrated liquid water path (Fig. 5). Understanding these kind of relationships are especially crucial in those studies that attempt to deduce various cloud properties using remote sensing techniques.

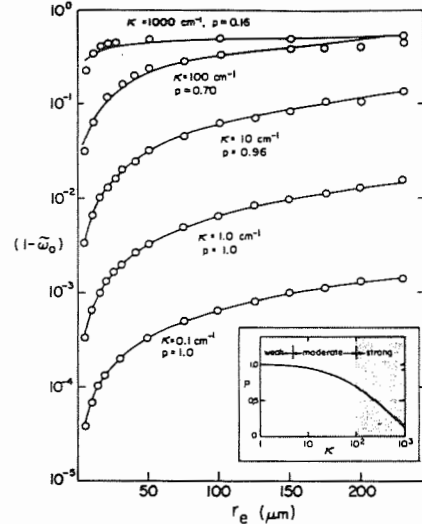


Fig. 4 Cosingle scattering albedo as a function of effective radius for selected values of  $\kappa$ . The solid curves represent the relationship described by (7) for the values of  $p$  indicated and the open circles apply to a scattering theory. The insert depicts the breakdown of the weak, moderate and strong absorption regimes (Ackerman and Stephens, 1987).

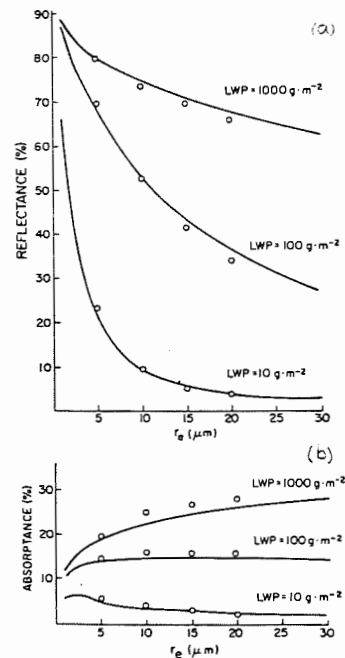


Fig. 5 Spectrally integrated ( $0.7\mu\text{m}$ ) values of (a) reflectance and (b) absorptance as a function of  $r_e$  for 3 values of integrated liquid water (LWP) (Ackerman and Stephens, 1987).

A number of issues thus emerge in our attempt to tie the radiative processes to cloud microphysical properties

- to what extent can  $\tilde{\omega}_o$  be parameterized solely in terms of cloud liquid water content?
- Can simple  $\tilde{\omega}_o$ -size relations like (7) be derived for non spherical ice particles?
- If so, to what extent can the bulk radiative properties of ice cloud be characterized in terms of ice water path?

A particularly vexing problem that seems to have grown over the years is the so called shortwave absorption paradox and perhaps points to current problems in specifying  $\tilde{\omega}_o$ . The paradox can be simply stated: many measurements of cloud absorption considerably exceed the largest values obtained from theory (Fig. 6). There are several reasons to be concerned with this general lack of agreement:

- absorption of solar radiation by some clouds is not negligible and can be as large as the cloud top longwave cooling,

- it is a measure of the uncertainty in our understanding of either the radiative transfer within cloud, or the microphysical structure of the cloud or both,

- it creates major uncertainties in the development of cloud remote sensing methods which are based on spectral measurements (e.g., Stephens and Platt, 1987 (Fig. 7)).

The explanations of the paradox range from

- lack of fidelity in measurements,
- improper characterization of the cloud microphysics in the calculation - large droplets and absorbing aerosols can enhance absorption, and
- heterogeneity of the cloud and the inappropriateness of the assumption of horizontal homogeneity in the calculations.

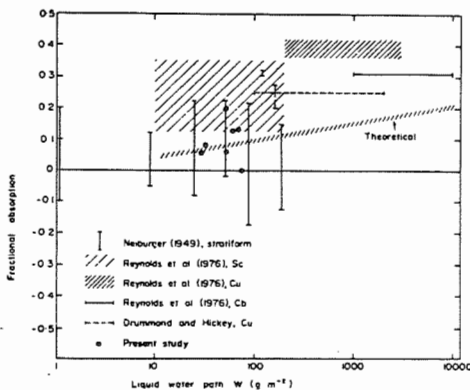


Fig. 6 Comparison of measured and calculated fractional shortwave absorption as a function of liquid water path. The shading about the line is the expected variability which may arise from differences in cloud type. The horizontal and vertical line, boxes and points are measured values (Stephens, 1978).

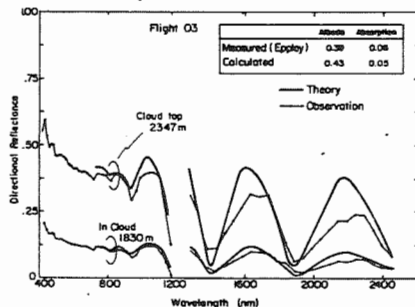


Fig. 7 Comparison of theoretically calculated and observed spectral bidirectional reflectance from stratocumulus clouds (Stephens and Platt, 1987).

### 3. Impact of Cloud Morphology On Radiative Transfer

The motivation for much of this work has come from the climate community who desire to characterize the bulk radiative properties of the atmosphere on some scale (hundreds of kilometers) which is typically larger than that associated with cloud structure. However, the same issues arise in cloud modeling in which the averaged radiative budget of the cloud is required over some scale (the model resolution). The subgrid scale structure that must be treated is done so in terms of the areal cloud coverage parameter  $H$  using some type of *ad hoc* relationship

$$A = A_o(1 - H) + A_c H \quad (8)$$

where  $A$ ,  $A_o$  and  $A_c$  are respectively the grid point radiative property,  $A_o$  the clear sky value and  $A_c$  the cloudy sky value. Yet (8) has no physical or theoretical basis. Even more significant, there is no unique relationship between  $A$  and  $H$ . Therefore, the issues that emerge are:

- What subgrid scale information do we need to characterize  $A$ ?  $H$  is not sufficient (and may not even be necessary).

- What is the form of the relationship between these new parameters and  $A$ ?

- How is this information connected to larger scale atmospheric variables?

Theoretical and observational studies have demonstrated that the radiative properties of cloud for most cases can be related to the vertically integrated cloud water in the more or less well defined way although it was noted above that exceptions to this relationship do exist. Other studies have also shown that the manner in which this water is distributed horizontally also significantly influences the characteristic radiative properties of the atmosphere. Results will be shown that demonstrate how cloud absorption, for instance, is organized in the horizontal according to the distribution of cloud liquid water content. It therefore seems that the radiation response in cloud is more intimately related to cloud structure including the organized scales of motion and turbulent scales of motion than previously thought.

### 4. Acknowledgement

This work was supported by the Atmospheric Sciences Section of the National Foundation under Contracts ATM-8519160 and ATM-8415127.

### 5. References

- Ackerman, S. A. and G. L. Stephens, 1987: The Absorption of Solar Radiation by Cloud Droplets: An Application of Anomalous Diffraction Theory. *J. Atmos. Sci.*, **44**, 1574-1588.
- Coakley, J., R. L. Bernstein, P. A. Durkee, 1987: Effect of ship-stack effluents on cloud reflectivity. *Science*, **37**, 1020-1022.
- Heymsfield, A. and C.M.R. Platt, 1984: A Parameterization of the particle size spectrum of ice clouds in terms of the ambient temperature and the ice water content. *J. Atmos. Sci.*, **41**, 849-855.
- Stephens, G. L. and C.M.R. Platt. 1987: Aircraft Observations of the Radiative and Microphysical Properties of Stratocumulus and Cumulus Cloud Fields. *J. Climate and Appl. Meteor.*, **26**, 1243-1269.
- Twomey, S., 1977: The influence of pollution on the shortwave albedo of cloud. *J. Atmos. Sci.*, **34**, 1149-1152.

THEORY ON THE UNCERTAINTY IN CLOUD MIROPHYSICAL PROCESSES AND CLIMATE

Kuo-Nan Liou and Szu-cheng S. Ou

Department of Meteorology, University of Utah  
Salt Lake City, Utah 84112, U.S.A.

1. INTRODUCTION

The objective of this paper is to investigate the interactive role of clouds and precipitation processes in a climate model. Section 2 presents the basic model structure and parameterizations for condensation, evaporation, and precipitation. Results simulated from the cloud-climate model are discussed in Section 3, where the potential link between microphysical cloud processes and climate is theorized. Finally, conclusions are given in Section 4.

2. THE CLOUDS AND CLIMATE MODEL

The present model for the investigation of the role of clouds and precipitation in climate is based on the 1-D climate model developed by Liou et al. (1985). However, we have modified the model by incorporating cloud liquid water and precipitation equations. In addition, we have also developed parameterization equations for condensation, precipitation, and evaporation terms, based on fundamental cloud microphysical processes in connection with the climate model. The basic 1-D, steady-state equations for the specific humidity  $q$ , cloud liquid water  $q_m$ , and precipitation flux  $\tilde{P}$  may be written in the forms

$$\frac{\partial}{\partial z} (\rho \overline{w'q'}) = -\eta \rho Q_c - (1-\eta) \rho E_r, \quad (1)$$

$$\frac{\partial}{\partial z} (\rho w_c q_m) = \eta \rho Q_c - \eta \rho P, \quad (2)$$

$$\frac{\partial}{\partial z} (\eta \tilde{P}) = \eta \rho P - (1-\eta) \rho E_r, \quad (3)$$

where  $\rho$  is the air density,  $\eta$  the cloud cover,  $Q_c$ ,  $E_r$ , and  $P$  the rates of condensation, evaporation, and precipitation generation,  $w_c$  the vertical velocity in the cloudy region, and  $\rho \overline{w'q'}$  the eddy flux of the specific humidity.

Let  $w_0$  and  $q_0$  denote the vertical velocity and specific humidity, respectively, in the clear region. It is assumed that there is a uniform distribution of large-scale parameters in clear and cloudy regions. This assumption has been widely used in the parameterization of cumulus convection. Thus, the eddy flux of the specific humidity  $\rho \overline{w'q'} = \eta w_c q_c + (1-\eta) w_0 q_0$ , where the specific humidity in the cloudy region  $q_c \approx q_s(T)$ , the saturation specific humidity. The horizontal averages of temperature  $T$ , specific humidity  $q$ , and vertical velocity  $w$ , may be expressed by  $\chi = \eta \chi_c + (1-\eta) \chi_0$ , where  $\chi$  can be  $T$ ,  $q$ , or  $w$ . For

large-scale cloud formation, we may safely assume that  $T_c = T_0 = T$ . Since there should be no vertical displacement in 1-D space, the vertical velocity  $w = 0 = \eta w_c + (1-\eta) w_0$ . Thus,  $w_0 = -\eta w_c / (1-\eta)$ . The vertical velocity in the cloudy region can be derived from Richardson's equation in a manner described in Liou et al. (1985). Finally, based on the horizontal averaging procedure, the cloud cover is related to the specific humidity in the form  $\eta = (q/q_s - h_0) / (1 - h_0)$ , where  $h_0 = q_0/q_s$  denotes the threshold relative humidity. The threshold relative humidity is parameterized in terms of its surface value in the form,  $h_0 = h_0(p^*) [(p/p^* - 0.02) / 0.98]$ , where  $p^*$  denotes the surface pressure, and  $h_0(p^*)$  is set to be 0.8.

On the basis of the steady-state, 1-D diffusion theory for water vapor and latent heat transports, the rate of condensation for a given particle size distribution may be expressed by

$$Q_c = k_c (q/q_s - 1), \quad (4)$$

where  $k_c$  represents the rate coefficient for condensation, which is a function of the mean particle radius  $\bar{r}$  and temperature. The rate of precipitation generation due to autoconversion and accretion, according to the collision theory, may be derived in the form

$$P = (k_1 + k_2 \tilde{P}^{0.791}) q_m, \quad (5)$$

where the rate coefficient for autoconversion,  $k_1 \approx 1.5 \times 10^{-7} \bar{r}^4$  ( $\mu\text{m}^{-4} \text{sec}^{-1}$ ), and  $k_2 \approx 0.931 \rho^{-0.105}$ , using the Marshall and Palmer rain-drop size distribution. This parameterization equation is similar to that developed by Kessler (1969) and Ogura and Takahashi (1971) for thunderstorm clouds, except that  $k_1$  in the present formulation is a function of the mean radius to the fourth power.

The time rate of change of mass for raindrops due to evaporation may be expressed in an equation analogous to the one for condensation. Including a ventilation factor (Beard and Pruppacher, 1971), we find

$$E_r = (k_{e1} \tilde{P}^{0.417} + k_{e2} \tilde{P}^{0.604}) (1 - q/q_s), \quad (6)$$

where the evaporation rate coefficients  $k_{e1}$  and  $k_{e2}$  are functions of the air density and temperature.

The rates of condensation, evaporation,

and precipitation generation are now parameterized in terms of the specific humidity  $q$ , cloud liquid water content  $q_m$ , and precipitation flux  $\bar{P}$ . The rate coefficients  $k_c$ ,  $k_{e1}$ , and  $k_{e2}$  are functions of temperature and are therefore interactive with the perturbation due to radiative forcings through the thermodynamic equation containing temperature and solar and IR fluxes.

### 3. NUMERICAL RESULTS AND THEORY ON THE ROLE OF CLOUD MICROPHYSICAL PROCESSES IN CLIMATE

In order to simulate the present mean annual condition (control run), we have used the following input data: a solar constant of  $1360 \text{ W m}^{-2}$ , average cosine of the solar zenith angle of 0.5, duration of sunlight of 12 h, surface albedo of 0.13, and  $\text{CO}_2$  concentration of 330 ppmv. The ozone and molecular profiles used correspond to the standard atmospheric condition. Parameterizations of the radiative properties of clouds and the scheme for the cloud cover follow those described in Liou et al. (1985). Moreover, based on the observed particle size distributions, we have assumed (climatological) mean particle radii  $\bar{r}_c$ , of 4, 5, and  $25 \mu\text{m}$  for low, middle, and high clouds, respectively.

In the control run, the temperature and specific humidity profiles computed from the model compare closely with climatological data. The liquid water contents simulated from the model are  $0.23$ ,  $0.14$ , and  $0.006 \text{ g m}^{-3}$  for low, middle, and high clouds, respectively. These values agree with the observed data presented by Matveev (1984). The total cloud cover and annual precipitation generated from the 1-D globally averaged model also agree well with climatological data.

In the perturbation experiments, we uniformly increase and decrease the climatological mean particle radii for all three cloud types by a value  $\Delta\bar{r} (= \bar{r} - \bar{r}_c)$  ranging from 0 to  $3 \mu\text{m}$ . We use a doubling of the  $\text{CO}_2$  concentration as the initial radiative forcing to investigate the effects and feedbacks of the mean particle radius on the climatic temperature perturbation. The results are illustrated in Fig. 1. For the fixed cloud cover, liquid water content, and mean particle radius, a doubling of  $\text{CO}_2$  produces a temperature increase  $\Delta T$  of  $2.3^\circ\text{C}$ , which is referred to as the standard temperature change. In our previous studies, we illustrated that the introduction of an interactive cloud cover program (Liou et al., 1985) and/or an interactive cloud liquid water content program (Ou and Liou, 1987), in connection with the climate model, leads to negative feedbacks. Increased temperatures will cause the surface evaporation to increase. Subsequently, cloud cover and liquid water content also increase, and less solar radiation is absorbed by the atmosphere and surface. Thus, clouds appear to stabilize the temperature perturbation due to the anticipated increase in  $\text{CO}_2$  concentration.

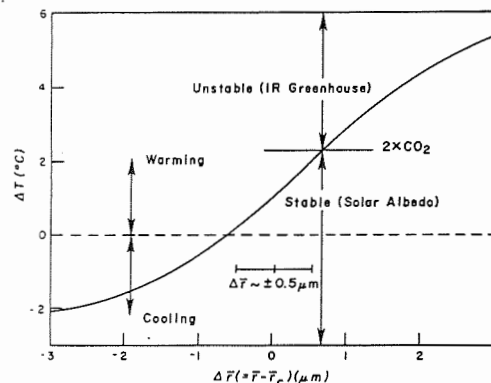


Fig. 1 Perturbation temperature change  $\Delta T$  as a function of the deviation from the climatological mean cloud particle radius  $\bar{r}_c$  resulting from a doubling of  $\text{CO}_2$ . The solid line ( $2\times\text{CO}_2$ ) denotes the standard temperature change when cloud cover, liquid water content, and mean particle radius are fixed in the experiment.

However, if we allow the cloud particle radius to vary in the interactive cloud and precipitation program, several temperature perturbations occur. If the perturbed cloud particle radius is within about  $0.5 \mu\text{m}$ ,  $0 < \Delta T < 2.3^\circ\text{C}$ , implying that the perturbation due to a doubling of  $\text{CO}_2$  is stabilized because of an increase in cloud cover and liquid water content. In this case, the solar albedo effects predominate and the presence of clouds produces a negative feedback to the climate system. If, however,  $\Delta\bar{r} > 0.5 \mu\text{m}$ , there would be a possibility for a runaway greenhouse effect, that is, the radiative forcing produced by a doubling of  $\text{CO}_2$  could produce a surface warming of  $5.6^\circ\text{C}$  (as opposed to  $2.3^\circ\text{C}$  when feedbacks from clouds were not considered) in the case when  $\Delta\bar{r} = 3 \mu\text{m}$ . On the other hand, if the perturbed particle radius  $\bar{r}$  is less than  $\bar{r}_c$  by  $0.5 \mu\text{m}$ , cooling instead of warming occurs when  $\text{CO}_2$  is doubled. The surface temperature could be cooled by as much as  $-2^\circ\text{C}$  due to a significant increase in cloud cover and liquid water content. Thus, there would be a possibility for the occurrence of an ice age.

On the basis of the preceding results, simulated from a 1-D climate model with an interactive cloud formation and precipitation program, the statistical and stochastic nature of cloud microphysical processes and their potential link to climate are theorized. Our theory is derived from the fact that the initiation of precipitation is directly proportional to the fourth power of the mean cloud particle radius.

Theory 1: If the perturbed mean cloud particle radius  $\bar{r}$  is less than the climatological mean cloud particle radius  $\bar{r}_c$ , precipitation decreases, leading to increases in cloud cover and liquid water content. Thus, the solar albedo effects outweigh the IR greenhouse effects. The perturbed temperature due to a positive radiative forcing is stabilized.

Theory 2: If the perturbed mean cloud particle radius  $\bar{r}$  is larger than the climatological mean cloud particle radius  $\bar{r}_c$ , precipita-

tion increases, leading to decreases in cloud cover and liquid water content. Thus, the IR greenhouse effects outweigh the solar albedo effects. The perturbed temperature due to a positive radiative forcing is amplified.

#### 4. CONCLUSIONS AND HYPOTHESES ON THE UNCERTAINTIES IN CLOUD MICROPHYSICAL PROCESSES

In Section 3, we theorized about the effects of clouds/radiation on climatic temperature perturbations based on the deviation of the perturbed cloud particle radius from the climatological mean value. We pointed out that cloud cover and liquid water content are directly related to precipitation processes, which are governed by the mean particle radius. In particular, we illustrated that the rate of precipitation generation is directly proportional to the fourth power of this radius. In the context of a 1-D cloud/radiation climate model, we further showed that uncertainties in the parameterized growth equations are largely attributable to uncertainties in the assumed particle size distribution. These uncertainties, in our view, are statistical and stochastic in nature and cannot be predicted entirely by the thermodynamic and dynamic laws governing the formation of clouds and precipitation.

In connection with our theories on the link between microphysical cloud processes and the stability of the climate and climatic perturbations, we propose the following two probabilities for perturbations of the climatological mean particle radius due to temperature feedbacks:

Hypothesis 1: The reaction rate involving the formation of embryonic sulfuric acid nuclei increases due to greenhouse warming. More nuclei are available to compete for water vapor, resulting in small cloud particles. The probability of the production of precipitation reduces and, at the same time, cloud cover and liquid water content increase in the atmosphere (stable climate).

Hypothesis 2: The condensation rate coefficient increases due to greenhouse warming. This leads to an increase in cloud liquid water content. There is a probability that large cloud particles could form and increase the production of precipitation. Subsequently, cloud cover and liquid water content decrease in the atmosphere (unstable climate).

In summary, the cloud mean particle radius is one of the critical elements that control the stability of the climate and climatic perturbations. Thus, we must develop a climatology of the mean particle radius for clouds over the globe in order to understand the role of clouds in climate.

#### 5. ACKNOWLEDGMENTS

This research was supported by NASA Grant NAG-732 and Air Force Office of Scientific Research Grant AFOSR-87-0294. Sharon Bennett typed and edited the manuscript.

#### REFERENCES

- Beard, K.V. and H.R. Pruppacher, 1971: A wind tunnel investigation of the rate of evaporation of small water drops falling at terminal velocity in the air. J. Atmos. Sci., 28, 1455-1464.
- Kessler, E., 1969: On the Distribution and Continuity of Water Substance in Atmospheric Circulations. Meteor. Mongr., No. 32, American Meteorological Society, 84 pp.
- Liou, K.N., S.C. Ou and P.J. Lu, 1985: Interactive cloud formation and climatic temperature perturbations. J. Atmos. Sci., 42, 1969-1981.
- Matveev, L.T., 1984: Cloud Dynamics. D. Reidel, Dordrecht, Holland, 340 pp.
- Ogura, Y. and T. Takahashi, 1971: Numerical simulation of the life cycle of a thunderstorm cell. Mon. Wea. Rev., 99, 895-911.
- Ou, S.C. and K.N. Liou, 1987: Effects of interactive cloud cover and liquid water content programs on climatic temperature perturbations. Atmospheric Radiation: Progress and Prospects, Science Press, Beijing, China, 433-440.

## IN SITU MEASUREMENTS OF "SHIP TRACKS"

Lawrence F. Radke, Jamie H. Lyons and Peter V. Hobbs  
Atmospheric Sciences Department, University of Washington  
Seattle, Washington 98195 USA  
and  
James E. Coakley  
National Center for Atmospheric Research  
Boulder, Colorado 80307 USA

### 1. INTRODUCTION

It has long been known that cloud droplet concentrations are strongly influenced by cloud condensation nuclei (CCN) (Twomey and Warner, 1967) and that anthropogenic sources of pollution can affect CCN concentrations (Radke and Hobbs, 1976). More recently it has been suggested that CCN may play an important role in climate through their effect on cloud albedo (Twomey et al., 1984; Charlson et al., 1987).

An interesting example of the effect of anthropogenic CCN on cloud albedo is the so-called "ship track" phenomenon. Ship tracks were first observed in satellite imagery when the ship's emissions were evidently needed for the formation of a visible cloud (Conover, 1966). However, they appear more frequently in satellite imagery as modifications to existing stratus and stratocumulus clouds. The tracks are seen most clearly in satellite imagery by comparing the radiance at  $3.7 \mu\text{m}$  with that at  $0.63$  and  $11 \mu\text{m}$  (Coakley et al., 1987). To account for the observed change in radiance, droplet concentrations must be high, and the mean size of the droplets small, in ship tracks.

In this note we describe what we believe to be the first *in situ* measurements in what appears to have been a ship track.

### 2. OBSERVATIONS

During the FIRE study of marine stratus off the coast of California in the summer of 1987, a number of ship-tracks were detected with  $3.7 \mu\text{m}$  satellite radiance measurements. Interceptions of ship track-like features by the University of Washington's C-131A research aircraft were made on July 2, 7 and 10. The July 10 case is described here.

On July 10 a ship track-like feature (hereafter referred to as "the feature") was penetrated by the aircraft between 1557 and 1615 UTC in the vicinity of  $32^\circ\text{N}$  and  $120^\circ\text{W}$ . The surface synoptic situation was dominated by a subtropical high off the California Coast with the winds from the N-NW. The GOES satellite imagery showed rather uniform stratocumulus in the area. Several ship track-like features are visible in the GOES 2015 UTC imagery. The satellite image that is closest in time to our aircraft observations is the NOAA-10 satellite imagery for 1537 UTC. This shows a linear track near the feature that we intercepted, however, there is a possibility that the feature on the satellite imagery is a mesoscale cloud boundary.

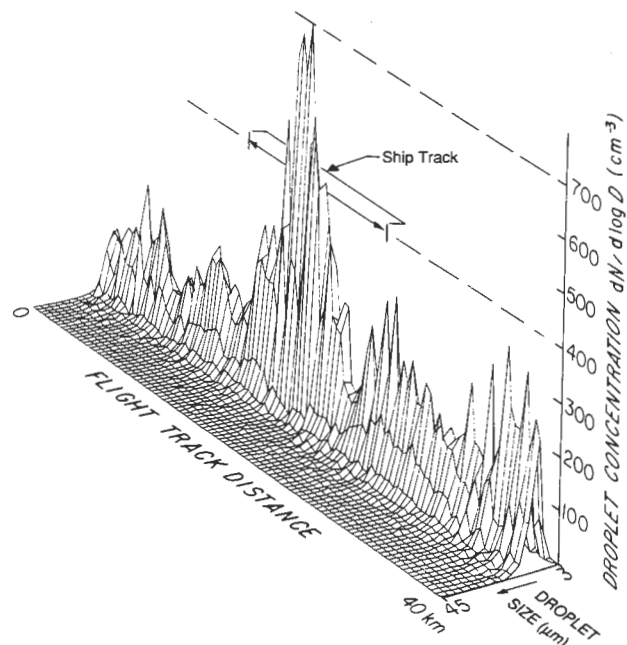


Figure 1: Cloud drop size distributions in 3-D perspective across the ship track-like feature on 10 July 1987.

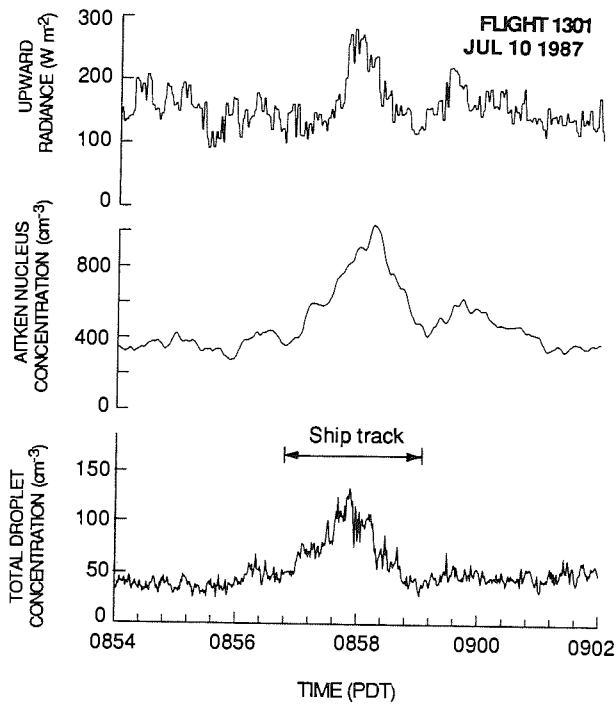


Figure 2: Total cloud drop concentrations, Aitken nucleus concentrations and broadband upward radiance measurements across the ship track-like feature on 10 July 1987.

The first aircraft penetration of the ship track-like feature was made at 1557 UTC, when the aircraft was located about midway between the top and bottom of a stratocumulus layer about 500 m thick. The change in the drop size distribution across the feature is clearly revealed by the microphysical measurements shown in Fig. 1. The feature can also be seen in Fig. 2, where total drop concentrations are shown. The increase in liquid water content in the feature was about 30%.

Also shown in Fig. 2 are measurements of Aitken nucleus concentrations, which show a sharp increase across the feature. The Aitken nucleus measurements were made within the cloud and represent mainly the cloud interstitial aerosol (Radke, 1983). However, a fraction of these nuclei may be the evaporated residues of cloud drops. Hence, while in cloud, a modest correlation is to be expected between drop and Aitken nucleus concentrations. Nevertheless, the sharp increase in Aitken nuclei in the feature must have been due to a dramatic increase in interstitial particles, particles that did not serve as CCN in the cloud. Such particles could well have been combustion products from a ship's engine.

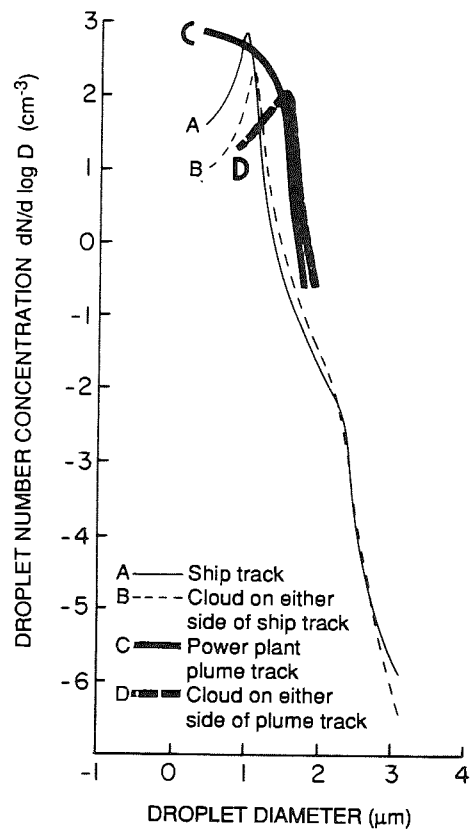


Figure 3: Cloud droplet size distributions averaged across (A) and on either side of (B) the ship track-like feature on 10 July 1987. Overprinted are corresponding data showing the effect on a cloud of the emissions from a coal-fired electric power plant (from Hobbs et al., 1980).

Coincident with the feature was an average increase of ~ 16% in upward radiance detected by the Eppley broad-band radiometer aboard the aircraft (Fig. 2). Coakley et al. (1988) show that the change in upward radiance,  $\Delta R$ , is related to a change in cloud drop concentration  $\Delta N$  by:

$$\Delta R \approx \frac{1}{12} \frac{\Delta N}{N} \quad (1)$$

Substituting the value of  $\frac{\Delta N}{N} (= \frac{100}{50})$  from our measurements into (1) yields  $\Delta R \approx 17\%$ .

### 3. DISCUSSION

Is it feasible that the modifications to the cloud structure described above could have been produced by emissions from a ship? In Fig. 3 we show the drop size distributions measured in and on either side of the feature. Also shown in Fig. 3 for comparison, are

measurements of the effect on the cloud drop size distribution of the emissions from a 1000 MW coal-fired electric power plant on a cloud 13 km downwind of the plant (data from Hobbs et al., 1980). It can be seen that the two effects are similar. Hobbs et al. calculated that the flux of CCN active at 0.2% supersaturation from the coal power plant, including gas-to-particle conversion in the plume, was  $\sim 10^{16} - 10^{17} \text{ s}^{-1}$ . This is a large source of CCN, comparable to the emissions from a large urban area or industrial complex (Radke and Hobbs, 1976).

Assuming a ship speed of  $10 \text{ m s}^{-1}$ , and using the measurements of 16 km and  $\sim 500 \text{ m}$  for the width and depth, respectively, of the feature, and an increase in droplet concentration in the feature of  $100 \text{ cm}^{-3}$ , we calculate that in order for a ship to produce the observed changes in drop concentrations it would have had to produce  $\sim 10^{16} \text{ CCN s}^{-1}$ . This requires the ship to be a very large (perhaps unreasonably large) source of CCN. However, in addition to fuel combustion, a ship can cause CCN to be lofted into the atmosphere by generating sea-salt particles through cavitation, splashing and bubble bursting. Particle production by these processes can produce substantial numbers of particles in the  $0.1 - 1 \mu\text{m}$  size range (Radke, 1977). Since these particles serve as very efficient CCN, they could augment the combustion products from a ship and thereby play a role in the formation of ship tracks. Also, the dynamic effects suggested by the increase in liquid water content in the feature would increase the supersaturation in the cloud and thereby activate additional CCN. A ship might also loft additional water vapor through emissions and/or stirring of the boundary layer.

Despite these various means by which ships might modify clouds, we have to conclude that ship tracks are a surprising phenomenon that is not yet fully explained.

*Acknowledgments.* This work was supported by National Science Foundation Grant ATM-8615344.

#### 4. REFERENCES

CHARLSON, R. J.; LOVELOCK, J. E.;

ANDREAE, M. O.; WARREN, S. G.: Oceanic

phytoplankton, atmospheric sulfur, cloud albedo and climate. *Nature*, 326 (1987), 655-661.

COAKLEY, J. A.; BERNSTEIN, R. L.;

DURKEE, P. A.: Effect of ship-track effluents on cloud reflectivity. *Science*, 237 (1987), 1020-1022.

COAKLEY, J. A.; BERNSTEIN, R. L.;

DURKEE, P. A.: Effect of ship-stack effluents on the radiative properties of marine stratocumulus:

Implications for man's impact on climate. In *Aerosols and Climate* (Eds. P. V. Hobbs and M. P.

McCormick). Hampton, VA: A. Deepak Publishing. 1988.

CONOVER, J. H.: Anomalous cloud lines. *J. Atmos. Sci.*, 23 (1966), 778-785.

HOBBS, P. V.; STITH, J. L.; RADKE, L. F.: Cloud active nuclei from coal-fired electric power plants and their interactions with clouds. *J. Appl. Meteor.*, 19 (1980), 439-451.

RADKE, L. F.; HOBBS, P. V.: Cloud condensation nuclei on the Atlantic seaboard of the United States. *Science*, 193 (1976), 999-1002.

RADKE, L. F.: Marine aerosol: simultaneous size distributions of the total aerosol and the sea-salt fraction from  $0.1$  to  $10 \mu\text{m}$  diameter. In *Atmospheric Aerosols and Nuclei* (Eds. A. F. Roddy and T. C. O'Conner). Galway, Ireland: Galway University Press. 1977.

RADKE, L. F.: Preliminary measurements of the size distribution of cloud interstitial aerosol. In *Precipitation Scavenging, Dry Deposition and Resuspension* (Eds. H. R. Pruppacher, R. G. Semonin and W. G. N. Slinn). New York: Elsevier. 1983.

TWOMEY, S. A.; PIERGRASS, M.; WOLFE, T. L.: An assessment of the impact of pollution on global cloud albedo. *Tellus*, 36B (1984), 356-366.

TWOMEY, S. A.; WARNER, J.: Comparisons of measurements of cloud droplets and cloud nuclei. *J. Atmos. Sci.*, 24 (1967), 702-703.

# RADIATION INDUCED GROWTH AND EVAPORATION OF DROPLETS IN BOUNDARY LAYER CLOUDS

Roger Davies

Department of Meteorology, McGill University, 805 Sherbrooke Street West,  
Montreal, Que H3A 2K6, Canada

## 1. INTRODUCTION

Long-lived boundary layer clouds are a major component of the climate system and may offer the best opportunity for experimental measurement of the response of clouds to radiative processes. We have examined some possible responses using a high resolution radiative transfer model, theoretical considerations of supersaturation feedback, and models of diffusional growth and sedimentation of cloud droplets. These theoretical predictions are presently being examined against the experimental measurements made in marine stratocumulus during the First International Satellite Cloud Climatology Program Regional Experiment (FIRE).

## 2. THEORY

The radiative transfer model uses high spectral and vertical resolution to produce broadband flux divergences of shortwave and longwave radiation. It includes the effects of droplet scattering, absorption and emission by both droplets and gas, and vertical discontinuities in temperature and liquid water content. The radiation budgets of individual droplets are also obtained as functions of their radius and position within the cloud.

Droplet growth rates are determined as by Davies (1985) and Alves (1987), allowing for supersaturation

feedback. In the absence of turbulence, droplet response to radiation is found to be significant, with droplets of all sizes growing under conditions of net longwave loss. The effect is greatest in the top few meters of the cloud where the longwave loss is a maximum. Inclusion of turbulence changes this result and reduces the overall growth rate. Smaller droplets now tend to evaporate, whereas the larger droplets maintain significant growth rates.

The theoretical result is illustrated in Figure 1, which shows the droplet growth rates predicted by our model for a typical boundary layer stratiform cloud under two limiting assumptions: (a) radiation alone with no turbulent heat exchange, and (b) radiation together with a fully efficient turbulent heat transfer. *In situ* measurements of cloud microphysics made by others during FIRE are currently being analyzed to see whether these limiting assumptions are consistent with observation.

## 3. REFERENCE

Adil R. Alves, "On the Interactions of Longwave Radiation, Microphysics, and Turbulence in Boundary Layer Clouds.", Ph. D. thesis, Purdue University, 184 pp, 1987.

R. Davies, "Response of Cloud Supersaturation to Radiative Forcing", *J. Atmos. Sci.*, 42, 2820-2825, 1985.

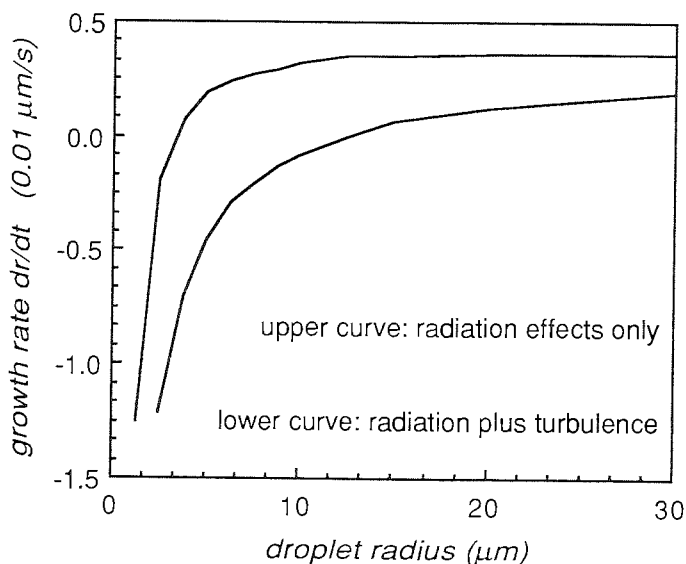


Fig. 1. Radiatively induced droplet growth at the top of a modeled stratiform cloud

## CLOUD AND AEROSOL OPTICAL DEPTHS

R. F. Pueschel(1), P. B. Russell(1), T. P. Ackerman(2),  
D. C. Colburn(1), R. C. Wrigley(1), M. A. Spanner(3), J. M. Livingston(4)

(1)NASA Ames Research Center, Moffett Field, CA 94035; (2)Pennsylvania State University, University Park, PA 16802; (3)TGS Technology, Moffett Field, CA 94035; (4)SRI International, Menlo Park, CA 94025

### 1. INTRODUCTION

Airborne sun photometry is essential to provide information on horizontal and vertical variations of optical depths in order to assess climatic feedback mechanisms of clouds. The Ames airborne sun photometer measures optical depths in six spectral intervals from 380 to 1020 nm simultaneously with a frequency of 0.5 Hz from outside an aircraft in a feedback-controlled active tracking mode. The instrument consists of a solar tracking system, a detector module, a temperature control system, a nitrogen purge system, a mechanical drive chain and a data acquisition system (MATSUMOTO 1987). In 1986/87, the instrument was operated in two large field programs. First, it was part of the instrument package aboard the NASA C-130 research aircraft that supported the First ISLSCP (International Satellite Land Surface Climatology Project) Field Experiment (FIFE) over the Konza Prairie in Kansas (38.9 - 39.1°N; 96.4 - 96.6°W). Second, it was flown on the Sandia National Laboratories Twin Otter research aircraft to measure the smoke optical depths of forest fires and a jet-fuel pool fire (PUESCHEL ET AL. 1988).

### 2. RESULTS AND DISCUSSION

#### 2.1 BACKGROUND OPTICAL DEPTHS

The FIFE intensive field campaigns between May and October 1987, and the fire investigations in the fall of 1986 provided opportunities to measure, respectively, the optical depths in clear atmospheres between the appearances of broken stratus clouds, and the optical depths in the vicinity of smokes. Typical background optical depths were 0.06-0.07 at 380 nm, decreasing to 0.006-0.007 at 1020 nm. The wavelength dependence of optical depths in the vicinity of forest fire smokes is rather steep: the Angstrom exponent,  $\alpha$ , of particulate optical depths (that is, total optical depths corrected for Rayleigh scattering, NO<sub>2</sub> and O<sub>3</sub> absorption) varied from a  $2.4 \pm 0.3$  near a Los Angeles controlled burn to  $3.3 \pm 0.6$  in the

vicinity of a fire near Fresno, CA. The atmosphere near Albuquerque, NM outside the jet-fuel smoke had a more typical Angstrom exponent of  $1.2 \pm 0.2$ . The background particulate optical depths in rural Kansas showed still less wavelength dependence with  $\alpha < 1.0$ . We conclude that (human) activities can alter the chemical and optical properties of background atmospheres to affect their spectral optical depths. Effects of water vapor adsorption on aerosol optical depths are apparent, based on data of the water vapor absorption band centered around 940 nm.

#### 2.2 SMOKE OPTICAL DEPTHS

Smoke optical depths show increases above the background atmosphere by up to two orders of magnitude. The Angstrom exponent of the undiscriminated data set shows a bimodal frequency distribution with modes  $2.0 < \alpha < 2.3$  and  $-0.3 < \alpha < 0$ . The latter mode becomes more pronounced as we discriminate against smaller optical depths. We conclude that the smoke aerosol is composed of two components. One component is dominated by particles that are relatively small in size and, consequently, scatter/absorb in the blue; this aerosol affects the optical properties of smokes at small optical depths. A second component, which is associated predominantly with high optical depths, is characterized by neutral, or slightly anomalous, extinction. The effects of dilution on the magnitude of optical depth, and of coagulation on its wavelength dependence in aging smokes have been documented by the measurements. Aged forest fire smoke shows anomalous extinction in 20% of all cases; the Angstrom exponent spectrum has modes of  $1.3 < \alpha < 1.5$  and  $-1.0 < \alpha < -0.8$ . The wavelength dependence of the optical depth of smoke from the jet-fuel fire showed a more neutral behavior than did that of the forest fire smokes. We conclude that the wavelength dependence of smoke optical depths depends critically on the fuels that

feed the fires, and on the residence time in the atmosphere of the smoke cloud. Under the assumption of similar opacity near 1000 nm it appears that, in the visible and near-ultraviolet, forest fire smokes would have greater opacity than jet fuel fire smokes. Beyond 1000 nm, however, forest fire smokes would have less opacity than fuel fire smokes.

### 2.3 CLOUD OPTICAL DEPTHS

On clear days, tenuous clouds of limited horizontal extent were observed. When the total optical depths measured through these clouds were corrected for molecular scattering and gaseous absorption by subtracting the total optical depths measured through the background atmosphere, the resultant values were lower than those of the background aerosol at short wavelengths. The spectral dependence of these cloud optical depths was neutral, however, in contrast to that of the background aerosol or the molecular atmosphere. This optical property of the atmosphere is attributed to high-altitude ice crystals at low concentrations. Similar to forest fire smokes, stratus clouds increase the optical depths by several orders of magnitude above that of background air. In contrast to forest fire smokes, however, their Angstrom exponent frequency spectra are unimodal. Separating out the effects of haze by discriminating against low optical depths, the Angstrom coefficient is  $\alpha \cong 1.0$ . The cloud optical properties have been linked to their microphysical properties by inverting the spectral optical depth data to derive columnar particle size distributions (KING ET AL. 1978).

KING, M. D.; BYRNE, D. M.; HERMAN, B. M.; REAGAN, J. A.: Aerosol Size Distributions Obtained by Inversion of Spectral Optical Depth Measurements. *J. Atmos. Sci.* 35 (1978), pp. 2153-2167.

MATSUMOTO, T.; RUSSELL, P. B.; MINA, C.; VAN ARK, W.; BANTA, V.: Airborne Tracking Sunphotometer. *J. Atmos. Ocean. Tech.* 4 (1987), pp. 336-339.

PUESCHEL, R. F.; LIVINGSTON, J. M.; RUSSELL, P. B.; COLBURN, D. A.; ACKERMAN, T. P.; ALLEN, D. A.; ZAK, B. D.; EINFELD, W.: Smoke Optical Depths: Magnitude, Variability and Wavelength Dependence. *J. Geophys. Res.* (submitted).

# AN OBSERVATIONAL STUDY OF RADIATIVELY DRIVEN CONVECTION

S Nicholls

Meteorological Office, Bracknell

## 1 INTRODUCTION

Interest in the cloud-topped boundary layer (CTBL) has increased considerably in recent years, acknowledging the importance of cloud-radiation feedback in climate simulations, the desire to interpret cloud structure from satellites and the requirement to provide more detailed local forecasts. Progress towards these goals demands a thorough understanding of the interaction of the physical processes active in CTBL's, including microphysics, radiation and turbulent transfer. One of the important differences of CTBL's compared to other types of boundary layer is that radiative effects can dominate the layer dynamics. For example, mixing may proceed entirely independently of surface processes in free, elevated cloud layers. This paper concentrates on aspects of the convective motion found such conditions and which are responsible for the cellular patterns commonly observed in stratocumulus. Understanding these motions is essential if the evolution of layer cloud is to be successfully modelled since they control both vertical transport and entrainment across layer boundaries. These results should also be useful in assessing the realism of large eddy simulations which are increasingly being employed to study entrainment.

Flight No	Cloud Depth (m)	$h$ (m)	$w_e$ (m/s)	$T_{vx}$ (K)	$q_{Tc}$ (g/kg)	$\Delta E$ (K)	$\langle T\psi \rangle$ (K)
511	320	370	0.57	0.026	0.028	0.021	-0.052
526	450	480	0.57	0.020	0.044	0.054	-0.040
528	190	480	0.63	0.024	0.021	-0.002	-0.048
620	340	700	0.78	0.025	0.028	0.031	-0.050

Table 1. Details of cases analysed (see also Ref 1)

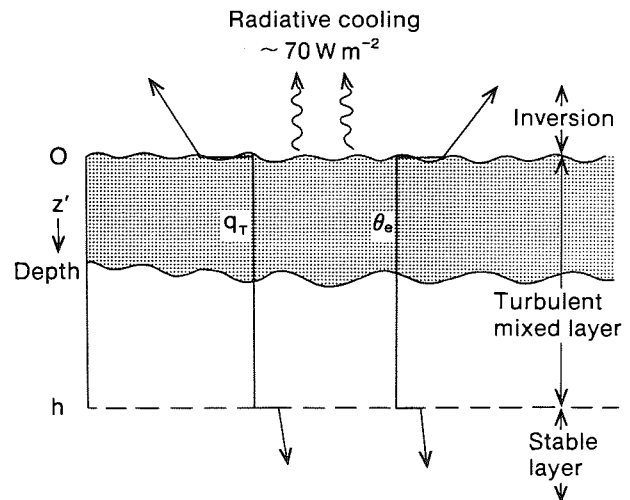


Fig 1 Schematic of conditions encountered. The cloud layer is shaded. The variation of equiv. potential temp. ( $\theta_e$ ) and total water mixing ratio ( $q_T$ ) with height are also shown.

## 2. THE DATA

These were collected on four flights by the MRF C130 aircraft in horizontally uniform, unbroken sheets of stratocumulus over the sea around the UK. See Table 1 for details. In each case, the cloud layer occupied the upper part of a mixed layer within which vertical gradients of the conserved quantities  $\theta_e$  and  $q_T$  were found to be small (Fig 1). Cloud top was marked by a strong inversion with a slightly stable region beneath the lower mixed layer boundary. The clouds were between 190m and 450m thick, while the mixed layer depth,  $h$ , varied from 370m to 700m. Mixed layer turbulence was being maintained by buoyant convection alone, with shear production negligible (Ref 2). Buoyancy production is largest just below cloud top (Ref 2) and is primarily due to radiative cooling. IR cooling from the top few tens of metres at cloud top is typically  $\sim 70 \text{ W m}^{-2}$ .

### 3. CONDITIONAL SAMPLING

The intense local cooling at cloud top sets up convective motion in the form of negatively buoyant downdraughts. These have been investigated using conditional sampling. Downdraughts (events) were defined by the nearest zero crossing points whenever the vertical velocity exceeded a threshold of  $-0.5w_*$  (Fig 2). The minimum acceptable width,  $d$ , was  $h/20$  ( $\sim 25\text{m}$ ) and events had to be separated by at least one data point ( $\sim 6\text{m}$ ). When scaled using the mixed layer quantities ( $w_*$ ,  $T_{v*}$ ,  $q_{T*}$ , defined in Ref 1 and see Table 1) a surprisingly consistent picture emerges.

Downdraughts occupy a maximum fractional area,  $\sim 0.37$ , just below cloud top (Fig 3). They are an efficient means of transport and are responsible for over half the heat, water vapour and liquid fluxes despite occupying well under half the area. The average intersected event width increases and the encounter frequency decreases with distance below cloud top ( $z'$ ). The distribution of intersected widths near cloud top can also be shown to be consistent with observed cellular patterns if downdraughts are assumed to occupy relatively narrow regions ( $\sim 0.1h$ - $0.15h$  wide) around the periphery of larger area updraughts (diameter  $\sim 0.5h$ ).

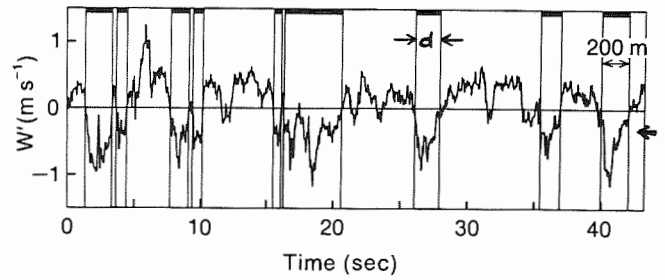


Fig 2. Vertical velocity data from part of a run near cloud top showing downdraughts chosen by the conditional sampling algorithm. The threshold ( $-0.5w_*$ ) is arrowed.

Conditionally sampled statistics show that, on average, downdraughts are both cooler and drier than their surroundings in the upper part of the mixed layer (Fig 4). These contrasts are largest near cloud top, decreasing to around zero near  $z'=0.5h$ , as downdraughts mix with surrounding cloud. Thus, downdraughts near cloud top contain both air which has been radiatively cooled as well as dry air entrained from above cloud top which has been cooled and moistened by evaporation. Since  $q_T$  is conserved over short timescales during mixing, the fraction of air within the downdraught originating from above cloud can be estimated using  $\langle q_T' \rangle$ . This can then be used to calculate the expected mean buoyancy change of the downdraughts due solely to mixing and subsequent evaporation,

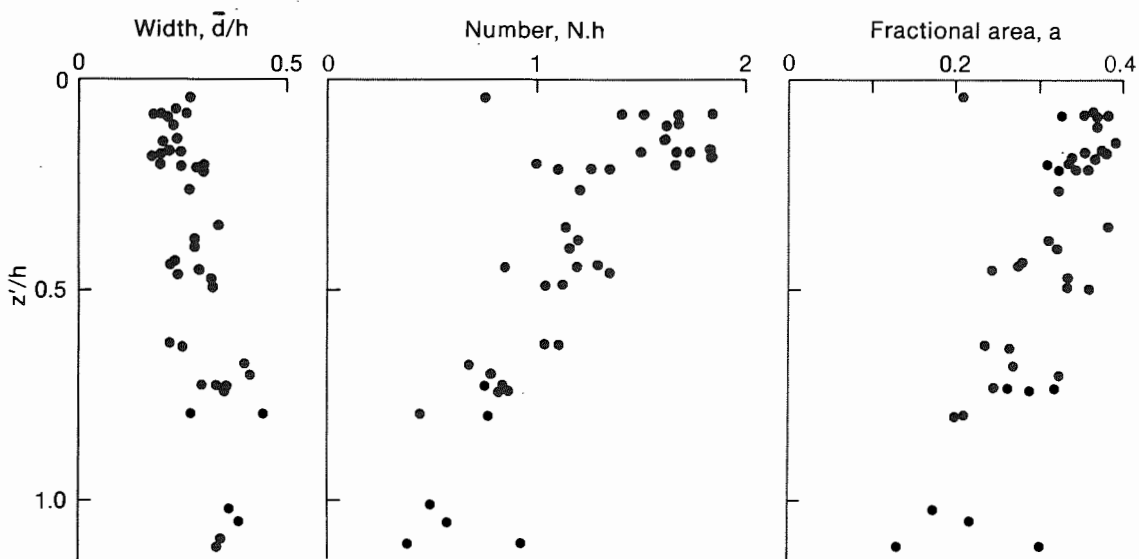


Fig 3. Run-averaged downdraught properties: mean event width ( $\bar{d}$ ), number encountered ( $N$ ) and area occupied.

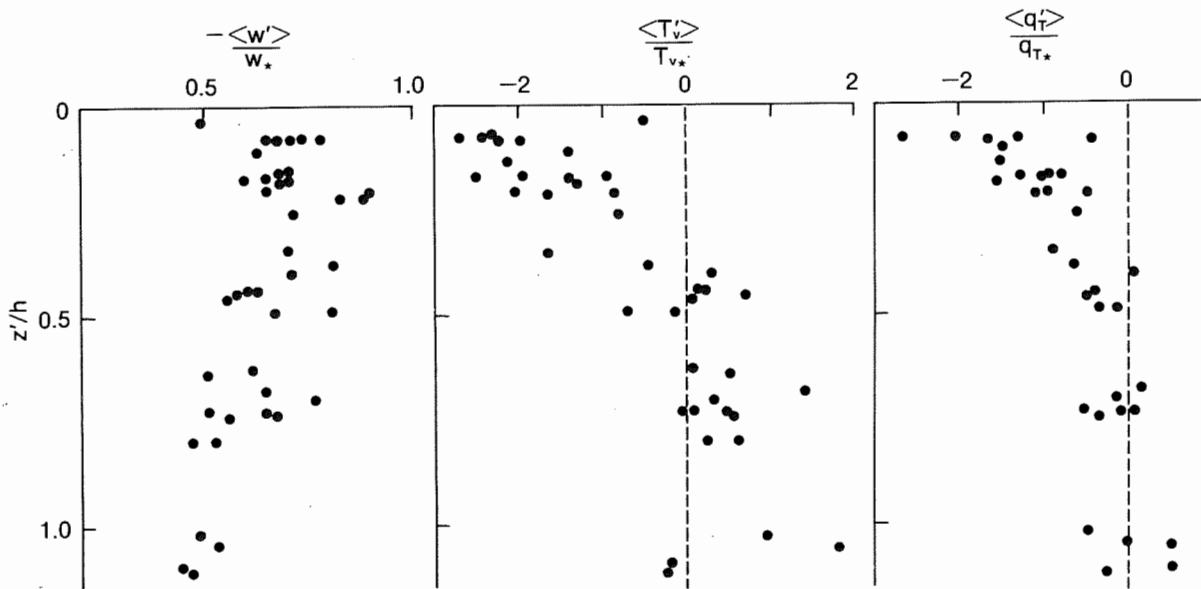


Fig 4. Event-mean vertical velocity  $\langle w' \rangle$ , virtual temperature  $\langle T'_v \rangle$  and total humidity  $\langle q'_T \rangle$  deviations from the run average. See Table 1 for scaling.

( $\Delta E$  in Table 1). These are small and have the wrong sign in all but one case to explain the observed values of  $\langle T'_v \rangle$  listed alongside. Only radiative cooling can produce the observed negative buoyancy. A few minutes exposure to the cooling rates of several degrees per hour calculated to exist at cloud top would be sufficient.

These temperature and moisture differences between events and their surroundings are smaller than those found in corresponding convective layers over heated land or sea surfaces (Refs 3,4), but this is compensated by the greater fractional area occupied by the downdraughts. The cloud top interface is thus ventilated more effectively than an aerodynamically rougher land or sea surface.

Although events near cloud top are relatively cool and dry on average, the conditional mean values are still quite small. Fluctuation levels within events are large compared to the mean deviation for all quantities except  $w$ . Downdraughts therefore also contain pockets which are both relatively moist and positively buoyant. The mean buoyancy deficit of the downdraughts is more than sufficient to explain their downward acceleration, but the poor correlation between  $w'$  and  $T'_v$  within

events suggests that the well defined event vertical velocity signature (near cloud top) results from the horizontal convergence of circulations constrained by the overlying inversion rather than direct buoyant instability at cloud top. In this interpretation, horizontal circulations formed by updraughts spreading out under the inversion scour the cloud top interface, incorporating air which has been radiatively cooled and/or partially mixed with inversion air before being forced down in narrow convergence zones. These downdraughts subsequently accelerate because of their net negative buoyancy, mixing internally and with the surrounding cloud. Updraughts compensating for this downward mass flux rise until they near the inversion where they are forced to spread out. This interpretation is also consistent with the measured turbulent kinetic energy balance (Ref 2).

#### 4 REFERENCES

1. Nicholls S & Leighton J R 1986 Quart J R Met Soc, 112, 431-460
2. McVean M & Nicholls S 1988 Proc Xth Intl Cloud Phys Conf, Bad Homburg
3. Lenschow D H & Stephens P L 1980 Boundary Layer Met, 19, 509-532
4. Greenhut G & Khalsa S 1985 J Atmos Sci, 42, 2550-2562

W.R. Cotton and S. Chen

Dept. of Atmospheric Science, Colorado State University, Fort Collins, CO 80523

G. Tripoli

University of Wisconsin, Dept. of Meteorology, Madison, WI 53715

## 1 Introduction

A number of researchers have speculated that radiative effects are important to the lifecycle of both tropical and extra-tropical mesoscale convective systems. Gray and Jacobson (1977), for example, noted that oceanic, tropical deep convection exhibits an early morning maximum and early evening minimum in heavy rainfall. It is also commonly observed that certain types of extratropical mesoscale convective systems (MCS), especially mesoscale convective complexes (MCCs), occur preferentially at night (Maddox, 1981; 1983). Wetzel *et al.* (1983) speculated that the destabilization caused by radiative cooling may be one factor contributing to the propensity for MCCs to form at night. It therefore seems worthwhile to examine the effects of longwave and shortwave radiation on simulated mesoscale convective systems.

In this paper we describe the results of model sensitivity experiments to long- and short-wave radiation using the Colorado State University Regional Atmospheric Modeling System (RAMS). The model response to radiation is investigated for three different MCSs: an isolated MCS over the High Plains of the United States, a pre-frontal squall line observed during the Australian Cold Fronts Research Program, and an orogenic MCS to the east of the Colorado mountains.

## 2 Summary of model

The model used in this study is the CSU RAMS which is derived from the cloud model described by Tripoli and Cotton (1982) and Cotton *et al.* (1982; 1986), and the mesoscale model described by Mahrer and Pielke (1977). The model contains physical parameterizations for cloud microphysics (Cotton *et al.*, 1982; 1986) which include liquid and ice phase precipitation processes. Longwave and shortwave radiative tendencies on  $\theta_{ii}$  (Chen and Cotton, 1983) are computed in cloudy regions by assuming all condensed water is in the liquid phase. No consideration is given to the unique radiative properties of the ice phase. Only longwave radiative effects are considered in the High Plains MCS whereas both short- and long-wave radiative effects are in the Australian squall line and the orogenic MCS. In the High Plains MCS and the Australian squall line, surface temperatures are specified and held fixed throughout the simulations. In the orogenic MCS simulation, soil temperature and soil moisture are predicted with an underlying soil model described by McCumber and Pielke (1981) and a surface energy balance model described by Tremback and Kessler (1985). Vertical and horizontal turbulent mixing is modeled using an eddy viscosity approach similar to that described by Tripoli and Cotton (1982).

The model equations are integrated by finite difference techniques described by Tripoli and Cotton (1982) for a non-hydrostatic, compressible system using a time-splitting procedure. Vertical grid resolution is 0.5 km in the High Plains MCS and the Australian squall line, whereas it is 0.25 km at low-levels and 0.75 km in the free atmosphere in the orogenic MCS. Horizontal grid resolution is 1.5 km (High Plains MCS), 1.0 km (Australian squall line) and 1.08 km (orogenic MCS).

## 3 Sensitivity to Radiation

### 3.1 High Plains MCS

In this case a two-dimensional version of RAMS was applied to the simulation of a U.S. High Plains MCS that was observed on July 14-15, 1984 during the AIMCS experiment. A detailed description of the experiment is given in Chen and Cotton (1988). A control simulation was established that exhibited many features in common with observed MCSs. The storm is dominated by a single persistent convective cell that contained a multi-branched updraft two of which fed the leading and trailing stratiform anvil cloud. A third updraft branch returned to the surface in what Knupp (1987) referred to as an "up-down" downdraft. This convective-scale downdraft mixed with mid-level air entering from the rear of the system. The contribution of longwave radiative flux divergence to the cloud heating rates is shown in Figure 1. A maximum of 35-40°C/day cooling near cloud top and a maximum of 20-25°C warming near the cloud base can be seen. The horizontal average of the longwave heating profile over the model domain yields approximately 16°C/day cooling at cloud top and 11°C/day warming at cloud base similar to results inferred by Cox and Griffith (1979) and Webster and Stephens (1980) in tropical clusters.

Turning off radiation reduced the warming within the stratiform cloud layer by 2°C, the magnitude of the surface cold pool was 1°C warmer, and the cloud top was 2°C warmer. The precipitation rate in the stratiform region with and without radiation is nearly identical. Likewise, differences in total surface precipitation after 4 h of simulation is small. It is possible that the slowly-settling ice crystals formed near the stratiform cloud top did not have enough time to reach the surface or seed the water-rich regions in the 4 h of simulation time. Also the ice crystal model tends to develop too many small ice crystals thus further reducing a surface precipitation response.

Although the microphysical structure failed to show significant changes due to the absence of longwave radiation, the internal cloud circulation increased noticeably when longwave radiation was activated. Figure 2a and 2b show the simulated circulation fields at 4 h for the radiation and no-radiation cases. The mesoscale updraft and downdraft strengths were similar in the leading stratiform regions while they were in general 0.5 to 1.0 m/s stronger when radiation was included. Likewise, peak convective-scale updraft strengths were in general stronger in the radiation experiment with the maximum value over 4 h being 28 m/s with radiation and 18 m/s without radiation. In the case with radiation, a nearly 80 km long, continuous band of jet-like

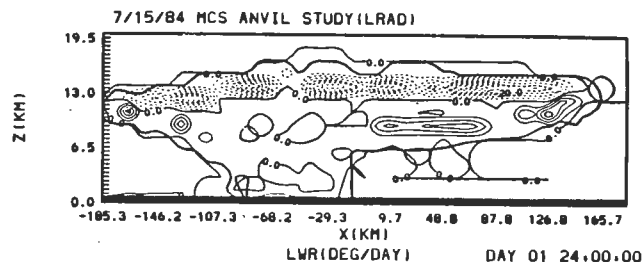


Figure 1: Longwave radiation cooling/heating rate. The contour interval is every 5°C.

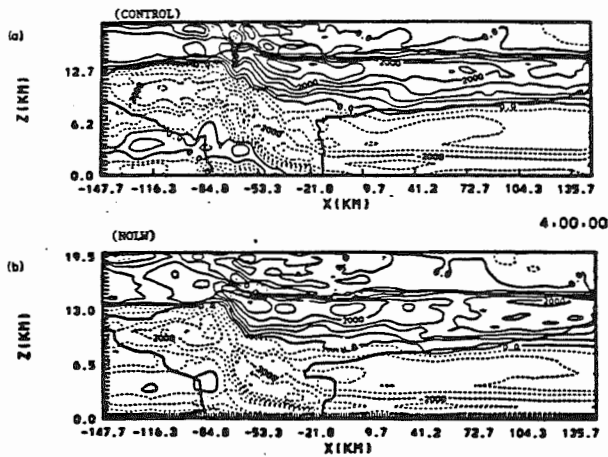


Figure 2: The horizontal velocity field for (a) control experiment and (b) no longwave radiation run. Dashed lines represent wind from the southwest and the solid lines represent wind from the northeast. The contour interval is  $5 \text{ m s}^{-1}$ .

rear-to-front, inflow at middle levels is evident with speeds of 3 to 5 m/s whereas it is only 2 to 4 m/s and not as continuous with radiation turned off.

### 3.2 The Australian squall line

In this case CSU RAMS was applied to the simulation of a squall line that was observed during the Australian Cold Fronts Research Program (CFRP) (Garrett *et al.*, 1985). The squall line occurred in a situation in which cold marine post-cool-frontal air from the south intermixes with hot and relatively dry air from the north. The cool marine air advancing from the south is relatively dry and stable, and produces some cloud near 1.5-2 km elevation. In advance of a frontal zone, a rising "conveyor belt" of relatively dry continental air advances southward from the north Australian interior. Because the relative humidity is low, saturation within this overrunning layer is not reached until it approaches 5 km MSL. This results in the formation of a shallow stratiform cloud in which all the potential convective instability is between the air residing at 500-700 mb and the air at 200-300 mb.

The simulations supported the hypothesis that unstable convection might be initiated by virga settling from the stratiform region of the conveyor belt into the post-frontal airmass. Initial evaporative cooling induced by virgae, generated vertical motions both upstream and downstream of the evaporatively cooled region. The sub-cloud circulations induced convergence in the subcloud layer which results in moderate intensity convection due to the conditional instability in the layer. Liquid water produced in the weak, conditionally unstable layer results in the formation of precipitation which further strengthens the sub-cloud convergence and the squall line circulation.

As in the High Plains MCS, longwave radiative flux divergences were turned off to examine the importance of radiation to the simulated squall line. Figure 3a and 3b show the simulated circulation fields and vertical velocity for the case with and without radiative effects, respectively, after 3 h of simulation. Turning off radiative effects weakened the system as a whole. Ice crystal mixing ratios diminished by over 0.5 g/kg and no precipitation reached the surface. Peak updraft and downdraft velocities weakened from the control by more than 50%. Downdraft velocities were actually stronger in the no radiation experiment early in the system lifecycle, but did not subsequently increase. The overall organization of the bands is strikingly different at 3 h with the no-radiation simulation exhibiting a stronger left band than the control.

The sensitivity to radiative effects in this case is not too surprising since the conditional instability in the upper parts of the cloud layer is relatively weak. Thus the destabilization caused by cloud top radiative cooling enhances the updrafts which, in turn,

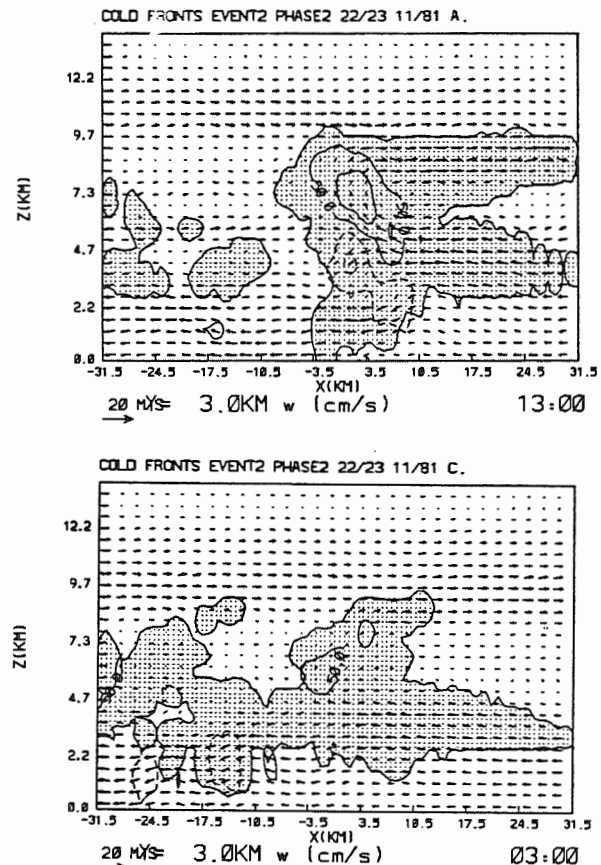


Figure 3: Predicted fields at 3 h of integration. In (a) radiation is included, thus integration corresponds to a time of day. Integration began at 10:00 CST and this time is therefore 13:00 CST. Vertical coordinate is height and horizontal coordinate is distance. Shading represents region where condensate exists, contoured fields are of  $w$  at intervals of  $1 \text{ m s}^{-1}$  beginning at  $0.5 \text{ m s}^{-1}$ . Radiation is turned off in (b). Because radiation is turned off, time begins at zero h.

produces more condensate and precipitation. The greater precipitation results in more sub-cloud evaporative cooling thus invigorating the downdraft circulation which perturbs the cloud layer divergence and so on. For further details see Ryan *et al.* (1988).

### 3.3 An Orographic MCS

The objective of this simulation was to examine the interactions between topographically-induced mesoscale circulations and deep convection as observed on a particular case study (Cotton *et al.*, 1983; Wetzell *et al.*, 1983). Shortwave and longwave radiation effected the surface energy budget as well as the thermodynamic structure of the cloudy and cloud-free atmosphere. The simulations described in detail by Tripoli (1986) and Tripoli and Cotton (1988a,b) were run for over 24 h on a two-dimensional domain that extended from the Colorado/Utah border eastward to central Kansas with 1.08 km horizontal resolution. As in the above experiments a control simulation was established and then the sensitivity of the model to radiative effects examined. In the sensitivity run longwave radiative flux divergences caused by clouds were neglected while daytime solar heating and radiative flux divergences in a cloud-free atmosphere were considered. In the control simulation deep convection first developed in the mountains and then organized into a mesoscale system which propagated over the plains to the east in the early afternoon. The MCS continued to propagate eastward on the plains undergoing cycles of intensification and decay. At sunset, longwave radiative cloud top cooling uninhibited by solar heating, destabilized the upper troposphere. The initial destabilization of the anvil leads to momentary explosive growth of the mesoscale circulation. Figure 4 illustrates the smoothed circulation field, at

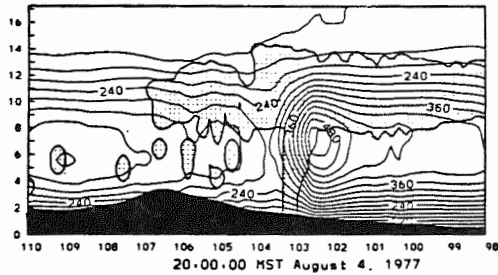


Figure 4: Predicted meso- $\beta$ -scale fields at 2000 MST for control case. Variables are as labeled. The fields represent 80 grid point (86 km) running averages of actual predicted variables. Streamfunction fields are calculated relative to the  $10 \text{ m s}^{-1}$  storm motion. Contour interval is  $500 \text{ g cm}^{-1} \text{ s}^{-1}$ . The boundary for condensate in excess of  $0.01 \text{ g kg}^{-1}$  (cloud boundary) is drawn by a heavy dark line and the region within is lightly shaded. The surface topography is depicted by the black shading. The vertical axis is height in km above mean sea level (MSL) and the horizontal axis is west longitude.

2000 MST at the time of sunset. Gravity waves which had previously been emitted into the stratosphere now became trapped after sunset by the unstable cloud top layer. As a result the previously singular meso- $\beta$ -scale upward circulation cell dispersed over several competing regions of meso- $\beta$ -scale upward motion.

Turning off longwave radiation cloud top cooling did not effect the simulation appreciably prior to sunset. At sunset, however, the explosive growth simulated in the control case was considerably weaker. Whereas the control convection dispersed into meso- $\beta$ -scale competing circulations after sunset, the no-longwave radiative cooling case remained concentrated in a single meso- $\beta$ -scale cell. The differences being largely due to the differences in the propagation of gravity waves due to lower stability in the cloud top radiation experiment. The impact of radiation on surface precipitation can be seen in Figure 5. The major difference occurs at a longitude of 103 (degree) where the control experienced pronounced intensification at sunset.

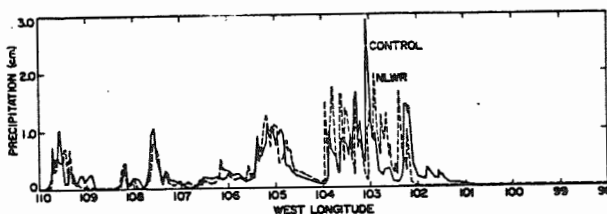


Figure 5: Accumulated precipitation in cm (vertical axis) versus horizontal location W longitude (horizontal axis). Curves for control case and NLWR case drawn.

## 4 Summary

These three cases illustrate that longwave radiation can have a significant influence on the behavior of mesoscale convective systems. The simulated interactions between radiation and the dynamics of MCSs is strong enough to merit further refinement in both the radiation and microphysical parameterizations. The impact of longwave radiation can involve some very complex interactions that in some cases is directly related to the destabilization of the cloud layer while in other cases the link is more indirect through the trapping of gravity wave energy in the troposphere.

## Acknowledgements

We acknowledge Brian Ryan's contribution to the Australian squall line simulations. Brenda Thompson processed the manuscript. The research was supported under National Science Foundation Grant

#ATM 8512480. Computations were performed at the National Center for Atmospheric Research (NCAR). NCAR is sponsored by the National Science Foundation.

## References

- Chen, C., and W.R. Cotton, 1983: A one-dimensional simulation of the stratocumulus-capped mixed layer. *Boundary-Layer Meteorol.*, **25**, 289-321.
- Cotton, W.R., M.A. Stephens, T. Nehr Korn, and G.J. Tripoli, 1982: The Colorado State University three-dimensional cloud/mesoscale model - 1982. Part II: An ice phase parameterization. *J. de Rech. Atmos.*, **16**, 295-320.
- Cotton, W.R., G.J. Tripoli, R.M. Rauber, and E.A. Mulvihill, 1986: Numerical simulation of the effects of varying ice crystal nucleation rates and aggregation processes on orographic snowfall. *J. Clim. Appl. Met.*, **25**, 1658-1680.
- Cotton, W.R., R.L. George, P.J. Wetzel and R.L. McAnelly, 1983: A long-lived mesoscale convective complex. Part I: The mountain-generated component. *Mon. Wea. Rev.*, **111**, 1893-1918.
- Cox, S.K., and K.T. Griffith, 1979: Estimates of radiative divergence during Phase III of the GARP Atlantic Tropical Experiment: Part II. Analysis of Phase III results. *J. Atmos. Sci.*, **36**, 586-601.
- Garrett, J.R., W.L. Physick, R.K. Smith, and A.J. Troup, 1985: The Australian summertime cool change. Part II: Mesoscale aspects. *Mon. Wea. Rev.*, **113**, 202-223.
- Gray, W.M., and R.W. Jacobson, Jr., 1977: Diurnal variation of deep cumulus convection. *Mon. Wea. Rev.*, **105**, 1171-1188.
- Knupp, K.R., 1987: Downdrafts within High Plains cumulonimbi. Part I: General kinematic structure. *J. Atmos. Sci.*, **44**, 987-1008.
- Maddox, R.A., 1981: The structure and life-cycle of midlatitude mesoscale convective complexes. Atmospheric Science Paper No. 336, Dept. of Atmospheric Science, Colorado State University, Fort Collins, Colorado, 80523, 311 pp.
- Maddox, R.A., 1983: Large-scale meteorological conditions associated with midlatitude, mesoscale convective complexes. *Mon. Wea. Rev.*, **111**, 1475-1493.
- Mahrer, Y. and R.A. Pielke, 1977: A numerical study of the airflow over irregular terrain. *Beitrage zur Physik der Atmosphäre*, **50**, 98-113.
- McCumber, M.C. and R.A. Pielke, 1981: Simulation of the effects of surface fluxes of heat and moisture in a mesoscale numerical model. Part I: Soil layer. *J. Geophys. Res.*, **86**, 9929-9938.
- Tremback, C.J. and R. Kessler, 1985: A surface temperature and moisture parameterization for use in mesoscale numerical models. Preprints, 7th Conference on Numerical Weather Prediction, 17-20 June 1985, Montreal, Canada, AMS.
- Tripoli, G.J., 1986: A numerical investigation of an orogenic mesoscale convective system. Ph.D. dissertation, Colorado State University, Dept. of Atmospheric Science, Fort Collins, Colorado 80523. (Atmospheric Science Paper No. 401).
- Tripoli, G.J., and W.R. Cotton, 1982: The Colorado State University three-dimensional cloud/mesoscale model - 1982. Part I: General theoretical framework and sensitivity experiments. *J. de Rech. Atmos.*, **16**, 185-220.
- Tripoli, G., and W.R. Cotton, 1988: A numerical study of an observed orogenic mesoscale convective system. Part 1. Simulated genesis and comparison with observations. Submitted for publication to *Mon. Wea. Rev.*
- Tripoli, G., and W.R. Cotton, 1988: A numerical study of an observed orogenic mesoscale convective system. Part 2. Analysis of governing dynamics. Submitted for publication to *Mon. Wea. Rev.*
- Webster, P.J. and G.L. Stephens, 1980: Tropical upper-tropospheric extended clouds: Inferences from Winter MONEX. *J. Atmos. Sci.*, **37**, 1521-1541.
- Wetzel, P.J., W.R. Cotton and R.L. McAnelly, 1983: A long-lived mesoscale convective complex. Part II: Evolution and structure of the mature complex. *Mon. Wea. Rev.*, **111**, 1919-1937.

# CIRRUS MICROPHYSICS AND INFRARED RADIATIVE TRANSFER: A CASE STUDY

Thomas P. Ackerman<sup>1</sup>, Andrew J. Heymsfield<sup>2</sup>, Francisco P. J. Valero<sup>3</sup>, Stefan Kinne<sup>3</sup>

<sup>1</sup>Department of Meteorology, Pennsylvania State University, University Park, PA

<sup>2</sup>NCAR, Boulder, CO

<sup>3</sup>NASA Ames Research Center, Moffett Field, CA

## 1. INTRODUCTION

The First ISCCP Regional Experiment (FIRE) consists of several research activities designed to study the role of clouds in global climate in support of the International Satellite Cloud Climatology Program (ISCCP). The first cirrus intensive field observation period was conducted from 13 October, 1986 to 2 November, 1986 in central Wisconsin, USA. The details of FIRE and the cirrus observation period can be found in Cox et al. (1987) and Starr (1987).

One of the primary objectives of FIRE was to acquire co-incident measurements of cirrus cloud microphysical properties such as particle size distribution and particle shape and morphology and measurements of infrared intensity and flux. On a variety of occasions during the observation period, data was acquired nearly simultaneously in space and time by the NCAR KingAir in cloud and by the NASA ER-2 at an altitude of about 19 km. In this paper, we have chosen to present data obtained on 28 October. The particular aircraft data of relevance to this case study consist of upwelling infrared intensities and fluxes measured from the ER-2 and observations of cloud particle size distributions and particle phase and morphology made from the KingAir. In addition, broad-band flux measurements were available both in and below the cirrus layer from the KingAir.

## 2. DATA

The synoptic situation on 28 October was characterized by a warm front passing through the observing network. Associated with the warm front passage was the development of various types of convective cirrus. Ground-based and airborne lidar showed numerous cirrus generating cells producing a cirrus layer with a variable optical thickness. For a period of approximately an hour (16:30 to 17:30 GMT), the two aircraft flew stacked, timed "racetracks" (a pattern of two longer parallel sides and shorter curved ends) in an area of developing cirrus. Due to the factor of 2-3 times greater speed of the ER-2 and the much shorter turning radius of the KingAir, the racetrack of the latter was completely enclosed by that of the ER-2, as well as being much shorter in length. Thus, only twice during each racetrack pattern were the two planes briefly observing the same general column of air. Furthermore, since the each aircraft's navigation has some error in position, the exact point of coin-

idence is difficult to define. Consequently, we have taken the approach of developing a composite cirrus layer from the KingAir observations taken during this time period and comparing it with average radiation fields observed by the ER-2.

The KingAir flew its racetrack legs at 7 altitudes ascending from 6 to 8 km. During each leg, several size distributions were acquired using PMS 2-D shadow probes. Glass slides were used to collect ice crystals by exposing the slide to the airstream and allowing crystals to impact on it. The slides were kept cold in CO<sub>2</sub> ice and returned to the ground for analysis of particle shape and size.

Observations of the upwelling 10.5  $\mu\text{m}$  and 6.5  $\mu\text{m}$  radiances and broad-band infrared flux were made from the ER-2. The radiance measurements were made with a 2-channel, nadir-viewing instrument continuously calibrated by a reference cell filled with liquid nitrogen. The instrument field of view is a 15° cone. The IR flux were measured by a flat plate radiometer that has a specially designed aperture with a cosine response.

## 3. DATA ANALYSIS

From the ice crystal slides and the 2-D shadow probe, it was observed that the majority of crystals were bullets and bullet rosettes, the latter typically consisting of 3 to 5 bullets. Using this information and the number of crystals per size bin, we are able to develop two different types of size distributions for model calculations. In the first, we simply compute the amount of ice water in a given size interval based on the average aspect ratio of the bullets. From the ice water amount, we can then compute the number of spheres for either equivalent volume or cross-section. The extinction coefficient for the spheres can then be computed from Mie theory. Average distributions and coefficients are computed for each aircraft leg, allowing us to develop a vertical profile of the composite cloud. Alternatively, we separate the rosettes into their individual bullets and bin the bullets into the appropriate size interval. We assume that the bullets can be approximated as cylinders and then compute the extinction and scattering coefficients. Again, average values are computed for each leg, allowing the development of vertical profiles.

The radiances are also analyzed statistically over the flight period. Histograms of the radiances are plotted

and means and variances calculated. Since the cloud temperature is known from radiosonde and KingAir measurements and the surface radiation temperature from below cloud measurements from the KingAir and clear-sky measurements from the ER-2, it is possible to convert the  $10 \mu m$  radiances to distributions of cirrus optical depth.

An infrared multiple-scattering model is then applied to the composite cloud and atmosphere. The calculated radiances and fluxes for the various assumed size distributions are compared to the observed radiances and fluxes. The mean and variances of the calculated radiation field, based on the observed variability in the size distributions, is compared with the observed mean and variances. On the basis of these calculations, we can assess the validity of various particle size and shape approximations. Given reasonable agreement, we can also assess the infrared radiative exchange within the cirrus layer and the average heating rates.

#### 4. REFERENCES

Cox, S. K.; McDougal, D. S.; Randall, D. A.; Schiffer, R. A.: FIRE - The First ISCCP Experiment. *Bull. Amer. Meteor. Soc.* 68 (1987) 114-118.

Starr, D. O'C.: A cirrus-cloud experiment: Intensive field observations planned for FIRE. *Bull. Amer. Meteor. Soc.* 68 (1987) 119-124.

# THE COLLECTION EFFICIENCY OF A MASSIVE FOG COLLECTOR

Robert S. Schemenauer and Paul I. Joe

Atmospheric Environment Service

4905 Dufferin St., Downsview, Ontario, Canada M3H 5T4

## 1. INTRODUCTION

The Camanchaca Project is designed to determine if fog water can serve as a new type of arid zones water supply. The background of the 2 year project is described in SCHEMENAUER et al. (1988). Estimates of the amounts of water that can be deposited by fogs are given in SCHEMENAUER (1986,p.303). Coastal stratocumulus cloud decks are blown onshore by the prevailing low level winds on the coast of Chile. The clouds are intercepted by the coastal mountains and extensive periods of high elevation fog (camanchaca) result. The fog is collected by large meshes called atrapanieblas. The choice of optimum sampling location is done by conducting preliminary experiments on relative fog water collection using small collectors (SCHEMENAUER et al. 1987, p.1285). This paper will describe the results of measurements designed to determine the collection efficiency of the atrapanieblas.

## 2. THE NOVEMBER 1987 FIELD PROJECT

### 2.1 FIELD SITE

The site is 60 km north of the city of La Serena in north central Chile. The main experimental location is on a ridge at 780 m (29° 26'S, 71° 15'W). It is 6 km from the village of Chungungo on the Pacific coast. Water from 60 large collectors on El Tofo will be delivered to Chungungo by the end of 1988.

### 2.2 INSTRUMENTATION

The 40 m<sup>2</sup> atrapanieblas are 10 m long and 4 m high. The top of each collector is 6 m above

ground. The collecting material is a double layer of black nylon mesh that is made in Chile. The mesh is a triangular weave of a flat fiber about 1 mm wide. The fiber is woven into a mesh with a pore size of about 1 cm. The atrapanieblas are being installed at several locations from 710 m to 780 m on El Tofo. Measurements of the characteristics of the fog droplet sizes and concentrations were made with two Particle Measuring Systems Forward Scattering Spectrometer Probes (FSSPs). One FSSP was mounted immediately in front of an atrapaniebla but moved 0.5 m off centre, Figure 1. The second FSSP was mounted behind the atrapaniebla 0.5 m off centre in the other direction. The calibrations of the FSSPs were checked before and after the two week field project using glass beads. Both FSSPs were equipped with aspirators to pull the droplets through

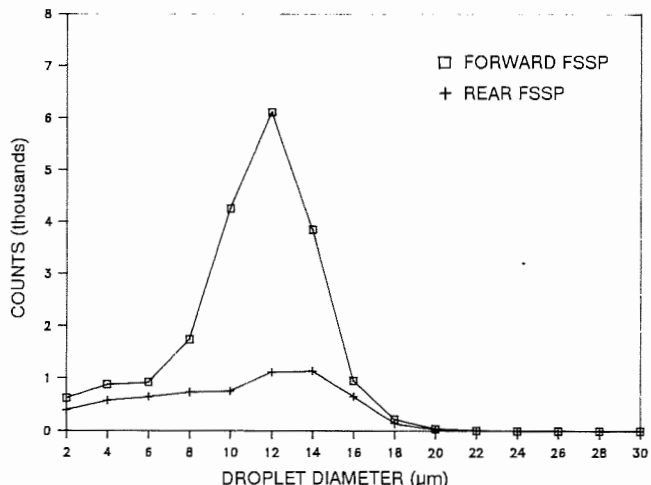


Fig. 1: Atrapaniebla with the forward FSSP.

the measuring section at a constant  $25 \text{ m s}^{-1}$ . A complete set of meteorological measurements was made 6 m in front of the forward FSSP and at the same height.

### 3. DROPLET SIZE DISTRIBUTIONS

The drop size distributions usually had a single peak with a mode near  $10 \mu\text{m}$ . Maximum sizes ranged from 15 to  $30 \mu\text{m}$  with larger droplets seen only rarely. Due to a data acquisition failure in the field, large amounts of data were not collected. However, some results from the FSSPs are available. Figure 2 shows the average number of droplets counted by the two FSSPs during four 5 s periods between 1735 and 1745 local time on 12 Nov 1987. The peak in the size distribution is at  $12 \mu\text{m}$  as the fog approaches the mesh.



**Fig. 2: Droplet size distributions.**

The peak is broader, 12 to  $14 \mu\text{m}$ , and much lower on the rear side of the mesh. In each location there was the occasional drop to  $28 \mu\text{m}$ . The average concentration in front of the mesh was  $231 \text{ cm}^{-3}$  and behind the mesh  $73 \text{ cm}^{-3}$ .

### 4. FOG LIQUID WATER CONTENT

The fog liquid water content (LWC) calculated from the distributions in Figure 2 was  $0.20 \text{ g m}^{-3}$  in front of the mesh and  $0.063 \text{ g m}^{-3}$  behind the mesh. On average, 69% of the fog water was removed by the mesh. Figure 3 shows how the fog LWC was distributed as a function of the droplet

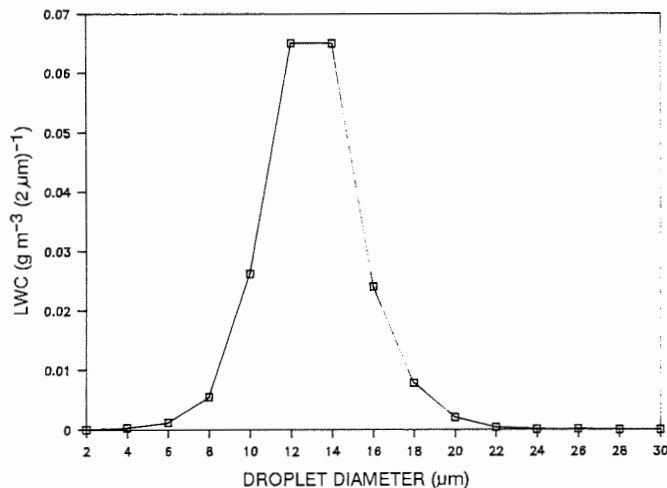


**Fig. 3: LWC distribution (forward FSSP).**

diameter in front of the mesh. Figure 4 shows the ratio of the LWC behind the mesh to that in front as a function of droplet diameter. The double layer of mesh appears

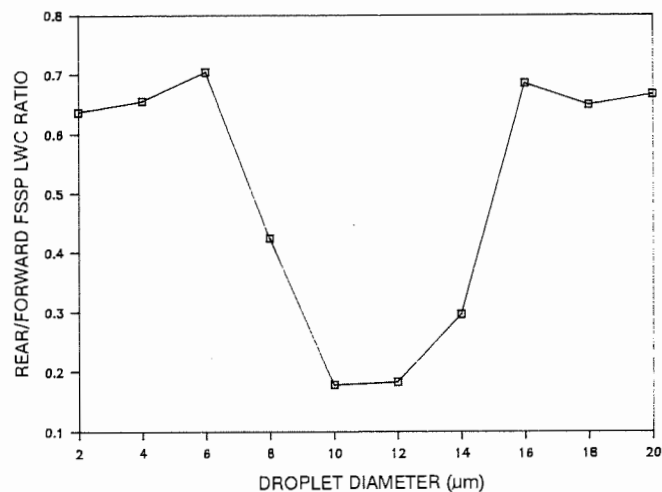


**Fig. 4: LWC ratio as a function of size.**

to be efficient in removing fog water in the part of the spectrum where most of the water is found. The ratios for droplets larger than  $20 \mu\text{m}$  are not shown since fewer than 10 droplets were counted in 5 s in these channels. In the 10 and  $12 \mu\text{m}$  size channels where the mode of the distribution is, only 18% of the fog water is passing through the mesh. At the time of these measurements, the wind was  $6.5 \text{ m s}^{-1}$  and the temperature  $10.8 \text{ }^\circ\text{C}$ .

### 5. MEASURED MESH EFFICIENCY

The double layer of mesh removed 69% of the fog water in the centre of the mesh. If we assume the fog LWC and wind speed were evenly distributed across the atrapaniebla,

then the  $40 \text{ m}^2$  collector should have had an output of  $36 \text{ cm}^3 \text{ s}^{-1}$ . The actual output as measured by a flowmeter averaged  $18.5 \text{ cm}^3 \text{ s}^{-1}$  for the 10 min period from 1735 to 1745. Some water, perhaps 15%, was being lost due to a poor design for the trough at the bottom of the atrapaniebla. But this cannot explain the fact that the output was only 52% of the estimated water available. This suggests there may be some unevenness in the water distribution or collection efficiency over the collector surface.

## 6. THEORETICAL COLLECTION EFFICIENCY

A single layer of the Rashell mesh covers  $\approx 50\%$  of the surface area defined by a  $40 \text{ m}^2$  atrapaniebla. The double layer of material covers only  $\approx 75\%$  of the area since fibers can overlap. Figure 5 gives the collection

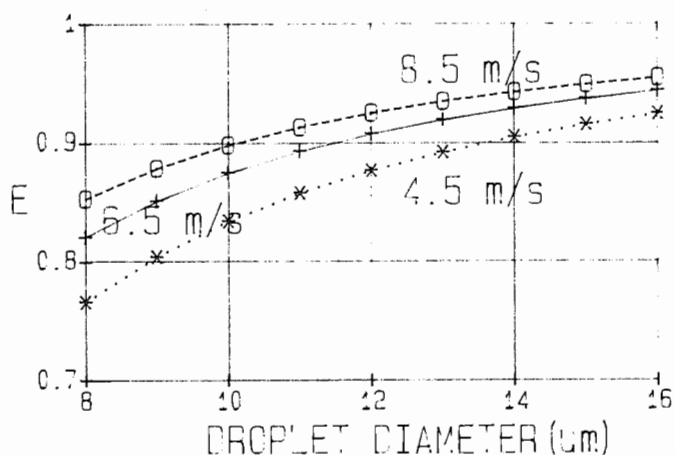


**Fig. 5: Collection efficiency calculations.**

efficiencies of a 1 mm ribbon as a function of air speed and droplet size according to the computations of Langmuir and Blodgett (1946). The ribbon will collect droplets of  $13 \mu\text{m}$  diameter (mid-point of LWC distribution) travelling at  $6.5 \text{ m s}^{-1}$  with an efficiency of 92%. The LWC passing through an unobstructed  $40 \text{ m}^2$  area is  $40 \text{ m}^2 \times 6.5 \text{ m s}^{-1} \times 0.2 \text{ g m}^{-3} = 52 \text{ g s}^{-1}$ . Introducing a mesh covering 75% of the area yields  $52 \text{ g s}^{-1} \times 0.75 \times 0.92 = 36 \text{ cm}^3 \text{ s}^{-1}$ . This is the same as the expected yield calculated from the FSSP data at the center of the collector. Both values are higher than the measured output of  $18.5 \text{ cm}^3 \text{ s}^{-1}$  even when increased by 15% to  $21 \text{ cm}^3 \text{ s}^{-1}$  to allow for trough losses.

Assuming a lower average wind speed of  $4.5 \text{ m s}^{-1}$  over the collector only reduces the collection efficiency to 0.89, resulting in an expected output of  $35 \text{ cm}^3 \text{ s}^{-1}$ . It appears that about 40% of the water in the swept out volume is not reaching the surface of the collector as a result of the air being forced around the collector and carrying the droplets with it. The wind flow around the collector will be examined in detail during the next field period.

## 7. CONCLUSIONS

The measured output from a  $40 \text{ m}^2$  fog water collector is  $\approx 58\%$  of the expected output based on measured and calculated collection efficiencies at the center of the collector. Reduced collection efficiencies due to a lower average wind over the mesh cannot explain the discrepancy. It is postulated that blockage of the wind by the large collector results in flow around the edges of the collector and thus a lower water droplet availability for collection.

## 8. REFERENCES

- LANGMUIR, I., BLODGETT, K.B.: A mathematical investigation of water droplet trajectories. Army Air Force Technical Report No. 5418, Washington, D.C., (1946) 68 pp.
- SCHEMENAUER, R.S.: Acidic Deposition to Forests: the 1985 Chemistry of High Elevation Fog (CHEF) Project. *Atmosphere-Ocean*, 24 (1986) #4, pp. 303-328.
- SCHEMENAUER, R.S., CERECEDA, P., CARVAJAL, N.: Measurements of Fog Water Deposition and Their Relationships to Terrain Features. *J. Clim. Appl. Meteor.*, 26, (1987) #9, pp. 1285-1291.
- SCHEMENAUER, R.S., FUENZALIDA, H., CERECEDA, P.: A neglected Water Resource: the Camanchaca of South America. *Bull. Amer. Meteor. Soc.*, 69 (1988) #2, pp. xx-xx.

THE USE OF AUTOMATIC PARTICLE RECOGNITION TO  
IMPROVE THE DETERMINATION OF BULK QUANTITIES  
FROM PMS 2-D PROBE DATA IN CIRRUS

A.G Darlison and P.R Brown

U.K Meteorological Office.

1. INTRODUCTION

Extracting results for bulk parameters from PMS 2d probe data requires us to determine the crystal habits present because crystals of different geometry have different average density and fall speed.

Although algorithms for classifying images have been developed their performance on cirrus data has not been tested. Here we investigate the behaviour of our classification software on typical cirrus images.

Furthermore the physical properties of some cirrus crystals are not well-known. We assess likely errors from this source by comparing alternative sets of density and fall speed formulae. We also test the validity of assuming a single dominant particle type.

2. PARTICLE CLASSIFICATION

The image classification scheme is based on the Fourier transform method of Duroure(1983), which detects symmetric images. The sum of the harmonics measures the edge 'roughness' which, together with the 'area ratio' (the product of the major and minor axes divided by image area) distinguishes non-symmetric particles. Images smaller than 6 diodes (150 microns) are not classified.

In the cirrus data we have examined bullet-rosettes and columns are common. Many images however have an irregular but roundish outline and are thought to be mainly irregular spatial crystals, presumably of thick plates and columns. They are frequently the dominant

particle type.

Figure 1 shows the effect of this scheme on some cloud probe data. Columns and bullet rosettes are correctly selected. This is verified by time-series plots of the concentrations of rosettes and irregular spatials, which confirm subjective impressions of the variation of dominant particle through the layer.

Out-of focus irregular spatials of size 150 to 200 microns are sometimes classified as bullet-rosettes (Figure 1(d)). The effects of this mis-classification are exacerbated because it results in incorrect depth-of field estimate and hence overcounting.

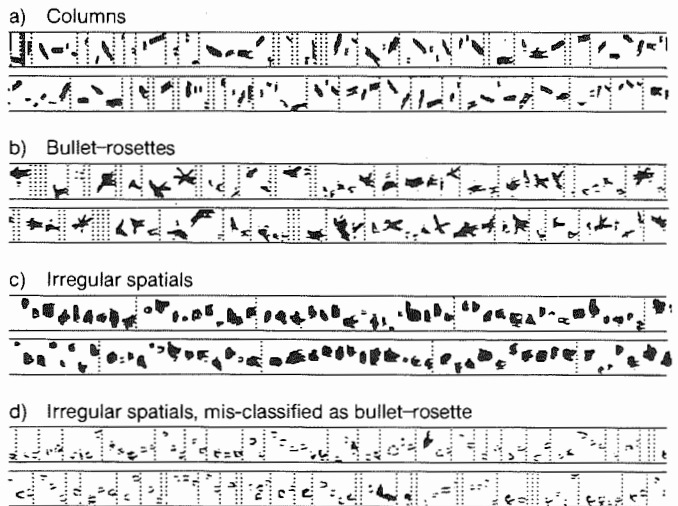


Figure 1. Sample results from the image classification scheme. Flight H786, ascent in frontal cirrus from 5 km altitude to 9 km.

3. MASS AND FALL SPEED FORMULAE

A summary of the various formulae for mass and fall speed appears in Table 1. They are based on the datasets of Heymsfield(1972), taken in

cirrus; Cunningham(1978), taken in U.S East Coast deep cyclonic systems; and Locatelli and Hobbs(1974). Note that in the 'equivalent sphere approximaton' for fall velocity, the particle is placed in an impermeable but massless circumscribed sphere and Stokes formula is used.

Suite 3 was not designed with cirrus in mind and has the following drawbacks i) no altitude correction is applied to fall velocities; and ii) the depth of field for bullet-rosettes is calculated using the maximum dimension rather than an estimate of the width of a branch.

values; a factor of 0.5 for IWC and 0.3 for precipitation rate.

Number concentrations are of course identical for particles larger than 150 microns but for small particles suite 1 undercounts by a factor of about 3 relative to suite 2. This accounts for the lower values of other bulk quantities.

Figure 2 shows the final result (summed over particle types for suites 1 and 2) together with the results from a run assuming blanket classification of bullet rosette (suite 3).

	SUITE 1	SUITE 2	SUITE 3
COLUMNS	$D = 0.82 A^{0.46}$ ; $A \leq 0.02$ $D = 0.61 A^{0.41}$ ; $A \geq 0.02$ (HEYMSFIELD)	$D = 0.42 A^{0.35}$ ; $A \leq 0.16$ $D = 0.52 A^{0.46}$ ; $A \geq 0.16$ (CUNNINGHAM)	AS SUITE 1
	$U = (-0.528 + 157.33 D_{MAX} - 85.27 D_{MAX}^2) \times 10^{-2}$ (HEYMSFIELD)	AS SUITE 1	$U = 0.7 D_{MAX}^{0.41}$
BULLET-ROSETTE	$D = 0.72 A^{0.47}$ ; $A \leq 0.088$ $D = 0.67 A^{0.44}$ ; $A \geq 0.088$ (TETRAHEDRON OF COLUMNS)	$D = 0.50 A^{0.39}$ ; $A \leq 0.21$ $D = 0.61 A^{0.51}$ ; $A \geq 0.21$ (CUNNINGHAM)	AS SUITE 2
	$U = (-1.2 + 97.86 D_{MAX} - 28.17 D_{MAX}^2) \times 10^{-2}$ (HEYMSFIELD)	$U = 0.69 D_{MAX}^{0.41}$ (LOCATELLI AND HOBBS)	$U = 0.7 D_{MAX}^{0.41}$
IRREGULAR SPATIAL	$D = 0.56 A^{0.32}$ (LOCATELLI AND HOBBS)	$D = 0.52 A^{0.40}$ (CUNNINGHAM)	—
	$U = 0.897 D_{MAX}^{0.41}$ (EQUIVALENT SPHERE)	$U = 0.69 D_{MAX}^{0.41}$ (LOCATELLI AND HOBBS)	—
SMALL ( $\leq 0.15$ mm)	$D = 0.935 A^{0.55}$ (SPHERE, DENSITY 0.57)	$D = 0.82 A^{0.46}$ (HEYMSFIELD)	DEPENDS ON BLANKET CLASSIFICATION
	$U = 7.24 D_{MAX}$ (STOKES' FORMULA)	AS SUITE 1 FOR COLUMNS	
DEPTH OF FIELD	MIN AXIS FOR COLUMNS WIDTH OF BRANCH FOR BULLET-ROSETTE MAJ AXIS FOR OTHERS	MIN AXIS FOR COLUMNS AND SMALL PARTICLES WIDTH OF BRANCH FOR BULLET-ROSETTE MAJ AXIS FOR OTHERS	MIN AXIS FOR COLUMNS MAJ AXIS FOR OTHERS

**Table 1.** Formulae for the melted diameter D (mm) and fall velocity, U, ( $m s^{-1}$ ) in terms of maximum particle dimension,  $D_{MAX}$  (mm), and projected area A ( $mm^2$ ).

#### 4. RESULTS AND DISCUSSION.

Generally we find that suite 1 produces larger values for bulk quantities than suite 2. For columns the factor is about 2 for both IWC and precipitation rate; for rosettes about 1.5; and for aggregates 3 to 4 for IWC and 2 for precipitation rate. However for small particles we find that suite 1 gives lower

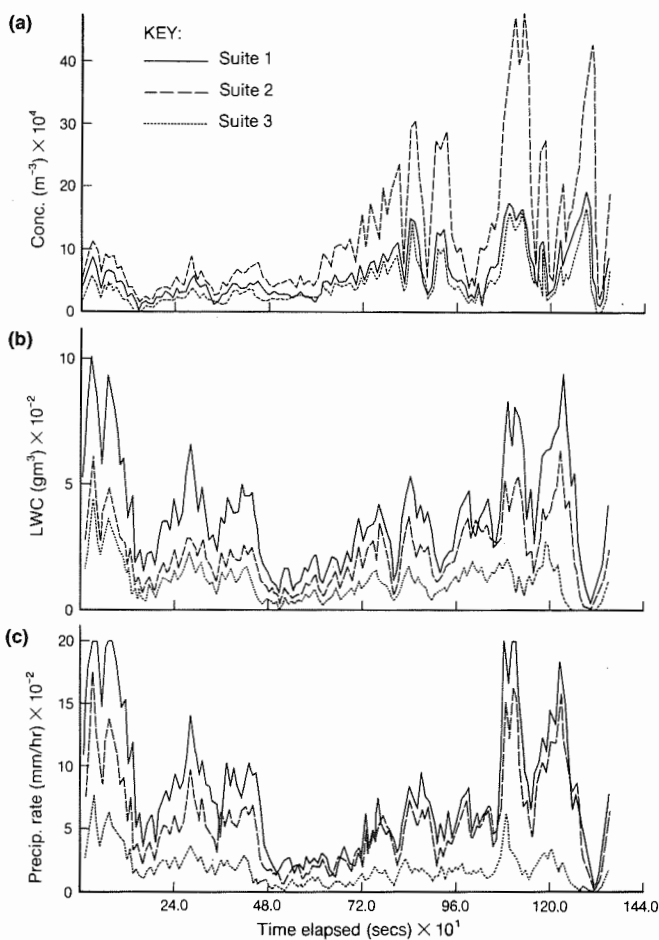


**Figure 2.** Bulk parameters derived from the same dataset used in Figure 1, using alternative mass and fall speed formulae.

First note that the general structure in the cloud does not depend on which suite is used. This is thought to arise from the negative correlation between average particle size and

concentration which is observed in this set of data.

The plot of particle concentration shows that suites 1 and 3 are in close agreement because the largest contribution comes from small particles which are treated in the same way. However (2) gives results up to three times higher due to the different depth of field calculation for small particles. When analysing 2d data some independent means of establishing the habit of small crystals, such as holography or replication, is clearly needed.

The plot of IWC shows (2) yielding higher values than (1), reflecting the higher estimates for the mass of most particle types in (1). Although (2) gives higher concentrations these do not contribute much to the IWC which resides mostly in larger particles. Suite 3 gives even lower values for IWC than (2) despite using similar mass formulae, highlighting the effects of naive depth of field calculation for bullet rosettes. Note however that (2) and (3) are similar at the start of the run where most particles are irregular spatials. Had the effects of mis-classification, mentioned above, been important this would not have been observed. Those particles which are mis-classified do not make a dominant contribution to the IWC. We conclude that providing particles are correctly classified and the depth of field calculated suitably, IWC estimates could be accurate to a factor of 2.

The trace for precipitation rate shows fairly close agreement for (1) and (2) because differences in fall velocity calculation tend to compensate for differences in mass calculation. This is fortuitous and the real uncertainty in precip. rate is probably a factor of 3 or 4. Note the much lower results from (3). These are still an underestimate

even when corrected for altitude ( $\times 1.7$ ), again reflecting the effects of naive depth of field calculation.

#### SUMMARY

- 1) An automatic particle recognition scheme based on both Fourier transforms and geometry is found to successfully distinguish cirrus particles.
- 2) Some poorly imaged crystals are mis-classified as bullet rosettes. Such images are over-counted because of depth-of-field effects, but this does not seriously affect bulk quantities.
- 3) Uncertainties in mass and fall speed relations introduce errors in the corresponding bulk quantities: a factor of 2 for IWC and 3 to 4 for precipitation rate.
- 4) Number concentrations inferred for small particles depend on what is assumed about their shape in the depth of field calculation. However this source of error is unlikely to affect other bulk parameters.

#### REFERENCES

- Cunningham, R.M 1978 Am. Met. Soc. Boston. iv Symp. Met. Obs & Instr, Denver. 345-9
- Durore, C 1978 J Rech Atmos 16 pp71-84
- Heymfield 1972 J. Atmos. Sci 29 1348
- Locatelli, J.D and Hobbs, P.V J. Geophys. Res. 79 2185

by

P.R.A. Brown and A.G. Darlison

Meteorological Office, Bracknell, UK

### 1. INTRODUCTION

Measurements of ice crystal concentrations have been made in glaciating maritime cumulus clouds using both PMS 2-D Optical Array Probes and an airborne holographic system (CONWAY et al, 1982; BROWN 1988). For columnar crystals of length greater than 140  $\mu\text{m}$ , the holographic values are a factor of about 5 larger than those from the 2-D probes. Similar factors are also found for irregular ice particles larger than 140  $\mu\text{m}$  and for all ice particles smaller than this limit. We examine various sources of error in both instruments in an attempt to explain the causes of this discrepancy.

### 2. DATA

The data were obtained during penetrations of two glaciating maritime cumulus clouds (BROWN et al., 1988). The concentration comparison is shown for columnar crystals in Fig. 1, in which the holographic data are averages from a single hologram and the 2-D values are 1 s averages which span the hologram exposure time. Fig. 2 shows size spectra of columnar crystals for data taken from part of a single cloud penetration, the holographic data being an average of four individual exposures and the 2-D data being a 5 s average covering this period. The average concentration difference factor for the whole data set is about 5, whilst for the data in Fig. 2 it is closer to 10. In the latter case the factor appears to be roughly constant over the size range 200–350  $\mu\text{m}$ .

### 3. ERRORS IN HOLOGRAPHIC DATA

The sample volume of the holographic device

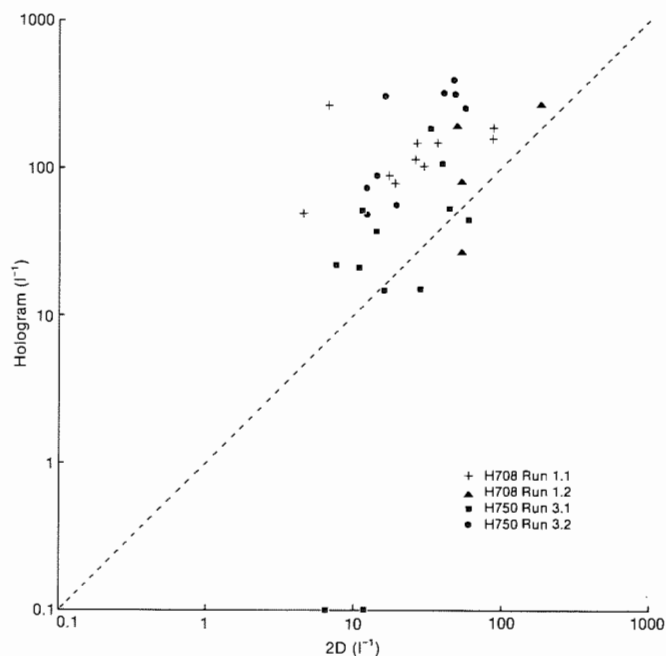


Fig. 1 Comparison of measurements of the concentration of columns with  $L > 140 \mu\text{m}$ .

is well-defined by the optical layout of the system (BROWN, 1988). Errors are therefore thought to be derived from two main sources. Firstly, the images themselves are of rather variable quality and it is possible, where the quality is very poor, to fail to identify some of them. This is however most significant for small sizes (less than 50  $\mu\text{m}$ ) and will in any case result in undercounting. Second is the effect of the airflow around the pod which houses the holographic camera. This has been examined using the simple model of KING (1984,1985), from which some generalized results may be obtained.

The shadow zone, bounded by a particle trajectory which grazes the pod nose (Fig. 3), has a maximum depth of about 3 cm, for

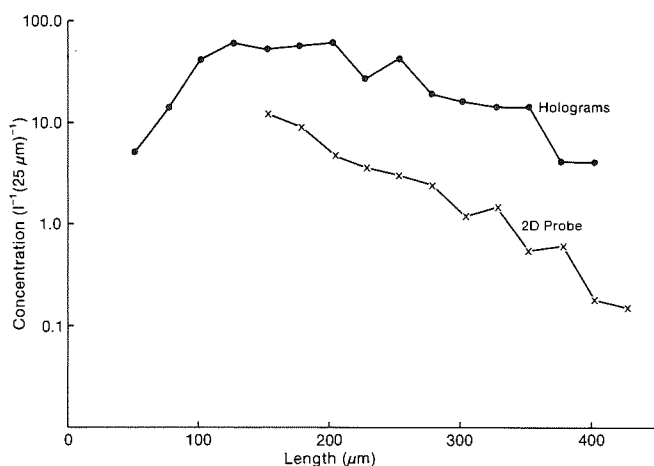


Fig.2 Size spectra of columns from holographic and 2-D data, flight H750. Temperature = -8.5 °C.

liquid droplets of about 30 μm in diameter or columns of about 170 μm in length. The former figure has been confirmed by measurements. Outside the shadow zone, the compression of particle trajectories increases the apparent concentration above the free-stream value by a factor which is a function of the particle size. This enhancement factor does however decrease rapidly away from the pod surface, and when averaged over the whole 25 cm depth of the holographic sample volume amounts to no more than about 30% for most sizes of columnar crystal. Those particles which strike the nose of the camera pod upstream of the sample aperture may fragment and give rise to spurious small ice particles. These however are generally easily identified by their concentration in the region close to the pod surface, and it is normal practice to exclude this from the hologram analysis.

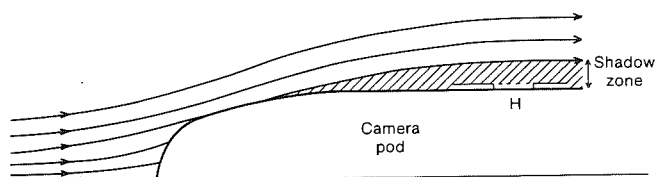


Fig. 3 Schematic view of particle trajectories around holography camera pod. H shows position of sampling aperture.

#### 4. ERRORS IN 2-D PROBE DATA

In the processing of 2-D data, individual images are automatically type-classified by a procedure described by DARLISON AND BROWN (1988). The comparison of this scheme with manual classification of some of the data from this study is shown in Table 1. The possible mis-classification of images may interact with other sources of error in 2-D data described below.

The depth of field for an individual image is given according to KNOLLENBERG (1970) by:

$$D_f = 3/2 * D_{eff}^2 / l \quad (1)$$

where  $D_{eff}$  is the effective dimension of an image which determines its diffraction properties and  $l$  is the illumination wavelength. For droplets and near-spherical ice particles,  $D_{eff}$  is taken to be the width of the widest slice, whereas for columnar crystals it is taken as the column width. The latter is significant as it means that the depth of field will be smaller than the probe sample gap for all columns shorter than 650 μm (assuming a 4:1 axis ratio).

Quasi-spherical irregular ice particles will generally have a minor axis larger by a factor of about 2 than that of a column of the same major axis length. Any such image mis-classified as a column will have its depth of field overestimated by a factor of 4. If 20% of irregulars are mis-classified as columns and vice-versa then the measured concentration of columns may be about 85% of the true value, whilst that of irregulars may be around 150%.

TABLE 1 Comparison of manual and automatic image type classification.

Manual	Automatic	
	Columns	Irregular
Columns	160	20
Irregular	36	128

TABLE 2 Software overestimate of 2-D sample volume for columns (4:1 axis ratio).

Length * width of shadow ( $\mu\text{m}$ )	Measured width	Sample Vol. overestimate
100 * 25	32.3	1.66
200 * 50	64.8	1.68
300 * 75	94.3	1.58

We have subsequently found that the algorithm used by the processing software to determine the column width gives a systematic overestimate, which will in turn cause an overestimate of the depth of field and hence the sample volume of the 2-D probe. The effect of this error for columns of different dimensions is shown in Table 2. These figures assume random orientation of crystals relative to the diode array. The sample volume overestimate may be larger for certain preferred orientations, and are also larger for larger axis ratios.

We have measured the time response of our 2-D cloud probe by monitoring the output from the photodetector amplifiers with the beam being chopped rapidly, and found a minimum rise/fall time of about 0.9  $\mu\text{s}$ , corresponding to 3-4 clock cycles at the normal aircraft true airspeed of 100  $\text{ms}^{-1}$ . The effects of this are twofold. Firstly, images with a dimension of less than about 100  $\mu\text{m}$  will not cause the probe to trigger. Secondly, images larger than this will be undersized in the direction perpendicular to the diode array by a factor of 2 for 100  $\mu\text{m}$  images, approaching unity at about 200  $\mu\text{m}$ . This undersizing can cause underestimates of the depth of field and sample volume in a similar manner to that described above. It will also act to shift the entire 2-D measured size spectrum towards smaller sizes.

##### 5. SUMMARY AND CONCLUSIONS.

The holographic sample volume is unambiguous in its definition and predictions about

airflow-induced distortions of holographic data have been at least partially tested by measurement. We therefore consider that the main causes of the concentration discrepancies lie with the 2-D system. No single source of error can account for the whole of the factor of 5-10 difference, although most act in the correct sense. We hope to model the operation of the 2-D probe, incorporating photodiode response and an improved calculation of the width of columns, with a view to developing more accurate sample volume estimates than those currently employed by our software.

The effects of probe response time will be of extra significance in cirrus cloud for two reasons, firstly because many of the particles are expected to be bullet-rosettes with a number of columnar arms, and secondly because the true airspeed at cirrus altitudes is in the range 120-140  $\text{ms}^{-1}$ . The diode response time is then of the order of 5 clock cycles and the possible non-detection and undersizing therefore extend to larger sizes.

##### REFERENCES

- BROWN P.R.A.: submitted to J.Atmos.Oceanic Technol (1988).  
 BROWN P.R.A., CHOULARTON T.W., and GRIGGS, D.J.: submitted to Quart.J.R.Met.Soc (1988).  
 CONWAY B.J., CAUGHEY S.J., BENTLEY A.N., and TURTON J.D.: Atmospheric Environment 16 (1982) pp1193-1207.  
 DARLISON A.G. and BROWN P.R.A.: Proceedings 10th Internatl. Cloud Physics Conf., 15-20 Aug. 1988.  
 KING W.D.: J.Atmos.Oceanic Technol. 1 (1984) pp5-13  
 KING W.D.: J.Atmos.Oceanic Technol. 2 (1985) pp539-547  
 KNOLLENBERG R.G.: J.Appl.Met. 9 (1970) pp86-103

# DEVELOPMENT OF HYDROMETEOR VIDEO SONDE

Masataka Murakami and Takayo Matsuo

Meteorological Research Institute,  
Tsukuba, Ibaraki 305, Japan

## 1. INTRODUCTION

In studies of cloud and precipitation formation, it is important to know the microphysical structure of clouds as well as the dynamical structure. Measurements of microphysical properties of precipitation clouds have been often made by airplanes equipped with a J-W hot wire device, a FSSP, and 2-D Optical Array Probes. Despite the convenience of these measuring instruments, they still have some problems. The instruments do not have sufficient ability to discriminate between cloud droplets and ice crystals nor the ability to reproduce a detailed shape of cloud and precipitation particles. Furthermore, from the viewpoint of airplane safety, research airplanes are sometimes restricted from operating in shallow orographic clouds and wintertime severe convective clouds.

To overcome these difficulties, we developed a special sonde called a Cloud Particle Video Sonde (CPVS) (Murakami *et al.*, 1987). It provided high quality images of cloud and precipitation particles up to 1 mm in size. However, for better understanding of precipitation formation processes, it is necessary to measure the precipitation particles larger than 1 mm. To meet this requirement, we have improved the CPVS in many respects, and made a Hydrometeor Video Sonde (HYVIS).

In this paper, we describe the HYVIS and expose its capabilities through a report of some observations.

## 2. OUTLINE OF HYDROMETEOR VIDEO SONDE SYSTEM

To obtain particle images together with meteorological data, the HYVIS and a standard rawinsonde are attached to the same balloon and are launched into clouds at ascent velocity of about 5 m/sec. The HYVIS transmits images of hydrometeors taken by two TV cameras over a 1,687 MHz microwave link to a ground station in real time so that it does not need to be retrieved later unlike a snow crystal sonde developed by Magono and Tazawa (1966). At the same time, meteorological elements such as temperature, humidity, and pressure are also transmitted at a frequency of 1,680 MHz (see Fig.1). These two microwaves of different frequencies are received by one antenna assembly with a 1.2 m parabolic dish. The received signals are fed through a Power Splitter to two receivers (RD65A and SAR-4; Meisei Electric Co.). The video signal from the HYVIS is detected at the SAR-4 receiver with FM Demodulator and

then fed to a Video Mixer. The video signal mixed with the time data from a Time Code Generator is recorded on a video cassette tape and is simultaneously displayed on a CRT.

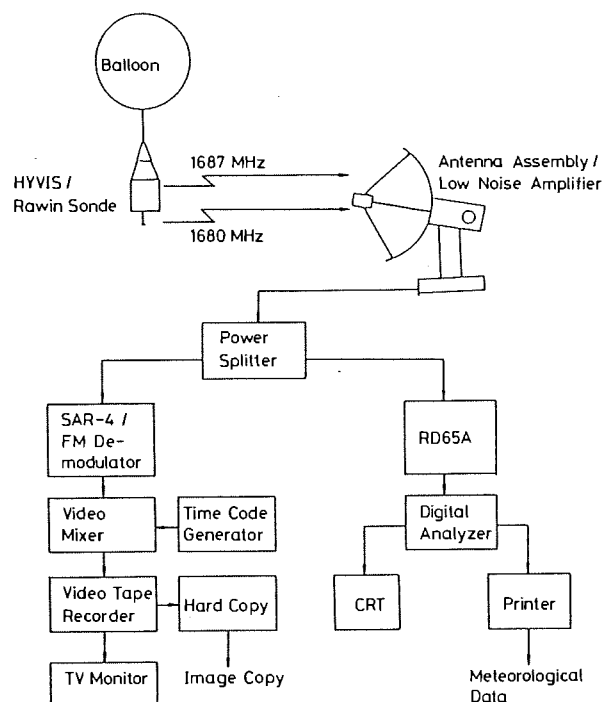


Fig.1. System diagram.

The meteorological signal is detected at RD65A receiver and processed through a Digital Analyzer to be displayed on a CRT and to be printed out in the form of temperature, relative humidity, pressure, height, windspeed, and wind direction in real time.

## 3. DESCRIPTION OF HYDROMETEOR VIDEO SONDE

As shown in Fig.2, the HYVIS has two small TV cameras with different magnifications to take pictures of hydrometeors from 7  $\mu$ m to 2 cm in size. Hydrometeors fall through the particle inlet (25 mm X 50 mm) and collect on a transparent particle dish. For first 4 seconds, TV camera A takes pictures of the cloud particles on the dish. Then TV camera B takes pictures of the precipitation particles for another 6 seconds. During the latter half of the shooting of TV camera B, a new part of the particle dish is pulled out.

TV cameras A and B have optical systems with magnifications of 7X and 0.33X, and takes pictures of 0.8 mm X 1.1 mm and 15 mm

X 20 mm areas on the particle dish, respectively. The particle dish is a roll of 35 mm leader film for procession. A special water-repellent coating is given to the surface of the film. The film is pulled out of a film magazine by a winding mechanism with a small DC motor and driving chains. Total length of the film is 15 m, and this capacity is long enough to continue an observation for 50 minutes and up to a height of 15 km.

The video signal from the TV cameras is transmitted to a ground receiving station through a Band-pass Filter (cut-off frequency=1 MHz), a Video Amplifier, and a FM Transmitter. The nominal transmission power is 0.6 W.

Two TV cameras, electronics circuits, and lithium batteries are stored in a heat insulating box to protect them from cold temperatures in the upper air. Dimensions of the HYVIS are 225 mm X 152 mm X 410 mm, and its weight is approximately 1.3 kg.

#### 4. DETERMINATION OF COLLECTION EFFICIENCY

In order to deduce the concentration of cloud and precipitation particles from the number collected on the particle dish, it is necessary to know the collection efficiency of the HYVIS for hydrometeors. To determine the collection efficiency of the HYVIS for water droplets, the collision experiment was carried out at various air speeds in a wind tunnel. The HYVIS and a reference ribbon of 3 mm width were simultaneously exposed to an air stream

containing sprayed water droplets, and the number of collected droplets was compared between the HYVIS and the ribbon. The collection efficiency showed no significant air speed dependency so that the mean value of the collection efficiency  $E$  expressed by the

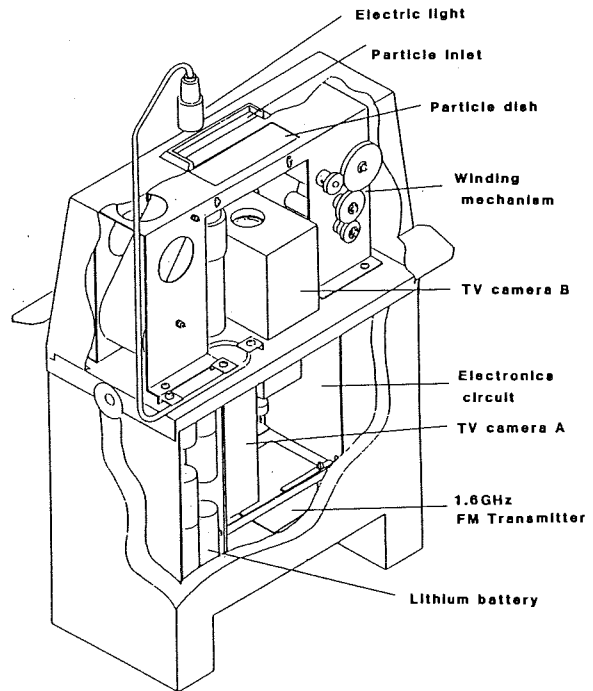


Fig.2. Cutout view of the HYVIS.

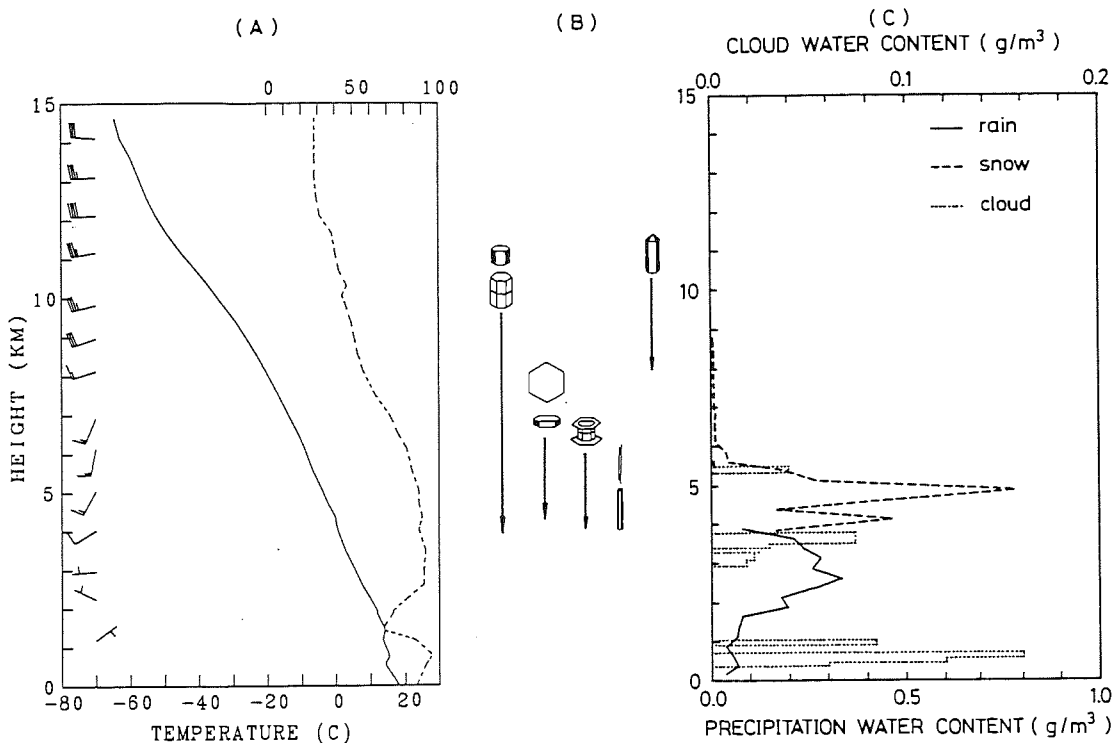


Fig.3. Microphysical structure of clouds along the ascent of the HYVIS: (A) temperature (solid line), relative humidity (broken line), and wind; (B) snow crystal types observed aloft; (C) rain water content (solid line), snow water content (broken line), and cloud liquid water content (dotted line).

following equation will be used regardless of air speed to calculate the number concentration of cloud droplets ( $D \leq 130 \mu\text{m}$ ) in the next section.

$$E = 0.0067D + 0.14 \quad (1)$$

The collection efficiency for droplets larger than  $130 \mu\text{m}$  is assumed to be unity.

As for wet snowflakes from 1.5 mm to 3.5 mm, the collection efficiency was determined to be 0.77 from field experiments although the data were scattered to a great extent. For dry snow crystals, it is difficult at the present time to determine a reliable collection efficiency because of a large scatter in collection efficiency data and bounce-off effect. Therefore, in calculating the number concentration of snow crystals, we corrected the raw data on the number concentration by a certain factor assuming the continuity of mass flux of precipitation particles across the melting layer.

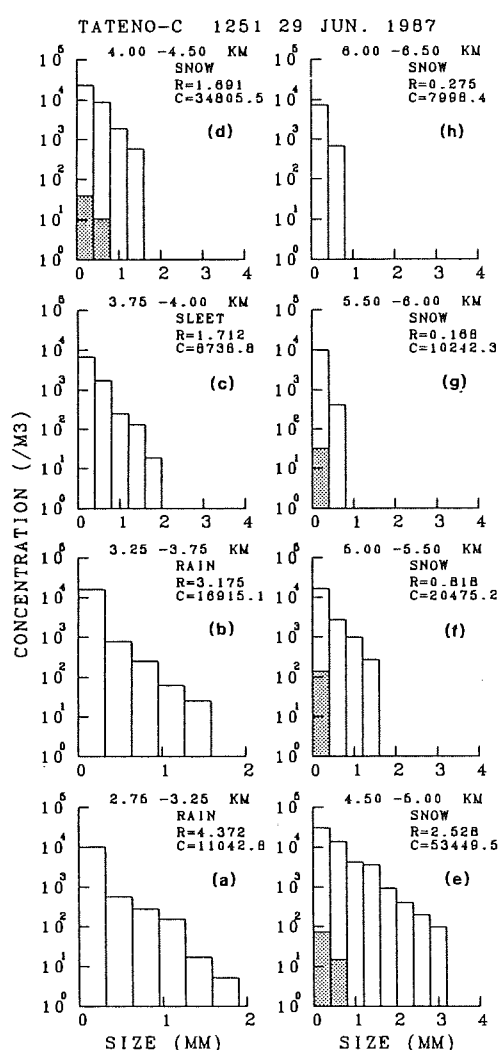


Fig.4. Change in size distributions of precipitation particles along the ascent of the HYVIS. Shaded bars represent supercooled drops. At the upper right of each figure shown are precipitation rate ( $R$ ; mm/hr) and total concentration of precipitation particles ( $C$ ; particles/ $\text{m}^3$ ).

## 5. AN EXAMPLE OF HYVIS OBSERVATION

By using the HYVIS along with a rawinsonde, the microphysical structure of stratiform precipitation clouds was observed over the Tsukuba Area of Kanto Plain, Japan, on 29 June 1987. The balloon equipped with the HYVIS and a rawinsonde was launched at 12:51 JST and required thirty minutes to make observations up to 11 km which was the cloud top height. At that time, this study area was located about 300 km north of a stationary front (Baiu front). Temperature, relative humidity, and wind profiles obtained from the balloon observation are shown together with snow crystal types observed aloft, cloud liquid water content, rain water content, and snow water content in Fig.3. Snow water content was computed from the size distribution of snow crystals using mass vs. maximum dimension relationships derived by Davis (1974).

A vertical change in size distributions of precipitation particles from 2.75 to 6.5 km MSL are shown in Fig.4. The HYVIS ascended in stratiform clouds except for the layer between heights of 4.5 and 6.0 km where it was under the influence of a convective region embedded in stratiform clouds. Broadening in size distributions in Figs.4e-4g indicated the rapid growth of needle type crystals in this region through a seeder-feeder mechanism. The upper part of the convective region consisted of supercooled cloud droplets. Also existed a sparse drizzle layer of 1.5 km depth just above the  $0^\circ\text{C}$  level. Rain drops grew through a collection of cloud droplets during their fall from 3.75 to 2.75 km MSL. Size distributions of clouds droplets in this layer and the convective region are shown together with those in lower cumulus clouds in Fig.5.

Examples of hydrometeor images taken by the HYVIS are shown in Fig.6. As seen from Fig.6b, most of elementary sheathes and

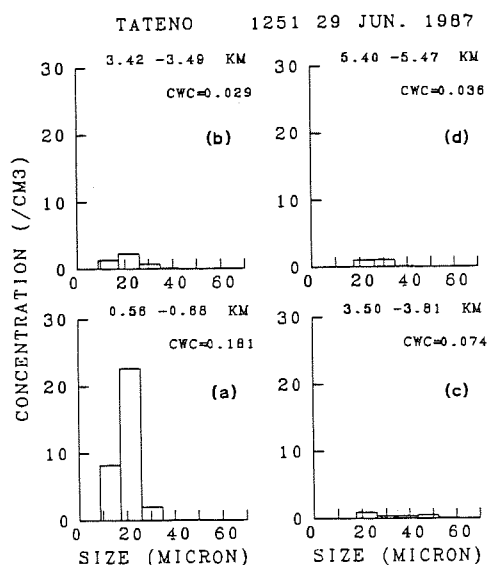


Fig.5. Size distributions of cloud droplets measured at different heights. At the upper right shown is cloud liquid water content ( $\text{g}/\text{m}^3$ ).

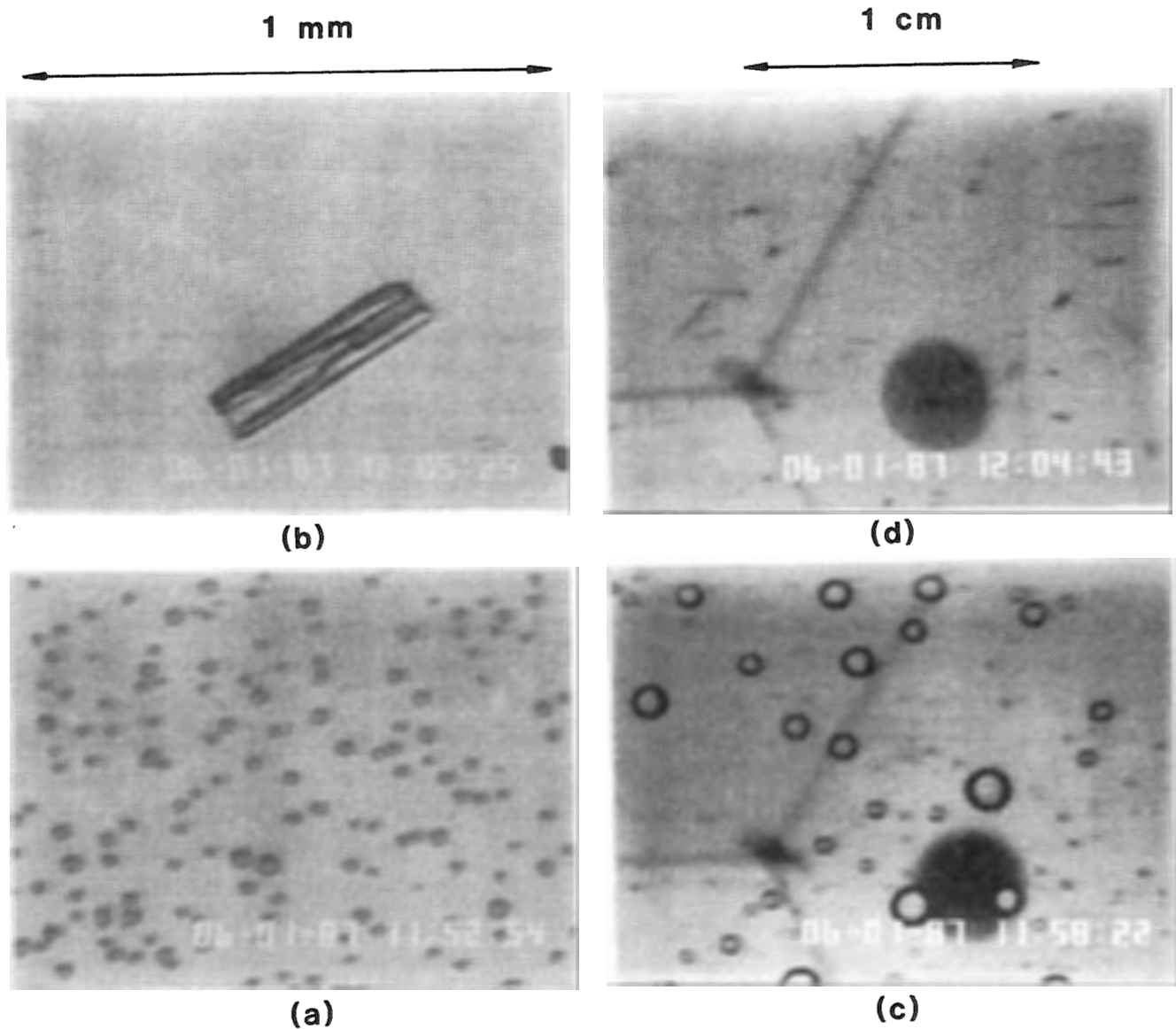


Fig.6. Examples of hydrometeor images: (a) cloud droplets observed at 0.6 km MSL (14.3 °C); (b) sheath at 4.9 km MSL (-3.4 °C); (c) rain drops at 2.5 km MSL (8.4 °C); (d) needle type crystals at 4.7 km MSL (-2.2 °C).

needles which rapidly grew in the convective region had no rime coverage on them although lightly rimed hexagonal plates were rarely observed there. This means that dominant mechanism of crystal growth in the feeder cloud was vapor deposition.

## 6. CONCLUSIONS

A special sonde (HYVIS) for measuring cloud and precipitation particles has been briefly described.

The HYVIS provides high quality images of hydrometeors from 7  $\mu\text{m}$  to 2 cm in size and a fine vertical resolution ( $\sim 50$  m) of microphysical structure in clouds. Advantages of the HYVIS have been demonstrated by briefly highlighting the observational results of stratiform clouds associated with a stationary front.

The capabilities of the HYVIS makes critical measurements possible in otherwise inaccessible clouds such as wintertime severe convective clouds and shallow orographic clouds. The HYVIS

measurements should lead to an improved understanding of clouds and precipitation formation processes and their modification potential.

## REFERENCES

- Davis, C. I. , 1974: *Ph.D. Thesis*, Dept. Environ. Sci., Univ. of Wyoming, Laramie, Wyoming.
- Magono, C. and S. Tazawa, 1966: Design of " snow crystal sonde". *J. Atmos. Sci.*, **23**, 618-625.
- Murakami, M., T. Matsuo, T. Nakayama and T. Tanaka, 1987: Development of Cloud Particle Video Sonde. *J. Meteor. Soc. Japan*, **65**, 803-809.

THE STUDY OF THE INTERSTITIAL AEROSOL PARTICLES AND CLOUD DROPLETS  
WITH DIGITAL IMAGE ANALYSIS OF DIFFRACTION IMAGES

R. Jaenicke and R. Sörensen

Institute for Meteorology, University of Mainz, FRG

## 1. INTRODUCTION

The study of airborne particles is currently limited to observation of their integral scattered light or by observation using microscopes. The latter has the disadvantage of studying the particles depart of their natural surrounding. The progress in computer science and manufacturing now makes it possible to look at the discrete particle in a different way. An approach to a new technique will be presented here. The method used can be described as "digital image processing".

There are significant hints in the diffraction image of a particle for defining it as a droplet, at least as a particle of spherical shape, or as a particle with rough surface (STRAUBEL, VAN DE HULST). A spherical droplet will show a diffraction image of circular geometry, while a dry one will not. The individual particle is illuminated by laser beam and the diffraction image is directly recorded by a video camera connected to either a recorder or a personal computer (Fig.1).

## 2. METHOD

### 2.1 PARTICLE DETECTION

The particles are sent through the laser beam using clean air sheet technique so that single particles can be isolated. With no particle present in the beam, the intensity maximum of the laser light is masked out so that the camera will not detect any scattered light except for some noise which is virtually always present. A particle crossing the beam will scatter the light and so the camera will see an increase in integral measured intensity. The computer is able to detect this increase and takes a snapshot of the camera image for

processing. As integral intensity measurement is not used for this method, there is only a small area scanned for changes in intensity. Only increasing intensities will be recognized. The detection of a particle lasts about 1/25 of a second. Fig.1 shows the system and its hardware components.

### 2.2 PROCESSING

When a snapshot of a particle has been made, there is no limit in time for processing its image. The time of processing can be regarded as non-sampling time. Currently, processing of an image lasts about 10 to 30 seconds depending on the complexity of the scattered image. At first, the computer will check a horizontal line for symmetry in intensity. If symmetry is given, another process takes place to detect circular symmetry, otherwise the particle is classified as non-spheric. The algorithm used is looking for areas of identical intensity, so constructing a polygone, framed by an inner and an outer circle. The construction of these circles may be seen in Fig.2. Fig.3 shows the scattering image of a large, irregular shaped particle. Fig.4 is a pseudo-three-dimensional view at the intensity distribution of a spherical shaped particle (droplet).

### 2.3 LIMITATIONS

As can be noted from above, the processing itself is relatively slow, depending on the used algorithms and the number of digitized images per second. So real time processing is not yet possible. If the time for computation can be reduced significantly, it might be possible to advance to about 30 images per second which will be classified. Another improve will be to

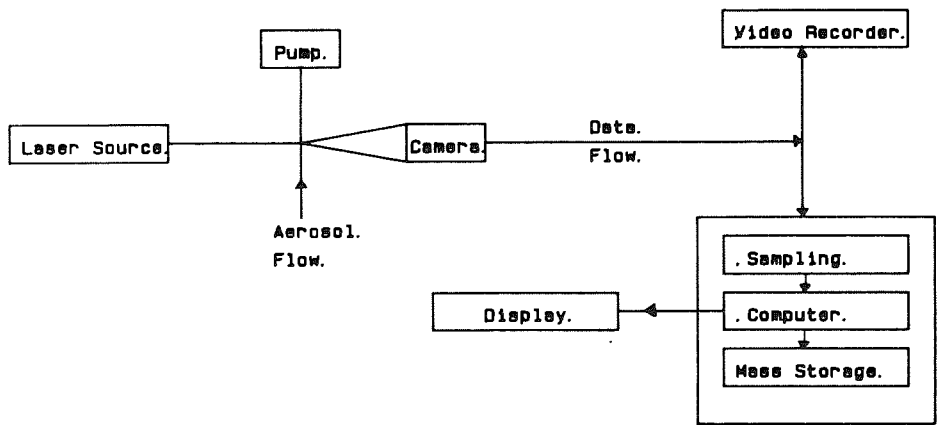


Fig. 1  
Required Hardware

SYSTEM OVERVIEW Digital Image Processing.

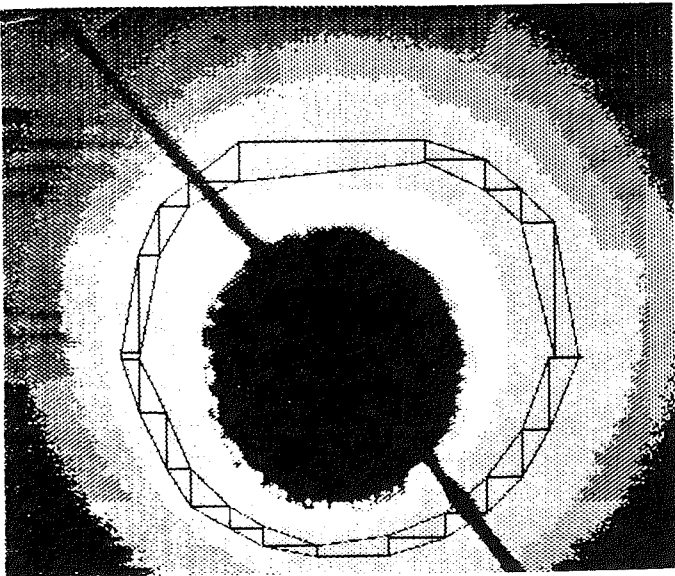


Fig.2: The process of detecting a circular shaped diffraction pattern

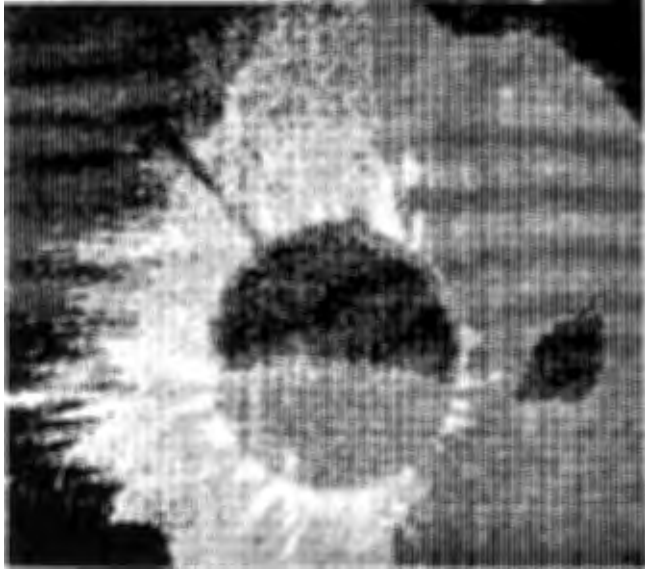


Fig.3: Printout of an irregularly shaped diffraction image



Fig.4  
Pseudo-three-dimensional intensity distribution produced by a spherical particle

abandon digital processing and reduce computation to the calculation of data, sampled by an analogous device like some circular mounted light detectors.

#### 2.4 ADVANTAGES

Digital image processing is very flexible. It is possible to develop strategies for various sampling problems depending on scattered light. When the structure and solution of a problem is evident, one is able to apply the knowledge to somewhat more specific machines. Another advantage is that one can observe the process of sampling and processing data on a monitor. The decision criteria may be manually corrected or interrupted. Any method of interpreting sampled data may be used, as integral intensity, intensity scattered into a specific sector or angle or pattern recognizing, i.e. contrast measurement. A large number of algorithms are available in helping with pattern matching, spectral analysis or noise reduction. Figs. 2 to 4 are matrix printouts of image data, the quality of the images is much better than on these printouts.

#### 3. USAGES

Currently a method is developed to use the shown apparatus in fog so that it is possible to obtain distributions of inactive particles and droplets. A real-time application is in progress to sample dry (inactive) particles for further analysis. For the present, the system is limited to laboratory usage. In field applications, one would sample images with a video recorder and analyze them in the laboratory; with the recorder as a "mass storage system", there is no need for real time processing of the sampled data.

#### 4. ACKNOWLEDGEMENT

The study is carried out with support of the German Science Foundation Sonderforschungsbereich "Chemistry and Dynamics of Hydro-meteors".

#### REFERENCES

- BERGMANN-SCHÄFER (1978): Lehrbuch der Experimentalphysik, Band III Optik. de Gruyter, 7th Ed.
- BORN & WOLF (1965): Principles of Optics. Pergamon Press, 3rd Ed.
- VAN DE HULST, H.C. (1957): Light scattering by small particles. Wiley & Sons.
- BROSSMAN, R. (1966): Die Lichtstreuung an kleinen Teilchen als Grundlage einer Teilchengrößenbestimmung. Dissertation an der TH Karlsruhe, Fakultät für Maschinenbau und Verfahrenstechnik.
- GIESE/DE BARY/BULLRICH/VINNEMANN (1962): Tabellen Miefunktionen. Akademie-Verlag Berlin.
- ROSENBERGER, D. (1975): Technische Anwendungen des Lasers. Springer-Verlag.
- STRAUBEL, H. (1981): Elektro-optische Messung von Aerosolen. Technisches Messen 48, Heft 6, p.199.
- STROKE, GEORGE W. (1969): An Introduction to Coherent Optics and Holography. Academic Press, 2nd Ed.
- VAN DE HULST, H.C. (1957): Light Scattering by small Particles. Wiley & Sons.

# ON THE DETERMINATION OF DROPLET SIZE DISTRIBUTIONS WITH THE COUNTER-FLOW VIRTUAL IMPACTOR

B. Johansson and J. Heintzenberg  
Department of Meteorology, University of Stockholm  
S-10691 Stockholm

## 1 INTRODUCTION

With the counter-flow virtual impactor (CVI) cloud droplets within an adjustable size range can be sampled for subsequent physical and chemical analyses without interference from gases and unactivated particles.

For a full understanding of the sampled cloud the analyses in the CVI need to be related to the cloud droplet size distribution.

Below, we present a new way of obtaining this size distribution through an inversion of parameters which are measured in the CVI. This method of retrieving the cloud drop size distribution has the advantage of yielding an internal consistency with the chemical properties measured in the same probe.

## 2 SOURCE OF DATA

The counter-flow virtual impactor takes size segregated samples of cloud droplets, separating them from the surrounding air and unactivated particles (OGREN ET AL. 1985; NOONE ET AL. 1988). The

sampled droplets are evaporated in a flow of warm, dry and particle free air. Then their liquid water content (LWC) is measured in the gas phase with a Lyman- $\alpha$  hygrometer (ZUBER and WITT, 1987). The non-volatile residues of the droplets are counted with a particle counter (CNC). By adjusting the cut-size, ( $r_{50}$ ), of the CVI, the lower size limit of the sampled droplets can be varied in a range from ca 2 to ca 20  $\mu\text{m}$  radius;  $r_{50}$  corresponds to a 50 % droplet collection efficiency. According to the CVI-calibration (NOONE ET AL., 1988), the collection efficiency for the droplet number concentration (CNC-efficiency) can be approximated by an incomplete  $\beta$ -function. Figure 1 shows an example for an  $r_{50} = 9 \mu\text{m}$ . The average absolute deviation, that is the square root of the sum of the squared deviations between the calibration curve and the approximating  $\beta$ -function, is .02 units on our efficiency scale.

### 3 INVERSION ALGORITHM

The measured property  $S$ , (droplet mass or number) is related to the droplet size distribution  $dN/dr$  through a Fredholm-integral equation where the kernel  $K(r)$  is the size dependent collection efficiency of the CVI in terms of either droplet number or liquid water content.

$$S = \int_0^{\infty} K(r) * dN(r)/dr) dr \quad (1)$$

By multiplying number-counting efficiencies with  $4\pi r^3/3$  the counting efficiencies are converted to mass collecting efficiencies, (using a density of  $1 \text{ g/cm}^3$  for water). Now, information from both CNC and LWC data can be used jointly to retrieve the drop size distribution.

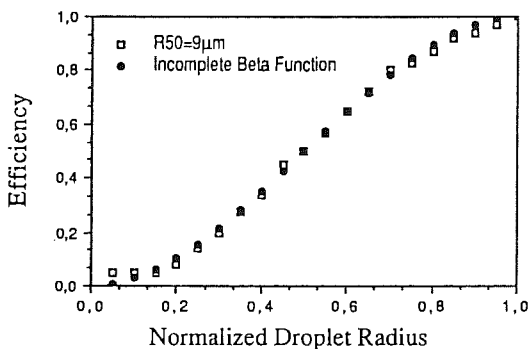


Fig. 1: Incomplete  $\beta$ -function, approximating the CVI collection efficiency at a cut radius  $r_{50} = 9 \mu\text{m}$ . This function is shifted left and right with varying  $r_{50}$ -value.

Equation (1) has no general analytical solution. However, by writing it as a finite sum (as in equation 2) we can find a numerical solution to the equation assuming a histogram representation of the size distribution instead of the continuous function in equation (1).

$$S = \sum_{l=1}^L K_l * (dN/dr)_l dr \quad (2)$$

$L$  is the total number of columns,  $(dN/dr)_l$  is the value of the drop size distribution in the histogram column,  $l$ ,  $K_l$  is the kernel averaged over the interval  $\delta r$ , of the column. The numerical method for solving equation (2) is based on the algorithm of HEINTZENBERG (1978). It is a randomized minimization search technique where the basic idea is to find a histogram-type size distribution whose properties (here CNC and LWC) have a minimum deviation from the measured (synthetic) properties. The minimization is done by an iterative least square fit.

### 4 RESULTS

Inverting synthetic data allows us to see how well the CVI has to perform to retrieve a good approximation of the drop size distribution. How many different size segregated

samples need to be taken to be able to yield an acceptable picture of the true size distribution? Is it necessary to increase the range in which size segregated samples can be taken (at present this range goes from ca 2 to ca 20  $\mu\text{m}$ )? How do realistic measurement errors affect the inversion result?

As an example, figure 2 shows an inversion result using 12 different cut radius settings in the hypothetical range from 2 to 40  $\mu\text{m}$ .

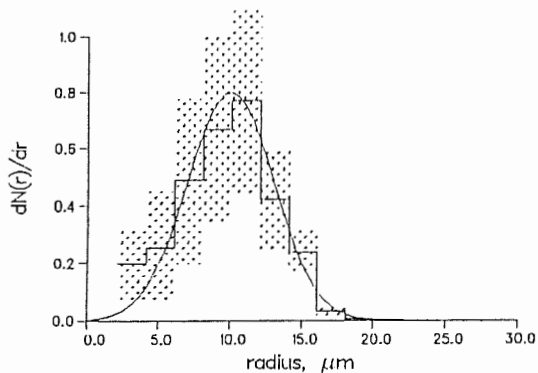


Fig. 2: Inversion results using  $r_{50} = 2, 4, 6, 8, 10, 12, 15, 20, 25, 30, 35,$  and 40  $\mu\text{m}$  and a 5% measuring error, (details, see text).

The synthetic data were calculated for the Gaussian distribution (shown by the full smooth line in figure 2). The histogram distribution is the mean of 80 separate inversions. The scatter of the inversion results is shown by the shaded bars. The measure-

ment error in the synthetic data of CNC and LWC was set to 5%. The average absolute deviation between the inverted size distribution and the initial size distribution was .06 units on our concentration scale. This deviation depends both on the measurement error and the error induced by the inversion.

#### REFERENCES

HEINTZENBERG, J.: Particle size distributions from scattering measurements of non-spherical particles via Mie-theory. *Contr. Atmos. Phys.* 51 (1978), p. 91-99.

NOONE, K.J.; CHARLSON, R.J.; COVERT, D.S.; OGREN, J.A.; HEINTZENBERG, J.: Design and calibration of a counterflow virtual impactor for sampling of atmospheric fog and cloud droplets. *Aerosol Sci. Technol.*, in press, 1988.

NOONE, K.J.; CHARLSON, R.J.; COVERT, D.S.; OGREN, J.A.; HEINTZENBERG, J.: Cloud droplets: Solute concentration is size dependent. *J. Geophys. Res.*, in press, 1988.

OGREN, J.A.; HEINTZENBERG, J.; CHARLSON, R.J.: In-situ sampling of clouds with a droplet to aerosol converter. *Geophys. Res. Lett.* 12 (1985), p. 121-124.

ZUBER, A.; WITT, G.: Optical hygrometer using Differential Absorption of the Hydrogen Lyman-alpha Radiation. *Appl. Optics* 26 (1987), p. 3083-3089.

# MULTIPARAMETER CHARACTERIZATION OF RAINDROP SIZE DISTRIBUTION

## BY THE POLARIMETRIC DFVLR RADAR: FIRST RESULTS

M. Chandra      A. Schroth      E. Lueneburg

DFVLR, Institut fuer HF-Technik, 8031 Wessling, West Germany

### 1. INTRODUCTION

The application of radar for obtaining the precipitation rate is important not only in the field of operational radar meteorology but also in microwave propagation research. Since the coherent polarimetric DFVLR radar, ref.(1), has become operational, efforts to obtain radar estimates of rainrates have been in progress. In this connection the radar determination of the raindropsize distribution via a two parameter description, ref.(2), and a three parameter description, ref.(3) are being investigated. In this paper we report demonstrative calculations involving the two parameter description of the radar determined, raindropsize distribution,  $N(D)$ . The results of the implementation of the mentioned three parameter technique in the sense of its applicability and limitations would be presented at the conference subject to the availability of appropriate radar data.

### 2. THEORY AND METHODOLOGY

The rainrate,  $R$  (mm/hr), is given by

$$R = 0.6\pi 10^{-3} \int V(D) N(D) dD \quad (1)$$

where  $V(D)$ , in m/s, is the fall-velocity of the raindrop of equivalent volume drop diameter,  $D$ (mm). The key to the radar determination of rainrate lies in its capability to characterize  $N(D)$ , from radar observables.

In the radar determination of  $N(D)$ , the microphysical interpretation of the polarimetric radar observables was obtained using the concept, ref.(3,4 & 5), entailed in the quantity  $\chi_{ij}^{pq}$ , which arises from the mean value of the product of polarimetric echoes  $S_{ij}$  and  $S_{pq}^*$  corresponding to the instantaneous scattering amplitudes of the scatter volume. The practical implementation of this quantity is, however, cumbersome for its formulation retains the sensor characteristics explicitly. A far more 'application friendly' use of this quantity is possible by defining an equivalent reflectivity  $Z_{ij}^{pq}$  related to  $\chi_{ij}^{pq}$ . This concept, invoked in ref.(3), may be seen as a polarimetric generalisation of the conventional single polarization equivalent reflectivity. This generalization may be formally described as:

$$Z_{ij}^{pq} = F \left( \frac{\lambda^4}{|K|^2 \pi^5} \right) \int_{D_{\min}}^{D_{\max}} s_{ij}(D) s_{pq}^*(D) N(D) dD \quad (2)$$

Here  $s_{ij}$  and  $s_{pq}$  are the polarimetric scattering amplitudes of the raindrop of equivalent volume drop diameter  $D$  appropriately averaged for the canting and or the shape oscillation effects, and the rest of the terminology conforms to the one in refs.(4, 5) excepting the factor  $F$ . This term is simply unity if the "user" chose to exclude in the above definition (i.e. by having corrected for) the influences of internal and external propagation effects and the Doppler phase term. Details of these influences may be found in refs.(3,5). Using this formalism, computer programmes were written for interpreting polarimetric quantities using an interpolation based inversion method (courtesy Dr. H. Schuster) for achieving a two and or three parameter radar description of the Gamma type  $N(D)$ :

$$N(D) = N_0 D^\mu e^{-(3.67 + \mu) D/D_0} \quad (3)$$

employing the techniques suggested in refs.(2,3). Here, we report sample calculations of the  $N_0$  and  $D_0$  parameters for certain pre-chosen values of the  $\mu$  parameter. The lack of necessary radar data (at the time of text formulation) prevent the reporting of the trials with the mentioned three parameter technique.

### 3. RADAR DATA AND ANALYSIS

Shown in figs. 1 are the RHI scans depicting the horizontal reflectivity ( $Z_{HH}^{HH}$  or simply  $Z_{HH}$ ), the  $Z_{DR}$  ( $= Z_{HH}^{HH} / Z_{VV}^{VV}$ ), and the LDR (included for additional information only) signatures of the event considered. The choice of this event was influenced by the presence of the intense convective kernel accompanied by unusually large  $Z_{DR}$  values typically 6.0 db or greater. The results to be now described, being demonstrative in nature, are restricted to the range bins located along the "ray" marked as a dark solid line in fig.1a. The  $Z_{HH}$ ,  $Z_{DR}$ , and LDR profiles along this "ray" are summarized in figs. 2. Shown in figs. 3 and 4 are the corresponding radar predicted values of the  $D_0$  and  $N_0$  parameters for the  $\mu$  values of -2,0 and 2. Also, shown in fig. 3 are the results obtained via the following empirical relationships ref.(6),  $Z = \alpha R^\beta$  and  $D_0 = \epsilon R^\delta$ , where for Joss- thunderstorm conditions  $\alpha = 500$ ,  $\beta = 1.5$ ,  $\epsilon = 1.2$  and  $\delta = 0.21$

Firstly, we note that the  $D_0$  determination from  $Z_{DR}$  measurement is limited to  $Z_{DR}$  values not exceeding 5.1, 5.2 and 5.3 for  $\mu$  values -2, 0, and 2, respectively. This limit is the natural consequence of the predefined axial ratios stemming from the Pruppacher - Pitter raindrop deformation rule, ref.(7). The calculations in the present case were done using a  $D_{\max}$  of 8.0 mm and the scatter crosssections were obtained for Pruppacher- Pitter spheroidal raindrops for  $T = 15^\circ\text{C}$  and  $f = 5.54$  GHz using the Waterman T-matrix algorithm.

The investigations presented here cover the unusually wide range of  $Z_{DR}$  values (0.5 to about 7.1 dB) in a single event. To facilitate at least tentative arguments, the radar predictions of  $N(D)$ , rainrate, etc, are presented along with the corresponding empirical results stemming from the reflectivity measurements alone. Bearing in mind that neither of the two results are more conclusive than the other and the severely limited size of the data base examined here, the "analysis" to be presented is meant to identify further investigations which would serve to clarify the detailed aspects of the use of the  $Z_{DR}$  and allied techniques. In this spirit, as a forward to this analysis, listed below are some investigations in progress, that would be, shortly, shown to be of importance in interpreting  $Z_{DR}$  values  $> 2$  dB :

1. The  $Z_{DR}$  due to water coated oblate hailstones, based on simple trial model of such particles in convective cells.
2. A reassessment of the influence of the integration limits of eqn.(2) and the raindrop axial ratios based on experimental and or theoretical sources different from the Pruppacher-Pitter deformation law. The resonance back-scattering effects ( $D \approx 5.5\text{mm}$ ) only add to the importance of these effects.
3. The significance of nearly monodisperse raindropsize distributions

Progress and appraisal of results arising from these investigations would be relegated to the conference meeting. Returning to the specific results an inspection of fig. 3 reveals that  $D_0$  predictions from  $Z_{DR}$  measurements and the corresponding empirical results for  $D_0$  show close agreement with the  $\mu = 0$  case for  $Z_{DR}$  values  $<$  about 1.5 dB. Furthermore, the remaining  $D_0$  values stemming from  $Z_{DR}$  larger than about 2 dB reveal greater and progressively increasing with  $Z_{DR}$  magnitudes, systematic departures from the empirical case. This suggests the need for a reexamination of the radar technique in light of the above listed items, particularly the latter two. In the results presented here, the untreated portions of the curves arising from the  $Z_{DR}$  values greater than the maximum interpretable values of  $Z_{DR}$  in rain, are left as broken-line horizontal flats. The results for  $N_0$  in fig. 4 show wide variations about the fixed Marshall-Palmer value of 8000, and thereby emphasising the usefulness of the radar technique. The rainrate profiles due to radar measurements are shown in fig. 5. These results reveal in comparison with the empirical law, large systematic departures (overestimates) for values of  $Z_{DR}$  greater than about 2.5 dB, tying up with the systematic departures observed in the  $D_0$  predictions (not fully illustrated due to large excursions with oscillatory behaviour). Similar inferences may be derived from the radar predictions of specific attenuation (for 20 GHz and horizontal polarization), shown in fig. 6 along with the corresponding empirical results due to the CCIR relationships using the empirical rainrate. These observations, yet again, are found in the corresponding results for the accumulated attenuation summarized in figure 7. These results in part emphasize the useful application of radar in obtaining attenuation estimates relevant to the propagation community and to the radar meteorologist from the point of correction of propagation contaminated radar echoes. The vertical line marked in the figure indicates the onset of the region of extra large values of  $Z_{DR}$  not analysible due to the reason mentioned earlier and therefore implying caution in the significance of the results beyond.

In fig. 8 we include, ad hoc, the results for radar predicted rainrates against the empirical values, as in figure 5, but this time for  $\mu$  values of 5, 10 and 15. These results somewhat surprisingly reveal a more correlated and a closer agreement between the empirical and the radar generated results for  $Z_{DR} < 2.5$  dB, in contrast to the results for  $\mu = -2, 0$  and 2 (not apparent in the illustrations). Also, the corresponding systematic departures observed in results of fig. 8, for  $Z_{DR} > 2.5$  but smaller than the critical  $Z_{DR}$  values, are less pronounced than the results of fig. 5. These observations, far from being conclusive, however, do point to the significance of the  $\mu$  parameter thus stressing the need of the radar determination of this parameter by methods such as of ref.(3).

#### 4. CONCLUSIONS

Using  $Z_{DR}$  and  $Z_{HH}$  radar measurements, firstly radar estimates of  $D_0$ ,  $N_0$  were obtained, which were then used for obtaining estimates of rainrate, specific attenuation, and the accumulated attenuation along a selected "ray". Comparison with corresponding empirical results, where appropriate, revealed three key observations linked to the magnitudes of  $Z_{DR}$  values:

1. In the region of  $Z_{DR} \leq 2.5$  dB or so, the radar predicted parameters (with the exception of  $N_0$ ) showed satisfactory and well correlated agreements with the empirical cases for predefined  $\mu$  values in the range -2 to 2, though systematic departures were noticeable for  $Z_{DR}$  values  $>$  about 1.5 dB. Interestingly, for larger  $\mu$  values (5 to 15) not only was the agreement, in the considered cases of rainrate, improved but also observed for  $Z_{DR}$  values up to 2.5 dB, thereby indicating the possible usefulness of the  $\mu$  parameter.

2. The, 2.5dB  $< Z_{DR} < 5.5$ dB values, interpreted as rain volumes, presented large systematic departures against the empirical results and in the same sense as observed in 1). This feature prompts the reexamination of the axial ratios of the larger raindrops  $> D=5$ mm, bearing the suggestion that these drops may be more deformed than the description due to Pruppacher - Pitter equilibrium rule, and or the simultaneous presence of melting oblate hydrometeors.
3.  $Z_{DR} > 6.5$ dB or so cannot be simply interpreted in terms of raindrop size distributions. For  $\mu = 15$  (a very monodispersive  $N(D)$ ) the largest  $Z_{DR}$  value interpretable, under the assumptions described in section 3 is about 5.5 dB and 6.5 dB for  $D_{max}$  of 8 and 6 mm, respectively. Hence, to be able to account for even larger  $Z_{DR}$  values observed, the need for considering mixed - phase hydrometeors in the convective shafts becomes important.

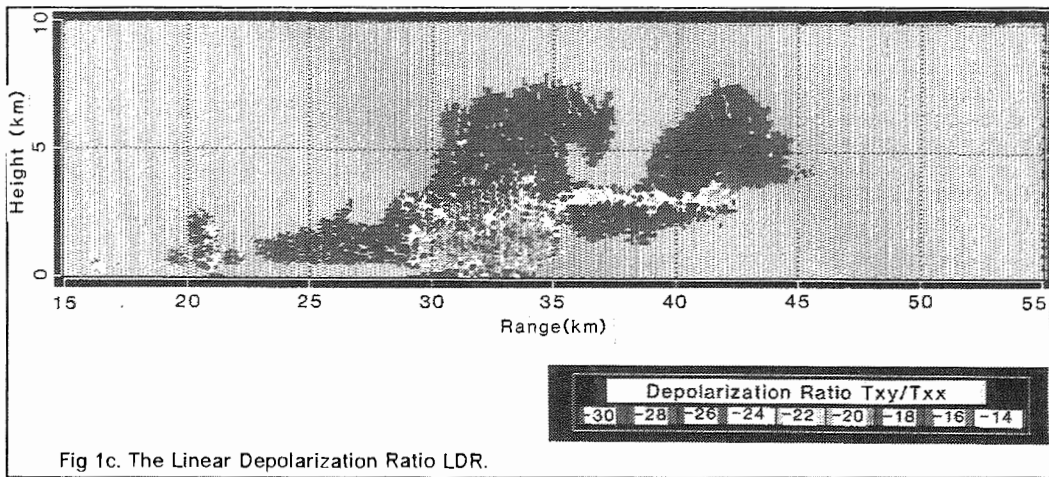
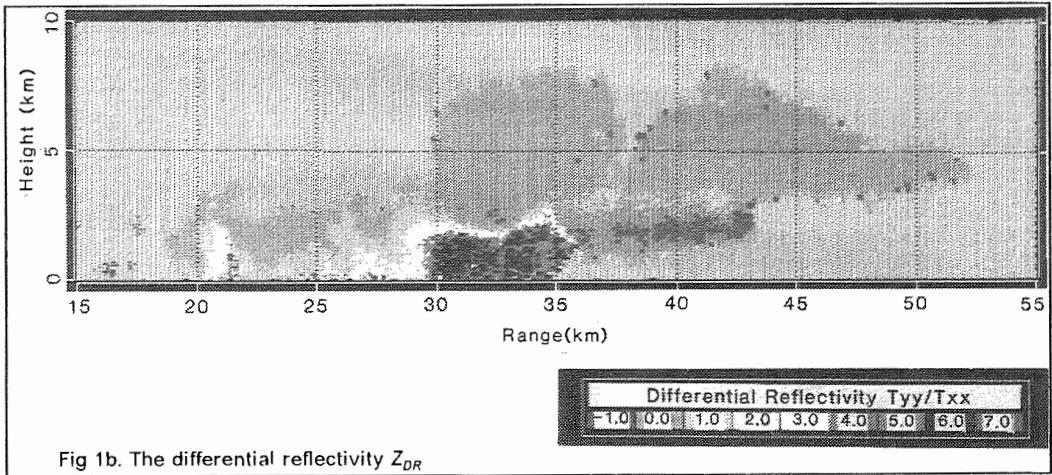
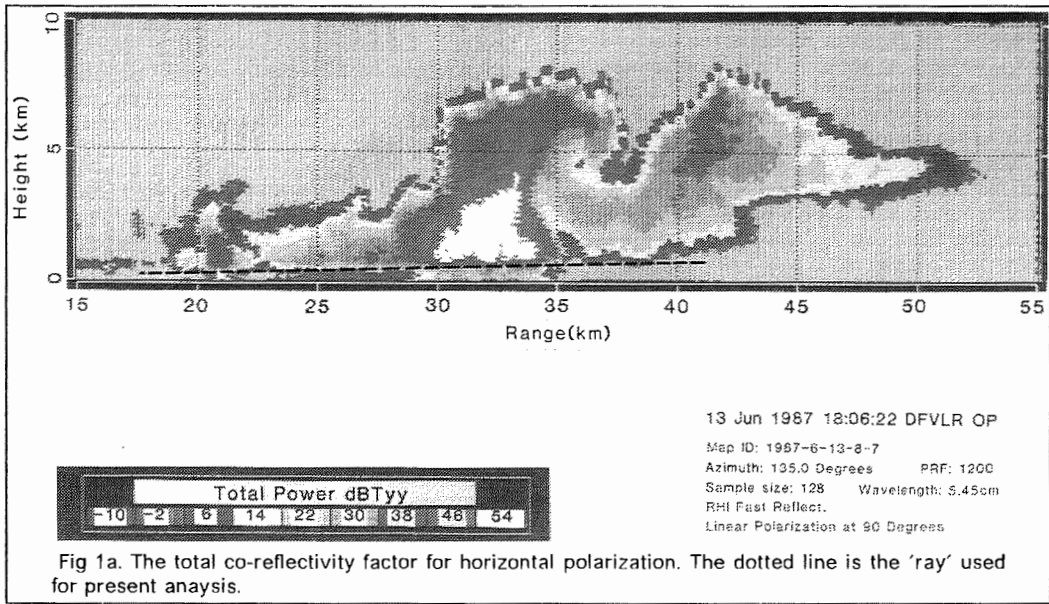
Finally, it may be added that any modelling of the hydrometeor volumes of the type suggested here should at some stage be qualified by additional ground based measurements (i.e. a distrometer, radio link, radiometer, etc.) or in situ aircraft measurements.

#### ACKNOWLEDGEMENTS

The authors gratefully acknowledge the help and contribution of several colleagues in the culmination of this work. In particular thanks are due to Dr. H. Hoeller for making available for this work the radar data collected by him. The help and generosity of Dr. H. Schuster is likewise acknowledged for allowing free access to his software (IP2PR and IP3PR) which enables a 2/3 parameter inversion of  $N(D)$  and a structured handling of radar data.

#### 5. REFERENCES

1. Schroth, A., et al, Jan 1988, " A C-Band Coherent polarimetric Radar for Propagation and Cloud Physics Research", to appear in J. Atm. & Oce. Tech.
2. Seliga, T. A. and Bringi, V. N., 1976, J. Appl. Met., 15, 69-76.
3. Chandra, M., et al, 1985, ICAP-85, Warwick, U. K., IEE Publ. Nr. 248, 11-17.
4. Chandra, M., et al, 1986, the 23-rd Rad. Met. Conf., Snowmass, Co., Paper Jp 19.38, Publ. by AMS.
5. Chandra, M., et al, 1987, ICAP-87, York, U. K., IEE Publ. Nr. 274, 328-333.
6. Joos, J, et al, 1968, Toronto, Int. Conf. Cloud Phy., 369-373.
7. Pruppacher, H. R. and Pitter, R. L., 1971, J. Atm. Sci, 28, 86-94
8. CCIR Doc.: Propagation in non-ionised media, vol. 5, Rep. 721-1, Geneva, 1982, 170-171.



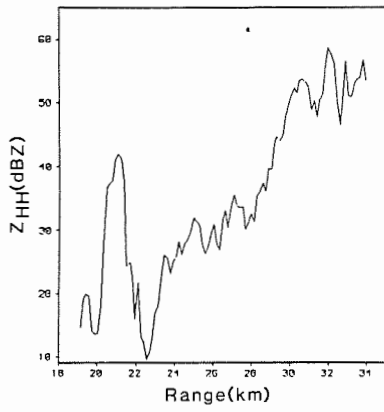


Fig 2a. The reflectivity (horizontal polarization) along the data ray.

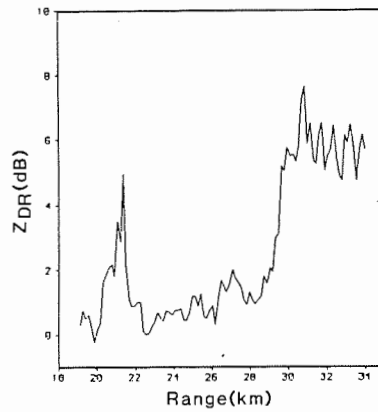


Fig 2b. The differential reflectivity along the data ray.

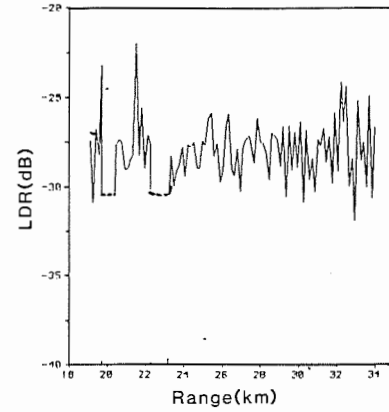


Fig 2c. The Linear Depolarization Ratio along the data ray.

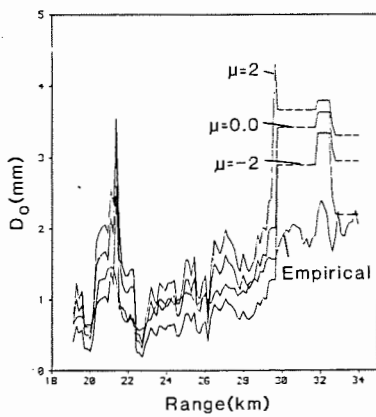


Fig 3.  $D_0$  against range for  $\mu = -2, 0, 2$  and the empirical law.

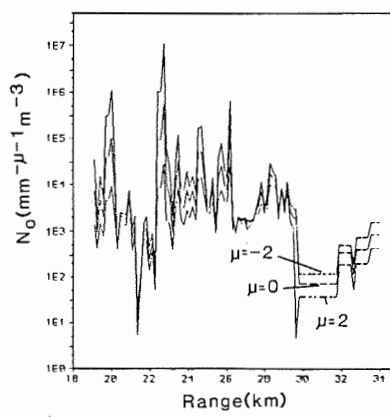


Fig 4.  $N_0$  against range for  $\mu = -2, 0, 2$ .

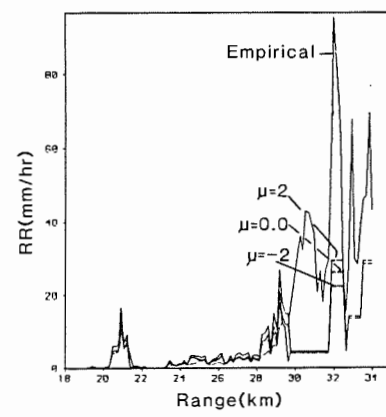


Fig 5. Rainrate against range for  $\mu = -2, 0, 2$  and the empirical law.

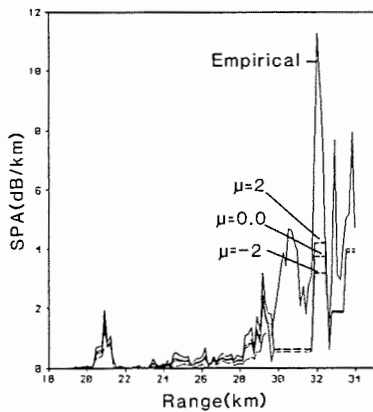


Fig 6. specific attenuation against range for  $\mu = -2, 0, 2$  and the CCIR empirical law for 20 GHz and horizontal polarization.

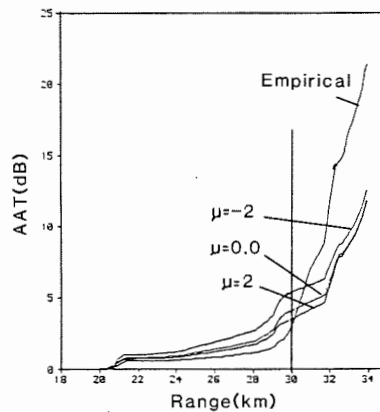


Fig 7. Accumulated (total) attenuation against range for  $\mu = -2, 0, 2$  and the CCIR empirical law for 20 GHz and horizontal polarization.

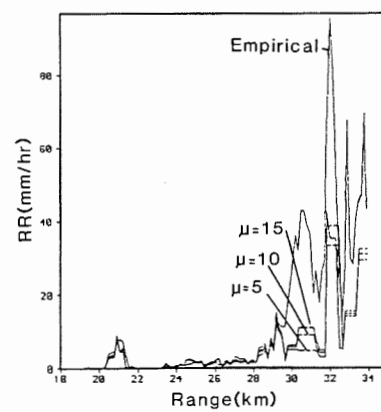


Fig 8. Rainrate against range for  $\mu = 5, 10, 15$  and the empirical law.

AN INVESTIGATION OF THE EFFECT OF  
ELECTRICAL CHARGES ON THE COLLISION  
EFFICIENCY OF CLOUD DROPS

V.M.Kim

The Institute of Experimental Meteorology  
Obninsk USSR

### 1. INTRODUCTION

The paper deals with theoretical investigations of the effects of drop electric charges on the gravitational coagulation process of drops of significantly various sizes with increasing their charge to the limiting values. The intermediate Reynolds numbers  $N_{Re}$  ranging from 10 to 60, which correspond to the falling velocities of the collector drops with radii  $R$  ranging from  $100\mu\text{m}$  to  $250\mu\text{m}$  are studied because of the lack of data on the strongly charged drop growth velocity due to coagulation with neutral and charged droplets of radii  $r$  from  $1\mu\text{m}$  to  $20\mu\text{m}$ . The drop size and charge range mentioned above is of practical importance because this is the range in which particle growth occurs in clouds including thunderstorm clouds (BARKER 1983, p. 631). The modification methods of warm clouds intended for precipitation growth enhancement are developed also in this range.

### 2. NUMERICAL MODEL

As far as in this work the size ratios of interacting drops  $r/R \leq 0.1$  were considered the approximation of purely inertial deposition with allowance for external force was used in the model to describe the process of drop collision. The effect of droplet hydrodynamical field on the collector drop hydrodynamical field was not considered in this approximation. A numerical solution (RIVKIND 1976, p. 8) of

the Navier-Stokes equations for flow-around a liquid sphere rather than a rigid one was taken as the field of velocities around a collector drop since the drag force coefficients of the collector drops available in the cited paper showed a more agreement with our experimental results for the drops (KIM 1986, p. 193). It was expected that the droplets are governed by the Stokes law. To determine coulomb and induction forces of interacting drops we used the expression obtained in (DAVIS 1964, p. 499) for two conducting electrically charged spheres. The collision efficiency of the drops was obtained from the formula  $E(R,r,Q,q) = y_c^2 (1 + r/R)^2$ , where  $Q$  and  $q$  are the electric charges on the collector drop and on the droplet, respectively and  $y_c$  is the dimensionless critical horizontal offset of the center of the droplet from the center of the collector drop, when the droplet is 30 collector drop radii upstream.

### 3. DISCUSSION OF RESULTS

We obtained the numerical results on the effect of the induction forces on  $E$  when the collector drop charge  $Q$  changed to the limiting Rayleigh charge and  $q = 0$  for  $N_{Re} = 10, 15, 30, 50, 60$ .  $E$  versus droplet sizes or their Stokes numbers  $K$  for  $N_{Re} = 10$  ( $R=103\mu\text{m}$ ) and  $50$  ( $R=216\mu\text{m}$ ) are presented in Fig.1 and the curves for the neutral collector drops are also given for

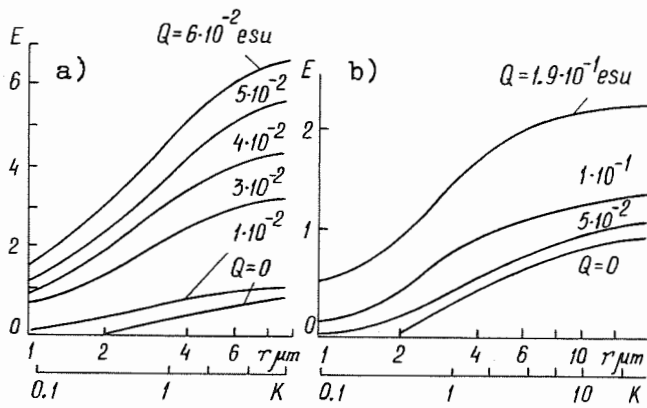


Fig.1: E versus r and K for various Q under the induction force: a)  $N_{Re} = 10$ ; b)  $N_{Re} = 50$

comparison. From these Figs one can see that for all droplet sizes studied E increases with increasing the collector drop charge, and the less r or the Stokes number of the droplet is the more E increases as compared to E for neutral droplets. For instance, for the limiting charge on the collector drop with radius  $103\mu\text{m}$  the collision efficiency of the droplet with  $r = 2\mu\text{m}$  is 200 times higher and the droplet with  $r = 10\mu\text{m}$  is only four times higher than the collision efficiency for neutral droplets. The induction force effect on the increase in collision efficiency enhances with decreasing  $N_{Re}$ , and the increase within the drop size and charge range considered reaches two orders of magnitude.

The analyses of droplet trajectories and different relations of the forces effecting on the droplet allow to draw the following conclusions. The collision efficiency does not practically depend on  $N_{Re}$  at  $N_{Re} \geq 30$  and at droplet Stokes numbers ranging from 0.1 to 40, if the parameter  $\beta$  is constant and more than 0.1 ( $\beta$  is the ratio of the induction force to the aerodynamic force affecting the droplet;

$\beta = Q^2 r^2 C_{sc} / 3 \pi \eta R^5 U_\infty$ , where  $\eta$  is the dynamic viscosity of air,  $U_\infty$  - terminal falling velocity of a collector drop and  $C_{sc}$  is the Stokes-Cunningham slip correction). E increases with increasing K at  $\beta < 1$  and decreases at  $\beta > 1$ . This derives from the fact that the increase of E at  $\beta > 1$  occurs only due to the increase of droplet deposition on the back of the sphere (Fig.2) hence the particle inertia

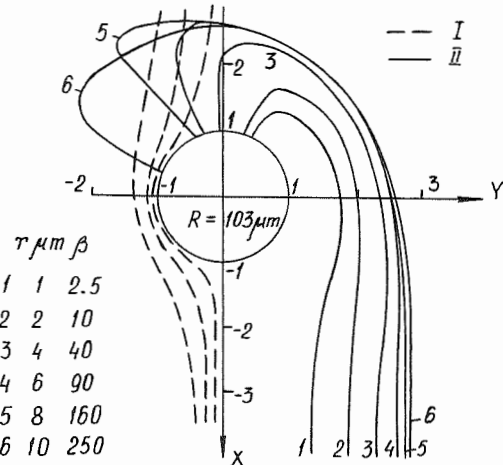


Fig.2: The critical trajectories of droplets with various sizes at the limiting charge on the collector drop with  $R = 103\mu\text{m}$  ( $N_{Re} = 10$ ): I-streamline; II-critical trajectories retards their deposition. The numerical results obtained for E at the induction interaction are in 10% agreement with our previous experimental results (BELYAEV 1984, p. 127). This indicates that the model is suitable for describing the coagulation process of electrically charged drops of significantly various sizes.

When considering simultaneous action of the coulomb and induction forces, the charge of the collector drop Q varied from 0 to its limiting value and the charge of droplets q was taken to be equal to the charge characteristic for thunderclouds,  $q = -20 r^2 \text{esu}$ . Fig.3 shows the value of E at

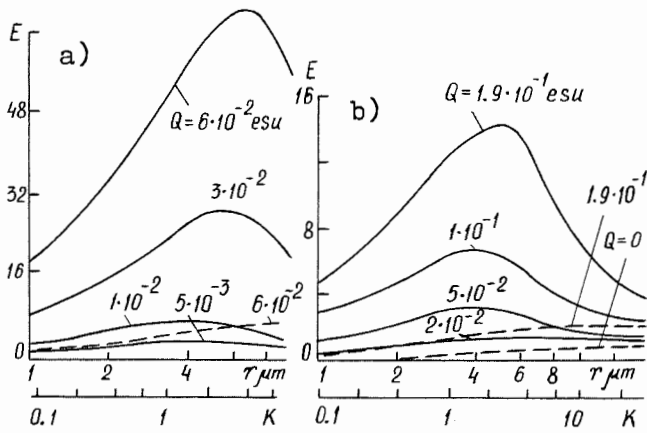


Fig.3: E versus r and K for various Q under the induction and coulomb forces: a)  $N_{Re} = 10$ ; b)  $N_{Re} = 50$ ; 1 -  $q = -20 r^2$  esu; 2 -  $q = 0$

$N_{Re} = 10$  and 50 for various charged on the collector drop and  $q = -20 r^2$  esu versus r or K. For comparison E are also shown for the induction interaction ( $q = 0$ ) at the limiting charge on a collector drop and E for neutral droplets. Under the simultaneous action of the coulomb and induction forces E at  $N_{Re} = 10$  can reach 3 orders of magnitude for  $r < 2 \mu\text{m}$  and one or two orders of magnitude for the other r compared to E for the neutral drops. The cylinder radius from which the droplets are scavenged reaches 8.5 collector drop radii. The action of the electrostatic forces decreases with increasing  $N_{Re}$ : the maximum value of E at  $N_{Re} = 10$  is 64 and at  $N_{Re} = 50$  is only 14. From Fig.3 and computation results for other  $N_{Re}$  it follows, that at all considered  $N_{Re}$  beginning from the particular collector drop charge Q the dependence of E on r or K becomes nonmonotonous, the maximum appears at  $r \approx (4 + 6) \mu\text{m}$  or  $K \approx (1.5 - 3)$ . The appearance of the maximum is accounted for by the dependence change of forces affecting the droplet.

#### 4. REFERENCES

BARKER, E.; BICKNELL, J.A.; GRIFFITS, R.E.; LATHAM, J.; VERMA, T.S.: The scavenging of particles by electrified drops: radar echo intensification following lightning. *Quart. J. Roy. Met. Soc.* 109 (1983), p.631-644.

BELYAEV, S.P.; KIM, V.M.; MATVEEV, V.N.: On coagulation of charged and neutral cloud drops. *Proc. of the 9th Intern. Physics Conf. Tallin.* 1(1984), p.127-130.

DAVIS, M.H.: Two charged spherical conductors in a uniform electric fields: Forces and field strength. *Quart. J. Mech. Appl. Math.* 17 (1964b), p.499-511.

KIM, V.M.: Coagulation of neutral and charged water drops of significantly various sizes at intermediate Reynolds numbers. *Phys. & Math. Cand. Degree Thesis.* Obninsk. 1986, 193p.

RIVKIND, V.J.; RYSKIN, G.M.: Structure of the flow about a spherical drop moving in a liquid medium at intermediate Reynolds numbers. *Fluid and Gas Mechanics.* (1976) No 1, p.8-15.

MICROPHYSICAL AND ELECTRICAL PHENOMENA  
DURING FREEZING OF WATER DROPS

Adzhiev A.Kh., Tomazov S.T.

High Mountain Geophysical Institute, Nalchik.

Process of charging of hydrometeors during cloud water freezing play an essential role in the formation of an electrical structure of thunder clouds. The study of this phenomenon has not begun until recently. The research is based on the occurrence of a considerable potential difference between the melt and solid phase, referred to as the effect of Workman-Reynolds-Ribeira (1954), and on the separation of considerable electric charges during an explosive splitting of freezing droplets.

The analysis of work on charge separation during water freezing ADZHIEV (1986, 42p.) shows that measurement of an inherent droplet charge involves great difficulties and the data obtained by various authors contradict in many aspects. The majority of studies of the above phenomenon dealt with a residual charge of a frozen droplet. Such approach does not allow an accurate estimation of the total quantity of the electric charge, separated during the freezing of a droplet. It is well-known, that contact charging, associated with mass fragmentation during freezing, is responsible for the charge. So, the charge value and sign are changing depending on the phase (solid, liquid or gase) and the fraction separated from the droplet. A residual charge, stored after multiple mass splitting from the freezing droplet, does not characterize the above process to the right degree. Some results of experimental studies of the influence of various

factors on the electric charge separation during water droplet freezing are presented. Evaluation of the charge is based on a continuous recording of the electric current from the freezing droplet. The source of the recorded electric current is the charge which originates on the freezing droplet due to mass fragmentation if there is a potential difference at the interface "vapor-water-ice". Voltmeter-electrometer "B7-30" with current sensitivity  $10^{-15}$  a at an input impedance  $5 \cdot 10^{11}$  ohms and capacity 20pF was used for studying charge separation during water droplet crystallization. Measuring error for the electric current from the freezing droplet was 1.8%, and the charge computation error was 2.6%. Besides, in order to study the electromagnetic radioemission during crystallization, we used amplitude- and frequency-response analyser XI-42, pulse analyser YP5-2 and spectrum analyser CK4-59.

A drop under study was put onto an electrode, connected to the electrometer. The electrode was placed into the cold chamber, cooled to  $-30^{\circ}\text{C}$  at a given rate. The drop was observed continuously with a microscope. The beginning and the end of crystallization were determined visually. The electric current variation with time was recorded by potentiometer OH-804/I. A more detailed information on the transient processes was obtained by a storage oscilloscope C8-17. In the process of crystallization we recorded temperatu-

re for the beginning (covering of a supercooled droplet with an ice shell) and the end (complete freezing of a droplet) of crystallization, ejection of microparticles, changes of the drop's shape, appearance of the surface cracks, projections and branches sometimes amounting to 3-5 mm. Water droplets were put into the cold chamber at 0°C and cooled till complete crystallization at a rate of 1-1.5 deg/min. As a rule, crystallization began from the surface of the drop, by the formation of an ice coating. Then, during crystallization the solid coating became partially distorted, and the interface moved over from the drop's surface to its center, creating excessive pressure inside the drop, which resulted in cracks producing airbubbles, microparticles of water and ice (section BC in Fig.1). The number

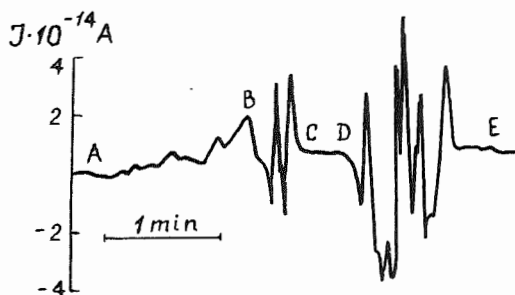


Fig.1. Current variation during droplet freezing (AC) and hail growth (DE). of individual events of charge separation in some experiments reached 30, and the most intensive charge separation occurred in the temperature range from -5 to -15°C. Normally, small pulses were observed when the droplet became ice-coated (A in Fig.1). In the experiments these pulses were positive in 99% of cases and negative in about 1%. Very often the droplets exploded into instantly freezing fragments. Maximum separation of electric charges is observed here. Explosive splitting of supercooled water droplets du-

ring crystallization is generally observed in the temperature range from -8 to -16°C. Probability of explosion here is 10-12% for water droplets with an electrical conduction  $2.4 \cdot 10^6$  ohm/cm and pH=5.3.

Results of our studies indicate that a maximum charge, separated during an explosive splitting of droplets, could reach a value of  $10^{-11}$  coul. If crystallization of the remainder continues after splitting, then the remainder of the droplet acquires a positive charge. If the explosive splitting occurs at the end of crystallization, then the charge of the remainder can be of any sign. The average value of the electric charge, separated in this process, is  $3 \cdot 10^{-10}$  coul. per 1g of frozen water.

Oscillography shows that the electric charge separation time for the explosive splitting is from 0.001 to 0.1s. The rate of current build-up is from  $10^{-11}$  to  $10^{-10}$  a/s with an average value of  $8 \cdot 10^{-11}$  a/s. When there is no visual explosion, the droplet charging is observed from the moment of ice-coating formation till the complete freezing of the droplet.

The average size of ejected microparticles and their number were found to increase with the droplet diameter during the droplet crystallization at the interface of two unmixing, optically transparent liquids. A millimeter size freezing droplet ejects on the average 30 particles, 10 of them are qualified as solid ones by their shape and colour. The size of the ejecting particles varied from 10 to  $100 \mu\text{m}$ , at an average value of  $35 \mu\text{m}$ . Chemical analysis of atmospheric precipitation revealed the presence of some ions:  $\text{K}^+$ ,  $\text{Ca}^+$ ,  $\text{Na}^+$ ,  $\text{SO}_4^-$ ,  $\text{NO}_3^-$ ,  $\text{NO}_2^-$ ,  $\text{Cl}^-$ ,  $\text{CO}_3^-$ . The following chemical substances were selected, which dissociate into the

same ions in the aqueous solution:  $K_2SO_4$ ,  $KNO_3$ ,  $KCl$ ,  $CaCl_2$ ,  $NaCl$ ,  $Na_2CO_3$ ,  $NaNO_3$ ,  $NaNO_2$ . Concentrations of the prepared solutions were of a wide range, i.e.  $10^{-6}$  -  $10^{-2}N$ . Studies of the crystallizing droplets of these solutions show that a concentration increase in excess of  $10^{-4} N$  results in a sharp decrease of the separating charge. Analysis of the obtained results allows us to conclude that added ions play an important role in the process of charging of crystallizing droplets of the solutions.

In the atmosphere the process of droplet charging continues even after their complete freezing due to the impaction of a frozen nucleus with a supercooled droplet. The latter freezes, while spreading over the nucleus surface, and increases the size of a growing hailstone and its charge. Charge separation was studied in the laboratory experiments with crystallization and hail growth in an air flow, containing water aerosol. The flow velocity varied between 5 and 10  $m s^{-1}$ . Temperature for the beginning of crystallization increased by 5-8°C and the charge increased up to  $10^{-10}$  -  $10^{-9} coul. \cdot min^{-1}$  per one gramme of water. Hail growth was accompanied by intensive charge separation (section DE in Fig.1).

Results of our studies show that dynamic structural changes at interfaces are accompanied by electromagnetic emission in the wide range of frequencies. Intensity of an acoustic signal was recorded by a piezoelectric sensor simultaneous to the recording of the electromagnetic spectrum. Spectrum analyzer and amplitude- and frequency-response analyser helped to follow the nature of the electromagnetic spectrum variation in the process of water crystallization. As a rule, this process begins from recording the maxima at 45

and 65 MHz, the spectrum is continuous with boundaries at 40-50 and 65-71 MHz. Further on, these maxima fade and new ones appear at 10-20 and 30-45 MHz, the spectrum nature here does not change. After that the process is accompanied by a considerable widening of the upper frequency band up to 50 MHz and by an increase of pulses in the region of the upper limit of the band. Later on a continuous spectrum with maxima at 42, 54, 64 MHz is observed in this frequency range, and small intensity maxima emerge in the range 8-25 MHz. Termination of the process is characterized by a transition from a continuous spectrum to separate lines at frequencies 52-56 MHz, 8-18 MHz and 24 MHz. Thus, the most typical frequencies can be singled out, i.e., 8-20 and 32-50 MHz. Analysis of pulses of electromagnetic emission indicates that they are a sequence of series, consisting of individual pulses of  $10^{-2}$  -  $0.5 \mu s$  duration. The electromagnetic emission strength grows considerably when the acoustic signals emerge. This growth is associated with the appearance of cracks and ejection of microparticles from the freezing surface. Electromagnetic emission intensifies with an increase of the freezing rate.

ADZHIEV, A.: Generation and Separation of Electric Charges in Clouds During Hailstone Formation and Melting. Review Meteorologia. Obninsk. 1986, 42 p.

WORKMAN, E.; REYNOLDS, S.: Electrical Phenomena Occuring During the Freezing of Dilute Aqueous Solution and Their Possible Relationship to Thunderstorm Electricity. Phys. Rev. 94 (1954), Nr. 4, p. 1073-1075.

A DESCRIPTION OF CONDENSATION PROCESSES IN A TURBULENT  
THREE-PHASE CLOUD

Novosyolov L.N., Stepanov A.S.

Research & Scientific Amalgamation "Typhoon", USSR

A closed system of second-order differential equations has been obtained under the diffusion approach for a description of cloud thermal, hydrodynamic and microphysical characteristics evolution at all the stages of its spatial and temporal development. Droplet and ice particles spectra  $f$  in the processes of condensation and turbulent mixing change according to kinetic equations like

$$\left(\frac{d}{dt} + \hat{K}_1 + \hat{K}_2\right) \frac{f}{\rho} = Q$$

$$\frac{d}{dt} = \frac{\partial}{\partial t} + w_i \frac{\partial}{\partial x_i}, \quad \hat{K}_1 = \frac{\partial}{\partial s} \dot{s} - \left(\frac{\partial}{\partial x_i} + \frac{\partial}{\partial s} A_i\right) K_{ij} \left(\frac{\partial}{\partial x_j} + \frac{\partial}{\partial s} A_j\right) \quad (1)$$

$$\hat{K}_2 = -K_{ij} \frac{\partial}{\partial s} \left(a_i \frac{\partial}{\partial x_j} + \frac{\partial}{\partial s} b_{ij}\right)$$

where  $\dot{s}$  is the particles surface area,  $K_{ij}$  is the eddy diffusivity tensor,  $Q$  are the sources of particles, of melting and of crystallization,  $\rho$  is the density of air,  $A_i, a_i, b_{ij}$  are the functions of cloud medium parameters,  $\vec{w}$  is the air flow velocity. Repetitive indices indicate summation. With the accuracy to a dimensional factor the component  $A_i$  are the mixing lengths in the size dimension domain controlling the contribution from turbulent mixing into the particles size dispersion growth rate  $\sigma$ :

$$\frac{d}{dt} \sigma \propto \frac{1}{2} K_{ij} A_i \left(A_j - 4 \frac{\partial \bar{s}}{\partial x_j}\right) \quad (2)$$

where  $\bar{s}$  is the mean surface area of the phase considered. The value of  $A_i$  varies within wide limits. In a three-phase medium it is determined primarily with the mean geometrical time of

phase relaxation and with the heterogeneity of potential and pseudopotential temperature fields. In a mixed supercooled cloud fluctuations of  $\frac{d}{dt} \sigma$  are possible at different stages of ice phase formation becoming both positive and negative. Therefore stochastic condensation does not obligatorily lead to the dispersion growth rate.

Universal expressions are obtained for turbulent heat and moisture fluxes in the inner and outer regions of a cloud. As it follows from the result obtained, heat- and mass-transfer take place somewhat differently from the phenomenological theory.

The latter complex operator  $\hat{K}_2$  in (1) has its origin in the effect of nonadiabaticity of air parcels, that is significant at cloud formation and for the processes occurring at cloud boundaries.

In view of a water-drop stratiform cloud comparative numerical calculations have been performed for drop spectrum evolution with the use of (1) and of equations of the turbulence semiempiric theory ( $A_i = a_i = b_{ij} = 0$ ). The tendencies of spectra evolution appeared to be different. According to (1) the spectrum attained with time an extremely pronounced maximum, in the second variant mechanical mixing caused a considerable broadening of the spectrum. Such tendencies are not universal: depending on certain profiles of thermal, hydrodynamic and microphysical parameters other situati-

ons are possible.

The mathematical tool obtained describes the whole set of condensation processes in a three-phase cloud medium. When necessary this technique can be generalized for the case of sedimentation and coagulation processes.

# EFFECT OF THE ELECTRIC FIELD ON THE RAINDROP SHAPE

Georgi Magradze

Geophysics Institute of the Georgian SSR Academy of  
Sciences, Z. Rukhadze Str. 1, Tbilisi 380093, USSR

Let us consider a raindrop of equivalent radius  $a_0$  falling with the terminal velocity  $\vec{v}$  under the action of aerodynamic and gravitational forces. The velocity vector  $\vec{v}$  is parallel to the electric field strength  $\vec{E}_0$  and to the oz-axis directed downwards. It is well-known that the equilibrium state of a liquid drop corresponds to the minimum value of free energy. Neglecting the internal water circulation and assuming that the temperature in the reference system connected with the drop centre is constant, we write an expression for free energy in the form

$$F = \alpha \int_{S_0} dS - \frac{E_0}{2} \int_{S_0} \sigma \cdot z \cdot dS - mgz_0 - \int_{V_0} p dV \quad (1)$$

where the first term is the surface energy, the second is the conductor energy in the external electric field, the third is the potential energy of a raindrop and the fourth is the action of external force;  $\alpha$  is the surface tension coefficient,  $\sigma$  is the surface charge distribution,  $z_0$  is the gravity centre position in the chosen reference system,  $p$  is aerodynamic pressure,  $S_0$  and  $V_0$  are respectively the surface and the volume of a drop.

We write expression (1) in terms of a spherical coordinate system; by virtue of symmetry considerations the drop must be symmetrical with respect to the oz-axis; therefore the surface radius-vector  $r(\theta, \varphi)$  depends only on the angle  $\theta$ . Since the exp-

ression for  $F$  depends only on the radius-vector of the drop surface, is a functional of  $r$  and the drop equilibrium corresponds to the minimum value of the functional  $F(r)$  on possible drop surface variations. The drop volume remains constant. Therefore an additional condition

$$\int_0^\pi r^3 \sin\theta d\theta = 2 \cdot a_0^3 \quad (2)$$

is imposed on  $r(\theta)$ . Condition (2) can be excluded by the substitution  $r(\theta) = C \cdot u(\theta)$ , where  $C$  is a constant determined from (2). After the substitution the finding of the drop equilibrium reduces to the finding of the absolute minimum value of functional (1) by successive approximations. For this the initial drop shape is given, for which the function  $\sigma(\theta)$  and the aerodynamic pressure distribution  $k(\theta)$  are calculated, while the surface is varied so as to obtain the minimum value for  $F(u)$ . Next,  $\sigma(\theta)$  and  $k(\theta)$  are calculated for a new value of  $r(\theta)$  and the variation process is repeated until the surface points converge with a given accuracy. If under the given conditions  $F(u)$  has no minimum value, then the minimization process diverges and in that case the drop instability is observed. In this approximation the minimization process is accomplished numerically by the method of local variations (CHERNOUS'KO and BANICHUK, 1973). In calculations for  $k(\theta)$  use was made of the function obtained experimental-

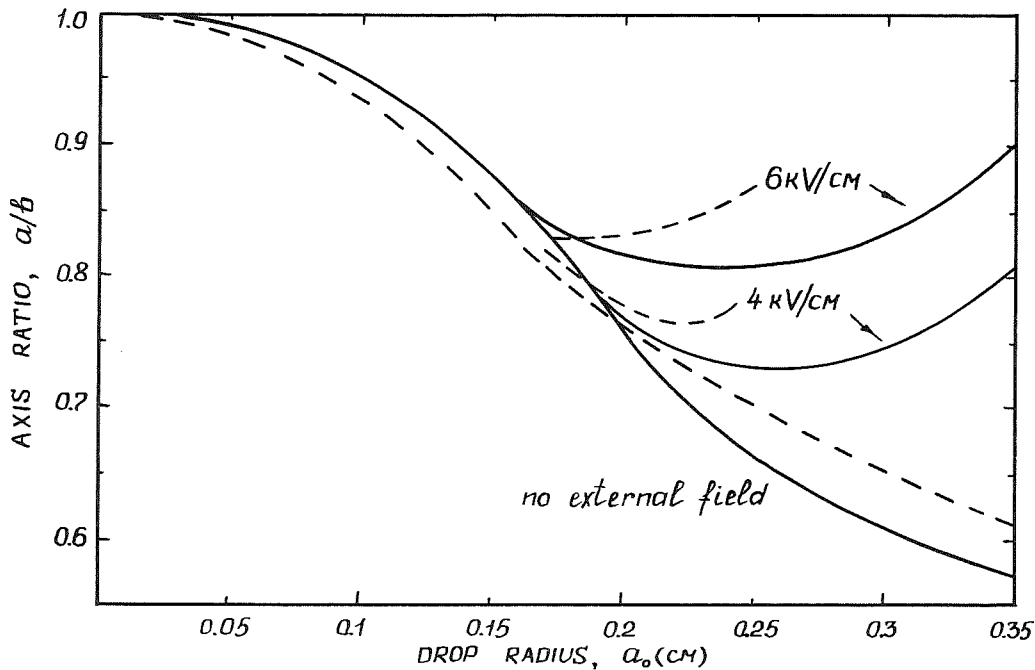


Fig. 1: Variation of the drop axis ratio  $a/b$  with the drop radius  $a_0$  for various values of  $E_0$ . The dotted line shows results from (RASMUSSEN et al. 1985) and (PRUPPACHER and PITTER 1971)

ly (FAGE 1937) with the correction for ellipsoidality suggested in (BEARD and CHUANG 1987). The correction for ellipsoidality was used with some modifications. The distribution of charge surface density was calculated by the numerical method based on the solution of a singular integral equation (MAGRADZE 1986).

When  $E_0 = 0$ , for drops of radius  $a_0 \geq 0.25$  cm a concavity develops in the drop bottom due to a strong aerodynamic pressure at the lower drop surface. The greater the radius, the larger the concavity. Similar results were obtained in (PRUPPACHER and PITTER 1971) for drops of  $a_0 \geq 0.2$  cm.

Fig. 1 shows the variation of the drop axis ratio  $a/b$ , where  $a$  is the vertical and  $b$  the horizontal drop size, with the radius  $a_0$  for various values of  $E_0$ .

The electric field strength  $E_0 \leq 6$  kV/cm practically has no effect on drops of radii less than 0.15 cm.

The electric field strength  $E_0 \leq 3$  kV/cm produces a weak effect on drops of radius  $0.15 \leq a_0 \leq 0.35$  cm. For  $E_0 \geq 3$  kV/cm large drops become elongated along the strength vector; the greater the radius, the stronger the elongation. Thus for a drop of  $a_0 = 0.3$  cm, the axis ratio  $a/b$  is equal to 0.62 when  $E_0 = 0$  but increases to 0.84 when  $E_0 = 6$  kV/cm.

The results obtained agree with experimental data from (RASMUSSEN et al. 1985). Our lower values of  $a/b$  as compared with experimental data can most probably be explained by using an inaccurate function in calculations of  $k(\theta)$ .

#### REFERENCES

- BEARD, K.V., and C. CHUANG: A new model for the equilibrium shape of raindrops. *J. Atmos. Sci.* 44 (1987), No.11, p. 1509-1524.
- CHERNOUS'KO, F.L., and N.V. BANICHUK: Variation problems of mechanics and control (in Russian). Moscow: Nauka 1973, 238 p.

FAGE, A. Experiments on a sphere at critical Reynolds numbers. Aero. Res. Comm. England, Rep. and Memo (1937), No. 1766, 20 p.

MAGRADZE, G.D.: Numerical method of calculating the electric field of water hydrometeors (in Russian). Abstracts All-Union Symp. on Atmospheric Electricity (1986), p. 127.

PRUPPACHER, H.R., and R.L. PITTER:  
A semi-empirical determination of the shape of cloud and rain drops. J. Atmos. Sci. (1971), v. 28, p. 86-94.

RASMUSSEN, R., C. WALCEK, H.R. PRUPPACHER, S.K. MITRA; J. LEW, V. IOVIZZANI, P.K. WANG, and V. BARTH: A wind tunnel investigation of the effect of an external electric field on the shape of electrically uncharged rain drops. J. Atmos. Sci. 42 (1985), No. 15, p. 1647-1052.

DAMPED-OSCILLATION REPRESENTATION OF DROP-SPECTRUM  
EVOLUTION DUE TO COALESCENCE AND BREAKUP

Philip S. Brown, Jr.

Trinity College  
Hartford, CT 06106, USA

1. INTRODUCTION

The research involves analysis and parameterization of model-generated raindrop spectra. In the model it is assumed that transient behavior of the drop spectrum is determined only by the effects of collisional breakup and coalescence. These binary drop-interaction processes are described by means of the fragment distribution function and coalescence efficiency of LOW AND LIST (1982a,b). The model-generated drop spectra are found to approach an equilibrium drop distribution that is unique in shape but that is proportional in size to the liquid water content of the system. When the initial drop spectra are assumed to have Marshall-Palmer form, the approach to equilibrium is not monotonic. Often the small-raindrop portion of the spectrum rapidly climbs to high concentration levels before settling back toward equilibrium. The phenomenon is evident in Fig. 1 which shows the log of number density  $n$  as a function of drop diameter  $D$  at various stages in the approach to equilibrium. (Also see LIST ET AL. 1987, p. 368.) It is the aim of this work to develop a simple parameterization that describes well the characteristic behavior of drop spectra evolving from Marshall-Palmer form. Such a parameterization could provide improved microphysics representation in moist convection models whose heavy demands on computer resources preclude detailed solution of the coalescence/breakup equation.

2. PARAMETERIZATION TECHNIQUE

The idea behind the parameterization is to represent  $n(D)$  by a discrete drop-size distribution  $n_i, i=1, \dots, I$ , and to express the set of values  $n_i$  in terms of exponential functions superimposed on the equilibrium distribution. The  $n_i$ 's are governed by a dynamical system that results from discretization of the coalescence/breakup equation (e.g., LIST AND GILLESPIE 1976, p. 2008). The local behavior of

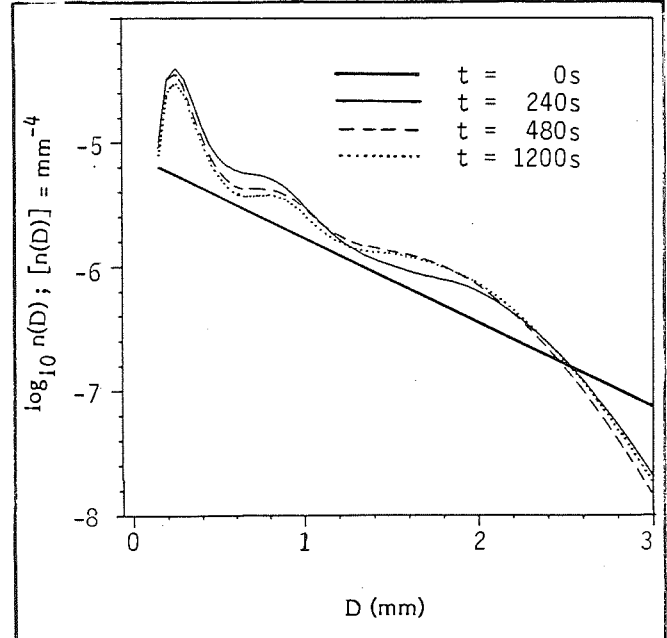


Fig. 1. Evolution of drop spectrum through coalescence and breakup. Initial distribution has Marshall-Palmer form  $n(D) = N_0 e^{-\Lambda D}$  where  $N_0 = 8 \times 10^{-6} \text{ mm}^{-4}$  and  $\Lambda = 1.559 \text{ mm}^{-1}$ . A non-monotonic approach to equilibrium is evident.

the system near equilibrium is represented by the equation

$$\frac{d\underline{\epsilon}}{dt} = \underline{A} \underline{\epsilon} \quad (1)$$

where  $\underline{\epsilon} = \{\epsilon_i\}$  denotes the departure of  $\{n_i\}$  from the equilibrium state  $\{(n_{eq_i})\}$  and where  $\underline{A}$  is the Jacobian matrix evaluated using equilibrium values of  $n_i$ . It follows from (1) that each component  $\epsilon_i = n_i - (n_{eq_i})_i$  is a linear combination of the functions  $e^{\lambda_j t}$ ,  $j=1, \dots, I$ , where the  $\lambda_j$ 's are the (complex) eigenvalues of  $\underline{A}$ . It happens that combinations involving only a small number of exponential functions describe well the behavior of the components  $n_i - (n_{eq_i})_i$  and thereby provide a simple parameterization of the evolving drop-size distribution.  $\{(n_{eq_i})_i\}$  is determined once and for all

by numerical solution of the coalescence/breakup equation; the solution is advanced in time until numerical equilibrium is reached.

### 3. ADJUSTMENT FOR LIQUID WATER CONTENT

For the parameterization to be useful, the approximating functions  $e^{\lambda_j t}$  and the equilibrium values  $(n_{eq})_i$  must be readily adjustable to accommodate systems with arbitrary liquid water content. It is an inherent property of the coalescence/breakup equation that both the "rate constants" (i.e. the  $\lambda_j$ 's) and the equilibrium drop size distribution are proportional to the liquid water content (SRIVASTAVA 1982, p. 1320). Once the  $\lambda_j$ 's and  $(n_{eq})_i$ 's are determined for a system with liquid water content  $L^*$ , multiplication by the scaling factor  $L/L^*$ , immediately determines the corresponding quantities for a system with liquid water content  $L$ . The generality of the parameterization depends upon these proportionality relations.

### 4. CASE STUDY

Calculation of the eigenvalues for the case treated in Fig. 1 shows (i) that  $\text{Re}(\lambda_j) < 0$  for each  $j$  so that the equilibrium is asymptotically stable, and (ii) that there are eigenvalues with  $\text{Im}(\lambda_j) \neq 0$  so that the drop spectrum will oscillate on its approach to equilibrium. Analysis of model-generated solutions shows that one particular damped oscillation describes rather well the nonmonotonic behavior of  $n_i - (n_{eq})_i$  for drop categories in the small raindrop portion of the spectrum. For these categories,

$$n_i(t) - (n_{eq})_i = c_i e^{-\mu t} \cos[\nu(t - t_i)] \quad (2)$$

where  $\lambda = \mu \pm i\nu$  are complex conjugate eigenvalues determined from the eigenanalysis and  $c_i, t_i$  are found by fitting the form (2) to the model-generated drop spectrum. The solid curve in Fig. 2 shows the model-generated solution  $n_i - (n_{eq})_i$  for index  $i$  corresponding to a drop diameter of .27 mm. (This component is contained in the overall spectrum shown in Fig. 1.) The dashed curve in Fig. 2 represents the damped oscillation (2). The particular function given in (2) provides a reasonable approximation to the transient behavior of the spectrum not only at  $D = .27$  mm but over the entire

small-drop range,  $D < .75$  mm. Other exponential functions can be used to model the mid-size and large-size portions of the spectrum. A composite of these submodels provides a parameterization that can represent the evolution of the overall spectrum shown in Fig. 1.

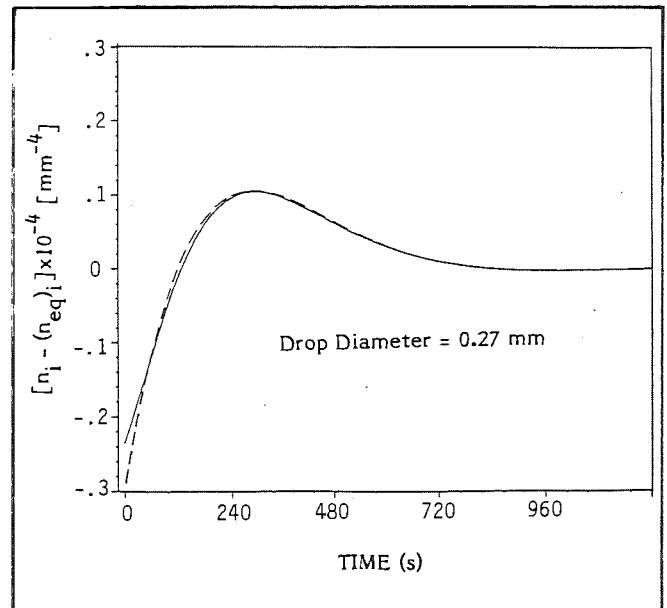


Fig. 2. Evolution of component  $\epsilon_i = n_i - (n_{eq})_i$ , where  $\epsilon_i$  is the departure of the drop spectrum from equilibrium for drop category  $i$  corresponding to mean drop diameter  $D = .27$  mm. Solid curve represents values obtained by numerical solution of the coalescence/breakup equation; dashed curve represents the parameterization established in (2).

### 5. CONCLUSION

The analysis is directed toward finding a simple mathematical form to describe the transient behavior of  $\{\epsilon_i(t)\}$  which represents the departure of the drop spectrum from equilibrium. The functions  $e^{\lambda_j t}$  provide such a description. The exponential functions damp in time, while some oscillate as they decay. One particular damped oscillation represents extremely well the departure of the drop spectrum from equilibrium in the small-drop range. The damped oscillation explains the non-monotonic behavior of a significant portion of the spectrum, and provides a convenient parameterization. Other representative functions of the form  $e^{\lambda_j t}$  can be found to describe the temporal behavior of the mid-size and large-drop portions of the drop-size distribution.

#### ACKNOWLEDGMENTS

This work was supported by the Division of Atmospheric Sciences, National Science Foundation, under Grant ATM-8521417.

#### REFERENCES

LIST, R.; DONALDSON, N.; STEWART, R.E.: Temporal evolution of drop spectra to collisional equilibrium in steady and pulsating rain. *J. Atmos. Sci.* 44 (1987), pp. 362-372.

LIST, R.; GILLESPIE, J.R.: Evolution of raindrop spectra with collision induced breakup. *J. Atmos. Sci.* 33 (1976), pp. 2007-2013.

LOW, T.B.; LIST, R.: Collision, coalescence and breakup of raindrops. Part I: Experimentally established coalescence efficiencies and fragment size distributions in breakup. *J. Atmos. Sci.* 39 (1982a), pp. 1591-1606.

LOW, T.B.; LIST, R.: Collision, coalescence and breakup of raindrops. Part II: Parameterization of fragment size distributions. *J. Atmos. Sci.* 39 (1982b), pp. 1607-1618.

SRIVASTAVA, R.C.: A simple model of particle coalescence and breakup. *J. Atmos. Sci.* 39 (1982), pp. 1317-1322.

# KINETIC EQUATION FOR POLLUTED CLOUD DROPLETS SPECTRUM

Isaac M. Erukashvily

Depart. for Research and Development, Israel Meteorological Service,  
P.O.Box 25, Bet-Dagan, Israel.

## 1. INTRODUCTION

Investigation of pollutants distribution in polluted cloud droplets (PCD) spectrum is very important in many applications of PCD microphysics such as cloud seeding simulation, scavenging of aerosol (including radio-active) particles or pollutant gas molecules, generation of cloud droplets electric charge.

To study the microphysical processes in PCD population the number density function  $n(x,y,t)$  depending on two characteristics of PCD has to be introduced (BEHENG, HERBERT, 1984 ; SMIRNOV ,NADEIKINA ,1984).

The value of  $n(x,y,t)dx dy$  represents the number of PCD which contain liquid water phase with mass in the range  $(x, x+dx)$  and pollutant with mass (or with charge for ions) in the range  $(y, y+dy)$ .  $t$  denotes time. In this study Kinetic equation for  $n(x,y,t)$  is derived taking into account the microphysical processes of coalescence and diffusional growth of PCD. Analytic solutions of the coalescence kinetic equation (CKE) for PCD with constant coalescence kernel are obtained and the numerical method of moments (ENUKASHVILY, 1980) is developed for numerical integrating CKE with an arbitrary coalescence kernel.

## 2. ANALYTIC SOLUTION OF CKE

To derive kinetic equation for  $n(x,y,t)$  time evolution taking into account the above mentioned microphysical processes the balance of the value  $n(x,y,t)dx dy$  in phase volume element  $dx dy$  has to be considered. Using the known method (PRUPPACHER, KLETT, 1978; SMIRNOV, NADEIKINA, 1984) we have

$$\begin{aligned} & \frac{\partial n(x,y,t)}{\partial t} + \frac{\partial((dx/dt) * n(x,y,t))}{\partial x} + \frac{\partial((dy/dt) * n(x,y,t))}{\partial y} = GCI - LCI \end{aligned} \quad (1)$$

where GCI and LCI are the gain and loss coalescence integrals respectively. CKE is obtained from (1) as:

$$\begin{aligned} & \frac{\partial n(x,y,t)}{\partial t} = -n(x,y,t) * \\ & * \int_0^\infty \int_0^\infty \sigma(x,y;u,v) n(u,v,t) du dv + \\ & + (1/2) \int_0^x du \int_0^y \sigma(x-u,y-v;u,v) * \\ & * n(x-u,y-v,t) n(u,v,t) dv \end{aligned} \quad (2)$$

where  $\sigma(x,y;u,v)$  represents the coalescence kernel. Now we introduce the number density function moments

$$M_{k_1}(t) = \int_0^\infty \int_0^\infty x^k y^l n(x,y,t) dx dy \quad (3)$$

so we have

$N(t) = M_{00}(t)$ ;  $L = M_{10}$ ;  $S = M_{01}$ ;  $M = L + S$ , where  $N(t)$  is the total number concentration of PCD;  $L$  and  $S$  are the total masses of liquid water phase and of pollutant respectively.  $M$  represents the total mass of PCD. The values

$$n(x,t) = \int_0^\infty n(x,y,t) dy \quad (4)$$

$$n(y,t) = \int_0^\infty n(x,y,t) dx \quad (4)$$

are the number density distribution functions of liquid water phase and of pollutant respectively in the PCD spectrum. From eq. (2) we obtain

$$\begin{aligned} & \frac{\partial M_{k_1}(t)}{\partial t} = \int_0^\infty \int_0^\infty n(u,v,t) du dv * \\ & * \int_0^\infty \int_0^\infty \sigma(x,y;u,v) ((1/2)(x+u)^k * \\ & * (y+v)^l - x^k y^l) n(x,y,t) dx dy \end{aligned} \quad (5)$$

The abbreviated set of coupled differential equations (5) may be used for approximative numerical integrating the CKE (2) for an arbitrary coalescence kernel (ENUKASHVILY, 1984; PRUPPACHER, KLETT, 1978)

Now we take the PCD initial spectrum in the form :

$$n(x,y,0) = A \exp(-\beta x - \tau y) \quad , (6)$$

where  $A, \beta, \tau$  parameters are determined by normalization conditions with given  $N(0), L$  and  $S$ . Setting  $\sigma(x,y;u,v) = \text{constant}$  in (2) and using the double Laplace transform to the CKE (2) as well we obtain

$$n(x,y,t) = \exp\{-(xN(0)/L) - (yN(0)/S)\} \{N(0)N(t)^2/LS\} * \sum_{m=0}^{\infty} \{(N(0)(N(0)-N(t)))/LS\}^m * (x^m y^m / (m!)^2) \quad , (7)$$

where  $N(t) = N(0) / (1 + (1/2) N(0)t)$ .

For the PCD monodisperse initial spectrum

$$n(x,y,0) = N(0) \delta(x-x_0) \delta(y-y_0)$$

where  $\delta$  is the Dirac delta function using again the double Laplace transform, we have

$$n(x,y,t) = (N(t)^2/N(0)) \sum_{m=0}^{\infty} \{(N(0)-N(t))/N(0)\}^m * \delta\{x-(m+1)x_0\} * \delta\{y-(m+1)y_0\} \quad , (8)$$

By substituting (7)-(8) in (4) the number density functions  $n(x,t)$  and  $n(y,t)$  are obtained. Analytic solutions (7)-(8) of the CKE (2) with  $\sigma = \text{constant}$  may be used as a test problem for numerical methods for integrating the CKE (2) with an arbitrary coalescence kernel.

### 3. NUMERICAL METHOD OF MOMENTS

The CKE (2) may be written also in the form

$$\begin{aligned} \partial n(x,y,t) / \partial t = & -n(x,y,t) * \\ & * \int_0^{\infty} \int_0^{\infty} \sigma(x,y;u,v) n(u,v,t) du dv + \\ & + \int_0^{x/2} \int_0^{y/2} \sigma(x-u,y-v;u,v) * \\ & * n(x-u,y-v,t) n(u,v,t) dv + \\ & + \int_0^{x/2} \int_0^{y/2} \sigma(x-u,v;u,y-v) n(x-u,v,t) * \\ & * n(u,y-v,t) dv \quad , (9) \end{aligned}$$

Method of moments for numerical integrating the CKE (9) is to seek a solution of the form (ENUKASHVILY, 1980)

$$n_{1,j}(x,y,t) = W_{1,j}(x,y,t) \sum_{k=0}^{\infty} \sum_{l=0}^{\infty} A_{1,j,k,l}(t) * L_{1,k}(x) L_{j,l}(y) \quad , (10)$$

where  $n_{1,j}(x,y,t)$  is the number density function in PCD packet

$(x_1, 2x_1; y_j, 2y_j)$  having liquid water mass in the range  $(x_1, 2x_1)$  and

having pollutant mass in the range  $(y_j, 2y_j)$ ;  $W_{1,j}(x,y,t)$  is the weighting function;

$A_{1,j,k,l}(t)$  are expansion coefficients.  $L_{1,k}(x)$  and  $L_{j,l}(y)$  are polynomials orthogonal in the ranges  $(x_1, 2x_1)$  and  $(y_j, 2y_j)$  respectively with  $W_{1,j}(x,y,t)$ . The expansion coefficients in (10) are expressed as a linear combinations

of the  $n_{1,j}(x,y,t)$  moments. Myltiplying the CKE (9) by  $x^k y^l dx dy$  and integrating from  $x_1$  to  $2x_1$  and from  $y_j$  to  $2y_j$  respectively, and using the Bleck's known idea of sectional computations of double integrals (BLECK, 1970) as well as replacing number density functions

$n_{1,j}(x,y,t)$  in coalescence integrals by expansion (10) we obtain for

$n_{1,j}(x,y,t)$  moments an infinite set of coupled differential equations. However by abbreviating (10) a finite set of coupled differential equations may be obtained to

compute finite number of  $n_{1,j}(x,y,t)$  moments in each separate PCD packets and to compute approximate

$n_{1,j}(x,y,t)$  as well. The expressions

of the coalescence integrals in  $n_{ij}(x,y,t)$  moments equations are derived as well.

#### 4. CONCLUDING REMARKS

4.1 Kinetic equation for the time evolution of PCD number density function  $n(x,y,t)$  is derived;  $n(x,y,t)$  evolves with time as a result of microphysical processes of coalescence, of condensation / evaporation and as a result of diffusion of pollutant gas molecules (or ions) from ambient air.

4.2 Analytic solutions of the CKE with constant coalescence kernel are obtained for exponential and monodisperse initial spectra of PCD using the double Laplace transform.

4.3 Numerical method of moments is developed for numerical integrating CKE with an arbitrary coalescence kernel.

4.4 To test the numerical method of moments a preliminary numerical computations are performed using as a test problem the above mentioned analytic solutions.

**Acknowledgements.** The author thanks A. Ianetz and H. Rosenthal for discussions.

#### 5. REFERENCES

5.1 BEHENG, K.D.; HERBERT, F.: Modelling the variation of aerosol concentration in drops as a result of scavenging and redistribution by coagulation. Proceedings of the 9th ICPC, 1(1984), Tallin, USSR, 207-208.

5.2 BLECK, R.: A fast approximative method for integrating the stochastic coalescence equation. J. Geophys. Res. 75(1970), 5165-5171

5.3 ENUKASHVILY, I.M.: On the solution of the kinetic coagulation equation. Izv. Acad. Nauk SSSR, ser. Geofiz. (1964), N10, 944-948.

5.4 ENUKASHVILY, I.M.: A numerical method for integrating the kinetic equation of coalescence and breakup of cloud droplets. J. Atmos. Sci. 37(1980), 2521-2534.

5.5 FRUPPACHER, H.R.; KLETT, I.D.: Microphysics of clouds and precipitation. D. Reidel, 1978.

5.6 SMIRNOV, V.I.; NADEIKINA, L.A.: Analytical solutions to a kinetic equation for the cloud drop size spectrum formed by condensation in a turbulent medium. Proceedings of the 9th ICPC, 1(1984), Tallin, USSR, 233-235.

# LIQUID WATER CONTENT, MEDIAN VOLUME DIAMETER, AND TEMPERATURE IN DEPENDENCE ON THE HEIGHT ABOVE THE CLOUD BASE FOR DIFFERENT TYPES OF CLOUDS

H.-E. Hoffmann and R. Roth

Institut für Physik der Atmosphäre, DFVLR, 8031 Oberpfaffenhofen, F.R.G.

## 1 Introduction

The 'Icing of Aircraft' is investigated since about five years in the DFVLR-Institute for Atmospheric Physics. For this purpose, an aircraft has been equipped as an icing research aircraft (Hoffmann et al., 1986). By the results of icing flights which were conducted with this aircraft, it was tried first to answer the question in which manner the normalized icing degree is depending on cloudphysical parameters (Hoffmann et al., 1987). For improving the forecast of normalized icing degrees (Weather Service, 1980) we tried also during these icing flights to get information about the dependence of the icing relevant cloudphysical parameters on cloud parameters. Here cloud parameters mean the cloud species and the height above the cloud base. We have always got these informations when we could fly through the whole cloud from its top to its base respectively vice versa. The data which we have collected during such vertical soundings of clouds, shall serve as input data for the extension of a climatology of icing relevant cloudphysical parameters (Roach et al., 1984).

After describing our test procedure in section 2, the figures of section 3 show the dependence of the cloudphysical parameters liquid water content LWC, temperature T, and median volume diameter MVD on the height above the cloudbase for different types of clouds. To learn something about the reliability of our measurements concerning the LWC, in the figures of section 4 the liquid water content values measured with the Johnson-Williams hot wire instrument and the Knollenberg instruments have been plotted.

## 2 Measuring instruments employed and performance of measurements

For the plottings of the following figures only the measured values of a part of the whole instrumentation of the icing research aircraft were used. In section 3 the values for the LWC were measured by a Johnson-Williams hot wire instrument, the values for the temperature by a Rosemount platinum-wire instrument Rosemount, and the values for the MVD by the Knollenberg instruments FSSP and OAP. In section 4, besides the LWC-values which were measured by means of the Johnson-Williams instrument, also those LWC-values were used which were

derived from the Knollenberg instruments FSSP and OAP.

The Johnson-Williams hot wire instrument and the Rosemount platinum-wire instrument are mounted on the nose cap, and the Knollenberg instruments FSSP and OAP at the lower side of the wings of the icing research aircraft. Their distance from the fuselage is about 4 m.

The measurements were carried out in the course of icing flights which were conducted in a region between the north edge of the Alps and a distance of about 100 km north of it. Each value of the points in the figures is the mean value formed on a flight time of 20 sec. That means a flight distance of about 1.2 km. Because of the greater reliability of the Knollenberg measuring values, for the figures of the sections 3 and 4 only flight sections have been taken when the cloud particles were fluid.

## 3 The dependence of cloudphysical parameters on the height above the cloud base

The following three figures are a selection of about 20 vertical structures of cloudphysical parameters which could be measured during our icing flights so far. In Fig. 1 LWC, T and MVD are depicted in dependence on the height above the cloud base in a St-cloud and in Fig. 2 the same parameters, but measured here in an Ac, As-cloud. During both these events there was no precipitation on the ground. The measurements for Fig. 3 have also taken place in an Ac, As-cloud but in this event, about 3 hours before, we had precipitations.

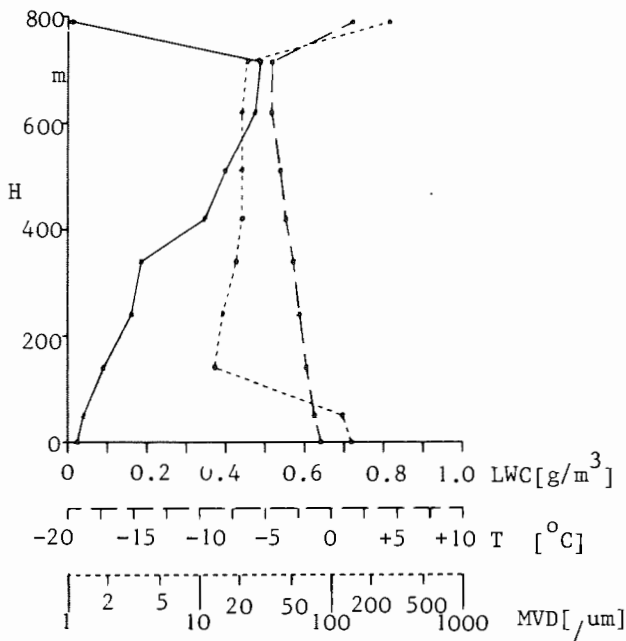


Fig. 1: The cloudphysical values liquid water content LWC, temperature T, median volume diameter MVD in dependence on the height above the cloud base H (St-Cloud).

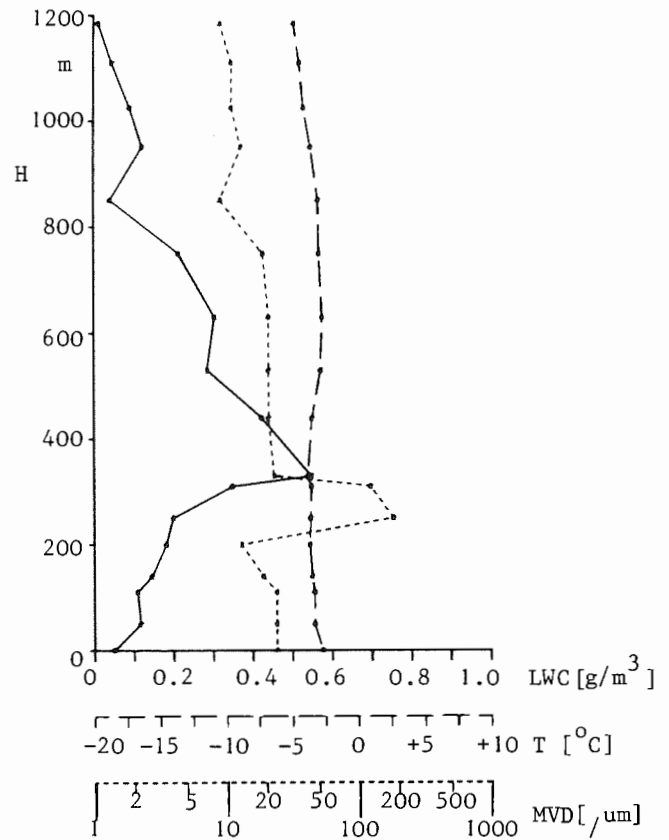


Fig. 3: The cloudphysical values liquid water content LWC, temperature T, median volume diameter MVD in dependence on the height above the cloud base H (Ac, As-Cloud).

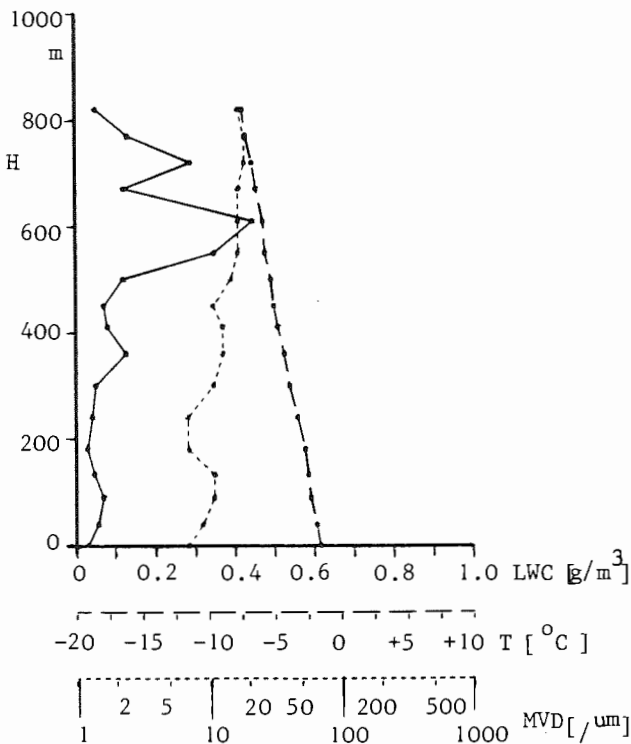


Fig.2: The cloudphysical values liquid water content LWC, temperature T, median volume diameter MVD in dependence on the height above the cloud base H (Ac, As-Cloud).

Some remarks to the results of the Fig. 1-3

1. In the St-cloud (see Fig. 1) the LWC was growing continuously from the base up to the top and had there its maximum value of about  $0.50 \text{ g/m}^3$ . In the interior of this St-cloud the MVD had nearly constant values of about  $20 \mu\text{m}$ . On the other hand, in the base and in the top the MVD had maximum values of about  $200$  and  $300 \mu\text{m}$ .
2. In the Ac, As-cloud without precipitation on the ground (see Fig. 2) in the upper third of the cloud the LWC had a significant maximum. In the whole cloud the MVD had nearly constant values between  $8$  and  $15 \mu\text{m}$ .
3. In the Ac, As-cloud, in which measuring was performed about 3h after precipitation on the ground, the maximum LWC value of about  $0.5 \text{ g/m}^3$  was located in the lower third of the cloud. In the lower third the MVD, too, had a significant maximum of about  $200 \mu\text{m}$ .

#### 4 The LWC values, measured by Johnson-Williams and by Knollenberg instruments

For the comparison of LWC measurements, carried out by the Johnson-Williams instrument and by the Knollenberg instruments, the same flight sections as in the figures 1 to 3 were used. In the following figures 4 to 6, besides the LWC values of the Johnson-Williams instrument, also the LWC values derived from measurements by the Knollenberg instruments FSSP and OAP were plotted. In this case the measuring values of the FSSP were taken for the particle diameter 2 to 32  $\mu\text{m}$  and for the particle diameters 34 to 600  $\mu\text{m}$  those of the OAP instrument.

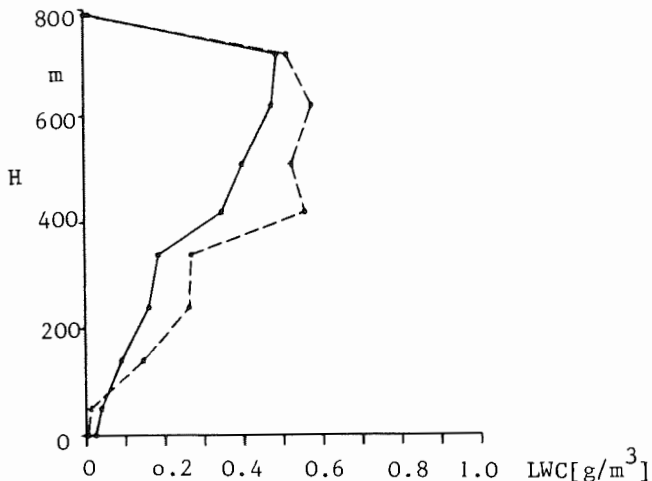


Fig. 4: Liquid water content LWC, measured by Johnson-Williams — and by Knollenberg instruments --- in dependence on the height above the cloud base H (s. also Fig. 1).

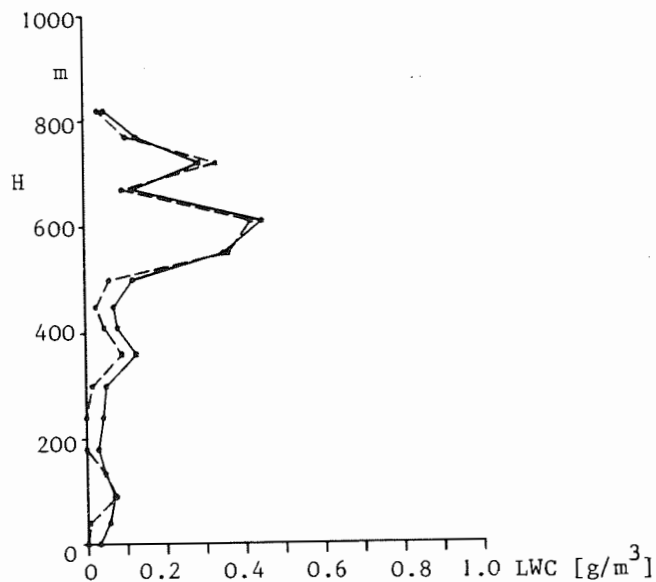


Fig. 5: Liquid water content LWC measured by Johnson-Williams — and by Knollenberg instruments --- in dependence on the height above the cloud base H (s. also Fig. 2).

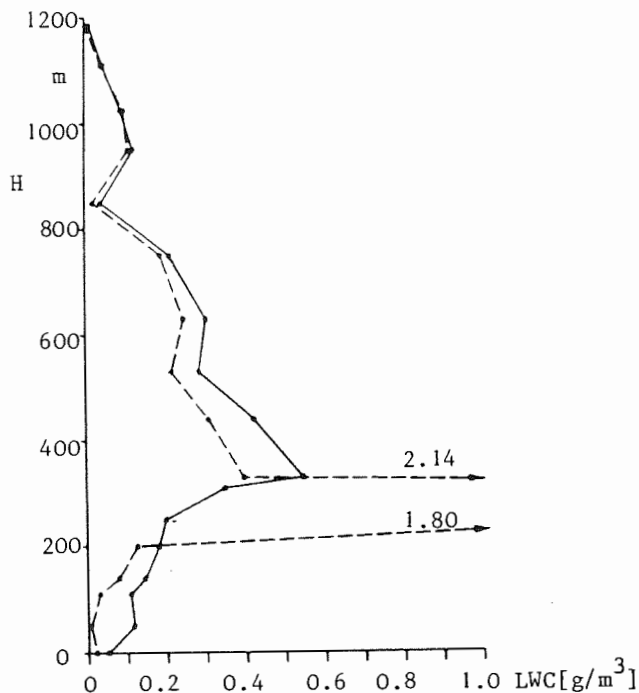


Fig. 6: Liquid water content LWC measured by Johnson-Williams — and by Knollenberg instruments --- in dependence on the height above the cloud base H (s. also Fig. 3).

Some remarks to the results of the Fig. 4-6

1. The type of dependence of the LWC values from the height above cloud base is reproduced in the same way by both the measurements.
2. The LWC values, determined by the Johnson-Williams instrument were smaller (see Fig. 4) or greater (see Fig. 6) than those determined by the Knollenberg instruments.
3. Nearly always the differences between the measuring values of the two instruments were smaller than 35%. Only on two measuring points (see Fig. 6), the measuring values showed extreme differences.

#### 5 References

HOFFMANN, H.-E., DEMMEL, J.: DFVLR's Icing Research Aircraft Do 28, D-IFMP, and its Measuring Equipment. ESA-TT-972 (1986)

HOFFMANN, H.-E., ROTH, R., DEMMEL, J.: Standardized Ice Accretion Thickness as a Function of Cloud Physics Parameters. ESA-TT-1080 (1987)

Weather Service: Forecaster's Guide on Aircraft Icing. AWS/TR-80/001, Air Weather Service, Scott AFB (1980)

ROACH, W.T., FORRESTER, D.A., CREWE, M.E., WATT, K.F.: An Icing Climatology for Helicopters. Special Investigations Memorandum 12, Meteorological Office Bracknell (1984).

A DETAILED EXAMINATION OF DISCONTINUITIES IN NATURAL RAIN SPECTRA

Harry C. Vaughan  
 Department of Meteorology  
 Iowa State University  
 Ames, Iowa 50011

I. INTRODUCTION

A natural distribution of free falling rain drops can be approximated by the Marshall-Palmer (M-P), 1948, relationship. However, close examination of short intervals of observed drop spectra show the slope ( $\Lambda$ ) and intercept ( $N_0$ ) vary considerably from the M-P distribution (Waldvogel, 1974). In addition, systematic perturbations are frequently observed in the minute-by-minute observations of drop spectra. It can be shown that these perturbations, first thought to be random noise in the data, are, in fact, well defined and generally fixed local peaks in the mass distribution of tropical warm rains. Niederdorfer (1932) reported orderly perturbations in the form of an arithmetic progression in the drop spectra which he expressed as its corresponding mass. His work was not verified and interest in the phenomenon was dropped (Mason, 1972). A plausible explanation for lack of verification will be discussed in Section III.

II. DATA AND ANALYSIS

In this study all samples were collected on 24 cm diameter Whatman I filter paper treated with a water soluble dye applied with a specially designed air brush (Wiesner, 1895). Samples were made singly or in pairs every minute through the duration of 16 rain episodes at El Verde, Puerto Rico. Additional data were collected at St. Thomas, USVI. These data were all supported by local 00 and 12Z upper air soundings. Cloud base computations from psychrometric readings, at the time of the episode, put the cloud base between 130 and 180 meters above the sampling point. Stain impressions were read to the nearest 0.1 mm; in the case of non-symmetrical impressions, the observer made a judgment regarding the mean diameter. The double samples were each read by two observers; differences between their readings were insignificant, with a resulting correlation of better than +0.9. Data was computed and displayed as follows: actual exposure time (raw spectra) histograms, normalized semi-log plots of each sample drop spectra and a mathematical transformation to mass per drop size, with an increment of 0.1 mm, was also plotted (Fig. 1).

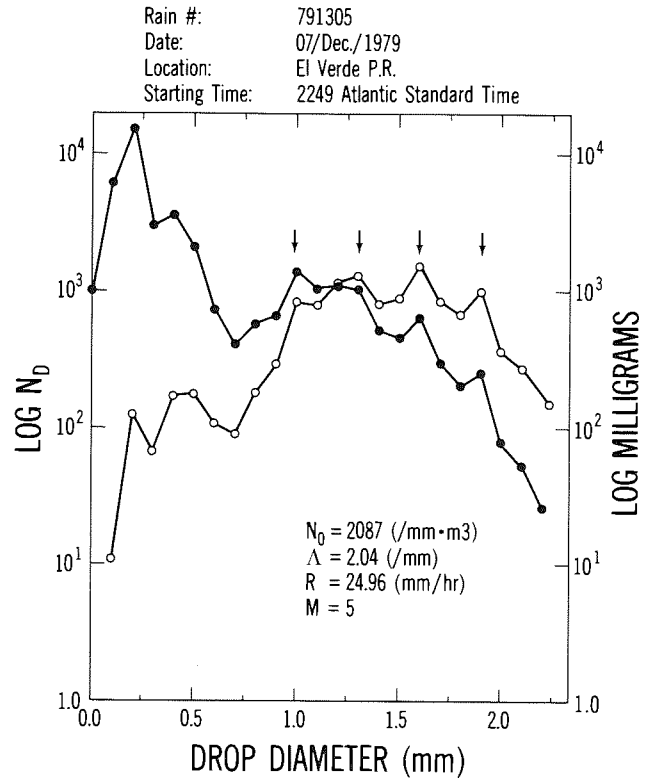


Fig. 1. The left-hand ordinate denotes the log of  $N_D/M^3/0.1$  mm diameter (closed circles), the right-hand ordinate denotes the log of drop mass in milligrams/0.1 mm increment (open circles). The four arrows point to the four open circle peaks each with a null width of 0.2 mm.

One hundred and twenty-three dye paper samples containing approximately fifty thousand individual stain impressions show discernible depressions, or in some cases gaps to be present in the spectra for almost every sample. Monodispersed drop spectra were observed in the final minute of a few episodes. In these cases the number of drops per second was increased two or three fold and the resulting semi-log plot shows no perturbations. The term perturbation as used here is intended to describe the series of peaks, nulls, and null widths which make up the total drop distribution in each spectral sample. The null width is defined as the number of 0.1 mm increments between, but not including, two adjacent peaks. Within this null width is the null minim, which like

perturbation peaks has an apparent physical significance. Obviously, if each of the null widths are equal, the series of perturbations comprises an arithmetic progression (Fig. 1). In general, the peak and null minim represent indices which are mutually exclusive. Further, irrespective of the sample rain rate there seems to be specific peak and null minim positions, drop spectra, which reoccur more frequently than others, with 1.3 mm as the mode value. In an attempt to illustrate the relocation and relative magnitude of the numerous perturbations an entire episode is plotted as a continuous three-dimensional surface (Fig. 2).

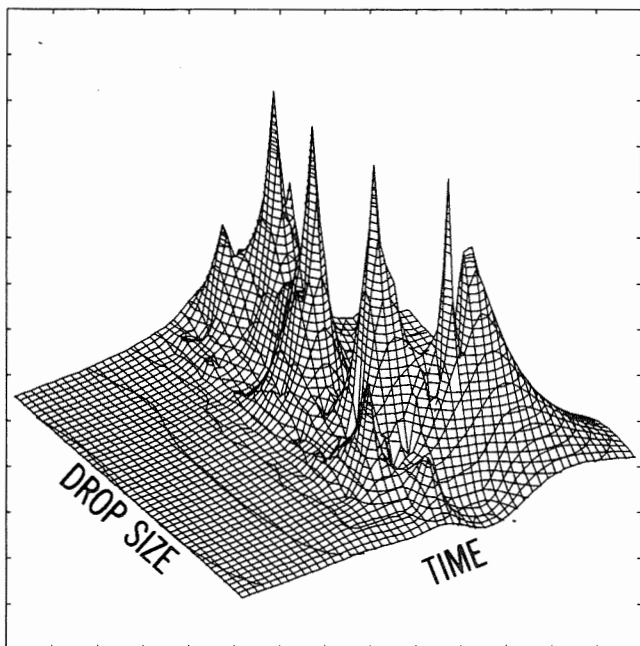


Fig. 2. The ordinate represents increasing drop size, the abscissa represents increasing time, and the Z axis, milligrams of water per drop size.

### III. MODEL

To aid in understanding the development of both transient and seemingly stationary perturbations, a primitive cloud droplet growth model was developed where only the accretion growth mechanism was considered. Using a single composite calibration curve (Hall, 1972), in conjunction with several published cloud droplet data sets which provided the environmental background, a number of cloud model drop spectra were generated (Vaughan, et al., 1988). Starting with a cloud droplet environment with a near normal distribution, the model was able to generate a series of transient and semi-permanent perturbations within its simulated drop spectra, which extended to drizzle size drops. A number of test droplet environments were used, each resulting in a different

positioning of the computer-generated perturbations. The perturbations observed in natural samples are supported by the model results and strongly suggest an ordered growth in a simple, warm rain process.

### IV. CONCLUSIONS

As the model output suggests, if in nature there is a tightly regimented mechanical growth process, the product would be perturbations resulting from discrete jumps where only select drop size ratios make lasting coalescence. Further, it is hard to reconcile the systematic distribution of these perturbations from the largest drop size down through the rain spectra by a breakup mechanism. It is clear the perturbations are real with differences as great as an order of magnitude, in mg, observed between adjacent null minim and peaks. It was found when three point smoothing was applied to raw data the perturbations were lost, particularly in low rain rate samples. This suggests that a finely-balanced accretion process occurs in the development of the drop spectra. Clearly, at least a portion of these data supports results previously reported by Niederdorfer. Since few rain drop data sets have been read to 0.1 mm, the possibility of seeing these perturbations may have been lost. A detailed account of this study has been submitted for publication.

### V. ACKNOWLEDGEMENTS

The author wishes to express sincere thanks to Gary R. White who assisted in collecting and testing much of the data and in writing portions of the data reduction program, and to Eric Quee for his work on the computer model and graphics.

### VI. REFERENCES

- Marshall, J. S. and W. Palmer, 1948. The distribution of rain-drops with size. *J. Meteor.*, 5:4, pp. 165-166.
- Mason, B. J., 1971. *The physics of clouds.* Oxford University Press, U.K.
- Niederdorfer, E., 1932. Messingem der Grosse der Regentropfen. *Meteor. Z.* 49:1, pp. 1-14.
- Vaughan, H. C., E. L. Quee, and S. Terronez, 1988. A primitive cloud droplet growth model to study perturbations in the natural rain spectra. WMO Second International Cloud Modeling Workshop, Toulouse, France.
- Waldvogel, A., 1974. The  $N_0$  jump of rain-drop spectra. *J. Atmos. Sci.* 31:5, pp. 1067-1078.
- Wiesner, J., 1985. Beitrage zur Kenntnis des Tropischen Regens. Sitzber. K. Akad. Wiss. Wien, Math.-naturw. Kl., 104, pp. 1397-1434.

## CRYSTALLIZATION OF SUPERCOOLED SOLUTIONS

K. Harrison and J. Hallett  
Desert Research Institute  
Reno, Nevada 89506

### 1. INTRODUCTION

Solution drops exist in the atmosphere in supercooled states down to temperatures approximately equal to the sum of the possible supercooling of water itself and the equilibrium freezing point depression of the solution. Initial nucleation of these drops can take place by particulate impurities in suspension or by contact with aerosol particles. Drops can also be nucleated by insoluble mineral particles or bacteria on the surface of vegetation. Crystals growing from these solution drops lead to changes in solution concentration, and possibly convection which enhances local supersaturation; both effects change the growth rate and shape of the crystals.

The aim of this research is to study crystallization of uniformly supercooled solutions ( $\text{Na}_2\text{SO}_4$ ,  $\text{NaCl}$ ,  $\text{H}_2\text{SO}_4$ ,  $\text{HNO}_3$ ,  $\text{HCl}$ ) and show how crystal growth velocity and habit depend on solution and concentration. The segregation coefficient for the solute in ice is measured by analysis of ice and solution, separated immediately after initial freezing, at different supercoolings. Subsequent solidification gives ion rejection at a varying rate depending on the geometry of the freezing, and may result in separation of hydrates, particularly when the initial concentration is high, as in haze (inactivated) droplets and low temperatures found in the Antarctic stratosphere. Electrical effects associated with rapid freezing are also investigated.

### 2. EXPERIMENTAL

A Schlieren optical system was used to investigate crystal growth and the presence of convection from the growing crystal. This system detects density gradients resulting from crystal growth and buoyant convection which could enhance growth and change ion segregation. Convection from a growing crystal could only be viewed if density and refractive index gradients were sufficient. In practice this requires concentrations  $> 0.2\text{M}$ .

Solutions were contained in cells with optical quality windows, volume 10 to 1000 ml, and located in a thermostated outer cell. Temperatures were uniform to  $\pm 0.2^\circ\text{C}$ , as judged by exploring the solution with a thermocouple. Nucleation was achieved by inserting a single crystal into the upper surface, or by inserting a seed crystal or a  $\text{LN}_2$  cooled wire into a narrow plastic tube ending in the middle of the solution. Crystals grew from the seeding site into the solution as flat dendrites or needles, where shape and velocity depended on solute, its concentration and the supercooling.

The segregation coefficient for ice was measured by analysis of the ice and solution immediately after freezing by separation of liquid and solid. After separation, the pH and temperatures of the liquid and solid phase (after melting) were measured using a SelectroMark Analyzer. In order to obtain more information about segregation, preliminary experiments were made to measure the potential difference between a growing ice crystal and the solution it grew in.

An electrometer was used to measure the potential difference between a thin wire attached to the nucleating crystal and another wire placed in the solution.

### 3. RESULTS

Fig. 1 shows crystal growth in different aqueous solutions. The Schlieren optical system is sensitive to gradients of refractive index integrated along the line of sight and shows convecting plumes as solute rejection occurs. Convection visualized in this system shows plumes ascending (solute incorporated preferentially) or descending (solute rejected) depending on the solute and illustrates how the convective plume interacts with the growing crystal tip.

Convection influence on crystal growth only occurs within a limited range of supercooling, where convective velocity is greater than the growth velocity of the individual crystal. Dendrite growth velocity is approximately proportional to the square of the supercooling,  $\Delta T$ .

Estimates of the segregation coefficient ( $\pm 10\%$ ) were obtained from measurement of the composition of the ice and the rejected solution, which were separated after the initial freezing process was complete and the temperature of the ice/solution mixture had approached its new equilibrium temperature to within  $0.2^\circ\text{C}$ . Preliminary experiments measuring ice and rejected

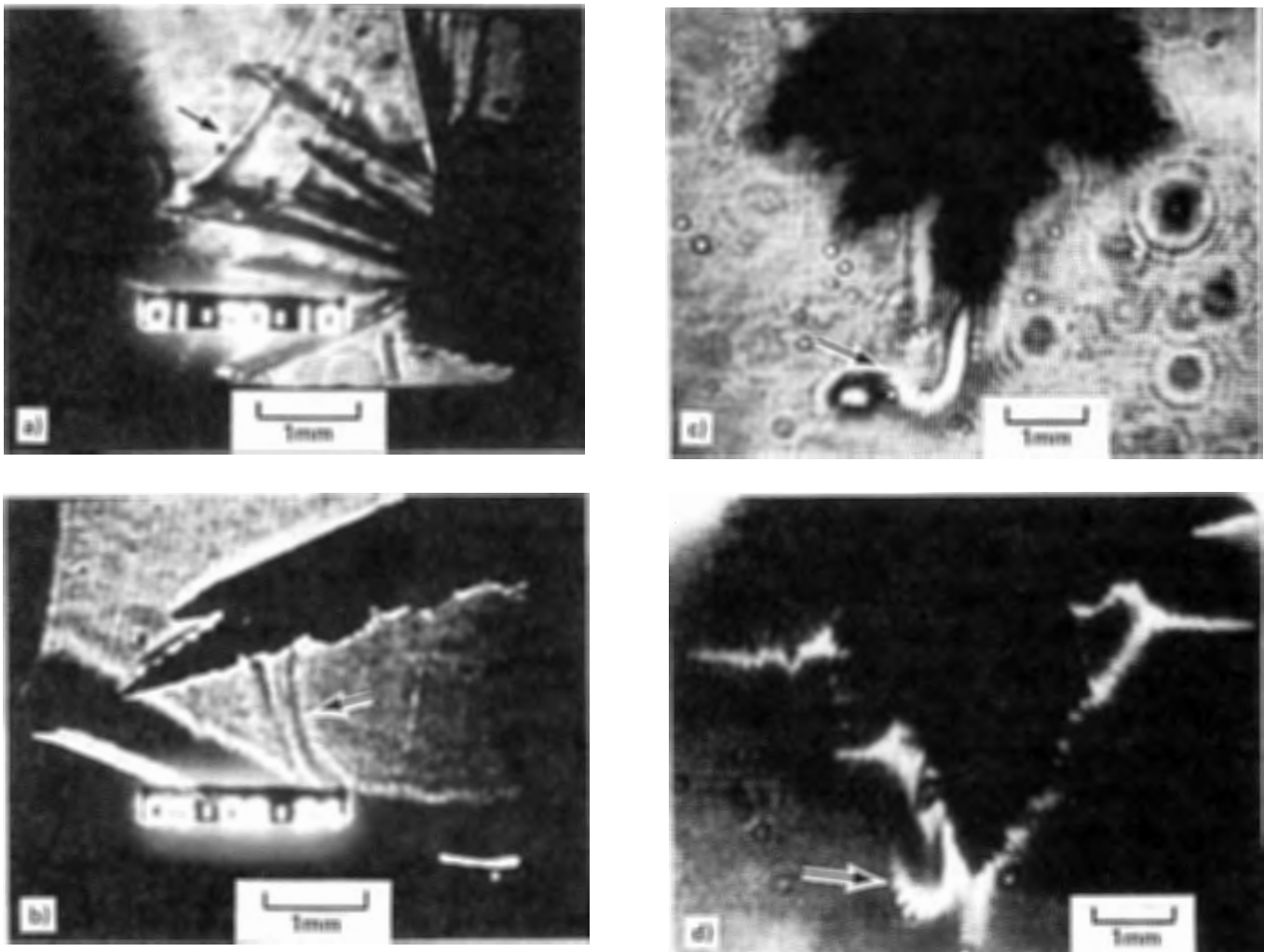


Fig. 1: Schlieren photographs of convection around growing crystals of: a) sodium sulfate decahydrate (2M,  $\Delta T = 3.7^\circ\text{C}$ ), b) ice in sodium chloride solution (0.8M,  $\Delta T = 0.4^\circ\text{C}$ ), c) ice in nitric acid solution (1M,  $\Delta T = 1.0^\circ\text{C}$ ), and d) ice in sulfuric acid solution (1M,  $\Delta T = 1.0^\circ\text{C}$ ).

solution indicate a pH decrease of 0.2 for  $H_2SO_4$  and 0.02 for  $HNO_3$ . Further insight into the segregation was obtained by measurement of the potential developed between the crystal and the solution, although this technique was of limited use because of the complicated geometry of the crystal solution. For laboratory distilled water a maximum potential of +0.4V was reached; +4.8 V for 1M  $HNO_3$ .

#### 4. DISCUSSION AND CONCLUSION

In the case of the decahydrate, it appears that stoichiometry is preserved and the convecting fluid results from solute loss at a fixed, but moving, boundary. In the case of ice, other possibilities exist. For  $H_2SO_4$  it appears that the sulfate ion can replace five water molecules, and become incorporated in molecular ratio 1:30 (DE MICHELI and IRIBARNE 1963, p.767). Whether this is important in the other substances is yet to be determined. Workman and Reynolds (1949, p. 254) measured electrical effects between ice-solution interfaces based on a linear growth front at a growth rate of  $\sim .01 \text{ cm s}^{-1}$ , compared with growth velocities of  $\sim .1 \text{ cm s}^{-1}$  in these experiments. For dilute solutions ( $10^{-3} - 10^{-6}N$ ) of NaCl they measured a potential difference of +30V and for dilute solutions of  $HNO_3$  and  $H_2SO_4$  effects were negligible. Our present results suggest that more extensive measurements need to be made in solutions at different supercoolings, and that substantial electrical effects may be present for higher concentrations under these conditions. Thus in hydrometeors, effects could occur at slow growth in weak solution, from selective shedding under wet growth, and also during freezing of highly supercooled individual drops.

From a different viewpoint substantial damage to vegetation could occur under specific conditions as concentrated solutions (possibly  $H_2SO_4$ ) are rejected in the freezing of rime or dew. These concentrated

solutions could dehydrate vegetation by osmosis, or lead to other damage. Solutions other than  $H_2SO_4$  could have similar effects. This damage would occur under quite specific meteorological conditions, when high concentration solutions are accreted and frozen. This suggests that accretion of supercooled polluted fog and dew formation under high levels of pollution, followed by freezing, appears more likely than "acid" rain to cause damage to vegetation.

The importance of such studies in ice crystal growth is also illustrated by our lack of knowledge of surface absorption and solute incorporation of ice crystals growing from the vapor in the Antarctic atmosphere (CRUTZEN 1986, p.651 and TOON 1986, p.1284). Here high concentrations of  $HNO_3/HCl$  exist at temperatures below  $-80^\circ C$ , where hydrate crystals may nucleate and give rise to quite unexpected structures and chemical reactions.

This research was funded by NASA Contract No. NAS7-918.

#### 5. REFERENCES

- COBB, A.W.; GROSS, G.W.: J. Electrochemical Soc. (1969) 116, p. 796-804.
- CRUTZEN, P.J.; ARNOLD, F.: Nitric Acid Cloud Formation in the Cold Antarctic Stratosphere: a major cause for the springtime 'ozone hole'. Nature (1986), 324, p.651-655.
- DE MICHELI, S.M.; IRIBARNE, J.: La Solubilité des Électrolytes Dans La Glace., J. Chem. Phys. (1962) 60, p. 767-774.
- HARRISON, K.; HALLETT, J.: On the Freezing of Supercooled Aqueous Solutions and Atmospheric Chemical Reactions. Conference on Cloud Physics, Snowmass, CO, Sept., 1986.
- TOON, O. B.; HAMILL, P.; TURCO, R.P.; PINTO, J.: Condensation of  $HNO_3$  and  $HCl$  in the winter polar stratospheres., Geophys. Res. Lett., (1986) 13, p. 1284-1287.
- WORKMAN, E.J.; REYNOLDS, S.E.: Electrical Phenomena Occurring during the Freezing of Dilute Aqueous Solutions and their Possible Relationship to Thunderstorm Electricity. Physical Review (1949) 78, p.254-257.

KINETICS OF ICE CRYSTAL FORMATION ON AEROSOL PARTICLES IN  
SUPERCOOLED FOG

Boris Gorbunov, Aleksandr Paschenko, Hatal'ya Kakutkina

Institute of Chemical Kinetics and Combustion

The experimental evidence on time characteristics of ice crystal formation is just scanty although their great importance for physics of clouds and governing the evolution of atmospheric processes cannot be denied. The present paper is concerned with the study of ice nucleation kinetics in a cloud chamber under the action of silver iodide, copper acetyl acetate, phloroglucine and some metal oxides at 268, 263 and 253 K. To obtain the kinetic dependences, a two-section cloud chamber with automatic registration was constructed (Gorbunov et al. 1987, p.261). It is composed of a two-section cylinder with inside diameters of 0.2 and 0.4 m, respectively, divided by a fluoroplastic partition with openings. Vapour is continuously supplied to the upper section from the boiler and after cooling it passes through the openings to the lower one. Herein, on reagent aerosol particles, the ice crystals are formed which fall out from supercooled fog and are detected by a photoelectric counter. The kinetic dependences were also determined in the isothermal cloud chamber of  $0.25 \text{ m}^3$  (Paschenko, Gorbunov 1987, p.269). A mass-mean size of aerosol particles was determined by electron microscopy.

Experimental kinetic curves exhibit three peculiarities: the presence of some time lag in crystal formation,

and the value of curve slopes at short and long times (Fig.1,2).

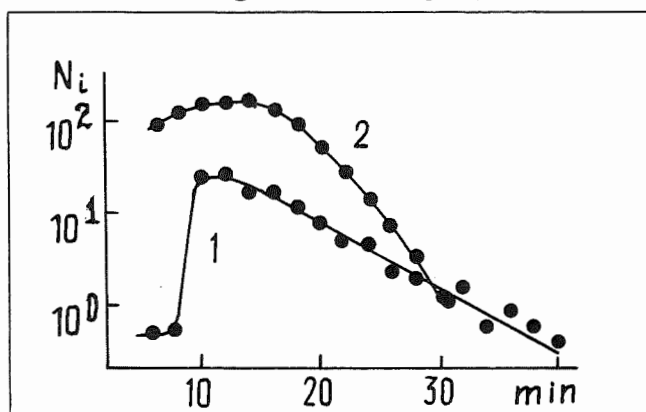


Fig.1: The kinetics of falling out of ice crystals formed on silver iodide aerosol particles in a  $0.018 \text{ m}^3$  chamber at 263 K.  $N_i$  - the number of crystals per  $1 \text{ mm}^3$  of chamber floor in 2 min. A mass-mean particle radius: 1 - 27 nm; 2 - 4 nm.

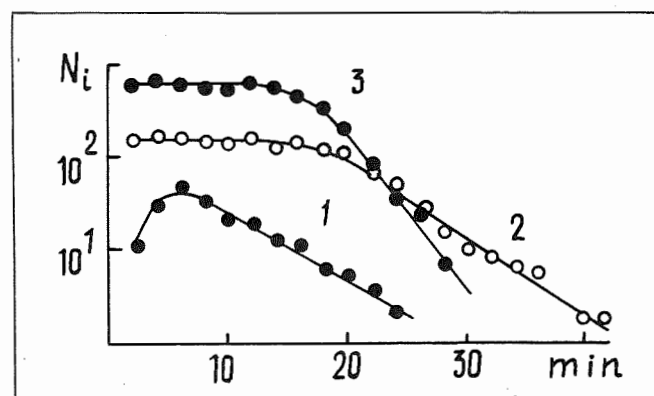


Fig.2: The same as in Fig.1 but for aerosol particles of copper acetyl acetate in a  $0.25 \text{ m}^3$  chamber at 263 K. A mass-mean particle radius: 1 - 120 nm; 2 - 85 nm; 3 - 110 nm (the curve if shifted by 0.5 along the ordinate).

It is shown that the time lag of ice crystal formation in the cloud cham-

ber is caused by the process of metastable medium relaxation after introduction of aerosols. An analysis of the slope of kinetic curves at long times showed that the ice crystal formation rate ( $K$ ) is practically independent of fog temperature, the size of aerosol particles, the concentration of aerosol particles introduced into the chamber, the concentration of ice crystals formed herein (Fig.3).

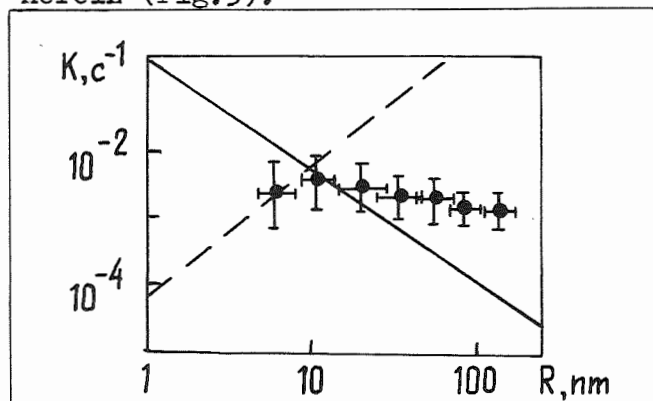


Fig.3: The dependence of ice crystal formation rate  $K = d \lg N_i / dt$  in cloud chamber at  $T = 263$  K on mean particle radius  $R$  for silver iodide. A solid line corresponds to a typical phenomenological dependence  $K$  on  $R$  calculated by a phenomenological theory. A dashed line corresponds to a collision mechanism of ice crystal formation.

At short times the dependence of the slope value on the ice crystal concentration in the chamber is revealed (Fig.4). This is observed at any temperature in both chambers and for all reagents. This dependence testifies to the interaction between the crystals during nucleation. Such a phenomenon, named the effects of vapour depletion, was observed earlier in diffusion chambers (Gorbunov et al. 1980, p.720). The interaction occurs at fairly large distances  $\sim 3$  mm (Fig.4). Such a consi-

derable influence may be accounted for by a high sensitivity of one of the stages of ice crystal formation (nucleation, growth or falling out) to the supersaturation in the chamber.

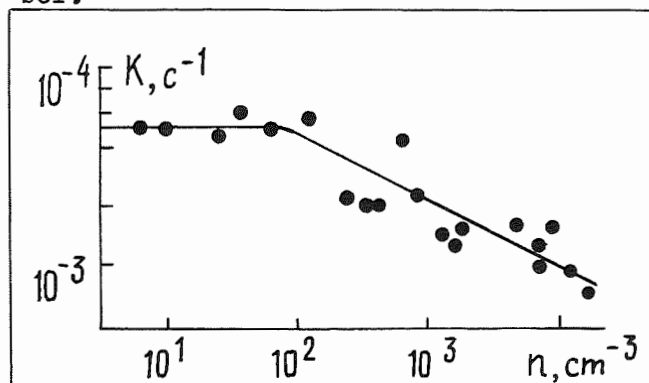


Fig.4: The dependence of ice crystal formation rate at the initial moment on the ice crystal concentration in a chamber ( $n$ ) for aerosol particles of silver iodide.

It is theoretically shown that the slope of kinetic curves at long times must strongly depend on particle radii (Fig.3). In practice it is not so which is difficult to fit to classical concepts about the process of heterogeneous nucleation.

GORBUNOV, B.; KAKUTKINA, N.; KOUTZENOGII, A.; PASCHENKO, A.; SAFATOV, A.: J. Aerosol Sci. 18 (1987) Nr. 3, S. 261-267.

GORBUNOV, B.; KAKUTKINA, N.; KOUTZENOGII, K.; PSHENICHNIKOV, N.: Izv. AN SSSR, 16 (1980) Ser. FAO, S. 720.

PASCHENKO, A.; GORBUNOV, B.: J. Aerosol Sci. 18 (1987) Nr. 3, S. 269-275.

# ABOUT SECONDARY ICE CRYSTAL PRODUCTION

T.Gzirishvili, V. Khorguani

Institute of geophysics, Acad. Sci., GSSR, Tbilisi, USSR

It has been shown earlier that in case of contact mechanism of nucleation on a free face of an aerosol particle placed at the surface of freezing drop, (Gzirishvili, 1967, p.58) the deposition of ice crystals can be observed. In the light of results received later (for example, GAGIN, NOZYCE, 1984, p.56) the above-mentioned effect can be explained by the origin of local supersaturations over the water, round a freezing "warm" drop and, as a result of this, by stimulation of nucleation and growth of ice on aerosol particles.

The present paper deals with the peculiarities of collision of supercooled water drops with the ice surface, kinetics of the process of their solidification and origin of secondary ice crystal in the presence or absence of the external electric field.

The experiments were carried out in a minor cloud camera in the central part of which with the aid of electrodes vertically oriented electric field was established. Electrodes presented round brass plates with the diameter 2 cm and thickness about 2 mm. On the lower electrode a layer of ice was freezed with the same thickness about 3,5 mm. A drop of twice distilled water was suspended by a metal hair covered with a thin vaseline layer. It was placed between the electrodes and was thrown off at a necessary moment.

The experiments were conducted at the same temperature of  $-16^{\circ}\text{C}$  while the drops were thrown off from the height of 10 cm.

In the absence of electric field, when colliding, the drop flattened and the extent of its spread about the ice surface turned to be the maximum, as a rule, - the freezing drop took the shapes from a spherical segment to cylindrical one with a conical top (Fig.1.)

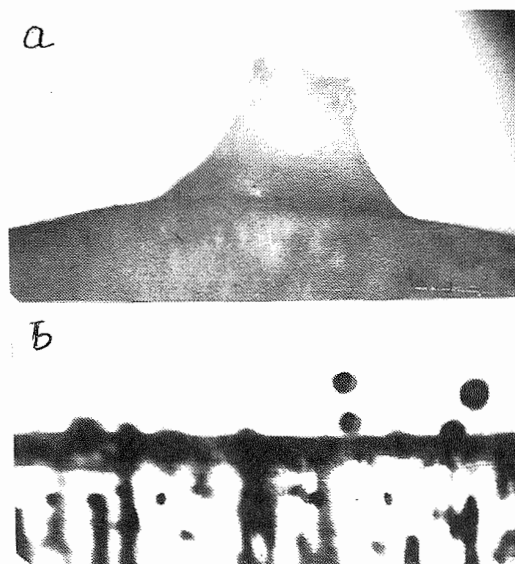


Fig.1- Crystallization of a droplet entrapped by an artificial hailstone b) generation of ice particles

In the presence of electric field the extent of spreading of the drop diminished. The drop took the shapes from spherical one to stretched ellipsoid (Fig.2). Calculations were made of relative change of the crystallized water mass  $w = 1 - \frac{m}{m_0}$  ( $m$  - the ice mass,  $m_0$  - the complete mass of a settled drop) and Fourier numbers  $F_0 = \frac{\alpha \tau}{L^2}$  ( $\alpha$  -

the coefficient of ice thermal diffusivity,  $L$ -characteristic length,  $\tau$ -the time of drop crystallization from the moment of its collision with the backing).

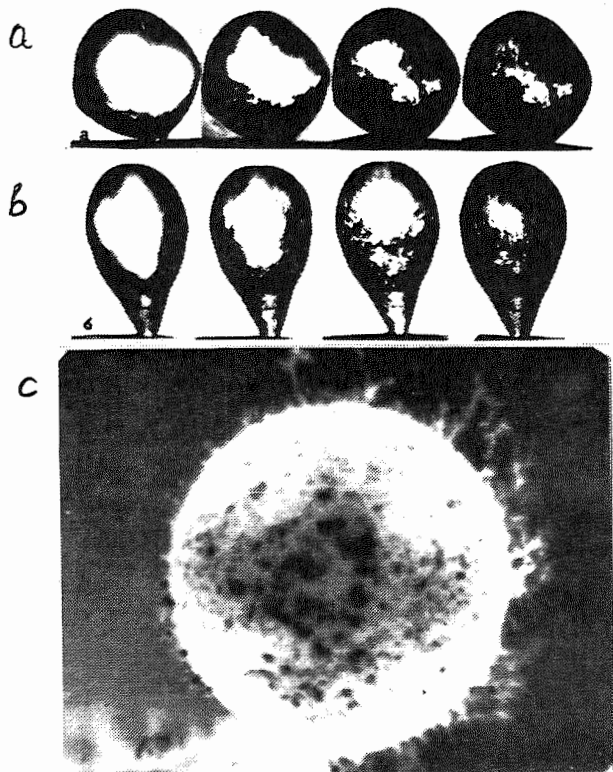


Fig. 2. Process of supercooled droplet crystallization after its collision with an ice substrate: a)  $S=4,1 \cdot 10^{-3}$ ,  $V=0$ ,  $\tau_1=5,05s$ ,  $\tau_2=48,5s$ ,  $\tau_3=75,0s$ ,  $\tau_4=87,0s$  b)  $S=8,9 \cdot 10^{-3}$ ,  $V=+3000v$ ,  $\tau_1=67,0s$ ,  $\tau_2=31,5s$ ,  $\tau_3=95,0s$ ,  $\tau_4=87,0s$  c) Origin and growth of ice crystals on  $SiO_2$  particles located on the freezing droplet surface.

When processing experimental data parameter  $S$  was introduced equal to the ratio of the area of joint base of the freezing drop to the area of its external surface. The curves of  $F_0$  dependence on  $w$  for the values  $S \geq 10^{-1}$  irrespective of the sign and of the potential magnitude, have the appearance given at Fig.3-a. One can see that their up-shift relative to each other is accompanied by the decrease of the value  $S$ . In case  $S \leq 10^{-2}$  (Fig.3-b) the nature of  $F_0$  dependence

on  $w$  is determined by the sign and value of the potential applied to the backing.

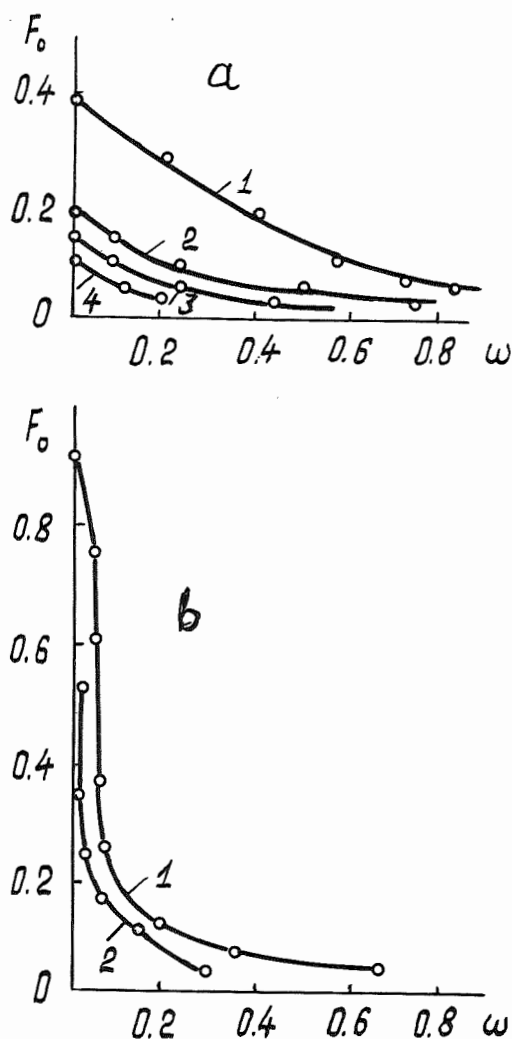


Fig 3. Dependence of  $F_0$ -Fourier number on  $w$ -parameter: a) 1-  $S=1,3 \cdot 10^{-1}$ ,  $V=-6000v$ ; 2-  $S=2,9 \cdot 10^{-1}$ ,  $V=+3000v$ ; 3-  $S=2,6 \cdot 10^{-1}$ ,  $V=0$ ; 4-  $S=8,4 \cdot 10^{-1}$ ,  $V=0$ ; b) 1-  $S=8,9 \cdot 10^{-3}$ ,  $V=+3000v$ ; 2-  $S=4,1 \cdot 10^{-3}$ ,  $V=0$ .

Unlike of  $S \geq 10^{-1}$ , in the present case, as  $S$  increases, the curves have a tendency to shift upwards relative to each other. Figs.1 and 2 give photos of overcooled drops in the process of freezing for  $S \approx 10^{-1}$  and  $S \leq 10^{-2}$ . For  $S \leq 10^{-2}$ , a counter advance of the crystallization front is observed from all the sides (Fig.2-a). The shape of the drop's ice cover does not change,

the process of crystallization is relatively protracted and the throw of ice splinters from the surface of a freezing drop is not observed. However in the presence of  $\text{SiO}_2$  aerosol particles on the drop surface, in the process of its crystallization, the nucleation of ice crystals can be observed as well as their intensive growth (Fig.2-b).

In the case of  $S > 10^{-1}$ , irrespective of the presence or absence of the electric field, when  $10^{-1} < S < 10^{-2}$ , at the negative values of the potential of the ice backing, the drop's crystallization front moves from its base to the summit causing the squeezing out of liquid masses of water and ice particles throw-off (Fig.1-b). The number of splinters is equal to 5 particles averagely. The activation of aerosol particles was not observed, as a rule  $S > 10^{-1}$

Thus, the above-mentioned results permit to mark out processes favouring the formation of ice crystals: in one case - as a result of mechanic action, in another - as a result of activation of heterogeneous nucleation of ice. A qualitative evaluation shows that the generation of ice crystals is much more in the latter case. The explanation of this phenomenon logically lies in the origin of comparatively significant oversaturation. Indeed, when  $S \leq 10^{-2}$ , because of a worse heat removal through the ice backing much greater overheat of freezing drop surface should be expected (to this indicates prolonged process of drop crystallization) and as a consequence of this - the rise of local oversaturation at its surface.

In the real atmosphere, in the presence of air flows, the picture apparently could not be changed qualitatively, as the thickness of temperature and dynamic boundary layers are roughly the same. This means that the heat transfer owing to thermal conductivity will be of the same order with the heat transfer owing to convection (Khorguani, 1984,p.95).

The above discussed phenomenon may be one of the causes of ice crystal generation in the hail clouds. On the other hand, in the case of capture by a hailstone of large overcooled drops in the regime  $S \leq 10^{-2}$  ice crystals will be formed. This, in its turn, would favour the growth of hail-stones in the medium with a mixed microstructure and promote the formation of spongy hailstones.

#### References:

- Gzirishvili T.G. Bulletin Academy Sci. Georgian SSR. Tbilisi, 1967, Vol.15 No.2, pp. 56-61.
- Gagin A.Nozyce H. Proc.11-th Int. Conf. Atm. Aeros. Cond. and Ice Nuclei. Budapest, vol.2, 1984, pp. 56-65.
- Khorguani V.G. Microphysics of hailstone generation and growth. Gidrometizdat, Moscow, 1984, p.183.

EXPERIMENTAL STUDIES ON SECONDARY  
ICE PARTICLE PRODUCTION

Akira Yamashita, Hiroyuki Konishi, Wataru Shimada,  
Masayoshi Miyatake and Keisuke Tani  
Osaka Kyoiku University, Tennoji-ku, Osaka

Mechanisms of secondary ice particle production were investigated by two series of experiments.

EXPERIMENT I

Artificially grown ice needles were evaporated in a subsaturation chamber placed under a stereoscopic microscope (Fig.1)

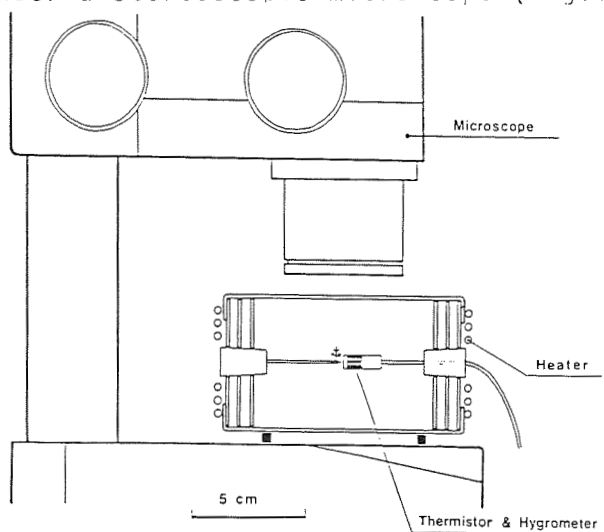


Fig.1 Section of apparatus and the whole evaporating process of a needle was observed in situ by a video camera. By a series of experiments it was found that the length of an ice needle decreased not only by evaporation but also by fragmentation, fracture or deformation of a tip. An example of fracture is shown in Fig.2. Fractured tip was folded or moved intermittently, and gradually evaporated. Fractured tips were also ejected from the mother crystal frequently as shown in Fig.3. The deformation of an evaporating needle occurred when its tip became very thin; the thin tip was curved like a whisker. Experiments were carried out at temperatures between  $-0.5^{\circ}\text{C}$  and  $-12^{\circ}\text{C}$  and at relative humidities between 40% and 97%.

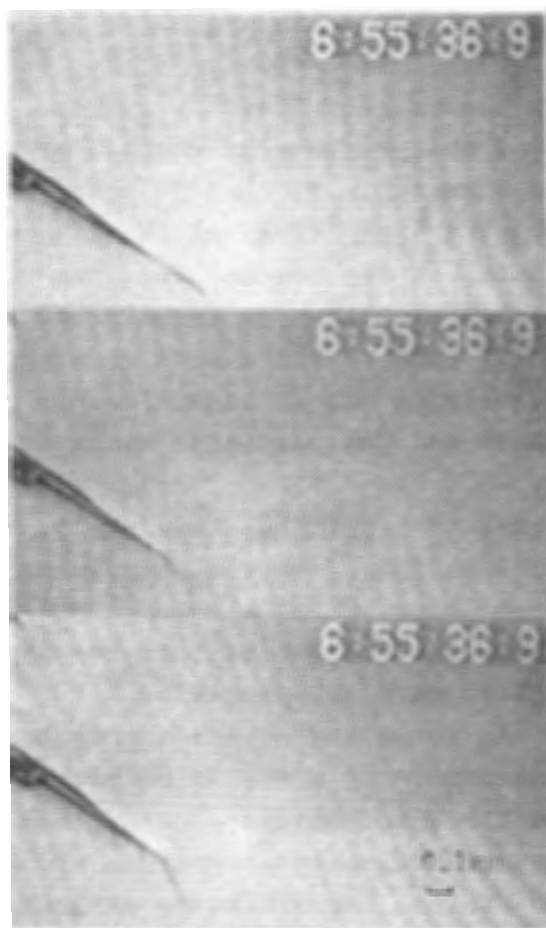


Fig.2 Fracture of needle. Three pictures show the change of the pointed tip in 0.1 second.

Experimental results are summarized in Fig.4. Fragmentations and fractures were observed at temperatures between  $-2.5^{\circ}\text{C}$  and  $-10^{\circ}\text{C}$  and at humidities lower than 85%, although they occurred rarely at humidities higher than 86% and at lower than 56%. As shown by double circles in this figure they occurred especially frequently at about  $-6^{\circ}\text{C}$  and at about 80%. These results suggest the possibility of secondary ice crystals produced by evaporating ice crystals might play

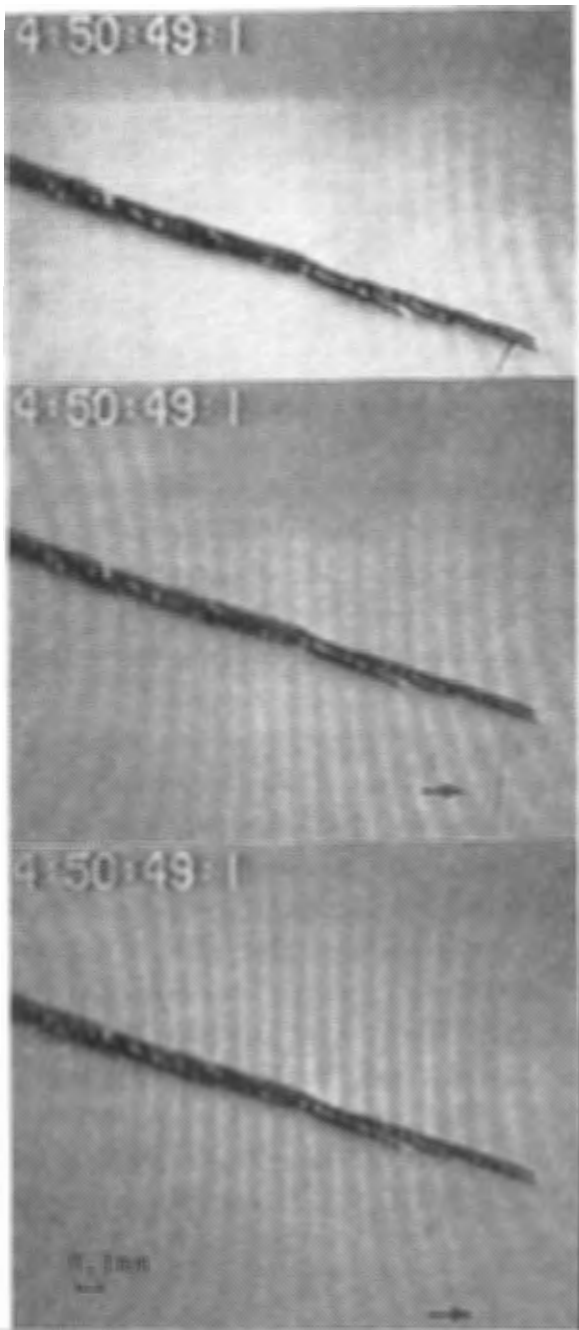


Fig.3 Fragmentation of needle.

Three pictures show the change of the pointed tip in 0.1 second.

important roles in nature.

#### EXPERIMENT II

Ice crystals including many gas enclosures were broken in a supercooled cloud for the purpose of clarifying the effect of expanding enclosed gas, and it was found that remarkable ice crystal enhancement occurred by the expansion of enclosed gas as large as 0.5-2.0mm in diameter. This type of secondary ice particle production also may be possible to occur in natural clouds because ice

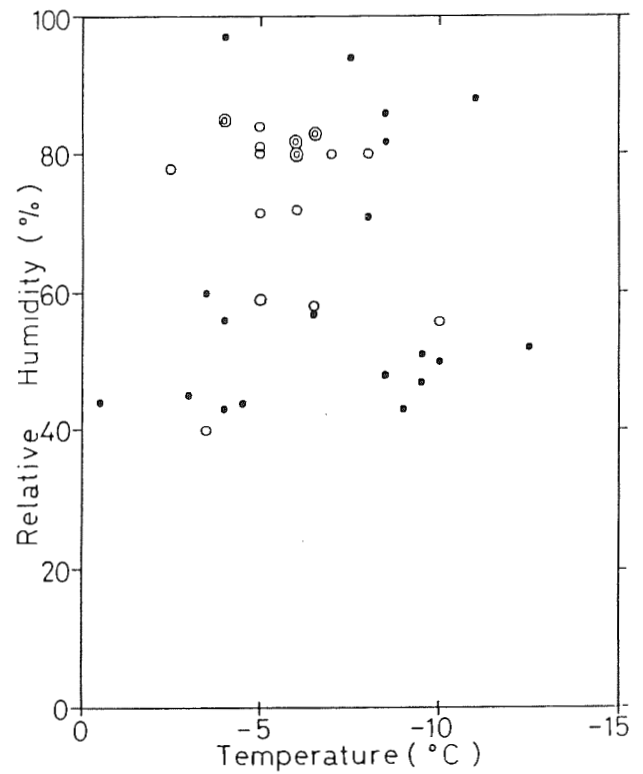


Fig.4 Conditions of experiments and occurrence of fragmentations and fractures

- : no fragmentation and fracture
- : fragmentations and/or fractures observed
- ⊙: the occurrence especially frequent

pellets observed in Osaka on 7 March 1987 were found to contain gas enclosures of about 0.5mm in diameter at the maximum.

# PROPORTION OF RIMING GROWTH PROCESS IN SNOWFALL PHENOMENA

Toshio Harimaya and Misao Sato

Department of Geophysics, Hokkaido University, Sapporo 060, Japan

## 1. INTRODUCTION

It is well known that snow particles grow through the processes of deposition, aggregation and riming. It is very important in the investigations of snow particle formation and precipitation mechanism to study the ratio of contribution by each process in the growth of a snow particle. But, no investigations have been made as yet. As snow particles fall to the ground maintaining the degree of aggregation growth as the number of snow crystals constituting an aggregated snow particle and the degree of riming growth as the riming amount, there is a possibility of measuring the ratio of contribution by each process. So we will concentrate on the riming growth process as the theme. The purposes of the present study are to establish the measuring method of riming amount on a snowflake and to study the difference of riming proportion in the growth of snow particles due to the difference of meteorological conditions and stages in the life cycle of snow clouds.

## 2. MEASURING METHOD OF RIMING AMOUNT ON A SNOWFLAKE

There are many studies on the riming properties of snow crystals (e.g. Harimaya 1975, p. 384). On the other hand, qualitative observations concerning riming amount on a snow particle were made by Hobbs et al. (1971,

p. 152), Reinking (1975, p.745), and Fujiyoshi and Wakahama(1985, p. 1667). In this study we will make quantitative measurements improving on their methods. The measurement was made as follows. Snowflakes were caught on a piece of velvet cloth and a snowflake was selected as their representative. It was disassembled into each snow crystal by a bamboo skewer on a glass plate as carefully as possible so that it would not fracture. Then, all snow crystals constituting a snowflake were photographed. Fig. 1 shows an example of a disassembled snowflake. Each snow crystal was classified into three types, Type I, Type II and Type III as seen in Fig. 1 according to degree of riming and graupel particles were referred to as Type IV. Meanwhile relations as seen

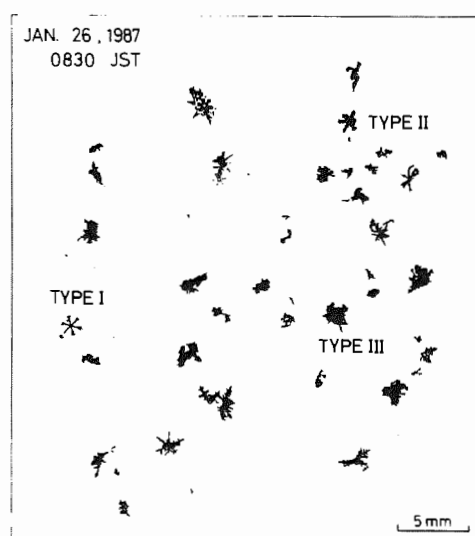


Fig. 1 All snow crystals constituting a snowflake. Examples in each type are shown by name.

in Fig. 2 were obtained from the measurements of the diameter and mass of snow crystals. The mass and riming mass of each snow crystal were obtained using these relations as follows. If we select a snow crystal of Type III and with a diameter of 3 mm by way of example, the mass is obtained from the equation of Type III as seen in Fig. 2 and the riming mass is estimated from the mass difference between a snow crystal (Type III) and unrimed snow crystals (Type I) with a diameter of 3 mm. Then, each mass and each riming mass were summed up and the riming proportion is presented by the ratio of total riming mass to total mass constituting a snowflake. The riming proportion of a graupel particle was assumed to be 100 %.

### 3. RESULTS

#### 3.1 DIFFERENCE OF RIMING PROPORTION DUE TO METEOROLOGICAL CONDITION

An example of radar reflectivity factor over the observation site, snowfall intensity, frequency of snow crystals in each type and riming proportion at the observation site is shown in Fig. 3. When a strong snow cloud passed over the observation site at about 0930 JST, the snowfall intensity increased, graupel particles fell and riming proportion increased. Then, the snowfall intensity continued to increase gradually and by contrast, the riming proportion decreased gradually. In the later stage, both the snowfall intensity and riming proportion became small. This time change is general during the passage of snow clouds. As it was inferred in Fig. 3 that the riming proportion is related to the snowfall intensity, the relation between the snowfall intensity

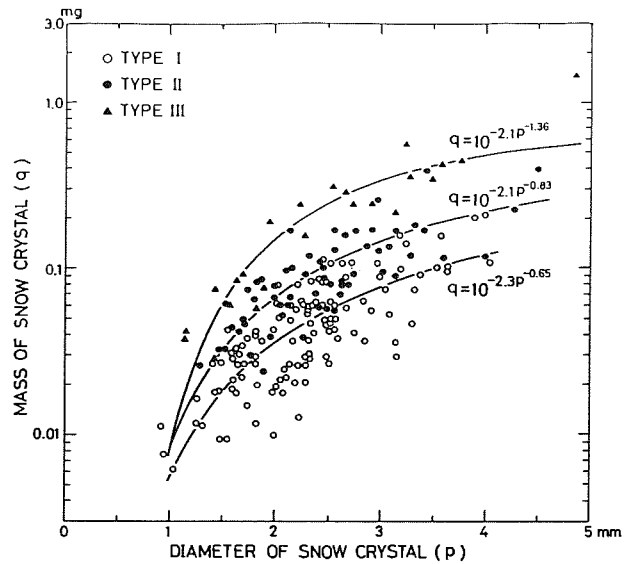


Fig. 2 Relation between the diameter and mass of snow crystals in each type.

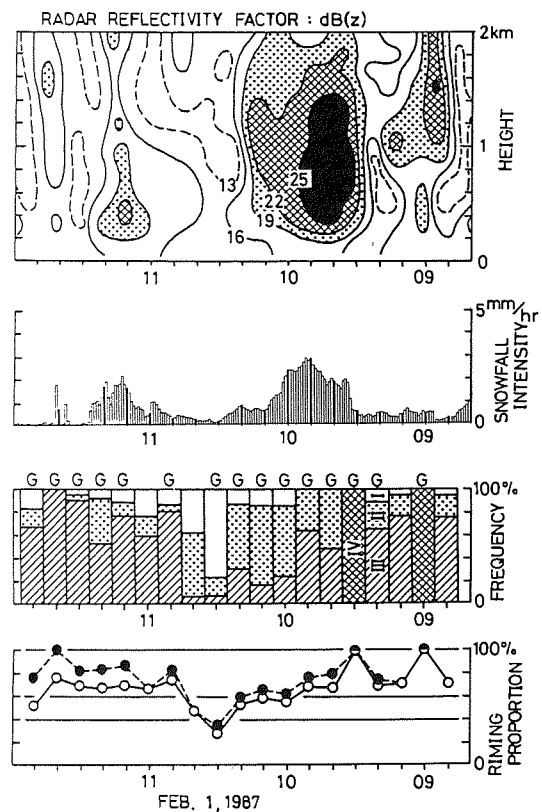


Fig. 3 Radar reflectivity factor over the observation site, snowfall intensity, frequency of snow crystals in each type and riming proportion at the observation site. Solid circles in the lower part indicate the riming proportion incorporating the effect of graupel particles.

and riming proportion was examined as shown in Fig. 4. The lower limit of riming proportion tends to increase with the increase of the snowfall intensity. Explained in detail, only the snowflakes with a large riming proportion fall when the snowfall intensity is strong and the snowflakes with a various value of riming proportion fall when the snowfall intensity is weak. But, in this part, the riming proportion is large when snow cloud is more active as represented by the radar echo pattern.

### 3.2 DIFFERENCE OF RIMING PROPORTION

#### DUE TO THE STAGE IN LIFE CYCLE OF SNOW CLOUDS

In order to study how the riming proportion changes with the growth stage of snow clouds, snow clouds were classified into three stages, i.e., developing, mature and dissipating, based on the growth stage of snow clouds passing over the observation site. The relation between the growth stage and riming proportion are shown in Fig. 5 under the conditions with an equal radar reflectivity factor. In a wide range of radar reflectivity factor, the riming proportion is large at the developing and mature stages and small at the dissipating stage.

### 4. DISCUSSION AND CONCLUSION

The lower limit of riming proportion tends to increase with the increase of snowfall intensity. Snowflakes with various values of riming proportion fall when the snowfall intensity is weak. This is considered to be explained by the sorting of snow particles and the difference of meteorological conditions. The riming proportion is large at the developing and mature stage of snow clouds and small at the

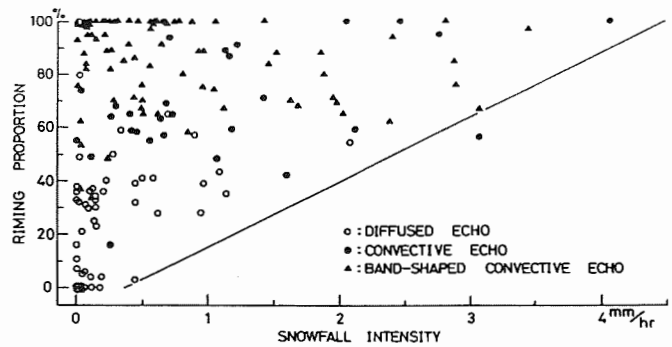


Fig. 4 Relation between snowfall intensity and riming proportion.

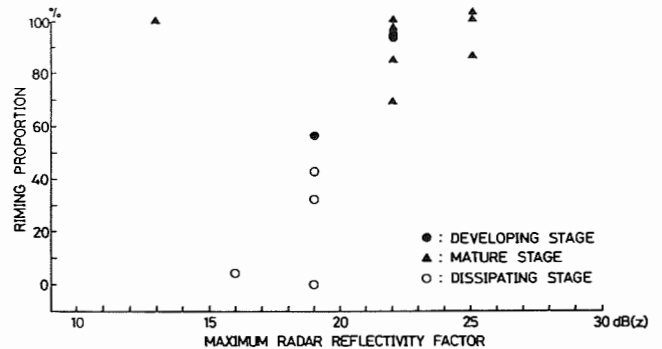


Fig. 5 Relation between the growth stage of snow clouds and riming proportion.

dissipating stage. This may probably be explained by the formation of cloud droplets and the riming process by snow particles.

### 5. REFERENCES

- Fujiyoshi, Y.; Wakahama, G.: On snow particles comprising an aggregate. *J. Atmos. Sci.* 42 (1985) No. 15, p. 1667-1674.
- Harimaya, T.: The riming properties of snow crystals. *J. Meteor. Soc. Japan* 53 (1975) No.6, p. 384-392.
- Hobbs, P. V.; Collaborators: Studies of winter cyclonic storms over the Cascade Mountains (1970-71). Res. Rept. 6 (1971), Dept. Atmos. Sci., University of Washington 306 pp.
- Reinking, R. F.: Formation of graupel. *J. Appl. Meteor.* 14 (1975) No. 5, p. 745-754.

THREE-DIMENSIONAL STRUCTURES OF SNOW CRYSTALS  
SHOWN BY STEREO-PHOTOMICROGRAPHS

Kunimoto Iwai

Faculty of Education, Shinshu University, Nagano  
Japan

### 1. Introduction

Photomicrographs of natural snow crystals have been taken with the microscope of low magnification by many investigators (Bentley and Humphreys, 1931, Nakaya, 1954, Magono and Lee, 1966).

Photomicrographs of plate-like snow crystals by Bentleys and Humphreys particularly have given the impression on a person that they are represented as two-dimensional nature. Few investigation about their three-dimensional structures has been done, even though Nakaya (1954) showed a few side view photomicrographs of them. Therefore, stereo-photomicrographs of snow crystals are desirable to clarify their three-dimensional nature. Iwai (1981), (1983) showed a simple method how to take their stereo-photomicrographs.

However, the author is anxious of that most personae cannot observe them stereo-scopically by naked eyes.

Therefore, at the poster session in the present conference, stereo-photomicrographs of snow crystals will be shown with the simple stereo-scopes.

### 2. Examples of stereo-photomicrographs of snow crystals.

Photo. 1 shows a pair of stereo-photomicrograph of snow crystal classified as malformed type. Its side view photographs is also shown. We cannot understand the surface structures of this crystal from only one plane photograph, because of its complexity.

However, we can immediately under-

stand that this crystal consists of two plates with different height, when we observe it stereo-scopically. we can see from the side view photomicrograph that these two plates are linked by a small and thin hexagonal plate. Two plates grow asymmetrically from the upper and lower parts of the small hexagonal plate and it becomes malformed crystal.

Photo. 2 shows stereo-photomicrograph of two resemble dendritic crystals. Both are the double plates which grow from the upper and lower parts of thin (crystal A, A' in side view) and thick (crystal B, B' in side view) hexagonal plates.

Photo. 3 shows a stereo-photomicrograph of a single bullet type crystal taken along the c-axis. From stereo-scopic view, we understand that apparent pyramidal faces are not crystallographic pyramidal faces but are mere skeleton structures. This finding will be important for explaining the halo with an angular radius of about  $8^\circ$ , which is rarely observed. Because, this halo is attributed to the ray path from the crystallographic pyramidal face to the prism face (Wallace and Hobbs, 1977).

### 3. Concluding Remarks

In this extended abstract, only 3 stereo-photomicrographs are shown. However, we have observed many natural snow crystals from the view point of three-dimensional structures for these 7 years.

The following are concluded:

- 1) Most of plate-like snow crystals (about 70 %) consist of 2 or more plate-like crystals having different forms and sizes.
  - 2) A simple dendritic plate is rarely observed.
  - 3) Apparent pyramidal faces of bullet crystal are not crystallographic faces but mere skeleton structures.
- The author believes that stereo-scopic view of snow crystals are very useful to clarify their three-dimensional nature.

#### References

- Bentley, W.A. and W.J. Humphreys, 1931: Snow crystals, McGraw-Hill, New York.
- Iwai, K., 1981: A simple method for taking stereo-photomicrographs of snow crystals. *Tenki*, 28, 377-380.
- Iwai, K., 1983: Three-dimensional Structure of plate-like snow crystals. *J. Met. Soc. Japan*, 61, 746-756.
- Magono, C. and C.W. Lee, 1966: Meteorological classification of natural snow crystals. *J. Fac. Sci. Hokkaido Univ. Ser. 7, 2*, 321-335.
- Nakaya, U., 1954: Snow crystals. Harvard Univ. Press.
- Wallace, J.M. and P.V. Hobbs: Atmospheric Science., Academic Press.

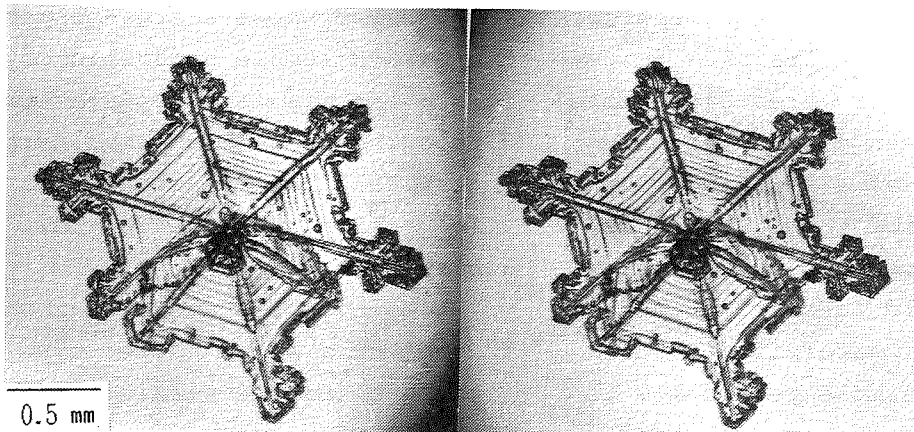


Photo. 1



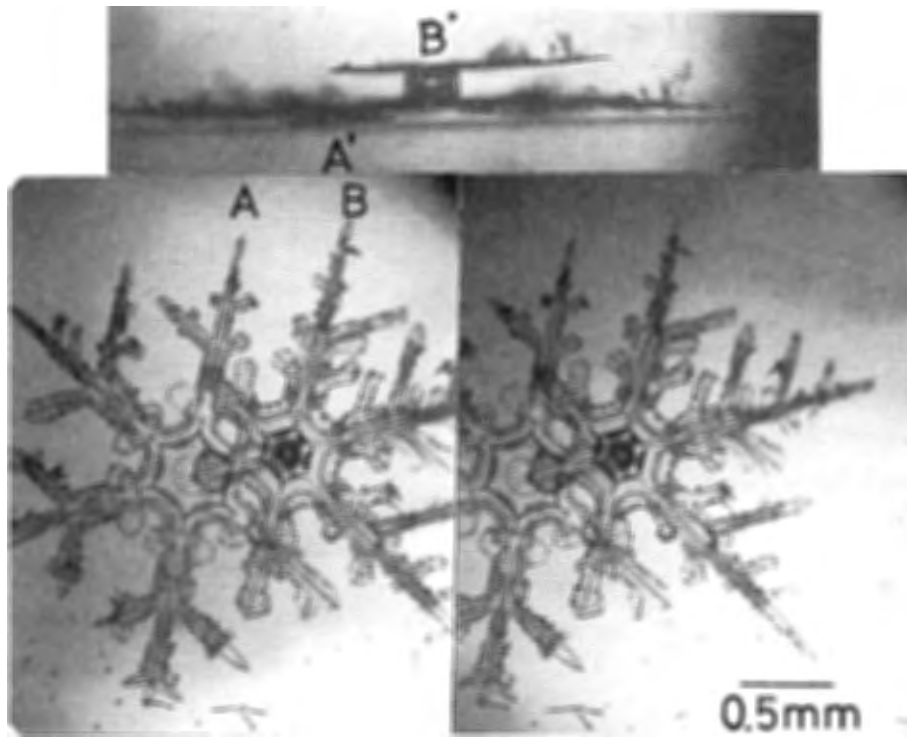


Photo. 2

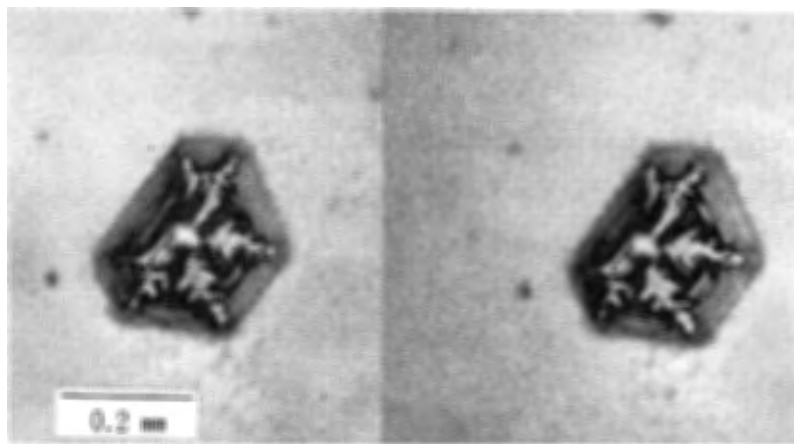


Photo. 3

# ON THE VARIATION OF FALLING VELOCITY OF EARLY SNOWFLAKES

Masahiro Kajikawa <sup>1</sup>  
Department of Earth Science  
Akita University  
Akita 010, Japan

## 1. INTRODUCTION

The aggregation of snow crystals to form snowflakes is an important process in the growth of precipitation particles in clouds. Information on the falling motion of snowflakes in the atmosphere is required to calculate their growth by the aggregation process, in addition to the falling velocity of snow crystals.

The falling motion of snowflakes is accompanied by the horizontal motion and both vertical and horizontal velocity variations (e.g., Sasyo, 1971, 1977; Zikmunda and Vali, 1972). Those velocity variations and horizontal motion are responsible for an increase in the collision efficiency of snowflakes. In the former observations (e.g., Sasyo, 1971, 1977), however, the available data of early snowflakes which are composed of several snow crystals, are not sufficient to study the aggregation process. In a previous paper (Kajikawa, 1982), the free-fall pattern of early snowflakes in still air and the number and shape of component crystals were analyzed. Early snowflakes are composed of two to six crystals, of which about 80% fall with a spiral or rotational motion. In this paper the correlations between velocity variations and features of unrimed early snowflakes will be analyzed and discussed.

## 2. METHOD OF OBSERVATION

Since the method of measurement of falling motion is the same as in the previous paper, the procedure will be described briefly. For the

measurement of three-dimensional motion, a falling snowflake was illuminated by stroboscopic light and photographed by means of a stereoscopic camera system. The coordinates of the snowflake were calculated from successive corresponding points (the center of images) on the pair of photographs. The fallen snowflakes were caught on a sampling plate and were microphotographed for determining shape, size, mass, and number of its component snow crystals. In this paper, data obtained from the analysis of fall pattern of spiral type involving rotational type were used to reveal the variations of vertical and horizontal velocities.

## 3. RESULTS

The relationships between the mass ( $M$ ) and the mean vertical velocity ( $\bar{V}$ ) and the mean horizontal velocity ( $\bar{V}_H$ ), are shown in Fig. 1. For the classification of snowflakes, the type describes the

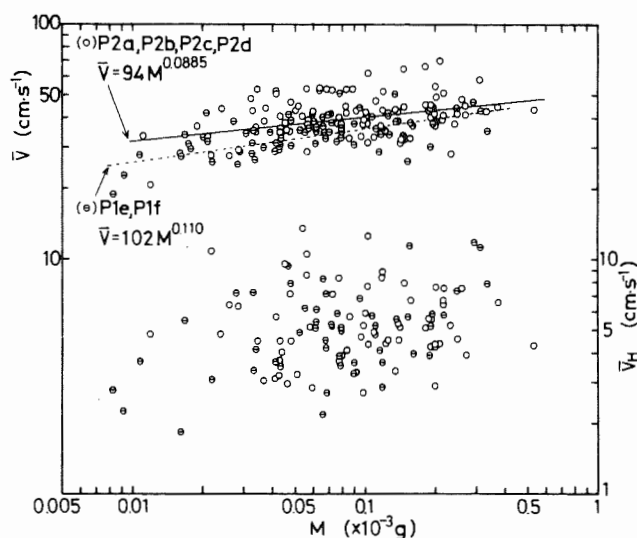


Figure 1. Relationships between the mass ( $M$ ) of early snowflakes and the mean vertical ( $\bar{V}$ ) and horizontal ( $\bar{V}_H$ ) velocity.

<sup>1</sup> Present Affiliation: Scientific Visitor, National Center for Atmospheric Research, Boulder, Colorado, U.S.A.

largest component crystals (Magano and Lee, 1966) was used. It is evident from this figure that  $\bar{V}_H$  has no relation to  $M$ . On the other hand,  $\bar{V}$  has reasonable correlation to  $M$ , although the large amount of scatter appear in the velocity values. Empirical equations were obtained by a least-squares technique.

Figure 2 shows the nondimensional amplitude ( $a' = a/d$ ) of the spiral motion, where  $a$  and  $d$  are the amplitude of the spiral motion and the size of snowflakes, respectively. It is clear that  $\bar{V}_H$  is proportional to  $a'$  and is independent of the main type of component snow crystals. On the other hand, there is some trend toward smaller  $\bar{V}$  with increasing  $a'$ .

The nondimensional frequency ( $n' = nd/\bar{V}$ ) of spiral motion increases as Reynolds number ( $Re = \bar{V}d/\nu$ ) increases and is independent of the shape of the component crystals, as seen in Fig. 3. Here  $n$  and  $\nu$  are the frequency of spiral motion and the kinematic viscosity of air, respectively.

Figure 4 is the relationship between  $a'$  and  $n'$ . It

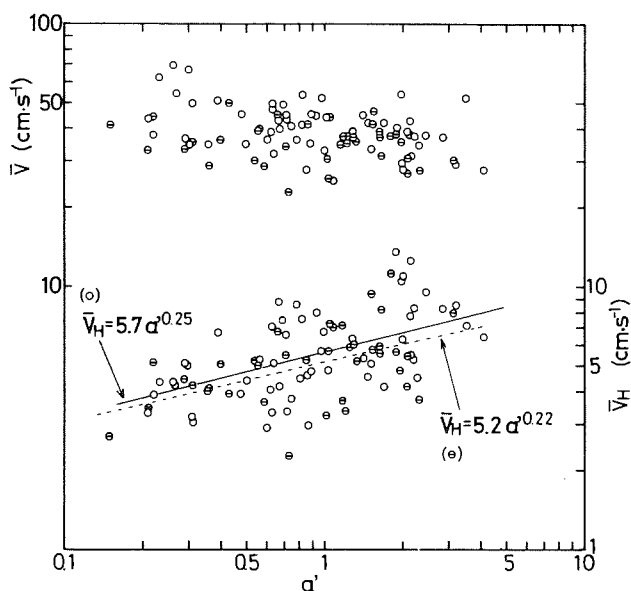


Figure 2. Relationships between the nondimensional amplitude ( $a'$ ) of the spiral or rotational motion and the mean vertical ( $\bar{V}$ ) and the horizontal ( $\bar{V}_H$ ) velocity. Symbols as in Fig. 1.

is evident that  $a'$  is inversely proportion to  $n'$  and is dependent in some degree of the shape of component snow crystals.

Figure 5 is the relationship between  $\bar{V}_H$  and the standard deviation ( $\sigma_v$ ) of the variation in vertical velocity ( $V$ ). Although  $\sigma_v$  increases slightly with  $\bar{V}_H$ , these values are usually smaller than 2 cm/sec (3 to 5% of  $\bar{V}$ ) and are independent on the main shape of component crystals.  $\sigma_v$  in this observation is smaller

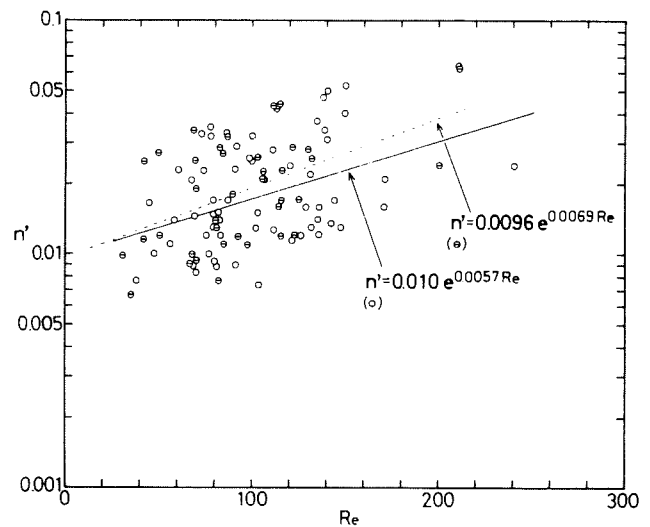


Figure 3. Relationship between the Reynolds number ( $Re$ ) with respect to the mean vertical velocity and the nondimensional frequency ( $n'$ ) of the spiral or rotational motion.

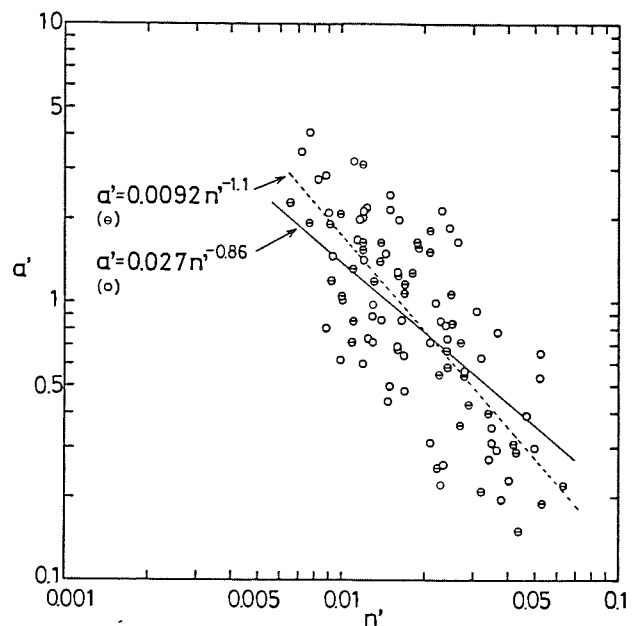


Figure 4. Relationship between the nondimensional frequency ( $n'$ ) and the nondimensional amplitude ( $a'$ ).

than the mean value (2.83 cm/sec) observed by Sasyo (1971). It seems that this difference is primarily due to the difference in the mean vertical velocity of the snowflakes in the two studies.

The relationship between  $\bar{V}_H$  and the standard deviation ( $\sigma_H$ ) of the variation in horizontal velocity ( $V_H$ ) is shown in Fig. 6. It can be seen that  $\sigma_H$  increases with  $\bar{V}_H$  and is independent of the shape of the component snow crystals.  $\sigma_H$  amounts to about 50% of  $\bar{V}_H$  and is larger than  $\sigma_v$ . These values of  $\sigma_H$  are comparable to the mean value (3.0 cm/sec) observed by Sasyo (1971). From the results described above, it seems likely that in particular the variation of the horizontal velocity plays an important role in the aggregation process of snowflakes.

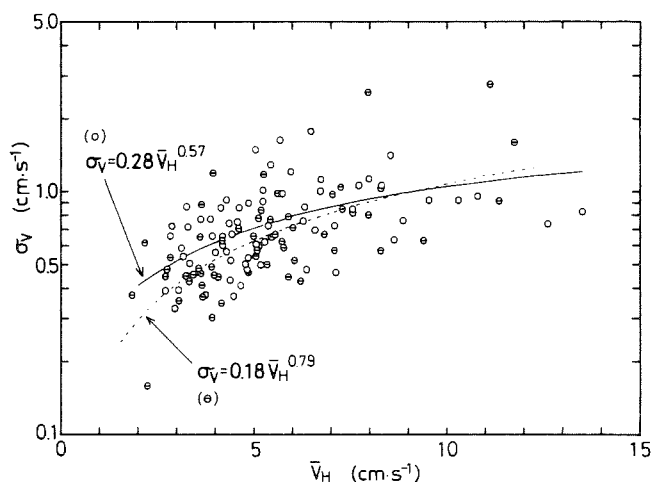


Figure 5. Relationship between the mean horizontal velocity ( $\bar{V}_H$ ) and the standard deviation ( $\sigma_v$ ) of variation in vertical velocity.

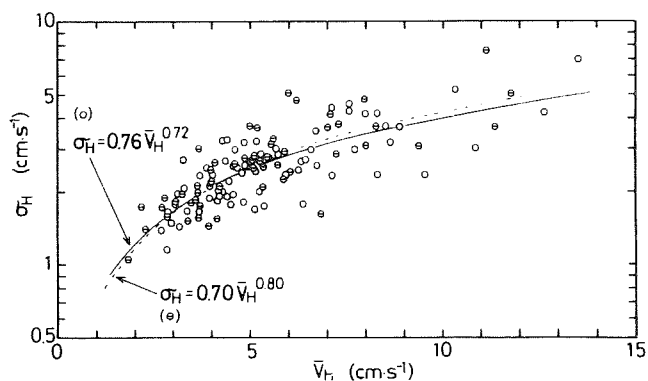


Figure 6. Relationship between the mean horizontal velocity ( $\bar{V}_H$ ) and the standard deviation ( $\sigma_H$ ) of variation in horizontal velocity.

#### 4. CONCLUDING REMARKS

The falling motion in still air of early snowflakes, which are composed of two to six crystals, was analyzed by means of a stereo-photogrammetry.

The variations of vertical and horizontal velocity in the spiral or rotational falling motion were empirically obtained, as shown in Figs. 5 and 6. The standard deviation of variation in vertical velocity is small. On the other hand, the standard deviation of variation in horizontal velocity is considerably larger and increases with mean horizontal velocity. Accordingly, it seems reasonable to conclude that in particular the variation of horizontal velocity plays an important role in the aggregation process of snowflakes.

The mean horizontal velocity can be estimated from the nondimensional amplitude of the spiral or rotational falling motion. The nondimensional amplitude is inversely related to the nondimensional frequency of spiral or rotational motion. And the nondimensional frequency can be estimated from the Reynolds number with respect to the mean vertical velocity of snowflakes.

#### 5. REFERENCES

- KAJIKAWA, M.: Observation of the falling motion of early snow flakes. Part I. Relationship between the free-fall pattern and the number and shape of component snow crystals. *J. Meteor. Soc. Japan.* **60** (1982) 797-803.
- MAGONO, C.; LEE, C. W.: Meteorological classification of natural snow crystals. *J. Fac. Sci. Hokkaido Univ. Serv.* **VII, 2** (1966) 321-335.
- SASYO, Y.: Study of the formation of precipitation by the aggregation of snow particles and the accretion of cloud droplets on snowflakes. *Pap. Meteor. Geophys.* **22** (1971) 69-142.
- SASYO, Y.: The collection efficiency of simulated snow particles for water droplets (II), On the oscillatory angular motion of the snowflake. *Pap. Meteor. Geophys.* **28** (1977) 159-168.
- ZIKMUNDA, J.; VALI, G.: Fall patterns and fall velocities of rimed ice crystals. *J. Atmos. Sci.* **29** (1972) 1334-1347.

A PARAMETRIZATION SCHEME FOR THE COALESCENCE OF WATER DROPS USING THE STOCHASTIC COLLECTION EQUATION

C. Lüpkes<sup>+</sup>, K. D. Beheng<sup>++</sup>, G. Doms<sup>+++</sup>

+ Institut für Meteorologie u. Geophysik der Universität Frankfurt/Main, FRG

++ Institut für Meteorologie u. Klimaforschung, Kernforschungszentrum Karlsruhe/Universität Karlsruhe, FRG

+++Deutscher Wetterdienst Offenbach, FRG

1. Introduction

In numerical simulation models the formation of precipitation due to the collision/coalescence process is usually treated by two methods: on the one hand, by numerically solving the stochastic collection equation (SCE) governing the time evolution of a drop size spectrum or, on the other hand, by using a parametrization scheme dealing with bulk quantities such as liquid water contents. With respect to the latter, the most prominent scheme is that of Kessler (1969). His concept is based on the partition of the total liquid water content into a cloudwater and a rainwater portion. The conversion of cloudwater into rainwater is thought to be the result of two basic conversion mechanisms: (i) autoconversion, which means the transformation of cloud water to rainwater and (ii) accretion, which means an increase of rainwater mass. The corresponding conversion rates as given by Kessler have been derived partly by intuition and partly by crude approximations.

In this paper we describe how the partitioning concept of Kessler can be applied to SCE and how rate equations analogous to those presented by Kessler can be formulated. Then we compare results obtained by this method with those obtained by Kessler's scheme. Starting from this basis finally a new parametrization scheme is outlined.

2. The concept

Applying Kessler's partitioning concept analogously to SCE the important question arises: Which drop radius separating cloud droplets from raindrops should be chosen? This question may be answered by the numerical-empirical result that, nearly independent of an initial drop spectrum, the evolving drop size distribution function (in a specifically transformed form) exhibits at about  $r^* = 40 \mu\text{m}$  radius a minimum value which is fairly stationary at longer simulation times. Thus, a drop radius of  $40 \mu\text{m}$  seems to be appropriate to distinguish cloud droplets from raindrops. Accordingly we split the size distribution function  $f(x)$ ,  $x$ : drop mass, into a cloud droplet part  $f_C(x)$

with  $x < x^* \sim (r^*)^3$  and into a raindrop part  $f_R(x)$  with  $x \geq x^*$  so that the total spectrum is given by  $f(x) = f_C(x) + f_R(x)$ . In the scope of this definition autoconversion and accretion denote the formation of raindrops with mass  $x = x_1 + x_2 \geq x^*$ , as shown in Fig.1, where  $x_1, x_2 < x^*$  as well as  $x_1 < x^*$  and  $x_2 \geq x^*$ , respectively.

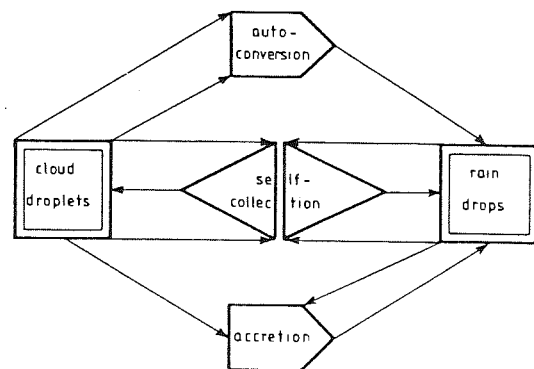


Fig.1 Scheme of the collection mechanisms

Additionally, selfcollection appears, which means the production of cloud droplets (raindrops) with mass  $x < x^*$  ( $x \geq x^*$ ) where  $x_1, x_2 < x^*$  ( $x_1, x_2 \geq x^*$ ). Obeying these mass relations and the separation of the drop size distribution function as indicated, the total rates of change of the cloud droplet and the raindrop part of the spectrum are then derivable as the sum of mode-specific 'differential' rates. From these rates mode-specific integral rates for arbitrary moments of both parts of the spectrum can be deduced. For the explicit formulation of both types of rates see Beheng & Doms (1986), Doms & Beheng (1986) and Beheng (1987).

The main results obtained from these investigations are as follows:

- Provided that the liquid water contents are the same, the shape of the initial drop spectrum strongly influences the magnitude and the time dependence of the conversion rates.
- Selfcollection of cloud droplets gradually leads to the formation of drops with mass  $x \sim x^*$ . Thus selfcollection is of special importance since drops in this size range are converted most effectively to raindrops by auto-

conversion.

- Concerning the cloud droplet range, autoconversion and selfcollection cause a narrowing and a broadening of that partial spectrum, respectively, resulting as a whole in a slight broadening; accretion has only a negligible effect on the spectrum's spread.

- Concerning the raindrop part of the spectrum, a strong broadening occurs due to the combined action of all collection modes.

- The autoconversion rate calculated by Kessler's formula is in principle unable to predict rates as have been computed by use of SCE.

All in all it can be stated that the major shortcomings of Kessler's scheme are that (i) cloud water is only represented by the liquid water content instead of a size spectrum and that (ii) raindrops are always described by an exponential function (Marshall-Palmer type) with constant number density for the hypothetical radius  $r=0$ . It has therefore been concluded that besides the cloud and rainwater content additional parameters have to be included to yield a more reliable parametrization scheme.

### 3. The new scheme

As a starting point the integral conversion rates derived by Beheng & Doms for the distinct modes of collection autoconversion, accretion and selfcollection have been used to predict, in addition to the rates of change of the liquid water contents, those of the number densities in each size range. In order to formulate these rates it was necessary to parametrize appropriately the collection kernel function  $K$  occurring in each integral expression. This was mostly done by assuming  $K \propto r^2$  (cf. Long, 1974). Unfortunately the parametrization developed in that way did not reproduce the results obtained by solving SCE. This deficiency was due to the fact that the structure of the distribution function near  $r^*$ , which turned out to be of great importance, was not grasped with necessary accuracy. Therefore, the cloud droplet range (see fig.2) was repartitioned into two sub-ranges (at a drop radius  $r^+$  of about 20  $\mu\text{m}$ ) and consequently the integral

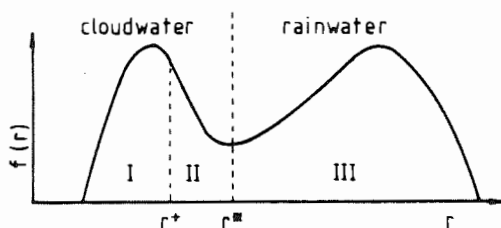


Fig.2 Scheme of the 3 drops ranges under consideration

conversion rates of Beheng & Doms were reformulated in correspondence with the new partitioning. A crucial point in this concept was that by applying the kernel approach mentioned above some integral rates could only be expressed as a function of the number densities at both separation radii  $r^+$  and  $r^*$  as well as the radar reflectivities in both cloud droplet ranges. To determine these open variables specific distribution functions in each drop range are assumed as a closure condition: in region I and II a Gamma and an inverse Gamma function, respectively, governed by three parameters, where in each function one parameter is set constant and the remaining two parameters  $\alpha_I, \alpha_{II}, \beta_I$  and  $\beta_{II}$ , resp., are chosen to be variable in time; in region III an exponential function containing two variable parameters. The time rates of change of the parameters of these distribution functions can be formulated in terms of time rates of change of certain moments of the spectra. In summary this results finally in a set of ten coupled prognostic equations: six for the number densities and liquid water contents in the three drop regions and four for the parameters  $\alpha_I, \alpha_{II}, \beta_I$  and  $\beta_{II}$ .

The procedure of the numerical solution of these equations is as follows:

(i) any given initial size distribution function is approximated by the specific functions prescribed in each size range. This consists in the determination of the four distribution parameters mentioned from the given number densities and liquid water contents in region I and II. In region III no drops are allowed to appear initially in order to exclude a contribution by accretion at the very beginning of the simulation. (ii) The prognostic equations for the three number densities and liquid water contents are solved by simple forward time integration. The open variables mentioned are calculated by iteration from the tendency equations for the four parameters.

### 4. Numerical results

In Figs.3 and 4 the results of the numerical simulation of the parameter scheme are compared to those obtained by solution of SCE, i.e. for the conversion rates due to accretion and autoconversion as well as for the time evolution of the rainwater content  $L_{III}$ . Two initial spectra  $s_1$  and  $s_2$  with liquid water contents  $L = 10^{-6} \text{ g cm}^{-3}$  and initial number densities  $N_0 = N(t=0) = 100 \text{ cm}^{-3}$  have been used which only differ by the specification of the initial radius dispersion coefficient  $v$  ( $v_1=0.25$  ( $s_1$ ),  $v_2=0.40$  ( $s_2$ )). The agreement between the two calculation

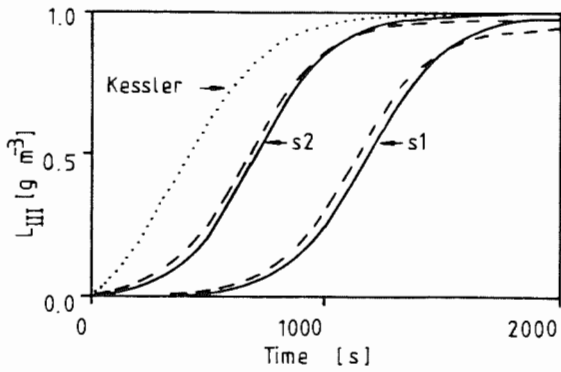


Fig. 3 Rainwater content  $L_{III}$  as function of model time for Spectrum s1 and s2 obtained by the solution of SCE (dashed lines), the new parameter model (solid lines) and Kessler's scheme.

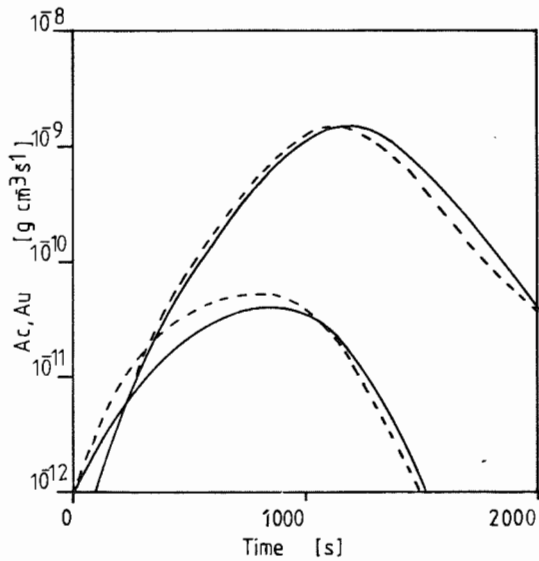


Fig. 4 Mass density conversion rates as function of model time for cloud water due to autoconversion (lower curves) and accretion (upper curves) obtained by the solution of SCE (dashed line) and the parameter model (solid line) for spectrum  $s_1$ .

methods is obviously good. Moreover, as already mentioned above, the structure of the initial size distribution function has a strong influence on the time evolution of the conversion rates and on that of the rain water content. Note that, when applying Kessler's scheme, only one curve occurs since for both initial spectra the same total liquid water content has been assumed.

## 5. References

- BEHENG, K.D.: Zur mikrophysikalischen Modelltheorie des Auswaschens von Aerosolteilchen sowie der Bildung von flüssigem und eisförmigem Niederschlag, Berichte des Instituts für Meteorologie u. Geophysik der Univ. Frankfurt a.M. 69 (1987), 78 p.
- BEHENG, K.D.; DOMS, G.: A general formulation of collection rates of cloud- and raindrops using the kinetic equation and comparison with parametrizations, Beitr. Phys. Atmos. 59 (1986), p. 66-84
- DOMS, G.; BEHENG, K.D.: Mathematical formulation of selfcollection, autoconversion and accretion rates of cloud- and raindrops, Meteorol. Rdsch. 39 (1986), p. 98-102
- KESSLER, E.: On the distribution and continuity of water substance in atmospheric circulations, Meteorol. Monogr. 32 (1969), 84 p.
- LONG, A.B.: Solutions to the droplet collection equation for polynomial kernels, J. Atmos. Sci. 31 (1974), p. 1040-1052

# ON THE DYNAMICS OF THE FALLING ICE CRYSTAL ZONE

Josef Podzimek

Department of Mechanical and Aerospace Engineering, and

Graduate Center for Cloud Physics Research

University of Missouri-Rolla, MO 65401

## 1. INTRODUCTION

This contribution focuses on aerodynamics of ice crystals or snowflakes in reference to evolution of falling ice crystal zone. The results of the investigation of particulate deposition on scavengers such as disks, plates, on thin oblate spheroids and long cylinders were published elsewhere (e.g., Podzimek and Martin, 1984).

## 2. MODELING OF THE ICE CRYSTAL ZONE

The numerical model is based on the previous work by Clark and List (1971) and Girard and List (1975) who assumed that body forces and aerodynamic drag of falling precipitation elements induce an air motion which affects the element dispersion and settling. In our two-dimensional model were neglected the thermodynamic terms related to water phase transition and to the thermal stratification of the atmosphere. To the standard equations for air mass conservation and linear momentum (with an isotropic turbulent exchange coefficient,  $K_t$ , and terms for the force acting on scavengers in gravitation field,  $-gq$ ) was added the continuity equation for scavenger mixing ratio,  $q$ , and the energy equation in the form

$$\frac{\partial q}{\partial t} + \frac{\partial(qu)}{\partial x} + \frac{\partial}{\partial z} [q(w-v_s)] = 0 ,$$

$$\frac{\partial}{\partial t} \iint \left[ \frac{1}{2}(u^2 + w^2) + gqz \right] dx dz = - \iint gq v_s dx dz - K_t \iint \left[ \left( \frac{\partial u}{\partial x} \right)^2 + \left( \frac{\partial u}{\partial z} \right)^2 + \left( \frac{\partial w}{\partial x} \right)^2 + \left( \frac{\partial w}{\partial z} \right)^2 \right] dx dz .$$

A simple relationship between the uniform size of scavengers and the settling velocity,  $V_s$ , was assumed. The effect of relaxation time for scavengers was neglected. Otherwise, the air velocity components,  $u$ ,  $w$ , were calculated from the stream function and related to the vorticity which was used in the transport equation.

## 3. RESULTS OF MODELING

The calculation has been done for calm, homogeneous atmosphere and for the atmosphere with uniform horizontal wind velocity. The initial and boundary conditions for calm atmosphere are similar to those in quoted articles. Following parameters were considered to affect the evolution of scavenger (precipitation) zone: mixing ratio  $q$  [in the range from  $0.01 g_s/g_a$  (scavengers)/ $g_a$  (air) to  $0.04 g_s/g_a$ ] scavenger settling rate,  $V_s$ , and turbulent exchange coefficient,  $K_t$ . Turbulent exchange coefficient was varying between 1.0 and  $2.500 \text{ m}^2/\text{s}$ .

The most important factor affecting the dispersion of precipitation elements and the induced downdrafts in the precipitation zone is the mixing ratio. This is documented well in Fig. 1 which shows the evolution of the downdraft velocities for  $q = 0.01 g_s/g_a$  and  $q = 0.04 g_s/g_a$ . The induced velocities have considerable impact on the mean height of the front center of the falling precipitation zone,  $z$ , in

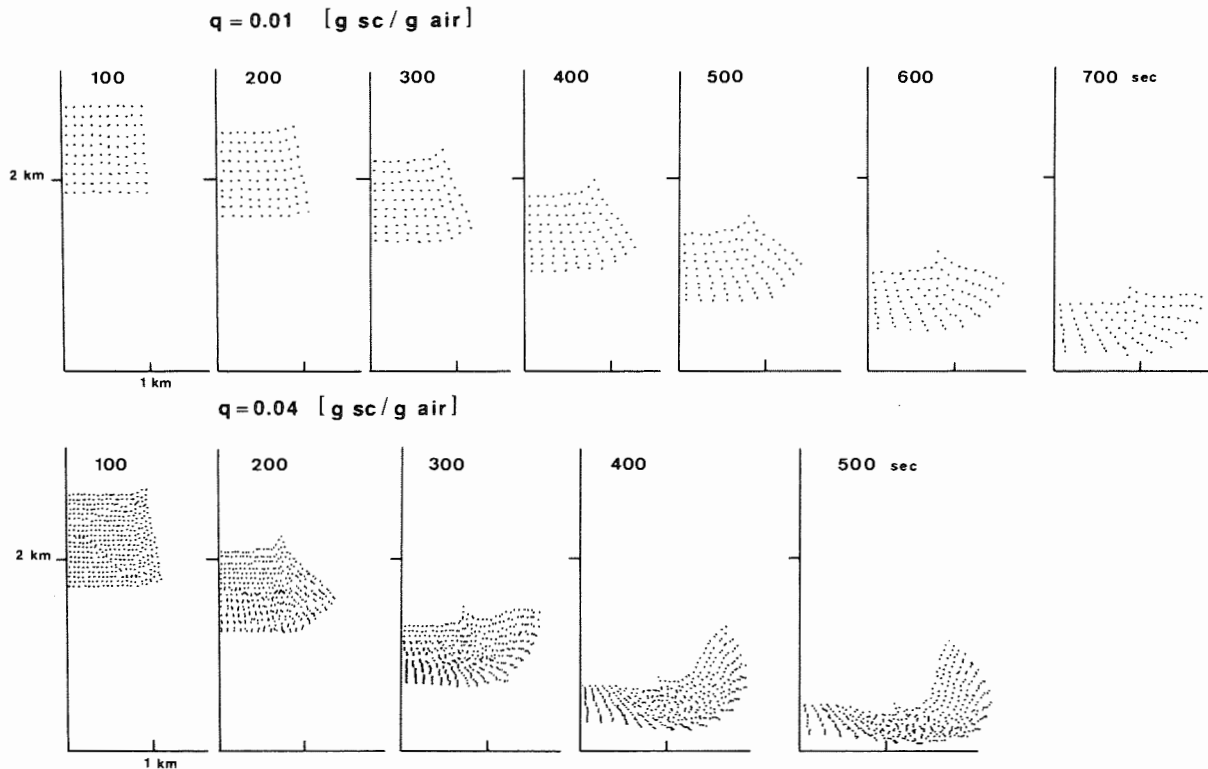


Fig. 1: Evolution of scavenger zone for  $q=0.01$  and  $0.04$ ,  $V_S=1.5$  m/s,  $K_t=1000$  m<sup>2</sup>/s.

Fig. 2 and on the maximum width of the dispersing zone,  $b_{max}$ . Less significant is the effect of turbulent exchange coefficient,  $K_t$ , on the induced velocities,  $u, w$ , and on the maximal width of the settling zone. Greater impact on the zone's evolution has the original shape of the initial scavenger zone. Thicker zones (e.g., 400 m x 400 m or 320 m x 500 m cross sections) induced downdrafts of around 0.2 m/s for scavenger settling velocity,  $V_S = 1.73$  m/s, mixing ratio,  $q = 0.01$  g<sub>s</sub>/g<sub>a</sub> and  $K_t = 1000$  m<sup>2</sup>/s. For comparison the downdrafts induced

by the scavenger zone of initial cross section of 800 m x 200 m after 400 seconds, amounted only to one half of those induced by thick scavenger zones. Usually several hundreds of seconds were necessary at a mixing ratio of 0.01 g<sub>s</sub>/g<sub>a</sub> for fully developed downdrafts.

The study of the impact of a uniform horizontal wind on the scavenger zone formation has been performed under the following assumptions: the component of the uniform horizontal wind velocity (in Fig. 3) was  $U = 1.0$  m/s affecting the deformation of the scavenger zone with cross section of 4000 m x 2000 m. Scavengers--of mixing ratio of 0.01 g<sub>s</sub>/g<sub>a</sub>--were released at a height  $H_R = 7$  km and constant turbulent exchange coefficient  $K_t = 1000$  m<sup>2</sup>/s. In this specific case the precipitation (scavenger) settling velocity was high,  $V_S = 6$  m/s, and the main field dimensions were 30 km x 10 km. With the boundary conditions  $u = U$ ,  $\zeta$  (vorticity) = 0,  $\frac{\partial \psi}{\partial x} = 0$  at the control

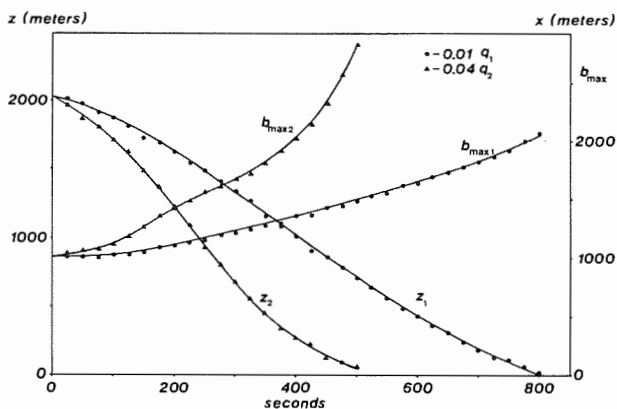


Fig. 2: Mean height,  $z$ , and the maximum width,  $b_{max}$ , of the scavenger zone.

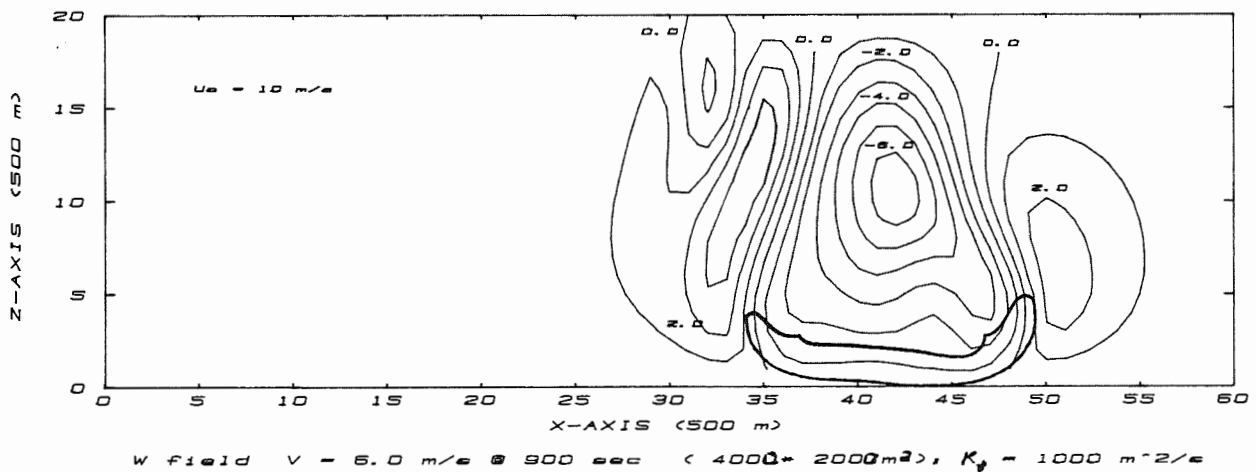


Fig. 3. Vertical components of velocities induced by falling scavenger zone.

volume (CV) entrance;  $w = 0$ ,  $\zeta_W = \zeta_{W+1}$ ,  $\psi = 0$  at the ground;  $\zeta = 0$ ,  $\frac{\partial \psi}{\partial x} = 0$  at the CV exit and  $w = 0$ ,  $\zeta = 0$ ,  $\psi = UH$  at the top of CV the induced velocities surpassed 10% of the scavenger free velocity. For very small individual ice crystals (with  $Re < 10$ ) one can modify the drag coefficients for drops in order to obtain the coefficients for ice crystals of different shape, however, of the same volume like drops. This equivalent radii enable us to determine the "effective mixing ratio",  $q$ , and the crystal settling velocity,  $V_S$ , in the equations of our numerical model. The author found a simple relationship between drag coefficient,  $C_D$  and the Reynolds number in the form  $C_D = A Re^{-0.466}$ , where  $A$  is changing its value from 16.5 (for disks and hexagonal plates) to 38.0 for dendrites in the domain of  $1 < Re < 200$ . The symmetrical plate type crystals start to oscillate around  $Re = 120$  and the stellar or dendritic type crystals in the domain of  $Re$  between 300 and 500. The columnar type crystals start to oscillate and perform the trochoidal motion at  $Re \approx 70$ . For small aggregates the application of the formula for the drag on porous bodies is possible.

## 5. CONCLUSION

Our study showed clearly that the most important parameter determining the evolution of a falling ice crystal zone is the "effective" mixing ratio of the crystals. The horizontal wind affects strongly the circulation inside and around the precipitation zone. Most of the crystals falling in nature do not perform an intense oscillatory motion except at side wind. Therefore the introduction of an "effective" mixing ratio in our falling precipitation zone equations is feasible.

## ACKNOWLEDGEMENT

The work was supported by the U.S. Army Research Office under grant DAAK-11-83-K-0007. Mr. Tom Smith and Vladimir Wojnar who ably performed numerical calculations and laboratory experiments. Mrs. Vickie Maples' help while preparing the article for publication is highly appreciated.

## REFERENCES

- Podzimek, J. and Martin, J.J.: Deposition of particulates on charged planar scavengers, Preprint Vol.: VII Int. Conf. on Atmospheric Electricity, Albany, AMS, Boston, 1984, p. 57-62.
- Clark, T.L. and List, R.: Dynamics of falling particle zone, J. Atmos. Sci. 28 (1971) P. 718-727.
- Girard, C. and List, R.: Thermodynamics of falling precipitation zones, Pageoph 113 (1975) p. 1035-1053.

A NEW DATABASE OF ICE PARTICLE SIZE SPECTRA  
FOR ALTITUDES UP TO 10 KM (30,000 FT)

Richard Jeck  
Naval Research Laboratory  
Washington, DC 20375 USA

## 1. INTRODUCTION

About 7600 nautical miles (14,000 km) of select ice particle measurements over the United States have been compiled into a single, computerized database for use in characterizing ice/snow particle size distributions and mass concentrations at flight altitudes. Data are from 50 research flights by six groups in eight projects with PMS 1-D and 2-D probes. Primary variables are average particle size spectra in the range 0.1 to 10mm from each of 1625 microphysically uniform cloud intervals or other convenient distances in wintertime clouds, snowstorms, cirrus and other high altitude clouds. This database provides an unusual, composite view of a large number of diverse ice particle measurements. Both the differences and similarities in ice particle characteristics among a wide variety of cloud and weather systems are evident. The database is illustrated here by plots of particle size, number density, and total mass as a function of temperature.

## 2. SOURCES OF DATA

Data were selected from published reports or archived computer tapes from flights in the following recent research projects (JECK, 1986): SCPP:1979-84 (REYNOLDS et al, 1986); NEWS:1982-83 (SELTZER et al, 1985); AFGL Cirrus:1977-79 (COHEN, 1981); AFGL LSCS (VARLEY, 1980); CCOPE:1981 (HEYMSFIELD, 1986); COSE-II:1979 (RAUBER, 1981); MIT Snow Growth:1980 (LO et al, 1982); OK-PRESTORM:1985 (CUNNING, 1986; HEYMSFIELD, 1987).

## 3. RESULTS

### 3.1 PARTICLE MASS

The ice particle mass that may be present at different flight altitudes is one of the primary interests in this newly assembled database. The mass,  $m$ , of individual particles is computed here using published (LOCATELLI and HOBBS, 1974) size-to-mass relationships of the form

$$m = A (d_{\max})^B,$$

where the nominal particle sizes associated with the PMS probe bins are used for  $d_{\max}$ , the largest dimension of the particle. The values of the parameters  $A$  and  $B$  depend on the type of particle (i.e., graupel, plates, unrimed dendrites, etc.). Particle types are often mixed or unknown, however, so for present purposes a "universal" equation with  $A=0.037$  and  $B=1.9$  is used for all particles. These two values represent most of the particles commonly observed in the database. The total ice particle mass (TIPM), or "ice water content" is obtained by summing the contributions from all the particle sizes represented by the available PMS probes. The greatest TIPM computed for any of the flights is about  $2.8 \text{ g/m}^3$ , in reasonable agreement with expectations.

The range and distribution of the computed TIPM's is seen in the scatterplot in figure 1. It appears that except for the relatively large mass concentrations possible in thunderstorm anvils (plotting symbol A in fig. 1) (HEYMSFIELD, 1986), TIPM's are likely to be less than  $0.2 \text{ g/m}^3$  at temperatures below about  $-30^\circ\text{C}$ . The data at these temperatures are mostly from cirrus,

with a few samples from the upper reaches of deep winter storms. The maximum TIPM's increase steadily as the temperature increases from -25°C, probably indicating the onset of dendritic growth, riming, and aggregation. The largest mass concentrations occur over the temperature range of 0° to -15°C. These extreme masses are associated with the trailing stratiform region of a mesoscale convective system (MCS) over Kansas (symbol M in fig. 1) (HEYMSFIELD, 1987), and from frontal rainbands windward of the Sierra Nevada mountains in east-central California.

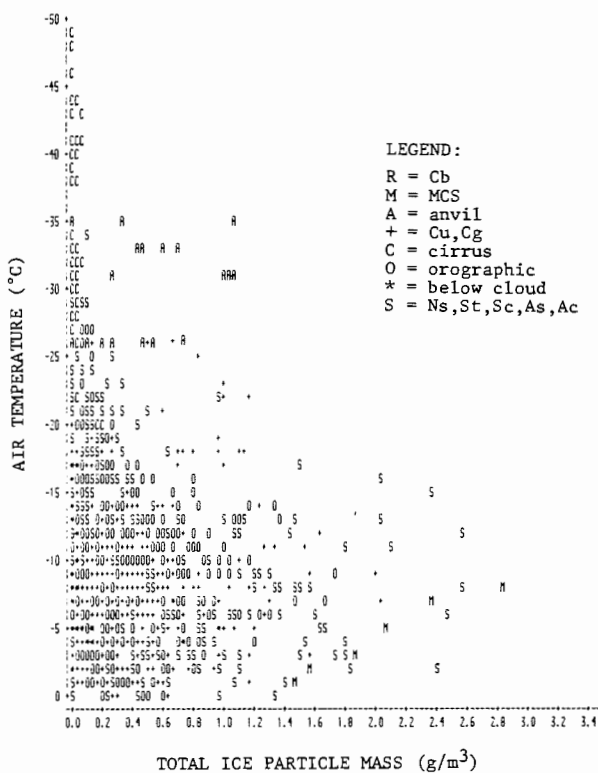


Fig.1: Total Mass vs. Temperature

### 3.2 PARTICLE CONCENTRATIONS

The numbers of ice particles ( $d_{max} > 100\mu\text{m}$ ) that have been recorded per liter of air as a function of temperature are shown in figure 2. There is a gradual increase in maximum concentrations as temperatures increase from -50° to -10°C and then a decline as temperatures approach 0°C. The increase is probably due to the growth of extremely small particles into the size range  $d_{max} > 100\mu\text{m}$  under consideration here.

The decline between -10° and 0°C is presumably due to aggregation and the fallout of precipitation sized particles in this temperature range. Peak concentrations are found between -5° and -10°C and appear to be no more than about 220/liter, except for MCS clouds where up to about 400/liter have been observed. At temperatures below about -30°C, maximum concentrations appear to be less than about 50/liter, except in thunderstorm anvils where nearly double those concentrations have been recorded. As with particle mass, extremes in particle concentration appear to reside in MCS and anvil clouds. Both are warm season phenomena and both are layer-type clouds associated with strongly convective systems.

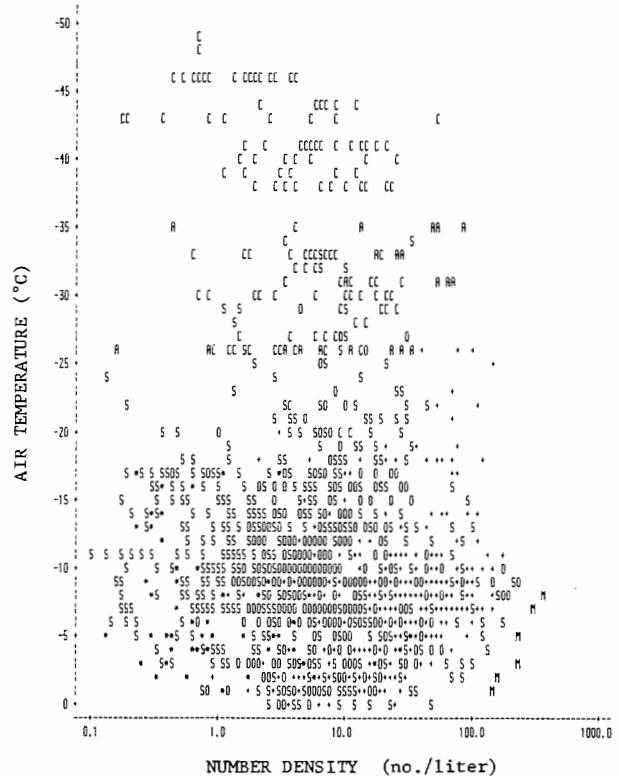


Fig. 2: Concentration vs. Temperature

### 3.3 PARTICLE SIZE

The non-conforming nature of anvil clouds stands out most clearly in a plot of maximum particle size vs. temperature (figure 3.) The maximum particle dimension (MPD) is determined from the highest PMS probe bin to contain at least one particle per cubic meter as an average over the uniform cloud

interval. Figure 3 shows the anvil data (symbol A) standing alone at temperatures between  $-25^{\circ}$  and  $-35^{\circ}\text{C}$ . Except for the large particles available in the anvil, there is otherwise a decrease in MPD with decreasing temperature below  $-15^{\circ}\text{C}$ . Looked at another way, (excepting the anvil data), there is a trend to larger MPD's as temperatures increase from  $-50^{\circ}$  up to about  $-12^{\circ}\text{C}$ . The steady increase is probably due to the appearance of stellars and dendrites at temperatures greater than about  $-20^{\circ}\text{C}$ , as well as to aggregation at the higher temperatures.

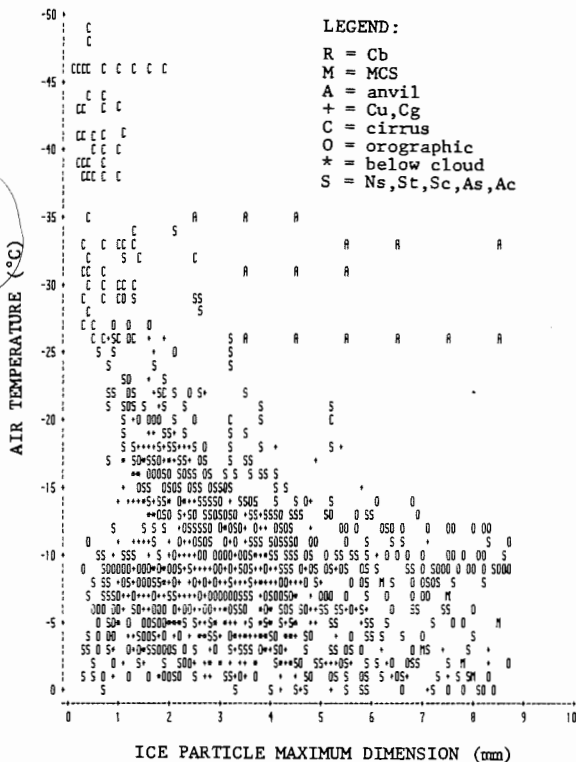


Fig. 3: Maximum Size vs. Temperature

#### 4. ACKNOWLEDGEMENT

This research was sponsored by the United States Department of Transportation, Federal Aviation Administration.

#### 5. REFERENCES

COHEN, I: Cirrus Particle Distribution Study, Part 8. Report No. AFGL-TR-81-0316(1981), Air Force Geophysics Laboratory, Hanscom AFB, Massachusetts 10731 U.S.A.

CUNNING, J: The Oklahoma-Kansas Preliminary Regional Experiment for STORM-Central. Bull. Amer. Met. Soc. 67 (1986) p. 1478ff.

HEYMSFIELD, A: Ice Particle Evolution in the Anvil of a Severe Thunderstorm during CCOPE. J. Atm. Sci. 43 (1986) p. 2463ff.

HEYMSFIELD, A: (1987) Private communication.

JECK, R: Airborne Cloud Physics Projects from 1974 through 1984. Bull. Amer. Met. Soc. 67 (1986) p. 1473-1477.

LO, K; PASSARELLI, R: The Growth of Snow in Winter Storms: An Airborne Observational Study. J. Atm. Sci. 39 (1982) p. 697-706.

LOCATELLI, J; HOBBS, P: Fall Speeds and Masses of Solid Precipitation Particles. J. Geophys. Research 79 (1974) p. 2185-2197.

RAUBER, R: Microphysical Processes in Two Stably Stratified Orographic Cloud Systems. Atm. Sci. paper No. 337 (1981). Colorado State Univ., Fort Collins, Colorado 80523.

REYNOLDS, D; DENNIS, A: A Review of the Sierra Cooperative Pilot Project. Bull. Amer. Met. Soc. 67 (1986) p. 513ff.

SELTZER, M; PASSARELLI, R; EMANUEL, K: The Possible Role of Symmetric Instability in the Formation of Precipitation Bands. J. Atm. Sci. 42 (1985) p. 2207-2219.

VARLEY, D: Microphysical Properties of a Large Scale Cloud System, 1-3 March 1978. Report No. AFGL-TR-80-0002 (1980). Air Force Geophysics Laboratory, Hanscom AFB, Massachusetts 01731 U.S.A.

A VERTICAL WIND TUNNEL FOR THE STUDY OF SNOWFLAKES AND  
EFFECTS OF ACCUMLATED SNOW ON MATERIALS

Kenji Isono (Nagoya University),  
Jutaro Kobayashi (Japan Weather Association),  
Takehiko Gonda (Science University of Tokyo),  
Yoshio Sasyo and Taro Mori (Suga Test Instruments Co., Ltd.)

1. INTRODUCTION

Most of vertical wind-tunnels for the study of snow have been designed and used for the study on the growth mode and other physical properties of snow crystals (for instance, Furukawa et al. 1980, P.29). Snow is often composed of snowflakes. The rates of snowfall and snow accumulation on ground and materials are affected by the features of aggregation of snow crystals and the size and other physical properties of snowflakes. A novel vertical wind-tunnel was constructed for the purpose of studying the process of snowflakes formation and effects of accumulated snow on materials for industrial use.

2. CONSTRUCTION AND PERFORMANCE

Fig. 1 shows a schematic diagram of the vertical wind-tunnel. Its main part, the snowfall tunnel ①, in which snowflakes are formed and fall against upward air current, is a cylindrical pipe made of stainless steel, 12 m in length and 55 cm in diameter. It stands vertically, penetrating four floors of a building. Its top end is connected to the return air duct ②, the lower end of which is connected to the air inlet on the wall of the tunnel near its lower end. This lower end is open to the test room in which observation, collection, examination of snow crystals and flakes, and tests of materials are made. The temperature of airstream in the snowfall tunnel and the return air duct is regulated by controlling the temperature of airstream surrounding them. The air temperature in the test room is maintained at temperatures not higher than that of airstream in which snow crystals and snowflakes grow, in order to prevent disturbances

caused by convection of air in the tunnel. Cooled water is injected through an ultrasonic atomizers ⑥ for the formation of supercooled clouds in which snow crystals and flakes grow at humidities of water saturation. Seeding of clouds is intermittently made by expanding

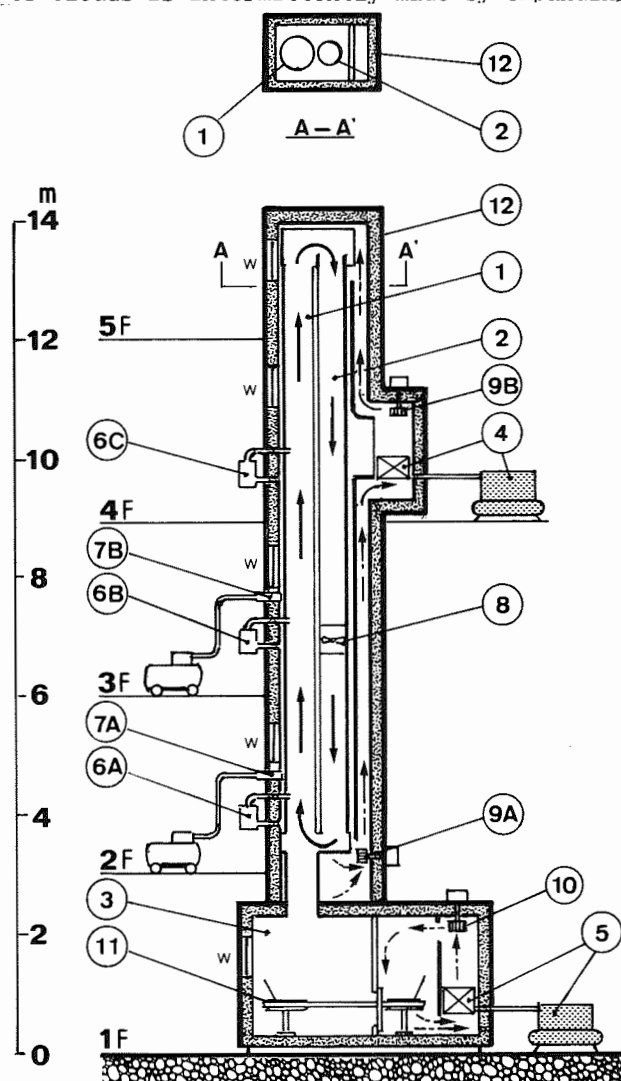


Fig. 1: The vertical wind-tunnel  
1. Snowfall tunnel, 2. Return air duct, 3. Test room, 4 and 5. Temperature regulators, 6. Ultrasonic atomizers A, B, C, 7. Seeding devices, 8,9 and 10. Fans, 11. Table, W. Window.

compressed air through one of the injection nozzles (for instance, 1 sec every 3 min). The speed of airstream is controlled in the range from 4 to 120 cm/s by regulating rotational speed of the fan  $\textcircled{8}$ . Air stream is warmed in the top part of the tunnel to prevent ice crystals and snowflakes from circulating through the return air duct and growing again in the snowfall tunnel.

### 3. EXPERIMENTAL

The result of a preliminary experiment showed that features of snowfall varied markedly with the change of environmental parameters such as cloud temperature, upward airstream speed, seeding rate, the rate of supply of water etc. For instance, when the speed of upward air current was changed properly in accordance with the growth of snow particles, keeping other parameters constant, snow crystals and snowflakes of sizes larger than those formed when air speed was kept constant were formed. In the present paper, the result of experiments on snowfall from supercooled clouds of different significant temperatures, -4, -7, -15, and -20 C will be described. The values of environmental parameters other than cloud temperature were kept constant as follows, The speed of upward airstream: 10 cm/s, The rate of water supply: 0.3 cc/s, The seeding rate: 600 ml of compressed ( $8 \text{ Kg/cm}^2$ ) air in 1 sec every 3 min. The mass of snowflakes fallen onto a plate of the size  $25.5 \times 20.1$  ( $512.55 \text{ cm}^2$ ) was measured with an electronic balance on which the plate mounted horizontally. Measured values were printed out every 1 min by a printer.

Snowfall process was watched through the windows on the wall of the tunnel and recorded continuously.

Fig. 2 shows a sample of snowflakes from clouds of -15 C. Fig. 3 shows photomicrographs of snowflakes formed in clouds of temperatures described above. These microphotographs shows the three-dimensional structures and constituent single crystals and frozen cloud droplets.

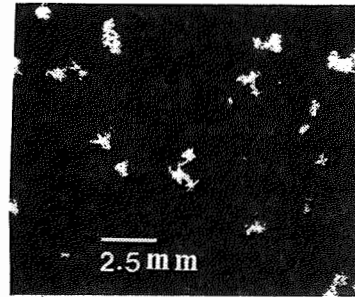


Fig. 2: Snowflakes  
Cloud temperature: -15 C

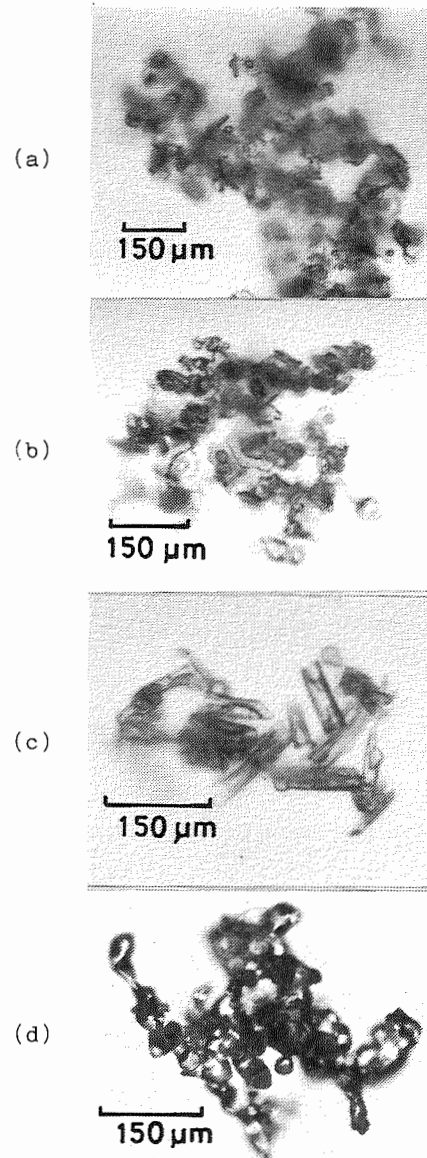


Fig. 3: Photomicrographs of snowflakes  
Upward air speed: 10 cm/s  
Cloud temperature: (a) -20, (b) -15, (c) -7 and (d) -4 C.  
Predominant shapes of constituent single ice crystals; (a) Hexagonal plate, (b) Sector and star, (c) Sheath, (d) Hexagonal plate.

The temperature dependence of the shapes of the constituent crystals in snowflakes examined almost coincides with that expected from Kobayashi' diagram (Kobayashi 1961, P. 1363). Fig. 4 shows the increase of mass of snowflakes accumulated on the plate with the elapse of time. The maximum rate of snowfall occurred at about -15 C.

Fig. 5 shows the increase of depth of accumulated snow on the plate. Table 1 shows the average values of snowfall rate in mass and the rate of accumulation on the plate.

It is to be noticed that ice crystals of the sizes in the range from 50 to 150  $\mu\text{m}$  aggregated and formed snow flakes so efficiently that snowfall was observed within 3 min in the test room.

More detailed results will be described elsewhere.

#### ACKNOWLEDGEMENT

Thanks are due to Mr. Nagaichi Suga, President of Suga Weathering Technology Foundation for his support for this work.

#### REFERENCES

- FURUKAWA, Y., ENDO, T., MIZUNO, Y., NARUSE, K. and TAKAHASHI, T: Experiment of artificial snow crystals by the use of a vertical wind tunnel, J. Japn. Soc. Snow Ice, 43 (1980), 147-150.
- KOBAYASHI, T.: The growth of snow crystals at low supersaturation, phil. Mag., 6 (1961), 1363-1370.

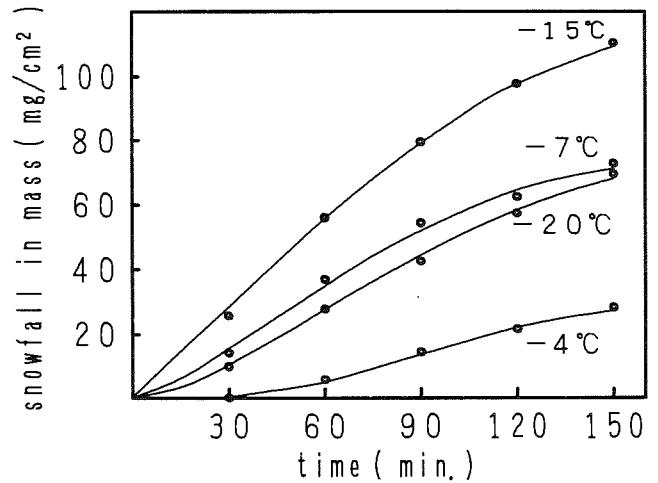


Fig. 4: Rate of snowfall  
Ordinate: Accumulated mass ( $\text{mg}/\text{cm}^2$ )  
Abcissa: Time after seeding

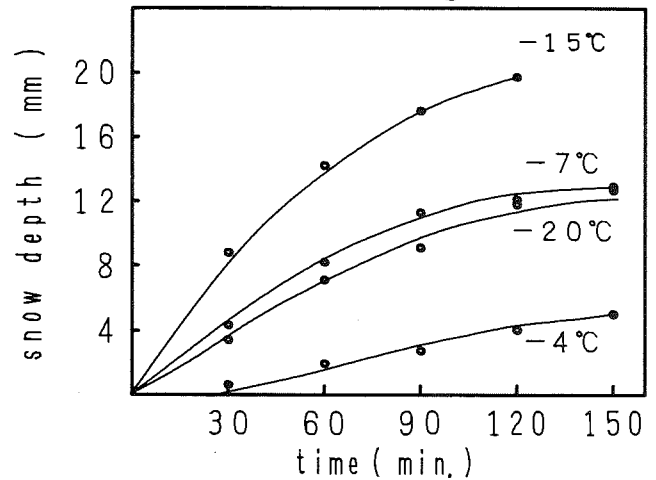


Fig. 5: Depth of accumulated snow

Cloud temperature (C)	Snowfall rate ( $\text{mg}/\text{cm}^2\text{hr}$ )	Accumulation (mm/hr)
-4	11	2
-7	29	5
-15	44	10
-20	28	5

Table 1: Average values of snowfall and snow accumulation